Research Topics

Exploration of innovative strategies focusing on advanced nanobiomaterials for optimizing oncological treatment and tissue restoration

Edited by
Weifeng Lin and Long Bai

Coordinated by
Johannes Greven and Xing Zhang

Published in
Frontiers in Bioengineering and Biotechnology

ISSN 1664-8714
ISBN 978-2-8325-3376-5
DOI 10.3389/978-2-8325-3376-5

About Frontiers

Frontiers is more than just an open access publisher of scholarly articles: it is a pioneering approach to the world of academia, radically improving the way scholarly research is managed. The grand vision of Frontiers is a world where all people have an equal opportunity to seek, share and generate knowledge. Frontiers provides immediate and permanent online open access to all its publications, but this alone is not enough to realize our grand goals.

Frontiers journal series

The Frontiers journal series is a multi-tier and interdisciplinary set of open-access, online journals, promising a paradigm shift from the current review, selection and dissemination processes in academic publishing. All Frontiers journals are driven by researchers for researchers; therefore, they constitute a service to the scholarly community. At the same time, the *Frontiers journal series* operates on a revolutionary invention, the tiered publishing system, initially addressing specific communities of scholars, and gradually climbing up to broader public understanding, thus serving the interests of the lay society, too.

Dedication to quality

Each Frontiers article is a landmark of the highest quality, thanks to genuinely collaborative interactions between authors and review editors, who include some of the world's best academicians. Research must be certified by peers before entering a stream of knowledge that may eventually reach the public - and shape society; therefore, Frontiers only applies the most rigorous and unbiased reviews. Frontiers revolutionizes research publishing by freely delivering the most outstanding research, evaluated with no bias from both the academic and social point of view. By applying the most advanced information technologies, Frontiers is catapulting scholarly publishing into a new generation.

What are Frontiers Research Topics?

Frontiers Research Topics are very popular trademarks of the *Frontiers journals series*: they are collections of at least ten articles, all centered on a particular subject. With their unique mix of varied contributions from Original Research to Review Articles, Frontiers Research Topics unify the most influential researchers, the latest key findings and historical advances in a hot research area.

Find out more on how to host your own Frontiers Research Topic or contribute to one as an author by contacting the Frontiers editorial office: frontiersin.org/about/contact

Exploration of innovative strategies focusing on advanced nanobiomaterials for optimizing oncological treatment and tissue restoration

Topic editors
Weifeng Lin — Weizmann Institute of Science, Israel
Long Bai — East China University of Science and Technology, China

Topic coordinators
Johannes Greven — University Hospital RWTH Aachen, Germany
Xing Zhang — University Hospital RWTH Aachen, Germany

Citation
Lin, W., Bai, L., Greven, J., Zhang, X., eds. (2023). *Exploration of innovative strategies focusing on advanced nanobiomaterials for optimizing oncological treatment and tissue restoration*. Lausanne: Frontiers Media SA. doi: 10.3389/978-2-8325-3376-5

Table of contents

frontiers | Frontiers in Bioengineering and Biotechnology

TYPE Editorial
PUBLISHED 15 August 2023
DOI 10.3389/fbioe.2023.1274758

OPEN ACCESS

EDITED AND REVIEWED BY
Gianni Ciofani,
Italian Institute of Technology (IIT), Italy

*CORRESPONDENCE
Xing Zhang,
✉ xinzhang@ukaachen.de

RECEIVED 08 August 2023
ACCEPTED 09 August 2023
PUBLISHED 15 August 2023

CITATION
Zhang X, Greven J, Bai L and Lin W (2023), Editorial: Exploration of innovative strategies focusing on advanced nanobiomaterials for optimizing oncological treatment and tissue restoration.
Front. Bioeng. Biotechnol. 11:1274758.
doi: 10.3389/fbioe.2023.1274758

Editorial: Exploration of innovative strategies focusing on advanced nanobiomaterials for optimizing oncological treatment and tissue restoration

Xing Zhang[1]*, Johannes Greven[1], Long Bai[2] and Weifeng Lin[3]

[1]Department of Orthopedics, Trauma and Reconstructive Surgery, University Hospital RWTH Aachen, Aachen, Germany, [2]Institute of Translational Medicine, Shanghai University, Shanghai, China, [3]School of Chemistry, Beihang University, Beijing, China

KEYWORDS

innovative strategies, versatile nano-/biomaterials, oncological treatment, tissue restoration, biological mechanism, precise nanomedicine, regenerative medicine, osteogenesis

Editorial on the Research Topic
Exploration of innovative strategies focusing on advanced nanobiomaterials for optimizing oncological treatment and tissue restoration

Recent progress in the nanotechnology and biotechnology has sparked a revolution in oncological therapy and tissue restoration, which led to a variety of brand-new nano/biomaterials with distinct structural and functional properties. The emergence of these "smart" nanoplatforms and biomaterials opens up a promising window to address the imperfections of conventional methods in cancer therapy and tissue regeneration, which has greatly improved therapeutic efficacy and accuracy. Exploration of innovative strategies to refine the use of nano/biomaterials is essential to fully exploit their potential.

The Research Topic "*Exploration of innovative strategies focusing on advanced nano-/biomaterials for optimizing oncological treatment and tissue restoration*" was conceived as a Research Topic and reviews spotlighting innovative strategies to potentiate the efficacy of oncological therapy and impaired tissue regeneration with the aid of nanoplatforms and biomaterials. Excitingly, a total of 17 articles have been collected with a well-balanced ratio: 2 comprehensive reviews and 15 original research articles. Herein, we provide a brief synopsis of the articles included in this Research Topic: one review summarizing the recent development of hydrogels for treating bone-related diseases, one review reporting recent advancements in nano-drug delivery for synergistic antitumor immunotherapy, and fifteen original articles presenting the latest advances in the investigation of nano-/biomaterials in the field of cancer treatment and tissue engineering. Our goal is to share innovative solutions to surmount current challenges and hurdles, which shed light on future directions of nano-/biomaterials-based disease interventions and treatment.

In recent years, immunotherapy has emerged as a powerful therapeutic strategy for treating cancer, and its advances have resulted in great improvements in clinical cancer outcomes. In this respect, Zhao et al. systematically review the latest developments in nano-drug delivery systems, classification of cancer immunotherapy, and recent progress in synergistic antitumor immunotherapies by application of nano-drug delivery systems. Nanodrug delivery systems-mediated cancer immunotherapy significantly alleviates the problems associated with immune tolerance and escape, immune side effects and poor tumor targeting, *etc*., by enhancing their stability and lengthening the circulation time.

To improve the therapeutic efficacy against solid tumors, hydrogel systems integrating various treatment modalities have been developed well. Tang et al. construct CuS nanoparticles and camptothecin (CPT) co-loaded thermosensitive injectable hydrogel (SCH) with self-supplied H_2O_2 capacity for enhancing chemodynamic therapy (CDT) in cancer therapy. When injecting SCH hydrogel into tumor sites, it achieves the synergism of photothermal therapy, precise drug release, and self-supply of H_2O_2, generating massive hydroxyl radicals and remarkably inducing tumor cell apoptosis. Sulfur dioxide (SO_2) gas therapy is an emerging therapeutic modality, holding great potential in treating multiple diseases. Huang et al. propose a SO_2 prodrug doped FeGA nanoparticles for enhanced CDT by photothermally triggered gas therapy (FBH) system, which is synthesized by wrapping a ratio of benzothiazolyl sulfonate (BTS) and FeGA NPs in the heat-sensitive hydrogel. This system can accurately control the release of SO_2 gas by virtue of the excellent photothermal conversion ability of FeGA NPs. The yielded SO_2 could induce cancer cell apoptosis but also consume excess GSH and increase the level of reactive oxygen species for improved therapeutic effect of the Fenton reaction. Lung cancer is also tackled in an original research article by Ning et al., developing a CLH hydrogel system that amplifies oxidative stress through cascade catalysis by co-loading CuS nanoparticles and β-lapachone (Lap) into agarose hydrogels. This CLH-mediated reactive oxygen burst strategy is expected to enhance the efficacy of antitumor therapy and reverse tumor chemoradiotherapy resistance in the future. In addition, Wang et al. design a copper-based nanozyme (CuP) and loaded it into agarose hydrogel to form CuP-based hydrogel system (named as CH) for second near-infrared (NIR-II) imaging and breast tumor treatment. This nanosystem could reduce the antioxidant potency of tumors and produce highly toxic OH for destroying the redox steady state, ultimately improving the effect of radiotherapy (RT). Together, these four contribution articles provide an outlook on the translation of “smart” hydrogel system-based strategy into real clinical applications.

Sonodynamic therapy (SDT) is a non-invasive emerging approach based on the interaction of ultrasound and sonoactive substances (sonosensitizers) for oncotherapy. Unfortunately, its clinical outcome is still unsatisfactory owing to the tendency to aggregate and weak targeting ability. In this context, Li et al. present a novel composite ECaC nanosystem by coating porous $CaCO_3$ NPs and Cur with the tumor cell-derived exosomes. Tumor cell-derived exosome membranes endow $CaCO_3$ with a new immune evasion ability, which enables it to actively evade the clearance of organs such as the liver and kidney, and specifically targets the tumor site to facilitate the release of Cur and Ca^{2+} in response to the degradation of tumor acidic microenvironment. Wang et al. construct a novel nanoplatform by loading Pyrogallol (PG) into mesoporous organosilica nanoparticles for cancer treatment, aiming at boosting intracellular and mitochondrial ROS levels, depleting glutathione (GSH), and downregulating GPX4. Particularly, MON@PG nanoplatforms were proven to significantly inhibit tumor proliferation and growth *in vitro* and *in vivo* by inducing ferroptotic cell death to sensitize radiotherapy. Interestingly, this work offers a promising chemoradiotherapy regimen for gastric cancer treatment by disrupting redox balance and augmenting ferroptosis. Bao et al. design the ferrimagnetic vortex nanoring Fe_3O_4@HA (FVNH) nanoparticles enclosing Doxorubicin for T2 MR imaging-guided hyperthermia therapy and chemotherapy. Notably, FVNH NPs show significantly extremally high magnetothermal conversion efficiency and shoring the transverse relaxation time for enhanced MRI imaging. Overall, FVNH loading with DOX nano-construct might hold great potential for combined magnetothermal-chemotherapy and targeted cancer imaging in future clinical trials.

Deep vein thrombosis (DVT) is a common cause of disability and cardiovascular death worldwide. Chen et al. realize the diagnosis and treatment of thrombus by applying low-power ultrasound combined with targeted microbubbles (MBt) bearing TNF-α antibody and urokinase (United Kingdom) in a DVT animal model. TNF-α is used as the target of thrombus to attract numerous targeted microbubbles to enrich locally in the thrombus and neutralize the inflammatory response, presenting an innovative strategy to treat thrombus, which is in line with the theme of our Research Topic. Lymphedema is a progressive disease caused by lymphatic transport dysfunction, imposing a substantial biomedical burden. Liu et al. reveal the relieving effect of low-intensity pulsed ultrasound (LIPUS) on secondary lymphedema, but also verify that LIPUS reduces lymphedema by regulating macrophage polarization and enhancing microcirculation. Accordingly, this innovative work offers a promising way for lymphedema treatment. Research conducted by Wang et al. delineates three primary aspects of nanoparticle-leukemia-related studies, including nanoparticles for diagnosis and treatment of leukemia, the specific molecular mechanism, and existing problems of the application of nanoparticles in leukemia. This offers preliminary and objective insights into nanoparticle-mediated leukemia studies.

Liu et al. contribute to this Research Topic with a review summarizing the evolution, properties, and preparation methods of hydrogels, and their latest application in bone-related diseases involving bone defects, fractures, cartilage damage, and osteosarcoma. The authors point out that hydrogel has great application potential as a functional polymer material in bone tissue engineering due to its unique advantages, such as porous structures similar to the extracellular matrix (ECM) and the soft texture reducing surrounding inflammatory responses. This review proposes customized suggestions for developing high-performance hydrogels suitable for bone-related diseases.

An excellent example of extracellular vesicles (EVs) for bone defect treatment is presented by Zhang et al., who develop dexamethasone-stimulated osteoblast-derived EVs ($OB\text{-}EV_{Dex}$) and investigate their osteogenic potential as a novel biomimetic tool to accelerate bone augmentation. The authors demonstrated that $OB\text{-}EV_{Dex}$ could markedly promote osteoblastic differentiation by positively upregulating crucial osteogenic genes, but also significantly augment capacities for *in vitro* proliferation, attachment, and viability of osteoblasts. Of note, the pro-osteogenic effect mediated by OB-EV$_{\text{Dex}}$ was even comparable to that of individual BMP-2 treatment. It is reasoned that irrespective of any clinical challenges, the prospective use of OB-EV$_{\text{Dex}}$ could function as a novel osteogenic accelerator for treating, or at least alleviating the symptoms of bone defects in future clinical practice.

Du et al. report a bifunctional Bi-BG composite scaffold with excellent photothermal effect and osteogenic activity, making it possible to treat large bone defects caused by surgical resection of bone tumors. This innovative strategy based on the Bi-BG scaffold allows the photothermal ablation of bone tumors and the augmentation of osteogenic capacity, which realizes the aim of "one stone, two birds". This work may provide new ideas for treating and repairing tumor-associated bone tissue defects by developing novel bifunctional scaffolds. Feng et al. propose a NIR light-assisted strategy to treat infected wounds based on the newly synthesized photothermal agent of CuSi nanowires, which could not only effectively combat bacteria, but also promote angiogenesis and facilitate wound healing due to the sustained release of bioactive Cu and Si ions. Qiang et al. contribute to this Research Topic with an original article reporting a high-strength Zn0.8Mn0.1Li alloy with calcium-phosphorus coatings for orthopedic implants. Such a self-designed implant significantly satisfies the clinical demands associated with improved osteogenic ability, biocompatibility, and biodegradability of medically degradable metal materials. The proper microenvironment is critical for the storage and transportation of embryonic stem cells (ESCs). Yang et al. propose an alternative approach that allows for facile storage and transportation of stem cells in ESCs-dynamic hydrogel construct (CDHC) under ambient conditions. This dynamic and self-biodegradable hydrogel provides a simple, cost-effective, and valuable tool for storing and transporting "ready-to-use" stem cells, facilitating "off-the-shelf" availability and widespread applications in biomedical fields and regenerative research.

In conclusion, this Research Topic presents state-of-the-art research work centering around the topic of nano-/biomaterials-based innovative strategies for oncological therapy and tissue restoration. There is a consensus among the authors that attention should be dedicated to optimizing the structure and properties of nano-/biomaterials for maximizing therapeutic efficacy. This Research Topic also provides distinct insight into overcoming the existing hurdles and challenges, and future directions associated with the design and development of these nano-/biomaterials. We hope this Research Topic could be of great interest to researchers and professionals, ultimately advancing advanced nano-/biomaterials towards clinical translation and improving clinical therapeutic outcomes.

Author contributions

XZ: Writing–original draft, Writing–review and editing. JG: Writing–review and editing. LB: Writing–review and editing. WL: Writing–review and editing.

Conflict of interest

The authors declare that the research was conducted in the absence of any commercial or financial relationships that could be construed as a potential conflict of interest.

Publisher's note

Frontiers in Bioengineering and Biotechnology

TYPE Original Research
PUBLISHED 29 August 2022
DOI 10.3389/fbioe.2022.1003777

EDITED BY
Long Bai,
East China University of Science and Technology, China

REVIEWED BY
Xin Li,
DWI—Leibniz-Institut für Interaktive Materialien, Germany
Kelong Ai,
Central South University, China
Ying Yang,
University of Michigan, United States

*CORRESPONDENCE
Qinqin Huang,
qqhuang@zzu.edu.cn

[†]These authors have contributed equally to this work

SPECIALTY SECTION
This article was submitted to Nanobiotechnology,
a section of the journal
Frontiers in Bioengineering and Biotechnology

RECEIVED 26 July 2022
ACCEPTED 10 August 2022
PUBLISHED 29 August 2022

CITATION
Tang W, Li X, Liu Z, Meng L, Zhu D and Huang Q (2022), CuS nanoparticles and camptothecin co-loaded thermosensitive injectable hydrogel with self-supplied H_2O_2 for enhanced chemodynamic therapy.
Front. Bioeng. Biotechnol. 10:1003777.
doi: 10.3389/fbioe.2022.1003777

CuS nanoparticles and camptothecin co-loaded thermosensitive injectable hydrogel with self-supplied H_2O_2 for enhanced chemodynamic therapy

Wenxue Tang[1†], Xiang Li[2†], Zeming Liu[3†], Lyu Meng[4], Daoming Zhu[5] and Qinqin Huang[1]*

[1]The Research and Application Center of Precision Medicine, The Second Affiliated Hospital, Zhengzhou University, Zhengzhou, China, [2]Department of Central Laboratory and Precision Medicine Center, Department of Nephrology, The Affiliated Huai'an Hospital of Xuzhou Medical University and Huai'an Second People's Hospital, Xuzhou, China, [3]Department of Plastic Surgery, Tongji Hospital, Tongji Medical College, Huazhong University of Science and Technology, Wuhan, China, [4]Department of Radiation and Medical Oncology, Hubei Key Laboratory of Tumor Biological Behaviors, Hubei Cancer Clinical Study Center, Zhongnan Hospital of Wuhan University, Wuhan, China, [5]Department of General Surgery and Guangdong Provincial Key Laboratory of Precision Medicine for Gastrointestinal Tumor, Nanfang Hospital, The First School of Clinical Medicine, Southern Medical University, Guangzhou, Guangdong, China

Chemodynamic therapy (CDT) is a kind of anti-tumor strategy emerging in recent years, but the concentration of hydrogen peroxide (H_2O_2) in the tumor microenvironment is insufficient, and it is difficult for a single CDT to completely inhibit tumor growth. Here, we designed a CuS nanoparticles (NPs) and camptothecin (CPT) co-loaded thermosensitive injectable hydrogel (SCH) with self-supplied H_2O_2 for enhanced CDT. SCH is composed of CuS NPs and CPT loaded into agarose hydrogel according to a certain ratio. We injected SCH into the tumor tissue of mice, and under the irradiation of near-infrared region (NIR) laser at 808 nm, CuS NPs converted the NIR laser into heat to realize photothermal therapy (PTT), and at the same time, the agarose hydrogel was changed into a sol state and CPT was released. CPT activates nicotinamide adenine dinucleotide phosphate oxidase, increases the level of H_2O_2 inside the tumor, and realizes the self-supply of H_2O_2. At the same time, CuS can accelerate the release of Cu^{2+} in an acidic environment and light, combined with H_2O_2 generated by CPT for CDT treatment, and consume glutathione in tumor and generate hydroxyl radical, thus inducing tumor cell apoptosis. The SCH system we constructed achieved an extremely high tumor inhibition rate *in vitro* and *in vivo*, presenting a new idea for designing future chemical kinetic systems.

KEYWORDS

chemodynamic therapy, hydrogel, CuS NPs, camptothecin, self-supplied H_2O_2

Introduction

By regulating the level of reactive oxygen species (ROS) in tumor cells, changing the redox balance in cancer cells, thereby inducing oxidative damage and death of cancer cells, is one of the effective methods for tumor therapy (Zhang et al., 2020; Zhu et al., 2020; Chen et al., 2021a; Wang et al., 2021a; Zhu et al., 2021a; Zhu et al., 2021b; Zhu et al., 2022a). Chemodynamic therapy (CDT) is a kind of anti-tumor strategy emerging in recent years (Lin et al., 2020; Sang et al., 2020; Chen et al., 2021b; Wang et al., 2021b; Chen et al., 2021c; Zhao et al., 2022). Generally, nano-catalyzed systems are used to induce *in situ* Fenton or Fenton-like reactions (In 1894, HJ·HFenton first pointed out that hydrogen peroxide has a strong oxidizing ability under the catalysis of Fe^{2+}, which can oxidize a variety of organic substances (Fenton, 1894); Fenton reagent is the combination of hydrogen peroxide (H_2O_2) and Fe^{2+}, in which Fe^{2+} is mainly used as a homogeneous catalyst, while H_2O_2 plays an oxidizing role. At the same time, in the study of Fenton method, it is found that in addition to Fe^{2+} can catalyze the decomposition of H_2O_2 to produce hydroxyl radical (•OH), other transition metal ions such as Mn^{2+}, Cu^{2+}, Co^{2+}, etc. Can also accelerate or replace Fe^{2+} to play this role. Catalysis to achieve oxidation.) in tumors, and the weakly oxidizing H_2O_2 is catalyzed (Li et al., 2021a; Deng et al., 2022). The process of transforming into strong oxidative active species such as •OH, •OH can not only damage the DNA chain, but also activate caspase-3 that promotes apoptosis, leading to programmed cell death of cancer cells (Zhang et al., 2019; Zhu et al., 2022b). Notably, this process requires no external stimulus. In contrast to other therapeutic strategies, CDT that is driven by endogenous chemical energy in the tumor microenvironment can successfully prevent oxidative damage to healthy tissues and is therefore tumor-specific (Dong et al., 2018; Liu et al., 2021a). Further, CDT

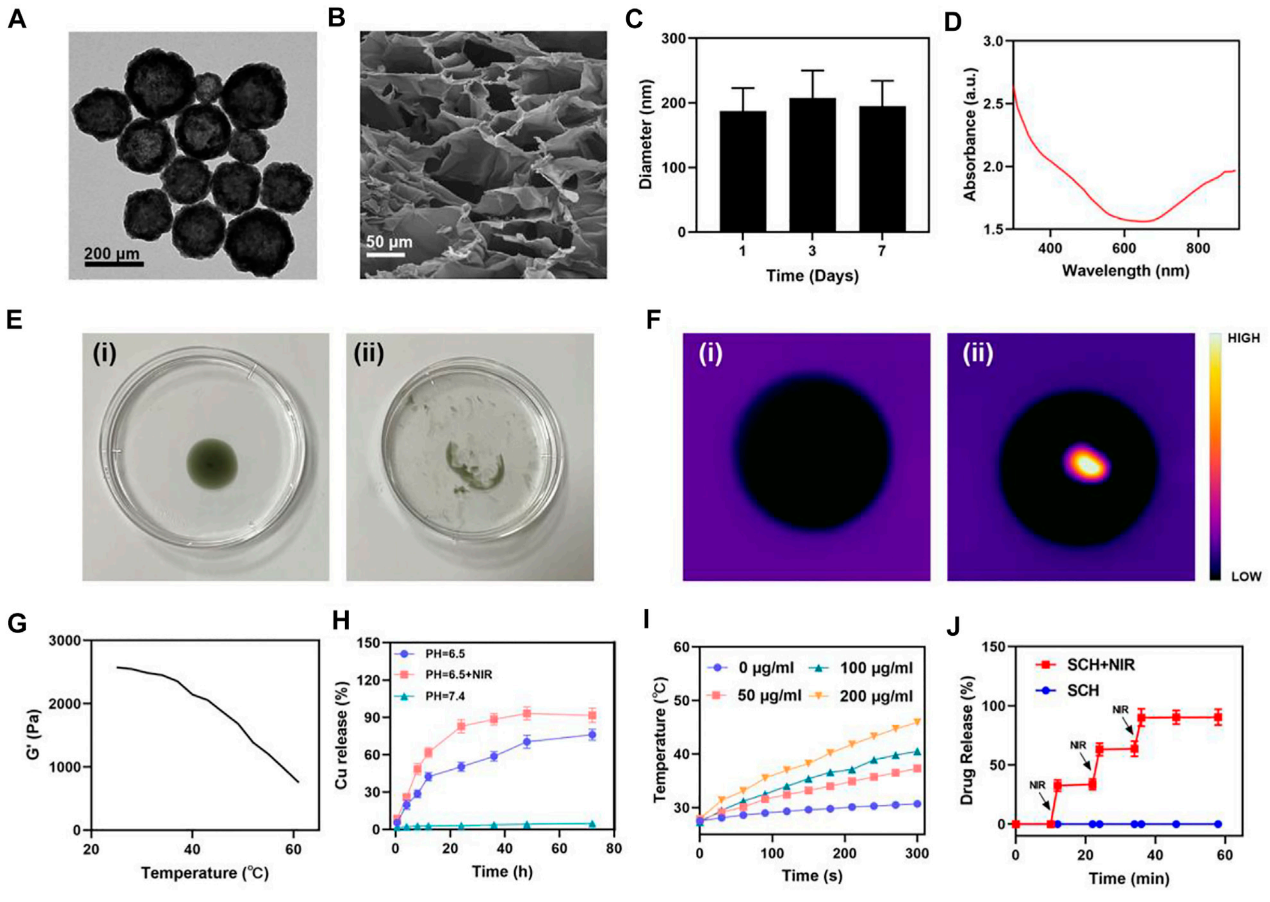

FIGURE 1
Characterization of SCH. **(A)** TEM image of CuS NPs. **(B)** SEM image of the SCH. **(C)** To determine the hydrodynamic diameter of CuS NPs (n = 3), DLS was employed. **(D)** CuS NPs absorbance spectra. **(E)**The morphology and **(F)**infrared thermal images of the prepared SCH before and after 0.5 W cm^{-2} 808 nm laser irradiation for 10 min **(G)**Temperature-dependent Rheological curves for the prepared SCH. **(H)**Time-dependent Cu^{2+} release from the SCH dispersed after different treatments. **(I)** Temperature changes of CuS NPs at various concentrations under a 5 min irradiation from an 808 nm laser at 0.5 W cm^{-2}. **(J)** Black arrows are utilized to denote the irradiation time points (n = 3) in an *in vitro* SCH release profile with and without 808 nm laser irradiation.

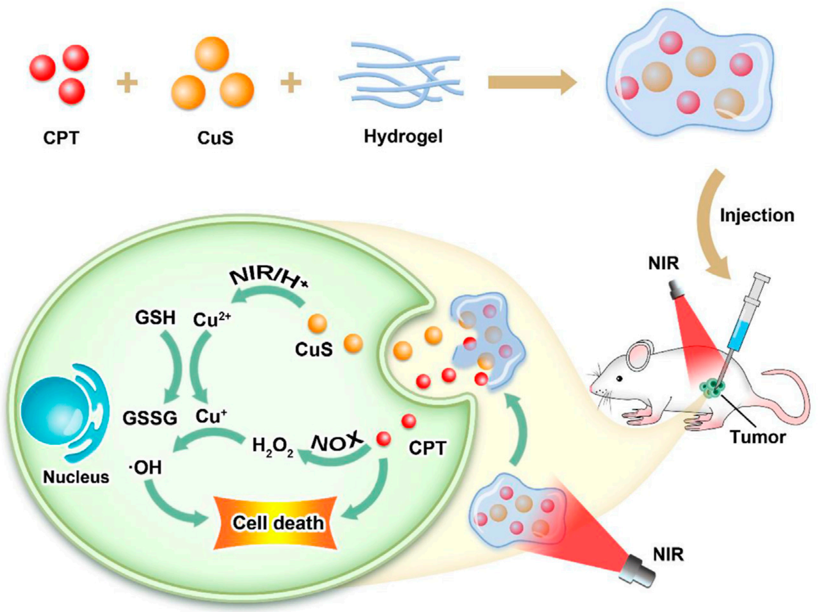

SCHEME 1
Schematic illustration of CuS NPs and CPT co-loaded thermosensitive injectable hydrogel with self-supplied H_2O_2 for enhanced CDT.

inhibits energy loss during therapy since it does not require sufficient oxygen (O_2) or external energy input (Feng et al., 2020). However, the insufficient concentration of H_2O_2 in the tumor microenvironment severely limits the therapeutic effect of chemokinetic (Zhou et al., 2021; Zhu et al., 2022c). At the same time, CDT alone does not effectively trigger immunological responses (Zhu et al., 2022b), therefore, it is very necessary to achieve high expression of H_2O_2 in the tumor microenvironment through a safe and effective method, and to promote the therapeutic effect of CDT through combined therapy, such as radiotherapy and photothermal therapy.

Camptothecin (CPT) is a class of alkaloids isolated from the traditional Chinese medicine Camptotheca. It has natural anti-tumor activity (Tang et al., 2019). Its main anti-tumor mechanism is to inhibit DNA synthesis by inhibiting the activity of S-phase enzyme I in the DNA replication of tumor cells, thereby mediating tumor cell apoptosis. Currently, CPT analogs (ie, irinotecan and topotecan) have been approved by the FDA for cancer treatment. However, CPT has poor water solubility and strong drug resistance, so it has certain limitations in clinical use. But surprisingly, CPT can also increase H_2O_2 levels of tumor cells via activation of nicotinamide adenine dinucleotide phosphate oxidase (Zhu et al., 2022b). By co-encapsulating Pd-C SAzymes and CPT in agarose hydrogel, Zhu et al. developed a light-controlled oxidative stress amplifier system that demonstrates improved synergistic anticancer action by creating H_2O_2 on its own and trans-forming “cold” tumors (Zhu et al., 2022b). The Pd-C SAzyme in this nanozyme hydrogel system transforms near-infrared laser into heat, which leads to agarose breakdown and subsequent CPT release. Through the activation of nicotinamide adenine dinucleotide phosphate oxidase, the CPT raises the amount of H_2O_2 in tumors while enhancing the catalytic activity of SAzymes with peroxidase-like action. In addition, combining photothermal therapy, chemotherapy and nanozyme-based catalytic therapy further promotes the immunogenic death of tumors and improves antitumor immunity. These outcomes demonstrate the synergistic antitumor capabilities of the new SAzyme/chemotherapeutics-based hydrogel system. Therefore, CPT may synergize with CDT to achieve self-supplied H_2O_2, effectively solving the problem of poor therapeutic effect of CDT due to insufficient concentration of H_2O_2 in the tumor microenvironment.

Semiconductor copper sulfide nanoparticles, with their superior electrical, optical and catalytic properties, have attracted extensive interest in the fields of photodegradation of pollutants, biomarkers, laser monitoring, and DNA detection (Liu et al., 2021b; Ding et al., 2022). As a semiconductor crystal material, CuS nanoparticles (NPs) have strong near-infrared absorption, and the main mechanism is the transition between electron d-d energy levels (Liu et al., 2015). Therefore, the absorption peak of CuS nanoparticles does not vary with the size of the particles. And shape, etc., have good photothermal stability. At the same time, CuS NPs has a strong local surface plasmon resonance effect in near-infrared (NIR), and also has a strong photothermal conversion efficiency, which also provides conditions for its application in photothermal therapy (PTT) (Wei et al., 2018). PTT is a non-invasive treatment (Li et al., 2017a; Li et al., 2017b; Li et al., 2021b; Li et al., 2021c; Li et al., 2022a; Li et al., 2022b). Li et al. prepared thioglycolic acid-modified CuS NPs by wet chemical method, and applied CuS NPs to photothermal therapy of tumors for the first time (Li et al., 2010). The particle size of the CuS NPs is about 3 nm, and it has a strong absorption peak in the NIR, with the maximum absorption peak at about 900 nm. Further MTT experiments show that this CuS NPs has outstanding photothermal treatment effect and good biocompatibility, they pointed out This CuS NPs preparation process is simple, low cost, has a small particle size, and has the advantages of unique optical properties and low biotoxicity. In addition, the Fenton-like reaction between Cu^{2+} ions released in the slightly acidic environment of the tumor and the endogenous H_2O_2 of the tumor leads to the generation of hydroxyl radicals for chemokinetic therapy (Ding et al., 2022; Meng et al., 2022), thereby inducing apoptosis. Studies have shown that ROS generated through the Fenton reaction may sensitize tumor cells to chemotherapeutic drugs and promote apoptosis of drug-resistant cells by destroying cytokines or nucleic acids (Cheng et al., 2021; Fu et al., 2021; Yan et al., 2022). Cu^{2+} can also oxidize GSH to oxidized glutathione (GSSG), which further promotes the generation of •OH (Meng et al., 2022). Therefore, CuS NPs can overcome the problem that single chemokinetic therapy is difficult to completely inhibit tumor growth.

Herein, we designed a CuS NPs and CPT co-loaded thermosensitive injectable hydrogel (SCH) with self-supplied H_2O_2 for enhanced CDT (Scheme 1). SCH is composed of CuS NPs and CPT loaded into agarose hydrogel according to a certain ratio. The hydrogel gradually solidifies after being injected into the tissue and is able to reside in the body for a long time. Therefore, it can be used repeatedly after one injection. The drug release rate can also be changed by adjusting the laser intensity, laser irradiation cycle and other parameters, which can well solve the problems of poor traditional drug loading, difficult manufacturing process, and early leakage or slow release of drugs. We injected SCH into the tumor tissue of mice, and under the illumination at 808nm, CuS NPs converted the near-infrared laser into heat to realize photothermal therapy, and at the same time, the agarose hydrogel was changed into a sol state and CPT was released of H_2O_2 inside the tumor, and realizes the self-supply of H_2O_2. At the same time, CuS NPs can accelerate the release of Cu^{2+} in an acidic environment and light, combined with H_2O_2 generated by CPT for chemokinetic treatment, and deplete glutathione inside the tumor. The SCH system we constructed achieved an extremely high tumor inhibition rate *in vitro* and *in vivo*, presenting a new idea for the design of future chemical kinetic systems.

Results and discussion

A previously described simple two-step synthesis procedure was employed for the synthesis of the CuS NPs (Ding et al., 2022). CuS NPs with an average particle size of about 190 nm are shown in (transmission electron microscope (TEM) images in Figure 1A. The pharmacological impact of NPs is limited since kidneys can easily remove NPs that are less than 10 nm in size. Thus, the hydrogel drug delivery system can significantly improve the usefulness of CuS NPs. The average hydrodynamic size of CuS NPs as determined by dynamic light scattering (DLS) measurement is approximately 196 ± 39 nm (Figure 1C), which is in good agreement with the TEM findings. The FDA has approved agarose hydrogel as a safe substance that dissolves easily, has no hazardous effects on the body, and can be metabolized by the natural metabolic processes of the body. We prepared the SCH system by mixing low melting point agarose hydrogel with CuS NPs and CPT in certain proportions with constant stirring at 60°. Figure 1B displays the scanning electron microscopy (SEM) image of the as-prepared SCH. When maintained at room temperature after preparation, SCH is fairly stable. Because CuS NPs can facilitate the transformation of light energy to heat energy, a rise in temperature results. A wide absorption region in the near-infrared region is visible in the UV-Vis absorption spectrum, which confirms that CuS NPs have an absorption value at 808 nm (Figure 1D). Consequently, SCH will slowly release CuS NPs under continuous laser irradiation, causing the solution to turn turbid (Figure 1E). The temperature difference between the pre- and post-irradiation states was authenticated by employing infrared thermal imaging (Figure 1F). As the temperature rises, SCH will progressively soften, and its storage modulus will continue to decline, according to the rheological measurement results of SCH at various temperatures (Figure 1G). This outcome is in line with the hydrogel's rheological characteristics. Additionally, we employed inductively coupled plasma-optical emission spectrometry (ICP-OES) to analyze how the laser affected the release of copper ions (Figure 1H), showing the NIR laser's ability to accelerate copper ion release in an acidic environment. SCH was produced with CuS NPs in a variety of concentrations (0, 50, 100, and 200 μg/ml) to examine their photothermal performance. Assuming no other variables change, Figure 1I demonstrates that when the concentration of CuS NPs rises, the heating impact also increases. After 5 min of laser irradiation, the temperature of SCH with 200 mg/ml CuS NPs elevated by around 18.0°C. The findings of our subsequent test of SCH's ability to control drug release are shown in Figure 1J. SCH can partly undergo disintegration under laser irradiation and releases the CPT.

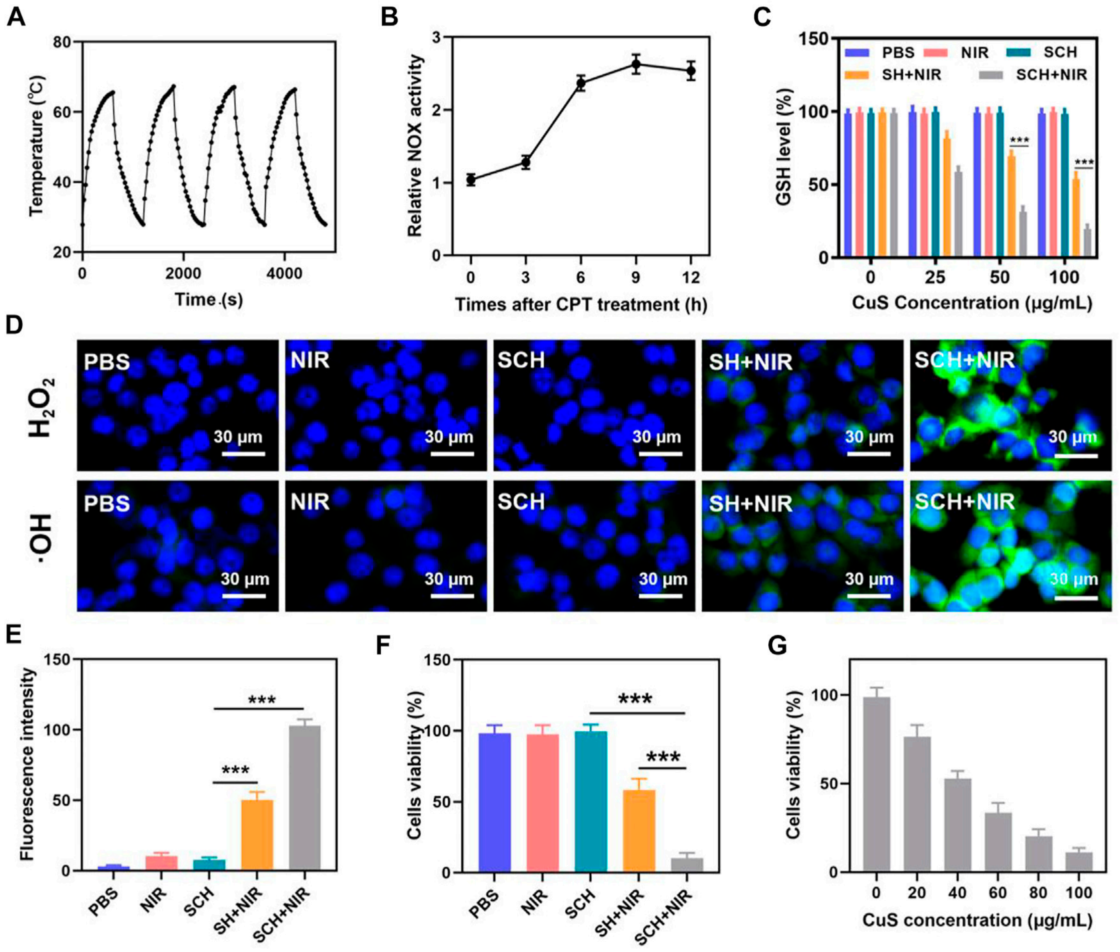

FIGURE 2
(A) Heating curve of SCH for four cycles having a $0.5\ W\ cm^{-2}$ power intensity under irradiation by 808 nm laser. **(B)** NADPH oxidase (NOX) activity assessment in CT26 cells following $10\ \mu g\ ml^{-1}$ CPT treatment at various time points. **(C)**The effect of different formulations on the intracellular GSH levels was determined by employing a GSH assay kit. (n = 3). **(D)** Confocal laser scanning microscopy images of different ROS produced in CT26 cells following various treatments. (n = 3). **(E)** Fluorescence intensity of OH from Figure 2D. (n = 3). **(F)** Various treatments' *in vitro* cytotoxicity towards CT26 cells. (n = 3).**(G)** Cytotoxicity of various concentrations of CuS NPs on CT26 cells. (n = 3).$^{*}p < 0.05$, $^{**}p < 0.01$, $^{***}p < 0.005$; Student's t-test.

Following the cessation of laser irradiation, the hydrogel cools and solidifies, protecting the drug. Our SCH system's potent capacity to control drug release is also shown by the fact that the drug is typically released entirely after four laser switching cycles.

Photothermal stability is a highly crucial aspect to consider when assessing photothermal agents (PTAs) (Liu et al., 2018; Ding et al., 2020; Chen et al., 2021d). Before verifying the tumor cell-killing effect of SCH system, we further evaluated the photothermal stability of SCH. An 808 nm NIR laser was utilized to constantly heat the SCH, and the switch was turned off after 10 min to let the SCH cool naturally to room temperature (Figure 2A). Four cycles of heating and cooling were carried out. The temperature graph demonstrates that the SCH peak temperature does not vary significantly, and the cooling trend is also consistent. In addition, we also calculated the photothermal conversion efficiency of CuS to be about 30.2% according to the previously reported method, which indicates that CuS has good photothermal performance. According to these results, the SCH has remarkable photothermal stability. After CPT treatment, a NOX activity detection kit was employed to confirm that the NOX in CT26 cells had been activated (Figure 2B). The anti-tumor activity based on ROS is inhibited by GSH's reaction with reactive oxygen species to be oxidized, which produces GSSG (Franco et al., 2007; Zhu et al., 2022d). Due to glutathione deficiency, free radicals damage cells' redox balance, induce oxidative stress and eventually result in cell apoptosis. We have established how

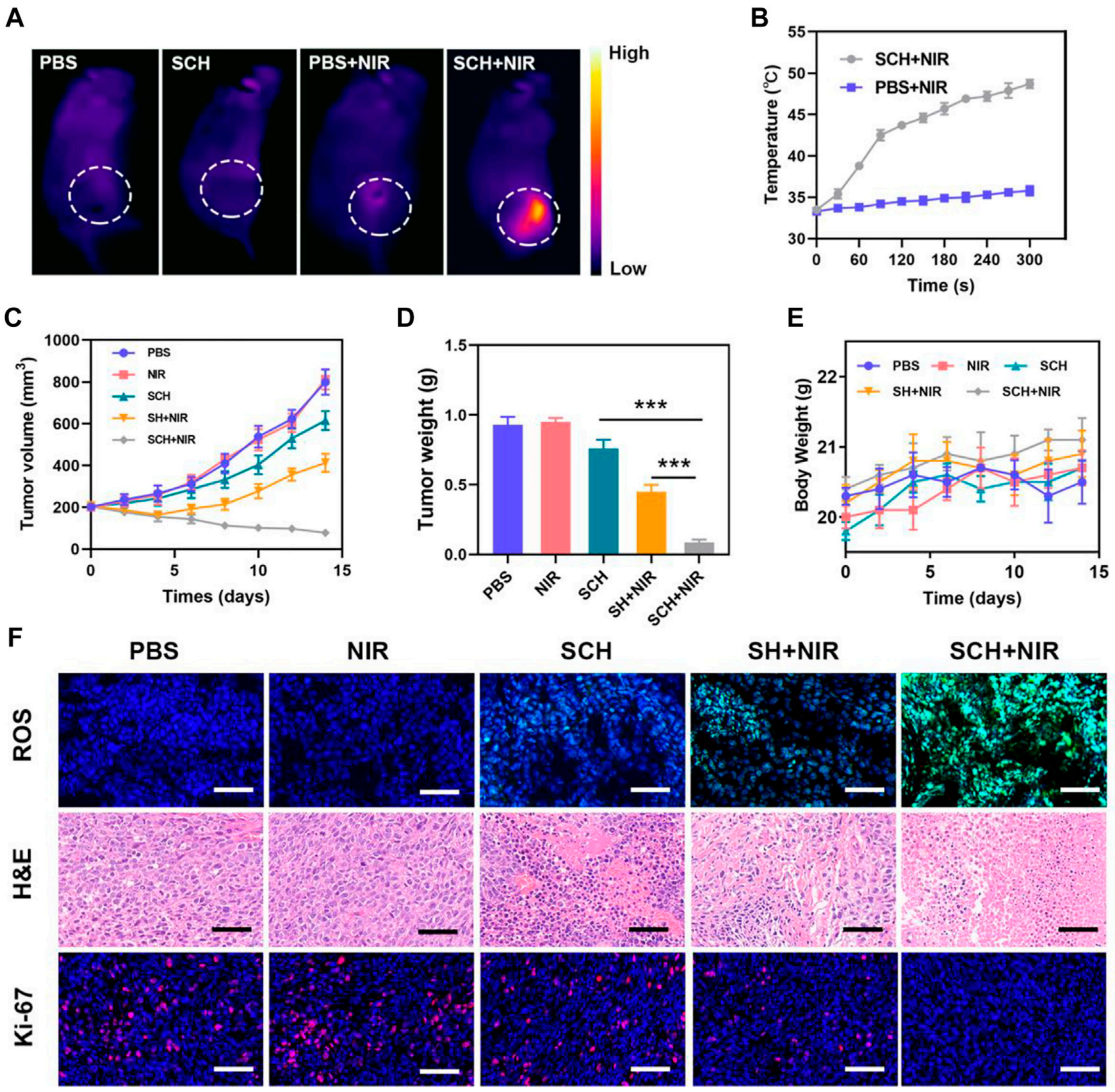

FIGURE 3
(A) Infrared thermal images of tumors in the specified treatment groups. **(B)** After being irradiated with 808 nm laser (0.5 W cm^{-2}) for 5 min, the temperature elevates in mice having CT26 tumor, in the specified treatment groups. **(C)** The treatment groups' tumor volume alters over time, as specified (n = 5). **(D)** Average tumor weight values associated with the indicated treatments (n = 5). **(E)** Changes in body weight in response to the indicated treatments (n = 5). **(F)** HPF, H&E, and Ki-67-stained tumor sections from the indicated treatment groups (n = 5). Scale bars: 100 μm ***p < 0.005; Student's t-test. The results were presented as mean ± SD.

SCH works in conjunction with NIR radiation for consuming GSH (Figure 2C). The findings demonstrate that Cu^{2+} may effectively lower intracellular GSH levels, while CPT can also generate a certain quantity of H_2O_2 to encourage GSH consumption, further enhancing the therapeutic effects of CDT. We utilized a hydrogen peroxide test kit as the probe for detecting intracellular H_2O_2 and hydroxyphenyl fluorescein (HPF) as the probe for detecting intracellular •OH to determine whether SCH may increase the generation of H_2O_2 in CT26 cells. The hydrogel coated with CuS (SH) was prepared to compare the experimental results. The control group's and SCH group's HPF fluorescence signals were both essentially nonexistent (Figures 2D,E). The SH in combination with the NIR group created a modest fluorescence effect, however, the SCH + NIR motivated the strongest green fluorescence because the SCH system yielded CPT under 808 nm irradiation, which then caused H_2O_2 to break down to produce •OH. We then administered various treatment combinations to CT26 tumor cells to verify the cytotoxicity of the SCH therapy. The viability of these cells was then evaluated via an MTT assay. In line with the inability of PBS, NIR, and SCH

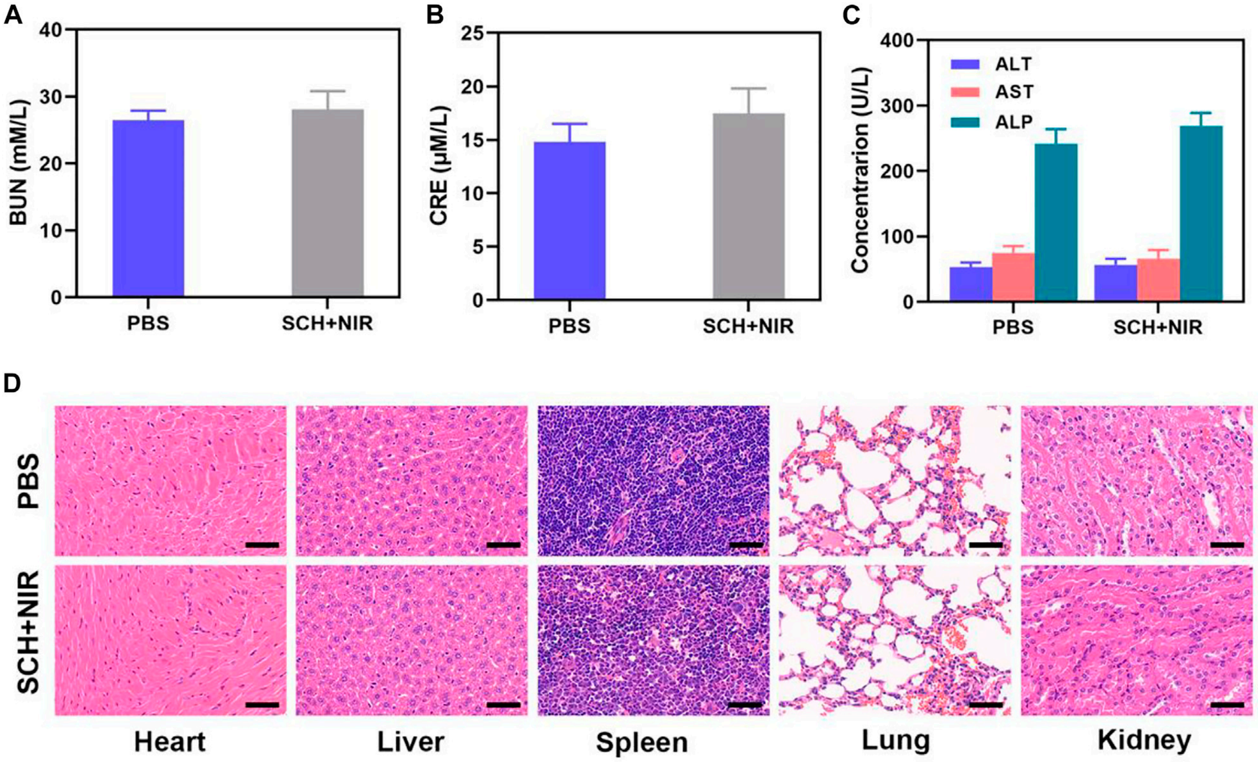

FIGURE 4
(A) Kidney function markers: BUN, **(B)** CRE, and **(C)** Liver function indicators: ALT, AST, and ALP following different treatments. (n = 3). **(D)** Results of histopathological examination (H&E-stained images) of the mice's major organs, including the heart, lung, liver, kidneys, and spleen, after exposure to various therapies 14 days after the injection. (n = 3). Scale bars: 50 μm.

therapies in stopping the growth of the tumor, cells in these treatment groups did not demonstrate any discernible cytotoxicity (Figure 2F). On the other hand, SH + NIR and SCH + NIR treatments significantly increased the tumor cell cytotoxicity, with SCH + NIR treatment proving to be more cytotoxic than SH + NIR treatment alone. This is explained by the fact that CPT in the hydrogel system disintegrated H_2O_2 to yield •OH, which further enhanced the efficacy of CDT, thereby inhibiting tumor growth. As a result, this combination therapy strategy has the ability to compensate for the tumor's deficiency of H_2O_2 and thereby improve treatment efficacy. As demonstrated in Figure 2G, we also developed SCH systems with various drug loading ratios and carried out MTT assays. The cell death was further boosted as CuS's concentration elevated, showing that SCH's cell killing was concentration-dependent.

We then examined this prepared SCH's capacity to induce the *in vivo* elimination of CT26 breast tumors in mice because they demonstrated positive antitumor activity *in vitro*. Following PBS or SCH treatment, the tumor site's temperature was measured for 5 min under an 808 nm (0.5 W cm^{-2}) laser. Temperatures in the SCH group were significantly higher than in the control group, according to IR thermal imaging (Figures 3A,B). The increase in temperature in the control group was insignificant (from 33.3 to 35.8°C), indicating that the increase in temperature in the SCH group was from 33.5 to 48.7°C. Since the heat resistance of tumor tissue is comparatively inferior to that of normal cells, SCH-mediated photothermal therapy can lead to the destruction of proteins and other active substances in tumor cells at elevated temperatures (42–47°C), thereby inducing apoptosis. On the other hand, SCH can release CuS NPs and CPT at high temperatures, enabling multiple rounds of treatments. The primary impact of SCH was determined by subcutaneously injecting 1 × 10^6 CT26 cells into BALB/c mice. The mice received treatment after their main tumor volume had reached almost 200 mm^3. Five groups of mice having tumors were created at random (5 mice in each group) (Zhang et al., 2020) PBS; (Chen et al., 2021a); NIR; (Zhu et al., 2021a); SCH; (Zhu et al., 2020); SH + NIR; and (Zhu et al., 2021b) SCH + NIR. The CuS NPs concentration was 20 mg/kg in groups 3, 4, and 5. After that, for 10 min, mice in groups 2, 4, and 5 were exposed to 808 nm laser radiation (0.5 W cm^{-2}). Every 2 days, the weight of the mice was recorded. The tumor volumes in the control group (PBS) and the NIR group dramatically increased throughout the continuous treatment cycle, whereas the SCH group showed a slight tumor suppressor effect, because the hydrogel would degrade slowly in the animal body in the absence of light, releasing a small part of drugs to cause a certain degree of killing effect on the tumor. A better therapeutic impact is exhibited by the SH + NIR group. Though SH in combination with the laser has a certain tumor-ablating impact, the intracellular H_2O_2 level restricts SH's ability to further induce the CDT effect. The group receiving treatment with SCH and NIR demonstrated the most effective tumor suppression (Figure 3C). Possibly following the laser irradiation, the chemotherapeutic drug CPT might boost H_2O_2 levels and further improve CuS NPs-mediated •OH generation in addition to promoting tumor cell apoptosis. Moreover, Cu^{2+} also could decrease intracellular GSH to cause oxidative stress damage. The weight of the tumor in mice following therapy matched the outcomes (Figure 3D). Throughout treatment, the mice's body weight did not alter abnormally, proving that the agarose hydrogel was safe and nontoxic and that our course of treatment was safe (Figure 3E). Moreover, when the production of •OH in these mice was assessed using HPF, considerably elevated levels were determined in mice treated with SCH + NIR, suggesting that the current treatment approach can improve the CDT effectiveness and thus inhibit tumor growth. After the SCH + NIR group received therapy, Ki-67 staining was performed, and it was seen to be reduced. The hematoxylin and eosin (H&E) staining results showed that upon treatments with SCH + NIR, the solid tumor tissue's structure was damaged, numerous tumor cells were necrotic, and the tissue's cells were constricted with vanished nuclei (Figure 3F). These findings indicate that laser irradiation and our CFH could work together to treat tumors.

We then assessed liver and renal functions which were not impaired and this ensured that there was no systemic toxicity caused by SCH (Figures 4A–C). Also, the outcomes of comprehensive histological examinations of H&E- stained lung, liver, heart, spleen, and kidney sections from these animals confirmed that there are no major anomalies in any mice (Figure 4D). Therefore, in these mice, SCH therapy did not cause any severe adverse events. In summary, we have demonstrated that the SCH system can achieve extremely high tumor suppression rates. In the treatment of tumors, CDT has been limited by insufficient hydrogen peroxide content in tumors. Our SCH system provides new ideas for CDT treatment of tumors in the future.

Conclusion

To conclude, we designed CuS NPs and CPT co-loaded thermosensitive injectable hydrogel with self-supplied H_2O_2 for enhanced Chemodynamic Therapy (SCH). We injected SCH into the tumor tissue of mice, and under the illumination at 808 nm, CuS NPs converted the near-infrared laser into heat to realize photothermal therapy, and at the same time, the agarose hydrogel was changed into a sol state and CPT was released. CPT activates nicotinamide adenine dinucleotide phosphate oxidase, increases the level of H_2O_2 inside the tumor, and realizes the self-supply of H_2O_2. At the same time, CuS NPs can accelerate the release of Cu^{2+} in an acidic environment and light, combined with H_2O_2 generated by CPT for chemokinetic treatment, and deplete glutathione inside the tumor. The SCH system we constructed achieved an extremely high tumor inhibition rate *in vitro* and *in vivo*, presenting a new idea for the design of future chemical kinetic systems. In the future, our system can be expected to be used in combination with advanced nanotechnology and immune technology concepts such as immunotherapy to further improve our therapeutic effect.

Data availability statement

The original contributions presented in the study are included in the article/Supplementary Material, further inquiries can be directed to the corresponding author.

Ethics statement

The animal study was reviewed and approved by wuhan university.

Author contributions

Conceived and designed the experiments: WT, XL, ZL, DZ, LM, and QH. Performed the experiments: WT, XL, LM, and ZL. Contributed reagents/materials/analysis tools: WT, XL, ZL, and QH. All authors contributed to the article and approved the submitted version.

Funding

This work was supported by National Natural Science Foundation of China (31800085).

Acknowledgments

The authors would like to thank Dr. Yufei Chen from Shiyanjia Lab (www.shiyanjia.com) for drawing schematic diagrams.

Conflict of interest

The authors declare that the research was conducted in the absence of any commercial or financial relationships that could be construed as a potential conflict of interest.

Publisher's note

Supplementary material

The Supplementary Material for this article can be found online at: https://www.frontiersin.org/articles/10.3389/fbioe.2022.1003777/full#supplementary-material

References

Chen, H., Zheng, D., Pan, W., Li, X., Lv, B., Gu, W., et al. (2021). Biomimetic nanotheranostics camouflaged with cancer cell membranes integrating persistent oxygen supply and homotypic targeting for hypoxic tumor elimination. *ACS Appl. Mat. Interfaces* 13 (17), 19710–19725. doi:10.1021/acsami.1c03010

Chen, L., Huang, Q., Zhao, T., Sui, L., Wang, S., Xiao, Z., et al. (2021). Nanotherapies for sepsis by regulating inflammatory signals and reactive oxygen and nitrogen species: New insight for treating COVID-19. *Redox Biol.* 45, 102046. doi:10.1016/j.redox.2021.102046

Chen, N., Fu, W., Zhou, J., Mei, L., Yang, J., Tian, Y., et al. (2021). Mn2+-doped ZrO2@PDA nanocomposite for multimodal imaging-guided chemo-photothermal combination therapy. *Chin. Chem. Lett.* 32 (8), 2405–2410. doi:10.1016/j.cclet.2021.02.030

Chen, X., Chen, Y., Wang, C., Jiang, Y., Chu, X., Wu, F., et al. (2021). NIR-triggered intracellular H+ transients for lamellipodia-collapsed antimetastasis and enhanced chemodynamic therapy. *Angew. Chem. Int. Ed.* 60, 21905–21910. doi:10.1002/anie.202107588

Cheng, J., Zhu, Y., Xing, X., Xiao, J., Chen, H., Zhang, H., et al. (2021). Manganese-deposited iron oxide promotes tumor-responsive ferroptosis that synergizes the apoptosis of cisplatin. *Theranostics* 11 (11), 5418–5429. doi:10.7150/thno.53346

Deng, H., Zhang, J., Yang, Y., Yang, J., Wei, Y., Ma, S., et al. (2022). Chemodynamic and photothermal combination therapy based on dual-modified metal-organic framework for inducing tumor ferroptosis/pyroptosis. *ACS Appl. Mat. Interfaces* 14, 24089–24101. doi:10.1021/acsami.2c00574

Ding, D., Mei, Z., Huang, H., Feng, W., Chen, L., Chen, Y., et al. (2022). Oxygen-Independent sulfate radical for stimuli-responsive tumor nanotherapy. *Adv. Sci. (Weinh).* 9, e2200974. doi:10.1002/advs.202200974

Ding, K., Zheng, C., Sun, L., Liu, X., Yin, Y., and Wang, L. (2020). NIR light-induced tumor phototherapy using ICG delivery system based on platelet-membrane-camouflaged hollow bismuth selenide nanoparticles. *Chin. Chem. Lett.* 31 (5), 1168–1172. doi:10.1016/j.cclet.2019.10.040

Dong, Z., Feng, L., Chao, Y., Hao, Y., Chen, M., Gong, F., et al. (2018). Amplification of tumor oxidative stresses with liposomal Fenton catalyst and glutathione inhibitor for enhanced cancer chemotherapy and radiotherapy. *Nano Lett.* 19, 805–815. doi:10.1021/acs.nanolett.8b03905

Feng, L., Liu, B., Xie, R., Wang, D., Qian, C., Zhou, W., et al. (2020). An ultrasmall SnFe2O4 nanozyme with endogenous oxygen generation and glutathione depletion for synergistic cancer therapy. *Adv. Funct. Mat.* 31 (5), 2006216. doi:10.1002/adfm.202006216

Fenton, H. J. H. (1894). LXXIII.—oxidation of tartaric acid in presence of iron. *J. Chem. Soc. Trans.* 65 (0), 899–910. doi:10.1039/CT8946500899

Franco, R., Panayiotidis, M. I., and Cidlowski, J. A. (2007). Glutathione depletion is necessary for apoptosis in lymphoid cells independent of reactive oxygen species formation. *J. Biol. Chem.* 282 (42), 30452–30465. doi:10.1074/jbc.M703091200

Fu, J., Li, T., Yang, Y., Jiang, L., Wang, W., Fu, L., et al. (2021). Activatable nanomedicine for overcoming hypoxia-induced resistance to chemotherapy and inhibiting tumor growth by inducing collaborative apoptosis and ferroptosis in solid tumors. *Biomaterials* 268, 120537. doi:10.1016/j.biomaterials.2020.120537

Li, X., Hetjens, L., Wolter, N., Li, H., Shi, X., and Pich, A. (2022). Charge-reversible and biodegradable chitosan-based microgels for lysozyme-triggered release of vancomycin. *J. Adv. Res.* 1, 1. doi:10.1016/j.jare.2022.02.014

Li, X., Kong, L., Hu, W., Zhang, C., Pich, A., Shi, X., et al. (2022). Safe and efficient 2D molybdenum disulfide platform for cooperative imaging-guided photothermal-selective chemotherapy: A preclinical study. *J. Adv. Res.* 37, 255–266. doi:10.1016/j.jare.2021.08.004

Li, X., Li, H., Zhang, C., Pich, A., Xing, L., and Shi, X. (2021). Intelligent nanogels with self-adaptive responsiveness for improved tumor drug delivery and augmented chemotherapy. *Bioact. Mat.* 6 (10), 3473–3484. doi:10.1016/j.bioactmat.2021.03.021

Li, X., Luo, R., Liang, X., Wu, Q., and Gong, C. (2021). Recent advances in enhancing reactive oxygen species based chemodynamic therapy. *Chin. Chem. Lett.* 33, 2213–2230. doi:10.1016/j.cclet.2021.11.048

Li, X., Ouyang, Z., Li, H., Hu, C., Saha, P., Xing, L., et al. (2021). Dendrimer-decorated nanogels: Efficient nanocarriers for biodistribution *in vivo* and chemotherapy of ovarian carcinoma. *Bioact. Mat.* 6 (10), 3244–3253. doi:10.1016/j.bioactmat.2021.02.031

Li, X., Xing, L., Hu, Y., Xiong, Z., Wang, R., Xu, X., et al. (2017). An RGD-modified hollow silica@Au core/shell nanoplatform for tumor combination therapy. *Acta Biomater.* 62, 273–283. doi:10.1016/j.actbio.2017.08.024

Li, X., Xing, L., Zheng, K., Wei, P., Du, L., Shen, M., et al. (2017). formation of gold nanostar-coated hollow mesoporous silica for tumor multimodality imaging and photothermal therapy. *ACS Appl. Mat. Interfaces* 9 (7), 5817–5827. doi:10.1021/acsami.6b15185

Li, Y., Lu, W., Huang, Q., Li, C., and Chen, W. (2010). Copper sulfide nanoparticles for photothermal ablation of tumor cells. *Nanomedicine* 5 (8), 1161–1171. doi:10.2217/nnm.10.85

Lin, L., Wang, S., Deng, H., Yang, W., Rao, L., Tian, R., et al. (2020). Endogenous labile iron pool-mediated free radical generation for cancer chemodynamic therapy. *J. Am. Chem. Soc.* 142 (36), 15320–15330. doi:10.1021/jacs.0c05604

Liu, W., Xiang, H., Tan, M., Chen, Q., Jiang, Q., Yang, L., et al. (2021). Nanomedicine enables drug-potency activation with tumor sensitivity and Hyperthermia Synergy in the Second near-infrared Biowindow. *ACS Nano* 15 (4), 6457–6470. doi:10.1021/acsnano.0c08848

Liu, X., Ren, Q., Fu, F., Zou, R., Wang, Q., Xin, G., et al. (2015). CuS@mSiO2-PEG core-shell nanoparticles as a NIR light responsive drug delivery nanoplatform for efficient chemo-photothermal therapy. *Dalton Trans.* 44 (22), 10343–10351. doi:10.1039/c5dt00198f

Liu, Y., Zhai, S., Jiang, X., Liu, Y., Wang, K., Wang, C., et al. (2021). Intracellular mutual promotion of redox homeostasis regulation and iron metabolism disruption for enduring chemodynamic therapy. *Adv. Funct. Mat.* 31 (17), 2010390. doi:10.1002/adfm.202010390

Liu, Y., Zhen, W., Jin, L., Zhang, S., Sun, G., Zhang, T., et al. (2018). All-in-One theranostic nanoagent with enhanced reactive oxygen species generation and modulating tumor microenvironment ability for effective tumor eradication. *ACS Nano* 12 (5), 4886–4893. doi:10.1021/acsnano.8b01893

Meng, X., Zhou, K., Qian, Y., Liu, H., Wang, X., Lin, Y., et al. (2022). Hollow cuprous Oxide@Nitrogen-doped carbon nanocapsules for cascade chemodynamic therapy. *Small* 18, e2107422. doi:10.1002/smll.202107422

Sang, Y., Cao, F., Li, W., Zhang, L., You, Y., Deng, Q., et al. (2020). Bioinspired construction of a nanozyme-based H2O2 homeostasis disruptor for intensive chemodynamic therapy. *J. Am. Chem. Soc.* 142 (11), 5177–5183. doi:10.1021/jacs.9b12873

Tang, Y., Lu, X., Yin, C., Zhao, H., Hu, W., Hu, X., et al. (2019). Chemiluminescence-initiated and *in situ*-enhanced photoisomerization for tissue-depth-independent photo-controlled drug release. *Chem. Sci.* 10 (5), 1401–1409. doi:10.1039/c8sc04012e

Wang, J., Sui, L., Huang, J., Miao, L., Nie, Y., Wang, K., et al. (2021). MoS2-based nanocomposites for cancer diagnosis and therapy. *Bioact. Mat.* 6 (11), 4209–4242. doi:10.1016/j.bioactmat.2021.04.021

Wang, Q., Gao, Z., Zhao, K., Zhang, P., Zhong, Q.-Z., Yu, Q., et al. (2021). Co-delivery of enzymes and photosensitizers via metal-phenolic network capsules for enhanced photodynamic therapy. *Chin. Chem. Lett.* 33, 1917–1922. doi:10.1016/j.cclet.2021.11.040

Wei, Q., Chen, Y., Ma, X., Ji, J., Qiao, Y., Zhou, B., et al. (2018). High-Efficient clearable nanoparticles for multi-modal imaging and image-guided cancer therapy. *Adv. Funct. Mat.* 28 (2), 1704634. doi:10.1002/adfm.201704634

Yan, J., Zhang, Y., Zheng, L., Wu, Y., Wang, T., Jiang, T., et al. (2022). Let-7i miRNA and platinum loaded nano-graphene oxide platform for detection/reversion of drug resistance and synergetic chemical-photothermal inhibition of cancer cell. *Chin. Chem. Lett.* 33 (2), 767–772. doi:10.1016/j.cclet.2021.08.018

Zhang, K., Yu, Z., Meng, X., Zhao, W., Shi, Z., Yang, Z., et al. (2019). A bacteriochlorin-based metal–organic framework nanosheet superoxide radical generator for photoacoustic imaging-guided highly efficient photodynamic therapy. *Adv. Sci.* 6 (14), 1900530. doi:10.1002/advs.201900530

Zhang, X., Ong'achwa Machuki, J., Pan, W., Cai, W., Xi, Z., Shen, F., et al. (2020). Carbon nitride hollow theranostic nanoregulators executing laser-activatable water splitting for enhanced ultrasound/fluorescence imaging and cooperative phototherapy. *ACS Nano* 14 (4), 4045–4060. doi:10.1021/acsnano.9b08737

Zhao, T., Wu, W., Sui, L., Huang, Q., Nan, Y., Liu, J., et al. (2022). Reactive oxygen species-based nanomaterials for the treatment of myocardial ischemia reperfusion injuries. *Bioact. Mat.* 7, 47–72. doi:10.1016/j.bioactmat.2021.06.006

Zhou, Q. M., Lu, Y. F., Zhou, J. P., Yang, X. Y., Wang, X. J., Yu, J. N., et al. (2021). Self-amplification of oxidative stress with tumour microenvironment-activatable iron-doped nanoplatform for targeting hepatocellular carcinoma synergistic cascade therapy and diagnosis. *J. Nanobiotechnology* 19 (1), 361. doi:10.1186/s12951-021-01102-0

Zhu, D., Chen, H., Huang, C., Li, G., Wang, X., Jiang, W., et al. (2022). H_2O_2 self-producing single-atom nanozyme hydrogels as light-controlled oxidative stress amplifier for enhanced synergistic therapy by transforming "cold" tumors. *Adv. Funct. Mat.* 32, 2110268. doi:10.1002/adfm.202110268

Zhu, D., Duo, Y., Meng, S., Zhao, Y., Xia, L., Zheng, Z., et al. (2020). Tumor-exocytosed exosome/aggregation-induced emission luminogen hybrid nanovesicles facilitate efficient tumor penetration and photodynamic therapy. *Angew. Chem. Int. Ed.* 59, 13836–13843. doi:10.1002/anie.202003672

Zhu, D., Ling, R., Chen, H., Lyu, M., Qian, H., Wu, K., et al. (2022). Biomimetic copper single-atom nanozyme system for self-enhanced nanocatalytic tumor therapy. *Nano Res.* 15, 7320–7328. doi:10.1007/s12274-022-4359-6

Zhu, D., Zhang, J., Luo, G., Duo, Y., and Tang, B. Z. (2021). Bright bacterium for hypoxia-tolerant photodynamic therapy against orthotopic colon tumors by an interventional method. *Adv. Sci. (Weinh).* 8, 2004769. doi:10.1002/advs.202004769

Zhu, D., Zhang, T., Li, Y., Huang, C., Suo, M., Xia, L., et al. (2022). Tumor-derived exosomes co-delivering aggregation-induced emission luminogens and proton pump inhibitors for tumor glutamine starvation therapy and enhanced type-I photodynamic therapy. *Biomaterials* 283, 121462. doi:10.1016/j.biomaterials.2022.121462

Zhu, D., Zheng, Z., Luo, G., Suo, M., Li, X., Duo, Y., et al. (2021). Single injection and multiple treatments: An injectable nanozyme hydrogel as AIEgen reservoir and release controller for efficient tumor therapy. *Nano Today* 37, 101091. doi:10.1016/j.nantod.2021.101091

Zhu, Y., Zhao, T., Liu, M., Wang, S., Liu, S., Yang, Y., et al. (2022). Rheumatoid arthritis microenvironment insights into treatment effect of nanomaterials. *Nano Today* 42, 101358. doi:10.1016/j.nantod.2021.101358

frontiers | Frontiers in Bioengineering and Biotechnology

TYPE Review
PUBLISHED 08 September 2022
DOI 10.3389/fbioe.2022.1010724

Recent advances in nano-drug delivery systems for synergistic antitumor immunotherapy

Bonan Zhao[1†], Xiang Li[2†], Ying Kong[3], Wenbo Wang[4], Tingting Wen[4], Yanru Zhang[4], Zhiyong Deng[5]*, Yafang Chen[4]* and Xian Zheng[4]*

[1]Leiden Academic Centre for Drug Research (LACDR), Leiden University, Leiden, Netherlands, [2]Department of Central Laboratory and Precision Medicine Center, Department of Nephrology, The Affiliated Huai'an Hospital of Xuzhou Medical University and Huai'an Second People's Hospital, Huai'an, China, [3]Department of Radiology, Affiliated Hospital of Xuzhou Medical University, Xuzhou, China, [4]Department of Pharmacy, Affiliated Kunshan Hospital of Jiangsu University, Kunshan, China, [5]Department of Pathology, Affiliated Kunshan Hospital of Jiangsu University, Kunshan, China

Check for updates

OPEN ACCESS

EDITED BY
Long Bai,
East China University of Science and Technology, China

REVIEWED BY
Fangnan Lv,
China Pharmaceutical University, China
Jin Zhu,
Westlake University, China
Xiang Xu,
King's College London, United Kingdom

*CORRESPONDENCE
Xian Zheng,
zhengxiannew@163.com
Yafang Chen,
yafang01@126.com
Zhiyong Deng,
yichun1988@yeah.net

†These authors have contributed equally to this work.

SPECIALTY SECTION
This article was submitted to Nanobiotechnology,
a section of the journal
Frontiers in Bioengineering and Biotechnology

RECEIVED 03 August 2022
ACCEPTED 22 August 2022
PUBLISHED 08 September 2022

CITATION
Zhao B, Li X, Kong Y, Wang W, Wen T, Zhang Y, Deng Z, Chen Y and Zheng X (2022), Recent advances in nano-drug delivery systems for synergistic antitumor immunotherapy.
Front. Bioeng. Biotechnol. 10:1010724.
doi: 10.3389/fbioe.2022.1010724

Immunotherapy has demonstrated great clinical success in the field of oncology in comparison with conventional cancer therapy. However, cancer immunotherapy still encounters major challenges that limit its efficacy against different types of cancers and the patients show minimal immune response to the immunotherapy. To overcome these limitations, combinatorial approaches with other therapeutics have been applied in the clinic. Simultaneously, nano-drug delivery system has played an important role in increasing the antitumor efficacy of various treatments and has been increasingly utilized for synergistic immunotherapy to further enhance the immunogenicity of the tumors. Specifically, they can promote the infiltration of immune cells within the tumors and create an environment that is more sensitive to immunotherapy, particularly in solid tumors, by accelerating tumor accumulation and permeability. Herein, this progress report provides a brief overview of the development of nano-drug delivery systems, classification of combinatory cancer immunotherapy and recent progress in tumor immune synergistic therapy in the application of nano-drug delivery systems.

KEYWORDS

cancer therapy, immunotherapy, synergistic treatment, nano-drug delivery systems, nanomedicine

1 Introduction

Tumors have surpassed cardiovascular diseases and become the leading cause of death worldwide, threatening human health and life (Mattiuzzi and Lippi, 2019; Bray et al., 2021). According to statistics from the World Health Organization, there were 18.1 million new cancer cases and 9.6 million cancer-related deaths globally in 2018 (Yates et al., 2020). In recent years, advances in immunotherapy have resulted in great improvements in cancer treatment (Yang, 2015). It is well known that the immune system plays an important role in cancer therapy, and several immunotherapies such as immune

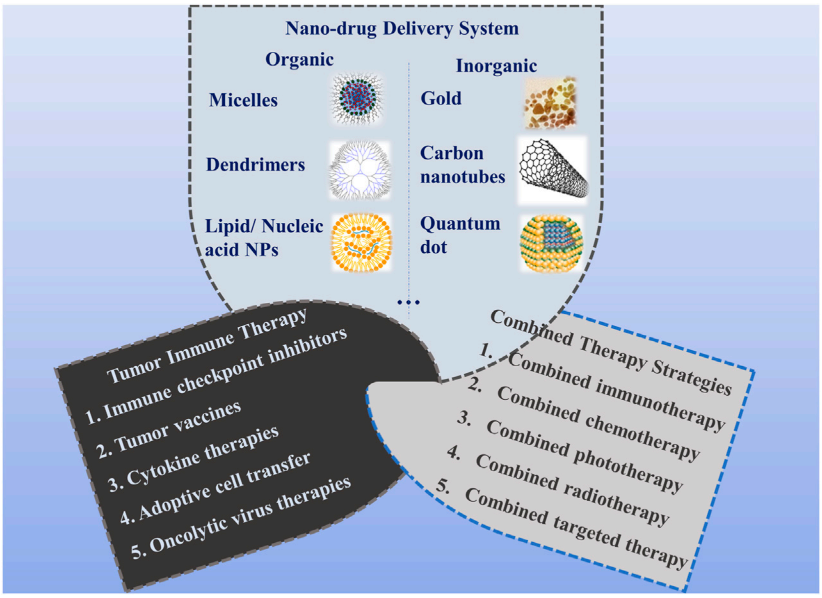

FIGURE 1
Classification of nano-drug delivery systems for synergistic antitumor immunotherapy.

checkpoint inhibitors (Bagchi et al., 2021), adoptive immunotherapy (Lee, 2019) and tumor vaccines (Rammensee et al., 2020) have emerged as effective therapeutic strategies for treating cancer patients. However, tumor immunotherapy still encounters serious challenges, wherein certain tumors barely respond to immunotherapy. The lack of immunogenicity and subsequent insufficient antitumor immune response is a major reason for the lack of efficacy of several immunotherapies (Pilla et al., 2018). Therefore, it is important to seek strategies to strengthen the immunogenicity of tumors to enhance the efficacy of immunotherapy and overcome immune tolerance and escape.

In recent years, increasing attention has been given to combination therapies (Bayat Mokhtari et al., 2017), especially in the nanomedicine area (Jin et al., 2020a). Compared to immunotherapy alone, synergistic treatments, such as in combination with chemotherapy or phototherapy, offer multiple advantages with fewer side effects by avoiding multidrug resistance. Thus, it is necessary to combine immunotherapies with other therapeutic strategies. Among them, nanomedicine is one of the most important therapeutic approaches, which has been extensively applied in the clinic and pre-clinical investigations (Bayda et al., 2019). Nanoparticles (NPs) are the key components of nanomedicine and have received wide interest as promising drug-delivery systems for cancer treatment. Nanoparticles applied as drug delivery systems refer to nanoscale (usually 10–200 nm in diameter) particles, devices, or systems synthesized from various materials (Jin and Ye, 2007), including polymers (micelles, nanobrushes), lipids (liposomes), etc. (Bauer et al., 2021; Kappel et al., 2021; Zhang et al., 2022). They can increase the intracellular concentration of drugs within the cancer cells while decreasing their toxicity to the normal cells through passive or active targeting strategies, which are greatly helpful for increasing tumor immunogenicity by inducing T cell-mediated immune responses, thereby achieving high antitumor efficacy (Huang et al., 2021a). Considerable efforts have been made to develop novel nanoparticle-assisted cancer therapies in recent years. In this review, we summarize the recent advance in the development of nano-drug delivery systems for synergistic antitumor immunotherapy [Figure 1].

2 Overview of nano-drug delivery systems for cancer therapy

In recent years, nano-drug delivery systems have rapidly developed with the application of nanotechnology in medicine, which can deliver therapeutic agents to the target site, including proteins, nucleic acids (Torres-Vanegas et al., 2021), small molecule chemotherapeutics (Wang et al., 2020), and imaging agents (Ehlerding et al., 2018). The therapeutic agent can be integrated into the nano-drug carrier through covalent bonding (Rianasari et al., 2013), physical packaging (Huang et al., 2021b), electrostatic force (Zhang et al., 2018a) or coordination complexation (Siemer et al., 2021), thereby solving the limitations of conventional chemotherapeutic drugs, such as low water solubility (Merisko-Liversidge and Liversidge, 2008),

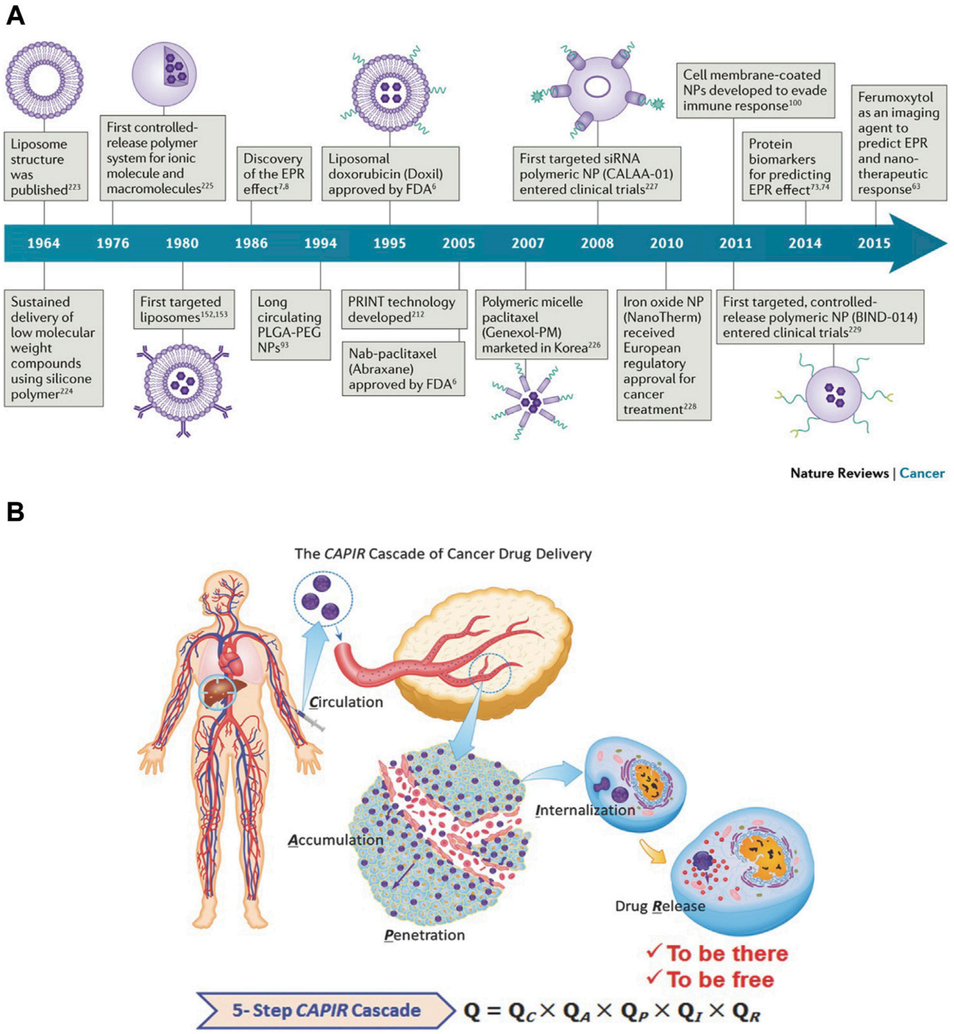

FIGURE 2
(A) Historical timeline of major developments in nano-drug delivery systems for cancer therapy (Shi et al., 2017). **(B)** A sketch of the CAPIR cascade of a nanomedicine to deliver a free drug into cancer cells (Sun et al., 2017).

instability in physiological conditions (Muthu and Feng, 2009), drug resistance (Siemer et al., 2021) and high toxicity (De Jong and Borm, 2008). Moreover, size effect of nanomedicine influences the pharmacokinetics of the drug, cellular uptake and penetration and accumulation in tumor tissues (Barua and Mitragotri, 2014). Besides, it can deliver tracer drugs and therapeutic drugs at the same time to realize the integration of tumor diagnosis and treatment (Jin et al., 2020b). Last but not least, co-delivery of multiple drugs or combined treatment with the second drug confers a synergistic antitumor therapeutic effect (Ma et al., 2013).

When it comes to the approaches to drug delivery *in vivo*, there are usually two ways that include passive and active targeting effects (Attia et al., 2019). On one hand, it is reported that size of NPs which range from approximately 40–400 nm is suitable to ensure long circulation time, enhanced accumulation in tumors with reduced renal clearance and is also known as enhanced permeation and retention (EPR) effect. Therefore, passive targeting is dependent on physiological features of tumor microenvironment (TME) like the abnormal vasculature, the surface charge of tumor cells, pH value and temperature (Shi et al., 2020; Wu, 2021). Although passive targeting has been widely developed and used, it is still faced numerous limitations such as the random targeting effects, which may result in insufficient drug diffusion into tumors. On the other hand, compared to passive targeting effects, active targeting effect could significantly increase the quality of delivery effects to target tumor cells. It can be achieved through the decoration of nano-drug carrier surfaces with ligands binding to receptors overexpressed onto tumor cells. Among the targeting ligands, folate, transferrin and epidermal growth factor receptors (EGFRs) have been widely used for the development of active targeting effect (Bertrand et al., 2014; Bazak et al., 2015).

2.1 Classification of nano-drug delivery systems

In the past few decades, nanotechnology has made major contributions to the oncology field. Nano-drug delivery systems have progressed several generations from liposomes to the discovery of EPR effect, nucleic acid nano-medicines (siRNA), targeted controlled release polymer nanoparticles, cell membrane coated nanoparticles, and nanoimaging agents, etc [Figure 2A, (Shi et al., 2017),]. According to the source of the materials, they can be divided into natural carriers and synthetic carriers. With regards to their composition, they can be divided into organic nano-carriers, inorganic nano-carriers and composite nano-carriers. Organic nanoparticles are made of organic materials, especially carriers based on lipids, viral capsids, polysaccharides or protein particles (Virlan et al., 2016). Inorganic nano-carriers include metal nanoparticles like gold or silver, ceramic nanoparticles, quantum dots (fluorescent semiconductor particles), and carbon particles (single-wall or double-wall carbon nanotubes) (Auffan et al., 2009). With the development of more novel nanocarriers, it may be possible further expand the clinical and translational applications of nanomedicine.

2.2 Systemic delivery of nano-medicine

After systemic administration, nanoparticles need to overcome multiple obstacles before entering the tumor cells to exert their therapeutic effects. At first, the nanoparticles in the blood circulation easily interact with plasma proteins and are taken up by the reticuloendothelial system (RES) (such as liver and spleen) (Nie, 2010). Therefore, the nanoparticles in circulation must first escape the RES and then should be enriched in the tumor tissue. Afterward, when the nanoparticles reach the tumor site, they also have to pass through two obstacles. Firstly, they need to be transported across the tumor blood vessels. Although leaky and tortuous tumor blood vessels allow nano-medicine enrichment, parietal cells such as pericytes and basement membranes limit the exudation of nano-medicine through openings in the capillary wall, thereby reducing the convective transport of nano-medicine. Secondly, the dense extracellular matrix (ECM), owing to its high osmotic pressure, inhibits the passive diffusion of nano-medicine. To conclude, the entire delivery process of nano-medicine after systemic administration can be summarized by "CAPIR": circulation, accumulation, penetration, internalization and release. Each step is independent and interconnected, involves a complicated process, and may affect the nanomedicine's ultimate antitumor efficacy [Figure 2B, (Sun et al., 2017)].

3 Synergistic anticancer immunotherapy

3.1 Classification of tumor immunotherapy

Tumor immunotherapy is a new type of treatment, which is different from conventional radiotherapy and chemotherapy. Different from killing tumor cells directly, it aims to activate the body's immune system and relies on the host's immune function to kill the tumor cells (Zolnik et al., 2010), which has strong specificity, remarkable curative effects and long-term effects. Therefore, it has received great attention in the field of cancer therapy. Based on clinical cancer immunotherapy strategies, it can be divided into five categories, including immune checkpoint inhibitors, tumor vaccines, cytokine therapies, adoptive cell transfer, and oncolytic virus therapies [Figure 3, (Zhang and Zhang, 2020)].

3.1.1 Immune checkpoint inhibitors

Immune checkpoint is a kind of immunosuppressive molecule, which plays a vital role in the maintenance of auto-immune tolerance and prevents normal tissues from being attacked by the immune system (Korman et al., 2022). However, during the development of cancers, tumor cells induce the high expression of immune checkpoint receptors through a variety of mechanisms to inhibit the function of T cells, thereby inhibiting the cytotoxic effect of the immune system and achieving tumor immune escape (Beatty and Gladney, 2015). Currently, the most widely used immune checkpoint inhibitors target the programmed death receptor-1 (PD-1), programmed death ligand-1 (PD-L1), cytotoxic T lymphocyte-associated antigen-4 (CTLA-4), lymphocyte activation gene-3 (LAG-3), which reactivate the tumoricidal effects of the immune system by interacting with the respective immune checkpoints to achieve antitumor immunotherapy (Franzin et al., 2020).

3.1.2 Tumor vaccines

As early as the end of the 19th century, William B. Coley, the father of tumor immunology, used the toxin secreted by Streptococcus to treat cancer and opened the door for tumor vaccines for the first time (McCarthy, 2006). Tumor vaccines use tumor antigens to enhance the ability of antigen-presenting cells (APCs), activate antigen-specific effects, and the tumoricidal effects of T cells. There is no specific way to classify tumor vaccines. According to the specific uses of the tumor vaccines,

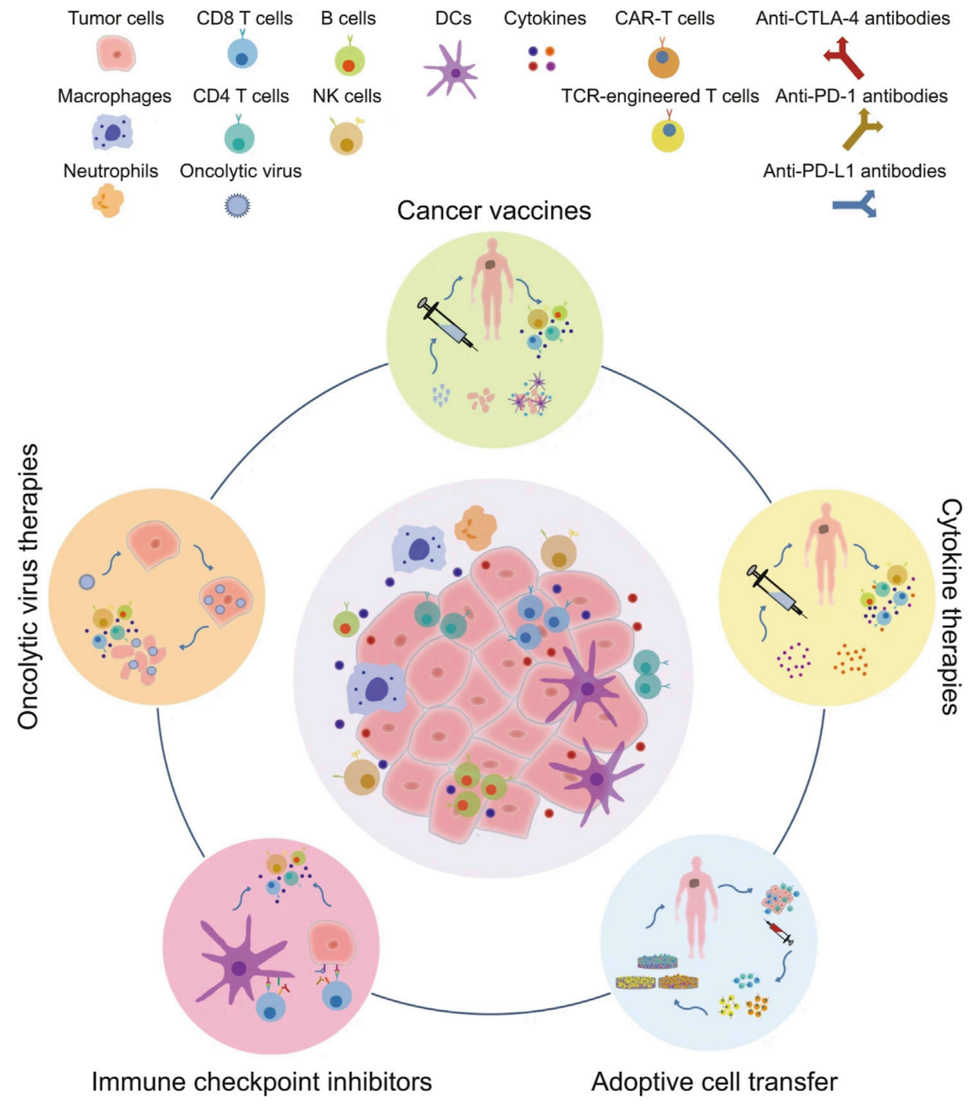

FIGURE 3
The major clinical categories of immunotherapy include oncolytic virus therapies, cancer vaccines, cytokine therapies, adoptive cell transfer, and immune checkpoint inhibitors (Zhang and Zhang, 2020).

they can be divided into two types: preventive vaccines (HBV, HPV) and personalized therapeutic vaccines (mRNA vaccine, DC vaccine) (Hollingsworth and Jansen, 2019). After the administration of the tumor vaccines, APCs present them to MHC II or MHC I and antigen-loaded DCs will migrate to lymph nodes to recruit and activate immune cells. Then activated B cells can promote tumor apoptosis through antibody-dependent cellular cytotoxicity and activated T cells can proliferate and differentiate into memory T cells or effector T cells. As a result, effector T cells will kill tumor cells directly or induce tumor cell apoptosis after traveling to TME. In 2010, the autologous DC-based prostate cancer vaccine Sipuleucel-T became the first human therapeutic cancer vaccine that was approved by the United States Food and Drug Administration (FDA) (Cheever and Higano, 2011).

3.1.3 Cytokine therapies

Cytokines are small, soluble signaling proteins with a short half-life, which initiate the immune response to external stimuli directly and rapidly (Conlon et al., 2019). They are important for the immune cells to kill tumor cells owing to their participation in nearly all cellular responses such as regulation of immune cell proliferation and differentiation. Interferon (IFN)-α was the first approved cytokine drug for tumor immunotherapy by the FDA in 1986 (Berraondo et al., 2019). Despite its advantages, cytokine therapy causes a variety of side effects and has a narrow therapeutic window, which limits its clinical use. Thus, cytokines-based immunotherapy regulates a complex network of signals with multipotent, multisource, multiterminal, and multimodal activity.

3.1.4 Adoptive cell transfer

Adoptive cell transfer (ACT) refers to the processing and modification of body's immune cells with the use of genetic engineering (Rosenberg et al., 2008). Herein, the immune cells are cultured and amplified *in vitro* to enhance their tumor-specific killing function. As a result, they are reinjected into the patient's body and ultimately kill the tumor cells. Compared with traditional surgical treatment, chemotherapy, or radiotherapy, immune cell therapy technology has remarkable advantages with regards to its curative effect, toxic and side effects, and tolerability. Clinically, adoptive immunotherapy includes tumor-infiltrating lymphocytes (TILs), T cell receptor (TCR) therapy, chimeric antigen receptor NK cell (CAR-NK) immunotherapy, and chimeric antigen receptor T cell (CAR-T) immunotherapy (Rohaan et al., 2019).

3.1.5 Oncolytic virus therapies

Oncolytic viruses (OVs) are viruses that can effectively infect and destroy cancer cells. It involves the generation of special oncolytic viruses through genetic modification of some weakly pathogenic viruses that exist in nature, and then use the inactivation or defects of the tumor suppressor genes in the target cells to selectively infect the tumor cells. Finally, the oncolytic viruses replicate to generate large numbers of viruses and eventually destroy the tumor cells (Chiocca and Rabkin, 2014). Furthermore, it can continue to stimulate an immune response and attract more immune cells for the sustained killing of the remnant cancer cells. Due to the characteristics of the oncolytic virus (Pol et al., 2016), this kind of immune therapy can be administered systemically or locally to treat primary and metastatic tumors. In 2015, the FDA approved T-VEC as the first oncolytic herpes virus (a modified herpes simplex virus) for the treatment of melanoma, and it is currently one of the most successful oncolytic viruses. Ribas et al. (2017) found that the combined use of the oncolytic virus drug (T-VEC) and the anti-PD-1 antibody (Keytruda) for melanoma treatment showed a tumor remission rate as high as 62%, of which 33% were complete remissions. Previous data showed that the remission rate of Keytruda single-drug therapy was 47%, and the complete remission rate was 14%. These data indicate that the combined administration of T-VEC and Keytruda can further enhance the potency of Keytruda.

3.2 Synergistic antitumor immunotherapy

Since several cancer patients show low response to single immunotherapy treatments, and some of the cancers have low immunogenicity along with tumor immunosuppressive microenvironment, the immunotherapies may not be efficacious against such tumors (Lv et al., 2022). Therefore, combination therapy is an alternative approach to overcome these problems. In addition to dual synergistic immunotherapy, an increasing number of studies are exploring the combination of immunotherapy with chemotherapy, radiotherapy, phototherapy, and targeted therapy in the clinic, which may achieve better antitumor efficacy than single immunotherapy administration (Perez-Gracia et al., 2009; Hagan et al., 2020; Liu et al., 2021; Zhao et al., 2021). Simultaneously, immunotherapy may also make up for the shortcomings of other antitumor treatment strategies, which may prevent the development of therapeutic resistance (Tan et al., 2020).

3.2.1 Synergistic immune checkpoint inhibition therapy

Unlike traditional and chemotherapy directly kill tumor cells, tumor immunotherapy aims to activate the body's immune system and relies on the autoimmune function to kill tumor cells. Among them, immune checkpoint inhibitors play an important role during the treatment process of tumor evasion and immune surveillance. However, the clinical tumor response to its separate treatment is still only less than 40%, which greatly limits its clinical application. Thus, the combined application of ICI may show a better tumor treatment effect by increasing tumor immunogenicity and response rate of ICI themselves. PD-1 inhibits T cell activation by binding to its ligand PD-L1 or PD-L2. When CTLA-4 binds to CD80 and CD86 on the surface of antigen-presenting cells, it inactivates the T cells. Competitive inhibition of PD-1 or CTLA-4 with antibodies blocks the above-mentioned mechanism, thereby enhancing the killing activity of T cells. The CTLA-4 pathway mainly acts on T cells interaction with APCs, which majorly affects the activation of T cells and the function of the effector cells. The PD-1 pathway mainly acts on the tumor cells and activated lymphocytes and reduces the extent of T cell activation and cytotoxicity. Both the above pathways can influence each other but are relatively independent (Buchbinder and Desai, 2016). Moreover, combination therapy of PD-1 with CTLA-4 inhibitors targeting the above pathways can make it feasible to reverse the cold/hot tumors. The immune escape mechanisms of hot tumors usually include the up-regulation of immune checkpoint molecules (e.g., PD-L1) recruitment of regulatory T cells (Treg), and loss of surface antigen expression, etc, but they still have a large number of tumor-infiltrating lymphocytes. As a result, this type of tumor often responds well to PD-1 inhibitors. On the contrary, cold tumors lack lymphocyte infiltration, PD-L1 expression, and the host innate immune recognition process during the immune escape, so they neither recruit effector T cells nor respond to PD-1 inhibitors. However, it was reported that when CTLA-4 inhibitors were applied to such cold tumors, $CD3^+/CD4+$ and $CD3^+/CD8+$ T cells could be recruited and even fully activated to increase the infiltration of lymphocytes in the tumor microenvironment and upregulate INF-γ, thereby up-regulating the expression of

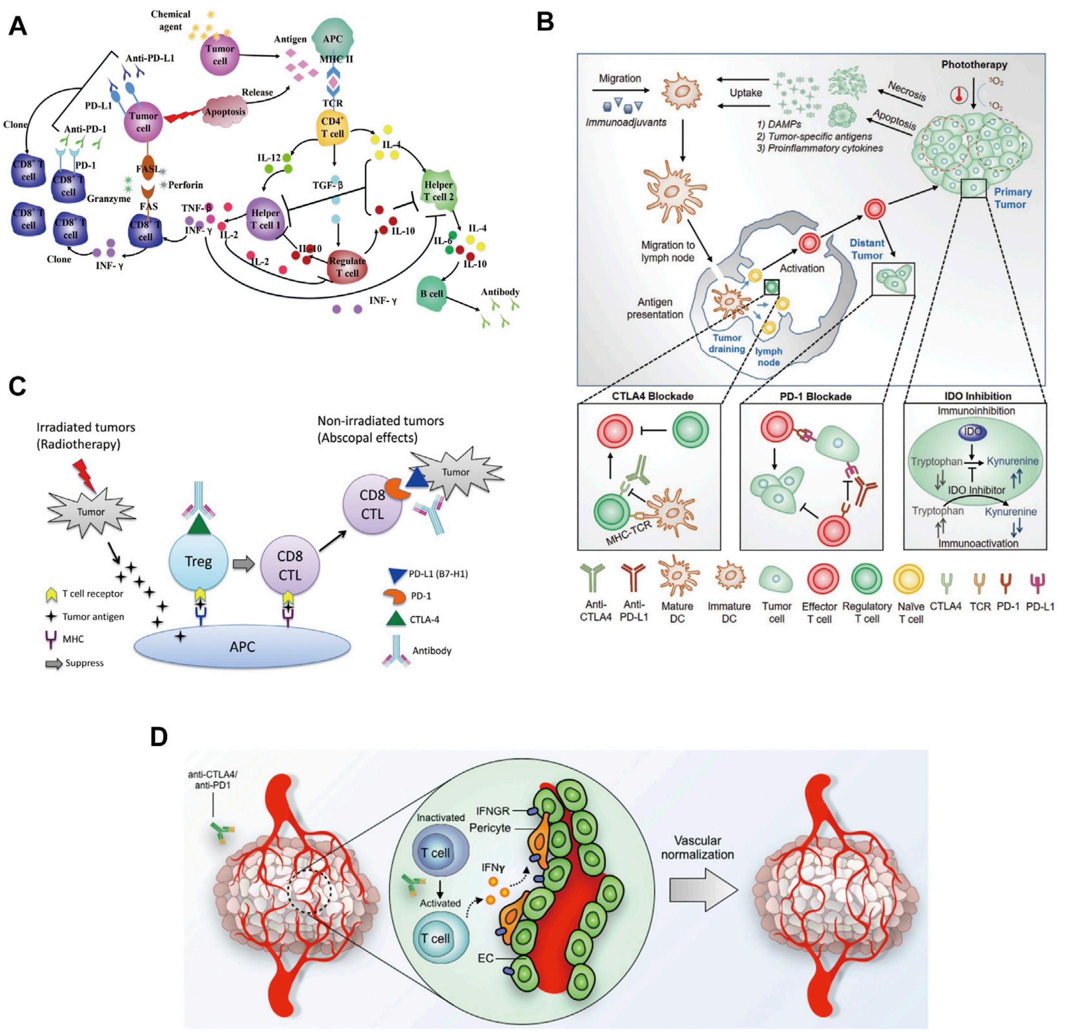

FIGURE 4
(A) Chemotherapeutic agents influence cytokines network in the antitumor immune system (Luo and Fu, 2016). **(B)** An overview of the combination of phototherapy and immunotherapy (Ng et al., 2018). **(C)** Potential mechanism of action of the combination of radiotherapy and immunotherapy (Mansfield et al., 2015). **(D)** Potential mechanism of immunotherapy-mediated tumor vascular normalization (Liu et al., 2019).

PD-L1 to resensitize the tumor cells to PD-1 inhibitors (Wei et al., 2017; Wu et al., 2019; Rupp et al., 2022). Therefore, the combined dual administration of CTLA-4 and PD-1 inhibitors may have a synergistic effect, or be effective in patients with negative expression of one ligand/receptor. Other combination therapies like LAG-3 and PD-L1 inhibitors are still under clinical trials, and the findings from these trials may further broaden the application of ICI in cancer treatment (Robert, 2021).

3.2.2 Synergistic combination of chemotherapy and cancer immunotherapy

The anti-tumor effects of chemotherapy combined with immunotherapy are multifaceted [Figure 4A, (Luo and Fu, 2016)]. Chemotherapy augments the effect of immunotherapy by enhancing tumor cell immunogenicity, suppressing immunosuppression, and inducing an antitumor immune response (e.g., immunogenic cell death, ICD). In addition, immunotherapy reverses the chemotherapy resistance of tumor cells, which improves the chemosensitivity of tumor cells and reduces their toxicity. In May 2017, the United States FDA accelerated the approval of the anti-PD-1 antibody pembrolizumab, pemetrexed and carboplatin for the first-line treatment of advanced or metastatic non-small cell lung cancer (NSCLC) (Qu et al., 2020). The results of the clinical trials showed that the group that received the combination of chemotherapy and immunotherapy had a significantly better objective remission rate (55% vs. 29%) and prolonged progression-free survival (PFS) (13.0 vs. 8.9 months) than the group that received the chemotherapy alone. At the 2021 American Society of Clinical Oncology (ASCO) annual meeting, the KEYNOTE-590 study that was presented was the first one reporting the international first-line application of anti-PD-1 antibody combined with cisplatin and 5-fluorouracil for the treatment of esophageal cancer. Moreover, the published results from a subgroup analysis in China were completely consistent with the results of the global study. Regardless of the expression of PD-L1, immunotherapy combined with chemotherapy may bring survival benefits for unresectable locally advanced or metastatic esophageal cancer patients receiving the first-line treatment (Kato et al., 2019; Li et al., 2021a). This result had a very significant and far-reaching impact on the treatment of esophageal cancer. At present, there are still other treatment strategies combining chemotherapy and immunotherapy in the clinic, However, further clinical evidence is needed to understand if those strategies can produce similar therapeutic effects or can be used for the treatment of multiple cancer types.

3.2.3 Synergistic combination of phototherapy and cancer immunotherapy

Phototherapy is a promising alternative approach that offers an elegant solution to eradicate tumors through the simple application of light irradiation (Wang et al., 2021). Meanwhile, it is also associated with antitumor immune response by inducing immunogenic cell death and enhancing the antitumor immunity. Phototherapy is comprised of photothermal and photodynamic therapy. In general, photothermal therapy (PTT) leads to cell death by necrosis (Hou et al., 2020), while photodynamic therapy (PDT) typically induces cellular apoptosis. Herein, the combination of phototherapy with cancer immunotherapy has been demonstrated to promote synergistic outcomes, promote cancer regression, and even induce immunologic memory [Figure 4B, (Ng et al., 2018)]. With promising discoveries in combination therapeutic approaches, it has been possible to achieve higher levels of proinflammatory cytokines, improved migration of dendritic cells, and an increased ratio of tumor-infiltrating cytotoxic T cells against regulatory T cells, making their clinical applications lucrative. Chen et al. reported that photothermal therapy could promote tumor infiltration of CAR-T cells and potentiate its antitumor activity (Chen et al., 2019). Desmoplastic structures and immunosuppressive microenvironment usually accounted for the reduced efficacy of CAR-T cells in solid tumors. Mild hyperthermia of the tumors reduced its compact structure and interstitial fluid pressure, increased blood perfusion, released antigens, and promoted the recruitment of endogenous immune cells. Hence, the combination of mild photothermal therapy with the adoptive transfer of CAR-T cells could potentially increase the therapeutic index of these cells in solid tumors. It was reported that infusing chondroitin sulfate proteoglycan-4 (CSPG4)-specific CAR-T cells into NOD SCID gamma mice engrafted with the human melanoma WM115 cells showed superior antitumor activity following photothermal ablation of the tumor. These findings suggested that photothermal therapy facilitated the accumulation and effector function of CAR-T cells within solid tumors. But future advances involving the combination of phototherapies with other strategies remain to be explored, which may help overcome the immunosuppressive environment at the tumor site (Li et al., 2021b; Huang et al., 2021c).

3.2.4 Synergistic combination of radiotherapy and cancer immunotherapy

The radiotherapy mechanism uses high-energy particles or waves such as X-rays to destroy or damage the cancer cells (Baskar et al., 2012). Radiotherapy causes radiation damage to the tumor and its surrounding normal tissues and cells (Barnett et al., 2009). Both normal and tumor cells can repair this damage, but normal cells are more capable of repairing radiation damage than tumors and these damages prevent cancer cells from growing and proliferating and ultimately killing them. Unlike chemotherapy, which exposes the whole body to anticancer agents, radiotherapy is usually localized to the tumor site. In most cases, it only targets and affects one part of the body, which is the treated area (Formenti and Demaria, 2009). In the PACIFIC study, durvalumab (10 mg/kg) was used for consolidation therapy in addition to radiotherapy and chemotherapy for patients with stage III NSCLC (non-small cell lung cancer) (Antonia et al., 2017). Compared with the placebo group, the median progression-free survival (mPFS) was significantly prolonged (16.8 vs. 5.6 months). But, so far, most of the studies reporting on radiotherapy combined with immune checkpoint inhibition are still retrospective studies or small group studies. A better strategy for the combination of radiotherapy and immunotherapy needs to be developed and verified by further clinical trials [Figure 4C, (Mansfield et al., 2015)].

3.2.5 Synergistic combination of vascular targeted therapy and cancer immunotherapy

Anti-angiogenesis therapy is one of the standard treatments for a variety of solid tumors (such as non-small cell lung cancer, breast cancer, colorectal cancer, etc.) in the clinic. Compared with general molecular targeting strategies, it can only be selectively administered based on specific biomarkers (Al-Abd et al., 2017). It is used for specific tumor classification, which is suitable for a wider group of patients. For liver cancer treatment, there is no specific single target that could serve as a biomarker and treatment with vascular targeted therapy could induce the production of many drug-resistant enzymes like phosphorylated extracellular signal-regulated kinase in these patients (Llovet et al., 2021). Therefore, multi-targeted drugs are needed for the treatment of liver cancer. Clinically approved drugs such as sorafenib which directly target the VEGF signaling pathway, act on multiple targets at the same time and show an anti-angiogenic effect through multiple mechanisms. Unfortunately, the actual effect of this treatment is not always satisfactory (Wilhelm et al., 2008). On the other hand, although the survival of liver cancer patients treated with PD-1 inhibitors as a single agent showed was prolonged, no statistically significant results were observed. Since single drugs tend to have a beneficial effect, there may be synergistic therapeutic combination strategies. Furthermore, normalizing the tumor vasculature has been shown to improve the efficacy of cancer immunotherapies, and emerging studies also suggest that enhanced immune stimulation, in turn, improves tumor vascular normalization, forming a mutually supportive loop [Figure 4D, (Liu et al., 2019)]. In the clinical study named IMbrave150, a total of 501 patients were enrolled globally. The patients received Atezolizumab (PD-L1 monoclonal antibody) and Bevacizumab (targeted for VEGF), simultaneously. The results showed that the median progression-free survival of the combined group was 6.8 months, and that of the sorafenib group was 4.3 months, reducing the risk of progression by 41%. Therefore, the combination of vascular targeted therapy with immunotherapy may bring revolutionary benefits to liver cancer patients (Finn et al., 2020). At the same time, related studies have shown that Vemurafenib (BRAF inhibitor) combined with Cobimetinib (MEK1/2 inhibitor) and Atezolizumab could significantly prolong the progression-free survival (PFS) of melanoma patients (Subbiah et al., 2020). Thus, the immune mediated vascular normalization opens up the possibility for identifying new cancer treatment strategies combining vascular targeting agents and immunotherapies.

4 Nano-drug delivery systems for synergistic antitumor immunotherapies

Clinically, synergistic antitumor immunotherapy is gaining wide attention nowadays. However, there are still many difficulties and challenges in controlling the proportion of the combined drugs, synergistic onset time, and adverse reactions (Senapati et al., 2018). Therefore, the rational design of the nano-delivery system to construct a synergistic combination treatment strategy is also conducive to promoting the development of personalized treatment and precision medicine. The co-delivery of immunotherapeutic drugs and other therapeutic drugs such as photosensitizers, chemotherapeutics and immune adjuvants have plenty of advantages, such as controlling the proportion of the combined drugs, prolonging the blood circulation time of drugs, realizing the targeted delivery of drugs at the tumor site and improving the tumor microenvironment (Huang et al., 2021d; Yang et al., 2021). But, for different combination regimens, specific nano-drug delivery systems are often required to meet the requirements of delivery and improve therapeutic efficacy (Patra et al., 2018)

4.1 Nano-drug delivery systems for combination of multiple immunotherapy strategies

In recent years, tumor immunotherapy, especially immune checkpoint blocking therapy, has rapidly advanced and is profoundly changing the treatment strategy for malignant tumors. Monoclonal antibodies have been widely used in tumor immunotherapy, but they suffer from drawbacks such as immune escape and drug resistance, which influence their anti-tumor efficacy in the clinic (Weiner et al., 2010). When compared with monoclonal antibodies, bispecific antibodies (BsAb) play a unique role in mediating the killing of tumor cells by the immune cells through their dual target signal blocking mechanism, which effectively prevents tumor cell drug resistance (Brinkmann and Kontermann, 2017). At the same time, the BsAb has stronger specificity, targeting ability and reduced off-target toxicity. However, ensuring the stability of BsAb antibodies, balancing the expression of the two antibodies and exploring an optimal format of the hinge region remain the major challenges for the development of novel therapeutic BsAbs. Therefore, the nanoplatform technology serves as an important method for the development of bispecific antibodies. Because the Fc segment of the therapeutic monoclonal antibody drugs in preclinical trials is highly consistent, Jiang et al. (2021) innovatively proposed the use of antibodies [anti-IgG (Fc specific) antibody, αFc] that can specifically recognize the Fc segment of antibodies to construct a universal antibody immobilization platform [Figures 5A–C, (Jiang et al., 2021),], through simple physical mixing of a new type of bispecific nanobody named "immunomodulating nano-adaptor." This nano-adaptor could be prepared conveniently, efficiently and controllably to realize the multivalency, bispecificity, and multifunctionality of the monoclonal antibody. Compared with conventional monoclonal antibody drugs, the nano-adaptor not only regulates the function of immune cells but also significantly enhances the interaction of immune cells (including T cells, macrophages, natural killer cells, etc.) with the tumor cells, effectively increasing the antitumor effects of the cloned antibody drugs. Nano-drug delivery system is an important technique that combines multiple immunotherapies and prevents the tumor immune escape arising from the single immune treatment. Furthermore, the co-delivery of multiple antibodies may induce further synergistic effects, similar to bi-specific antibodies and multi-specific antibodies, which is a highly promising strategy (Parker et al., 2019; Bai et al., 2020).

Nano-drug delivery systems for the combination of chemotherapy and cancer immunotherapy.

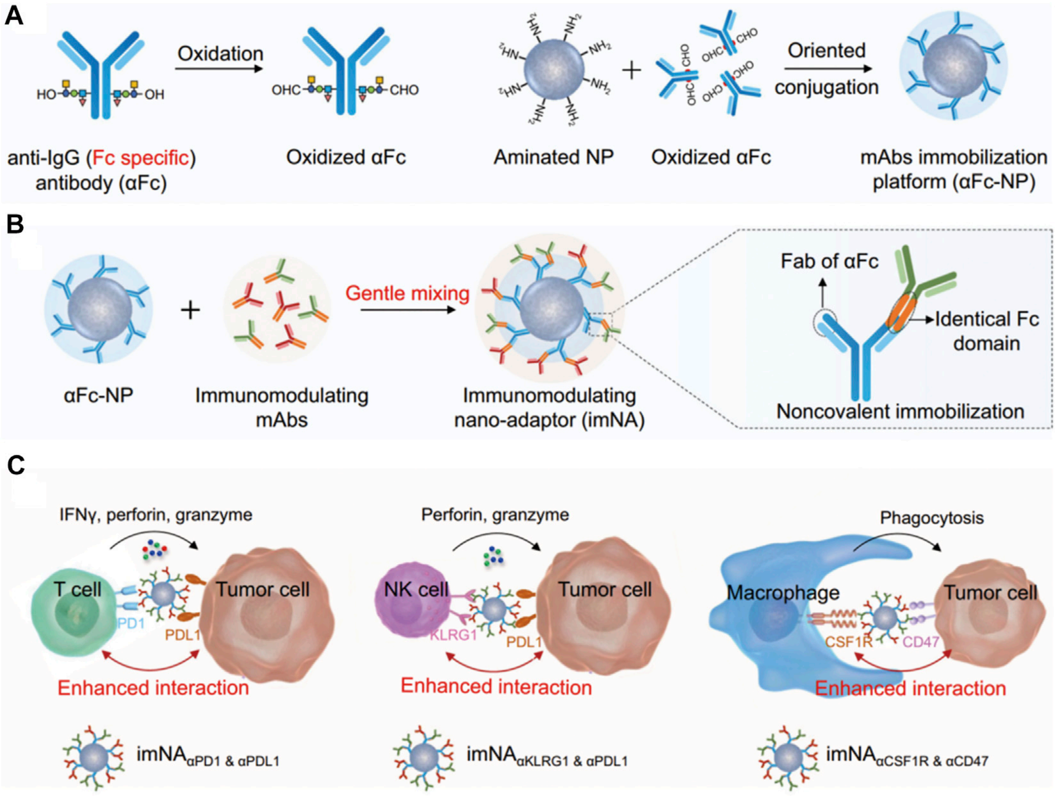

FIGURE 5
(A–C) Schematic illustrating the design of imNAs and their potential to improve antibody-based cancer immunotherapy (Jiang et al., 2021).

The strategy of combining immunotherapy with chemotherapy is a classic approach for antitumor therapy. The nano drug delivery system used for its co-delivery needs to be able to load the antibody drugs along with the small molecule chemotherapeutic drugs to achieve the controlled release of both the drugs at the tumor site and improve both the pharmacokinetics and biodistribution of these drugs (Din et al., 2017; Senapati et al., 2018). These carriers include liposomes (Zununi Vahed et al., 2017), polymer micelles (Krishnamurthy et al., 2015), inorganic silica nanoparticles (Chen et al., 2014), metal-organic framework materials and so on (Ding et al., 2020). Triple-negative breast cancer (TNBC) is an aggressive malignancy with a high recurrence rate and poor outcomes in the clinic. Because tumor-associated macrophages (TAMs) were found to be enriched in TNBC, Chen *et al.* (2021) designed and synthesized a matrix metalloprotease 2 (MMP2) responsive integrated strategy [Figures 6A,B, (Chen et al., 2021). It could deliver paclitaxel (PTX) and anti-CD47 (aCD47) using detachable immune liposomes (ILips). In the TNBC microenvironment, the "two-in-one" ILips facilitated the MMP2-responsive release of aCD47 to efficiently polarize the M2 macrophages toward the M1 phenotype to enhance the phagocytosis of tumor cells and activate the systemic T-cell immune response. Together with the immune effect, the detached PTX-loaded liposomes were internalized by the MDA-MB-231 cells to synergistically inhibit tumor cell proliferation and metastasis. In the TNBC-bearing mouse model, PTX-loaded ILips demonstrated superior antitumor efficacy and inhibited tumor recurrence. This integrated strategy represented a promising approach to synchronously enhance the immune response and tumor-killing effects, improving the therapeutic efficacy against TNBC. In addition, researchers also tried to achieve immunochemotherapeutic therapy by designing different ways to administer chemical drugs and immunotherapy through nano-drug delivery systems. Zhao et al. (2021) used poly (L-Aspartic acid)-*b*-poly (ethylene glycol) loaded with combretastatin A4 through ester bond. It could be self-assembled to form nanomicelles (CA4-NPs), which were aimed to significantly disrupt new blood vessel formation in the tumor tissues for targeted liver cancer therapy [Figure 6C, (Zhao et al., 2021)]. Here, CA4-NPs were mainly distributed at the tumor site because of the triple targeting effects, namely EPR effect, acid-sensitive (pH = 5.5) effect in the tumor microenvironment, and good selectivity of CA4 for the central tumor blood vessel. Considering that CA4-NPs might induce severe hypoxic conditions resulting in the high expression of

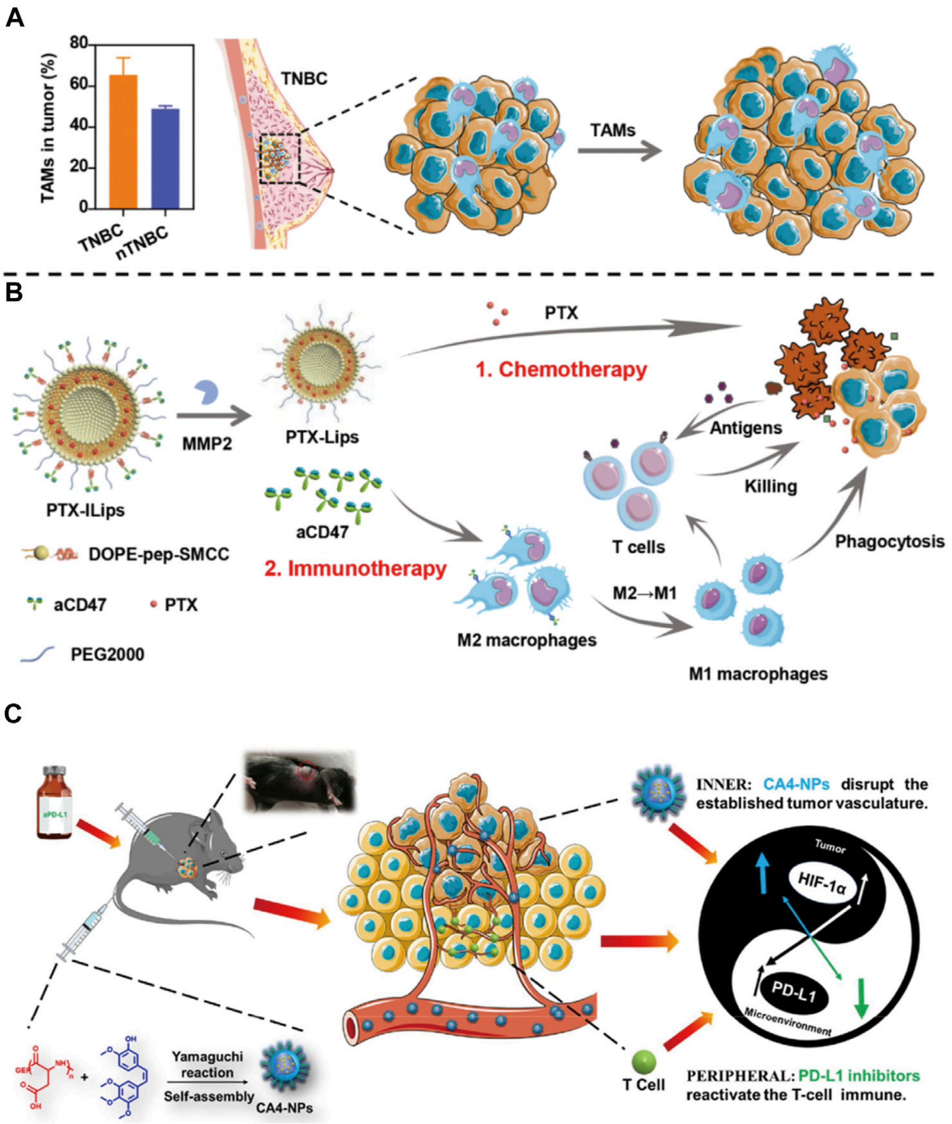

Scheme 1 CA4-NPs arrest the tumor by disrupting the established central tumor vasculature, which can induce severe hypoxic conditions and high expression of HIF-1α in tumor tissues. The hypoxic condition can increase the expression of PD-L1 in tumor microenvironment, so the PD-L1 inhibitors can release the 'immune brake' to reactivate the T-cell immune response to the tumor effect in the peripheral area

FIGURE 6
(A) Tumor-associated macrophages (TAMs) promote tumor growth in triple-negative breast cancer (TNBC) and **(B)** PTX-ILips designed for the enhanced efficacy of immunochemotherapy against TNBC (Chen et al., 2021). **(C)** Mechanism of action of the combination of CA4-NPs and aPD-L1 (Zhao et al., 2021).

HIF-1α by the tumor tissues, which could induce the overexpression of PD-L1, the researchers also used an anti-PD-L1 antibody (aPD-L1) to prevent immunosuppression. This way of complementary combination was able to achieve an ideal therapeutic effect at tumor sites where CA4-NPs and aPD-L1 could respond to the inner area and peripheral area, respectively. As a result, a significant decrease in tumor volume and weight were observed in the combination group that received CA4-NPs and aPD-L1 compared with CA4-NPs or aPD-L1 monotherapy in subcutaneous Hepa1-6 hepatic tumor models.

Overall, in recent years, benefiting from the results of a large number of clinical trials of immunotherapy combined with chemotherapy, this kind of strategy has become the first-line treatment regimen for many cancers, including non-small cell lung cancer, small cell lung cancer, head and neck cancer, breast cancer, etc (Salas-Benito et al., 2021). The application of nano-delivery systems in combination treatment strategies can further improve the effect of antitumor therapies, and enable the development of further therapies combining immunotherapy and chemotherapy.

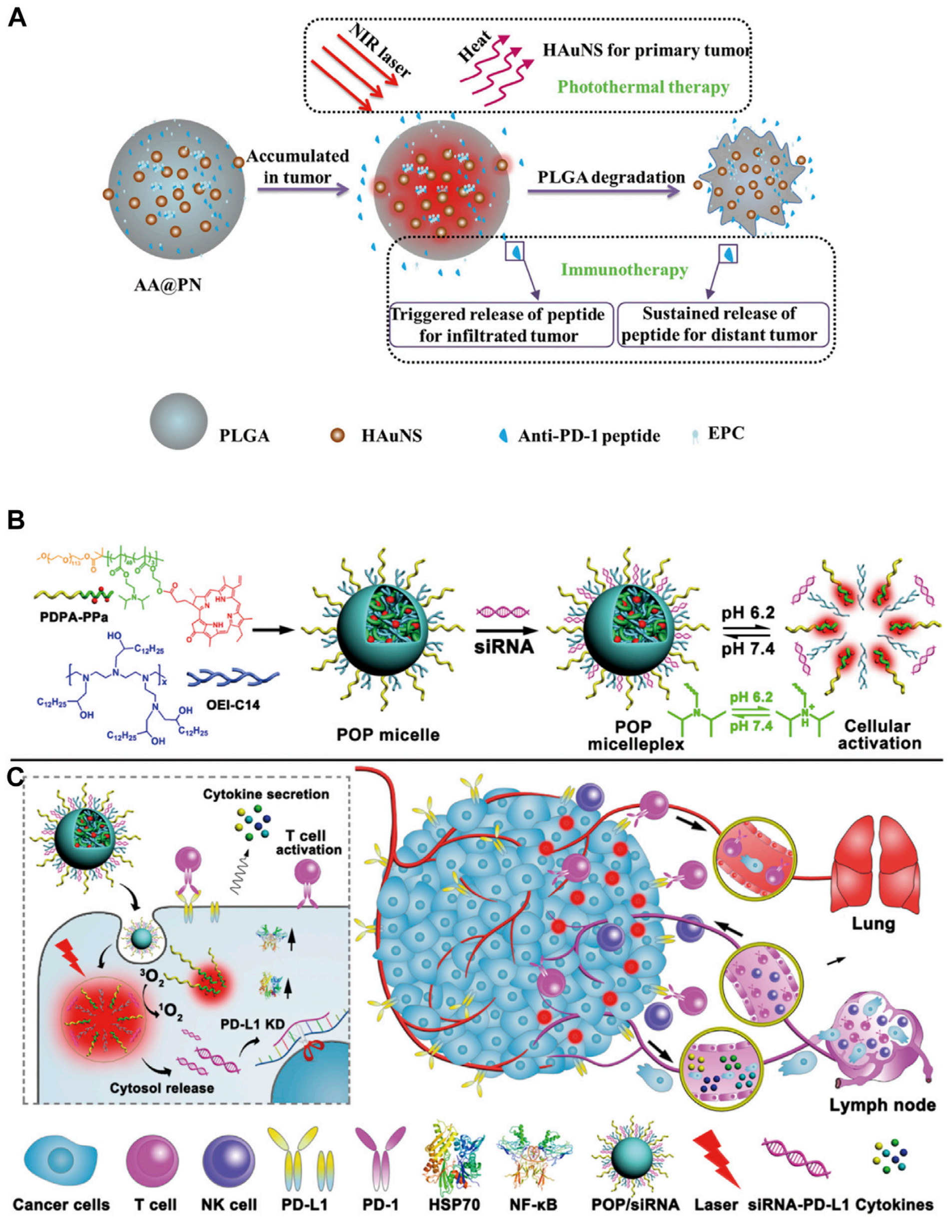

FIGURE 7
(A) Scheme showing the preparation and structure of AA@PN as well as its combined therapeutic modalities (Luo et al., 2018). **(B,C)** Cartoon schematic of POP–PD-L1 micelleplex mediated photodynamic cancer immunotherapy (Wang et al., 2016).

4.2 Nano-drug delivery systems for combined photothermal therapy and cancer immunotherapy

Nano drug delivery systems used for combined immunotherapy and photothermal therapy mostly contain nanomaterials with near-infrared photothermal conversion function, including inorganic materials such as gold (Liu et al., 2018), copper sulfide (Guo et al., 2014), organic materials such as heptamethine (ICG, IR780, IR820) (Alves et al., 2022), and some carbon quantum dots (Zhang et al., 2018b). A new strategy was proposed by Luo *et al.* (2018) that combined PD-1 blockers with photothermal ablation for treating malignant tumors by co-encapsulating anti-PD-1 peptide and hollow gold nanoshell into biodegradable PLGA [Figure 7A, (Luo et al., 2018),]. The results showed that the slow and continuous release of anti-PD-L1 antibodies from PLGA could be achieved from 0 to 40 days, and this release was easily accelerated by illumination with a near-infrared (NIR) laser. Overall, a clear

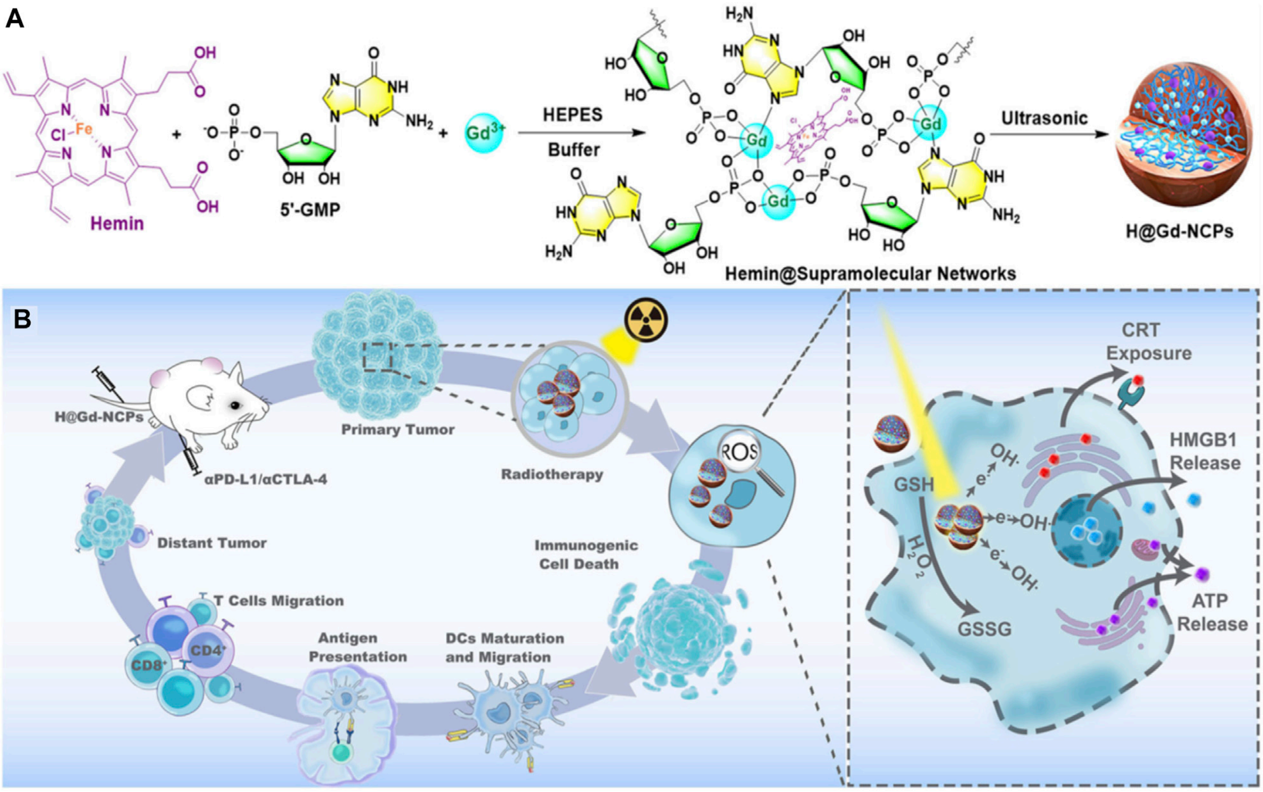

FIGURE 8
(A,B) The preparation and mechanism of action of H@Gd-NCPs (Huang et al., 2021c).

killing effect on distant tumor cells was observed after the combination therapy, reflecting the activation of the antitumor immune response. The use of nano-systems to deliver photothermal materials was conducive to its improved long-term photothermal effects at the tumor site. Meanwhile, continuous immune responses were triggered by immunogenic cell death to enhance the antitumor immunity, which had a synergistic therapeutic effect with immunotherapy.

In the second kind of phototherapy, photodynamic therapy, the excited photosensitizer releases reactive oxygen species in the tumor tissues to induce tumor cell apoptosis and it is also associated with anti-tumor immune response. However, the immunosuppressive tumor microenvironment limits the immune response induced by PDT. Thus, it is necessary to combine PDT with immune checkpoint inhibitors and immunoadjuvant therapy for synergistic treatment of the tumors. Moreover, PDT also requires photosensitizers to accumulate at the tumor site, therefore, the nano delivery systems are required to deliver them. Some nano-delivery materials are inherently photosensitive. Therefore, the photosensitizer can be loaded into the nano drug delivery system, or the carrier material with photosensitivity can be used to prepare the nanoparticles. At present, the photosensitizers commonly used for combination with immunotherapy include ICG (Shirata et al., 2017), Ce6 (Li et al., 2014), temoporfin (Tan et al., 2010), pheophorbide A (PPa) (Tang et al., 2010), etc. In the study from Wang *et al.* (2016), they demonstrated that PDT-mediated cancer immunotherapy could be augmented by PD-L1 knockdown in the tumor cells [Figures 7B,C, (Wang et al., 2016)]. Hence, they designed a versatile micelleplex by integrating an acid-activatable cationic micelle, PPa, and small interfering RNA (siRNA). The micelleplex was inert at physiological pH conditions and was activated only upon internalization into the acidic endocytic vesicles of the tumor cells for fluorescence imaging and PDT. These results showed that compared to PDT alone, the combination of PDT and siRNA showed significantly enhanced efficacy for inhibiting tumor growth and distant metastasis in a B16-F10 melanoma xenograft tumor model. It has been suggested that acid-activatable micelleplexes utilizing PDT-induced cancer immunotherapy were more effective when combined with siRNA-mediated PD-L1 blockade, which could provide a general strategy for enhancing the therapeutic efficacy of PDT.

Nano-drug delivery systems for combined radiotherapy and cancer immunotherapy.

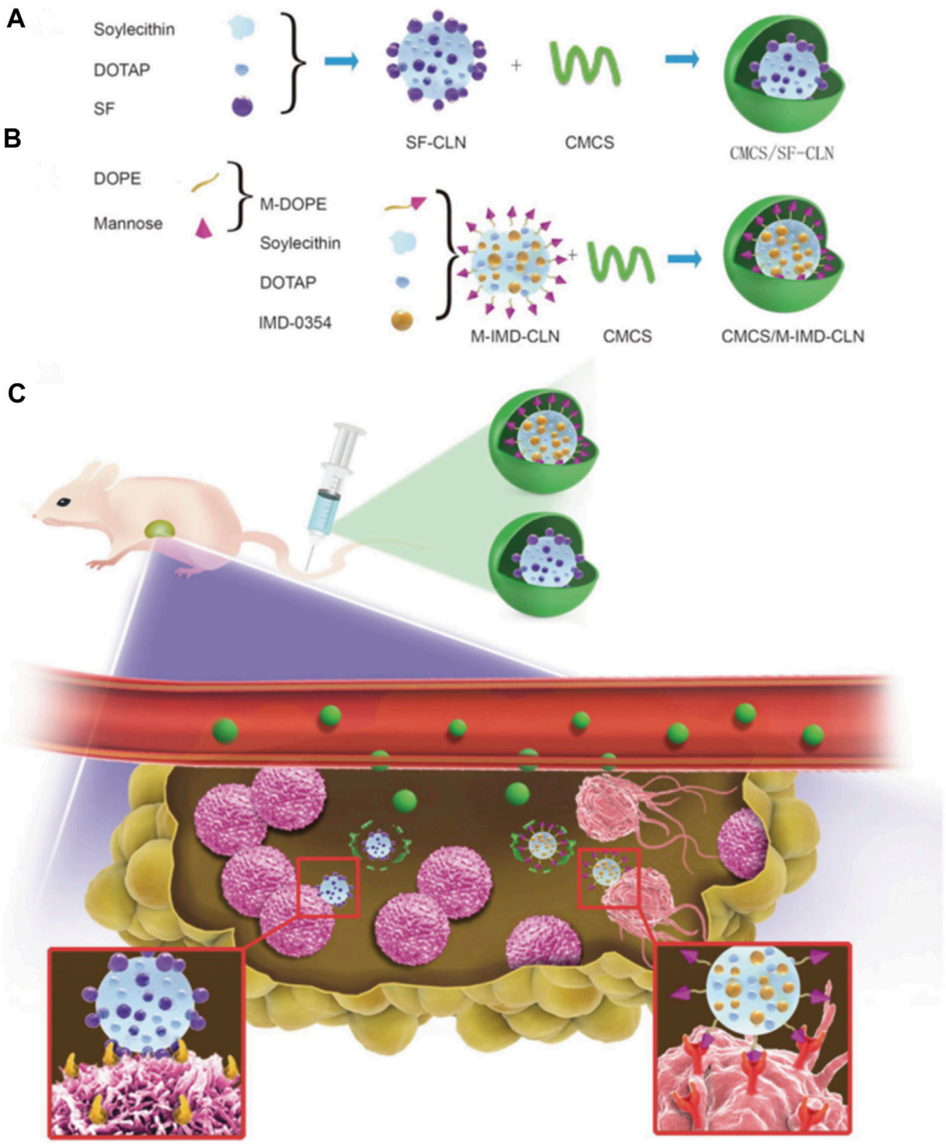

FIGURE 9
(A–C) Scheme of twin-like core-shell nanoparticles (CMCS/SF-CLN + CMCS/M-IMD-CLN) for synchronous biodistribution and targeted delivery to enhance chemo-immunotherapy (Wang et al., 2019).

Radiotherapy is currently one of the most widely used cancer treatment methods in the clinic, but poor specificity of traditional *in vivo* radiotherapy, short-term effects in the tumor tissue and side effects on normal tissues, limit its wide application. Some multifunctional nanomaterials themselves can be used as radiotherapy sensitizing agents and radiation dose enhancers to effectively improve the efficacy of radiotherapy against the tumor lesions, thereby overcoming the dose tolerance constraints of healthy tissues and enhancing radiosensitization (Yu et al., 2022). On the other hand, nanomaterials can be used as drug carriers to load different kinds of drugs to help regulate signaling pathways and cell cycles, inhibit DNA repair mechanisms, indirectly promote tumor cell apoptosis or selectively kill tumor cells and modulate the tumor microenvironment, which could improve the overall radiotherapy sensitivity (Kwatra et al., 2013). Huang et al. (2021a) constructed nano-scale gadolinium-based coordination polymers (H@Gd-NCPs) by combining gadolinium (Gd3+), 5′-guanylic acid (5′-GMP) and one peroxidase activity agent-Hemin [Figures 8A,B, (Huang et al., 2021b)]. Due to the existence of "Gadolinium," it could not only be used as an excellent nuclear magnetic contrast agent, but also as a high-order atom Gd to effectively deposit X-rays at a relatively low dose of radiotherapy, and increase the effect of local radiotherapy. Moreover, Hemin encapsulated within H@Gd-

NCPs could enhance the peroxidase-like properties to utilize the overexpressed H_2O_2 in the tumor microenvironment, leading to GSH depletion. The integration of ROS enhancement and GSH depletion eventually amplifies irradiation-mediated oxidative stress and induces ICD.

Nano-drug delivery systems for the combination of targeted therapy with cancer immunotherapy.

Based on the constantly changing anti-angiogenesis mechanisms and related targets, researchers have shifted from solely focusing on vascular endothelial cells and other components of the blood vessel itself to the components of tumor extracellular matrix (such as collagen, hyaluronic acid), tumor-related fibroblasts cells, immune cells and stem cells in targeted tumor treatment area (Richards et al., 2010; Henke et al., 2019; Baghban et al., 2020). In addition, it is also possible to explore further combination treatment strategies of angiogenesis targeted therapy with other therapeutic methods such as immunotherapy, for clinical application. During the process of developing combined targeted therapies, researchers found that nano-delivery systems can exert their unique synergistic effects. In addition to the characteristics of long circulation and good tumor site permeability to improve the delivery efficiency, they can also integrate various functional components to actively target the tumor blood vessels, improve hypoxia within the TME, and regulate immunity, resulting in a "cocktail effect" (Abou Khouzam et al., 2021; Janji and Chouaib, 2022). Tumor-associated macrophage (TAM)-based immunotherapy has been presented as a promising strategy for cancer therapy (Kumari and Choi, 2022). Therefore, the combination of TAM-based immunotherapy with sorafenib (SF), one of the most important multikinase targeted inhibitors, may be more effective for treating hepatocellular carcinoma (HCC). In a previous study from Wang *et al.* (2019), the researchers designed and synthesized twin-like core-shell nanoparticles (TCN) for synchronous biodistribution and separated cell-targeted delivery of SF and TAM re-polarization agents IMD-0354, to cancer cells to enhance tumor-localized chemo-immunotherapy [Figure 9, (Wang et al., 2019)]. The analysis of the antitumor efficiency *in vivo* and phenotypic analysis of the TAMs in the tumor tissues showed that the combination therapy group exhibited superior synergistic antitumor efficacy and M2-type TAM polarization ability as compared with the SF mono-therapy group in Hepa1-6 tumor-bearing mice. Consequently, TCN enabled the co-administration of the drug combination and served as a nano-drug delivery system, and showed great potential for application in tumor targeted-immunotherapy in the clinic.

5 Conclusion

To conclude, although cancer immunotherapy has garnered wide attention clinically, it still suffers from several limitations such as generating immune tolerance and escape, immune side effects and poor tumor targeting, etc. The application of nano-drug delivery systems may significantly alleviate the above problems by enhancing the stability and lengthening the circulation time, which is beneficial for cellular uptake to stimulate the antitumor immune response. An increasing number of studies have revealed that the combined treatment with nano-immunotherapy had more advantages, such as further improvement in the therapeutic efficacy, reduced side effects, reduced immune tolerance and escape. However, such treatment strategies also suffer from different limitations such as the toxic and side effects mediated by the nano-drug carrier itself during the process of treatment *in vivo*. Besides, it is reported that although a large amount of anti-tumor studies showed encouraging efficacies in animal models, the clinical and translational application of nano-drug delivery systems for synergistic tumor immunotherapy is still in progress and many issues still need to be addressed. We believe that further breakthroughs and discoveries will appear in the tumor immune synergistic therapy with nano-drug delivery systems, which may help expand their clinical applications in the future.

Author contributions

BZ and LX wrote the original draft; YK, WW, TW, and YZ reviewed and edited the manuscript; XZ, ZD, and YC supervised the study and acquired funding for the same. All authors approved the final version of this manuscript.

Funding

The work was supported by the Natural Science Foundation of Jiangsu Province (BK20220299).

Conflict of interest

The authors declare that the research was conducted in the absence of any commercial or financial relationships that could be construed as a potential conflict of interest.

Publisher's note

References

Abou Khouzam, R., Brodaczewska, K., Filipiak, A., Zeinelabdin, N. A., Buart, S., Szczylik, C., et al. (2021). Tumor hypoxia regulates immune escape/invasion: Influence on angiogenesis and potential impact of hypoxic biomarkers on cancer therapies. *Front. Immunol.* 11, 613114. doi:10.3389/fimmu.2020.613114

Al-Abd, A. M., Alamoudi, A. J., Abdel-Naim, A. B., Neamatallah, T. A., and Ashour, O. M. (2017). Anti-angiogenic agents for the treatment of solid tumors: Potential pathways, therapy and current strategies-A review. *J. Adv. Res.* 8 (6), 591–605. doi:10.1016/j.jare.2017.06.006

Alves, C. G., Lima-Sousa, R., Melo, B. L., Moreira, A. F., Correia, I. J., and de Melo-Diogo, D. (2022). Heptamethine cyanine-loaded nanomaterials for cancer immuno-photothermal/photodynamic therapy: A review. *Pharmaceutics* 14 (5), 1015. doi:10.3390/pharmaceutics14051015

Antonia, S. J., Villegas, A., Daniel, D., Vicente, D., Murakami, S., Hui, R., et al. (2017). Durvalumab after chemoradiotherapy in stage III non–small-cell lung cancer. *N. Engl. J. Med.* 377 (20), 1919–1929. doi:10.1056/NEJMoa1709937

Attia, M. F., Anton, N., Wallyn, J., Omran, Z., and Vandamme, T. F. (2019). An overview of active and passive targeting strategies to improve the nanocarriers efficiency to tumour sites. *J. Pharm. Pharmacol.* 71 (8), 1185–1198. doi:10.1111/jphp.13098

Auffan, M., Rose, J., Bottero, J.-Y., Lowry, G. V., Jolivet, J.-P., and Wiesner, M. R. (2009). Towards a definition of inorganic nanoparticles from an environmental, health and safety perspective. *Nat. Nanotechnol.* 4 (10), 634–641. doi:10.1038/nnano.2009.242

Bagchi, S., Yuan, R., and Engleman, E. G. (2021). Immune checkpoint inhibitors for the treatment of cancer: Clinical impact and mechanisms of response and resistance. *Annu. Rev. Pathol. Mech. Dis.* 16, 223–249. doi:10.1146/annurev-pathol-042020-042741

Baghban, R., Roshangar, L., Jahanban-Esfahlan, R., Seidi, K., Ebrahimi-Kalan, A., Jaymand, M., et al. (2020). Tumor microenvironment complexity and therapeutic implications at a glance. *Cell Commun. Signal.* 18 (1), 59. doi:10.1186/s12964-020-0530-4

Bai, C., Hu, P., Zhang, W., Song, L., Liu, D., Chen, Y., et al. (2020). Modular design of Bi-specific nanoplatform engaged in malignant lymphoma immunotherapy. *Nanoscale* 12 (35), 18418–18428. doi:10.1039/D0NR04450D

Barnett, G. C., West, C. M., Dunning, A. M., Elliott, R. M., Coles, C. E., Pharoah, P. D., et al. (2009). Normal tissue reactions to radiotherapy: Towards tailoring treatment dose by genotype. *Nat. Rev. Cancer* 9 (2), 134–142. doi:10.1038/nrc2587

Barua, S., and Mitragotri, S. (2014). Challenges associated with penetration of nanoparticles across cell and tissue barriers: A review of current status and future prospects. *Nano Today* 9 (2), 223–243. doi:10.1016/j.nantod.2014.04.008

Baskar, R., Lee, K. A., Yeo, R., and Yeoh, K. W. (2012). Cancer and radiation therapy: Current advances and future directions. *Int. J. Med. Sci.* 9 (3), 193–199. doi:10.7150/ijms.3635

Bauer, T. A., Horvat, N. K., Marques, O., Chocarro, S., Mertens, C., Colucci, S., et al. (2021). Core cross-linked polymeric micelles for specific iron delivery: Inducing sterile inflammation in macrophages. *Adv. Healthc. Mat.* 10 (19), e2100385. doi:10.1002/adhm.202100385

Bayat Mokhtari, R., Homayouni, T. S., Baluch, N., Morgatskaya, E., Kumar, S., Das, B., et al. (2017). Combination therapy in combating cancer. *Oncotarget* 8 (23), 38022–38043. doi:10.18632/oncotarget.16723

Bayda, S., Adeel, M., Tuccinardi, T., Cordani, M., and Rizzolio, F. (2019). The history of nanoscience and nanotechnology: From chemical-physical applications to nanomedicine. *Molecules* 25 (1), 112. doi:10.3390/molecules25010112

Bazak, R., Houri, M., El Achy, S., Kamel, S., and Refaat, T. (2015). Cancer active targeting by nanoparticles: A comprehensive review of literature. *J. Cancer Res. Clin. Oncol.* 141 (5), 769–784. doi:10.1007/s00432-014-1767-3

Beatty, G. L., and Gladney, W. L. (2015). Immune escape mechanisms as a guide for cancer immunotherapy. *Clin. Cancer Res.* 21 (4), 687–692. doi:10.1158/1078-0432.Ccr-14-1860

Berraondo, P., Sanmamed, M. F., Ochoa, M. C., Etxeberria, I., Aznar, M. A., Pérez-Gracia, J. L., et al. (2019). Cytokines in clinical cancer immunotherapy. *Br. J. Cancer* 120 (1), 6–15. doi:10.1038/s41416-018-0328-y

Bertrand, N., Wu, J., Xu, X., Kamaly, N., and Farokhzad, O. C. (2014). Cancer nanotechnology: The impact of passive and active targeting in the era of modern cancer biology. *Adv. Drug Deliv. Rev.* 66, 2–25. doi:10.1016/j.addr.2013.11.009

Bray, F., Laversanne, M., Weiderpass, E., and Soerjomataram, I. (2021). The ever-increasing importance of cancer as a leading cause of premature death worldwide. *Cancer* 127 (16), 3029–3030. doi:10.1002/cncr.33587

Brinkmann, U., and Kontermann, R. E. (2017). The making of bispecific antibodies. *Mabs* 9 (2), 182–212. doi:10.1080/19420862.2016.1268307

Buchbinder, E. I., and Desai, A. (2016). CTLA-4 and PD-1 pathways: Similarities, differences, and implications of their inhibition. *Am. J. Clin. Oncol.* 39 (1), 98–106. doi:10.1097/coc.0000000000000239

Cheever, M. A., and Higano, C. S. (2011). PROVENGE (Sipuleucel-T) in prostate cancer: The first FDA-approved therapeutic cancer vaccine. *Clin. Cancer Res.* 17 (11), 3520–3526. doi:10.1158/1078-0432.Ccr-10-3126

Chen, M., Miao, Y., Qian, K., Zhou, X., Guo, L., Qiu, Y., et al. (2021). Detachable liposomes combined immunochemotherapy for enhanced triple-negative breast cancer treatment through reprogramming of tumor-associated macrophages. *Nano Lett.* 21 (14), 6031–6041. doi:10.1021/acs.nanolett.1c01210

Chen, Q., Hu, Q., Dukhovlinova, E., Chen, G., Ahn, S., Wang, C., et al. (2019). Photothermal therapy promotes tumor infiltration and antitumor activity of CAR T cells. *Adv. Mat.* 31 (23), 1900192. doi:10.1002/adma.201900192

Chen, Y., Chen, H., and Shi, J. (2014). Inorganic nanoparticle-based drug codelivery nanosystems to overcome the multidrug resistance of cancer cells. *Mol. Pharm.* 11 (8), 2495–2510. doi:10.1021/mp400596v

Chiocca, E. A., and Rabkin, S. D. (2014). Oncolytic viruses and their application to cancer immunotherapy. *Cancer Immunol. Res.* 2 (4), 295–300. doi:10.1158/2326-6066.Cir-14-0015

Conlon, K. C., Miljkovic, M. D., and Waldmann, T. A. (2019). Cytokines in the treatment of cancer. *J. Interferon Cytokine Res.* 39 (1), 6–21. doi:10.1089/jir.2018.0019

De Jong, W. H., and Borm, P. J. (2008). Drug delivery and nanoparticles: Applications and hazards. *Int. J. Nanomedicine* 3 (2), 133–149. doi:10.2147/ijn.s596

Din, F. U., Aman, W., Ullah, I., Qureshi, O. S., Mustapha, O., Shafique, S., et al. (2017). Effective use of nanocarriers as drug delivery systems for the treatment of selected tumors. *Int. J. Nanomedicine* 12, 7291–7309. doi:10.2147/ijn.S146315

Ding, L., Lin, X., Lin, Z., Wu, Y., Liu, X., Liu, J., et al. (2020). Cancer cell-targeted photosensitizer and therapeutic protein co-delivery nanoplatform based on a metal–organic framework for enhanced synergistic photodynamic and protein therapy. *ACS Appl. Mat. Interfaces* 12 (33), 36906–36916. doi:10.1021/acsami.0c09657

Ehlerding, E. B., Grodzinski, P., Cai, W., and Liu, C. H. (2018). Big potential from small agents: Nanoparticles for imaging-based companion diagnostics. *ACS Nano* 12 (3), 2106–2121. doi:10.1021/acsnano.7b07252

Finn, R. S., Qin, S., Ikeda, M., Galle, P. R., Ducreux, M., Kim, T. Y., et al. (2020). Atezolizumab plus Bevacizumab in unresectable hepatocellular carcinoma. *N. Engl. J. Med.* 382 (20), 1894–1905. doi:10.1056/NEJMoa1915745

Formenti, S. C., and Demaria, S. (2009). Systemic effects of local radiotherapy. *Lancet Oncol.* 10 (7), 718–726. doi:10.1016/s1470-2045(09)70082-8

Franzin, R., Netti, G. S., Spadaccino, F., Porta, C., Gesualdo, L., Stallone, G., et al. (2020). The use of immune checkpoint inhibitors in oncology and the occurrence of AKI: Where do we stand? *Front. Immunol.* 11, 574271. doi:10.3389/fimmu.2020.574271

Guo, L., Yan, D. D., Yang, D., Li, Y., Wang, X., Zalewski, O., et al. (2014). Combinatorial photothermal and immuno cancer therapy using chitosan-coated hollow copper sulfide nanoparticles. *ACS Nano* 8 (6), 5670–5681. doi:10.1021/nn5002112

Hagan, C. T. t., Mi, Y., Knape, N. M., and Wang, A. Z. (2020). Enhancing combined immunotherapy and radiotherapy through nanomedicine. *Bioconjug. Chem.* 31 (12), 2668–2678. doi:10.1021/acs.bioconjchem.0c00520

Henke, E., Nandigama, R., and Ergün, S. (2019). Extracellular matrix in the tumor microenvironment and its impact on cancer therapy. *Front. Mol. Biosci.* 6, 160. doi:10.3389/fmolb.2019.00160

Hollingsworth, R. E., and Jansen, K. (2019). Turning the corner on therapeutic cancer vaccines. *NPJ Vaccines* 4 (1), 7. doi:10.1038/s41541-019-0103-y

Hou, Y. J., Yang, X. X., Liu, R. Q., Zhao, D., Guo, C. X., Zhu, A. C., et al. (2020). Pathological mechanism of photodynamic therapy and photothermal therapy based on nanoparticles. *Int. J. Nanomedicine* 15, 6827–6838. doi:10.2147/ijn.S269321

Huang, J., Yang, B., Peng, Y., Huang, J., Wong, S. H. D., Bian, L., et al. (2021a). Nanomedicine-boosting tumor immunogenicity for enhanced immunotherapy. *Adv. Funct. Mat.* 31 (21), 2011171. doi:10.1002/adfm.202011171

Huang, L., Zhao, S., Fang, F., Xu, T., Lan, M., and Zhang, J. (2021b). Advances and perspectives in carrier-free nanodrugs for cancer chemo-monotherapy and combination therapy. *Biomaterials* 268, 120557. doi:10.1016/j.biomaterials.2020.120557

Huang, X., Lu, Y., Guo, M., Du, S., and Han, N. (2021c). Recent strategies for nano-based PTT combined with immunotherapy: From a biomaterial point of view. *Theranostics* 11 (15), 7546–7569. doi:10.7150/thno.56482

Huang, Z., Wang, Y., Yao, D., Wu, J., Hu, Y., and Yuan, A. (2021d). Nanoscale coordination polymers induce immunogenic cell death by amplifying radiation therapy mediated oxidative stress. *Nat. Commun.* 12 (1), 145. doi:10.1038/s41467-020-20243-8

Janji, B., and Chouaib, S. (2022). The promise of targeting hypoxia to improve cancer immunotherapy: Mirage or reality? *Front. Immunol.* 13, 880810. doi:10.3389/fimmu.2022.880810

Jiang, C. T., Chen, K. G., Liu, A., Huang, H., Fan, Y. N., Zhao, D. K., et al. (2021). Immunomodulating nano-adaptors potentiate antibody-based cancer immunotherapy. *Nat. Commun.* 12 (1), 1359. doi:10.1038/s41467-021-21497-6

Jin, C., Wang, K., Oppong-Gyebi, A., and Hu, J. (2020a). Application of nanotechnology in cancer diagnosis and therapy-A mini-review. *Int. J. Med. Sci.* 17 (18), 2964–2973. doi:10.7150/ijms.49801

Jin, S., and Ye, K. (2007). Nanoparticle-mediated drug delivery and gene therapy. *Biotechnol. Prog.* 23 (1), 32–41. doi:10.1021/bp060348j

Jin, W., Dong, C., Yang, D., Zhang, R., Jiang, T., and Wu, D. (2020b). Nano-carriers of combination tumor physical stimuli-responsive therapies. *Curr. Drug Deliv.* 17 (7), 577–587. doi:10.2174/1567201817666200525004225

Kappel, C., Seidl, C., Medina-Montano, C., Schinnerer, M., Alberg, I., Leps, C., et al. (2021). Density of conjugated antibody determines the extent of Fc receptor dependent capture of nanoparticles by liver sinusoidal endothelial cells. *ACS Nano* 15 (9), 15191–15209. doi:10.1021/acsnano.1c05713

Kato, K., Shah, M. A., Enzinger, P., Bennouna, J., Shen, L., Adenis, A., et al. (2019). KEYNOTE-590: Phase III study of first-line chemotherapy with or without pembrolizumab for advanced esophageal cancer. *Future Oncol.* 15 (10), 1057–1066. doi:10.2217/fon-2018-0609

Korman, A. J., Garrett-Thomson, S. C., and Lonberg, N. (2022). The foundations of immune checkpoint blockade and the ipilimumab approval decennial. *Nat. Rev. Drug Discov.* 21 (7), 509–528. doi:10.1038/s41573-021-00345-8

Krishnamurthy, S., Ng, V. W., Gao, S., Tan, M. H., Hedrick, J. L., and Yang, Y. Y. (2015). Codelivery of dual drugs from polymeric micelles for simultaneous targeting of both cancer cells and cancer stem cells. *Nanomedicine* 10 (18), 2819–2832. doi:10.2217/nnm.15.109

Kumari, N., and Choi, S. H. (2022). Tumor-associated macrophages in cancer: Recent advancements in cancer nanoimmunotherapies. *J. Exp. Clin. Cancer Res.* 41 (1), 68. doi:10.1186/s13046-022-02272-x

Kwatra, D., Venugopal, A., and Anant, S. J. T. C. R. (2013). Nanoparticles in radiation therapy: A summary of various approaches to enhance radiosensitization in cancer. *Transl. Cancer. Res.* 2 (4), 330–342. doi:10.3978/j.issn.2218-676X.2013.08.06

Lee, D. A. (2019). Cellular therapy: Adoptive immunotherapy with expanded natural killer cells. *Immunol. Rev.* 290 (1), 85–99. doi:10.1111/imr.12793

Li, Q., Wang, X., Wang, P., Zhang, K., Wang, H., Feng, X., et al. (2014). Efficacy of chlorin e6-mediated sono-photodynamic therapy on 4T1 cells. *Cancer biother. Radiopharm.* 29 (1), 42–52. doi:10.1089/cbr.2013.1526

Li, X., Zhen, Y., and Li, S. (2021a). Review on combination strategy of immune checkpoint blockade, photodynamic therapy and nanomedicine against solid tumor. *Mat. Des.* 209, 109958. doi:10.1016/j.matdes.2021.109958

Li, Z., Sun, Y., Ye, F., Ma, D., Yin, X., Zhuang, W., et al. (2021b). First-line pembrolizumab plus chemotherapy versus chemotherapy in patients with advanced esophageal cancer: Chinese subgroup analysis of KEYNOTE-590. *J. Clin. Oncol.* 39, 4049. doi:10.1200/JCO.2021.39.15_suppl.4049

Liu, Y., Crawford, B. M., and Vo-Dinh, T. (2018). Gold nanoparticles-mediated photothermal therapy and immunotherapy. *Immunotherapy* 10 (13), 1175–1188. doi:10.2217/imt-2018-0029

Liu, Z., Wang, Y., Huang, Y., Kim, B. Y. S., Shan, H., Wu, D., et al. (2019). Tumor vasculatures: A new target for cancer immunotherapy. *Trends Pharmacol. Sci.* 40 (9), 613–623. doi:10.1016/j.tips.2019.07.001

Liu, Z., Xie, Z., Li, W., Wu, X., Jiang, X., Li, G., et al. (2021). Photodynamic immunotherapy of cancers based on nanotechnology: Recent advances and future challenges. *J. Nanobiotechnology* 19 (1), 160. doi:10.1186/s12951-021-00903-7

Llovet, J. M., Kelley, R. K., Villanueva, A., Singal, A. G., Pikarsky, E., Roayaie, S., et al. (2021). Hepatocellular carcinoma. *Nat. Rev. Dis. Prim.* 7 (1), 6. doi:10.1038/s41572-020-00240-3

Luo, L., Yang, J., Zhu, C., Jiang, M., Guo, X., Li, W., et al. (2018). Sustained release of anti-PD-1 peptide for perdurable immunotherapy together with photothermal ablation against primary and distant tumors. *J. Control. Release* 278, 87–99. doi:10.1016/j.jconrel.2018.04.002

Luo, M., and Fu, L. (2016). The effect of chemotherapy on programmed cell death 1/programmed cell death 1 ligand axis: Some chemotherapeutical drugs may finally work through immune response. *Oncotarget* 7 (20), 29794–29803. doi:10.18632/oncotarget.7631

Lv, B., Wang, Y., Ma, D., Cheng, W., Liu, J., Yong, T., et al. (2022). Immunotherapy: Reshape the tumor immune microenvironment. *Front. Immunol.* 13, 844142. doi:10.3389/fimmu.2022.844142

Ma, L., Kohli, M., and Smith, A. (2013). Nanoparticles for combination drug therapy. *ACS Nano* 7 (11), 9518–9525. doi:10.1021/nn405674m

Mansfield, A. S., Park, S. S., and Dong, H. (2015). Synergy of cancer immunotherapy and radiotherapy. *Aging (Albany NY)* 7 (3), 144–145. doi:10.18632/aging.100730

Mattiuzzi, C., and Lippi, G. (2019). Current cancer epidemiology. *J. Epidemiol. Glob. Health* 9 (4), 217–222. doi:10.2991/jegh.k.191008.001

McCarthy, E. F. (2006). The toxins of William B. Coley and the treatment of bone and soft-tissue sarcomas. *Iowa Orthop. J.* 26, 154–158.

Merisko-Liversidge, E. M., and Liversidge, G. G. (2008). Drug nanoparticles: Formulating poorly water-soluble compounds. *Toxicol. Pathol.* 36 (1), 43–48. doi:10.1177/0192623307310946

Muthu, M. S., and Feng, S.-S. (2009). Pharmaceutical stability aspects of nanomedicines. *Nanomedicine* 4 (8), 857–860. doi:10.2217/nnm.09.75

Ng, C. W., Li, J., and Pu, K. (2018). Recent progresses in phototherapy-synergized cancer immunotherapy. *Adv. Funct. Mat.* 28 (46), 1804688. doi:10.1002/adfm.201804688

Nie, S. (2010). Understanding and overcoming major barriers in cancer nanomedicine. *Nanomedicine* 5 (4), 523–528. doi:10.2217/nnm.10.23

Parker, C. L., McSweeney, M. D., Lucas, A. T., Jacobs, T. M., Wadsworth, D., Zamboni, W. C., et al. (2019). Pretargeted delivery of PEG-coated drug carriers to breast tumors using multivalent, bispecific antibody against polyethylene glycol and HER2. *Nanomedicine Nanotechnol. Biol. Med.* 21, 102076. doi:10.1016/j.nano.2019.102076

Patra, J. K., Das, G., Fraceto, L. F., Campos, E. V. R., Rodriguez-Torres, M. d. P., Acosta-Torres, L. S., et al. (2018). Nano based drug delivery systems: Recent developments and future prospects. *J. Nanobiotechnol.* 16 (1), 71. doi:10.1186/s12951-018-0392-8

Perez-Gracia, J. L., Berraondo, P., Martinez-Forero, I., Alfaro, C., Suarez, N., Gurpide, A., et al. (2009). Clinical development of combination strategies in immunotherapy: Are we ready for more than one investigational product in an early clinical trial? *Immunotherapy* 1 (5), 845–853. doi:10.2217/imt.09.51

Pilla, L., Ferrone, S., and Maccalli, C. (2018). Methods for improving the immunogenicity and efficacy of cancer vaccines. *Expert Opin. Biol. Ther.* 18 (7), 765–784. doi:10.1080/14712598.2018.1485649

Pol, J., Kroemer, G., and Galluzzi, L. (2016). First oncolytic virus approved for melanoma immunotherapy. *Oncoimmunology* 5 (1), e1115641. doi:10.1080/2162402x.2015.1115641

Qu, J., Wang, L., Jiang, M., Zhao, D., Wang, Y., Zhang, F., et al. (2020). A review about pembrolizumab in first-line treatment of advanced NSCLC: Focus on KEYNOTE studies. *Cancer Manag. Res.* 12, 6493–6509. doi:10.2147/cmar.S257188

Rammensee, H. G., Löffler, M. W., Walz, J. S., Bokemeyer, C., Haen, S. P., and Gouttefangeas, C. (2020). Tumor vaccines-therapeutic vaccination against cancer. *Internist (Berl)* 61 (7), 690–698. doi:10.1007/s00108-020-00814-z

Rianasari, I., de Jong, M. P., Huskens, J., and van der Wiel, W. G. (2013). Covalent coupling of nanoparticles with low-density functional ligands to surfaces via click chemistry. *Int. J. Mol. Sci.* 14 (2), 3705–3717. doi:10.3390/ijms14023705

Ribas, A., Dummer, R., Puzanov, I., VanderWalde, A., Andtbacka, R. H. I., Michielin, O., et al. (2017). Oncolytic virotherapy promotes intratumoral T Cell infiltration and improves anti-PD-1 immunotherapy. *Cell* 170 (6), 1109–1119.e10. doi:10.1016/j.cell.2017.08.027

Richards, O. C., Raines, S. M., and Attie, A. D. (2010). The role of blood vessels, endothelial cells, and vascular pericytes in insulin secretion and peripheral insulin action. *Endocr. Rev.* 31 (3), 343–363. doi:10.1210/er.2009-0035

Robert, C. (2021). LAG-3 and PD-1 blockade raises the bar for melanoma. *Nat. Cancer* 2 (12), 1251–1253. doi:10.1038/s43018-021-00276-8

Rohaan, M. W., Wilgenhof, S., and Haanen, J. (2019). Adoptive cellular therapies: The current landscape. *Virchows Arch.* 474 (4), 449–461. doi:10.1007/s00428-018-2484-0

Rosenberg, S. A., Restifo, N. P., Yang, J. C., Morgan, R. A., and Dudley, M. E. (2008). Adoptive cell transfer: A clinical path to effective cancer immunotherapy. *Nat. Rev. Cancer* 8 (4), 299–308. doi:10.1038/nrc2355

Rupp, T., Genest, L., Babin, D., Legrand, C., Hunault, M., Froget, G., et al. (2022). Anti-CTLA-4 and anti-PD-1 immunotherapies repress tumor progression in preclinical breast and colon model with independent regulatory T cells response. *Transl. Oncol.* 20, 101405. doi:10.1016/j.tranon.2022.101405

Salas-Benito, D., Pérez-Gracia, J. L., Ponz-Sarvisé, M., Rodriguez-Ruiz, M. E., Martínez-Forero, I., Castañón, E., et al. (2021). Paradigms on immunotherapy combinations with chemotherapy. *Cancer Discov.* 11 (6), 1353–1367. doi:10.1158/2159-8290.CD-20-1312

Senapati, S., Mahanta, A. K., Kumar, S., and Maiti, P. (2018). Controlled drug delivery vehicles for cancer treatment and their performance. *Signal Transduct. Target. Ther.* 3, 7. doi:10.1038/s41392-017-0004-3

Shi, J., Kantoff, P. W., Wooster, R., and Farokhzad, O. C. (2017). Cancer nanomedicine: Progress, challenges and opportunities. *Nat. Rev. Cancer* 17 (1), 20–37. doi:10.1038/nrc.2016.108

Shi, Y., van der Meel, R., Chen, X., and Lammers, T. (2020). The EPR effect and beyond: Strategies to improve tumor targeting and cancer nanomedicine treatment efficacy. *Theranostics* 10 (17), 7921–7924. doi:10.7150/thno.49577

Shirata, C., Kaneko, J., Inagaki, Y., Kokudo, T., Sato, M., Kiritani, S., et al. (2017). Near-infrared photothermal/photodynamic therapy with indocyanine green induces apoptosis of hepatocellular carcinoma cells through oxidative stress. *Sci. Rep.* 7 (1), 13958. doi:10.1038/s41598-017-14401-0

Siemer, S., Bauer, T. A., Scholz, P., Breder, C., Fenaroli, F., Harms, G., et al. (2021). Targeting cancer chemotherapy resistance by precision medicine-driven nanoparticle-formulated cisplatin. *ACS Nano* 15 (11), 18541–18556. doi:10.1021/acsnano.1c08632

Subbiah, V., Baik, C., and Kirkwood, J. M. (2020). Clinical development of BRAF plus MEK inhibitor combinations. *Trends Cancer* 6 (9), 797–810. doi:10.1016/j.trecan.2020.05.009

Sun, Q., Zhou, Z., Qiu, N., and Shen, Y. (2017). Rational design of cancer nanomedicine: Nanoproperty integration and synchronization. *Adv. Mat.* 29 (14), 1606628. doi:10.1002/adma.201606628

Tan, I. B., Dolivet, G., Ceruse, P., Vander Poorten, V., Roest, G., and Rauschning, W. (2010). Temoporfin-mediated photodynamic therapy in patients with advanced, incurable head and neck cancer: A multicenter study. *Head. Neck* 32 (12), 1597–1604. doi:10.1002/hed.21368

Tan, S., Li, D., and Zhu, X. (2020). Cancer immunotherapy: Pros, cons and beyond. *Biomed. Pharmacother.* 124, 109821. doi:10.1016/j.biopha.2020.109821

Tang, P. M., Bui-Xuan, N. H., Wong, C. K., Fong, W. P., and Fung, K. P. (2010). Pheophorbide a-mediated photodynamic therapy triggers HLA Class I-restricted antigen presentation in human hepatocellular carcinoma. *Transl. Oncol.* 3 (2), 114–122. doi:10.1593/tlo.09262

Torres-Vanegas, J. D., Cruz, J. C., and Reyes, L. H. (2021). Delivery Systems for nucleic acids and proteins: Barriers, cell capture pathways and nanocarriers. *Pharmaceutics* 13 (3), 428. doi:10.3390/pharmaceutics13030428

Virlan, M. J., Miricescu, D., Radulescu, R., Sabliov, C. M., Totan, A., Calenic, B., et al. (2016). Organic nanomaterials and their applications in the treatment of oral diseases. *Molecules* 21 (2), 207. doi:10.3390/molecules21020207

Wang, D., Wang, T., Liu, J., Yu, H., Jiao, S., Feng, B., et al. (2016). Acid-activatable versatile micelleplexes for PD-L1 blockade-enhanced cancer photodynamic immunotherapy. *Nano Lett.* 16 (9), 5503–5513. doi:10.1021/acs.nanolett.6b01994

Wang, M., Rao, J., Wang, M., Li, X., Liu, K., Naylor, M. F., et al. (2021). Cancer photo-immunotherapy: From bench to bedside. *Theranostics* 11 (5), 2218–2231. doi:10.7150/thno.53056

Wang, Q. Y., Xu, Y. S., Zhang, N. X., Dong, Z. P., Zhao, B. N., Liu, L. C., et al. (2020). Phenylboronic ester-modified anionic micelles for ROS-stimuli response in HeLa cell. *Drug Deliv. (Lond).* 27 (1), 681–690. doi:10.1080/10717544.2020.1748761

Wang, T., Zhang, J., Hou, T., Yin, X., and Zhang, N. (2019). Selective targeting of tumor cells and tumor associated macrophages separately by twin-like core-shell nanoparticles for enhanced tumor-localized chemoimmunotherapy. *Nanoscale* 11 (29), 13934–13946. doi:10.1039/c9nr03374b

Wei, S. C., Levine, J. H., Cogdill, A. P., Zhao, Y., Anang, N. A. S., Andrews, M. C., et al. (2017). Distinct cellular mechanisms underlie anti-CTLA-4 and anti-PD-1 checkpoint blockade. *Cell* 170 (6), 1120–1133.e17. doi:10.1016/j.cell.2017.07.024

Weiner, L. M., Surana, R., and Wang, S. (2010). Monoclonal antibodies: Versatile platforms for cancer immunotherapy. *Nat. Rev. Immunol.* 10 (5), 317–327. doi:10.1038/nri2744

Wilhelm, S. M., Adnane, L., Newell, P., Villanueva, A., Llovet, J. M., and Lynch, M. (2008). Preclinical overview of sorafenib, a multikinase inhibitor that targets both Raf and VEGF and PDGF receptor tyrosine kinase signaling. *Mol. Cancer Ther.* 7 (10), 3129–3140. doi:10.1158/1535-7163.Mct-08-0013

Wu, J. (2021). The enhanced permeability and retention (EPR) effect: The significance of the concept and methods to enhance its application. *J. Pers. Med.* 11 (8), 771. doi:10.3390/jpm11080771

Wu, K., Yi, M., Qin, S., Chu, Q., Zheng, X., and Wu, K. (2019). The efficacy and safety of combination of PD-1 and CTLA-4 inhibitors: A meta-analysis. *Exp. Hematol. Oncol.* 8 (1), 26. doi:10.1186/s40164-019-0150-0

Yang, M., Li, J., Gu, P., and Fan, X. (2021). The application of nanoparticles in cancer immunotherapy: Targeting tumor microenvironment. *Bioact. Mat.* 6 (7), 1973–1987. doi:10.1016/j.bioactmat.2020.12.010

Yang, Y. (2015). Cancer immunotherapy: Harnessing the immune system to battle cancer. *J. Clin. Invest.* 125 (9), 3335–3337. doi:10.1172/jci83871

Yates, P., Charalambous, A., Fennimore, L., So, W. K. W., Suh, E. E., Woodford, E., et al. (2020). Cancer nursing's potential to reduce the growing burden of cancer across the world. *Oncol. Nurs. Forum* 47 (6), 625–627. doi:10.1188/20.Onf.625-627

Yu, S., Wang, Y., He, P., Shao, B., Liu, F., Xiang, Z., et al. (2022). Effective combinations of immunotherapy and radiotherapy for cancer treatment. *Front. Oncol.* 12, 809304. doi:10.3389/fonc.2022.809304

Zhang, H., Bussmann, J., Huhnke, F. H., Devoldere, J., Minnaert, A.-K., Jiskoot, W., et al. (2022). Together is better: mRNA co-encapsulation in lipoplexes is required to obtain ratiometric co-delivery and protein expression on the single cell level. *Adv. Sci. (Weinh).* 9 (4), 2102072. doi:10.1002/advs.202102072

Zhang, H., De Smedt, S. C., and Remaut, K. (2018a). Fluorescence correlation spectroscopy to find the critical balance between extracellular association and intracellular dissociation of mRNA complexes. *Acta Biomater.* 75, 358–370. doi:10.1016/j.actbio.2018.05.016

Zhang, M., Wang, W., Cui, Y., Zhou, N., and Shen, J. (2018b). Magnetofluorescent carbon quantum dot decorated multiwalled carbon nanotubes for dual-modal targeted imaging in chemo-photothermal synergistic therapy. *ACS Biomater. Sci. Eng.* 4 (1), 151–162. doi:10.1021/acsbiomaterials.7b00531

Zhang, Y., and Zhang, Z. (2020). The history and advances in cancer immunotherapy: Understanding the characteristics of tumor-infiltrating immune cells and their therapeutic implications. *Cell. Mol. Immunol.* 17 (8), 807–821. doi:10.1038/s41423-020-0488-6

Zhao, B., Dong, Z., Liu, W., Lou, F., Wang, Q., Hong, H., et al. (2021). Co-administration of combretastatin A4 nanoparticles and anti-PD-L1 for synergistic therapy of hepatocellular carcinoma. *J. Nanobiotechnology* 19 (1), 124. doi:10.1186/s12951-021-00865-w

Zolnik, B. S., González-Fernández, A., Sadrieh, N., and Dobrovolskaia, M. A. (2010). Minireview: Nanoparticles and the immune system. *Endocrinology* 151 (2), 458–465. doi:10.1210/en.2009-1082

Zununi Vahed, S., Salehi, R., Davaran, S., and Sharifi, S. (2017). Liposome-based drug co-delivery systems in cancer cells. *Mater. Sci. Eng. C* 71, 1327–1341. doi:10.1016/j.msec.2016.11.073

frontiers | Frontiers in Bioengineering and Biotechnology

TYPE Review
PUBLISHED 12 September 2022
DOI 10.3389/fbioe.2022.998988

OPEN ACCESS

EDITED BY
Weifeng Lin,
Weizmann Institute of Science, Israel

REVIEWED BY
Guanglong Ma,
University of Southampton,
United Kingdom
Wenxian Du,
Shanghai Jiao Tong University, China
Yong Xu,
Technical University Dresden, Germany
Sihang Liu,
Shanghai Jiao Tong University, China

*CORRESPONDENCE
Ran Kang,
kangran126@126.com
Lin Xie,
xielin@njucm.edu.cn
Xin Liu,
liuxin@njucm.edu.cn

[†]These authors have contributed equally to this work

SPECIALTY SECTION
This article was submitted to Nanobiotechnology, a section of the journal Frontiers in Bioengineering and Biotechnology

RECEIVED 20 July 2022
ACCEPTED 29 August 2022
PUBLISHED 12 September 2022

CITATION
Liu X, Sun S, Wang N, Kang R, Xie L and Liu X (2022), Therapeutic application of hydrogels for bone-related diseases. *Front. Bioeng. Biotechnol.* 10:998988. doi: 10.3389/fbioe.2022.998988

Therapeutic application of hydrogels for bone-related diseases

Xiyu Liu[1†], Shuoshuo Sun[1†], Nan Wang[1], Ran Kang[1,2*], Lin Xie[1*] and Xin Liu[1,2*]

[1]Third School of Clinical Medicine, Nanjing University of Traditional Chinese Medicine, Nanjing, China, [2]Department of Orthopedics, Nanjing Lishui Hospital of Traditional Chinese Medicine, Nanjing, China

Bone-related diseases caused by trauma, infection, and aging affect people's health and quality of life. The prevalence of bone-related diseases has been increasing yearly in recent years. Mild bone diseases can still be treated with conservative drugs and can be cured confidently. However, serious bone injuries caused by large-scale trauma, fractures, bone tumors, and other diseases are challenging to heal on their own. Open surgery must be used for intervention. The treatment method also faces the problems of a long cycle, high cost, and serious side effects. Studies have found that hydrogels have attracted much attention due to their good biocompatibility and biodegradability and show great potential in treating bone-related diseases. This paper mainly introduces the properties and preparation methods of hydrogels, reviews the application of hydrogels in bone-related diseases (including bone defects, bone fracture, cartilage injuries, and osteosarcoma) in recent years. We also put forward suggestions according to the current development status, pointing out a new direction for developing high-performance hydrogels more suitable for bone-related diseases.

KEYWORDS

hydrogels, bone-related diseases, tissue engineering, biocompatibility, biodegradability

1 Introduction

The skeletal system is closely related to the movement of the body and its defenses. It may manage basic human physiological functions, which help maintain homeostasis in the body's internal environment and store minerals (Khiabani et al., 2021). The destruction of the skeletal system leads to endless consequences. Bone-related diseases are mainly associated with a variety of factors, such as trauma, infection, and age (Loeffler et al., 2018). Severe bone damage cannot heal on their own, significantly affecting the life quality of patients (Yue et al., 2020). Traditional surgical treatment methods mainly include prostheses implantation and bone transplantation. Despite their clinical efficacy, they might have side effects such as infection and pain and have disadvantages such as high surgical costs and the need for additional surgery (Kretlow and Mikos, 2007; Khan et al., 2008; Liu et al., 2017; Yue et al., 2020). Of more than two million bone grafts performed worldwide annually, delayed healing occurs in more than 20% of patients. Regrettably, there is currently no satisfactory bone grafting protocol (Chen et al., 2012; Yu et al., 2020; Yue et al., 2020). Up to now, the dominating alternative has been the use of donated, the commonly used allografts have only weak effects of bone induction and bone regeneration. Nevertheless, the development of autologous bone grafting is constrained by factors related to the morbidity of the donor site and the insufficient volume of graft material (Kurien et al., 2013; Gibbs et al., 2016). Therefore, the emergence of new technologies or modifications to existing treatment modalities is urgently sought to provide individuals with utmost care and help patients return to their everyday lives (Nallusamy and Das, 2021).

Tissue engineering (TE) facilitates the creation of three-dimensional (3D) substitutes that closely resemble human tissue to restore and maintain the integrity of tissue structure and physical enginery, which holds promise from repair to human tissue regeneration and individual health restoration (Ghosal and Kaushik, 2020). Combining TE technology with orthopedics is expected to bring unprecedented benefits. Bone TE (BTE)-related techniques are often used in some cases of bone-related diseases, such as blocked bone regeneration (Li J. J. et al., 2018). Cells, growth factors, scaffolds and bioreactors are main components of BTE (Vermonden et al., 2012; Li J. J. et al., 2018). In BTE, scaffolds are key elements for building biological structures that resemble natural bone. Recently, a satisfactory 3D scaffold design with numerous advantageous features has been proposed (Nallusamy and Das, 2021).

To date, polymeric materials widely used in the biomedical field have attracted much attention due to their characteristic superiorities such as biocompatibility, processability and low cost (Henry et al., 1998; Sigfridsson et al., 2009; Tuan-Mahmood et al., 2013). Nowadays, polymeric patches of ingeniously designed with stimuli-responsive properties are widely used as biomedical scaffolds in biomedical field. Currently, materials associated with such polymers mainly include hydrogels, microneedles (MNs), microcapsules, microspheres, and fibers, which exhibit excellent biocompatibility and biodegradability (Shahiwala, 2011).

In BTE, hydrogels are prominent among the numerous available biomaterials that constitute scaffolds (Nallusamy and Das, 2021). A unique advantage of the hydrogels must be pointed out, their specific porous structures similar to the extracellular matrix (ECM) can serve as carriers for various growth factors (Ulery et al., 2011; Buwalda et al., 2016; Liu et al., 2018). Moreover, their soft texture reduces surrounding inflammatory responses (Buwalda et al., 2016). In consequence, hydrogels are quite appropriate as scaffold-related materials for BTE (Yue et al., 2020). This article reviews the application of hydrogels in bone-related diseases in recent years, involving bone defects, fractures, cartilage damage and osteosarcoma. The above research hopes that this contribution will further guide scientists to develop high-quality hydrogels suitable for bone regeneration.

2 Hydrogels

Hydrogels are highly hydrated 3D networks of hydrophilic polymers. The cross-linking of polymer chains enables them to absorb and retain large amounts of water in a porous structure (Gan et al., 2001; Loh et al., 2011; Nguyen et al., 2011; Barouti et al., 2016, 2016; Gibbs et al., 2016; Jiang et al., 2019; Yue et al., 2020; Lin et al., 2021; Oliveira et al., 2021; Liu et al., 2022). Due to the similarity between hydrogels and tissue ECM, they are widely used in the biomedical field as a biocompatible polymeric material (Caló and Khutoryanskiy, 2015). In accordance with many biological materials, hydrogels can be divided into two categories: natural polymers and synthetic polymers (Ahmed, 2015; Zhu et al., 2022). So far, many different kinds of hydrogels have been applied in the pharmaceutical industry. Hyaluronic acid, gelatin, alginate, dextran, chitosan, collagen, elastin and albumin are all natural polymers that can be complexed into hydrogels (Rivory et al., 1994; Bouhadir et al., 2001; Liu et al., 2006; McDaniel et al., 2010; Yue et al., 2020). These materials generally have good biocompatibility and biodegradability, combined with practicality and durability. Hydrogels produced through their self-assembly or cross-linking have been widely exploited in drug delivery systems (He et al., 2018; Zhu et al., 2022). In addition, smart delivery nanoplatforms constructed with some natural polymers have been used as hydrogel drug depots (Zhu et al., 2022). However, these natural polymers have inconsistent hydration and elastic properties. Common biosynthetic materials include poly (ethylene glycol) (PEG), poly (N-isopropylacrylamide) (PNIPAAm), polycaprolactone (PCL), poly (L-glutamic acid) (PGA), polypropylene fiber (PPF), and polyvinyl alcohol (PVA) (Yue et al., 2020). Synthetic polymers-derived hydrogels offer controllability and reproducibility to improve consistency and alter properties (Ahmed, 2015; Gibbs et al., 2016). Whereas, synthetic biomaterials' biocompatibility and safety are weak, that own lower biological activity than natural biomaterials (Amini and Nair, 2012). Both natural and synthetic polymers have pros and cons. In order to take full advantage of their excellent properties, several materials can be used in combination (BaoLin and Ma, 2014; Oliveira et al., 2021). In BTE, the application of hydrogels has advantages and limitations; thus, it is often applied to specific scenarios according to the characteristics of each hydrogel. It is particularly emphasized that composite hydrogels are often prepared to reduce the limitations and maximize the advantages. In each bone-related disease, we will exemplify the specific applications of representative hydrogels in detail.

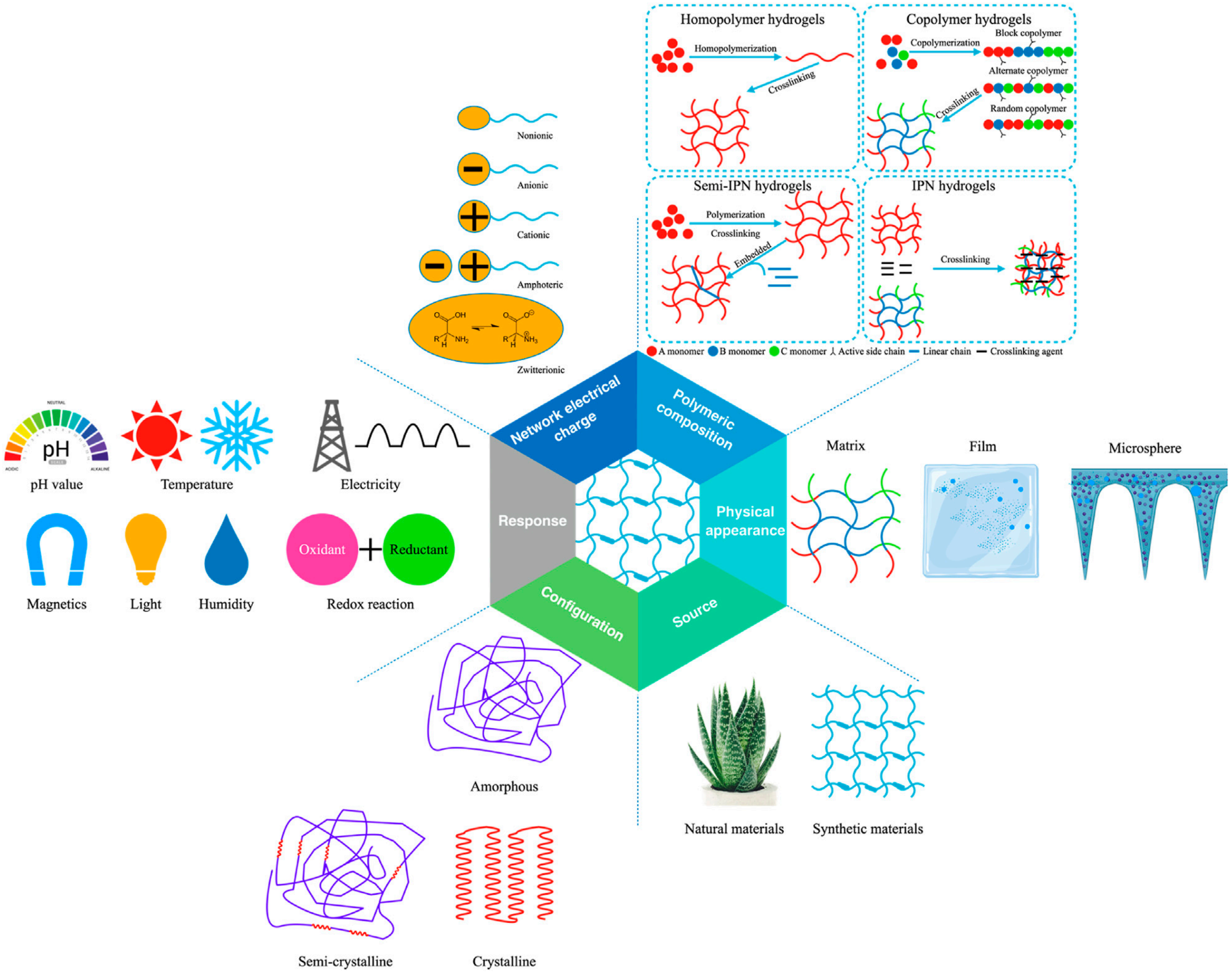

FIGURE 1
Classification of hydrogels based on properties.

2.1 The evolution of hydrogels

Its evolution has gone through several generations (Nallusamy and Das, 2021). In 1960, the porous polymers named poly (2-hydroxyethyl methacrylate [HEMA]) were used to fabricate contact lenses (Wichterle and Lím, 1960; Nallusamy and Das, 2021). The first-generation hydrogels are mainly about a single chemical polymer network. Second-generation hydrogels refer to stimulus-responsive hydrogels that respond when the environment changes (Hodgson et al., 2017; Nallusamy and Das, 2021). The third-generation hydrogels established cross-linking methods with physical interactions, which were expected to tune the properties (Buwalda et al., 2016; Nallusamy and Das, 2021). Up to now, the fourth-generation hydrogels have been developed into smart hydrogels, which possess strong stability and stable performance to achieve more accurate targeted delivery (Buwalda et al., 2014; Nallusamy and Das, 2021).

2.2 Main properties of hydrogels

Hydrogels have been widely used in tissue engineering due to their unique performance advantages, such as softness, water absorption, tunable mechanical strength, and controllable degradability. Especially in BTE, hydrogels have promise as functional scaffolds for growth factor transport and cell adhesion (Yue et al., 2020).

Hydrogels have a great characteristic of absorbing a large amount of water or biological liquid, among many material forms. This characteristic gives hydrogels excellent softness, biocompatibility, and hydrophilicity and shows a good fit with the softness of living tissue. This beneficial characteristic is also a prerequisite for biological application (Caló and Khutoryanskiy, 2015; Kondiah et al., 2016; Nakka and Mungray, 2016; Chai et al., 2017; Nallusamy and Das, 2021). In addition, the structure and coordination of hydrogels in their hydrated form guarantee structural strength and also facilitate the flow of liquids, metabolites, nutrients or agents (Khiabani et al., 2021). The unique physical properties of hydrogels make them the workhorse of drug delivery systems (Chai et al., 2017). The porosity of the hydrogel is used to encapsulate the drug into the gel, while the diffusion coefficient of the molecules in the hydrogel network determines the drug release rate (Li and Mooney, 2016). Notably, the properties of hydrogels can be adapted to slow drug release patterns, maintaining higher drug concentrations where they are administered for prolonged periods (Hoare and Kohane, 2008; Narayanaswamy and Torchilin, 2019). It can also be matched with environmental conditions to release and degrade controlled drugs (Hunt et al., 2014; Li and Su, 2018; Mantha et al., 2019; Oliveira et al., 2021). It is worth mentioning that, as “smart gels”, hydrogels are exceptionally sensitive to external stimuli such as ionic strength, pH and temperature, demonstrating their high efficiency (Vashist et al., 2014). More importantly, the hydrogels are durable and show high stability during storage. Based on their different properties, hydrogels have been classified into the following categories (Figure 1) (Lee and Shin, 2007; Ahmed, 2015; Thakur and Thakur, 2018; Ghosal and Kaushik, 2020; Yue et al., 2020; Nallusamy and Das, 2021). It should be pointed out that, according to different classification methods, we mainly classify from source, physical appearance, polymeric composition, network electrical charge, response, and configuration.

2.3 Main influencing factors for the preparation of hydrogels suitable for bone TE

The 3D space formed by the scaffold material in BTE provides a region for cells to survive. Integrins are heterodimeric receptors in cell membranes that connect cells to substrates by binding to adhesion proteins on the biomaterial surface (Clark et al., 2020). Among them, the key factors regulating cell behavior in biomaterials are listed as follows: chemical component, mechanical property, morphology and hydrophilia. According to information, ideally beneficial scaffold material should be matched to specific conditions, as listed below: 1) excellent biocompatibility and degradability; 2) good porosity and 3D structure (Yue et al., 2020). For example, many macromolecules structurally similar to the ECM are ordinarily used to prepare hydrogels to modulate the properties of attached cells. Such molecular materials mainly contain collagen, fibronectin and laminin (Yue et al., 2020). Therefore, the preparation methods of hydrogels should be integrated with superior materials and sophisticated technologies to make them more suitable for treating bone-related diseases.

In BTE, various mechanical properties (tension, compression, bending, swelling, deswelling, indentation, pore diameter, pore shape, and interpore connectivity) should be considered to fabricate suitable scaffolds (Pacifici et al., 2018). The mechanical strength of most bioactive hydrogels is not strong, which limits the application of hydrogels in BTE (Utech and Boccaccini, 2016; Xue et al., 2021). Based on these, It is crucial to prepare hard and tough hydrogels with tunable mechanics. Processing should be carried out to improve the properties according to its imitations. Advanced techniques in different fields can be used to process hydrogels into desired structures. For example, 3D bioprinting is highly representative (Ansari et al., 2017; Pacifici et al., 2018). We can incorporate inorganic fillers into the polymer matrixes or perform chemical modification techniques during processing to improve mechanical stability. The properties of tensile strength, shape recovery, and energy dissipation can be improved by adding extra physical cross-linking points (Utech and Boccaccini, 2016). Hydrogel matrices can enhance strength and stiffness by incorporating nanotechnology. Additional ions can also be appended to overcome the drawbacks (Kilpadi et al., 2001; Hoppe et al., 2011). Although the addition of inorganic materials can effectively improve the physical structure of hydrogels, there are also some shortcomings, such as the dissolution of harmful substances into adjacent cells and the mechanical stability needs to be further improved. Rauner et al. (2017) achieved significant progress in the development of mechanically tunable hybrid hydrogels by exploiting the changes under enzymatic reaction to obtain hydrogels with extremely strong hardness and tenacity. So far, there is a view that it is crucial to focus on the inherent structure of bone, which helps to optimize the mechanical properties and provides a new perspective for designing bionic materials that aid in bone regeneration (Xue et al., 2021).

Nanoparticles, ranging in diameter from 1 to 100 nm, are solid colloidal particles composed of natural synthetic or semi-synthetic polymers. They are commonly used as reservoirs for nanoparticle systems and as carriers for drug delivery systems (Gan et al., 2019). In exploring emerging drug replacement therapy methods, nanoparticle drug delivery systems have two outstanding advantages, which can not only enhance drug penetration, but also prolong the effective circulation time of drugs in the body (Wu et al., 2022). It is worth mentioning that some macromolecular nanomaterials composed of nanoparticles (such as nanosheets, nanotubes, mesoporous materials, etc.) are often used as nanoplatforms to carry drugs to treat diseases (Yan J. et al., 2021; Wang Y.-C. et al., 2021; Zhu et al., 2021). To date, nanomaterials have been widely used in various fields of medical treatment (Zhu et al., 2018, 2019). With its superior physical and chemical properties, it has been extensively explored and developed in various therapeutic modalities (Zhu et al., 2022). Based on the different configurations of hydrogels that have been used in BTE, the aforementioned fusion of nanotechnologies will help provide state-of-the-art strategies for facing bone-related diseases with hydrogels. The incorporation of nanoparticles into the polymeric matrix could lead to improving the mechanical and electrical features for obtaining satisfactory therapeutic efficacy (Zhu et al., 2022).

The pore size of the hydrogels also plays a key role in guiding the cells into the hydrogel networks. It is necessary to control the appropriate pore size to prepare hydrogels with high performance related to bone repair. At present, there are mainly three types of apertures. Different pore sizes are associated with the appearance of different cellular behaviors. Hydrogels with small pore sizes (2–50 nm) utilize large enough surface area to load drugs, resulting in a good therapeutic effect (Huang et al., 2015). Hydrogels with a moderate pore size (10 μm) can promote the formation of hydroxyapatite and introduce bone morphogenetic proteins by increasing the exchange rate of calcium, magnesium, zinc and other mineral ions (Schröter et al., 2020). Large pore size (above 100 μm) can significantly accelerate cell migration and adhesiveness (Li Y. et al., 2017). Although hydrogels with diverse pore sizes have multiple functional benefits. Nevertheless, they still exist morphological limitations. To address these types of problems, 3D printing and other techniques related to elaborate processing have been exploited far and wide to precisely fabricate hydrogels with matched mechanical properties, tailored porosity and structure for BTE (Gauvin et al., 2012; Chen et al., 2020; Matai et al., 2020; Wang et al., 2020, Wang et al., 2021 C.).

2.4 Preparation methods of hydrogel

In general, hydrogels are mainly associated with two types of cross-linking modes: physical cross-linking and chemical cross-linking (Yue et al., 2020). Physical hydrogels' attachment modalities include ion interactions, electrostatic interactions, hydrogen bonds, hydrophobic interactions and crystallization (Nabavi et al., 2020; Neves et al., 2020; Khiabani et al., 2021). Methods for synthesizing chemically cross-linked hydrogels include Michael addition reactions, Schiff base reactions, Diels–Alder cycloadditions, radical polymerization, and other click chemistry (Neves et al., 2020). In recent years, physically and chemically related triggering conditions have been commonly utilized to fabricate hydrogels (Hennink and van Nostrum, 2002; Hu W. et al., 2019). In physically triggered conditions, light or temperature stimulates hydrogels' cross-linking. Whereas under chemically triggered conditions, molecular or ionic cross-linking agents can make covalent bonds or coordinative bonds between polymer chains to form steady hydrogel networks (Voorhaar and Hoogenboom, 2016). Among them, hydrogels manufactured under physical trigger conditions have some outstanding features of clinical application. For example, their mild formation temperature and low toxicity in cross-linking reaction are extremely reliable and trustworthy. The hydrogels prepared by this method have great potential application value in pinhole bone defects and fractures. Whereas chemically triggered hydrogels are covalently cross-linked *via* monovalent, bivalent, or multivalent, they tend to intervene in those hard and large bone defects (Xue et al., 2021).

2.4.1 Physically cross-linked hydrogels

The gelation process of physically cross-linked hydrogels occurs under mild conditions, the interactions involved are mainly ionic. The triggering conditions are often related to temperature (Nonoyama et al., 2020; Xue et al., 2021). Interestingly, ions also play critical roles in maintaining body homeostasis (Zhang et al., 2021b; 2021c). For example, natural polysaccharide hydrogels are usually prepared adopting the principle of ionic interactions. Such hydrogels have valuable potential applications in BTE, effectively supporting the adhesion, proliferation and differentiation of angiogenic and osteoblasts cells (Han et al., 2013). Many injectable hydrogels are also formed through physical interactions. For example, Hou et al. (2015) researched a self-assembled injectable hydrogel linked by hydrogen bonding with striking biocompatibility, biodegradability, and sustainable release of biomolecules, which could interact with different types of biomolecules for BTE. Regarding temperature-triggered hydrogels, thermosensitive hydrogels are fabricated by covalent cross-linking thermo-responsive chains into polymers. PNIPAAm, poly (N,N-diethyl acrylamide), poly (lactic-co-glycolic acid)-PEG and soluplus are some of the commonly-used thermo-responsive polymers (Li X. et al., 2017; Wu et al., 2017; Ekerdt et al., 2018; Hanyková et al., 2020; Xue et al., 2021). Temperature-responsive polymers have great potential for application in drug delivery, of which PNIPAAm is a typical representative due to its ability to reversibly swell in aqueous solutions (Vadnere et al., 1984; Mortensen and Pedersen, 1993; Khiabani et al., 2021). However, pristine hydrogels' adjustable mechanical capabilities and rheological properties are limited. Hence, bonding PNIPAAm with other polymer chains can enhance its stabilities and mechanical properties (Li J. et al., 2018). The survey report showed that hyaluronic acid (HA), elastin-like protein (ELP), alginate (AAlg), gelatin, monoacryloyloxyethyl phosphate (MAEP), furfurylamine grafted chondroitin sulfate (ChS-F) and hydroxyapatite (HAp) incorporated into PNIPAAm could effectively improve mechanical strength, thermo sensitivity, degree of crystallization, swelling ratio and other related properties (Khiabani et al., 2021).

2.4.2 Chemical cross-linked hydrogels

Chemical reactions can significantly improve the control of flexibility and precision associated with crosslinking, stabilize the hydrogel matrix, enhance mechanical properties and increase stability (Zhang and Khademhosseini, 2017; Xue et al., 2021). Moreover, for the application of hydrogels in substance delivery, the chemically cross-linked form may supply more efficient release dynamics (Khiabani et al., 2021). To date, numerous chemical cross-linking modes have been exploited in hydrogel systems, which comprise small molecule cross-linking, photo-induced cross-linking, and enzyme-induced cross-linking (Xue et al., 2021).

Small-molecule crosslinkers include tannic acid (TA), glutaraldehyde, dopamine, genipin. Since glutaraldehyde has limited use due to toxic side effects on cells and tissues, TA, dopamine, genipin, and caffeic acid are often used as ideal substitutes in polymer networks to enhance the biological properties of materials (Oryan et al., 2018; Xue et al., 2021). Advanced hydrogels cross-linked by different molecular reagents show many compelling merits, including extended selectivity, rapid gel-formation ability, and tunable mechanical properties (Xue et al., 2021).

Photo-triggered hydrogels are triggered by specific wavelengths of light (ultraviolet (UV) or visible light) to induce the formation and morphological changes of 3D networks of gel (Zhu H. et al., 2020). Multiple nature/synthetic-derived polymers are modified with light-responsive cross-linking groups. For example, natural sources such as collagen, HA, and gelatin polymers are modified to obtain such hydrogels. The photo-crosslinking method facilitates the formation of *in situ* gels and achieves precise spatio-temporal control. Relevant optical properties include wavelength, distance, power, and exposure time of the applied light (Zhang K. et al., 2021; Kirillova et al., 2021). It is worth noting that the photo-crosslinking process of the gel must exist photoinitiators, which determine the wavelength of exposure and the quality of gel formation (Xue et al., 2021). However, toxic photoinitiators affect the cell-loaden type and biocompatibility and destroy the hydrogel's friendly internal environment, limiting the hydrogel's application in BTE (Balakrishnan and Banerjee, 2011).

Due to the potential toxicity of small-molecule chemical crosslinkers and residual reagents, other methods should be sought to avoid this tricky problem. Enzymatically cross-linked hydrogels have excellent biocompatibility, tunable stiffness and rapid gelation (Akhtar et al., 2016). Thus, focusing on enzymatically catalyzed gel-formation may point a hopeful direction for the subsequent development in BTE. Among them, a representative example is a cross-linking reaction initiated by horseradish peroxidase (HRP) (Xue et al., 2021).

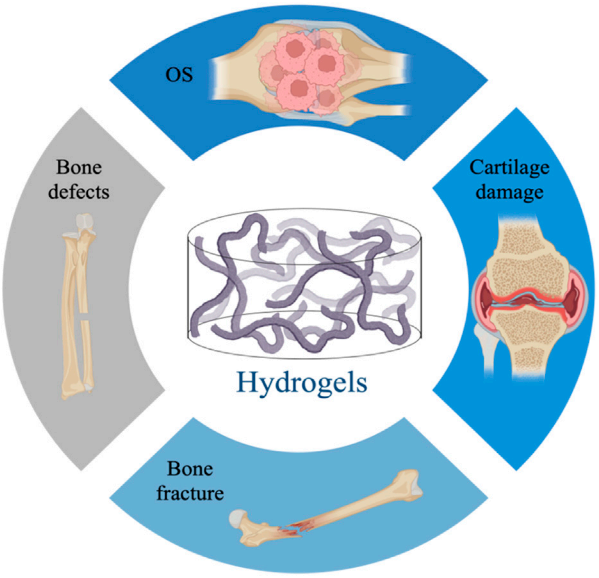

FIGURE 2
Application of hydrogels in bone diseases, including bone defects, fractures, cartilage damage, osteoarthritis.

3 Hydrogels in bone diseases

Combined with tremendous improvements in the preparation of hydrogels, which exhibit excellent physical and chemical properties, making them cutting-edge biomaterials. How these materials can ultimately be applied clinically and tuned for specific clinical applications has been investigated (Zhang and Khademhosseini, 2017). During these decades of progress, an increasing number of novel hydrogels have been applied to targetable drug delivery and treatment of diseases in BTE (Yu et al., 2020; Yue et al., 2020).

As the scaffold material in BTE, hydrogels mainly play the following functions: 1) to transport the cells to specific sites; 2) to facilitate interactions between cells and biomaterials, and promote cell attachment; 3) to guarantee cell survival, vascularization, proliferation, and differentiation (carriers for protection and delivery of substances); 4) to control tissue structure and function (essential subunits providing mechanical strength); and 5) to ensure safety (negligible inflammation or toxicity) (Langer and Tirrell, 2004; Preethi Soundarya et al., 2018).

In BTE, injectable hydrogels are usually employed, which can be minimally invasive to reach the defect site to fill internal large or irregular defects. Injectable forms of hydrogels can treat deformities of any shape, as well as deliver drugs and immobilize injured bone tissue. Factors such as curvature, pore geometry, pore size, and porosity associated with

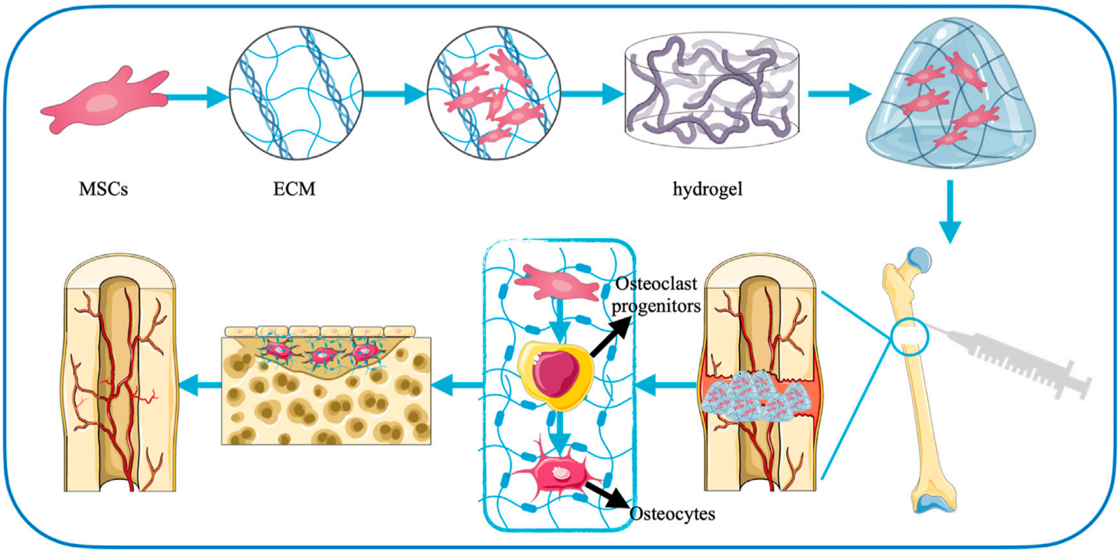

FIGURE 3
The role of hydrogels in the treatment of bone defects.

composite scaffold materials play a key role in bone formation (Zadpoor, 2015). Typically, composite materials are incorporated into hydrogels with the main purpose of maintaining the cohesiveness of the particles both during injection and after delivery to the defect site. In BTE, common examples include Oligo [poly (ethylene glycol) fumarate] and calcium phosphate (apatite), gelatin methacrylate and HAP, cyclic acetal hydrogels and nano-HAP (hydroxyapatite), poly (ethylene glycol) diacrylate and clay, alginate and 45S5 bioactive glass (BG), elastin-like polypeptide collagen and 45S5 BG, et al.(Chang et al., 2010; Patel et al., 2010; Bongio et al., 2011; Wheeler et al., 2013; Zeng et al., 2014; Sadat-Shojai et al., 2015; Utech and Boccaccini, 2016; Nallusamy and Das, 2021). However, prolonged usage of injectable hydrogels can also lead to damage to surrounding tissues, limiting the maintenance of mechanical and biological properties. Fortunately, shape memory and self-healing hydrogels can help solve this problem by preserving the functional level of cells and tissues. Shape memory hydrogels exhibit extremely high tensile strength. Self-healing hydrogels possess both high tensile strength and superior elongation at break (Mehrotra et al., 2020).

The preparation of biomimetic hydrogels in the field of BTE provides a broad prospect for the treatment of bone-related diseases (Xue et al., 2021). Below we describe the application of hydrogels in bone defects, fractures, cartilage injuries, and osteoarthritis, where regeneration of bone loss is a key consideration for their therapeutic goals (Benjamin, 2010) (Figure 2).

3.1 Bone defects

Bone defects are mainly severe painful injuries caused by fractures, infections, trauma, tumor resection or skeletal abnormalities (Yu et al., 2020). At present, although autologous bone grafting is still the momentous means of treatment, the availability of the source and the secondary injury it causes limit its widespread use. Bone graft scaffolds are gradually being widely used because they can overcome the above problems and have remarkable clinical application effects (Bauer and Muschler, 2000; Henkel et al., 2013; Perez et al., 2018). Notably, in bone defect repair, the ECM plays an important role as bridging in signal transduction and interchange of material between the regenerating tissue and the original structure. The network structure of the hydrogel can effectively mimic the ECM (Cui et al., 2019; Shang et al., 2021).

Therefore, hydrogel materials have natural advantages as scaffolds for new bone tissue growth, which exhibit great potential in treating delayed bone repairing or wound healing (Figure 3). In addition, the repair of bone defects is actually an osteogenic effect, which is mainly based on the growth, multiplication, and maturation of osteoblasts. When the self-recovery ability is insufficient, growth factors and cells pass through the hydrogels to promote the proliferation and differentiation of mesenchymal stem cells (MSCs) and accelerate bone synthesis (Chaudhuri et al., 2016; Yue et al., 2020). At present, there are various cross-linking influencing substances used to prepare hydrogels suitable for bone defects, mainly mineral ions, thermosensitive polymers, small molecule cross-linking agents, photoresponsive polymers, enzymes, exosomes, and molecular therapies.

Mineral ions are an integral part of maintaining the physiological balance and stabilization of body and can form functional hydrogels by linking with polymer chains to accelerate bone regeneration (Xue et al., 2021). Thus, ionic-based hydrogels are frequently used in bone-related diseases to promote osteoanagenesis. Irons are often incorporated into biomimetic materials to improve blood vessel formation during bone regeneration. Copper can also effectively maintain the bone quantity and accelerate wound repair. The data have shown that adding copper ions to the hydrogels could maintain its network structure for a long time and ensure the sustained-release behavior of biologically active substance (Pontremoli et al., 2018; Xue et al., 2021). Not only that, recent studies have shown that Mg^{2+} has unlimited potential. Its role in promoting bone differentiation and bone regeneration in bone defects is very obvious (Lin et al., 2018; Obata et al., 2019). Pan et al. (2020) incorporated MgO nanoparticles into hydrogels and found that the addition of Mg^{2+} enhanced the osteoblast differentiation of bone mesenchymal stem cells (BMSCs) and accelerated bone tissue regeneration. In addition, a 3D hydrogel scaffold combined with hydroxyapatite/MgO nanocrystal designed by a research group also enhanced the repair of bone defect in diabetic rats.

Thermosensitive polymers (such as PNIPAAm, Soluplus) can be incorporated into the backbone to fabricate highly biocompatible thermoresponsive hydrogels for bone defects requiring minimally invasive surgery (Xue et al., 2021). However, such hydrogels usually have poor mechanical properties and need to be composited with other materials to enhance the strength of the matrix (Ahmed, 2015; Bahram et al., 2016; Fuchs et al., 2020; Ji and Kim, 2021). It has been found that incorporating of HA into thermally responsive hydrogel systems can enhance the physical mechanics performance of the hydrogels. HA becomes the main hydrophilic chain of such hydrogels due to the presence of hydroxyl and carboxyl groups (Ekerdt et al., 2018). Furthermore, HA is also a major part of ECM, which facilitates a range of cellular behaviors *in vivo*. Studies have shown that HA-PNIPAAm polymers are mainly generated by modifying the thiol-terminated PNIPAAm with the pendant vinyl groups of HA-VS (Ekerdt et al., 2018; Xue et al., 2021). And the constructed hydrogels have regulated mechanical behavior adapted to specific stem cell differentiation, for example, which greatly promoted the osteogenic differentiation of BMSCs (Rape et al., 2015).

Small-molecule crosslinkers, including dopamine, nanoclays, genipin and TA, are frequently introduced into polymer networks as ideal substitutes for enhancing the properties of biomaterials. Li et al. (2016) found that introducing metal ions (Fe^{3+}) and phenolic hydroxyl groups into dopamine-modified polymers can form dynamic covalent bonds, ultimately enhancing the controllability of hydrogels' mechanical properties. It must be mentioned that, due to the reversibility of the structure of metal coordination bonds, this hydrogel also has a self-healing capacity. That is to say, this type of hydrogel has both tunable mechanical properties and self-healing ability. As a broad-spectrum hydrogel model, it is not only suitable for soft tissue defects (skin wounds) but also has a remarkable curative effect on bone defects. In addition, the fusion of nanotechnology and hydrogels provides a novel idea for bone defect repair. Introducing nanoclay as the crosslinking agent at the nanoscale into the caffeic acid-modified chitosan system can form versatile, self-rehabilitation hydrogels (Xue et al., 2021). The nanoclay-crosslinked hydrogel shows good osteoinductivity by modulating the Wnt/β-catenin pathway and can be used in arbitrary bone defects. Genipin also acts as a cross-linking agent to enhance the mechanical properties of 3D scaffold. Another study have shown that TA-related hybrid hydrogels could guide bone regeneration in an experimental mouse model (Bai et al., 2020).

Photoresponsive polymer is a kind of polymer that can produce reversible changes in various physical properties under the action of light. Gelatin is a photoresponsive polymer that can be modified by photo-crosslinked groups, mainly containing acrylamide, methacryloyl, and norbornene. Gelatin methacrylate (GelMA) is the most typical photo-crosslinked polymer, which exhibits biological and mechanical properties vary with the degree of methacrylation and hydrogels' concentration (Zhao et al., 2016). It should be pointed out that GelMA itself has low osteogenic activity; some bioactive components need to be introduced to enhance the bone regeneration ability of GelMA (Xue et al., 2021). Osteogenic growth peptide (OGP) is an active compound that enhances bone repair *in vivo* (Gabarin et al., 2001). Studies suggest that OGP-crosslinked GelMA hydrogels can improve cellular adherence and growth and accelerate the expression of osteogenesis-related genes, promoting the regeneration capacity of new tissue in bone defects. Qiao et al. (2020) prepared a novel hydrogel by utilizing the form of covalent linkage between GelMA and OGP under UV light to enhance the osteogenesis potential of GelMA-based hydrogels. In a rat distal femoral defect model, this hydrogel demonstrated enhanced repair capacity *in vivo* and an accelerated rate of new bone regeneration.

Studies have shown that hydrogels under the action of enzymes can also promote bone repair, showing great application prospects. For example, Xue et al. (2021) prepared an enzymatic hydrogel with chondroitin sulfate (CS) and HA in the presence of H_2O_2 and HRP in a specific environment. The researchers conducted *in vitro* and *in vivo* experiments. The results showed that the microenvironment provided by the newly prepared hydrogel is favorable for the osteoblastic differentiation of BMSCs and the bone tissue repairing of rat femur.

In addition to using traditional and common cross-linked polymers to prepare hydrogels with excellent properties for bone defects, many emerging strategies for hydrogel innovation have also been proposed to enrich the field of bone defect treatment. The secretory process of paracrine signaling is closely linked to tissue damage repair (Al-Samadi et al., 2017). Exosomes are essential for the inflammatory response after injury and can promote the regeneration and reconstruction of damaged tissues (Jing et al., 2018). Currently, many studies have focused on loading exosomes in hydrogel systems. It has been indicated that exosomes from human bone marrow-derived MSCs could effectively enhance osteogenic differentiation (Pethő et al., 2018). Animal model studies have also shown that exosomes loaded in hydrogels can help boost osteogenesis and healing of damaged bones in the rat models (Yang et al., 2020). Various studies indicate that this hydrogel exhibits excellent bone repair ability while possessing superior properties (such as strong self-repair ability, high biocompatibility, and low toxicity.) (Pishavar et al., 2021).

Currently, diagnosis and treatment of diseases at the molecular and cellular levels have been explored from multiple perspectives, such as RNA interference (RNAi) technology. It is mediated by microRNAs (miRNAs) and small interfering RNAs (siRNAs) and is an effective strategy for post-transcriptional gene regulation. Nevertheless, the adhibition of RNAi therapies related to bone regeneration has not yet entered the clinical trial stage, so there is still a lot of research space. One of the major difficulties is the inability to achieve sustained release of RNA molecules in the target site of bone defect and surrounding cells. We still lack a suitable carriers to accompany the safe operation and get effective results. A likely approach is to encapsulate RNAi molecules into hydrogels, which can also be delivered in combination with nanoparticle technology (Yu et al., 2020). Nanomaterials, which have been mentioned earlier, are often incorporated into polymer matrices as promising reinforcement materials for next-generation BTE applications (Zhu et al., 2022).

3.2 Bone fracture

The bone fracture usually occurs under high-force shock or pressure. Bone formation and growth are crucial for treating bone fractures (such as avulsion, comminuted, and crush fractures) (AI-Aql et al., 2008; Yun et al., 2021). At present, most fractured bone tissue heals itself, while complex fractures require interventions to promote bone repair (Agarwal and García, 2015). Minor fractures can be recovered without surgical intervention, but the recovery period is long and affects the patient's quality of life (AI-Aql et al., 2008). In contrast, multiple complex fractures have poor recovery and often require invasive surgery (AI-Aql et al., 2008; López et al., 2014). The application of 3D polymer matrix to repair damaged bone tissue in fracture patients is a hot research direction currently (Han et al., 2021; Khiabani et al., 2021).

Using autologous bone and prosthetic implants to improve bone reconstruction can accelerate bone healing and maintain the degree of recovery to minimize surgical intervention. In the process of exploring treatment methods for bone fractures, a research group proposed to use hydrogel-type bone-derived decellularized extracellular matrix (bdECM) and β-tricalcium phosphate (β-TCP) to immobilize 3D-printed polycaprolactone scaffolds. Using three treatments of two different materials (bone-derived ECM, beta-TCP, and a combination of both), the researchers evaluated their performance as materials for inducing fusion in native bone grafts. A porous-structured polycaprolactone (PCL) scaffold was placed in the centre of the rat calvarial defects model. Then, each material was used to fill the gap between the PCL scaffold and the defective bone. The bone formation capacity in the organism was finally assessed by histological analysis. *In vitro* experiments, the properties of the materials were also evaluated with MG63 cells. The results showed that the bone-derived ECM-β-TCP mixture showed faster bone formation in rats and was an ideal osteogenic promoter for the therapy of bone fractures (Yun et al., 2021).

For patients with undisplaced fractures, who do not require bone grafting and are treated conservatively, injectable hydrogel-mediated growth factor delivery vehicles may be considered to accelerate fracture healing (Gibbs et al., 2016). Wang et al. (2008) investigated the ability of collagen-based gels containing nerve growth factor (NGF) and nano-hydroxyapatite particles to strengthen bone formation and explored the potential clinical efficacy of hydrogels in conservative treatment of fractures. The research team injected the gel into the callus of the rabbit mandible and found that the hydrogel facilitated growth factor-mediated osteogenesis (Wang et al., 2008; Gibbs et al., 2016). Sasaki et al. (2013) also proposed that a gelatin-based hydrogel containing basic fibroblast growth factor (bFGF) could boost the healing of fracture of the proximal sesamoid bone. The hydrogels are not only safely applied to the injured region, but also the level of degradation can be regulated by adjusting the degree of cross-linking (Sasaki et al., 2013) (Figure 4). In addition, the research data suggested that the mixed growth factor delivery system based on alginate and electrospun nanofibrous mesh-based hydrogels may promote bone regeneration during fracture nonunion, providing preliminary basic support for follow-up studies (Kolambkar et al., 2011). Regarding the development of nanotechnology, there are also studies to explore the effect of gelatin on the stability of silver nanoparticles (AgNPs) and the application of related polymers in fracture treatment. The experimental group prepared AgNPs-loaded Gel hydrogels under sunlight using gelatin as a stabilizer. The researchers found that the synthetic hydrogels were not harmful to osteoblasts. And they further effectively improved the survival rate and diffuse of osteoblasts, showing the potential ability to regulate fracture healing (Han et al., 2021).

It has to be mentioned that fracture repair is often accompanied by the risk of infection (Metsemakers et al.,

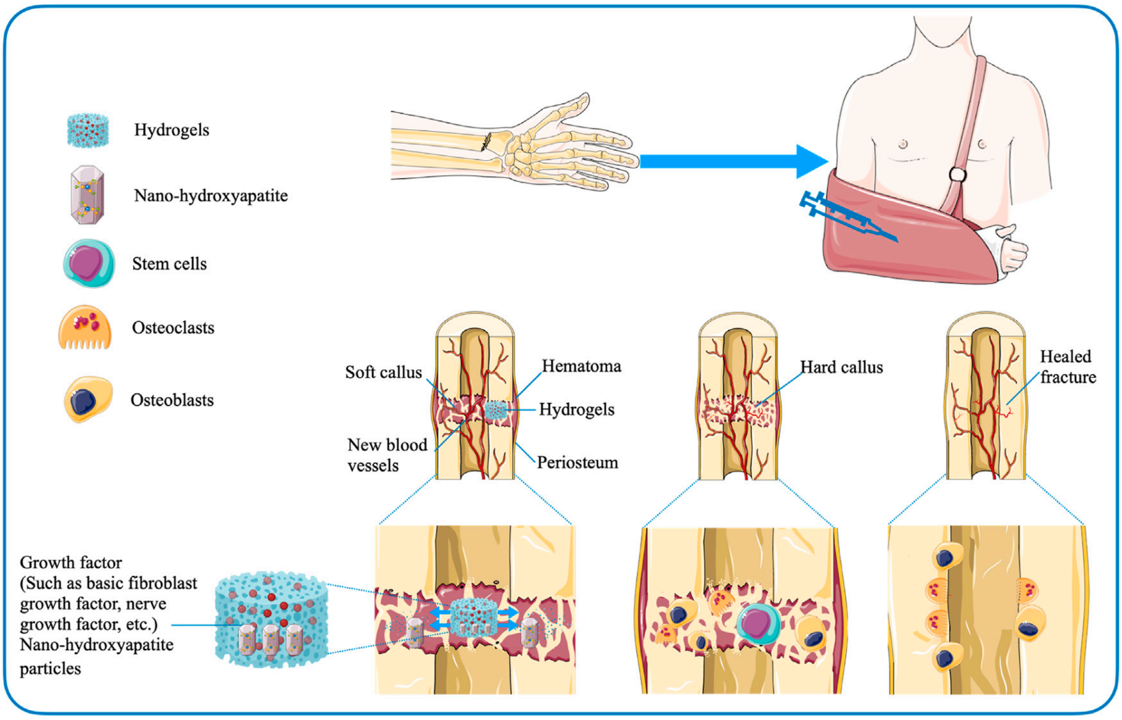

FIGURE 4
Hydrogel-mediated sustained release of growth factors accelerates fracture healing.

2015). Prophylactic antibiotic therapy can effectively reduce the incidence of infection. However, edema, destruction of vasculature and tissue often limit the penetration of antibiotics, reducing the therapeutic efficacy. Fortunately, this conundrum can be overcome through the application of hydrogels. The carriers transport antibiotics to specific sites to exert their effects. Boo et al.(Ter Boo et al., 2018) demonstrated the great feasibility of the gentamicin-loaded hydrogel in preventing infection in a rabbit humeral osteotomy model. Moreover, Lu et al. (2018) proposed that copper-containing hydrogels also exhibited obvious antibacterial activity.

3.3 Cartilage damage

Damage to cartilage and osteochondral tissue is a common global public health problem. Its occurrence is closely related to diseases such as joint trauma, osteochondritis dissecans, and osteoarthritis. The prevalence rate of cartilage and osteochondral injuries in the general population is 60% (Liu et al., 2017). Cartilage is avascular and lacks sufficient progenitor cells and nutrients to heal itself when damaged (Huey et al., 2012). If left untreated, cartilage damage will progress and become irreversible, leading to osteoarthritis that can eventually lead to disability (Chen et al., 2009). Current treatment strategies mainly include repair of microfractures, and autologous chondrocyte implantation, osteochondral autografts and allografts (Benazzo et al., 2008; Selmi et al., 2008; Hamblin et al., 2010; Haene et al., 2012; MacDonald et al., 2016; Polat et al., 2016; Gou et al., 2020). Despite their widespread usage, these approaches have significant drawbacks and limitations (Dai et al., 2020). At present, therapeutic techniques targeting cartilage lesions are difficult to cure cartilage damage, thereby accelerating the development of alternative tissue engineering strategies. Combined with BTE, it is a feasible idea to create artificial structures that mimic the structural characteristics, mechanical properties and biological functions of cartilage tissue. Cartilage tissue has high intensity, elasticity, and shock absorption (Pascual-Garrido et al., 2018). Consequently, it is promising to prepare high-intensitive, whippy hydrogels to mimic the mechanical characters of natural articular cartilage (Dai et al., 2020).

Regarding the physical cross-linking of hydrogels, although their effects on chondrogenic differentiation have rarely been investigated, some studies have considered the influence of the ionic effect of physical cross-linking of hydrogels on the biological behavior of cartilage. Xu's group (Xu et al., 2018) developed a biomaterial that binds copper to promote cartilage formation. *In vitro* studies showed that Cu promoted morphological changes of MSCs, the production of glycosaminoglycan (GAG) and the expression of chondrogenic genes. To prepare hydrogels that can be applied to soft tissue, in the presence of positively charged quaternary poly (ethylene imine) (Q-PEI) and micelles formed by Pluronic F127 diacrylate, Mahapatra et al.(Das Mahapatra et al., 2020) prepared hydrogels with excellent tenacity by means of dual networks cross-linking. At the same time, this system also contains Ca^{2+} and Cu^{2+} ions, which form coordination bonds and effectively elevate the tensile strength and mechanical intensity of the hydrogels. Hydrogels with dual-ion cross-linked networks and hyper-extensibility have been successfully designed (Xue et al., 2021). In the field of chemically cross-linked hydrogels, Zhang's research group (Zhang et al., 2020) designed a bi-component hydrogel based on HRP-induced cross-linking reaction, which is composed of collagen type I-tyramine (Col-TA) and hyaluronic acid-tyramine (HA-TA). The hydrogel possessed remarkable physicochemical properties and the conjugated TGF-β1 released from the hydrogel greatly promoted the BMSCs' capacity of chondrogenic differentiation *in vitro*. Besides, *in vivo* experiments, histological and immunohistochemical analyses revealed that this enzyme-catalyzed hydrogel could exhibit the superior effects of cartilage repair.

Overall, hydrogels formed without covalency possess tunable mechanical performance and self-healing power, holding great promise in evaluating biomaterials for cartilage tissue regeneration. Combined with the rapid development of modern information technology, it is suggested that the introduction of 3D bioprinting in the field of hydrogel preparation may help meet the needs of patients. The biological structure can be quickly designed through automated and computerized technology to mimic natural cartilage tissue. The development of elastic and high-strength hydrogels for 3D printing in repairing cartilage defects and the osteochondral interface is crucial. It is extremely important to develop highly powerful and flexible hydrogels for 3D printing in repairing cartilage damage. This type of hydrogels may provide novel insights into treating cartilage diseases (Dai et al., 2020).

3.3.1 Osteoarthritis

Joint cartilage is fragile and prone to damage. As mentioned above, cartilage tissue lacks blood vessels and has low metabolic activity, so the associated damage is usually irreversible (Zhang et al., 2016). Long-term damage to articular cartilage ultimately gives rise to the development of OA. OA is a prevailing degenerative joint disease. Its occurrence is highly correlated with the damage to cartilage structure and the up-regulation of permeability, mainly showing the characteristics of cartilage lesions (Hochberg, 2012; Zhang et al., 2016; Quicke et al., 2022). To date, the main treatment modalities for OA include lifestyle interventions, drug therapy (nonsteroidal anti-inflammatory drug, NSAID), and intra-articular therapy (Quicke et al., 2022). Current treatments are limited and only relieve symptoms (Zhang et al., 2008). There is an urgent need to find suitable treatments to impede the progression of OA (Zhao et al., 2022). Although the treatment of OA is hindered by the limitation of the anatomical structure of the joint cavity, the applicability of hydrogels provides new ways of thinking about it (Zhao et al., 2022). Hydrogels are elastic and adhesive, with a range of superior mechanical properties, making them particularly suitable for application in small and relatively isolated joint cavities (Kim et al., 2011). Hydrogels have promising applications in BTE as platforms for loading stem cells and medicines. With regard to hydrogels for OA treatment, there has been substantial research evidence of their effectiveness, accelerating tissue regeneration and the delivery of drugs.

The synovial joints carry a significant load on the human body and have extremely low friction under physiological stress when healthy. Normal frictional stress is typically required to maintain cartilage homeostasis (URBAN, 1994). When cartilage damage occurs (caused by sports, accidental trauma, or old age wear), the boundary layer on the outer surface of the cartilage is destroyed, resulting in dysfunction of cartilage lubrication and increased friction and wear. The limited self-healing ability of articular cartilage cannot cope with high friction, leading to the occurrence of OA, which is mainly characterized by progressive degeneration of articular cartilage (Sellam and Berenbaum, 2010; Goldring and Goldring, 2016; Morgese et al., 2018). In the treatment of OA, reducing friction between articular cartilage surfaces remains an important issue. Hydrogels with idealized mechanical properties and high water content, such as double-network hydrogels, contain highly hydrated lubricating carriers that can provide reservoirs to complement the boundary layer on the gel surface (Lin et al., 2020; Shoaib and Espinosa-Marzal, 2020; Liu Y. et al., 2021; Wang J. et al., 2021; Hilšer et al., 2021; Xie et al., 2021; Chen et al., 2022). These layers work through a hydration lubrication mechanism, resulting in extremely low friction, which is replenished when worn, providing long-term lubrication (Lin and Klein, 2022). It is reported that cartilage-lubricating brush-like polymers (hyaluronic acidgraft-poly-2-acrylamide-2-methylpropanesulfonic acid sodium salt (HA/PA) and hyaluronic acid-graft- poly-2-methacryloyloxyethyl phosphoryl choline (HA/PM)) could effectively combine on the cartilage surface to form a stable boundary layer *in vitro* and *in vivo*, which can lubricate and regenerate cartilage (Xie et al., 2021). On this basis, Chen et al. (2022) blended HA/PA and HA/PM (HPX) with polyvinyl alcohol (PVA) to construct biomimetic cartilage-lubricating hydrogels (HPX/PVA). The hydrogels exhibit low friction and wear, effectively addressing the main drawback of PVA hydrogels used as cartilage implants. It can be seen that the addition of HA/PA and HA/PM can improve the tribological properties and biomimetic properties of PVA hydrogels, which provides the possibility of introducing the boundary lubrication mechanism in the hydrogels (Rong et al., 2020; Lin and Klein, 2021; Branco et al., 2022).

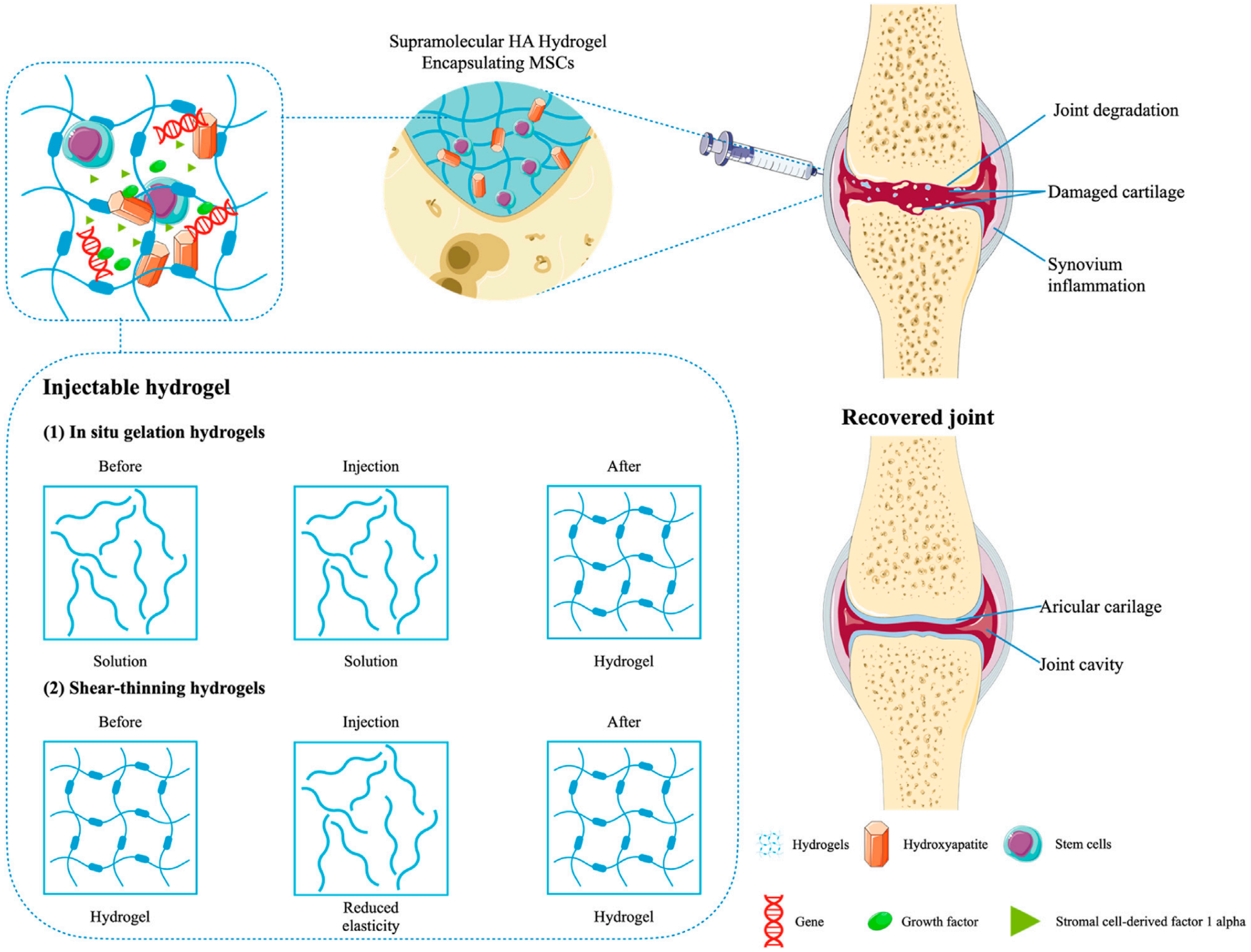

FIGURE 5
Injection therapy of hydrogels in OA.

Additionally, it should be noted that HA-based hydrogels have therapeutic efforts on OA, with data showing respectable pain relief by intra-articular injection of HA and chondroitin sulfate (Zhang et al., 2008). The hydrogels replenish joint fluid and reduce friction between articular cartilage surfaces. In order to improve the efficacy and retention rate of HA, it can be injected into the joint cavity together with the coupling with a thermosensitive polymer. The biocompatibility is maintained by reducing enzyme sensitivity (Maudens et al., 2018). One clinical study suggested that oral NSAIDs could be combined with intra-articular HA and corticosteroids in OA patients with persistent symptoms. Especially in the case of no reactions caused by other drugs, it was more applicable (Alexander et al., 2021). As mentioned previously, HA-based hydrogels are effective in relieving OA-related pain. This is because hydrogels with polyporous structures can expedite cell multiplication and tissue formation by slowly releasing drugs into the synovial cavity, ultimately suppressing inflammation and repairing cartilage damage (Jeuken et al., 2016). Not only that, the hydrogel scaffolds can also host cells and promote cell growth by transmitting signals and nutrients (Jeuken et al., 2016; Bao et al., 2020). For example, Thiolated gelatin/poly (ethylene glycol) diacrylate (PEGDA) interpenetrating network (IPN) hydrogels can simultaneously deliver progenitor cell populations and insulin-like growth factor-1 (IGF-1). By the way, the attachment of IGF-1 to the hydrogels can further support the long-lasting role of stem cells in their proliferation and the regeneration of tissue (Cho et al., 2020). Furthermore, in the treatment of OA, the formation of hyaline-like persistent cartilage is often promoted by implanting MSCs during surgery (Kristjánsson and Honsawek, 2014). Stromal cell-derived factor 1 alpha (SDF-1α) is a crucial factor in MSCs-related biological processes that involve activation, mobilization, homing, and migration of MSCs. Using a chitosan-based

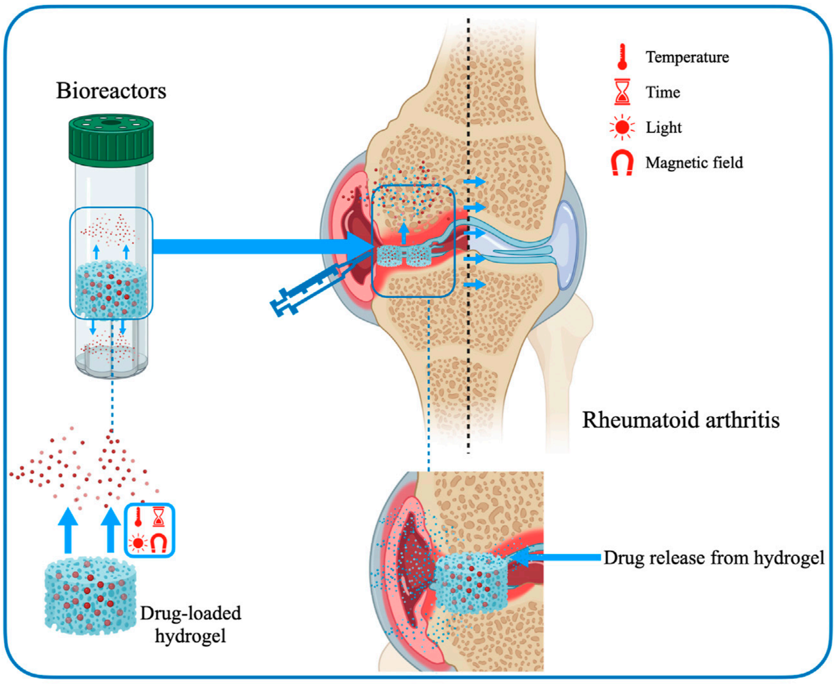

FIGURE 6
Drug delivery hydrogels in suppressing of RA.

hydrogel inset with SDF1α to affect the migration of MSCs significantly promoted homing of the stem cells and repair of cartilage in the OA model (Liu H. et al., 2021). In addition, DNA supramolecular hydrogels are promising cell delivery systems for MSCs therapy, with significant protective effects on MSCs both *in vitro* and *in vivo*, which can be used to treat severe OA models. Studies have shown that DNA supramolecular hydrogels could promote the formation of high-quality cartilage under high-friction conditions of osteoarthritis (Yan X. et al., 2021) (Figure 5).

3.3.2 Rheumatoid arthritis

RA is an autoimmune and chronic inflammatory disease that primarily affects articulationes synoviales and frequently involves injures to both arthroidal cartilage and bone (Hilkens and Isaacs, 2013; Oliveira et al., 2021). The definite pathological mechanism associated with RA remains unknown, but it is generally believed to be related to the breakdown of the state of immune tolerance (Weyand and Goronzy, 2020). Currently, several conservative treatments for RA are mainly used for pain relief and control inflammation. However, traditional modes of administration are not fully effective and have serious adverse side effects. Most immunomodulators suffer from deficiencies such as increased size, low stability, poor permeability to lesion sites and limited ability to cross cell membranes. Hydrogels can be used as carriers for drug delivery to effectively improve the therapeutic effect of biopharmaceuticals (Xiao et al., 2021). Hydrogels as drug delivery systems are a very attractive platform to ensure that these barriers are reduced and the therapeutic effects of drugs are maximized. Furthermore, hydrogels can mimic physiological microenvironments and possess the mechanical behaviors required for use as *in vitro* models of cartilage (Oliveira et al., 2021) (Figure 6). The specific advantages of hydrogels mainly include expanding blood circulation, promoting penetration of diseased tissue, improving accumulation, increasing uptake, enhancing drug-carrying capacity and being easy to modify physicochemical properties (Ahmed and Bae, 2016; Lu et al., 2016; Donahue et al., 2019; Su et al., 2019; Zhu Y. et al., 2020; He et al., 2020).

Tacrolimus-loaded soluplus hydrogel responds to sensitive temperature and is a hopeful vehicle of drug transport for RA therapy (Xue et al., 2021). Researchers used soluplus and tacrolimus to create a micelle-linked hydrogel for the treatment of RA (Wu et al., 2017). Combining the two components greatly modulated the drug release rate and improved the mechanical properties. Specifically, soluplus formed micelles by self-assembly and loaded tacrolimus. The hydrogel was formed under hydrophobic interactions, creating an internal environment with stable mechanical properties to store topical drugs. Furthermore, experiments in the rat models confirmed that the tacrolimus-loaded soluplus hydrogel has a better treatment effect on RA compared to the known poloxamer 407 delivery system.

3.4 Osteosarcoma

OS is the most common primary bone tumour among adolescents and children (Siegel et al., 2021). The traditional therapeutic method is surgical resection combined with chemotherapy regimens, but there are some limitations, leading to systemic side effects, postoperative recurrence, infection, and massive bone loss, while chemotherapy drugs have poor selectivity and drug resistance (Chen et al., 2021). Therefore, it is necessary to find new therapeutic strategies to improve the therapeutic effect and avoid any side effects. Nanoparticle-based drug delivery systems have been exploited to form a promising new-style alternative therapeutic strategy, which can both deliver drugs accurately to tumor sites and repair bone defects after tumor excision (Angulo et al., 2017; Chi et al., 2017; Corre et al., 2020; Yan J. et al., 2021; Gill and Gorlick, 2021; Zhu et al., 2021; Wu et al., 2022). Yin's research group (Yin et al., 2020) developed a new-type nanoimplant SP@MX-TOB/GelMA with multiple functions. Under 808 nm near-infrared (NIR) irradiation, this effect under thermal ablation can efficiently remove OS cells and promote bone regeneration *via* hyperthermia. On the side, SP@MX-TOB/GelMA can carry high-efficiency antibacterial agents to prevent infection. In conclusion, this multipurpose implant under photothermal control can greatly eliminate OS cells, fight infection and enhance osteogenic ability (Wu et al., 2022). Although hydrogel nanoparticles have many benefits, their inherent properties also inevitably limit their clinical applications. For example, the specific hydrophilic nature of hydrogels may complicate the formulation of high drug loading and sustained drug release. For another example, studies have shown that nanoparticles with a diameter of more than 100 nm cannot form stabilized hydrogels; hence the diameter and amount of nanoparticles should be strictly controlled (Beckett et al., 2020; Wu et al., 2022). In the future, more work will be needed on the preparation.

4 Conclusion

At present, there are many opportunities to apply small molecule substances and biomaterials in clinical applications. It has been argued that the final objective is to ameliorate the biological response and rebuild nascent systems. On the long road to finding ideal biomedical materials used in clinics, efforts should be made toward composite hydrogels. For example, numerous biologically active substances possess osteoinductive properties that can be studied and analyzed in combination with hydrogels, mainly including steroids, collagen, casein phosphopeptides, prostaglandin agonists and amelogenin (Yue et al., 2020).

Hydrogels have been intensively studied because of their stability, but their preparation and application remain challenging by reason of the complicacy of the inherent properties of this class of materials. Numerous research groups have focused on developing new polymerization methods to synthesize polymers with different structures while avoiding using large amounts of harmful solvents. In this process, the molecular structures have been adjusted to design high-performance hydrogels required in specific circumstances, hoping that patients will benefit from them in the near future. Although the research results of hydrogels in BTE are gratifying, providing similar results to natural tissues, further research and development are still needed to seek the optimal research objects in each performance segment (aspects of physics and biology) and then enter into clinical translation (Nallusamy and Das, 2021).

It must be pointed out that there is still a long way to go to penetrate the market owing to insufficient clinical research evidence to prove the efficacy of hydrogels. The large-scale production of such new biomaterials faces technical and economic difficulties. It is predicted to be challenging to introduce them into the clinic and the market (Haugen et al., 2019; Liu et al., 2022). It needs to be emphasized again that improving the safety and adaptability of hydrogels is a pivotal issue that should be addressed in our future research. Conducting *in vivo* study designs is a critical and highly challenging part of testing biomaterials for safety and efficacy. The effect of hydrogels in BTE can be studied in relatively simple small animal models. Depending on different research purposes, the settings of the animal model can be adjusted and modified. However, final pre-clinical testing in larger animals should be performed to understand the suitability of the hydrogels and determine if it is conditioned for the optimal transition from the bench to the bedside.

Most of the research is only in the experimental phase and has not yet begun to be applied to the stage of clinical therapeutics. Here, the following recommendations are summarized. 1) Major factors such as hydrophilicity have been adjusted to design hydrogels with superior performance, but it is still essential to establish a complete set of methods to assess the biocompatibility of hydrogels with humans (Yue et al., 2020; Khiabani et al., 2021). 2) Many different hydrogels have been studied in animal models. However, Further standardization of animal models and procedures is needed to improve the comparability of studies to elucidate the therapeutic effects of hydrogels on bone-related diseases and assess safety and applicability (Kim and Kim, 2013; Nikravesh et al., 2020; Yue et al., 2020). 3) In bone-related diseases, many studies on hydrogels based on human models should be carried out (Xue et al., 2021).

As a new functional polymer material, the hydrogel has great application value in BTE. Understanding the properties, preparation and cross-linking methods of hydrogels can help us further grasp the progress of their applications in bone-related diseases. The idea of combining hydrogels with other biomaterials has gradually become a general strategy for treating bone-related diseases (Chen et al., 2016; Ghosh et al., 2018; Hu X.-B. et al., 2019, 4; Liu et al., 2022; Sun et al., 2022). Overall, though hydrogel-related biological materials are still under development and have many challenges, they undeniably have great potential in future clinical treatments (Yue et al., 2020). The application of hydrogels builds a bridge for therapeutics of bone-related diseases.

Author contributions

XL (1st author): Conceptualization, Methodology, Investigation, Writing-original draft. SS: Conceptualization, Datum analysis. NW: Writing-review and; editing. LX, XL (6th author), and KR: Writing, Revising, Supervision.

Funding

This work was funded by the Natural Science Foundation of Jiangsu Province (BK20220464), Jiangsu Provincial Traditional Chinese Medicine Science and Technology Development Plan Project (2020 ZD202008), Science and technology projects in Jiangsu Province (2019 BE2019765), and National Natural Science of China (81772356).

Conflict of interest

The authors declare that the research was conducted in the absence of any commercial or financial relationships that could be construed as a potential conflict of interest.

Publisher's note

References

Agarwal, R., and García, A. J. (2015). Biomaterial strategies for engineering implants for enhanced osseointegration and bone repair. *Adv. Drug Deliv. Rev.* 94, 53–62. doi:10.1016/j.addr.2015.03.013

Ahmed, E. M. (2015). Hydrogel: Preparation, characterization, and applications: A review. *J. Adv. Res.* 6, 105–121. doi:10.1016/j.jare.2013.07.006

Ahmed, M. S., and Bae, Y.-S. (2016). Dendritic cell-based immunotherapy for rheumatoid arthritis: From bench to bedside. *Immune Netw.* 16, 44–51. doi:10.4110/in.2016.16.1.44

Ai-Aql, Z. S., Alagl, A. S., Graves, D. T., Gerstenfeld, L. C., and Einhorn, T. A. (2008). Molecular mechanisms controlling bone formation during fracture healing and distraction osteogenesis. *J. Dent. Res.* 87, 107–118. doi:10.1177/154405910808700215

Akhtar, M. F., Hanif, M., and Ranjha, N. M. (2016). Methods of synthesis of hydrogels. A review A review. *Saudi Pharm. J.* 24, 554–559. doi:10.1016/j.jsps.2015.03.022

Al-Samadi, A., Awad, S. A., Tuomainen, K., Zhao, Y., Salem, A., Parikka, M., et al. (2017). Crosstalk between tongue carcinoma cells, extracellular vesicles, and immune cells in *in vitro* and *in vivo* models. *Oncotarget* 8, 60123–60134. doi:10.18632/oncotarget.17768

Alexander, L. A. M., Ln, D., Eg, Z., Is, D., Ay, K., Ss, R., et al. (2021). Pharmacological management of osteoarthritis with a focus on symptomatic slow-acting drugs: Recommendations from leading Russian experts. *J. Clin. Rheumatol.* 27, e533–e539. doi:10.1097/RHU.0000000000001507

Amini, A. A., and Nair, L. S. (2012). Injectable hydrogels for bone and cartilage repair. *Biomed. Mat.* 7, 024105. doi:10.1088/1748-6041/7/2/024105

Angulo, P., Kaushik, G., Subramaniam, D., Dandawate, P., Neville, K., Chastain, K., et al. (2017). Natural compounds targeting major cell signaling pathways: A novel paradigm for osteosarcoma therapy. *J. Hematol. Oncol.* 10, 10. doi:10.1186/s13045-016-0373-z

Ansari, S., Seagroves, J. T., Chen, C., Shah, K., Aghaloo, T., Wu, B. M., et al. (2017). Dental and orofacial mesenchymal stem cells in craniofacial regeneration: The prosthodontist's point of view. *J. Prosthet. Dent.* 118, 455–461. doi:10.1016/j.prosdent.2016.11.021

Bahram, M., Mohseni, N., and Moghtader, M. (2016). An introduction to hydrogels and some recent applications. *IntechOpen*. doi:10.5772/64301

Bai, S., Zhang, X., Lv, X., Zhang, M., Huang, X., Shi, Y., et al. (2020). Bioinspired mineral–organic bone adhesives for stable fracture fixation and accelerated bone regeneration. *Adv. Funct. Mat.* 30, 1908381. doi:10.1002/adfm.201908381

Balakrishnan, B., and Banerjee, R. (2011). Biopolymer-based hydrogels for cartilage tissue engineering. *Chem. Rev.* 111, 4453–4474. doi:10.1021/cr100123h

Bao, W., Li, M., Yang, Y., Wan, Y., Wang, X., Bi, N., et al. (2020). Advancements and Frontiers in the high performance of natural hydrogels for cartilage tissue engineering. *Front. Chem.* 8, 53. doi:10.3389/fchem.2020.00053

BaoLin, G., and Ma, P. X. (2014). Synthetic biodegradable functional polymers for tissue engineering: A brief review. *Sci. China Chem.* 57, 490–500. doi:10.1007/s11426-014-5086-y

Barouti, G., Liow, S. S., Dou, Q., Ye, H., Orione, C., Guillaume, S. M., et al. (2016). New linear and star-shaped thermogelling poly([R]-3-hydroxybutyrate) copolymers. *Chem. Eur. J.* 22, 10501–10512. doi:10.1002/chem.201601404

Bauer, T. W., and Muschler, G. F. (2000). Bone graft materials. An overview of the basic science. *Clin. Orthop. Relat. Res.* 371, 10–27. doi:10.1097/00003086-200002000-00003

Beckett, L. E., Lewis, J. T., Tonge, T. K., and Korley, L. T. J. (2020). Enhancement of the mechanical properties of hydrogels with continuous fibrous reinforcement. *ACS Biomater. Sci. Eng.* 6, 5453–5473. doi:10.1021/acsbiomaterials.0c00911

Benazzo, F., Cadossi, M., Cavani, F., Fini, M., Giavaresi, G., Setti, S., et al. (2008). Cartilage repair with osteochondral autografts in sheep: Effect of biophysical stimulation with pulsed electromagnetic fields. *J. Orthop. Res.* 26, 631–642. doi:10.1002/jor.20530

Benjamin, R. M. (2010). Bone health: Preventing osteoporosis. *Public Health Rep.* 125, 368–370. Available at: https://www.ncbi.nlm.nih.gov/pmc/articles/PMC2848259/. doi:10.1177/003335491012500302Accessed May 14, 2022)

Bongio, M., van den Beucken, J. J. J. P., Nejadnik, M. R., Leeuwenburgh, S. C. G., Kinard, L. A., Kasper, F. K., et al. (2011). Biomimetic modification of synthetic hydrogels by incorporation of adhesive peptides and calcium phosphate nanoparticles: *In vitro* evaluation of cell behavior. *Eur. Cell. Mat.* 22, 359–376. doi:10.22203/ecm.v022a27

Bouhadir, K. H., Alsberg, E., and Mooney, D. J. (2001). Hydrogels for combination delivery of antineoplastic agents. *Biomaterials* 22, 2625–2633. doi:10.1016/S0142-9612(01)00003-5

Branco, A. C., Oliveira, A. S., Monteiro, I., Nolasco, P., Silva, D. C., Figueiredo-Pina, C. G., et al. (2022). PVA-based hydrogels loaded with diclofenac for cartilage replacement. *Gels* 8, 143. doi:10.3390/gels8030143

Buwalda, S. J., Boere, K. W. M., Dijkstra, P. J., Feijen, J., Vermonden, T., and Hennink, W. E. (2014). Hydrogels in a historical perspective: From simple networks to smart materials. *J. Control. Release* 190, 254–273. doi:10.1016/j.jconrel.2014.03.052

Buwalda, S. J., Vermonden, T., and Hennink, W. E. (2016). Hydrogels for therapeutic delivery: Current developments and future directions. *Biomacromolecules* 18, 316–330. doi:10.1021/acs.biomac.6b01604

Caló, E., and Khutoryanskiy, V. V. (2015). Biomedical applications of hydrogels: A review of patents and commercial products. *Eur. Polym. J.* 65, 252–267. doi:10.1016/j.eurpolymj.2014.11.024

Chai, Q., Jiao, Y., and Yu, X. (2017). Hydrogels for biomedical applications: Their characteristics and the mechanisms behind them. *Gels* 3, 6. doi:10.3390/gels3010006

Chang, C.-W., Spreeuwel, A. van, Zhang, C., and Varghese, S. (2010). PEG/clay nanocomposite hydrogel: A mechanically robust tissue engineering scaffold. *Soft Matter* 6, 5157–5164. doi:10.1039/C0SM00067A

Chaudhuri, O., Gu, L., Klumpers, D., Darnell, M., Bencherif, S. A., Weaver, J. C., et al. (2016). Hydrogels with tunable stress relaxation regulate stem cell fate and activity. *Nat. Mat.* 15, 326–334. doi:10.1038/nmat4489

Chen, C., Chi, Y.-J., Zhao, M.-Y., and Lv, L. (2012). Purification and identification of antioxidant peptides from egg white protein hydrolysate. *Amino Acids* 43, 457–466. doi:10.1007/s00726-011-1102-0

Chen, H., Sun, J., Hoemann, C. D., Lascau-Coman, V., Ouyang, W., McKee, M. D., et al. (2009). Drilling and microfracture lead to different bone structure and necrosis during bone-marrow stimulation for cartilage repair. *J. Orthop. Res.* 27, 1432–1438. doi:10.1002/jor.20905

Chen, P., Xia, C., Mei, S., Wang, J., Shan, Z., Lin, X., et al. (2016). Intra-articular delivery of sinomenium encapsulated by chitosan microspheres and photo-crosslinked GelMA hydrogel ameliorates osteoarthritis by effectively regulating autophagy. *Biomaterials* 81, 1–13. doi:10.1016/j.biomaterials.2015.12.006

Chen, Q., Liu, S., Yuan, Z., Yang, H., Xie, R., and Ren, L. (2022). Construction and tribological properties of biomimetic cartilage-lubricating hydrogels. *Gels* 8, 415. doi:10.3390/gels8070415

Chen, W., Xu, Y., Li, Y., Jia, L., Mo, X., Jiang, G., et al. (2020). 3D printing electrospinning fiber-reinforced decellularized extracellular matrix for cartilage regeneration. *Chem. Eng. J.* 382, 122986. doi:10.1016/j.cej.2019.122986

Chen, Y., Liu, R., Wang, W., Wang, C., Zhang, N., Shao, X., et al. (2021). Advances in targeted therapy for osteosarcoma based on molecular classification. *Pharmacol. Res.* 169, 105684. doi:10.1016/j.phrs.2021.105684

Chi, Y., Yin, X., Sun, K., Feng, S., Liu, J., Chen, D., et al. (2017). Redox-sensitive and hyaluronic acid functionalized liposomes for cytoplasmic drug delivery to osteosarcoma in animal models. *J. Control. Release* 261, 113–125. doi:10.1016/j.jconrel.2017.06.027

Cho, H., Kim, J., Kim, S., Jung, Y. C., Wang, Y., Kang, B.-J., et al. (2020). Dual delivery of stem cells and insulin-like growth factor-1 in coacervate-embedded composite hydrogels for enhanced cartilage regeneration in osteochondral defects. *J. Control. Release* 327, 284–295. doi:10.1016/j.jconrel.2020.08.002

Clark, A. Y., Martin, K. E., García, J. R., Johnson, C. T., Theriault, H. S., Han, W. M., et al. (2020). Integrin-specific hydrogels modulate transplanted human bone marrow-derived mesenchymal stem cell survival, engraftment, and reparative activities. *Nat. Commun.* 11, 114. doi:10.1038/s41467-019-14000-9

Corre, I., Verrecchia, F., Crenn, V., Redini, F., and Trichet, V. (2020). The osteosarcoma microenvironment: A complex but targetable ecosystem. *Cells* 9, 976. doi:10.3390/cells9040976

Cui, Z.-K., Kim, S., Baljon, J. J., Wu, B. M., Aghaloo, T., and Lee, M. (2019). Microporous methacrylated glycol chitosan-montmorillonite nanocomposite hydrogel for bone tissue engineering. *Nat. Commun.* 10, 3523. doi:10.1038/s41467-019-11511-3

Dai, W., Sun, M., Leng, X., Hu, X., and Ao, Y. (2020). Recent progress in 3D printing of elastic and high-strength hydrogels for the treatment of osteochondral and cartilage diseases. *Front. Bioeng. Biotechnol.* 8, 604814. doi:10.3389/fbioe.2020.604814

Das Mahapatra, R., Imani, K. B. C., and Yoon, J. (2020). Integration of macro-cross-linker and metal coordination: A super stretchable hydrogel with high toughness. *ACS Appl. Mat. Interfaces* 12, 40786–40793. doi:10.1021/acsami.0c11167

Donahue, N. D., Acar, H., and Wilhelm, S. (2019). Concepts of nanoparticle cellular uptake, intracellular trafficking, and kinetics in nanomedicine. *Adv. Drug Deliv. Rev.* 143, 68–96. doi:10.1016/j.addr.2019.04.008

Ekerdt, B. L., Fuentes, C. M., Lei, Y., Adil, M. M., Ramasubramanian, A., Segalman, R. A., et al. (2018). Thermoreversible hyaluronic acid-PNIPAAm hydrogel systems for 3D stem cell culture. *Adv. Healthc. Mat.* 7, e1800225. doi:10.1002/adhm.201800225

Fuchs, S., Shariati, K., and Ma, M. (2020). Specialty tough hydrogels and their biomedical applications. *Adv. Healthc. Mat.* 9, e1901396. doi:10.1002/adhm.201901396

Gabarin, N., Gavish, H., Muhlrad, A., Chen, Y. C., Namdar-Attar, M., Nissenson, R. A., et al. (2001). Mitogenic G(i) protein-MAP kinase signaling cascade in mc3t3-E1 osteogenic cells: Activation by C-terminal pentapeptide of osteogenic growth peptide [OGP(10-14)] and attenuation of activation by cAMP. *J. Cell. Biochem.* 81, 594–603. doi:10.1002/jcb.1083

Gan, L. H., Roshan Deen, G., Loh, X. J., and Gan, Y. Y. (2001). New stimuli-responsive copolymers of N-acryloyl-N′-alkyl piperazine and methyl methacrylate and their hydrogels. *Polymer* 42, 65–69. doi:10.1016/S0032-3861(00)00296-2

Gan, N., Sun, Q., Zhao, L., Tang, P., Suo, Z., Zhang, S., et al. (2019). Protein corona of metal-organic framework nanoparticals: Study on the adsorption behavior of protein and cell interaction. *Int. J. Biol. Macromol.* 140, 709–718. doi:10.1016/j.ijbiomac.2019.08.183

Gauvin, R., Chen, Y.-C., Lee, J. W., Soman, P., Zorlutuna, P., Nichol, J. W., et al. (2012). Microfabrication of complex porous tissue engineering scaffolds using 3D projection stereolithography. *Biomaterials* 33, 3824–3834. doi:10.1016/j.biomaterials.2012.01.048

Ghosal, A., and Kaushik, A. (2020). *Intelligent hydrogels in diagnostics and therapeutics*. Boca Raton, Florida: CRC Press.

Ghosh, S., Mukherjee, B., Chaudhuri, S., Roy, T., Mukherjee, A., and Sengupta, S. (2018). Methotrexate aspasomes against rheumatoid arthritis: Optimized hydrogel loaded liposomal formulation with *in vivo* evaluation in wistar rats. *AAPS PharmSciTech* 19, 1320–1336. doi:10.1208/s12249-017-0939-2

Gibbs, D. M. R., Black, C. R. M., Dawson, J. I., and Oreffo, R. O. C. (2016). A review of hydrogel use in fracture healing and bone regeneration: Hydrogel use in fracture healing and bone regeneration. *J. Tissue Eng. Regen. Med.* 10, 187–198. doi:10.1002/term.1968

Gill, J., and Gorlick, R. (2021). Advancing therapy for osteosarcoma. *Nat. Rev. Clin. Oncol.* 18, 609–624. doi:10.1038/s41571-021-00519-8

Goldring, S. R., and Goldring, M. B. (2016). Changes in the osteochondral unit during osteoarthritis: Structure, function and cartilage–bone crosstalk. *Nat. Rev. Rheumatol.* 12, 632–644. doi:10.1038/nrrheum.2016.148

Gou, G.-H., Tseng, F.-J., Wang, S.-H., Chen, P.-J., Shyu, J.-F., Weng, C.-F., et al. (2020). Autologous chondrocyte implantation versus microfracture in the knee: A meta-analysis and systematic review. *Arthrosc. J. Arthrosc. Relat. Surg.* 36, 289–303. doi:10.1016/j.arthro.2019.06.033

Haene, R., Qamirani, E., Story, R. A., Pinsker, E., and Daniels, T. R. (2012). Intermediate outcomes of fresh talar osteochondral allografts for treatment of large osteochondral lesions of the talus. *J. Bone Jt. Surg.* 94, 1105–1110. doi:10.2106/JBJS.J.02010

Hamblin, T., Curtis, S. H., D'Astous, J., and Aoki, S. K. (2010). Childhood obesity and low-velocity knee dislocation in a fifteen-year-old girl: A case report. *J. Bone Jt. Surgery-American Volume* 92, 2216–2219. doi:10.2106/JBJS.J.00115

Han, X., He, J., Wang, Z., Bai, Z., Qu, P., Song, Z., et al. (2021). Fabrication of silver nanoparticles/gelatin hydrogel system for bone regeneration and fracture treatment. *Drug Deliv. (Lond).* 28, 319–324. doi:10.1080/10717544.2020.1869865

Han, Y., Zeng, Q., Li, H., and Chang, J. (2013). The calcium silicate/alginate composite: Preparation and evaluation of its behavior as bioactive injectable hydrogels. *Acta Biomater.* 9, 9107–9117. doi:10.1016/j.actbio.2013.06.022

Hanyková, L., Krakovský, I., Šestáková, E., Šťastná, J., and Labuta, J. (2020). Poly(N, N'-Diethylacrylamide)-Based thermoresponsive hydrogels with double network structure. *Polymers* 12, E2502. doi:10.3390/polym12112502

Haugen, H. J., Lyngstadaas, S. P., Rossi, F., and Perale, G. (2019). Bone grafts: Which is the ideal biomaterial? *J. Clin. Periodontol.* 46 (21), 92–102. doi:10.1111/jcpe.13058

He, Q., Huang, Y., and Wang, S. (2018). Hofmeister effect-assisted one step fabrication of ductile and strong gelatin hydrogels. *Adv. Funct. Mat.* 28, 1705069. doi:10.1002/adfm.201705069

He, W., Kapate, N., Shields, C. W., and Mitragotri, S. (2020). Drug delivery to macrophages: A review of targeting drugs and drug carriers to macrophages for inflammatory diseases. *Adv. Drug Deliv. Rev.* 166, 15–40. doi:10.1016/j.addr.2019.12.001

Henkel, J., Woodruff, M. A., Epari, D. R., Steck, R., Glatt, V., Dickinson, I. C., et al. (2013). Bone regeneration based on tissue engineering conceptions — a 21st century perspective. *Bone Res.* 1, 216–248. doi:10.4248/BR201303002

Hennink, W. E., and van Nostrum, C. F. (2002). Novel crosslinking methods to design hydrogels. *Adv. Drug Deliv. Rev.* 54, 13–36. doi:10.1016/s0169-409x(01)00240-x

Henry, S., McAllister, D. V., Allen, M. G., and Prausnitz, M. R. (1998). Microfabricated microneedles: A novel approach to transdermal drug delivery. *J. Pharm. Sci.* 87, 922–925. doi:10.1021/js980042+

Hilkens, C. M. U., and Isaacs, J. D. (2013). Tolerogenic dendritic cell therapy for rheumatoid arthritis: Where are we now? *Clin. Exp. Immunol.* 172, 148–157. doi:10.1111/cei.12038

Hilšer, P., Suchánková, A., Mendová, K., Filipič, K. E., Daniel, M., and Vrbka, M. (2021). A new insight into more effective viscosupplementation based on the synergy of hyaluronic acid and phospholipids for cartilage friction reduction. *Biotribology* 25, 100166. doi:10.1016/j.biotri.2021.100166

Hoare, T. R., and Kohane, D. S. (2008). Hydrogels in drug delivery: Progress and challenges. *Polymer* 49, 1993. doi:10.1016/j.polymer.2008.01.027

Hochberg, M. C. (2012). Osteoarthritis year 2012 in review: Clinical. *Osteoarthr. Cartil.* 20, 1465–1469. doi:10.1016/j.joca.2012.07.022

Hodgson, S. M., McNelles, S. A., Abdullahu, L., Marozas, I. A., Anseth, K. S., and Adronov, A. (2017). Reproducible dendronized PEG hydrogels via SPAAC cross-linking. *Biomacromolecules* 18, 4054–4059. doi:10.1021/acs.biomac.7b01115

Hoppe, A., Güldal, N. S., and Boccaccini, A. R. (2011). A review of the biological response to ionic dissolution products from bioactive glasses and glass-ceramics. *Biomaterials* 32, 2757–2774. doi:10.1016/j.biomaterials.2011.01.004

Hou, S., Wang, X., Park, S., Jin, X., and Ma, P. X. (2015). Rapid self-integrating, injectable hydrogel for tissue complex regeneration. *Adv. Healthc. Mat.* 4, 1491–1495. doi:10.1002/adhm.201500093

Hu, W., Wang, Z., Xiao, Y., Zhang, S., and Wang, J. (2019a). Advances in crosslinking strategies of biomedical hydrogels. *Biomater. Sci.* 7, 843–855. doi:10.1039/c8bm01246f

Hu, X.-B., Kang, R.-R., Tang, T.-T., Li, Y.-J., Wu, J.-Y., Wang, J.-M., et al. (2019b). Topical delivery of 3, 5, 4'-trimethoxy-trans-stilbene-loaded microemulsion-based hydrogel for the treatment of osteoarthritis in a rabbit model. *Drug Deliv. Transl. Res.* 9, 357–365. doi:10.1007/s13346-018-00604-z

Huang, B., Yuan, Y., Ding, S., Li, J., Ren, J., Feng, B., et al. (2015). Nanostructured hydroxyapatite surfaces-mediated adsorption alters recognition of BMP receptor IA and bioactivity of bone morphogenetic protein-2. *Acta Biomater.* 27, 275–285. doi:10.1016/j.actbio.2015.09.007

Huey, D. J., Hu, J. C., and Athanasiou, K. A. (2012). Unlike bone, cartilage regeneration remains elusive. *Science* 338, 917–921. doi:10.1126/science.1222454

Hunt, J. A., Chen, R., Veen, T. van, and Bryan, N. (2014). Hydrogels for tissue engineering and regenerative medicine. *J. Mat. Chem. B* 2, 5319–5338. doi:10.1039/C4TB00775A

Jeuken, R. M., Roth, A. K., Peters, R. J. R. W., Van Donkelaar, C. C., Thies, J. C., Van Rhijn, L. W., et al. (2016). Polymers in cartilage defect repair of the knee: Current status and future prospects. *Polymers* 8, 219. doi:10.3390/polym8060219

Ji, D., and Kim, J. (2021). Recent strategies for strengthening and stiffening tough hydrogels. *Adv. NanoBiomed Res.* 1, 2100026. doi:10.1002/anbr.202100026

Jiang, L., Luo, Z., Loh, X. J., Wu, Y.-L., and Li, Z. (2019). PHA-based thermogel as a controlled zero-order chemotherapeutic delivery system for the effective treatment of melanoma. *ACS Appl. Bio Mat.* 2, 3591–3600. doi:10.1021/acsabm.9b00467

Jing, H., He, X., and Zheng, J. (2018). Exosomes and regenerative medicine: State of the art and perspectives. *Transl. Res.* 196, 1–16. doi:10.1016/j.trsl.2018.01.005

Khan, Y., Yaszemski, M. J., Mikos, A. G., and Laurencin, C. T. (2008). Tissue engineering of bone: Material and matrix considerations. *J. Bone Jt. Surg.* 90 (1), 36–42. doi:10.2106/JBJS.G.01260

Khiabani, S. S., Aghazadeh, M., Rakhtshah, J., and Davaran, S. (2021). A review of hydrogel systems based on poly(N-isopropyl acrylamide) for use in the engineering of bone tissues. *Colloids Surfaces B Biointerfaces* 208, 112035. doi:10.1016/j.colsurfb.2021.112035

Kilpadi, K. L., Chang, P. L., and Bellis, S. L. (2001). Hydroxylapatite binds more serum proteins, purified integrins, and osteoblast precursor cells than titanium or steel. *J. Biomed. Mat. Res.* 57, 258–267. doi:10.1002/1097-4636(200111)57:2<258::aid-jbm1166>3.0.co;2-r

Kim, I. L., Mauck, R. L., and Burdick, J. A. (2011). Hydrogel design for cartilage tissue engineering: A case study with hyaluronic acid. *Biomaterials* 32, 8771–8782. doi:10.1016/j.biomaterials.2011.08.073

Kim, J.-H., and Kim, H.-W. (2013). Rat defect models for bone grafts and tissue engineered bone constructs. *Tissue Eng. Regen. Med.* 10, 310–316. doi:10.1007/s13770-013-1093-x

Kirillova, A., Yeazel, T. R., Asheghali, D., Petersen, S. R., Dort, S., Gall, K., et al. (2021). Fabrication of biomedical scaffolds using biodegradable polymers. *Chem. Rev.* 121, 11238–11304. doi:10.1021/acs.chemrev.0c01200

Kolambkar, Y. M., Dupont, K. M., Boerckel, J. D., Huebsch, N., Mooney, D. J., Hutmacher, D. W., et al. (2011). An alginate-based hybrid system for growth factor delivery in the functional repair of large bone defects. *Biomaterials* 32, 65–74. doi:10.1016/j.biomaterials.2010.08.074

Kondiah, P. J., Choonara, Y. E., Kondiah, P. P. D., Marimuthu, T., Kumar, P., Du Toit, L. C., et al. (2016). A review of injectable polymeric hydrogel systems for application in bone tissue engineering. *Molecules* 21, 1580. doi:10.3390/molecules21111580

Kretlow, J. D., and Mikos, A. G. (2007). Review: Mineralization of synthetic polymer scaffolds for bone tissue engineering. *Tissue Eng.* 13, 927–938. doi:10.1089/ten.2006.0394

Kristjánsson, B., and Honsawek, S. (2014). Current perspectives in mesenchymal stem cell therapies for osteoarthritis. *Stem Cells Int.* 2014, 1–13. doi:10.1155/2014/194318

Kurien, T., Pearson, R. G., and Scammell, B. E. (2013). Bone graft substitutes currently available in orthopaedic practice: The evidence for their use. *Bone Jt. J.* 95-B, 583–597. doi:10.1302/0301-620X.95B5.30286

Langer, R., and Tirrell, D. A. (2004). Designing materials for biology and medicine. *Nature* 428, 487–492. doi:10.1038/nature02388

Lee, S.-H., and Shin, H. (2007). Matrices and scaffolds for delivery of bioactive molecules in bone and cartilage tissue engineering. *Adv. Drug Deliv. Rev.* 59, 339–359. doi:10.1016/j.addr.2007.03.016

Li, J. J., Ebied, M., Xu, J., and Zreiqat, H. (2018a). Current approaches to bone tissue engineering: The interface between biology and engineering. *Adv. Healthc. Mat.* 7, e1701061. doi:10.1002/adhm.201701061

Li, J., and Mooney, D. J. (2016). Designing hydrogels for controlled drug delivery. *Nat. Rev. Mat.* 1, 16071. doi:10.1038/natrevmats.2016.71

Li, J., Wang, B., Lin, J., Cheng, D., and Lu, Y. (2018b). Multifunctional surface modification of mulberry silk fabric via PNIPAAm/chitosan/PEO nanofibers coating and cross-linking technology. *Coatings* 8, 68. doi:10.3390/coatings8020068

Li, Q., Barrett, D. G., Messersmith, P. B., and Holten-Andersen, N. (2016). Controlling hydrogel mechanics via bio-inspired polymer-nanoparticle bond dynamics. *ACS Nano* 10, 1317–1324. doi:10.1021/acsnano.5b06692

Li, X., Chen, L., Lin, H., Cao, L., Cheng, J., Dong, J., et al. (2017a). Efficacy of poly(D, L-lactic acid-co-glycolic acid)-poly(ethylene glycol)-poly(D, L-lactic acid-co-glycolic acid) thermogel as a barrier to prevent spinal epidural fibrosis in a postlaminectomy rat model. *Clin. Spine Surg.* 30, E283–E290. doi:10.1097/BSD.0000000000000221

Li, X., and Su, X. (2018). Multifunctional smart hydrogels: Potential in tissue engineering and cancer therapy. *J. Mat. Chem. B* 6, 4714–4730. doi:10.1039/C8TB01078A

Li, Y., Xiao, Y., and Liu, C. (2017b). The horizon of materiobiology: A perspective on material-guided cell behaviors and tissue engineering. *Chem. Rev.* 117, 4376–4421. doi:10.1021/acs.chemrev.6b00654

Lin, Q., Lim, J. Y. C., Xue, K., Su, X., and Loh, X. J. (2021). Polymeric hydrogels as a vitreous replacement strategy in the eye. *Biomaterials* 268, 120547. doi:10.1016/j.biomaterials.2020.120547

Lin, W., and Klein, J. (2022). Hydration lubrication in biomedical applications: From cartilage to hydrogels. *Acc. Mat. Res.* 3, 213–223. doi:10.1021/accountsmr.1c00219

Lin, W., and Klein, J. (2021). Recent progress in cartilage lubrication. *Adv. Mat.* 33, 2005513. doi:10.1002/adma.202005513

Lin, W., Kluzek, M., Iuster, N., Shimoni, E., Kampf, N., Goldberg, R., et al. (2020). Cartilage-inspired, lipid-based boundary-lubricated hydrogels. *Science* 370, 335–338. doi:10.1126/science.aay8276

Lin, Z., Wu, J., Qiao, W., Zhao, Y., Wong, K. H. M., Chu, P. K., et al. (2018). Precisely controlled delivery of magnesium ions thru sponge-like monodisperse PLGA/nano-MgO-alginate core-shell microsphere device to enable *in-situ* bone regeneration. *Biomaterials* 174, 1–16. doi:10.1016/j.biomaterials.2018.05.011

Liu, H., Xiang, X., Huang, J., Zhu, B., Wang, L., Tang, Y., et al. (2021a). Ultrasound augmenting injectable chemotaxis hydrogel for articular cartilage repair in osteoarthritis. *Chin. Chem. Lett.* 32, 1759–1764. doi:10.1016/j.cclet.2020.12.004

Liu, M., Nakasaki, M., Shih, Y.-R. V., and Varghese, S. (2018). Effect of age on biomaterial-mediated *in situ* bone tissue regeneration. *Acta Biomater.* 78, 329–340. doi:10.1016/j.actbio.2018.06.035

Liu, M., Zeng, X., Ma, C., Yi, H., Ali, Z., Mou, X., et al. (2017). Injectable hydrogels for cartilage and bone tissue engineering. *Bone Res.* 5, 17014. doi:10.1038/boneres.2017.14

Liu, X., Heng, W. S., PaulLi, Q., and Chan, L. W. (2006). Novel polymeric microspheres containing norcantharidin for chemoembolization. *J. Control. Release* 116, 35–41. doi:10.1016/j.jconrel.2006.08.022

Liu, X., Sun, Y., Chen, B., Li, Y., Zhu, P., Wang, P., et al. (2022). Novel magnetic silk fibroin scaffolds with delayed degradation for potential long-distance vascular repair. *Bioact. Mat.* 7, 126–143. doi:10.1016/j.bioactmat.2021.04.036

Liu, Y., Xiong, D., and Zhao, X. (2021b). A bionic PEEK composite structure with negatively charged surface adsorbing molecular brushes possessing improved biotribological properties for artificial joints. *Tribol. Int.* 155, 106808. doi:10.1016/j.triboint.2020.106808

Loeffler, J., Duda, G. N., Sass, F. A., and Dienelt, A. (2018). The metabolic microenvironment steers bone tissue regeneration. *Trends Endocrinol. Metab.* 29, 99–110. doi:10.1016/j.tem.2017.11.008

Loh, X. J., Nguyen, V. P. N., Kuo, N., and Li, J. (2011). Encapsulation of basic fibroblast growth factor in thermogelling copolymers preserves its bioactivity. *J. Mat. Chem.* 21, 2246–2254. doi:10.1039/C0JM03051A

López, D., García-German, D., and Egea, R. (2014). Multiple fracture of the upper limb. Case report. *Acta Ortop. Mex.* 28, 54–56.

Lu, Y., Li, L., Zhu, Y., Wang, X., Li, M., Lin, Z., et al. (2018). Multifunctional copper-containing carboxymethyl chitosan/alginate scaffolds for eradicating clinical bacterial infection and promoting bone formation. *ACS Appl. Mat. Interfaces* 10, 127–138. doi:10.1021/acsami.7b13750

Lu, Y., Li, Y., and Wu, W. (2016). Injected nanocrystals for targeted drug delivery. *Acta Pharm. Sin. B* 6, 106–113. doi:10.1016/j.apsb.2015.11.005

MacDonald, A. E., Bedi, A., Horner, N. S., Sa, D. de, Simunovic, N., Philippon, M. J., et al. (2016). Indications and outcomes for microfracture as an adjunct to hip arthroscopy for treatment of chondral defects in patients with femoroacetabular impingement: A systematic review. *Arthrosc. J. Arthrosc. Relat. Surg.* 32, 190–200.e2. doi:10.1016/j.arthro.2015.06.041

Mantha, S., Pillai, S., Khayambashi, P., Upadhyay, A., Zhang, Y., Tao, O., et al. (2019). Smart hydrogels in tissue engineering and regenerative medicine. *Materials* 12, 3323. doi:10.3390/ma12203323

Matai, I., Kaur, G., Seyedsalehi, A., McClinton, A., and Laurencin, C. T. (2020). Progress in 3D bioprinting technology for tissue/organ regenerative engineering. *Biomaterials* 226, 119536. doi:10.1016/j.biomaterials.2019.119536

Maudens, P., Meyer, S., Seemayer, C. A., Jordan, O., and Allémann, E. (2018). Self-assembled thermoresponsive nanostructures of hyaluronic acid conjugates for osteoarthritis therapy. *Nanoscale* 10, 1845–1854. doi:10.1039/C7NR07614B

McDaniel, J. R., Callahan, D. J., and Chilkoti, A. (2010). Drug delivery to solid tumors by elastin-like polypeptides. *Adv. Drug Deliv. Rev.* 62, 1456–1467. doi:10.1016/j.addr.2010.05.004

Mehrotra, D., Dwivedi, R., Nandana, D., and Singh, R. K. (2020). From injectable to 3D printed hydrogels in maxillofacial tissue engineering: A review. *J. Oral Biol. Craniofac. Res.* 10, 680–689. doi:10.1016/j.jobcr.2020.09.006

Metsemakers, W.-J., Handojo, K., Reynders, P., Sermon, A., Vanderschot, P., and Nijs, S. (2015). Individual risk factors for deep infection and compromised fracture healing after intramedullary nailing of tibial shaft fractures: A single centre experience of 480 patients. *Injury* 46, 740–745. doi:10.1016/j.injury.2014.12.018

Morgese, G., Benetti, E. M., and Zenobi-Wong, M. (2018). Molecularly engineered biolubricants for articular cartilage. *Adv. Healthc. Mat.* 7, e1701463. doi:10.1002/adhm.201701463

Mortensen, K., and Pedersen, J. S. (1993). Structural study on the micelle formation of poly(ethylene oxide)-poly(propylene oxide)-poly(ethylene oxide) triblock copolymer in aqueous solution. *Macromolecules* 26, 805–812. doi:10.1021/ma00056a035

Nabavi, M. H., Salehi, M., Ehterami, A., Bastami, F., Semyari, H., Tehranchi, M., et al. (2020). A collagen-based hydrogel containing tacrolimus for bone tissue engineering. *Drug Deliv. Transl. Res.* 10, 108–121. doi:10.1007/s13346-019-00666-7

Nakka, R., and Mungray, A. A. (2016). Biodegradable and biocompatible temperature sensitive triblock copolymer hydrogels as draw agents for forward osmosis. *Sep. Purif. Technol.* 168, 83–92. doi:10.1016/j.seppur.2016.05.021

Nallusamy, J., and Das, R. K. (2021). Hydrogels and their role in bone tissue engineering: An overview. *J. Pharm. Bioallied Sci.* 13, S908–S912. doi:10.4103/jpbs.jpbs_237_21

Narayanaswamy, R., and Torchilin, V. P. (2019). Hydrogels and their applications in targeted drug delivery. *Molecules* 24, 603. doi:10.3390/molecules24030603

Neves, M. I., Araújo, M., Moroni, L., da Silva, R. M. P., and Barrias, C. C. (2020). Glycosaminoglycan-Inspired biomaterials for the development of bioactive hydrogel networks. *Molecules* 25, E978. doi:10.3390/molecules25040978

Nguyen, V. P. N., Kuo, N., and Loh, X. J. (2011). New biocompatible thermogelling copolymers containing ethylene-butylene segments exhibiting very low gelation concentrations. *Soft Matter* 7, 2150–2159. doi:10.1039/C0SM00764A

Nikravesh, N., Borchard, G., Hofmann, H., Philipp, E., Flühmann, B., and Wick, P. (2020). Factors influencing safety and efficacy of intravenous iron-carbohydrate nanomedicines: From production to clinical practice. *Nanomedicine Nanotechnol. Biol. Med.* 26, 102178. doi:10.1016/j.nano.2020.102178

Nonoyama, T., Lee, Y. W., Ota, K., Fujioka, K., Hong, W., and Gong, J. P. (2020). Instant thermal switching from soft hydrogel to rigid plastics inspired by thermophile proteins. *Adv. Mat.* 32, e1905878. doi:10.1002/adma.201905878

Obata, A., Ogasawara, T., and Kasuga, T. (2019). Combinatorial effects of inorganic ions on adhesion and proliferation of osteoblast-like cells. *J. Biomed. Mat. Res. A* 107, 1042–1051. doi:10.1002/jbm.a.36623

Oliveira, I. M., Fernandes, D. C., Cengiz, I. F., Reis, R. L., and Oliveira, J. M. (2021). Hydrogels in the treatment of rheumatoid arthritis: Drug delivery systems and artificial matrices for dynamic *in vitro* models. *J. Mat. Sci. Mat. Med.* 32, 74. doi:10.1007/s10856-021-06547-1

Oryan, A., Kamali, A., Moshiri, A., Baharvand, H., and Daemi, H. (2018). Chemical crosslinking of biopolymeric scaffolds: Current knowledge and future directions of crosslinked engineered bone scaffolds. *Int. J. Biol. Macromol.* 107, 678–688. doi:10.1016/j.ijbiomac.2017.08.184

Pacifici, A., Laino, L., Gargari, M., Guzzo, F., Velandia Luz, A., Polimeni, A., et al. (2018). Decellularized hydrogels in bone tissue engineering: A topical review. *Int. J. Med. Sci.* 15, 492–497. doi:10.7150/ijms.22789

Pan, H., Gao, H., Li, Q., Lin, Z., Feng, Q., Yu, C., et al. (2020). Engineered macroporous hydrogel scaffolds via pickering emulsions stabilized by MgO nanoparticles promote bone regeneration. *J. Mat. Chem. B* 8, 6100–6114. doi:10.1039/d0tb00901f

Pascual-Garrido, C., Rodriguez-Fontan, F., Aisenbrey, E. A., Payne, K. A., Chahla, J., Goodrich, L. R., et al. (2018). Current and novel injectable hydrogels to treat focal chondral lesions: Properties and applicability. *J. Orthop. Res.* 36, 64–75. doi:10.1002/jor.23760

Patel, M., Patel, K. J., Caccamese, J. F., Coletti, D. P., Sauk, J. J., and Fisher, J. P. (2010). Characterization of cyclic acetal hydroxyapatite nanocomposites for craniofacial tissue engineering. *J. Biomed. Mat. Res. A* 94, 408–418. doi:10.1002/jbm.a.32683

Perez, J. R., Kouroupis, D., Li, D. J., Best, T. M., Kaplan, L., and Correa, D. (2018). Tissue engineering and cell-based therapies for fractures and bone defects. *Front. Bioeng. Biotechnol.* 6, 105. doi:10.3389/fbioe.2018.00105

Pethő, A., Chen, Y., and George, A. (2018). Exosomes in extracellular matrix bone biology. *Curr. Osteoporos. Rep.* 16, 58–64. doi:10.1007/s11914-018-0419-y

Pishavar, E., Luo, H., Naserifar, M., Hashemi, M., Toosi, S., Atala, A., et al. (2021). Advanced hydrogels as exosome delivery systems for osteogenic differentiation of MSCs: Application in bone regeneration. *Int. J. Mol. Sci.* 22, 6203. doi:10.3390/ijms22126203

Polat, G., Erşen, A., Erdil, M. E., Kızılkurt, T., Kılıçoğlu, Ö., and Aşık, M. (2016). Long-term results of microfracture in the treatment of talus osteochondral lesions. *Knee Surg. Sports Traumatol. Arthrosc.* 24, 1299–1303. doi:10.1007/s00167-016-3990-8

Pontremoli, C., Boffito, M., Fiorilli, S., Laurano, R., Torchio, A., Bari, A., et al. (2018). Hybrid injectable platforms for the *in situ* delivery of therapeutic ions from mesoporous glasses. *Chem. Eng. J.* 340, 103–113. doi:10.1016/j.cej.2018.01.073

Preethi Soundarya, S., Haritha Menon, A., Viji Chandran, S., and Selvamurugan, N. (2018). Bone tissue engineering: Scaffold preparation using chitosan and other biomaterials with different design and fabrication techniques. *Int. J. Biol. Macromol.* 119, 1228–1239. doi:10.1016/j.ijbiomac.2018.08.056

Qiao, Y., Liu, X., Zhou, X., Zhang, H., Zhang, W., Xiao, W., et al. (2020). Gelatin templated polypeptide Co-Cross-Linked hydrogel for bone regeneration. *Adv. Healthc. Mat.* 9, e1901239. doi:10.1002/adhm.201901239

Quicke, J. G., Conaghan, P. G., Corp, N., and Peat, G. (2022). Osteoarthritis year in review 2021: Epidemiology & therapy. *Osteoarthr. Cartil.* 30, 196–206. doi:10.1016/j.joca.2021.10.003

Rape, A. D., Zibinsky, M., Murthy, N., and Kumar, S. (2015). A synthetic hydrogel for the high-throughput study of cell–ECM interactions. *Nat. Commun.* 6, 8129–9. doi:10.1038/ncomms9129

Rauner, N., Meuris, M., Zoric, M., and Tiller, J. C. (2017). Enzymatic mineralization generates ultrastiff and tough hydrogels with tunable mechanics. *Nature* 543, 407–410. doi:10.1038/nature21392

Rivory, L. P., Chatelut, E., Canal, P., Mathieu-Boué, A., Robert, J., and MAthieu-Boue, A. (1994). Kinetics of the *in vivo* interconversion of the carboxylate and lactone forms of irinotecan (CPT-11) and of its metabolite SN-38 in patients. *Cancer Res.* 54, 6330–6333.

Rong, M., Liu, H., Scaraggi, M., Bai, Y., Bao, L., Ma, S., et al. (2020). High lubricity meets load capacity: Cartilage mimicking bilayer structure by brushing up stiff hydrogels from subsurface. *Adv. Funct. Mat.* 30, 2004062. doi:10.1002/adfm.202004062

Sadat-Shojai, M., Khorasani, M.-T., and Jamshidi, A. (2015). 3-Dimensional cell-laden nano-hydroxyapatite/protein hydrogels for bone regeneration applications. *Mater. Sci. Eng. C* 49, 835–843. doi:10.1016/j.msec.2015.01.067

Sasaki, N., Nishii, S., Yamada, K., Huruoka, H., and Tabata, Y. (2013). Effect of gelatin hydrogel sheet containing basic fibroblast growth factor on proximal sesamoid bone transverse fracture healing in the horse. *J. Equine Vet. Sci.* 33, 210–214. doi:10.1016/j.jevs.2012.06.012

Schröter, L., Kaiser, F., Stein, S., Gbureck, U., and Ignatius, A. (2020). Biological and mechanical performance and degradation characteristics of calcium phosphate cements in large animals and humans. *Acta Biomater.* 117, 1–20. doi:10.1016/j.actbio.2020.09.031

Sellam, J., and Berenbaum, F. (2010). The role of synovitis in pathophysiology and clinical symptoms of osteoarthritis. *Nat. Rev. Rheumatol.* 6, 625–635. doi:10.1038/nrrheum.2010.159

Selmi, T. a. S., Verdonk, P., Chambat, P., Dubrana, F., Potel, J.-F., Barnouin, L., et al. (2008). Autologous chondrocyte implantation in a novel alginate-agarose hydrogel. *J. Bone Jt. Surg. Br. volume* 90-B, 597–604. doi:10.1302/0301-620X.90B5.20360

Shahiwala, A. (2011). Formulation approaches in enhancement of patient compliance to oral drug therapy. *Expert Opin. Drug Deliv.* 8, 1521–1529. doi:10.1517/17425247.2011.628311

Shang, F., Yu, Y., Liu, S., Ming, L., Zhang, Y., Zhou, Z., et al. (2021). Advancing application of mesenchymal stem cell-based bone tissue regeneration. *Bioact. Mat.* 6, 666–683. doi:10.1016/j.bioactmat.2020.08.014

Shoaib, T., and Espinosa-Marzal, R. M. (2020). Advances in understanding hydrogel lubrication. *Colloids Interfaces* 4, 54. doi:10.3390/colloids4040054

Siegel, R. L., Miller, K. D., Fuchs, H. E., and Jemal, A. (2021). Cancer statistics, 2021. *Ca. A Cancer J. Clin.* 71, 7–33. doi:10.3322/caac.21654

Sigfridsson, K., Lundqvist, A. J., and Strimfors, M. (2009). Particle size reduction for improvement of oral absorption of the poorly soluble drug UG558 in rats during early development. *Drug Dev. Ind. Pharm.* 35, 1479–1486. doi:10.3109/03639040903025855

Su, C., Liu, Y., Li, R., Wu, W., Fawcett, J. P., and Gu, J. (2019). Absorption, distribution, metabolism and excretion of the biomaterials used in Nanocarrier drug delivery systems. *Adv. Drug Deliv. Rev.* 143, 97–114. doi:10.1016/j.addr.2019.06.008

Sun, Y., Liu, X., Wang, L., Xu, L., Liu, K., Xu, L., et al. (2022). High-performance SOD mimetic enzyme Au@Ce for arresting cell cycle and proliferation of acute myeloid leukemia. *Bioact. Mat.* 10, 117–130. doi:10.1016/j.bioactmat.2021.08.012

Ter Boo, G. J., Schmid, T., Zderic, I., Nehrbass, D., Camenisch, K., Richards, R. G., et al. (2018). Local application of a gentamicin-loaded thermo-responsive hydrogel allows for fracture healing upon clearance of a high *Staphylococcus aureus* load in a rabbit model. *Eur. Cell. Mat.* 35, 151–164. doi:10.22203/ecm.v035a11

Thakur, V. K., and Thakur, M. K. (2018). *Hydrogels: Recent advances*. Charm: Springer.

Tuan-Mahmood, T.-M., McCrudden, M. T. C., Torrisi, B. M., McAlister, E., Garland, M. J., Singh, T. R. R., et al. (2013). Microneedles for intradermal and transdermal drug delivery. *Eur. J. Pharm. Sci.* 50, 623–637. doi:10.1016/j.ejps.2013.05.005

Ulery, B. D., Nair, L. S., and Laurencin, C. T. (2011). Biomedical applications of biodegradable polymers. *J. Polym. Sci. B. Polym. Phys.* 49, 832–864. doi:10.1002/polb.22259

Urban, J. P. G. (1994). The chondrocyte: A cell under pressure. *Rheumatology* 33, 901–908. doi:10.1093/rheumatology/33.10.901

Utech, S., and Boccaccini, A. R. (2016). A review of hydrogel-based composites for biomedical applications: Enhancement of hydrogel properties by addition of rigid inorganic fillers. *J. Mat. Sci.* 51, 271–310. doi:10.1007/s10853-015-9382-5

Vadnere, M., Amidon, G., Lindenbaum, S., and Haslam, J. L. (1984). Thermodynamic studies on the gel-sol transition of some pluronic polyols. *Int. J. Pharm. X.* 22, 207–218. doi:10.1016/0378-5173(84)90022-X

Vashist, A., Vashist, A., Gupta, Y. K., and Ahmad, S. (2014). Recent advances in hydrogel based drug delivery systems for the human body. *J. Mat. Chem. B* 2, 147–166. doi:10.1039/c3tb21016b

Vermonden, T., Censi, R., and Hennink, W. E. (2012). Hydrogels for protein delivery. *Chem. Rev.* 112, 2853–2888. doi:10.1021/cr200157d

Voorhaar, L., and Hoogenboom, R. (2016). Supramolecular polymer networks: Hydrogels and bulk materials. *Chem. Soc. Rev.* 45, 4013–4031. doi:10.1039/c6cs00130k

Wang, C., Huang, W., Zhou, Y., He, L., He, Z., Chen, Z., et al. (2020). 3D printing of bone tissue engineering scaffolds. *Bioact. Mat.* 5, 82–91. doi:10.1016/j.bioactmat.2020.01.004

Wang, C., Lai, J., Li, K., Zhu, S., Lu, B., Liu, J., et al. (2021a). Cryogenic 3D printing of dual-delivery scaffolds for improved bone regeneration with enhanced vascularization. *Bioact. Mat.* 6, 137–145. doi:10.1016/j.bioactmat.2020.07.007

Wang, J., Zhang, X., Zhang, S., Kang, J., Guo, Z., Feng, B., et al. (2021b). Semi-convertible hydrogel enabled photoresponsive lubrication. *Matter* 4, 675–687. doi:10.1016/j.matt.2020.11.018

Wang, X., Kluge, J. A., Leisk, G. G., and Kaplan, D. L. (2008). Sonication-induced gelation of silk fibroin for cell encapsulation. *Biomaterials* 29, 1054–1064. doi:10.1016/j.biomaterials.2007.11.003

Wang, Y.-C., Dai, H.-L., Li, Z.-H., Meng, Z.-Y., Xiao, Y., and Zhao, Z. (2021c). Mesoporous polydopamine-coated hydroxyapatite nano-composites for ROS-triggered nitric oxide-enhanced photothermal therapy of osteosarcoma. *J. Mat. Chem. B* 9, 7401–7408. doi:10.1039/d1tb01084k

Weyand, C. M., and Goronzy, J. J. (2020). Immunometabolism in the development of rheumatoid arthritis. *Immunol. Rev.* 294, 177–187. doi:10.1111/imr.12838

Wheeler, T. S., Sbravati, N. D., and Janorkar, A. V. (2013). Mechanical & cell culture properties of elastin-like polypeptide, collagen, bioglass, and carbon nanosphere composites. *Ann. Biomed. Eng.* 41, 2042–2055. doi:10.1007/s10439-013-0825-3

Wichterle, O., and Lím, D. (1960). Hydrophilic gels for biological use. *Nature* 185, 117–118. doi:10.1038/185117a0

Wu, H., Wang, K., Wang, H., Chen, F., Huang, W., Chen, Y., et al. (2017). Novel self-assembled tacrolimus nanoparticles cross-linking thermosensitive hydrogels for local rheumatoid arthritis therapy. *Colloids Surfaces B Biointerfaces* 149, 97–104. doi:10.1016/j.colsurfb.2016.10.013

Wu, K., Yu, B., Li, D., Tian, Y., Liu, Y., and Jiang, J. (2022). Recent advances in nanoplatforms for the treatment of osteosarcoma. *Front. Oncol.* 12, 805978. doi:10.3389/fonc.2022.805978

Xiao, Q., Li, X., Li, Y., Wu, Z., Xu, C., Chen, Z., et al. (2021). Biological drug and drug delivery-mediated immunotherapy. *Acta Pharm. Sin. B* 11, 941–960. doi:10.1016/j.apsb.2020.12.018

Xie, R., Yao, H., Mao, A. S., Zhu, Y., Qi, D., Jia, Y., et al. (2021). Biomimetic cartilage-lubricating polymers regenerate cartilage in rats with early osteoarthritis. *Nat. Biomed. Eng.* 5, 1189–1201. doi:10.1038/s41551-021-00785-y

Xu, C., Chen, J., Li, L., Pu, X., Chu, X., Wang, X., et al. (2018). Promotion of chondrogenic differentiation of mesenchymal stem cells by copper: Implications for new cartilage repair biomaterials. *Mater. Sci. Eng. C* 93, 106–114. doi:10.1016/j.msec.2018.07.074

Xue, X., Hu, Y., Wang, S., Chen, X., Jiang, Y., and Su, J. (2021). Fabrication of physical and chemical crosslinked hydrogels for bone tissue engineering. *Bioact. Mat.* 12, 327–339. doi:10.1016/j.bioactmat.2021.10.029

Yan, J., Wang, Y., Ran, M., Mustafa, R. A., Luo, H., Wang, J., et al. (2021a). Peritumoral microgel reservoir for long-term light-controlled triple-synergistic treatment of osteosarcoma with single ultra-low dose. *Small* 17, e2100479. doi:10.1002/smll.202100479

Yan, X., Yang, B., Chen, Y., Song, Y., Ye, J., Pan, Y., et al. (2021b). Anti-friction MSCs delivery system improves the therapy for severe osteoarthritis. *Adv. Mat.* 33, 2104758. doi:10.1002/adma.202104758

Yang, S., Zhu, B., Yin, P., Zhao, L., Wang, Y., Fu, Z., et al. (2020). Integration of human umbilical cord mesenchymal stem cells-derived exosomes with hydroxyapatite-embedded hyaluronic acid-alginate hydrogel for bone regeneration. *ACS Biomater. Sci. Eng.* 6, 1590–1602. doi:10.1021/acsbiomaterials.9b01363

Yin, J., Han, Q., Zhang, J., Liu, Y., Gan, X., Xie, K., et al. (2020). MXene-based hydrogels endow polyetheretherketone with effective osteogenicity and combined treatment of osteosarcoma and bacterial infection. *ACS Appl. Mat. Interfaces* 12, 45891–45903. doi:10.1021/acsami.0c14752

Yu, T., Wang, H., Zhang, Y., Wang, X., and Han, B. (2020). The delivery of RNA-interference therapies based on engineered hydrogels for bone tissue regeneration. *Front. Bioeng. Biotechnol.* 8, 445. doi:10.3389/fbioe.2020.00445

Yue, S., He, H., Li, B., and Hou, T. (2020). Hydrogel as a biomaterial for bone tissue engineering: A review. *Nanomaterials* 10, 1511. doi:10.3390/nano10081511

Yun, S., Choi, D., Choi, D.-J., Jin, S., Yun, W.-S., Huh, J.-B., et al. (2021). Bone fracture-treatment method: Fixing 3D-printed polycaprolactone scaffolds with hydrogel type bone-derived extracellular matrix and β-tricalcium phosphate as an osteogenic promoter. *Int. J. Mol. Sci.* 22, 9084. doi:10.3390/ijms22169084

Zadpoor, A. A. (2015). Bone tissue regeneration: The role of scaffold geometry. *Biomater. Sci.* 3, 231–245. doi:10.1039/c4bm00291a

Zeng, Q., Han, Y., Li, H., and Chang, J. (2014). Bioglass/alginate composite hydrogel beads as cell carriers for bone regeneration. *J. Biomed. Mat. Res.* 102, 42–51. doi:10.1002/jbm.b.32978

Zhang, K., Feng, Q., Fang, Z., Gu, L., and Bian, L. (2021a). Structurally dynamic hydrogels for biomedical applications: Pursuing a fine balance between macroscopic stability and microscopic dynamics. *Chem. Rev.* 121, 11149–11193. doi:10.1021/acs.chemrev.1c00071

Zhang, W., Moskowitz, R. W., Nuki, G., Abramson, S., Altman, R. D., Arden, N., et al. (2008). OARSI recommendations for the management of hip and knee osteoarthritis, Part II: OARSI evidence-based, expert consensus guidelines. *Osteoarthr. Cartil.* 16, 137–162. doi:10.1016/j.joca.2007.12.013

Zhang, W., Ouyang, H., Dass, C. R., and Xu, J. (2016). Current research on pharmacologic and regenerative therapies for osteoarthritis. *Bone Res.* 4, 15040. doi:10.1038/boneres.2015.40

Zhang, Y., Cao, Y., Zhao, H., Zhang, L., Ni, T., Liu, Y., et al. (2020). An injectable BMSC-laden enzyme-catalyzed crosslinking collagen-hyaluronic acid hydrogel for cartilage repair and regeneration. *J. Mat. Chem. B* 8, 4237–4244. doi:10.1039/d0tb00291g

Zhang, Y. S., and Khademhosseini, A. (2017). Advances in engineering hydrogels. *Science* 356, eaaf3627. doi:10.1126/science.aaf3627

Zhang, Z., Jia, B., Yang, H., Han, Y., Wu, Q., Dai, K., et al. (2021b). Biodegradable ZnLiCa ternary alloys for critical-sized bone defect regeneration at load-bearing sites: *In vitro* and *in vivo* studies. *Bioact. Mat.* 6, 3999–4013. doi:10.1016/j.bioactmat.2021.03.045

Zhang, Z., Jia, B., Yang, H., Han, Y., Wu, Q., Dai, K., et al. (2021c). Zn0.8Li0.1Sr-a biodegradable metal with high mechanical strength comparable to pure Ti for the treatment of osteoporotic bone fractures: *In vitro* and *in vivo* studies. *Biomaterials* 275, 120905. doi:10.1016/j.biomaterials.2021.120905

Zhao, T., Wei, Z., Zhu, W., and Weng, X. (2022). Recent developments and current applications of hydrogels in osteoarthritis. *Bioeng. (Basel).* 9, 132. doi:10.3390/bioengineering9040132

Zhao, X., Lang, Q., Yildirimer, L., Lin, Z. Y., Cui, W., Annabi, N., et al. (2016). Photocrosslinkable gelatin hydrogel for epidermal tissue engineering. *Adv. Healthc. Mat.* 5, 108–118. doi:10.1002/adhm.201500005

Zhu, C., He, M., Sun, D., Huang, Y., Huang, L., Du, M., et al. (2021). 3D-Printed multifunctional polyetheretherketone bone scaffold for multimodal treatment of osteosarcoma and osteomyelitis. *ACS Appl. Mat. Interfaces* 13, 47327–47340. doi:10.1021/acsami.1c10898

Zhu, H., Cheng, P., Chen, P., and Pu, K. (2018). Recent progress in the development of near-infrared organic photothermal and photodynamic nanotherapeutics. *Biomater. Sci.* 6, 746–765. doi:10.1039/C7BM01210A

Zhu, H., Mah Jian Qiang, J., Wang, C. G., Chan, C. Y., Zhu, Q., Ye, E., et al. (2022). Flexible polymeric patch based nanotherapeutics against non-cancer therapy. *Bioact. Mat.* 18, 471–491. doi:10.1016/j.bioactmat.2022.03.034

Zhu, H., Ni, N., Govindarajan, S., Ding, X., and Leong, D. T. (2019). Phototherapy with layered materials derived quantum dots. *Nanoscale* 12, 43–57. doi:10.1039/C9NR07886J

Zhu, H., Yang, H., Ma, Y., Lu, T. J., Xu, F., Genin, G. M., et al. (2020a). Spatiotemporally controlled photoresponsive hydrogels: Design and predictive modeling from processing through application. *Adv. Funct. Mat.* 30, 2000639. doi:10.1002/adfm.202000639

Zhu, Y., Yu, X., Thamphiwatana, S. D., Zheng, Y., and Pang, Z. (2020b). Nanomedicines modulating tumor immunosuppressive cells to enhance cancer immunotherapy. *Acta Pharm. Sin. B* 10, 2054–2074. doi:10.1016/j.apsb.2020.08.010

frontiers | Frontiers in Bioengineering and Biotechnology

TYPE Original Research
PUBLISHED 14 September 2022
DOI 10.3389/fbioe.2022.1013097

EDITED BY
Long Bai,
East China University of Science and Technology, China

REVIEWED BY
Chen Yang,
Wenzhou Institute (CAS), China
Zengjie Fan,
Lanzhou University, China
Kun Hu,
Beijing Institute of Graphic Communication, China

*CORRESPONDENCE
Feng-Zhen Liu,
ldcllfz@163.com
Xi-Meng Chen,
827825736@qq.com
Yu-Jue Zhang,
zhangyujue@126.com

SPECIALTY SECTION
This article was submitted to Nanobiotechnology, a section of the journal Frontiers in Bioengineering and Biotechnology

RECEIVED 06 August 2022
ACCEPTED 29 August 2022
PUBLISHED 14 September 2022

CITATION
Qiang H-F, Lv Z-Y, Hou C-Y, Luo X, Li J, Liu K, Meng C-X, Du W-Q, Zhang Y-J, Chen X-M and Liu F-Z (2022), Development of biodegradable Zn-Mn-Li and CaP coatings on Zn-Mn-Li alloys and cytocompatibility evaluation for bone graft.
Front. Bioeng. Biotechnol. 10:1013097.
doi: 10.3389/fbioe.2022.1013097

Development of biodegradable Zn-Mn-Li and CaP coatings on Zn-Mn-Li alloys and cytocompatibility evaluation for bone graft

Hui-Fen Qiang[1], Zhao-Yong Lv[2], Cai-Yao Hou[1], Xin Luo[2], Jun Li[2], Kun Liu[2], Chun-Xiu Meng[2], Wan-Qing Du[2], Yu-Jue Zhang[2]*, Xi-Meng Chen[2]* and Feng-Zhen Liu[1,2]*

[1]Department of Materials Science and Engineering, Liaocheng University, Liaocheng, China,
[2]Liaocheng People's Hospital, Dongchangfu Hospital of Liaocheng Hospital, Liaocheng, China

Zn-based alloys are considered as new kind of potential biodegradable implanted biomaterials recently. The difficulty of metal implanted biomaterials and bone tissue integration seriously affects the applications of metal implanted scaffolds in bone tissue-related fields. Herein, we self-designed Zn0.8Mn and Zn0.8Mn0.1Li alloys and CaP coated Zn0.8Mn and Zn0.8Mn0.1Li alloys, then evaluated the degradation property and cytocompatibility. The results demonstrated that the Zn0.8Mn0.1Li alloys had profoundly modified the degradation property and cytocompatibility, but Zn0.8Mn0.1Li alloys had particularly adverse effects on the surface morphology of osteoblasts. The results furtherly showed that the CaP-coated Zn0.8Mn and Zn0.8Mn0.1Li alloys scaffold had better biocompatibility, which would further guarantee the biosafety of this new kind of biodegradable Zn-based alloys implants for future clinical applications.

KEYWORDS

zn-based alloys, mechanical property, degradation property, cytocompatibility, osteogenesis

1 Introduction

In recent years, biodegradable ferroalloy and magnesium alloy as the main representatives of medical metal materials with biodegradable properties have attracted extensive attention (Gu et al., 2012). The unique surface and mechanical properties of metals make them more attractive implanted scaffolds. At present, magnesium alloy and ferroalloy are widely studied, but they all have certain clinical defects, which limit their applications in the clinical biodegradable field (Li et al., 2021).

Zn-based biodegradable materials have been introduced in the last few years. Zinc is a common nutrient in the human body and plays a momentous role in immunity, the nervous system, and so on (Yang et al., 2022). The response of host tissue is the most critical factor in determining the success of biodegradable bone implantation, and the response of host tissue is largely determined by its degradation behavior. Based on the chemical activity of element, Zn is between Mg and Fe (the standard electrode potential of Mg is −0.237V, Fe is −0.440V, and Zn is −0.763 V), it can be preliminarily inferred that the degradation rate of Zn is slower than Mg and faster than Fe, which meets the requirements of being degradable metal biomaterials from corrosiveness. Therefore, the research on the design and biocompatibility evaluations of Zn-based alloys will have great significance. In terms of orthopedic implants, pure Zn has low hardness and cannot meet the requirements of clinical implants (Zhang et al., 2021). However, the addition of alloying elements can effectively solve this problem (Yin et al., 2019). Alloying elements such as Mn, Li, Cr, Sn, and Ge that exhibit eutectic reactions at the Zn-rich end are preferred to avoid large brittle intermetallic compounds (Shi et al., 2020; Zhang et al., 2019). Li is an important alloying element, it can refine the grain size of Zn-based alloys and improve the mechanical properties of Zn-based alloys, and the addition of Li can reduce the mass of pure Zn because the density of Li is the lowest among alloying elements (Zhao et al., 2017). Li group reported the microstructure evolution, mechanical properties, *in vitro* degradation, and cytocompatibility evaluations of ZnLi alloys, which had well optimal scaffold performance (Li et al., 2020). Sun group reported that this new Zn-Mn-Mg alloy had the mechanical and biodegradable properties required for ligament reconstruction fixation (Sun et al., 2021). But until now, Zn-Mn-Li alloys were not reported.

Various chemical, physical and biological cues have been revealed to regulate the adhesion and differentiation of stem cells (Yao et al., 2013a; Yao et al., 2021). Surface properties of biomaterials such as roughness, surface morphology, and element composition can influence ambient cells (Yao et al., 2013b). Surface properties can be modified with micro-arc oxidation, ion implantation, bionic deposition, chemical transformation, and so on (Jablonská et al., 2016). Osseointegration is a complex process. Bai group reported that changing the surface properties of biodegradable implant materials, such as morphology and composition, can modulate their osteogenic properties and accelerate bone healing (Bai et al., 2021). Phosphate chemical conversion technology is a process of chemical and electrochemical combination, which is used to form CaP coatings and bind them firmly to substrates (Zhao et al., 2021a; Zhao et al., 2021b). In the process of coatings design, elements with bone promoting function can be introduced, and the coatings have high crystallinity and stability, and the degradation rate and the ion release are slow, which guarantees the long-term stability of the implants. In addition, the degradation product PO_4^{3-} is also a major component of bone and can participate in bone mineralization (Zhao et al., 2019). The CaP coatings composited immediately on the Zn implants surface can adjust the corrosion resistance, roughness, and hydrophilicity of Zn-based alloys, create a suitable environment for cell survival and effectively improve the adhesion of osteoblasts (Su et al., 2019; Acheson et al., 2022). Calcium is used in a variety of biomaterials and is a major ingredient in the body's bones (Ling et al., 2021). Moreover, degradation products of calcium-rich phosphate not only contribute to the integration of Zn implants with host bone, but also regulate the microenvironment of tissues around implants and promote new bone formation (Wang et al., 2021). Theoretically, the surface modification of Zn-based alloys by phosphate chemical conversion technology has a broad application prospect.

Therefore, in this study, alloying elements manganese and lithium will be added to the zinc matrix, and the mechanical properties, degradation behavior, and cytocompatibility of Zn, Zn0.8Mn, and Zn0.8Mn0.1Li alloys will be compared longitude, simultaneously, CaP coatings on the surface of Zn-based alloys were synthesized by phosphate chemical conversion technology. The degradation and osteogenic ability of CaP coatings were studied. This study will further optimize the biosafety of novel biodegradable Zn-based alloys implants and provide a theoretical basis for future clinical applications.

2 Materials and methods

2.1 Materials and coating processes

Zn0.8Mn, Zn0.8Mn0.1Li alloys were prepared from high purity Zn, Mn, and Li metal powders of 99.95 wt%. Figure 1 briefly showed the preparation process of the alloys. Under the protection of the Ar atmosphere, put the raw materials into a ZG−0.01 vacuum induction furnace, kept the constant temperature at 500°C for 40 min, placed it at room temperature, and then poured it into the graphite mold to obtain the cylindrical ingot. All cylindrical ingots were homogenized at 250°C for 2 h, then at 350°C for 2 h, and finally put into the furnace for cooling. The actual compositions of the alloy were measured by ICP-AES (Thermo Science M Series). The results were shown in Table 1.

The pure Zn, Zn0.8Mn alloy, and Zn0.8Mn0.1Li alloy were cut into a disk with a diameter of 10 mm and a thickness of 1 mm, then grounded with 240–5,000 silicon carbide sandpaper, and polished to obtain a smooth surface. Ultrasonic cleaning was then performed in acetone, alcohol, and deionized water. As Figure 2 shown, the prepared Zn disk was connected to the pure Fe clip and then acid etched for pretreatment. The pretreated samples were then immersed in a phosphate chemical conversion solution with the design composition, in which the ratio of calcium to phosphorus was 1.67 at 70°C for 60 min. The pH of the phosphate chemical conversion solution was adjusted to

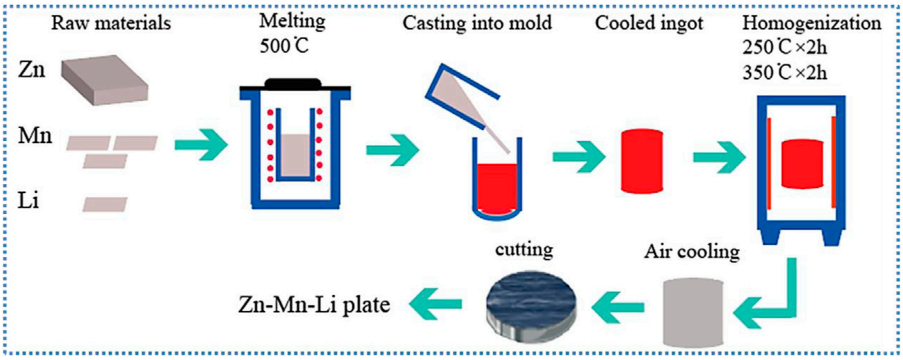

FIGURE 1
Schematic diagram of the alloys preparation route.

TABLE 1 Actual composition of Zn-based alloys.

Types of alloy	Zn/wt%	Mn/wt%	Li/wt%
Pure Zn	99.99	—	—
Zn0.8Mn	Balance	0.82	—
Zn0.8Mn0.1Li	Balance	0.82	0.11

2.5–3.5 using H_3PO_4 or $Ca(OH)_2$. Then, placed the reaction beaker in an ultrasonic cleaner for 60 min. In the last, the samples were cleaned with deionized water and dried at room temperature.

2.2 Characterizations of Zn-based alloys and CaP coatings on Zn-based alloys

The phase composition of the samples was measured by XRD (Rigaku D-max/2500 PC, Japan). The surface morphology of all samples was watched by FE-SEM (SU-4800, Hitachi, Japan), and the microstructure was observed by FE-SEM after etching with 4% nitric acid solution. Under the condition of 300 g load and 10 s loading time, the microhardness of the materials was measured by microhardness tester. For the accuracy of the results, we have tested at least five parallel samples. The wetting angle was measured with a contact angle meter to evaluate the surface wettability of the sample (DSA100S, KRUSS, Germany).

XRD was employed to detect the crystal structure of the coatings. The surface morphology of the CaP coatings was manifested using FE-SEM. The surface chemical constituent was determined using the FE-SEM equipped with EDS. The surface wettability was evaluated by DSA100S, and the surface roughness was analyzed by atomic force microscope (AFM, spa-300hv).

2.3 *In Vitro* degradation test

The electrochemical properties of the materials were tested by an electrochemical analyzer (modular XM, AMETEK, United States). Working electrode, placed on a specific mold, with an exposed study surface area of 0.237 cm^2. Before measurement, the samples were soaked in SBF solution for 30 min to obtain a stable surface state. The open circuit potential was set to 1,800 s to achieve stability. The potential dynamic polarization (PDP) test was performed in the range of ±0.3 V. Constant scanning rate was 1 mVs^{-1}. Electrochemical impedance spectroscopy (EIS) was performed in the frequency range of 10^5 Hz to 10^{-2} Hz. ZSimpWin software was used to analyze the impedance data and fit it with the equivalent curve.

Early corrosion behaviors of Zn, Zn0.8Mn, and Zn0.8Mn0.1Li were researched in SBF at 37 ± 0.5°C for 14 and 28 days. Microscopical images and chemical compositions were obtained using FE-SEM equipped with EDS. The corrosion products were analyzed by XRD with radiation and 4°/min scanning speed.

2.4 *In Vitro* biosafety test

2.4.1 The sample processing

Before the tests, the samples were polished and soaked in 75% ethanol solution for 20 min, followed by UV irradiation for 20 min.

2.4.2 Mouse embryonic osteoblast precursor cells culture

The osteoblast precursor cell line (MC3T3-E1) was selected for cell tests. The culture medium was α-DMEM (Gibco, United States) supplemented with 10% FBS (Gibco, United States), 1% L-glutamine, and 10% penicillin-streptomycin at 37°C in 5% CO_2 atmosphere.

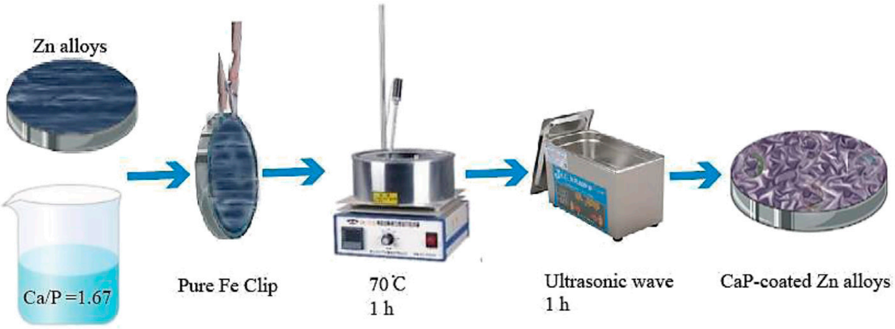

FIGURE 2
Flow diagram of the experimental procedure.

2.4.3 Cytotoxicity test

After the cells were cultured on the scaffold for 1, 3, and 7 days, 10% CCK-8 reagent was added and placed in an incubator with 5% CO_2 at 37°C for 3 h. The cellular activity was assessed on a microtiter plate reader (Thermo, America).

2.4.4 Cell adhesion test

The 2×10^5 MC3T3-E1 cells were inoculated for 3 days and fixed in 4% paraformaldehyde (Sangon Biotech) for 30 min. Washed three times and then dehydrated with 30%, 50%, 75%, 90%, 95%, and 100% gradient ethanol (Biogenic organism) solutions for 5 min each time. Finally, it dried slowly at room temperature. The sample morphology was observed by FE-SEM. And cell adhesion numbers were performed with DAPI (Sigma) after cultured for 3 days.

2.4.5 Cell viability test

The 2×10^5 MC3T3-E1 cells were inoculated for 1, 3, and 7 days. Added 2 μl of Calcein-AM Solution (2 mM) and 6 μl of Propidium iodide (PI, 1.5 mM) to 1×buffer and mixed well. Then added 200 μl mixture to the surface of the Zn-based alloys and stained it for 20 min without light. Finally viewed under a fluorescence microscope (Nikon, Japan).

2.4.6 Cell morphology evaluation

The 2×10^5 MC3T3-E1 cells were inoculated for 1, 3, and 7 days. Then, the cells were fixed with 4% paraformaldehyde for 15 min and infiltrated with 0.1% Triton for 20 min. Finally, 200 μl podophyllotoxin dye and 100 μl 1% bovine serum albumin were dyed at room temperature for 30 min.

TABLE 2 Primer sequences used in the study.

Gene	Primer	Sequences (5′-3′)
RUNX2	Forward	AAATGCCTCCGCTGTTATGAA
	Reverse	GCTCCGGCCCACAAATCT
COL-1	Forward	GCTGGAGTTTCCGTGCCT
	Reverse	GACCTCGGGGACCCATTG
GAPDH	Forward	TGACCACAGTCCATGCCATC
	Reverse	GACGGACACATTGGGGGTAG

2.4.7 Measurement of Alkaline Phosphatase Activity and extracellular matrix mineralization

Osteogenic differentiation was induced by adding osteogenic induction solution (β-glycerophosphate, ascorbic acid, and dexamethasone) into the complete medium. After 7 days of culture, alkaline phosphatase (ALP) activity was detected by BCIP/NBT ALP Color Development Kit (Beyotime), and after 14 days of culture, extracellular matrix mineralization was detected by alizarin red S(Sigma) staining.

2.4.8 Cytokine determinations of MC3T3-E1

To further investigate the effects of different scaffold materials on the osteogenic expression of MC3T3E1, the expression of RUNX2 and COL-1 were detected by real-time quantitative polymerase chain reaction (RT-qPCR) after the cells were cultured on the scaffold for 7 days. Total RNA was extracted by TRIzol reagent (Life Technologies). Complementary DNA was synthesized from 1,000 ng of total RNA using the SensiFAST™ cDNA Synthesis Kit (Byolin, Australia) according to the manufacturer's protocol. The gene expression was then quantified using an

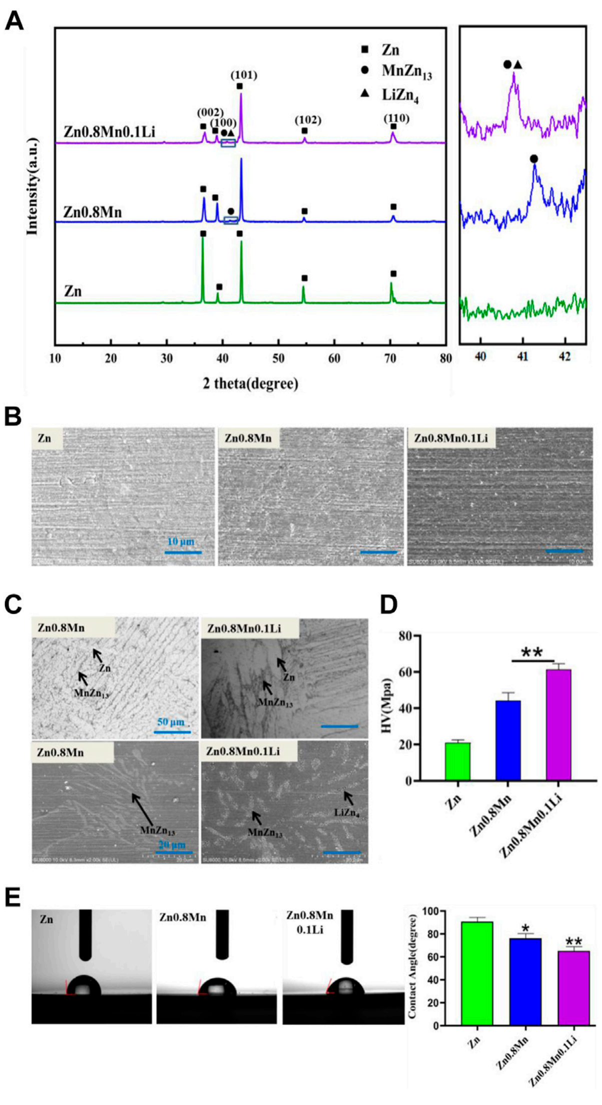

FIGURE 3
Characterizations of Zn, Zn0.8Mn, and Zn0.8Mn0.1Li. **(A)** X-ray diffraction patterns. **(B)** Surface morphologies by FESEM. **(C)** The metallographic structure. **(D)** Microhardness. **(E)** Water contact angles.*$p < 0.05$ compared to pure Zn, **$p < 0.01$ compared to pure Zn.

SYBR Green quantitative polymerase chain reaction kit (Invitrogen) in a 7500 RT-PCR system (QuantStudio™, applied biosystems) with a procedure of 95°C for 3 min and 95°C for 3 s, followed by 40 cycles at 60°C for 30 s. Gene expression was normalized to GAPDH using the ΔΔCt method. The primer sequences were shown in Table 2.

2.5 Statistical analysis

Using SPSS 22.0 statistical software, The data were demonstrated as means ± standard deviation (SD). Using one-way ANOVA to analyze the statistical difference. The distinction was significant at $p < 0.05$.

3 Results

3.1 Characterizations of Zn-based alloys

Pure Zn, Zn0.8Mn, and Zn0.8Mn0.1Li alloys had been selected for phase analysis and biological analysis *in vitro*. Figure 3A showed the XRD patterns of Zn-based alloys. $MnZn_{13}$ phase was detected in Zn0.8Mn, and $MnZn_{13}$ and $LiZn_4$ phases were detected in Zn0.8Mn0.1Li alloys. Figure 3B presented the surface morphologies of Zn-based alloys. As can be seen, Zn, Zn0.8Mn, and Zn0.8Mn0.1Li had smooth surface morphology. As we can see from Figure 3C, $MnZn_{13}$ and $LiZn_4$ were detected in the Zn0.8Mn0.1Li alloy. $LiZn_4$ particles attached to $MnZn_{13}$ particles and formed $MnZn_{13}$/$LiZn_4$ compound structure. By comparing the two figures, the addition of Li refined the microstructure significantly. Systematically, the microhardness of the alloy was significantly increased from 20.94 HV of pure Zn to 61.2 HV of Zn0.8Mn0.1Li alloy (Figure 3D). Figure 3E showed a digital image of the droplet morphology and the matching calculation of the contact angle. The contact angle of Zn, Zn 0.8Mn, and Zn0.8Mn0.1Li decreased in order. They were 90.6 ± 4.32°, 76.4 ± 4.47°, and 65.3 ± 4.1°, respectively. Mainly because after adding alloying elements, the eutectic structure was formed and the grain was refined, the contact angle was reduced and wettability was improved.

3.2 Degradation of Zn-based alloys

The polarization curves of pure Zn, Zn0.8Mn, and Zn0.8Mn0.1Li were given in Figure 4A. The fitting results were shown in Table 3. Conduct PDP test to compare the corrosion resistance of samples. The slopes of anode and cathode Tafel curves changed with the change of Mn/Li content, which indicated that Mn/Li affected the dissolution and oxygen consumption of Zn matrix. Among all materials, the Ecorr value of Zn was the lowest (−1.17 VCE). As for Zn0.8Mn and Zn0.8Mn0.1Li, Ecorr values increased with Mn/Li content. And the icorr values of Zn0.8Mn were lower than that of Zn0.8Mn0.1Li. The corrosion rate (CR) of Zn0.8Mn0.1Li was 0.046 mm/y, which was slower than that of pure Zn. Figure 4B showed the EIS plots of pure Zn, Zn0.8Mn, and Zn08Mn0.1Li. As shown in the Nyquist curves (Figure 4B), compared to pure Zn, Zn0.8Mn0.1Li had a bigger semicircle diameter, which indicated its lower corrosion rate. After adding Mn/Li, Zn0.8Mn0.1Li showed the characteristics of diffusion impedance in the low-frequency scope, the slope of the curve in the low-frequency scope increased, and the smallest frequency impedance modulus (|z|) increased (Figures 4C,D). The fitted equivalent circuit was

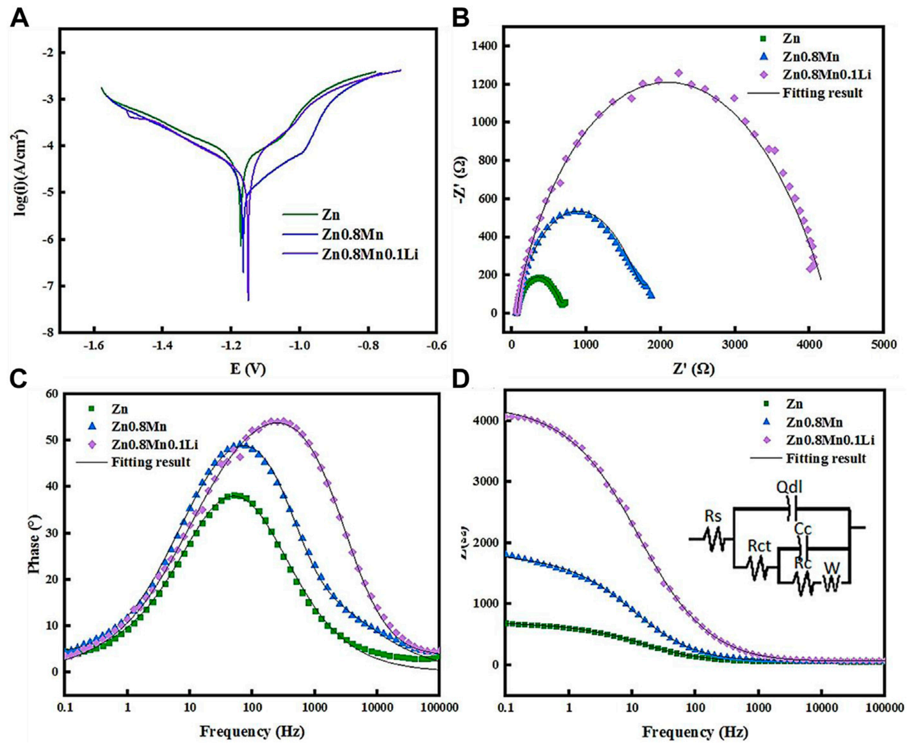

FIGURE 4
Polarization curves and EIS results of pure Zn and Zn-based alloys in SBF. **(A)** Potentiodynamic polarization curves. **(B)** Nyquist plots. **(C)** Bode plots of phase angle vs. Frequency. **(D)** Bode plots of |Z| vs. Frequency. The inset in Figure 4D is an equivalent circuit for fitting the EIS spectra.

TABLE 3 Polarization data of pure zinc and zinc alloy samples in SBF.

Materials	βa (mV/dec)	−βc (mV/dec)	Ecorr (V/SCE)	Icorr (μA/cm2)	CR (mm/a)
Zn	166.30 ± 21.57	288.7 ± 0.55	−1.1710	53.70	0.085
Zn0.8Mn	175.55 ± 3.51	265.36 ± 0.58	−1.1565	30.90	0.055
Zn0.8Mn0.1Li	125.96 ± 0.83	248.14 ± 0.95	−1.1504	26.92	0.046
CaP Zn	64.83 ± 1.04	253.57 ± 6.42	−0.9532	3.45	0.00059
CaP Zn0.8Mn	124.88 ± 1.55	272.63 ± 1.15	−0.9394	7.74	0.0014
CaP Zn0.8Mn0.1Li	282.32 ± 5.11	219.81 ± 2.60	−0.3710	0.25	0.000045

TABLE 4 Fitting parameters in SBF.

Materials	Rs (Ωcm^2)	Qdl (S.sec^n/m^2)	n1 (0<*n*<1)	Rct (Ωcm^2)	Cc (F/m^2)	Rc (Ωcm^2)	W (S.sec^5/cm^2)
Zn	61.95	0.7875	0.74	577.6	24.37	30.66	0.02775
Zn0.8Mn	58.6	0.4185	0.6747	81.8	0.02064	1,607	0.01152
Zn0.8Mn0.1Li	64.22	0.1866	0.6226	17.88	0.005532	4200	1354000000
CaP Zn	85.77	0.006744	0.7084	815.7	0.006736	1,121	0.02532
CaP Zn0.8Mn	93.42	0.3512	0.6713	66.23	0.01724	1,257	0.02178
CaPZn0.8Mn.1Li	89.69	0.1385	0.5966	5,247	1.684	8595	0.00008695

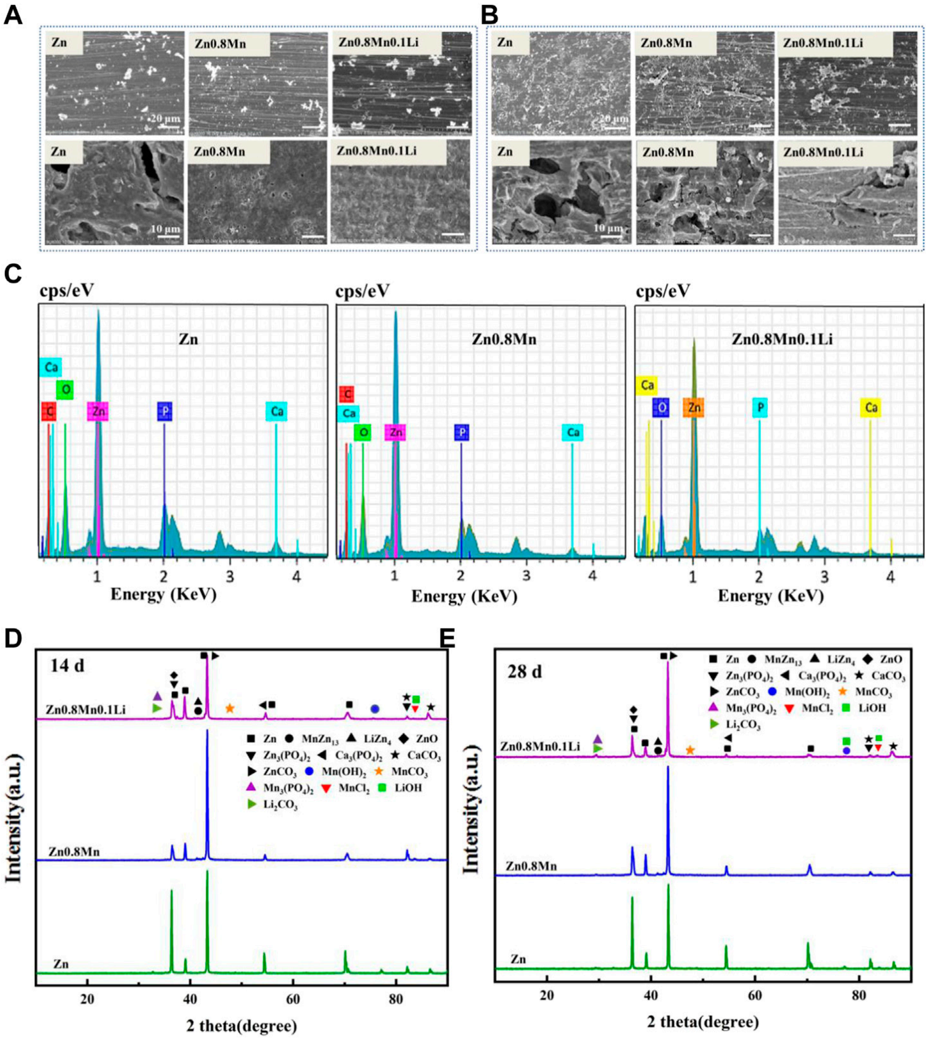

FIGURE 5
In vitro degradation tests. **(A)** Degradation morphology under FESEM after 14 days immersion in SBF. **(B)** Degradation morphology under FESEM after 28 days immersion in SBF. **(C)** The EDS spectra of Zn, Zn0.8Mn, and Zn0.8Mn0.1Li after 28 days immersion in SBF. **(D)** XRD diffraction patterns of degradation products after 14 days immersion in SBF. **(E)** XRD diffraction patterns of degradation products after 28 days immersion in SBF.

shown in Figure 4D. Rs, Rct, and Rc were solution resistance, charge transferring resistance between samples and SBF solution, and resistance of corrosion products layer, respectively. Qc represented the capacitance of the corrosion products layer. Qdl was a constant phase element (CPE) corresponding to the double layer capacitance. There were many reasons for CPE, such as non-uniformity, electrode pores, surface roughness, slow adsorption reaction, uneven distribution of potential and current, et al. The fitting results were shown in Table 4. The R_C of the alloy can be calculated as Zn0.8Mn0.1Li > Zn0.8Mn > Zn descending sort, so as their corrosion resistances.

The samples were immersed in SBF solution for 14 and 28 days to observe the morphology of the corrosion products. After removing the corrosion products, the surface corrosion was also observed (Figure 5A). After 14 days of immersion, a small number of corrosion products were observed on the surface. The initial corrosion products on the surface of pure Zn and Zn-based alloys were round cloud aggregates. After removing the corrosion products, local corrosion pits appeared on the surface of pure Zn. While Zn0.8Mn and Zn0.8Mn0.1Li exhibited much more uniform degradation morphology. After soaking for 28 days, the corrosion products of the three alloys all increased to a certain extent. As shown in Figure 5B, the surface corrosion products of pure Zn and Zn0.8Mn showed an elongated crystal shape and accumulated in large quantities in local areas. After the removal of corrosion products, pure Zn and Zn0.8Mn showed characteristic uneven corrosion, accompanied by a large area of corrosion pits. However, the

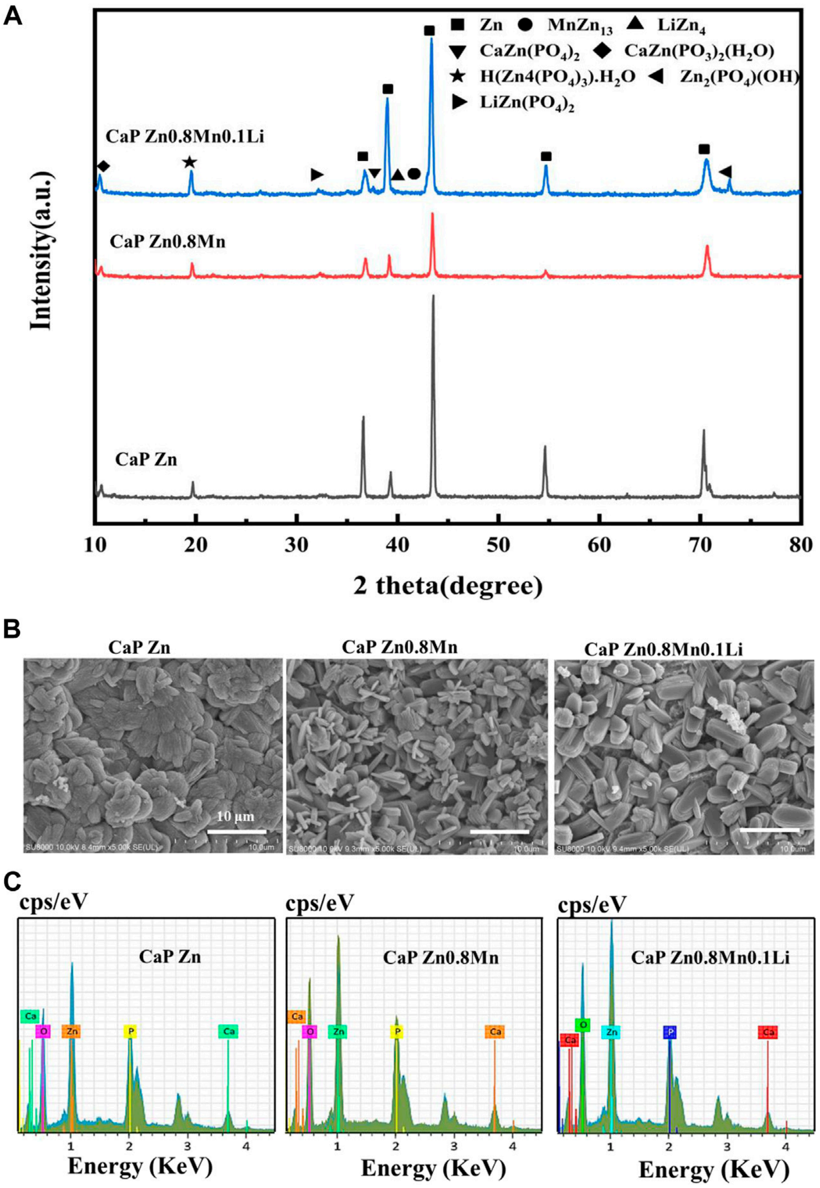

FIGURE 6
The microstructure and composition of CaP-coated Zn, Zn0.8Mn, and Zn0.8Mn0.1Li. **(A)** XRD spectrum. **(B)** Surface morphologies by FESEM. **(C)** The EDS spectra and relative contents of each element.

surface of Zn0.8Mn0.1Li showed flower-like corrosion products, which showed a smaller corrosion area and no obvious corrosion pits compared with the other two samples. All these results showed Zn0.8Mn0.1Li manifested more uniform degradation behavior. Additionally, the EDS analyses of the corrosion products after 28 days were performed. EDS spectrum showed that the white particles were mainly composed of Zn, P, O, C, and a small amount of Ca (Figure 5C). The degradation products were mainly ZnO, $ZnPO_4$, $CaPO_4$, $ZnCO_3$, and $CaCO_3$ indicated from XRD patterns (Figures 5D,E). This result showed the diffraction peak of corrosion products was significantly enhanced after immersion for 28 days.

3.3 Surface Morphology and Composition of CaP coatings on Zn-based Alloys

The Zn/Fe coupling system includes zinc and iron clamp to form a point contact. Due to the corrosion potential

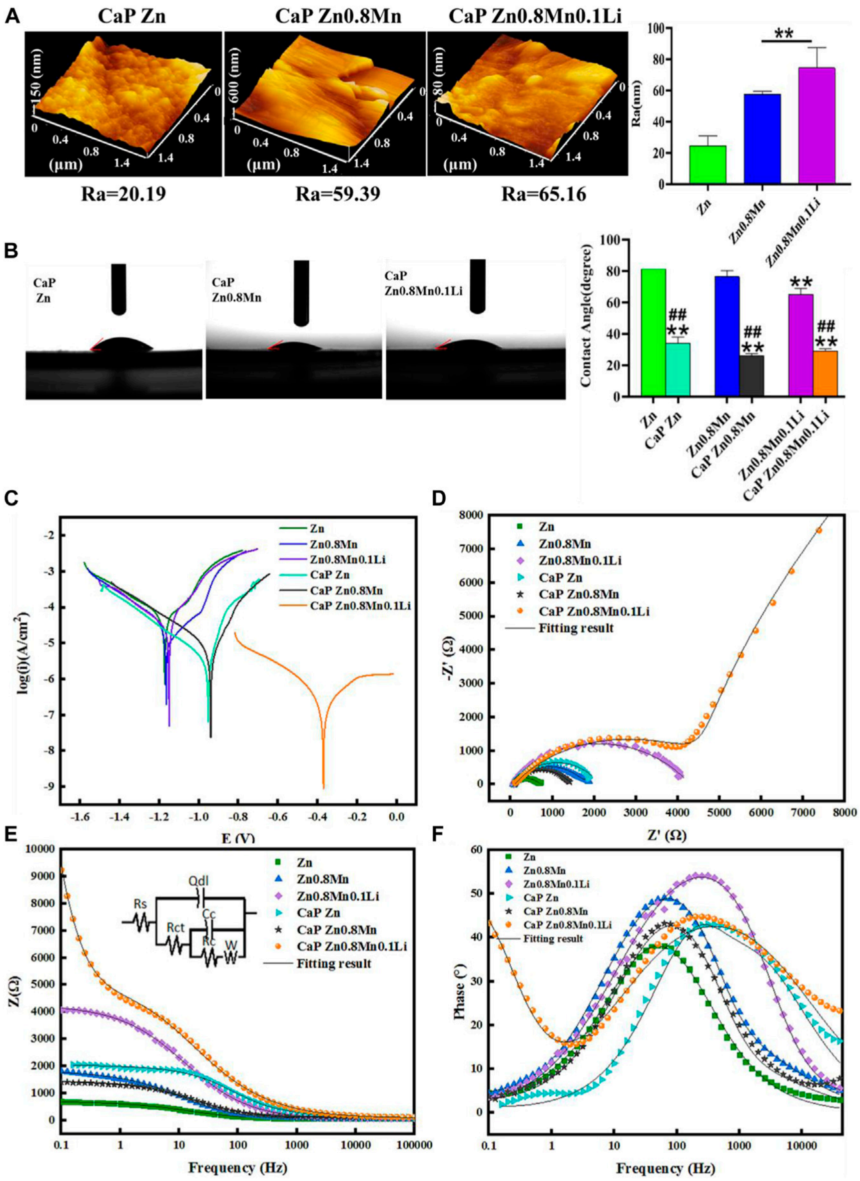

FIGURE 7
Characterization of CaP-coated Zn, Zn0.8Mn, and Zn0.8Mn0.1Li. **(A)** The surface roughness of the surfaces obtained by AFM. **(B)** Water contact angles. **(C)** Potentiodynamic polarization curves of CaP Zn, CaP Zn0.8Mn, and Zn0.8Mn0.1Li. **(D)** Nyquist plots. **(E)** Bode plots of |Z| vs Frequency. The insets in Figure 7E is equivalent circuit for fitting the EIS spectra. **(F)** Bode plots of phase angle vs Frequency. $*p < 0.05$ compared to pure Zn, $**p < 0.01$ compared to pure Zn, $\#\#p < 0.01$ compared to no coatings.

difference, the iron clamp can be regarded as the coupled anode, zinc as the coupled cathode in the acid phosphate chemical conversion solution. And the initial power of this reaction was provided by the corrosion of the iron clamp. In addition, the transient high temperatures and high pressures generated by ultrasound on the Zn surface caused partial supersaturation of the ion concentration near the Zn surface, leading to heteronucleation growth of phosphate crystals. Finally, complete CaP coatings were formed.

As can be seen from Figure 6A, CaP Zn, CaP Zn0.8Mn and CaP Zn0.8Mn0.1Li had similar XRD diffraction peaks. The phase composition were $CaZn_2(PO_4)_2$, $CaZn_2(PO_3)2(H_2O)$, $H(Zn_4(PO_4)_3)H_2O$, and $Zn_2(PO_4)(OH)$. The CaP Zn0.8Mn0.1Li consisted a small amount of $LiZn(PO_4)_2$ phase. The diffraction peak intensity of CaP Zn was obviously stronger than CaP Zn0.8Mn and CaP Zn0.8Mn0.1Li. The surface morphologies of CaP Zn, CaP Zn0.8Mn and CaP Zn0.8Mn0.1Li were shown in Figure 6B. Apparently, diverse

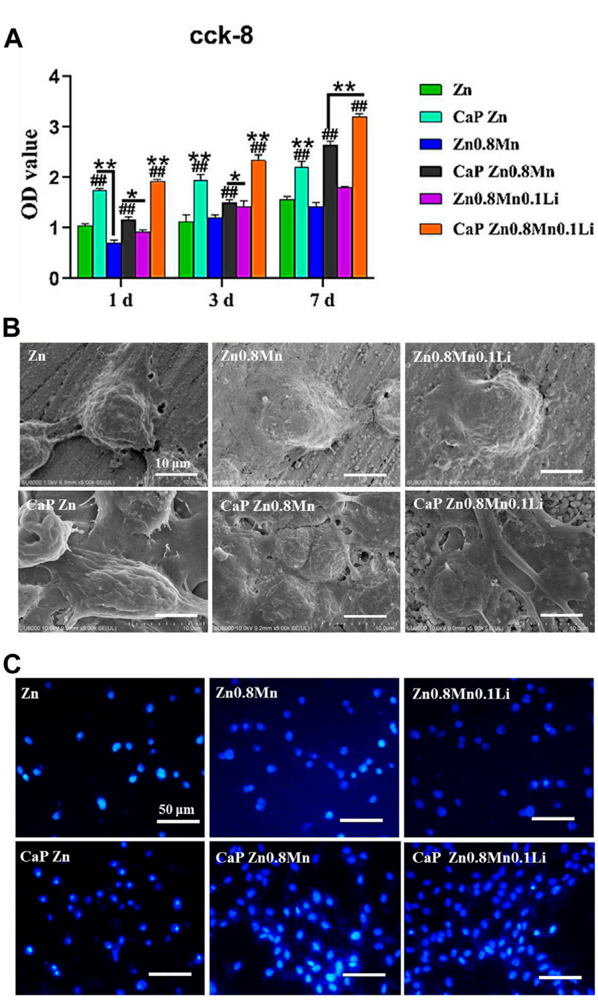

FIGURE 8
Cytocompatibility of Zn-based alloys and CaP-coated Zn-based alloys. **(A)** CCK-8 cells proliferation experiment of MC3T3-E1 after cultured 1, 3, and 7 days *in vitro*. **(B)** SEM and **(C)** DAPI nuclear staining pictures of MC3T3- E1 cells on different samples surface after cultured 3 days *$p < 0.05$ compared to pure Zn, **$p < 0.01$ compared to pure Zn, ##$p < 0.01$ compared to no coatings.

dense and uniform coatings were formed on the surface of pure Zn and Zn-based alloys after chemical conversion. The morphologies between these three kinds of coatings were quite different. CaP Zn was composed of regular fibrous crystals that were tightly bound to each other without any gaps. Compared with CaP Zn, the microstructure of CaP Zn0.8Mn changed significantly and became relatively loose surface state composed of interwoven rod-like crystals. CaP Zn0.8Mn0.1Li was composed of uniform elliptic sheet crystals with regular shape and uniform sizes. As can be seen from Figure 6C, EDS results showed that the main elements of the coatings were O, P, Zn, and Ca, which confirmed the successful introduction of Ca and P elements on the coatings.

AFM test showed that the roughness of the samples surface increased significantly with the surface morphology (Figure 7A). Wettability results showed that both the CaP Zn, CaP Zn0.8Mn, and CaP Zn0.8Mn0.1Li became more hydrophilic (Figure 7B). The contact angle of CaP Zn, CaP Zn0.8Mn, and CaP Zn0.8Mn0.1Li decreased significantly, with values of 34.3 ± 3.66°, 29.9 ± 5.60°, and 29.0 ± 1.57°, respectively. However, there was a certain gap between the single particles of CaP Zn0.8Mn and CaP Zn0.8Mn0.1Li, resulting in a decrease in contact angle and an increase in hydrophilicity. Figure 7C showed the potentiodynamic polarization curve of the CaP coatings with pure Zn and Zn-based alloys. The electrochemical parameters calculated by Tafel extrapolation were shown in Table 2. Generally, the higher the corrosion voltage (Ecorr) and the lower the corrosion current density (Icorr) indicated that the corrosion rate was slower and the metal was more resistant to corrosion. As shown in Table 2, the Ecorr of CaP coatings were higher than the pure Zn and Zn-based alloys while the Icorr of CaP coatings were smaller, and the Icorr of CaP Zn0.8Mn0.1Li was the lowest, this showed the higher corrosion resistance of the CaP Zn0.8Mn0.1Li. As shown in the Nyquist curves (Figure 7D), CaP Zn0.8Mn0.1Li had a bigger semicircle diameter and had the largest impedance modulus (|z|) in the low-frequency region, which indicated its lower corrosion rate (Figure 7E). There were two-time constants in the Bode curve of CaP Zn0.8Mn0.1Li (Figure 7F), so two-time constant models with W diffusion impedance were used to fit the EIS data of all the specimens. The fitted equivalent circuit results were listed in Table 3, the Rc of CaP Zn0.8Mn0.1Li was the highest, so it had the highest corrosion resistance. These structural features were essential to enhance the osteogenesis-related cell attachment and accelerate tissue growth during osseointegration.

3.4 Biocompatibility of MC3T3-E1 cells

Good proliferation and adhesion of cells on scaffolds were two important factors in the construction of bone tissue engineering scaffolds. For the sake of estimating the proliferation ability of MC3T3-E1 cells cultured on scaffolds, CCK-8 was measured on days 1, 3, and 7 after cells inoculation. Results were shown in Figure 8A, the OD value of MC3T3-E1 cells was raised on day 3 and day 7. Compared with Zn and Zn0.8Mn, Zn0.8Mn0.1Li had a higher OD value and faster growth rate, which proved that Zn0.8Mn0.1Li had better biocompatibility. And Zn-based alloys were expected to become ideal bone osteogenesis materials. Moreover, compared with Zn, Zn0.8Mn, and Zn0.8Mn01Li, the OD value of the platforms coated with CaP coatings was significantly increased, and the CaP Zn0.8Mn0.1Li had the most considerable OD value, followed by CaP Zn0.8Mn and CaP Zn. The adhesive ability of MC3T3-E1 cells on the surfaces

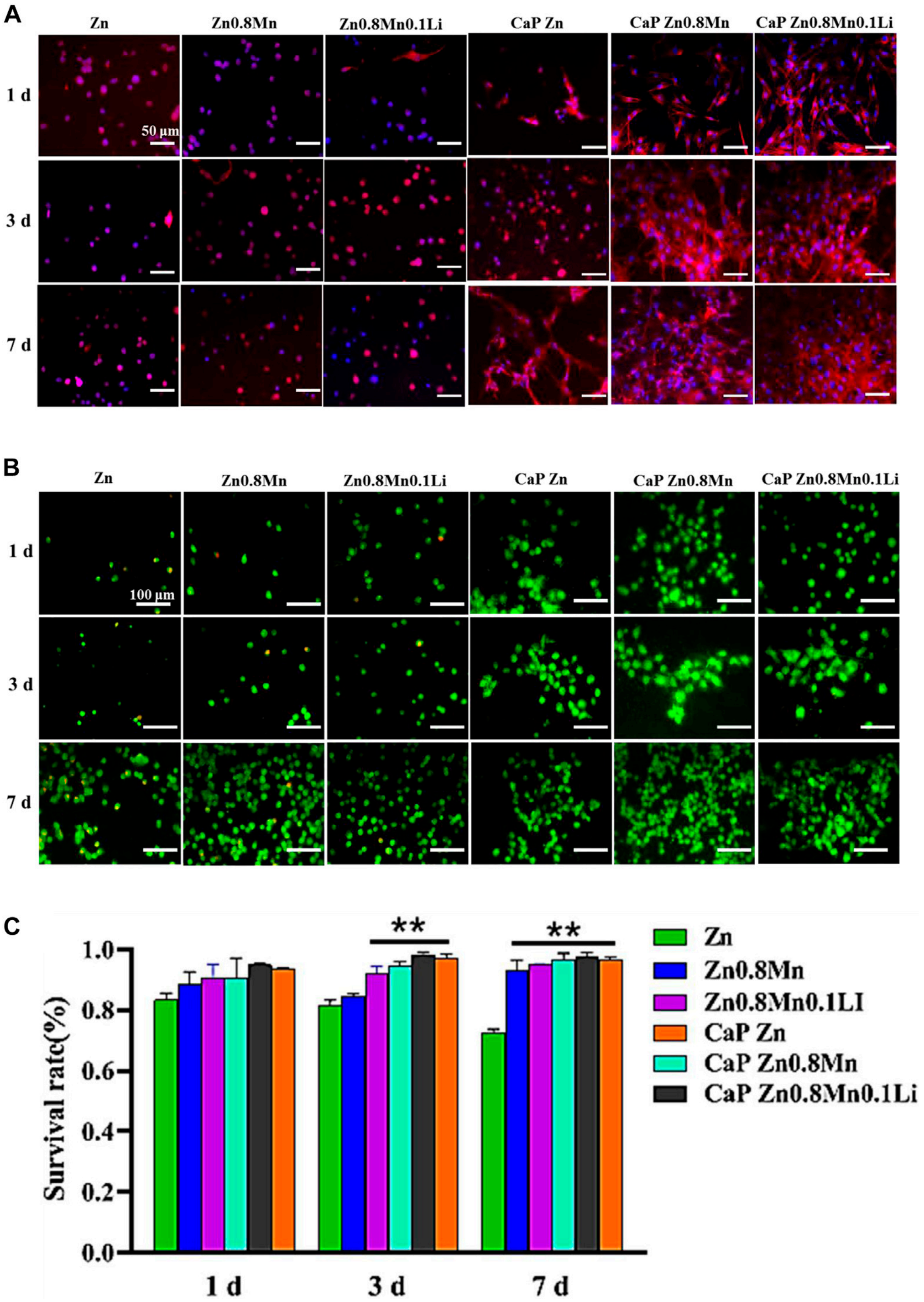

FIGURE 9
(A) The AM/PI staining results about cell activity *in vitro*. **(B)** Cell survival ratio by fluorescence expression quantity. **(C)** The morphology of MC3T3-E1 cells after seeding on the different scaffolds for 1, 3, and 7 days $^{**}p < 0.01$ compared to pure Zn.

was evaluated by FE-SEM analysis and DAPI staining (Figures 8B,C). MC3T3-E1 cells were round on the surface of pure Zn and Zn-based alloys, with almost no pseudopods protruding. However, after adding CaP coatings, MC3T3-E1 cells were fusiform. It can be seen that MC3T3-E1 had obvious pseudopods protrusion on the surface of CaP Zn0.8Mn0.1Li,

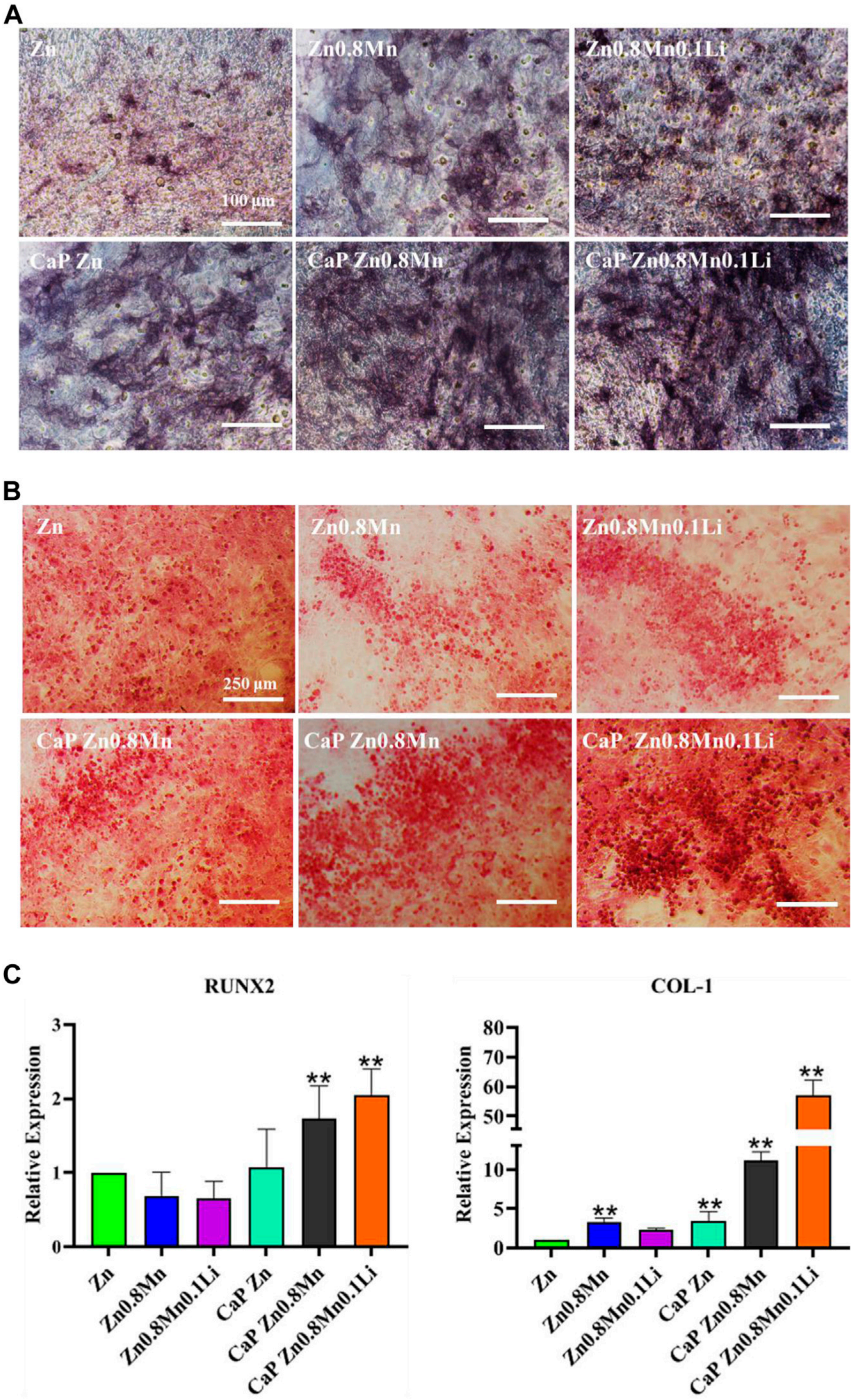

FIGURE 10
Osteogenic differentiation of MC3T3-E1 cells. **(A)** ALP staining and quantification in MC3T3-E1 cells. **(B)** Alizarin red S staining and quantification in MC3T3-E1 cells. **(C)** The expression of osteogenic gene was detected by qRT-PCR. $^{*}p < 0.05$, $^{**}p < 0.01$ represent significant differences between the indicated columns.

which connected with adjacent cells compactly. The number of attached cells increased significantly after Zn0.8Mn and Zn0.8Mn0.1Li were inoculated for 3 days while compared with the pure Zn. After adding CaP coatings, the number of MC3T3-E1 increased significantly, especially CaP Zn0.8Mn0.1Li.

Figure 9A showed the staining of MC3T3-E1 cells on the scaffold surface. The red was the cytoskeleton factin and the blue was the nucleus. The cells cultured on the pristine Zn-based alloys showed a circular shape with very few pseudopods. The morphology of MC3T3-E1 on CaP Zn was slightly expanded on day 7. And the morphology of MC3T3-E1 revealed spindle-like shapes on the CaP Zn0.8Mn and CaP Zn0.8Mn0.1Li. Compared with MC3T3-E1 on the CaP Zn0.8Mn, the sizes of the MC3T3-E1 were wider on the CaP Zn0.8Mn0.1Li, and it was fully paved on 7 days. AM/PI staining was performed to assess cell viability and calculate survival rate. As shown in Figure 9B, when cells were dyed with AM/PI, dead cells showed typical red fluorescence, while living cells showed green fluorescence. The survival rate of the pure Zn group showed a downward trend, and a large number of dead cells occurred on day 7. These results showed that the cells had a higher survival rate at Zn0.8Mn and Zn0.8Mn0.1Li than pure Zn. (Figure 9C). No dead cells were found in the coating group, therefore, the biocompatibility of CaP coatings was good. The results showed very little or no effect on the survival rate of MC3T3-E1 cells compared to no coated. Confocal laser scanning microscope (CLSM) analysis was used to observe the morphology of cell attachment and spreading after being cultured for 1, 3, and 7 days.

For the sake of the early stage osteogenic activity of scaffolds, we observed the ALP staining of MC3T3-E1 cells cultured on different scaffolds for 7 days. As shown in Figure 10A, only a small amount of gray deposits can be observed on the pure Zn, the gray deposits of Zn0.8Mn0.1Li was obviously more and darker than that of pure Zn. After the introduction of CaP coatings on the Zn-based alloys, the gray sediments had increased to a certain extent. However, more black sediments were produced on CaP Zn0.8Mn0.1Li. Calcium deposition reflected the efficiency of the mineralization stage. After MC3T3-E1 cells were inoculated on different scaffolds for 14 days, the mineralization of calcium nodules was measured by ARS. According to Figure 10B, a small raise in the number of calcium nodules was surveyed on Zn0.8Mn and Zn0.8Mn0.1Li alloys compared with that of pure Zn, but there were quite a few calcium nodules on the CaP-coated Zn-based alloys. This showed that surface-modified CaP was more conducive to the secretion of mineralized extracellular matrix and can promote osteogenic activity, especially CaP Zn0.8Mn0.1Li. The expression of osteogenic genes COL1 and RUNX2 were detected by RT-PCR. From RT-PCR results, we can see the expression of osteogenic genes in MC3T3-E1 on CaP-coated Zn-based alloys was significantly higher than pure Zn. Especially the CaP Zn0.8Mn0.1Li had the highest expression of osteogenic genes (Figure 10C). These results indicated that CaP Zn0.8Mn0.1Li can effectively promote the osteogenic differentiation of MC3T3-E1 cells.

4 Discussion

In this study, we first self-designed high-strength Zn0.8Mn0.1Li alloy to study the performance of Zn-based alloys in orthopedic implants. According to Zn-Mn phase diagram, the solid solubility of Mn in Zn reached a maximum of 0.8% at eutectic reaction temperature (Shi et al., 2018). With the addition of alloying elements, the microhardness of the alloy is significantly improved, which can meet the requirements of clinical orthopedic implants. This was attributed to that $MnZn_{13}$ particles stimulated the recrystallization of Zn grains at room temperature and released the internal stress during the tensile test (Sun et al., 2021). Further alloying 0.1% Li in Zn-Mn alloy introduced finer $LiZn_4$ second phase, refined the grain, and significantly improved its strength. The formation of the second phase can also avoid serious pitting and local corrosion in the degradation process of Zn alloys.

It is positive impact on the corrosion resistance of Zn-Mn alloy for the addition of Li because the structure of Zn0.8Mn0.1Li alloy was more uniform and finer. When Zn0.8Mn0.1Li alloy was immersed in SBF, Zn controlled the anodic and cathodic reactions, which accounted for more than 98 wt% of the alloy (Li et al., 2020; Sun et al., 2021). The corrosion mechanism diagram of Zn0.8Mn0.1Li alloy in SBF was shown in Figure 11. The reactions were as follows:

$$Zn \rightarrow Zn^{2+} + e^{-} \tag{1}$$

$$O_2 + 2H_2O + 4e^{-} \rightarrow 4OH^{-} \tag{2}$$

$$Zn^{2+} + 2OH^{-} \rightarrow Zn(OH)_2 \tag{3}$$

The dissolved Zn^{2+} can severally draw HPO_4^{2-} and Ca^{2+} in the SBF, resulting in the deposition of $Ca_3(PO_4)_2$, $CaCO_3$, $Zn_3(PO_4)_2$, and $ZnCO_3$, which were specific corrosion products of Zn and its alloys in physiological environment (Ma et al., 2016; Yang et al., 2016; Zhao et al., 2019). Partial $Zn(OH)_2$ was seemly to be dehydrated to produce ZnO through subsequent reaction:

$$Zn^{2+} + HPO_4^{2-}/CO_3^{2-} \rightarrow Zn_3(PO_4)_2/ZnCO_3 \tag{4}$$

$$Ca^{2+} + HPO_4^{2-}/CO_3^{2-} \rightarrow Ca_3(PO_4)_2/CaCO_3 \tag{5}$$

$$Zn(OH)_2 \rightarrow ZnO + H_2O \tag{6}$$

The ions released from the alloy were primarily Zn^{2+}, $Mn^{2+,}$ and Li^{+}. Guided by the XRD profile in Figures 5D,E, the metallic ions (Mn^{2+} and Li^{+}) can respectively attract with OH^{-}, HCO_3^{-}, HPO_4^{2-}, and Cl^{-} in the SBF as follows:

$$Mn^{2+} + 2OH^{-} \rightarrow Mn(OH)_2 \tag{7}$$

$$Mn^{2+} + HCO_3^{-} \rightarrow H^{+} + MnCO_3 \tag{8}$$

$$3Mn^{2+} + 2HPO_4^{2-} \rightarrow 2H^{+} + Mn_3(PO_4)_2 \tag{9}$$

$$Mn^{2+} + 2Cl^{-} \rightarrow MnCl_2 \tag{10}$$

Li showed great fluidity and activity in the corrosive layer and was easy to react with dissolved O_2 in the water environment,

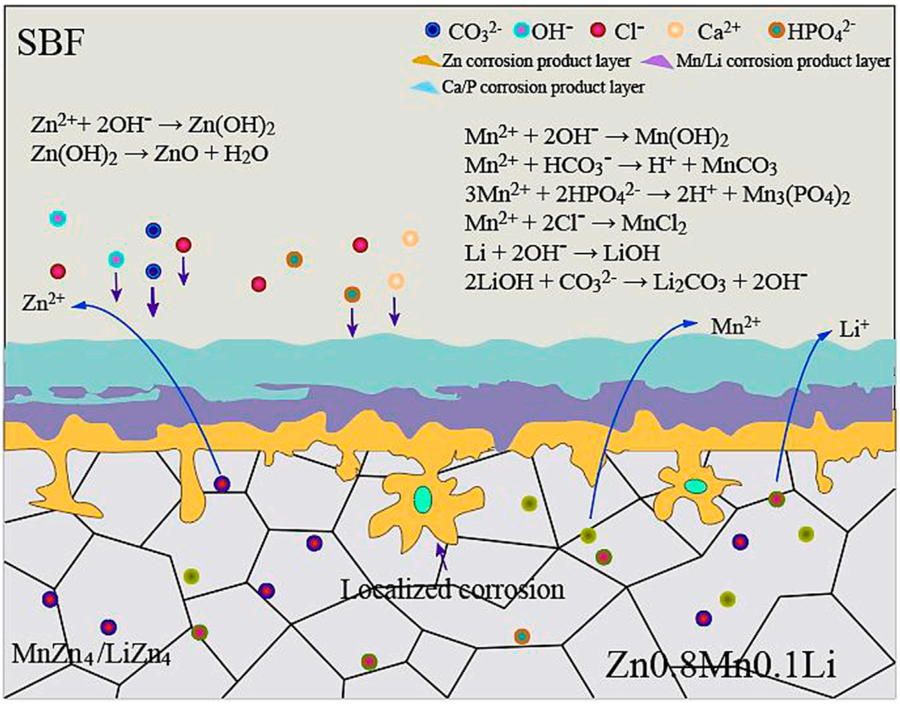

FIGURE 11
Corrosion mechanism diagram of Zn0.8Mn0.1Li alloy in SBF.

forming Li_2O in the outer corrosive layer (Li et al., 2020). Combined with XRD (Figure 1), water-insoluble lithium-rich corrosion products were formed according to the following reactions:

$$2Li + 2H_2O \rightarrow 2LiOH + H_2 \tag{11}$$

$$2LiOH + CO_3^{2-} \rightarrow Li_2CO_3 + 2OH^- \tag{12}$$

The results of *in vitro* experiments showed that all samples had no toxic side effects on cell proliferation and adhesion, showing a good proliferation trend. But experiments had demonstrated that Zn-based alloys had certain effects on the morphology of MC3T3-E1 cells, the cells do not spread well on it. However, the spread area of osteoblasts on CaP Zn0.8Mn0.1Li was larger, and the aspect ratio was about 2:1. Relevant studies had also confirmed that the cytoskeleton guides cells to regulate their adhesion or other behaviors to adapt to the corresponding microenvironment (Jing et al., 2021). It had been reported that more cell contact and larger cell spread are conducive to osteogenic differentiation of MC3T3-E1 cells (Yao et al., 2013c). This may be the reason for the highest expression of osteogenic characteristic genes under CaP Zn0.8Mn0.1Li stimulation (Yao et al., 2019). A similar elongated cell morphology had also been reported to increase cell viability, which may provide another advantage for CaP Zn0.8Mn0.1Li scaffolds in improving cell viability and cell proliferation (Zou et al., 2021).

The survival rate of Zn0.8Mn and Zn0.8Mn0.1Li alloys showed an increasing trend, which indicated that the processed Zn-based alloys had certain biocompatibility. However, the cell survival rate on the surface of pure Zn showed a downward trend, which may be caused by the rapid degradation of pure Zn and the high local Zn^{2+} concentration. It has been reported that the cytocompatibility of pure Zn and Zn alloys exhibited a concentration-dependent phenomenon, the low concentrations of Zn^+ were beneficial to cells and high concentrations were harmful to cells. For example, Ma demonstrated that Zn^{2+} promoted cell proliferation at low concentrations of 60 μM and inhibit cell proliferation at concentrations greater than 80 μM (Ma et al., 2015).

The additions of Mn and Li to Zn-based alloys have statistically modified the biocompatibility to some extent. Mn is the immune system and a variety of enzymes necessary trace elements play an important role in bone growth and development of animals. Mn deficiency can lead to poor bone growth, reproductive disorders, and neurological disorders (Sun et al., 2021). Li is also necessary for human body nutrition elements, the latest research showed that Li can stimulate the osteogenic differentiation of bone marrow mesenchymal stem cells and promote bone reconstruction (Li et al., 2020).

It was considered that the coexistence of Mn^{2+} and Li + promoted Mn^{2+} and Li^{+} influx into MC3T3-E1 cells, inhibited Zn^{2+} effusion, effectively activated Runx2, and induced osteogenic differentiation of MC3T3-E1 cells (Yu et al., 2017). The osteogenic effect of Zn0.8Mn0.1Li may be attributed to the synergistic effect of Li^{+} and Zn^{2+}. Although the content of Li (0.1%) is low in the alloy, it is preferentially released during degradation due to its high chemical reactivity. This can effectively regulate the release of Zn^{2+} and avoid the adverse effect of excessive local zinc ion concentration on the osteogenic effect.

In the future design of Zn-based alloys for orthopedic, we should select elements with osteogenic effects and low electrode potential to balance their synergistic effects and reduce the release rate of Zn^{2+} moderately. Therefore, Zn0.8Mn0.1Li alloy had good comprehensive properties and was expected to become a candidate material for the development of biodegradable alloys.

The physicochemical properties of the material surface were the key factors to regulate the bone-implant bonding. The adhesion, proliferation, and differentiation of cells were intensely dependent on the surface of materials, including surface composition, charge, and hydrophilicity. Such as the effect of roughness on protein adsorption will directly affect cell adhesion and diffusion (Yang et al., 2021; Yuan et al., 2022). It has been shown that cell fate can be determined by designing the surface topography to give specific physicochemical parameters (Priyadarshini et al., 2019). Phosphate chemical conversion technology is an effective technique to adjust the surface morphology and element composition by forming different transformation films on the surface of implants. The formation of phosphate can effectively slow down the corrosion rate, mainly because of the low solubility product constant of phosphate. Calcium phosphate was the main component of hard tissue, so it had a positive effect on the adhesion and growth of bone cells on biomaterials (Su et al., 2019). Moreover, the hydrophilicity and roughness of the scaffolds were significantly improved after the preparation of CaP coatings on the scaffolds, which were more suitable for cell attachment (Ling et al., 2021). It is necessary to accelerate bone repair in the process of promoting bone regeneration. Zn0.8Mn0.1Li alloy will be a promising bone implant to achieve these results. The study proved CaP coatings could significantly promote bone regeneration.

5 Conclusion

All in all, to satisfy the clinical demands of osteogenic ability, biocompatibility, and biodegradability of medical degradable metal materials, a high-strength Zn0.8Mn0.1Li alloy was designed. To further improve its cytocompatibility, we modified its surface and prepared calcium-phosphorus coatings. It decreased the ion release and subsequently also decreased toxicity and enhanced MC3T3-E1 cells proliferation and adhesion. Therefore, this study will propose an innovative strategy for the surface design of biomedical implants.

Data availability statement

The raw data supporting the conclusion of this article will be made available by the authors, without undue reservation.

Author contributions

XL, Z-YL, C-YH assisted H-FQ performed all experimental work of this article. H-FQ wrote and Y-JZ edited the manuscript. F-ZL reviewed this manuscript, contributed, and approved the final manuscript. Y-JZ, X-MC, and F-ZL contributed to the conception, design, and leadership of the program.

Funding

This work was in part supported by the Science Foundation of Shandong Province of China (Grant No. ZR2021MH026) and Medicine and Health Science Technology Development plan of Shandong Province of China (Grant No. 202108020440), and Liaocheng People's Hospital Youth Fund Project (Grant No. LYQN201914).

Conflict of interest

The authors declare that the research was conducted in the absence of any commercial or financial relationships that could be construed as a potential conflict of interest.

Publisher's note

References

Acheson, J.- G., Gallagher, E.-A., Ward, J., McKillop, S., FitzGibbon, B., Boyd, A., et al. (2022). Shear testing and failure modelling of calcium phosphate coated AZ31 magnesium alloys for orthopaedic applications. *Surf. Coat. Technol.* 429, 127944. doi:10.1016/j.surfcoat.2021.127944

Bai, L., Chen, P., Zhao, Y., Hang, R., Yao, X., Tang, B., et al. (2021). A micro/nano-biomimetic coating on titanium orchestrates osteo/angio-genesis and osteoimmunomodulation for advanced osseointegration. *Biomaterials* 278, 121162. doi:10.1016/j.biomaterials.2021.121162

Gu, X.-N., Xie, X.-H., Li, N., Zheng, Y.-F., and Qin, L. (2012). *In vitro* and *in vivo* studies on a Mg-Sr binary alloy system developed as a new kind of biodegradable metal. *Acta Biomater.* 8, 2360–2374. doi:10.1016/j.actbio.2012.02.018

Jablonská, E., Vojtěch, D., Fousová, M., Kubásek, J., Lipov, J., Fojt, J., et al. (2016). Influence of surface pre-treatment on the cytocompatibility of a novel biodegradable ZnMg alloy. *Mater. Sci. Eng. C* 68, 198–204. doi:10.1016/j.msec.2016.05.114

Jing, Ling-zhi., Fan, Suna., Yao, Xiang., and Zhang, Yao-peng. (2021). Effects of compound stimulation of fluid shear stress plus ultrasound on stem cell proliferation and osteogenesis. *Regen. Biomater.* 8, rbab066–10. doi:10.1093/rb/rbab066

Li, W., Qiao, W., Liu, X., Bian, D., Shen, D., Zheng, Y., et al. (2021). Biomimicking bone-implant interface facilitates the bioadaption of a new degradable magnesium alloy to the bone tissue microenvironment. *Adv. Sci.* 8, 2102035. doi:10.1002/advs.202102035

Li, Z., Shi, Z.-Z., Hao, Y., Li, H.-F., Zhang, H.-J., Liu, X.-F., et al. (2020). Insight into role and mechanism of Li on the key aspects of biodegradable Zn Li alloys: Microstructure evolution, mechanical properties, corrosion behavior and cytotoxicity. *Mater. Sci. Eng. C* 114, 111049. doi:10.1016/j.msec.2020.111049

Ling, L., Cai, S., Li, Q., Sun, J., Bao, X., and Xu, G. (2021). Recent advances in hydrothermal modification of calcium phosphorus coating on magnesium alloy. *J. Magnesium Alloys* 10, 62–80. doi:10.1016/j.jma.2021.05.014

Ma, J., Zhao, N., and Zhu, D. (2016). Bioabsorbable zinc ion induced biphasic cellular responses in vascular smooth muscle cells. *Sci. Rep.* 6, 1–10. doi:10.1038/srep26661

Ma, Jun., Zhao, Nan., and Zhu, Dong-hui. (2015). Endothelial cellular responses to biodegradable metal zinc. *ACS Biomater. Sci. Eng.* 1, 1174–1182. doi:10.1021/acsbiomaterials.5b00319

Priyadarshini, B., Rama, M., Chetanand Vijayalakshmi, U. (2019). Bioactive coating as a surface modification technique for biocompatible metallic implants: A review. *J. Asian Ceram. Soc.* 7, 397–406. doi:10.1080/21870764.2019.1669861

Shi, Z.-Z., Gao, X.-X., Zhang, H.-J., Liu, X.-F., Li, H.-Y., Zhou, C., et al. (2020). Design biodegradable Zn alloys: Second phases and their significant influences on alloy properties. *Bioact. Mat.* 5, 210–218. doi:10.1016/j.bioactmat.2020.02.010

Shi, Z.-Z., Yu, J., and Liu, X.-F. (2018). Microalloyed Zn-Mn alloys: From extremely brittle to extraordinarily ductile at room temperature. *Mat. Des.* 144, 343–352. doi:10.1016/j.matdes.2018.02.049

Su, Y.-C., Wang, K., Gao, J.-L., Yang, Y., Qin, Y. X., Zheng, Y., et al. (2019). Enhanced cytocompatibility and antibacterial property of zinc phosphate coating on biodegradable zinc materials. *Acta Biomater.* 98, 174–185. doi:10.1016/j.actbio.2019.03.055

Sun, J., Zhang, X., Shi, Z.-Z., Gao, X.-X., Li, H.-Y., Zhao, F.-Y., et al. (2021). Development of a high-strength Zn-Mn-Mg alloy for ligament reconstruction fixation. *Acta Biomater.* 119, 485–498. doi:10.1016/j.actbio.2020.10.032

Sun, S., Ye, G., Lu, Z., Weng, Y., Ma, G., and Liu, J. (2021). Surface treatment of Zn-Mn-Mg alloys by micro-arc oxidation in silicate-based solutions with different NaF concentrations. *Materials* 14, 4289. doi:10.3390/ma14154289

Wang, J., Pan, Y., Wang, W., Cui, H., Feng, R., Cui, X., et al. (2021). Effect of zinc content on the microstructure, *in vitro* bioactivity, and corrosion behavior of the microarc oxidized Mg-xZn-0.6Ca (x= 3.0, 4.5, 6.0) alloy. *Biointerphases* 16, 011007. doi:10.1116/6.0000579

Yang, G., Liu, H., Cui, Y., Li, J., Zhang, S., Wang, N., et al. (2021). Bioinspired membrane provides periosteum-mimetic microenvironment for accelerating vascularized bone regeneration. *Biomaterials* 268, 120561. doi:10.1016/j.biomaterials.2020.120561

Yang, J., Yim, C.-D., and You, B.-S. (2016). Effects of solute Zn on corrosion film of Mg-Sn-Zn alloy formed in NaCl solution. *J. Electrochem. Soc.* 163, C839–C844. doi:10.1149/2.0401614jes

Yang, N., Venezuela, J., Almathami, S., and Dargusch, M. (2022). Zinc-nutrient element based alloys for absorbable wound closure devices fabrication: Current status, challenges, and future prospects. *Biomaterials* 280, 121301. doi:10.1016/j.biomaterials.2021.121301

Yao, X., Hu, Yi-wen., Cao, Bin., Peng, Rong., and Ding, Jian-dong. (2013a). Effects of surface molecular chirality on adhesion and differentiation of stem cells. *Biomaterials* 34, 9001–9009. doi:10.1016/j.biomaterials.2013.08.013

Yao, Xiang., Liu, Rui-li., Liang, Xiang-yu., and Ding, Jian-dong. (2019). Critical areas of proliferation of single cells on micropatterned surfaces and corresponding cell type dependence. *ACS Appl. Mat. Interfaces* 11, 15366–15380. doi:10.1021/acsami.9b03780

Yao, Xiang., Peng, Rong., and Ding, Jian-dong. (2013c). Effects of aspect ratios of stem cells on lineage commitments with and without induction media. *Biomaterials* 34, 930–939.

Yao, Xiang., Wang, Xin-lei., and Ding, Jian-dong. (2021). Exploration of possible cell chirality using material techniques of surface patterning. *Acta Biomater.* 126, 92–108. doi:10.1016/j.actbio.2021.02.032

Yao, X., Peng, Rong., and Ding, Jian-dong. (2013b). Cell–material interactions revealed via material techniques of surface patterning. *Adv. Mat.* 25, 5257–5286. doi:10.1002/adma.201301762

Yin, Y.-X., Zhou, C., Shi, Y.-P., Shi, Z.-Z., Lu, T.-H., Hao, Y., et al. (2019). Hemocompatibility of biodegradable Zn-0.8 wt% (Cu, Mn, Li) alloys. *Mater. Sci. Eng. C* 104, 109896. doi:10.1016/j.msec.2019.109896

Yu, Yi-qiang., Jin, Guo-dong., Xue, Yang., Wang, Dong-hui., Liu, Xuan-yong., and Sun, Jiao. (2017). Multifunctions of dual Zn/Mg ion co-implanted titanium on osteogenesis, angiogenesis and bacteria inhibition for dental implants. *Acta Biomater.* 49, 590–603. doi:10.1016/j.actbio.2016.11.067

Yuan, W., Xia, D., Wu, S., Zheng, Y., Guan, Z., and Rau, J. V. (2022). A review on current research status of the surface modification of Zn-based biodegradable metals. *Bioact. Mat.* 7, 192–216. doi:10.1016/j.bioactmat.2021.05.018

Zhang, Y., Yan, Y., Xu, X.-M., Lu, Y.-J., Chen, L.-G., Li, D., et al. (2019). Investigation on the microstructure, mechanical properties, *in vitro* degradation behavior and biocompatibility of newly developed Zn-0.8% Li-(Mg, Ag) alloys for guided bone regeneration. *Mater. Sci. Eng. C* 99, 1021–1034. doi:10.1016/j.msec.2019.01.120

Zhang, Z., Jia, B., Yang, H., Han, Y., Wu, Q., Dai, K., et al. (2021). Zn0.8Li0.1Sr-a biodegradable metal with high mechanical strength comparable to pure Ti for the treatment of osteoporotic bone fractures: *In vitro* and *in vivo* studies. *Biomaterials* 275, 120905. doi:10.1016/j.biomaterials.2021.120905

Zhao, D.-W., Zuo, K.-Q., Wang, K., Sun, Z. Y., Lu, Y. P., Cheng, L., et al. (2021a). Interleukin-4 assisted calcium-strontium-zinc-phosphate coating induces controllable macrophage polarization and promotes osseointegration on titanium implant. *Mater. Sci. Eng. C* 118, 111512. doi:10.1016/j.msec.2020.111512

Zhao, D.-W., Liu, C., Zuo, K.-Q., Su, P., Li, L. B., Xiao, G. Y., et al. (2021b). Strontium-zinc phosphate chemical conversion coating improves the osseointegration of titanium implants by regulating macrophage polarization. *Chem. Eng. J.* 408, 127362. doi:10.1016/j.cej.2020.127362

Zhao, L., Wang, X., Wang, T., Xia, Y., and Cui, C. (2019). Mechanical properties and biodegradation of porous Zn-1Al alloy scaffolds. *Mat. Lett.* 24, 775–778. doi:10.1016/j.matlet.2019.03.097

Zhao, P.-P., Hu, H.-R., Liu, J.-Y., Ke, Q.-F., Peng, X.-Y., Ding, H., et al. (2019). Gadolinium phosphate/chitosan scaffolds promote new bone regeneration via Smad/Runx2 pathway. *Chem. Eng. J.* 359, 1120–1129. doi:10.1016/j.cej.2018.11.071

Zhao, S., Seitz, J.-M., Eifler, R., Maier, H.-J., Guillory, R.-J., II, Earley, E.-J., et al. (2017). Zn-Li alloy after extrusion and drawing: Structural, mechanical characterization, and biodegradation in abdominal aorta of rat. *Mater. Sci. Eng. C* 76, 301–312. doi:10.1016/j.msec.2017.02.167

Zou, Sheng-zhi., Wang, Xin-ru., Fan, Suna., Yao, Xiang., Zhang, Yao-peng., and Shao, Hui-li. (2021). Electrospun regenerated *Antheraea pernyi* silk fibroin scaffolds with improved pore size, mechanical properties and cytocompatibility using mesh collectors. *J. Mat. Chem. B* 9, 5514–5527. doi:10.1039/d1tb00944c

frontiers | Frontiers in Bioengineering and Biotechnology

TYPE Original Research
PUBLISHED 29 September 2022
DOI 10.3389/fbioe.2022.1024089

Hydrogel co-loading SO_2 prodrug and FeGA nanoparticles for enhancing chemodynamic therapy by photothermal-triggered SO_2 gas therapy

Qinqin Huang[1], Meng Lyu[2], Wenxue Tang[1]*, Pengyuan Qi[3]* and Hongzhi Hu[4]*

[1]The Research and Application Center of Precision Medicine, The Second Affiliated Hospital, Zhengzhou University, Zhengzhou, China, [2]Department of Radiation and Medical Oncology, Hubei Key Laboratory of Tumor Biological Behaviors, Hubei Cancer Clinical Study Center, Zhongnan Hospital of Wuhan University, Wuhan, China, [3]Cancer Center, Union Hospital, Tongji Medical College, Huazhong University of Science and Technology, Wuhan, China, [4]Department of Orthopaedics, Union Hospital, Tongji Medical College, Huazhong University of Science and Technology, Wuhan, China

Chemodynamic therapy (CDT) is an effective anti-tumor method, while CDT alone cannot achieve a good therapeutic effect. Moreover, the overexpression of glutathione (GSH) in tumor cells dramatically limits the efficiency of CDT. Here, we proposed a hydrogel co-loading SO_2 prodrug and FeGA nanoparticles (NPs) for enhancing CDT by photothermal-triggered SO_2 gas therapy (FBH) system by mixing benzothiazolyl sulfonates (BTS) and FeGA NPs in a certain ratio and encapsulating them in a heat-sensitive hydrogel. FeGA NPs could accelerate the release of Fe^{2+} under acidic conditions and light, and combine with excess H_2O_2 in the tumor for chemokinetic treatment. BTS, as a water-soluble prodrug of SO_2, can accurately control the release of SO_2 gas by virtue of the excellent photothermal conversion ability of FeGA NPs and the acidic pH value of tumor site. SO_2 can not only induce cell apoptosis, but also consume excess GSH in cancer cells and increase the content of reactive oxygen species, which seriously destroyed the redox balance in cancer cells and further promotes the therapeutic effect of Fenton reaction. The intelligent FBH system provided a new approach for the synergistic treatment of CDT and SO_2 gas, which demonstrated good anticancer effects both *in vivo* and *in vitro*.

KEYWORDS

chemodynamic therapy, fega nanoparticles, SO2 gas therapy, glutathione, hydrogel

OPEN ACCESS

EDITED BY
Long Bai,
East China University of Science and Technology, China

REVIEWED BY
Qiuyue Ding,
Guizhou Provincial People's Hospital, China
Xiaoke Zhang,
Xi'an Jiaotong University, China
Shuai Chen,
Hunan Institute of Technology, China
Wenliang Song,
University of Shanghai for Science and Technology, China

*CORRESPONDENCE
Wenxue Tang,
twx@zzu.edu.cn
Pengyuan Qi,
qpengyuan@outlook.com
Hongzhi Hu,
13720105746@163.com

SPECIALTY SECTION
This article was submitted to Nanobiotechnology, a section of the journal Frontiers in Bioengineering and Biotechnology

RECEIVED 21 August 2022
ACCEPTED 12 September 2022
PUBLISHED 29 September 2022

CITATION
Huang Q, Lyu M, Tang W, Qi P and Hu H (2022), Hydrogel co-loading SO_2 prodrug and FeGA nanoparticles for enhancing chemodynamic therapy by photothermal-triggered SO_2 gas therapy.
Front. Bioeng. Biotechnol. 10:1024089.
doi: 10.3389/fbioe.2022.1024089

Introduction

Nanoparticles mediated drug delivery and chemodynamic treatment (CDT) is gaining popularity as a form of tumor therapy (Liu et al., 2021; Zhang et al., 2022a; Zhang et al., 2022b; Tang et al., 2022; Zhang et al., 2022). The Fenton or Fenton-like reaction is used by CDT to catalyze the conversion of weakly oxidizing hydrogen peroxide (H_2O_2) into strongly oxidizing hydroxyl radical (•OH), which increases intracellular oxidation levels, protein inactivation, DNA necrosis, lipid oxidation, and ultimately induces cancer cell apoptosis (Liu et al., 2018; Lin et al., 2020; Chen et al., 2021; Lin et al., 2021; Xu et al., 2021; Deng et al., 2022). This process takes advantage of the weak acidity and the presence of excess H_2O_2 in the tumor microenvironment (Ma et al., 2018; Zhang et al., 2020; Zhu et al., 2022a). CDT has the characteristics of strong specificity and independence, and is suitable for the treatment of tumors deep in the tissue. It is a research hotspot of cancer treatment in recent years. Compared with photodynamic therapy and sonodynamic therapy, CDT does not depend on the oxygen (O_2) inside the tumor, nor does it require the input of external energy (light energy, ultrasound) (Zhu et al., 2020; Zhu et al., 2021a; Zhu et al., 2022b). It is independent and suitable for the treatment of tumors deep in the tissue, and has a good application prospect in tumor treatment (Li et al., 2017a; Fu et al., 2021). For instance Lin and others showed that copper-based CDT could cause tumor cells to die and release tumor-associated antigens, which could then elicit immunological reactions in the tumor. Nevertheless, since CDT is still in the development stage, the therapeutic efficiency of single CDT therapy is not ideal (Li et al., 2021a; Xin Li et al., 2021; Zhou et al., 2021; Li et al., 2022a; Li et al., 2022b; Guo et al., 2022). On the other hand, glutathione (GSH), as an important antioxidant in cells, can remove the produced •OH, which is the key to cell survival against oxidative stress, this antioxidant defense in cancer cells has become a major obstacle to the efficacy of CDT (Chang et al., 2019; Li et al., 2021b; Hu et al., 2021; Zhou et al., 2021). Depleting the GSH in the tumor microenvironment or using other therapies in combination with CDT is therefore urgently needed to enhance its therapeutic impact. Gas therapy is gaining popularity as a new therapeutic approach for the treatment of tumors (Zhu et al., 2021b). Numerous therapeutic gases, including carbon monoxide, nitric oxide, hydrogen sulfide, oxygen, and sulfur dioxide, have shown promise in the treatment of various diseases, including cancer (Wang et al., 2021; Zhu et al., 2022c). These gases also play important regulatory roles in various physiological processes of cells, tissues, or organisms. Gas therapy is preferable in comparison to chemotherapy, radiation, and other existing treatments due to its enhanced permeability and retention (EPR) impact on tumor tissue (Li et al., 2017b; Zhang et al., 2020; Zhao et al., 2022), which can boost the aggregation of nanoparticles at tumor locations. It also has less drug resistance to tumor cells. Recent research has revealed that sulfur dioxide (SO_2), long thought to be a hazardous environmental pollutant and a byproduct of industrial processing, also has beneficial benefits on mammals in addition to its poisonous ones. According to reports, SO_2 has a lot of potential as a gas for the treatment of several diseases, including cancer, inflammation, and cardiac ischemia-reperfusion (I/R) injury (Li et al., 2021a; Li et al., 2021b; Li et al., 2022c). The study also found that SO_2 can not only cause oxidative damage to various tissues and organs in mice, affecting the activities of various antioxidant enzymes, but also reduce the content of GSH in the tumor microenvironment (Fenton, 1894; Li et al., 2017a; Liang et al., 2021). For example, Wei et al. designed and fabricated a glutathione GSH-reactive SO_2 polymeric prodrug that synergistically acts with doxorubicin (DOX) on McF-7 ADR in human breast cancer cells. They demonstrated that the released SO_2 could promote the level of reactive oxygen species (ROS) in tumor cells (Lu et al., 2020). Therefore, combining CDT with SO_2 gas therapy may enhance the anticancer effect (Shen et al., 2018). However, owing to the rapid diffusion of gas molecules and inadequate tissue penetration, achieving precise SO_2 release doses in space and time is crucial for on-demand gas therapy. Therefore, nano systems with good biocompatibility and biodegradability for the controllable release of CDT and SO_2 from tumor tissues are urgently needed.

Having a 1:1 iron/gallate stoichiometry, FeGA is a hexacoordinate complex with a slightly distorted geometry due to the Jahn-Teller effect (Yuan et al., 2021). Each iron center is complexed *via* a total of six iron-oxygen bonds to the benzoic and carboxylate oxygens of four gallate molecules. The five oxygen atoms of gallate act as electron donors due to its pseudo-radical electronic structure, which in turn is beneficial for the reduction of ligands to metals. Gallic acid ligand and iron center exhibit strong metal-ligand exchange coupling, which induces strong electron delocalization throughout the polymer, improving light absorption significantly and turning it dark black while also bringing the spin density of the ionic center closer to the value for high-spin iron (II) (Cun et al., 2022). As a result, the metal-gallate complex's ionic center serves as its active site, allowing the gallate ligand to transfer electrons to nearby free oxygen molecules, reducing oxygen and producing reactive ROS, and subsequently reducing the iron center (Wang et al., 2020). In acidic environments, the electron loss of Gallate causes degradation of the surrounding ligand field, producing highly oxidized hydroxyl radicals (•OH) that lead to cell death. FeGA nanoparticles (NPs) can also demonstrate a synergistic therapeutic effect of high photothermal therapy (PTT) and CDT, i.e., PTT/CDT, because of its favorable photothermal characteristics [(Li et al., 2019), (Li et al., 2017a)]. GSH, a potent ROS scavenger, can, however, adaptively maintain intracellular redox equilibrium and lessen the cell-killing effects of ROS when it is overexpressed in tumor cells. Developing plausible strategies for GSH depletion in tumors is therefore crucial for promoting the therapeutic effect of the Fenton reaction on tumor death.

Here, we propose a SO_2 prodrug doped FeGA NPs for enhanced CDT by photothermally triggered gas therapy (FBH) system, which is synthesized by mixing benzothiazolyl sulfonate (BTS) and FeGA NPs in a certain proportion and wrapping in heat-sensitive hydrogel. With the excellent photothermal conversion ability of FeGA NPs and the acidic environment of the tumor site, BTS, as a water-soluble SO_2 prodrug, can precisely control the release of SO_2 gas by photothermal. Studies have found that cytotoxic SO_2 can not only induce apoptosis, but also consume excess glutathione in cancer cells and increase the quantity of reactive oxygen species, thereby severely disrupting the redox balance in cancer cells. FeGA can accelerate the release of Fe^{2+} in an acidic environment and under light, and combine with the excess H_2O_2 in the tumor for chemokinetic treatment. At the same time, SO_2 can deplete GSH in the tumor, which can further assist the therapeutic influence of Fenton reaction on tumor killing. This FBH system provides a new approach for CDT and SO_2 gas synergistic therapy and shows excellent anticancer effects *in vivo* and *in vitro*.

Results and discussion

We prepared FeGA NPs according to the studies in the literature [(Xin Li et al., 2021)] and showed its transmission electron microscope (TEM) image (Figure 1A), then we synthesized the FBH system by encapsulating the prepared FeGA NPs and BTS in 2% agarose hydrogel, and it was imaged by scanning electron microscopy (SEM) (Figure 1B). We then determined the average hydrated particle size of FeGA NPs by dynamic light scattering (DLS) method (Figure 1C), and the results were in good agreement with TEM. The UV-Vis absorption spectra observed that FBH has broad absorption in the NIR (Figure 1D), which indicates that the metal-organic coordination polymer formed by the coordination of GA with iron ions may have better photothermal properties. The photothermal conversion performance was investigated by preparing FBHs containing FeGA NPs at different concentrations (0, 50, 100, 200 μg/ml) and exposing them to a 808 nm laser at 0.5 W/cm2 for 5 min. The resulting concentration- and time-dependent temperature rise curves are shown in Figure 1E. For example, the temperature of FBH containing 200 μg/ml FeGA NPs increased from 27.9 to 51.9 C after laser irradiation. In addition, the laser power dependent photothermal effect (0, 0.2, 0.5, 0.8, and 1.0 W/cm2) was also demonstrated (Figure 1F). This indicates that the temperature

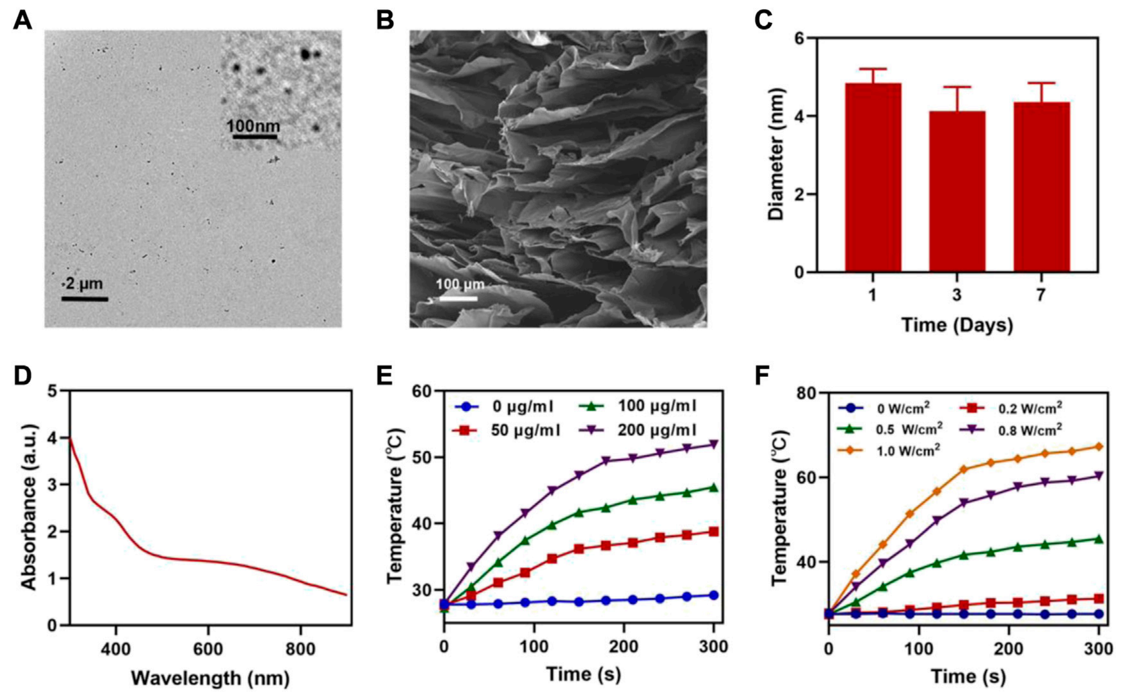

FIGURE 1
(A) TEM image of FeGA NPs (inset FeGA). **(B)** SEM image of FBH. **(C)** Hydrodynamic sizes of FeGA NPs. **(D)** UV-Vis absorption spectrum of FBH. **(E)** Temperature curves of FBH containing FeGA NPs with different concentrations under 808 nm laser at 0.5 W/cm^2 irradiation. **(F)** Temperature curves of FBH containing 100 μg/ml FeGA NPs under different power densities.

increases of the FBH containing FeGA NPs can be tuned from 27.7°C (0 W/cm2) to 67.3°C (1.0 W/cm2) by controlling the power density of the 808 nm laser, demonstrating the photothermal conversion dependence of performance on laser power density. Notably, the photothermal performance of FBH did not regress significantly during four laser on/off cycles, indicating that the as-prepared FBH has high photothermal stability for photothermal therapy (Figure 2A). These results indicate that FeGA nanoparticles have good photothermal stability. According to the photothermal conversion efficiency formula, the photothermal conversion efficiency of FeGA is 45.7%, which is higher than that of Au nanorods (21%) [(Xiong et al., 2021)]. Therefore, FeGA nanoparticles are an excellent photothermal conversion reagent. In our system, the hydrogel-encapsulated SO2 pre-drug BTS is a crystalline white solid with excellent water solubility. Studies have found that BTS can selectively generate SO2 in the acidic

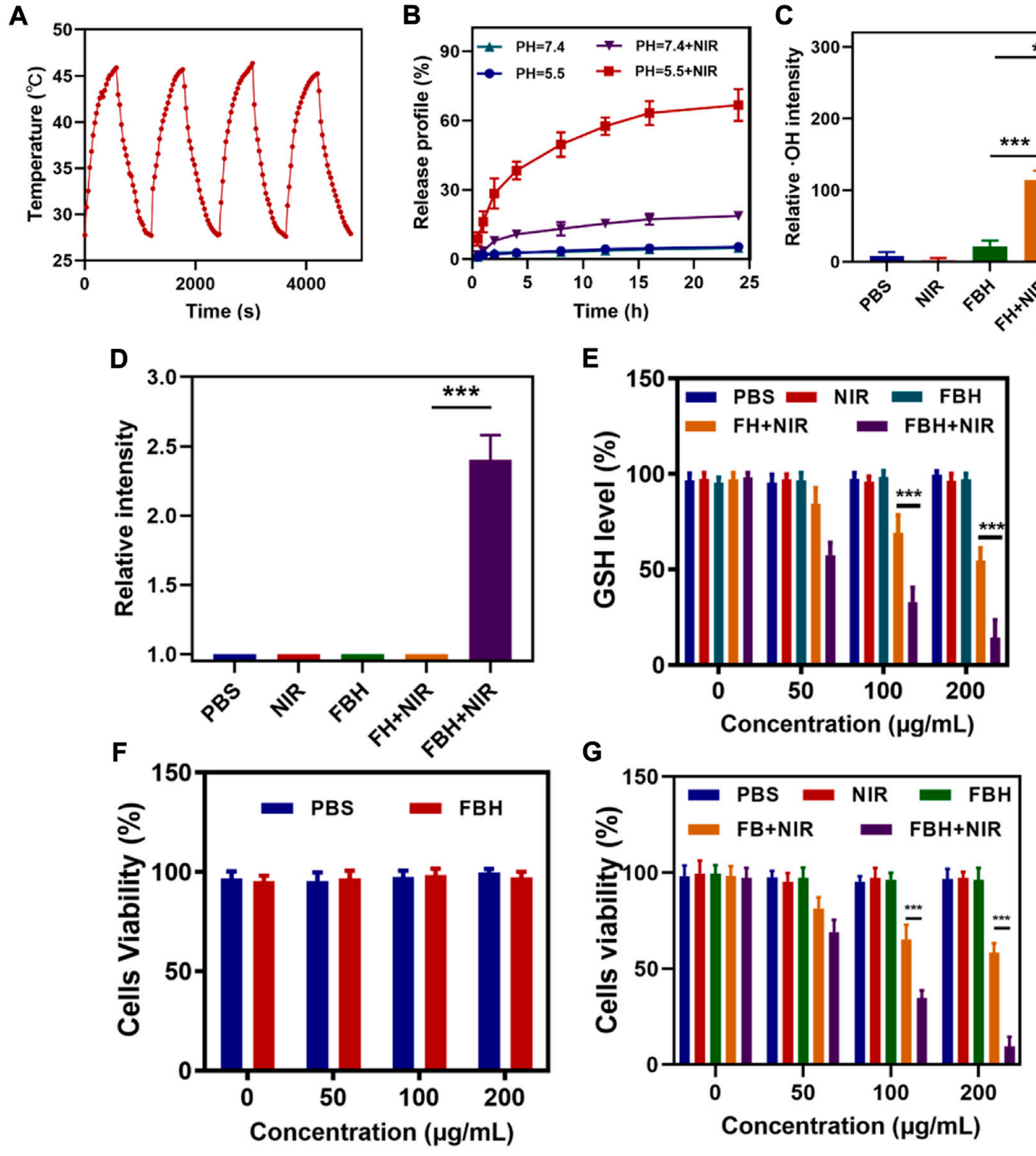

FIGURE 2
(A) Heating curve of FBH under four cycles of heating and cooling processes. **(B)** The release curve of SO_2 from FBH after different treatments. **(C)** Relative OH intensity in cells after treated by different experimental groups (n = 3). **(D)** Relative SO_2 intensity in cells after treated by different experimental groups (n = 3). **(E)** The effect of different formulations on the intracellular GSH levels was determined by employing a GSH assay kit (n = 3). **(F)** Cell viabilities of control group (PBS) and FBH system without NIR irradiation (n = 3). **(G)**Various treatments' *in vitro* cytotoxicity towards 4T1 cells (n = 3). *$p < 0.05$, **$p < 0.01$, ***$p < 0.005$; Student's t-test.

environment of tumors [(Yuan et al., 2021)]. Therefore, we further verified the SO2 release efficiency of the BTS-loaded FBH under light-stimulated acidic environment (Figure 2B). As mentioned before, under laser irradiation, our FBH system will achieve a photothermal response, which causes the agarose hydrogel to melt and release BTS. We found that the SO2 release efficiency of the system was significantly enhanced under acidic conditions. At neutral pH (7.4) the reaction is much slower. But in the absence of light, our FBH is in a solidified state at room temperature, and it is difficult to decompose to release BTS, so no SO2 is produced. This further proves that the FBH system prepared by us can controllably perform gas treatment and subsequent further treatment.

As previously shown, FeGA can accelerate the release of Fe^{2+} in an acidic environment and under light, and combine with the excess H_2O_2 in the tumor for chemokinetic treatment. To detect FBH-induced ·OH production in cells, we stained 4T1 cells with different treatments using the OH detection probe HPF. As illustrated in Figure 2C, the PBS group, the NIR group and the FBH alone group had almost no OH production, which means that OH was almost absent in normal cells and was not affected by NIR light stimulation, the FBH group alone did not cause cell damage because it was difficult to decompose and release drugs due to the encapsulation of hydrogel. In addition, a hydrogel containing only FeGA NPs (FH) was prepared for exploratory experiments. The FH + NIR group produced OH of moderate intensity, while the FBH + NIR group produced OH of maximum intensity. ROS can cause damage to DNA and cellular protein, leading to tumor cell death. However, in order to maintain cellular redox homeostasis, overexpressed glutathione GSH exists in the tumor microenvironment, and

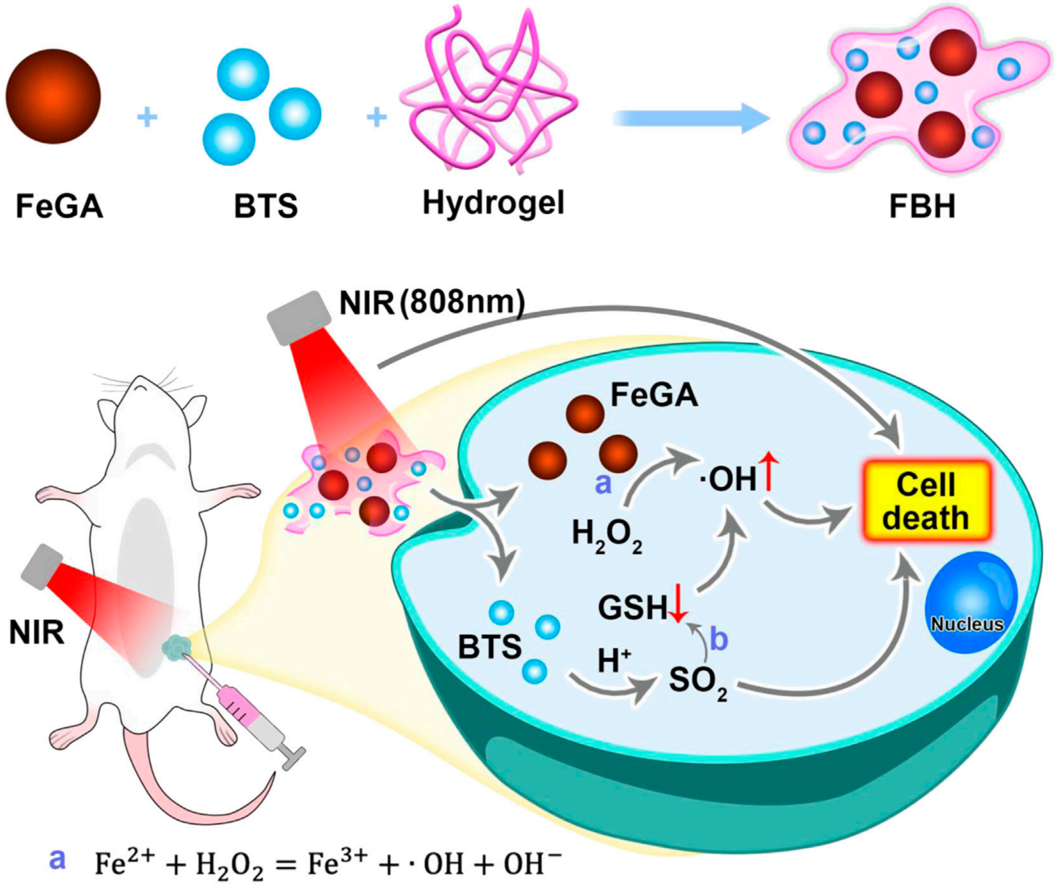

$$\text{a}\quad Fe^{2+} + H_2O_2 = Fe^{3+} + \cdot OH + OH^-$$

$$\text{b}\quad SO_2 + H_2O = HSO_3^- + H^+$$

$$GSH \underset{Gred}{\overset{\cdot OH}{\rightleftharpoons}} GSSG + HSO_3^- \rightarrow GSSO_3^-$$

SCHEME 1
Schematic illustration of hydrogel co-loading SO_2 prodrug and FeGA NPs for enhancing CDT by photothermal-triggered SO_2 gas therapy.

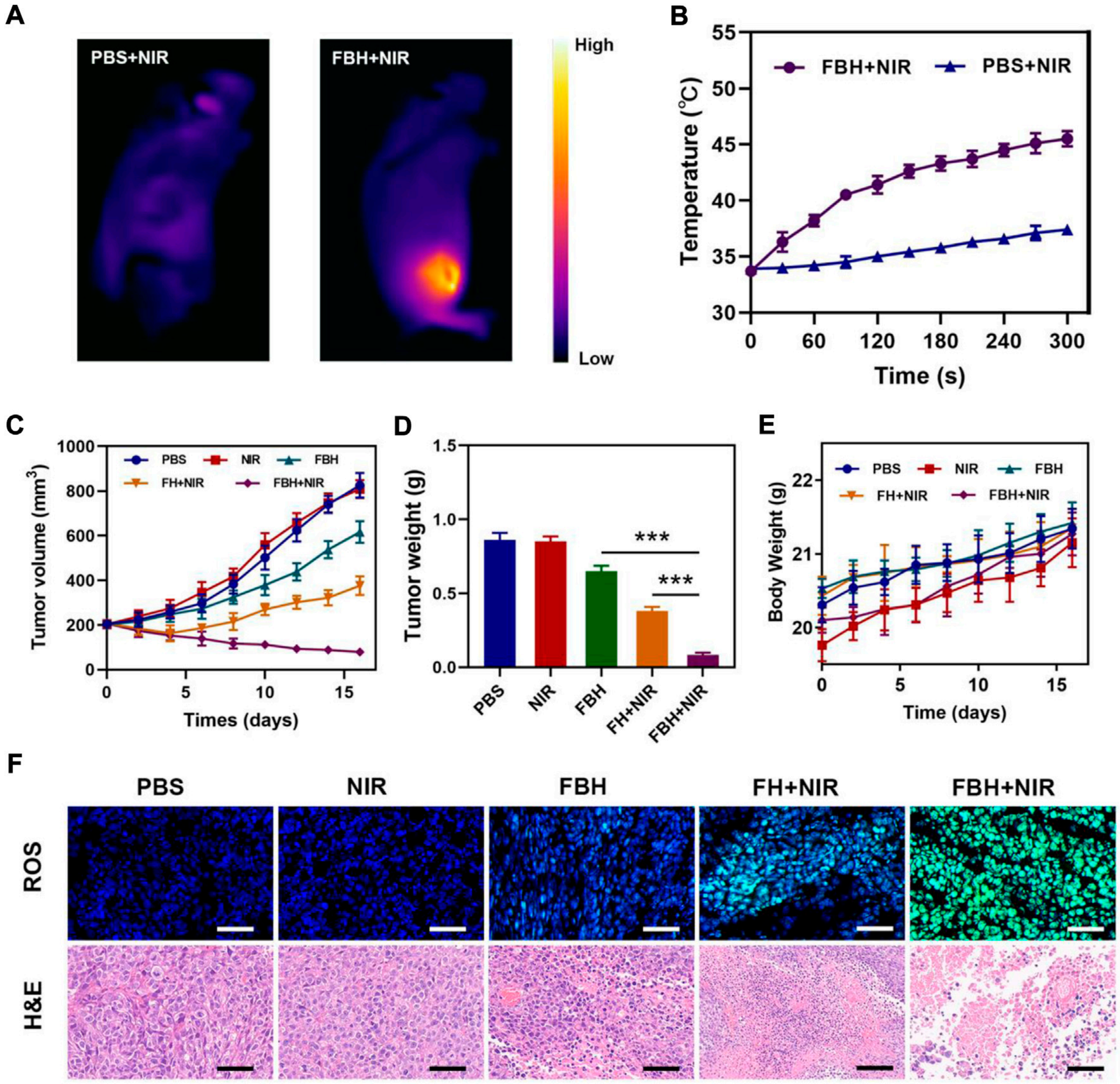

FIGURE 3
(A) Infrared thermal images of tumors in the specified treatment groups. **(B)** After being irradiated with 808 nm laser (0.5 W/cm^2) for 5 min, the temperature elevates in mice having 4T1 tumor, in the specified treatment groups. **(C)**The treatment groups' tumor volume alters over time (n = 5). **(D)** Average tumor weight values associated with the indicated treatments (n = 5). **(E)** Changes in body weight in response to the indicated treatments (n = 5). **(F)** HPF and H&E-stained tumor sections from the indicated treatment groups (n = 5). Scale bars: 100 μm $^*p < 0.05$, $^{**}p < 0.01$, $^{***}p < 0.005$; Student's t-test.

GSH can react with oxidative reactive substances to be oxidized to form oxidized glutathione (GSSG), thus resulting in an inhibition of the anti-tumor effect based on ROS. According to research, the SO_2 produced by BTS will consume GSSG excessively, and the generated S-sulphoglutathione ($GSSO_3^-$) will be excreted in the form of thiosulfate, thereby disrupting the normal GSH cycle, reducing the GSH content, thereby increasing the level of ROS, changing the redox balance of cells, and producing oxidative stress. Stimulated, eventually triggering apoptosis (Osi et al., 2021). Therefore, we first studied the production of SO_2 in different treatment groups by cell experiments. As shown in Figure 2D. The results show that only under laser irradiation, our FBH system can melt agarose hydrogel and release BTS to generate SO_2 due to the photothermal effect. This also proves that our FBH system can be controlled for gas release. We then investigated GSH consumption in different cell treatment groups, as shown in Figure 2E. The results show that FBH and NIR radiation can fully consume GSH. Combined with the conclusion in Figure 2C, it is sufficient to prove that SO_2 produced by our FBH system can promote the consumption of GSH, which is conducive to the subsequent FeGA-mediated Fenton reaction. In order to evaluate the cytotoxicity of FBH, we employed 4T1 cancer cells to conduct

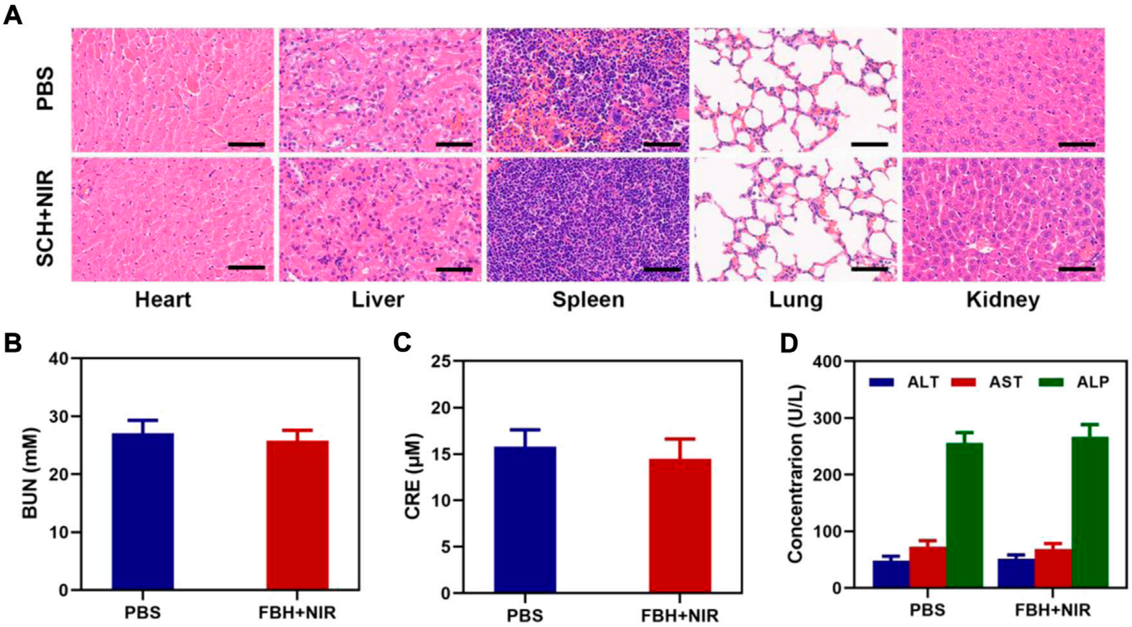

FIGURE 4
(A) Results of H&E-stained images for the mice's major organs, including the heart, lung, liver, kidneys, and spleen, after exposure to various therapies 16 days after the injection. Scale bars: 100 μm. **(B)** Kidney function markers: BUN, **(C)** CRE, and **(D)** liver function indicators: ALT, AST, and ALP following different treatments.

the standard MTT assay (Zuo et al., 2022). As shown in Figure 2F, FBH exhibited little cytotoxicity in the absence of irradiation. Furthermore, we evaluated the antitumor efficacy of FBH through MTT assay (Figure 2G). 4T1 cells were incubated with PBS, NIR (0.5 W/cm^2, 5 min), FBH, FH + NIR (0.5 W/cm^2, 5 min) and FBH + NIR (0.5 W/cm^2, 5 min). From the results, the treatment effects of the control group, the NIR group and the FBH alone group were not satisfactory. In particular, FBH alone showed little cytotoxicity even at the highest doses. This is due to the encapsulation of the hydrogel, and FBH cannot have an effect on the cells. The FBH + NIR group treatment showed more significant cytotoxicity than the FB + NIR group treatment, which may be explained by the photothermal effect opening the SO_2 release. As anticipated, the FBH + NIR group not only showed the synergistic treatment results of photothermal therapy and gas therapy, but also enhanced FeGA-mediated CDT killing ability of cancer cells by depleting glutathione of cancer cells through SO_2. This additionally demonstrates that FBH + NIR has good antitumor.

Before studying the antitumor efficacy of FBH *in vivo*, we first studied the photothermal efficacy of the prepared FBH in mice. After intratumoral injection of PBS and FBH, respectively, the mice were exposed to 808 nm (0.5 W/cm^2) laser light for 5 min, as shown in Figures 3A,B, Photothermal images showed that the tumor temperature in the control group only increased around $\Delta T = 4°C$. In contrast, after light activation, the temperature of the tumor area in mice injected with FBH showed a rapid warming of $\Delta T = 17°C$. This important result suggests that FBH may serve as an excellent therapeutic agent for the synergistic anticancer efficacy of FeGA-mediated CDT/PTT. We then examined the ability of this prepared FBH to induce the elimination of 4T1 mammary tumors in mice as they exhibited positive antitumor activity *in vitro*. We randomly divided unilateral 4T1 tumor-bearing mice with tumor volumes of approximately 200 mm^3 into five groups: (Zhang et al., 2022a): PBS; (Zhang et al., 2022b); NIR; (Tang et al., 2022); FBH; (Zhang et al., 2022); FH + NIR; (Liu et al., 2021); FBH + NIR. As shown in Figures 3C,D, compared with the PBS, NIR group, the FBH alone group had a slight inhibitory effect on the tumor. Notably, this does not appear to be fully responsive to *in vitro* MTT results. This is because the encapsulated agarose can be slowly decomposed in the body, and the mechanism may be related to the action of some biological enzymes. While the FB + NIR group significantly reduced tumor growth, the FBH + NIR group exhibited higher tumor inhibition rates than FBH and FB + NIR alone. This can be attributed to the synergistic anticancer effects of FeGA-mediated CDT and SO_2-mediated gas therapy released from FBH in response to light as described above, as well as enhanced CDT killing of cancer cells by disrupting redox homeostasis of the tumor microenvironment through GSH depletion by SO_2. Furthermore, the high stability of FBH avoids premature drug release in the tumor site. Similarly, none of the groups demonstrated any weight loss during the medication (Figure 3E), indicating that FBH is safe *in vivo*. These findings imply that by photothermally activating the gas treatment, our synthetic FBHs can improve CDT effectiveness against tumor cells. To further explore the antitumor mechanism of FBH, we used the HPF kit to verify the *in vivo* OH production after different treatments (Figure 3F). Green fluorescence was hardly seen in the PBS and NIR groups, and the degradation rate of FBH alone was slow under the action of biological enzymes *in vivo*, so the production of OH was not high. While FH + NIR can also observe obvious fluorescence, but the production of OH is limited because GSH can consume OH. The amount of ROS in the FBH + NIR group was significantly higher than that in the FH + NIR group, showing that SO_2 can increase the level of intracellular OH. Using H&E staining, the histology of tumor tissue was investigated. The findings demonstrated dense tumor tissue in the PBS and NIR groups, and necrotic tumor cells in the FBH group alone. The FH + NIR group would obviously induce tumor cell necrosis, and its nuclei would shrink or even disappear, while the FBH + NIR group treated tumors. The area of tissue necrosis was larger than that of FBH alone or FH + NIR group, indicating that the killing effect of FBH + NIR on tumor was higher than that of FBH or FH + NIR group. There were hardly any apoptotic cells in the PBS and NIR groups. Taken together, these results indicated that our prepared FBH system could effectively inhibit tumor cell proliferation and promote apoptosis.

Additionally, mice in good health were used to test FBH's long-term biocompatibility. Each group's mice had their major organs removed and subjected to H&E examination. As seen in Figure 4A, the lung, liver, heart, spleen, and kidney sections of these animals displayed normal histological morphology and no evident pathological alterations, demonstrating that FBH has a low level of systemic toxicity *in vivo*. Blood from FBH-treated mice ($n = 5$) was obtained 16 days after treatment, and hematological and blood biochemical analyses were performed to assess blood cell and major organ function in mice during treatment (Figures 4B–D). Urea (BUN) and creatinine (CRE) are biomarkers of renal function, and alanine aminotransferase (ALT), aspartate aminotransferase (AST), and alkaline phosphatase (ALP) are biomarkers of liver function. These biomarkers did not differ significantly from those of the control group, indicating that the substance did not have any obvious hepatotoxicity or nephrotoxicity. All of the aforementioned findings imply that FBH is a secure medication delivery method with minimal systemic toxicity.

Conclusion

In summary, we proposed a hydrogel co-loading SO_2 prodrug and FeGA NPs for enhancing CDT by photothermal-triggered SO_2 gas therapy system. With the excellent photothermal conversion ability of FeGA NPs and the acidic conditions of the tumor site, BTS can precisely control the release of SO_2 gas under NIR irradiation. Under NIR irradiation, FeGA could accelerate the release of Fe^{2+} in the acidic tumor microenvironment and react with the excess H_2O_2 in the tumor for chemokinetic treatment. At the same time, SO_2 can deplete GSH in the tumor, which can further enhance the therapeutic impact of Fenton reaction on tumor killing. This FBH system provides a new approach for CDT and SO_2 gas synergistic therapy and shows excellent anticancer effects *in vivo* and *in vitro*.

Data availability statement

The raw data supporting the conclusions of this article will be made available by the authors, without undue reservation.

Ethics statement

The animal study was reviewed and approved by the Wuhan University.

Author contributions

QH and PQ performed the experiments, analyzed all the data, drafted all the figures, and prepared the manuscript. WT performed the experiments. ML and HH conceived, designed the experiments, and revised the manuscript.

Funding

Henan Province Medical Science and Technology Research Program Joint Construction Project (LHGJ20190326).

Acknowledgments

The authors would like to thank Yufei Chen from Shiyanjia Lab (www.shiyanjia.com) for drawing schematic diagrams.

Conflict of interest

The authors declare that the research was conducted in the absence of any commercial or financial relationships that could be construed as a potential conflict of interest.

Publisher's note

References

Chang, M., Wang, M., Wang, M., Shu, M., Ding, B., Li, C., et al. (2019). A multifunctional cascade bioreactor based on hollow-structured Cu2 MoS4 for synergetic cancer chemo-dynamic therapy/starvation therapy/phototherapy/immunotherapy with remarkably enhanced efficacy. *Adv. Mat.* 31 (51), e1905271. doi:10.1002/adma.201905271

Chen, X., Chen, Y., Wang, C., Jiang, Y., Chu, X., Wu, F., et al. (2021). NIR-triggered intracellular H+ transients for lamellipodia-collapsed antimetastasis and enhanced chemodynamic therapy. *Angew. Chem. Int. Ed.* 60, 21905–21910. doi:10.1002/anie.202107588

Cun, J. E., Pan, Y., Zhang, Z., Lu, Y., Li, J., Pan, Q., et al. (2022). Photo-enhanced upcycling H2O2 into hydroxyl radicals by IR780-embedded Fe3O4@MIL-100 for intense nanocatalytic tumor therapy. *Biomaterials* 287, 121687. doi:10.1016/j.biomaterials.2022.121687

Deng, H., Zhang, J., Yang, Y., Yang, J., Wei, Y., Ma, S., et al. (2022). Chemodynamic and photothermal combination therapy based on dual-modified metal-organic framework for inducing tumor ferroptosis/pyroptosis. *ACS Appl. Mat. Interfaces* 14, 24089–24101. doi:10.1021/acsami.2c00574

Fenton, H. J. H. (1894). LXXIII.—oxidation of tartaric acid in presence of iron. *J. Chem. Soc. Trans.* 65 (0), 899–910. doi:10.1039/CT8946500899

Fu, J., Li, T., Yang, Y., Jiang, L., Wang, W., Fu, L., et al. (2021). Activatable nanomedicine for overcoming hypoxia-induced resistance to chemotherapy and inhibiting tumor growth by inducing collaborative apoptosis and ferroptosis in solid tumors. *Biomaterials* 268, 120537. doi:10.1016/j.biomaterials.2020.120537

Guo, Q. L., Dai, X. L., Yin, M. Y., Cheng, H. W., Qian, H. S., Wang, H., et al. (2022). Nanosensitizers for sonodynamic therapy for glioblastoma multiforme: Current progress and future perspectives. *Mil. Med. Res.* 9 (1), 26. doi:10.1186/s40779-022-00386-z

Hu, H., Yang, W., Liang, Z., Zhou, Z., Song, Q., Liu, W., et al. (2021). Amplification of oxidative stress with lycorine and gold-based nanocomposites for synergistic cascade cancer therapy. *J. Nanobiotechnology* 19 (1), 221. doi:10.1186/s12951-021-00933-1

Li, X., Hetjens, L., Wolter, N., Li, H., Shi, X., and Pich, A. (2022c). Charge-reversible and biodegradable chitosan-based microgels for lysozyme-triggered release of vancomycin. *J. Adv. Res.* [in press]. doi:10.1016/j.jare.2022.02.014

Li, X., Kong, L., Hu, W., Zhang, C., Pich, A., Shi, X., et al. (2022b). Safe and efficient 2D molybdenum disulfide platform for cooperative imaging-guided photothermal-selective chemotherapy: A preclinical study. *J. Adv. Res.* 37, 255–266. doi:10.1016/j.jare.2021.08.004

Li, X., Li, H., Zhang, C., Pich, A., Xing, L., and Shi, X. (2021a). Intelligent nanogels with self-adaptive responsiveness for improved tumor drug delivery and augmented chemotherapy. *Bioact. Mat.* 6 (10), 3473–3484. doi:10.1016/j.bioactmat.2021.03.021

Li, X., Lu, S., Xiong, Z., Hu, Y., Ma, D., Lou, W., et al. (2019). Light-addressable nanoclusters of ultrasmall iron oxide nanoparticles for enhanced and dynamic magnetic resonance imaging of arthritis. *Adv. Sci.* 6 (19), 1901800. doi:10.1002/advs.201901800

Li, X., Lu, Y., and Hu, Y. (2022a). A wireless and battery-free DNA hydrogel biosensor for wound infection monitoring. *Matter* 5 (8), 2473–2475. doi:10.1016/j.matt.2022.06.021

Li, X., Ouyang, Z., Li, H., Hu, C., Saha, P., Xing, L., et al. (2021b). Dendrimer-decorated nanogels: Efficient nanocarriers for biodistribution *in vivo* and chemotherapy of ovarian carcinoma. *Bioact. Mat.* 6 (10), 3244–3253. doi:10.1016/j.bioactmat.2021.02.031

Li, X., Xing, L., Hu, Y., Xiong, Z., Wang, R., Xu, X., et al. (2017b). An RGD-modified hollow silica@Au core/shell nanoplatform for tumor combination therapy. *Acta Biomater.* 62, 273–283. doi:10.1016/j.actbio.2017.08.024

Li, X., Xing, L., Zheng, K., Wei, P., Du, L., Shen, M., et al. (2017a). Formation of gold nanostar-coated hollow mesoporous silica for tumor multimodality imaging and photothermal therapy. *ACS Appl. Mat. Interfaces* 9 (7), 5817–5827. doi:10.1021/acsami.6b15185

Liang, L., Wen, L., Weng, Y., Song, J., Li, H., Zhang, Y., et al. (2021). Homologous-targeted and tumor microenvironment-activated hydroxyl radical nanogenerator for enhanced chemoimmunotherapy of non-small cell lung cancer. *Chem. Eng. J.* 425, 131451. doi:10.1016/j.cej.2021.131451

Lin, L., Wang, S., Deng, H., Yang, W., Rao, L., Tian, R., et al. (2020). Endogenous labile iron pool-mediated free radical generation for cancer chemodynamic therapy. *J. Am. Chem. Soc.* 142 (36), 15320–15330. doi:10.1021/jacs.0c05604

Lin, X., Li, L., Li, S., Li, Q., Xie, D., Zhou, M., et al. (2021). Targeting the opening of mitochondrial permeability transition pores potentiates nanoparticle drug delivery and mitigates cancer metastasis. *Adv. Sci.* 8 (4), 2002834. doi:10.1002/advs.202002834

Liu, Y., Zhai, S., Jiang, X., Liu, Y., Wang, K., Wang, C., et al. (2021). Intracellular mutual promotion of redox homeostasis regulation and iron metabolism disruption for enduring chemodynamic therapy. *Adv. Funct. Mat.* 31 (17), 2010390. doi:10.1002/adfm.202010390

Liu, Y., Zhen, W., Jin, L., Zhang, S., Sun, G., Zhang, T., et al. (2018). All-in-One theranostic nanoagent with enhanced reactive oxygen species generation and modulating tumor microenvironment ability for effective tumor eradication. *ACS Nano* 12 (5), 4886–4893. doi:10.1021/acsnano.8b01893

Lu, Q., Lu, T., Xu, M., Yang, L., Song, Y., and Li, N. (2020). SO2 prodrug doped nanorattles with extra-high drug payload for "collusion inside and outside" photothermal/pH triggered - gas therapy. *Biomaterials* 257, 120236. doi:10.1016/j.biomaterials.2020.120236

Ma, B., Wang, S., Liu, F., Zhang, S., Duan, J., Li, Z., et al. (2018). Self-assembled copper-amino acid nanoparticles for *in situ* glutathione "AND" H2O2 sequentially triggered chemodynamic therapy. *J. Am. Chem. Soc.* 141, 849–857. doi:10.1021/jacs.8b08714

Osi, A. R., Zhang, H., Chen, J., Zhou, Y., Wang, R., Fu, J., et al. (2021). Three-dimensional-printable thermo/photo-cross-linked methacrylated chitosan-gelatin hydrogel composites for tissue engineering. *ACS Appl. Mat. Interfaces* 13 (19), 22902–22913. doi:10.1021/acsami.1c01321

Shen, W., Liu, W., Yang, H., Zhang, P., Xiao, C., and Chen, X. (2018). A glutathione-responsive sulfur dioxide polymer prodrug as a nanocarrier for combating drug-resistance in cancer chemotherapy. *Biomaterials* 178, 706–719. doi:10.1016/j.biomaterials.2018.02.011

Tang, Y., Varyambath, A., Ding, Y., Chen, B., Huang, X., Zhang, Y., et al. (2022). Porous organic polymers for drug delivery: Hierarchical pore structures, variable morphologies, and biological properties. *Biomater. Sci.* [in press]. doi:10.1039/d2bm00719c

Wang, J., Sui, L., Huang, J., Miao, L., Nie, Y., Wang, K., et al. (2021). MoS2-based nanocomposites for cancer diagnosis and therapy. *Bioact. Mat.* 6 (11), 4209–4242. doi:10.1016/j.bioactmat.2021.04.021

Wang, X., Zhong, X., Bai, L., Xu, J., Gong, F., Dong, Z., et al. (2020). Ultrafine titanium monoxide (TiO_{1+x}) nanorods for enhanced sonodynamic therapy. *J. Am. Chem. Soc.* 142 (14), 6527–6537. doi:10.1021/jacs.9b10228

Xin Li, H. S., Li, H., Hu, C., Luo, Y., Shi, X., Pich, A., et al. (2021). Multi-responsive biodegradable cationic nanogels for highly efficient treatment of tumors. *Adv. Funct. Mat.* 31, 2100227. doi:10.1002/adfm.202100227

Xiong, Z., Achavananthadith, S., Lian, S., Madden, L. E., Ong, Z. X., Chua, W., et al. (2021). A wireless and battery-free wound infection sensor based on DNA hydrogel. *Sci. Adv.* 7 (47), eabj1617. doi:10.1126/sciadv.abj1617

Xu, L., Xu, R., Saw, P. E., Wu, J., Cheng, S. X., and Xu, X. (2021). Nanoparticle-mediated inhibition of mitochondrial glutaminolysis to amplify oxidative stress for combination cancer therapy. *Nano Lett.* 21 (18), 7569–7578. doi:10.1021/acs.nanolett.1c02073

Yuan, H., Han, Z., Chen, Y., Qi, F., Fang, H., Guo, Z., et al. (2021). Ferroptosis photoinduced by new cyclometalated iridium(III) complexes and its synergism with apoptosis in tumor cell inhibition. *Angew. Chem. Int. Ed.* 60 (15), 8174–8181. doi:10.1002/anie.202014959

Zhang, X., Ong'achwa Machuki, J., Pan, W., Cai, W., Xi, Z., Shen, F., et al. (2020). Carbon nitride hollow theranostic nanoregulators executing laser-activatable water splitting for enhanced ultrasound/fluorescence imaging and cooperative phototherapy. *ACS Nano* 14 (4), 4045–4060. doi:10.1021/acsnano.9b08737

Supplementary material

The Supplementary Material for this article can be found online at: https://www.frontiersin.org/articles/10.3389/fbioe.2022.1024089/full#supplementary-material

Zhang, Y., Kim, I., Lu, Y., Xu, Y., Yu, D. G., and Song, W. (2022). Intelligent poly(l-histidine)-based nanovehicles for controlled drug delivery. *J. Control. Release* 349, 963–982. doi:10.1016/j.jconrel.2022.08.005

Zhang, Y., Li, S., Xu, Y., Shi, X., Zhang, M., Huang, Y., et al. (2022b). Engineering of hollow polymeric nanosphere-supported imidazolium-based ionic liquids with enhanced antimicrobial activities. *Nano Res.* 15 (6), 5556–5568. doi:10.1007/s12274-022-4160-6

Zhang, Y., Song, W., Lu, Y., Xu, Y., Wang, C., Yu, D. G., et al. (2022a). Recent advances in poly(α-L-glutamic acid)-based nanomaterials for drug delivery. *Biomolecules* 12 (5), 636. doi:10.3390/biom12050636

Zhao, T., Wu, W., Sui, L., Huang, Q., Nan, Y., Liu, J., et al. (2022). Reactive oxygen species-based nanomaterials for the treatment of myocardial ischemia reperfusion injuries. *Bioact. Mat.* 7, 47–72. doi:10.1016/j.bioactmat.2021.06.006

Zhou, Q. M., Lu, Y. F., Zhou, J. P., Yang, X. Y., Wang, X. J., Yu, J. N., et al. (2021). Self-amplification of oxidative stress with tumour microenvironment-activatable iron-doped nanoplatform for targeting hepatocellular carcinoma synergistic cascade therapy and diagnosis. *J. Nanobiotechnology* 19 (1), 361. doi:10.1186/s12951-021-01102-0

Zhu, D., Chen, H., Huang, C., Li, G., Wang, X., Jiang, W., et al. (2022a). H_2O_2 self-producing single-atom nanozyme hydrogels as light-controlled oxidative stress amplifier for enhanced synergistic therapy by transforming "cold" tumors. *Adv. Funct. Mat.* 32, 2110268. doi:10.1002/adfm.202110268

Zhu, D., Duo, Y., Meng, S., Zhao, Y., Xia, L., Zheng, Z., et al. (2020). Tumor-exocytosed exosome/aggregation-induced emission luminogen hybrid nanovesicles facilitate efficient tumor penetration and photodynamic therapy. *Angew. Chem. Int. Ed.* 59, 13836–13843. doi:10.1002/anie.202003672

Zhu, D., Liu, Z., Li, Y., Huang, Q., Xia, L., and Li, K. (2021b). Delivery of manganese carbonyl to the tumor microenvironment using Tumor-Derived exosomes for cancer gas therapy and low dose radiotherapy. *Biomaterials* 274, 120894. doi:10.1016/j.biomaterials.2021.120894

Zhu, D., Zhang, J., Luo, G., Duo, Y., and Tang, B. Z. (2021a). Bright bacterium for hypoxia-tolerant photodynamic therapy against orthotopic colon tumors by an interventional method. *Adv. Sci. (Weinh).* 8, 2004769. doi:10.1002/advs.202004769

Zhu, D., Zhang, T., Li, Y., Huang, C., Suo, M., Xia, L., et al. (2022b). Tumor-derived exosomes co-delivering aggregation-induced emission luminogens and proton pump inhibitors for tumor glutamine starvation therapy and enhanced type-I photodynamic therapy. *Biomaterials* 283, 121462. doi:10.1016/j.biomaterials.2022.121462

Zhu, Y., Zhao, T., Liu, M., Wang, S., Liu, S., Yang, Y., et al. (2022c). Rheumatoid arthritis microenvironment insights into treatment effect of nanomaterials. *Nano Today* 42, 101358. doi:10.1016/j.nantod.2021.101358

Zuo, H., Qiang, J., Wang, Y., Wang, R., Wang, G., Chai, L., et al. (2022). Design of red blood cell membrane-cloaked dihydroartemisinin nanoparticles with enhanced antimalarial efficacy. *Int. J. Pharm. X.* 618, 121665. doi:10.1016/j.ijpharm.2022.121665

frontiers | Frontiers in Bioengineering and Biotechnology

TYPE Original Research
PUBLISHED 06 October 2022
DOI 10.3389/fbioe.2022.1005719

OPEN ACCESS

EDITED BY
Long Bai,
East China University of Science and Technology, China

REVIEWED BY
Ming Wang,
University of Rochester, United States
Yi Wang,
Chongqing Medical University, China
Zhao Zhihao,
National University of Singapore, Singapore

*CORRESPONDENCE
Fengshou Zhang,
fengshouzhang@163.com
Lei Xu,
haeyxulei@163.com

†These authors have contributed equally to this work

SPECIALTY SECTION
This article was submitted to Nanobiotechnology, a section of the journal Frontiers in Bioengineering and Biotechnology

RECEIVED 28 July 2022
ACCEPTED 26 September 2022
PUBLISHED 06 October 2022

CITATION
Bao J, Tu H, Li J, Dong Y, Dang L, Yurievna KE, Zhang F and Xu L (2022), Interfacial engineered iron oxide nanoring for T2-weighted magnetic resonance imaging-guided magnetothermal-chemotherapy.
Front. Bioeng. Biotechnol. 10:1005719.
doi: 10.3389/fbioe.2022.1005719

Interfacial engineered iron oxide nanoring for T2-weighted magnetic resonance imaging-guided magnetothermal-chemotherapy

Jianfeng Bao[1,2†], Hui Tu[1†], Jing Li[3], Yanbo Dong[4], Le Dang[4], Korjova Elena Yurievna[5], Fengshou Zhang[1]* and Lei Xu[6]*

[1]School of Medical Technology and Engineering, Henan University of Science and Technology, Luoyang, China, [2]Functional Magnetic Resonance and Molecular Imaging Key Laboratory of Henan Province, The First Affiliated Hospital of Zhengzhou University, Zhengzhou University, Zhengzhou, China, [3]Office of Science and Technology, Henan University of Science and Technology, Luoyang, China, [4]School of Education, Pingdingshan University, Pingdingshan, China, [5]Institute of Psychology, The Herzen State Pedagogical University of Russia, Saint Petersburg, Russia, [6]Department of Clinical Laboratory, Huai'an Second People's Hospital, The Affiliated Huai'an Hospital of Xuzhou Medical University, Huai'an, Jiangsu, China

Due to no penetration depth limitation, low cost, and easy control, magnetic nanoparticles mediated magnetic hyperthermia therapy (MHT) has shown great potential in experimental and clinal treatments of various diseases. However, the low heating conversion efficiencies and short circulation times are major drawback for most existing magnetic-thermal materials. Additionally, single MHT treatment always leads to resistance and recurrence. Herein, a highly efficient magnetic-thermal conversion, ferrimagnetic vortex nanoring Fe_3O_4 coated with hyaluronic acid (HA) nanoparticles (Fe_3O_4@HA, FVNH NPs) was firstly constructed. Additionally, the doxorubicin (DOX) was successfully enclosed inside the FVNH and released remotely for synergetic magnetic–thermal/chemo cancer therapy. Due to the ferrimagnetic vortex-domain state, the ring shape Fe_3O_4 displays a high specific absorption rate (SAR) under an external alternating magnetic field (AMF). Additionally, antitumor drug (DOX) can be encapsulated inside the single large hole of FVNH by the hyaluronic acid (HA) shell and quickly released in response the tumor acidic microenvironments and AMF. What's more, the non-loaded FVNH NPs show good biocompatibility but high cytotoxicity after loading DOX under AMF. Furthermore, the synthesized FVNH can efficiently reduce the transverse relaxation time and enhance negative magnetic resonance imaging (MRI). The impressive *in vivo* systemic therapeutic efficacy of FVNH was also proved in this work. Taken together, the results of this study demonstrate that the synthesized FVNH NPs offer the promise of serving as multifunctional theranostic nanoplatforms for medical imaging-guided tumor therapies.

KEYWORDS

theranostic nanoparticles, vortex nanoring, magnetic hyperthermia therapy, hyaluronic acid, magnetic resonance imaging

Introduction

In recent years, with the vast development of nanotechnology, the biomedical field has been greeted with tremendous excitement, especially for antitumor applications (Mccarroll et al., 2014; Cryer and Thorley, 2019; Barani et al., 2021). Chemotherapy is one of the most common cancer treatments in clinical practice. However, most chemotherapeutics lack the property of tumor targeting, resulting in various side effects (Lindley et al., 1999; Wu et al., 2005). In order to improve the efficiency of the drug and reduce damage to the normal tissues, many researchers have significantly paid diligently (Zhang et al., 2020a; Yang et al., 2020; Cheng et al., 2021). Among various methods employed to overcome this limitation, designing smart nanocarriers, which can load small molecule antitumor drugs, has shown great promise in precise treatments (Vines et al., 2019; Farzin et al., 2020). Thus, carrying material, encapsulating material, and targeting material is essential for intelligent drug transport (Ahn et al., 2018; Yoo et al., 2019). The porous material is one kind of ideal material for drug loading because of the inherent free space, such as hollow SiO_2 (Zhu et al., 2010; Hu et al., 2015), mesoporous carbon (Hussain and Guo, 2019; Zhang et al., 2020a), liposomes (Al-Jamal and Kostarelos, 2011; Zhao et al., 2019), and metal-organic frameworks (Luo et al., 2019; Lawson et al., 2021; Ni et al., 2022). For the extra encapsulating material, easy to decorated organic polymers, like the polypyrrole, polyethylene glycol, and polydopamine, are commonly used as a gatekeeper to control the drug release (Wen et al., 2017). The implementation of targeted delivery, small molecule ligands, such as folic acid, Arginine-Glycine-Aspartic acid, and specific base sequences (Steichen et al., 2013; Bazak et al., 2015). Thus, the approach of establishing smart drug delivery nanocarriers can be achieved by integrating all the above-mentioned components.

Conventional medical management is two independent operations in cancer diagnosis and therapy (Litwin and Tan, 2017; Waks and Winer, 2019). Thus, usually, two different drugs are needed for different purposes. This may cause some potential problems: the time interval between the diagnosis and treatment process is long, which may miss the best treatment opportunity; additionally, the treatment depends on the initial diagnosis and can not keep pace with the progression of the disease. So it will be much more meaningful for clinical practice if the diagnosis and treatment can be integrated into one activity, which will help the physician to improve the accuracy of the disease treatment and cut the odds of trouble (Kelkar and Reineke, 2011; Lim et al., 2015). Among all approaches presented in the literature, the multifunctional nanomaterials mediated cancer therapy shows great promise (Janib et al., 2010; Zhang et al., 2019). In the past decades, numerous theranostic nanoplatforms have been developed for combing imaging and therapy in one nanocomposite (Madamsetty et al., 2019). The lipid-based nanoparticles, polymeric nanocarriers, and inorganic nanoplatforms are three major classes of basic materials (Zhao et al., 2020). Among them, iron oxide is usually used for multiple purposes due to its biocompatibility and low prices, such as magnetic resonance imaging (MRI) T1 and T2 enhancement, photoacoustic imaging enhancement, near-infrared imaging, and magnetic hyperthermia (MHT), magnetic targeting drug delivery and ferroptosis induced cell death (Semkina et al., 2015; Ge et al., 2016; Zhou et al., 2018). In addition, the iron oxide nanoparticles will show active targeting, intelligent controlled drug release, and extra multimodal imaging after a simple modification.

In this work, we designed and prepared the ferrimagnetic vortex nanoring Fe_3O_4@HA nanoparticles (FVNH NPs) enclosing Doxorubicin for T2 MR imaging-guided hyperthermia therapy and chemotherapy. The base nanoring material has a single huge hole at the nanometer size, giving FVNH unique magnetic properties. These include extremely low coercivity and high saturated magnetization, which are prerequisites for high-performance negative MRI imaging and magnetothermal purpose. At the same time, the weak dipole-dipole interactions of the ring structure at the microscopic level behave as a stable colloidal state at the macroscopic level. The properties of synthesized FVNH were fully characterized, and its antitumor therapeutic efficacy was evaluated *in vitro* and *in vivo*. The preliminary findings in this work suggested that DOX-loading FVNH nanocomposite can be used as a novel drug delivery nanocarrier with the potential for cancer theranostic use.

Materials and methods

Chemicals and materials

All reagents were of analytical grade and obtained from several different vendors. $FeCl_3$, NH_4SO_4, NH_4HPO_4, polyethylenimine (PEI, molecular weight = 25,000 Da), N-hydroxysuccinimide, and dialysis bag (3,500 Da) were purchased from Aladdin Biochemical Technology Co., Ltd (Shanghai, China), China. The hyaluronic acid (HA, molecular weight = 5,000–10,000 Da) was purchased from Zhanxun Biotechnology Co., Ltd (Xi'an, China). Dimethyl sulfoxide (DMSO) and absolute ethyl alcohol were purchased from Luoyang Chemical Regent Factory (Luoyang, China). 3-(4, 5-dimethylthiazol-2-yl)-2, 5-diphenyltetrazoliun bromide (MTT), doxorubicin hydrochloride (DOX), and dulbecco minimum essential medium (DMEM) medium was purchased from Yuanye Bio-Technology Co., Ltd (Shanghai, China). The calcein acetoxymethyl ester (Calcein-AM) and Propidium Iodide (PI) were obtained from Biyuntian Biotechnology (Shanghai, China). The 4T1 cell line was purchased from the Cell Bank of the Chinese Academy of Sciences. Milli-Q water (18.2 MΩ·cm) was used in all experiments.

Nanoring α-Fe_2O_3 synthesis

The based single porous material, nanoring α-Fe_2O_3, was prepared through a hydrothermal approach according to previous studies (Jia et al., 2008; Bao et al., 2022). Briefly, 1 ml 0.5 mol/L $FeCl_3$, 500 µl 0.01 mol/L NH_4HPO_4, 500 µl 0.03 mol/L NH_4SO_4, and 78 ml water were added into the 100 ml Teflon and then stirred severally for 30 min. Then, the Teflon tank was transferred into the high-pressure reactor and heated to 220°C in the silicone oil bath. After the 24-h reaction, the orange product was collected using a centrifugal machine with 10,000°r/min for 10 min. Then the nanoring α-Fe_2O_3 was washed three times with water and ethanol, separately, and then dried at 60°C overnight.

Reduction of nanoring α-Fe_2O_3

The nanoring α-Fe_2O_3 was reduced into Fe_3O_4 by hydrogen. Briefly, the nanoring α-Fe_2O_3 was flat out on the horizontal corundum pot and then put the pot in the tube furnace. The reduction reaction was performed with 5% H_2/Ar mixture gas and kept at 480°C for 2 h. The color of nanoring changed from orange to black, indicating that the hematite has been changed into magnetite and that a magnet can easily collect the final product.

Coating the nanoring Fe_3O_4 with hyaluronic acid and loading doxorubicin

250 mg of previously reduced nanoring Fe_3O_4 was dispersed in the de-ionized 100 ml water and then placed in an ultrasonic tank for 30 min at 85°C. Then 50 mg PEI in 10 ml water was added to the above solution, stirring the mixture for another 24 h. After that, the HA was conjugated to the Fe_3O_4@PEI surface according to previous work (Li et al., 2014). For coating the HA, 200 mg HA was dissolved in 20 ml of water at a temperature of 70°C. After cooling to room temperature, 20 ml DMSO with 20 mg carbodiimide and 10 mg N-hydroxysuccinimide was added to the HA solution with vigorous magnetic stirring for 3 h. Then activated HA mixture was put into the previous Fe_3O_4@PEI solution using the drop-by-drop mode with stirring for another 3 days in the dark. Finally, the ring ferrimagnetic vortex nanoring Fe_3O_4@HA nanoparticles (FVNH NPs) was separated from the waste solution using a magnet and dried using a freeze-dryer. For loading the DOX, the 5 mg DOX was added into the nanoring Fe_3O_4 solution in the PEI coating step and with the same following reactions.

Characterization of FVNH NPs

The synthesized FVNH NPs were fully characterized. The microtopography was observed by scanning electron microscopy (SEM, JSM−5600LV) and electronic transmission microscopy (TEM, JEOL-2100). The crystal structure of obtained samples was determined from x-ray powder diffraction (XRD, D8 Advance Bruker) data. The dynamic light scattering (DLS, Malvern Nano-ZS90) instruments were used to measure the zeta potential and average particle size. The magnetic properties of all samples were measured on a SQUID magnetometer (Quantum Design, MPMS-XL7). An infrared thermal (IR) camera was used to record the thermal images and temperatures (Testo-875). The Nanodrop 2000 spectrophotometer was used to measure the UV-vis spectrum (Thermo Scientific). The cells were evaluated by ELISA plate reader (DNM-9606, PuLang New Technology Ltd) at 490 nm and laser confocal microscopy (FV1000, OLYMPUS).

Magnetic hyperthermia assessed

The alternating magnetic field (AMF) was generated by using an inductive heating device (ASPG-10A-II, Shuangping). Different concentration (0–100 µg/ml) of FVNH dissolved in the water was put in the center of the coil of the AMF. After charging with fixed currents and frequency (273 kHz, 600 G), the temperatures of different samples were recorded using an IR camera. What's more, the heating stability and the efficiency of FVNH (100 µg/ml) were also accessed with several circles of on-off of AMF (273 kHz, 600 G) and the specific absorption rates (SAR) under different field strengths (200–800 G) were calculated according to a previously reported method (Quinto et al., 2015). The SAR was calculated using following formula:

$$SAR = Cm\frac{\Delta T}{\Delta T} \times \frac{m_v}{m_{np}}$$

where Cm is the medium heat capacity, ΔT/Δt is the rate of temperature increase in 60 s, m_v and m_{np} are the mass of the suspension and the iron content.

T2 relaxation and magnetic resonance imaging

In this experiment, a clinical 3.0 T MRI scanner was used for magnetic resonance experiments. To measure the T2 relaxation time, different concentrations of FVNH samples were dissolved in the water with different concertation (0.1–2 mg/ml) and then fixed with 0.5% agarose gel in 2 ml centrifuge tubes. In order to accurately measure the R2, the amount of Fe in the PBS solution before relaxation measurement was quantified by ICP-MS. T2 relaxation time was measured using Carr–Purcell–Meiboom–Gill (CPMG) pulse sequence with the following parameters: repetition time (TR) = 10,000 ms, echo time (TE) = 20, 40, 60, 80, 100, 120, 160, 200, 240 ms and the relaxation rate was obtained by fitting data points to calculate slope. For T2-weighted scan, following parameters were adopted: TR = 5,000 ms, TE = 60 ms, slice thickness = 5 mm, field of view = 50 × 50 mm, matrix = 128 × 128.

Evaluation of the doxorubicin loading and doxorubicin releasing

To take it one step further, the obtained FVNH was explored as the drug-carrying to deliver DOX due to the large hole in the center of the nanoring. The absorption value directly measured the content of the DOX at 490 nm by a UV–Vis spectrophotometry. As previously reported (Zhang et al., 2012), the standard curve of DOX content was fitted using least squares with several known concentrations (1–200 mg/L) of DOX and corresponding absorption values at 490 nm. As mentioned above, the loading nanocarriers were collected with a magnet, and the free DOX in the supernate was separated from the nanocarriers. The AMF (273 kHz, 600 G) as an external stimulus was applied for 10 min to explore whether it would enhance the DOX release. The concentration of DOX was determined by measuring the light absorption intensity of the upper layer liquid, and the drug loading efficiency of DOX was further determined according to Eq. 1

$$DOX\,loading\,efficiency\ (\%) = \frac{\text{Amount of encapsulated DOX}}{\text{Amount of FVNH}} \times 100\% \tag{1}$$

And the cumulative release was calculated according to Eq. 2

$$cumulative\ release\ (\%) = \frac{5\sum_1^N C_i + 50C_N}{M_{DOX}} \times 100\% \tag{2}$$

Where N is the number of samplings, C is the DOX concentration and M is the total content of DOX. The volume for the whole system and each sampling is 50 and 5 ml, separately. Three parallel tests obtain all the measurements.

Cytotoxicity experiments

In vitro cytotoxicity tests of free DOX, FVNH, and FVNH-DOX were performed using 4T1 *breast* cancer cells with the standard MTT method as follows: 1×10^4 4T1 cells, which were in the logarithmic phase, were seeded to 96-wells plate and then different samples were added into the wells with various concentration (0–50 μg/ml). After 4 h of incubation, the previous medium was replaced by a fresh medium, and the cells were cultured for another 24/48 h. Then, 10 μl, 5 mg/ml MTT in the PBS was added to each well and incubated with the cells for extra 3 h at 37°C. The medium was abandoned, and 200 μl DMSO was added to each well to dissolve the cells. After shocking gently for 10 min, the 96-well plate was put into a microplate spectrophotometer (PULANG, DNM-9606, Beijing, China), and the absorbance values at 490 nm were recorded. Cell viability was further assessed by different treatments 1) DOX; 2) FVNH-DOX; 3) FVNH + AMF; 4) FVNH-DOX + AMF, and each group has three repetitions, and the mean value was used for analyzing. Calcein-AM/PI staining inspections were applied, to directly observe the therapeutic efficiency. Briefly, 4T1 cells were seeded to a 24-well plate at pH = 6.0 for 4 h, and then different treatments were performed as mentioned above. Subsequently, the calcein-AM and PI solution was added to each well for the double-staining, and then the dyes were incubated with cells in an incubator for another 20 min before washing off with PBS. Then the CLSM was used to observe and record the live/dead cells in the plate.

In vivo experiments

The 4T1 mouse breast cancer cells (1×10^7 per mouse) were injected into the right hind limb of 30, 4-week-old BALB/c mice. When the tumor volume reached 100 mm^3, the mice were divided into five groups. The mice in the experimental group were intratumorally injected with 100 μl FVNH + DOX 1 mg/ml in PBS suspension and then placed in an AMF, for 10 min. For the other four control groups: 1) injected with the same volume of PBS; 2) injected with the same volume of FVNH-DOX; 3) injected with 100 μl free DOX, 4) injected with 100 μl FVNH + AMF, 5) injected with 100 μl FVNH-DOX + AMF (the amount of DOX was 5 mg/kg, AMF: 273 kHz, 600 G, 10 min). The treatment was repeated the day after the first treatment to enhance the effect. Five major organs and tumor tissue were excised for H&E staining. Twenty days later, all tumor-bearing mice were sacrificed. The length (L) and width (W) of the tumors were recorded every 2 days using vernier calipers, as well as the weight of the mice was monitored. The tumor volume (V) was estimated by the following formula: $V= (L\times W^2)/2$. The relative volume of the tumor was calculated as V/V_0 (V_0 was the initial tumor volume before treatments for each mouse).

Statistical analysis

The measurement values were presented as mean ± standard deviation (SD). All statistical analysis was performed by using *t-test* analysis. $^*p < 0.05$ and $^{**}p < 0.01$ were accepted as significant and high significant level.

Results and discussion

Synthesis and characterization of FVNH

The ring shape of nanoparticles forms progressively as expected through a classical nucleation-aggregation-dissolution process under high pressure and temperature condition. Specifically, the nano hematite disks were first formed by the $FeCl_3$. The electronegative ions, SO_4^{2-} and PO_4^{3-}, will coordinate competitively with the surface iron and replace the oxygen. Finally, as previously reported, the ring hole is formatted after

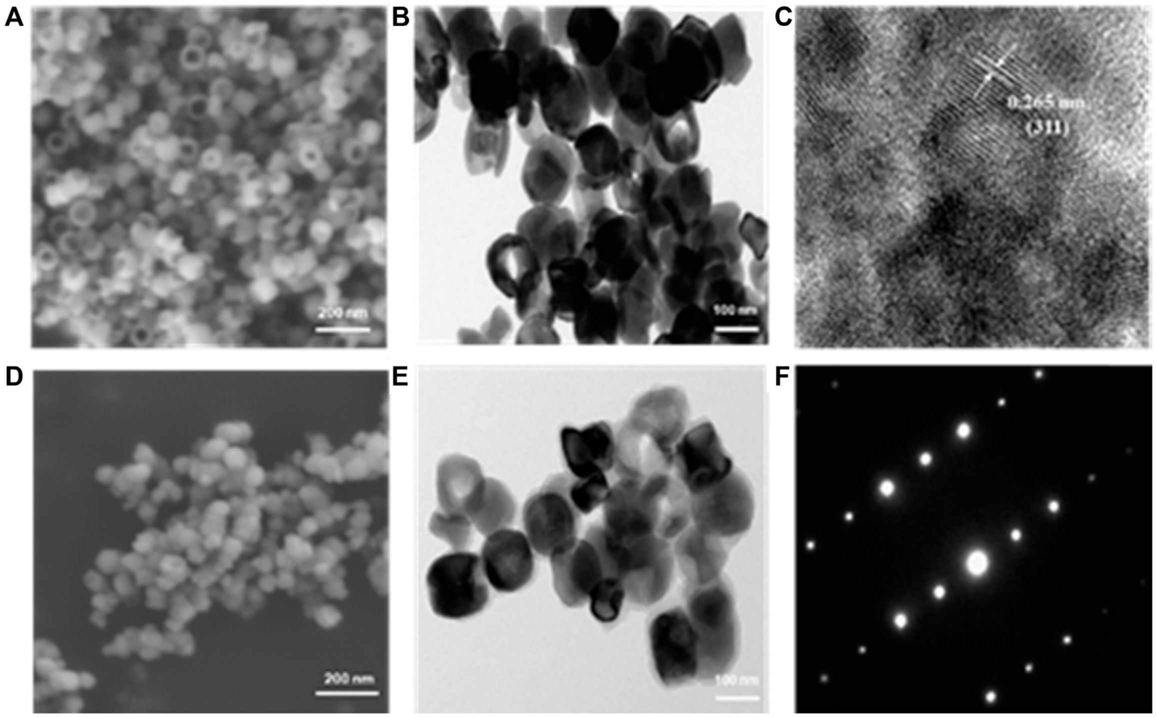

FIGURE 1
Morphology images of obtained samples. SEM **(A)** and TEM **(B)** images of naked nanoring Fe_3O_4. **(C)** High-resolution TEM image recorded on Fe and the interlayer spacings matched with that of magnetite. SEM **(D)** and TEM **(E)** images of HA-coated nanoring Fe_3O_4 and **(F)** corresponding fast Fourier transforms electron diffraction patterns.

the reaction duration can control dissolution accrued on the exposed crystal plane and the hole size (Jia et al., 2008). The morphology of ferrimagnetic nanoring is observed by SEM (Figure 1A), and the uniform ring shape of nanoparticles can be clearly seen. The average external and inner diameters are around 119 ± 11 nm and 69 ± 7 nm. The ring thickness and height are about 32 ± 4 nm and 82 ± 6 nm. The TEM image and high-resolution TEM image of the ferrimagnetic nanoring are shown in Figures 1A,B. Besides the ring shape of the synthesized nanoparticles being further confirmed, the d-spacing of lattice fringes is 0.265 nm (Figure 1C), which is in line with (311) plane of Fe_3O_4. After coating with the HA, no significant changes were observed in SEM images (Figure 1D). However, a layer of a mistlike slice, about 11 nm thick, can be identified on the TEM image (Figure 1E). The fast Fourier transforms electron diffraction patterns (Figure 1F) display well-defined sharp diffraction spots and thus further verifying that the synthesized nanoring Fe_3O_4 particles are single crystals.

The XRD technique was used further to analyze the nanoring crystal structure and its derivatives. As shown in Figure 2A, all the diffraction peaks belong to the crystal peaks of Fe_3O_4. It should be noted that there were no other peaks, which further showed that the compositions of both samples are pure. For the FVNH, the XRD pattern is very similar to the naked nanoring Fe_3O_4, except for a slightly elevated envelope between the 20–30-degree region caused by the PEI and HA, which was caused by the PEI and HA together. Since the surface charge is one factor influencing the materials entering cells, the zeta potential of different samples was measured. What's more, consistent with previous studies (Jiang et al., 2008; Yeh et al., 2013), HA was successfully decorated to the nanoring Fe_3O_4-PEI, and the zeta potential dropped down to about −13.5 mV from 18.2 mV accordingly. After the FVNH was dispersed in water, the average hydrodynamic diameter was 181.2 nm measured by DLS (Figure 2B), much higher than the size measured from the SEM image. This discrepancy can be attributed to the invisible shell layer for the latter. What's more, the colloidal stability of FVNH was explored by monitoring the hydrodynamic diameter over 1 week and the result demonstrate the suitable stability (Supplementary Figure S1). As shown in Figure 2C, the zeta potential for naked nanoring α-Fe_2O_3 and Fe_3O_4 is −3.3 mV and −13.5 mV. After the polymerization of PEI and HA, the zeta potential decreased to −22.6 mV. Theoretically, the negative charge of FVNH will aid the NPs enter cells (Asati et al., 2010; Prijic et al., 2010). As shown in Figure 2D, the hysteresis loops of FVNH were evaluated. FVNH show relatively large saturation magnetization, 69.8 emu/g, which means that the FVNH may

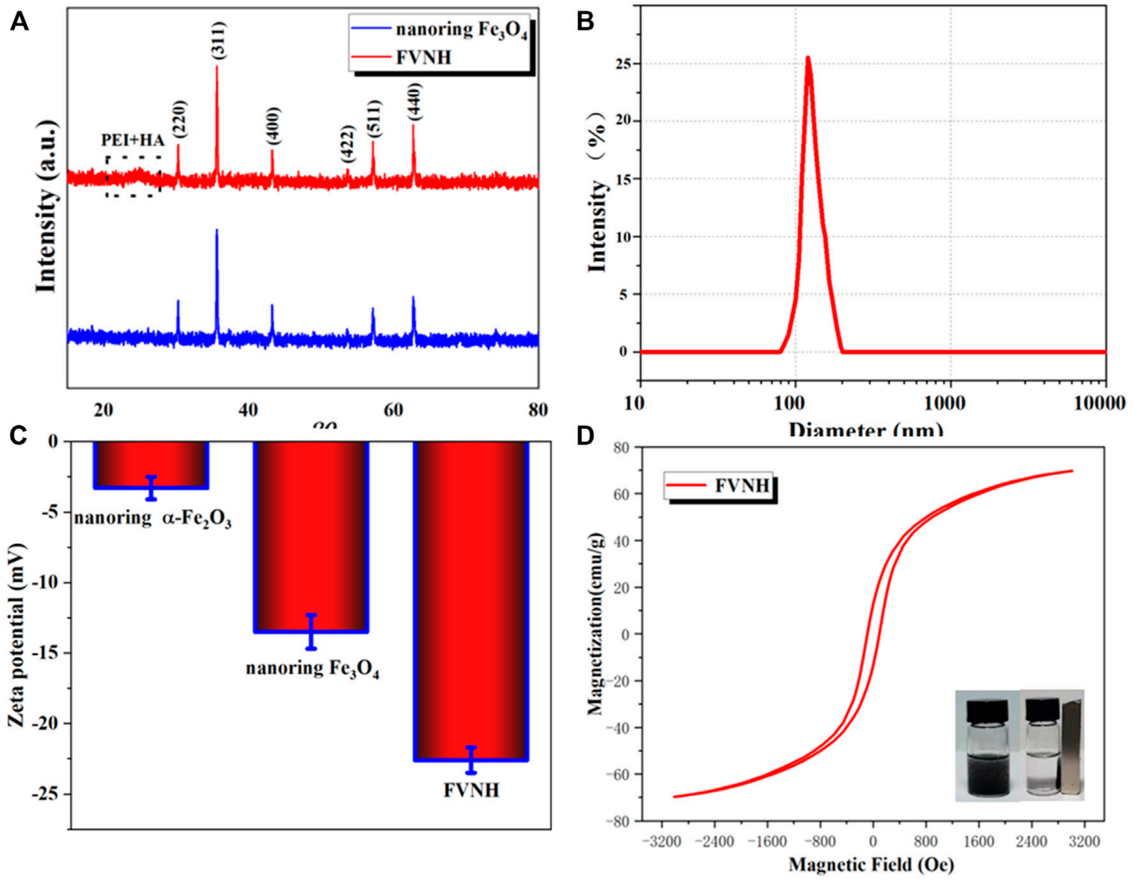

FIGURE 2
(A) X-ray diffraction patterns of naked nanoring Fe_3O_4 and FVNH. **(B)**The hydrodynamic diameter distribution of synthesized FVNH in water measured by DLS. **(C)** Zeta potentials of the nanoparticles for different synthetic steps. **(D)** The hysteresis curves of Ferrimagnetic FVNH nanoparticles and photographs of the FVNH solution in PBS with and without a magnet nearby.

have great potential to enhance the MHT and MRI. What's more, both coercivity and remanence of FVNH are very low. Thus stable magnetic sol–gel can be realized by reducing the dipole-dipole interaction like the superparamagnetic iron oxide nanoparticles. In addition, as shown in the photo, FVNH can be easily absorbed by a magnet, further indicating that the synthesized material has excellent magnetic properties, which can be used for tumor magnetic target treatment.

Subsequently, the magnetic-thermal property of FVNH under the AMF was explored, and the results are shown in Figure 3. The temperature rose rapidly in the initial several minutes and then reached to flattened phase gradually within 10 min. Figure 3A shows the temperature-increasing profiles of AMF-caused heat generation for different FVNH concentrations (0–100 μg/ml). Furthermore, the temperature changes were recorded with fixed strength of 600 G, as shown in Figure 3A, the faster rate of temperature increases with the increase of FVNH concentration. For the same FVNH concentration (100 μg/ml), the higher magnetic field strength will increase a magnetic heating effect, and higher SAR values can be achieved (Figure 3B). The high SAR values of FVNH can be attributed to two factors: 1) the magnetic vortex structure generates large hysteresis loss, and 2) the magnetization reversal process of vortex-to-onion. The magnetothermal stability of FVNH dispersion was also investigated, as can be seen in Figure 3C, the temperature of FVNH dispersion raised from room temperature (~26°C) to the maximum balance temperature (~55°C) during the five cycles of AMF on-off. It can be preliminarily determined that the proposed FNVH has high magnetothermal stability, which may be suitable for multiple treatments with only one injection. What's more, the thermal images of different times (100 μg/ml, 600 G) are shown in Figure 3D. When the AMF duration was increased from 0 to 10 min, the thermal images became much hotter, which is in line

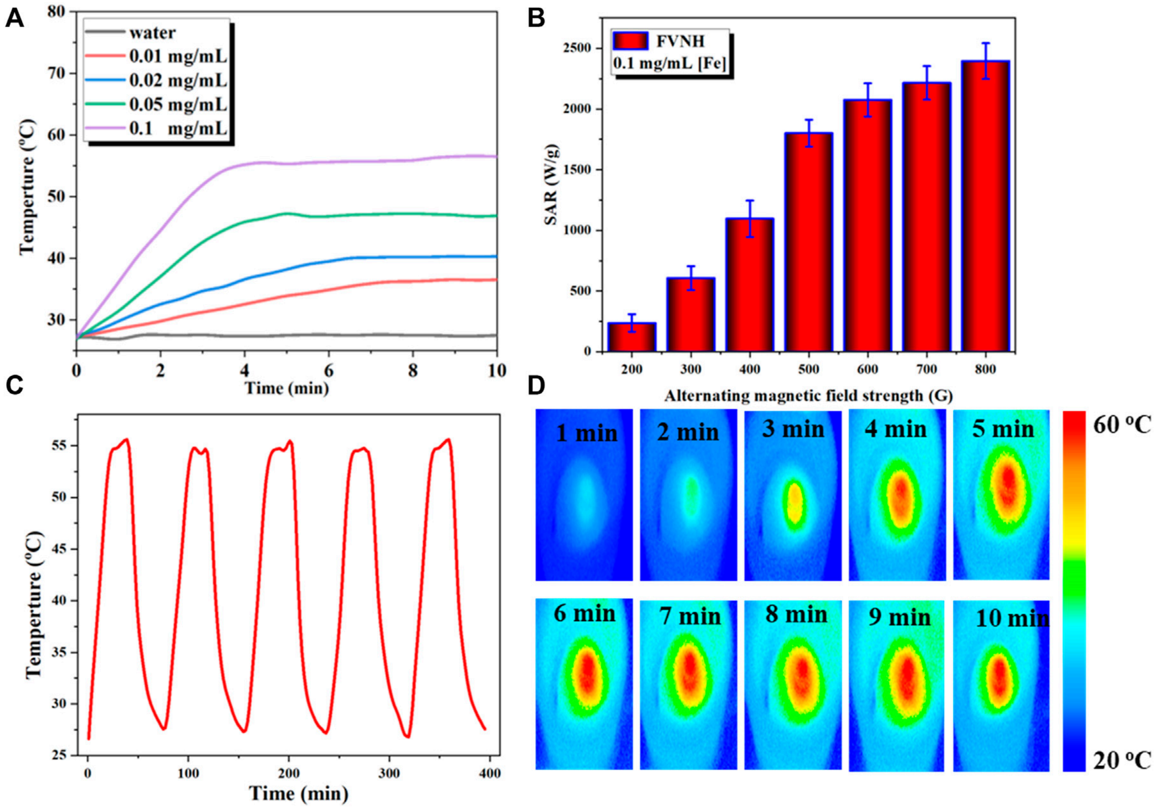

FIGURE 3
(A) Temperature increase profiles for water and different concentration of FVNH under AMF (273 kHz, 600 G) for 10 min. **(B)** Specific absorption rate dependence on the amplitude of AMF. **(C)** Magnetothermal stability of FVNH over a repeated magnetic field on/off cycles. **(D)** Photothermal images of FVNH suspension (200 μg/ml) under AMF (273 kHz, 600 G) for different time durations.

with the temperature-increasing curves. Preliminarily, the obtained FVNH shows excellent magnetic heating characteristics and may have potential application in MHT.

T2 weighted magnetic resonance images

For modern medicine, MRI plays an essential role in tumor diagnosis. Besides the morphological examination, MRI is the primary way to evaluate benign and malignant conditions through the injection of the contrast agent. Various gadolinium-based small molecules are currently used as T1W contrast agents, which will make the tissues much brighter but have biological security problems. On the other hand, the T2W contrast agent developed slowly. Superparamagnetic nanoparticles, well known for their good biocompatibility, are considered an ideal contrast agent that can efficiently shortenthe T2. As a similar magnetic material, the potential of obtained FVNH as T2 contrast agents were preliminary explored in this work at 3 T. As shown in Figure 4A, the T2W images become dark gradually as the concentration of the FVNH increase. Additionally, the transverse relaxivity (r2) value of the FVNH NPs reached 56.25 mM^{-1} S^{-1}, which indicats that the synthesized material has a great ability to shorten T2. The amount of relaxation change depended on the distance between the Fe of nanoring Fe_3O_4 core and the nearby proton of water. Due to shielding effects from the PEI-HA shell, the saturation magnetization decreased slightly, and the transverse relaxation rate decreased accordingly for the same reason, which is consistent with previous studies. It should notice that the FVNH also shows higher T2 values than conventional spherical iron oxide nanoparticles, which can be attributed to the vortex property. T2W images are shown in Figure 4B, with the increase of FVNH concentration from left to right tubes, the image becomes darker. Then the sample was injected into a tumor-bearing mouse, as can be seen in Figure 4C, after the injection, the tumor (red dash circles) showed much lower MRI signal intensity, which means FVNM NPs have been concentrated in the tumor site. Additionally, MR signal intensity is significantly lower after 6 h injection than that of 2 h injection (Figure 4D), which indicates the sample concentration is higher for the former time point. The results

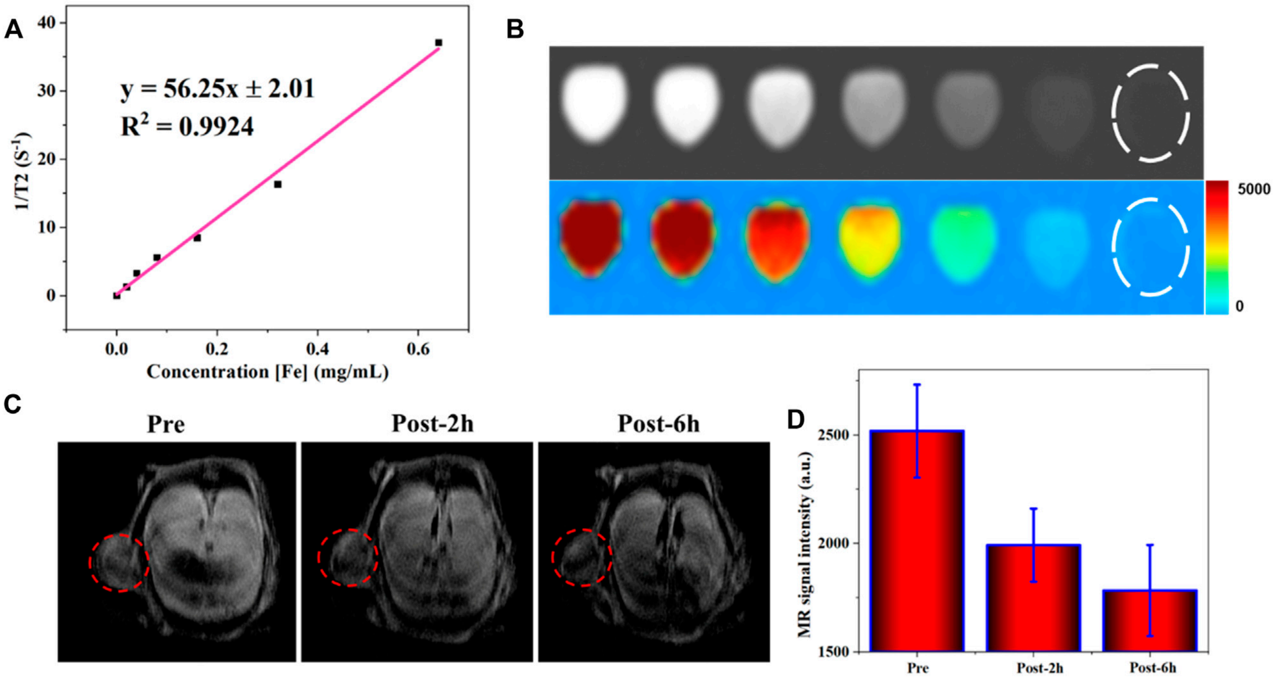

FIGURE 4
MR contrast enhancing ability of FVNH. **(A)** The transverse relaxation rate (1/T2, s-1) as a function of Fe concentration (mM) for FVNH at clinal 3.0 T MRI scanner. **(B)** T2W MR and pseudo-color images at Fe concentrations. **(C)** *In vivo* MR (T2W) images in cancer before and after injection of FVNH NPs. **(D)** MRI signal intensity changes in the tumor region.

revealed that FVNH NPs had an outstanding performance for enhancing T2W MRI both *in vivo* and *in vitro*, and could serve as a potential contrast agent for MR image-guided MHT.

Drug loading and release

The UV-Vis spectrophotometer evaluated the DOX loading in FVNH by the absorption value at 490 nm. Moreover, the calculated loading capacity of DOX for the synthesized NPs is 31.5%. The relatively high value of the drug loading capacity can be attributed to two factors: 1) There is a very large hole in the center of the ring shape basic nanomaterial; and 2) The other may be the intermolecular interactions, like the hydrogen bonding interaction. The *in vitro* DOX release behaviors were explored at different pH (7.4, 6.0, and 5.0) using dialysis bags. As shown in Figure 5A, the release profiles were plotted for 48 h duration according to the absorbance values. The fluorescent intensity was much higher for pH 5.0 than 6.0 and 7.4, which means the lower value environments will accelerate the DOX release. The cumulative released amount in 48 h is 13.0%, 26.6% and 41.2% for pH 5.0, 6.0, and 7.4, separately. It should be noticed that the efficient release under acidic conditions is very adaptable to the tumor microenvironments. The results are in line with previous similar studies (Fang et al., 2019; Wu et al., 2019). This phenomenon is attributed to the interaction effects between DOX and nanocarrier disappearing and the dissociation of carboxylic acid groups. The responses of drug release excited by the magnetothermal thermal were assessed subsequently. As shown in Figure 5B, the fluorescence intensity shows a leaping increase when applying AMF, while the leaping phenomenon disappears when the AMF is absent. The smart "on-off" effect may be that the increased temperature will debilitate the interaction between DOX and nanocarrier, weakening the electrostatic force.

Cell viability assay

Subsequently, we studied the cell viability with various treatments by the standard MTT method, and the results are shown in Figures 6A,B. FVNH has a negligible effect on the 4T1 cell viability even at a concentration of 500 μg/ml and 48 h incubation, which preliminary evidence it is excellent biocompatible nature. The amount of iron internalized in the cells was quantified using ICP-MS. As shown in Supplementary Figure S2, higher cellular iron levels were observed with higher FVNH concentration from 0 to 0.2 mM [Fe] as expected. While for different treatments (free DOX, FVNH-DOX, FVNH + AMF, FVNH-DOX + AMF), with the decrease in the concentrations of

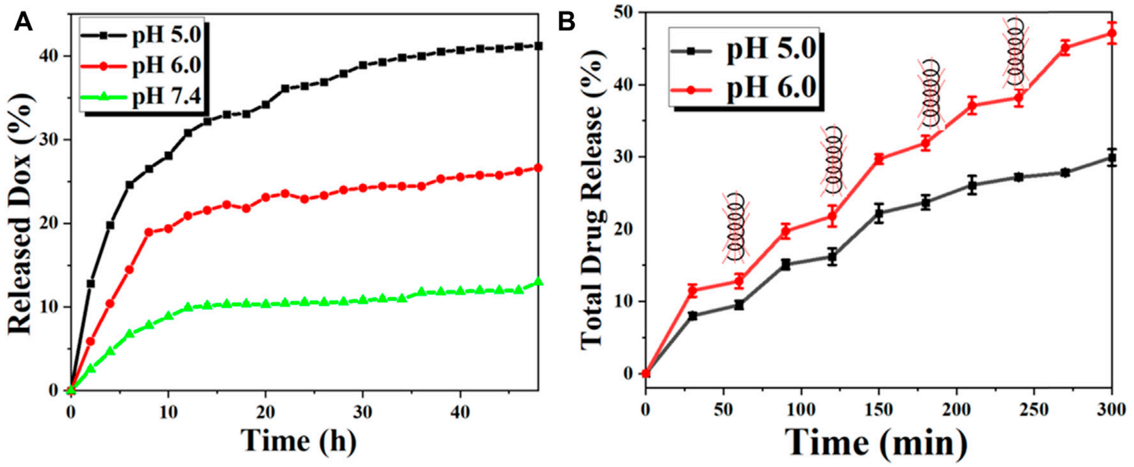

FIGURE 5
The *in vitro* DOX release behavior of the FVNH-DOX. **(A)** Cumulative DOX release profiles of FVNH-DOX at different pH within 2 days and **(B)** In the presence and absence of AMF with a 400 kHz 600 G at different time points (each time point lasts 10 min) under different pH within 5 h.

samples (conversion of DOX content), the cytotoxicity for 4T1 cells increased accordingly. As expected, for FVNH-DOX + AMF group, the cell viability is significantly lower than in any other group. That is to say, the synergistic therapy is better than each independent treatment. In order to observe the cell killing, a live-dead cell stain was further applied as well. As shown in Figure 6C, the live cells were stained with green color, and the dead cells were stained with red color. The largest red fluorescence area appeared in the synergistic group, which is consistent with the MTT experiments. Altogether, these results proved that the designed FVNH-DOX had a very good combined MHT-chemo effect for *in vitro* antitumor cell efficiency.

The *in vivo* therapeutic efficacy

In vivo combined antitumor tests were performed on tumor-bearing mice using FVNH-DOX as a therapeutic reagent. To monitor the magnetothermal effect of synthesized FVNH *in vivo*, temperature changes in the tumor site under the AMF were recorded using an IR camera. As shown in Figure 7A, the temperature of the tumor increased rapidly under the AMF, rising significantly from approximately 37°C to about 45°C within 1 min. In contrast, the temperature of the control tumors remained almost unchanged under the same AMF. As tumor cells are more heat sensitive than normal cells, these results further demonstrate the promise of FVNH-DOX as an effective agent for both chemo-magnetothermal therapy. Although the magnetic nanorings have been used as magnetothermal agents to treat tumors, the potential use of it encapsulated with DOX for synergistic cancer treatment has not been reported. The changes in relative tumor volumes in 4T1 tumor-bearing mice further demonstrated the anti-tumor capacity (Figure 7B). All treatment groups showed a slight overall increase in body weight over the 18-day study (Figure 7C), further indicating few side effects of the FVNH and the magnetothermal treatment. The FVNH-DOX + AMF treatment group showed significant tumor suppression after 18 days of treatment, but for the other four groups, PBS, FVNH-DOX, free DOX, and FVNH + AMF groups still had various degrees of tumors growth. The FVNH-DOX + AMF treatment group had the smallest tumor volume, even disappeared (Figure 7D), of the five groups, confirming that the combination treatment was much better than the other single treatment groups. Furthermore, as seen in the H&E-stained tumor tissue sections, there was more necrosis and apoptosis in the tumor tissue of the FVNH-DOX + AMF treated group (Figure 7E), but no significant necrotic cells in other major organs (Supplementary Figure S3). Histological analysis of diferent organs in tumor-bearing mice stained with H&E are displayed in Supplementary Figure S3. All the organs from five gruops were normal, preliminary indicating that less toxicity of FVNH and treaments to the major organs. Overall, the FVNH loading with DOX nanocomposites in the present of AMF could be a promising nanoplatform for combined magnetothermal-chemotherapy of cancer in future clinical trials.

Due to the lack of depth limitation, low cost, and suitability for remote control, magnetothermal therapy, and chemotherapy, based on magnetic nanoparticles in combination with controlled drug delivery systems, have been extensively studied in recent years. To improve the biocompatibility of magnetic nanoparticles and to achieve superior diagnostic and therapeutic purposes, scientists have made a number of material-based strategies. Fan et al. (2010) and our previous study demonstrated that the ring shape nano magnetite has magnetic vortex properties and thus

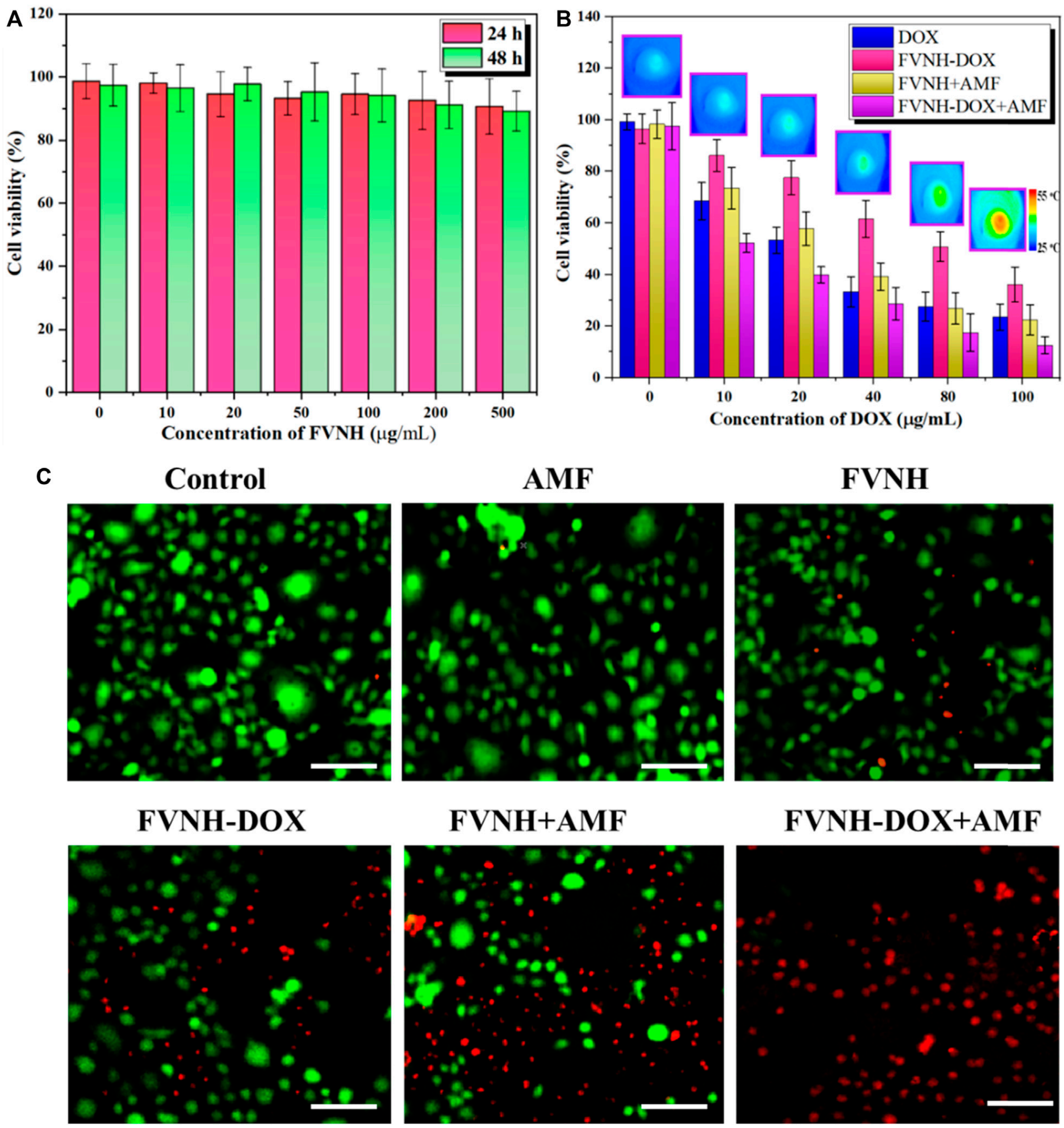

FIGURE 6
Cell viability assay. **(A)** Cell viability after incubation with different FVNH for 24 and 48 h. **(B)** Cell viability upon various kinds of treatments at different concentrations of DOX and representive thermal images of FVNH-DOX + AMF group. **(C)** Fluorescence images of co-stained with calcein-AM (green) and PI (red) 4T1 cells after different therapies. (*n* = 3, mean ± SD), (Scale bar = 100 μm).

excellent magnetothermal properties for magnetothermal tumors therapy as well as enhancing MRI (Bao et al., 2021); By modifying HA on graphene and attaching the composite to iron oxide nanoparticles after wrapping DOX, Pramanik et al. found that this nanoplatform could not only control the drug release by an external magnetic field, but it would kill much more breast cancer cells than the non-magnetic thermal control group (Pramanik et al., 2019). Recently, Zhang et al. (2020b) synthesized an iron oxide nanoparticle with super magneto-thermal efficiency through a green biomineralization process,

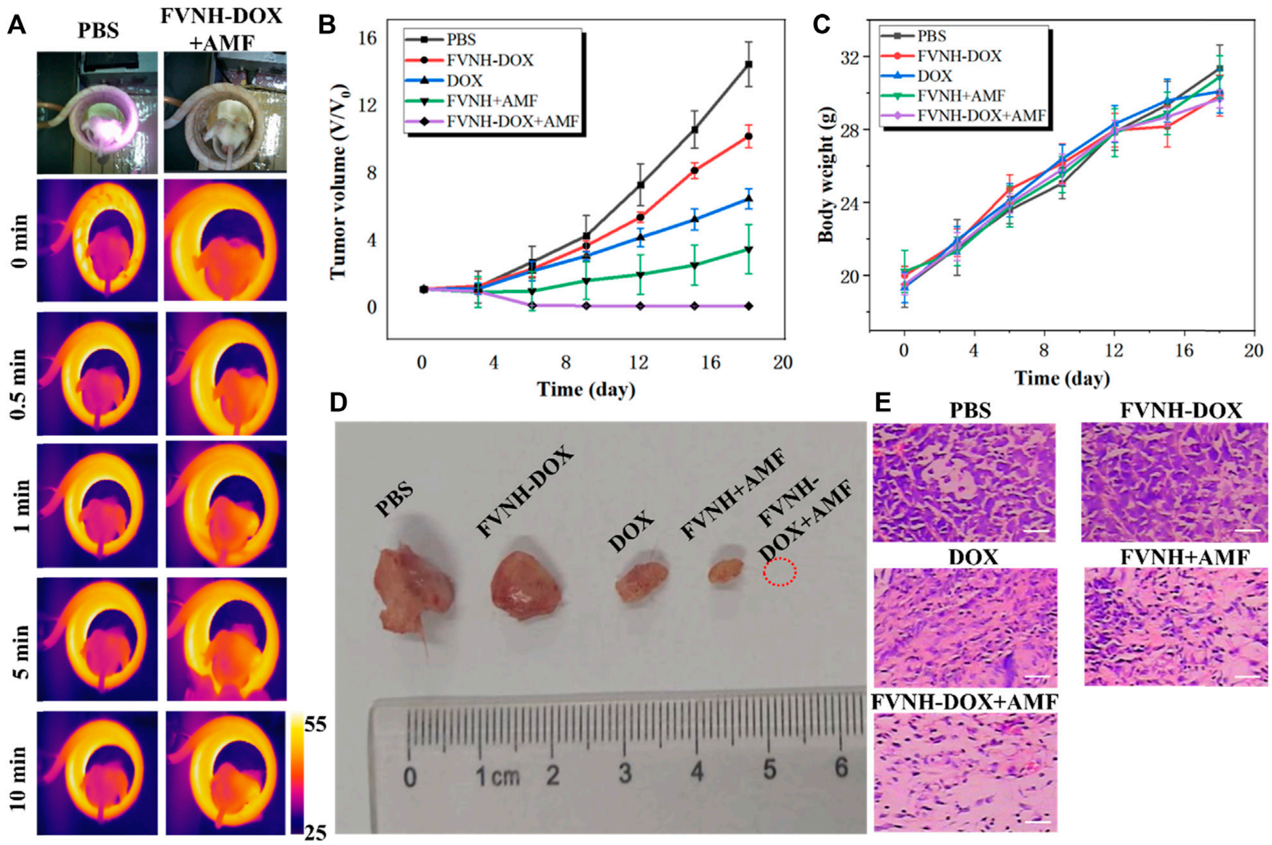

FIGURE 7
In vivo cancer magnetothermal-chemotherapy in tumor-bearing mice models with 4T1 cancer cells. **(A)** Photos and corresponding thermal images of tumor-bearing mice under AMF at different time points after injection with PBS or FVNH-DOX; **(B)** The relative tumor growth curves of different groups; **(C)** Body weight curves for different groups after treatment; **(D)** Representative tumors picture from different treatment groups after the experiments; **(E)** The H&E images of tumors collected from different treated groups. (Scale bar = 100 μm).

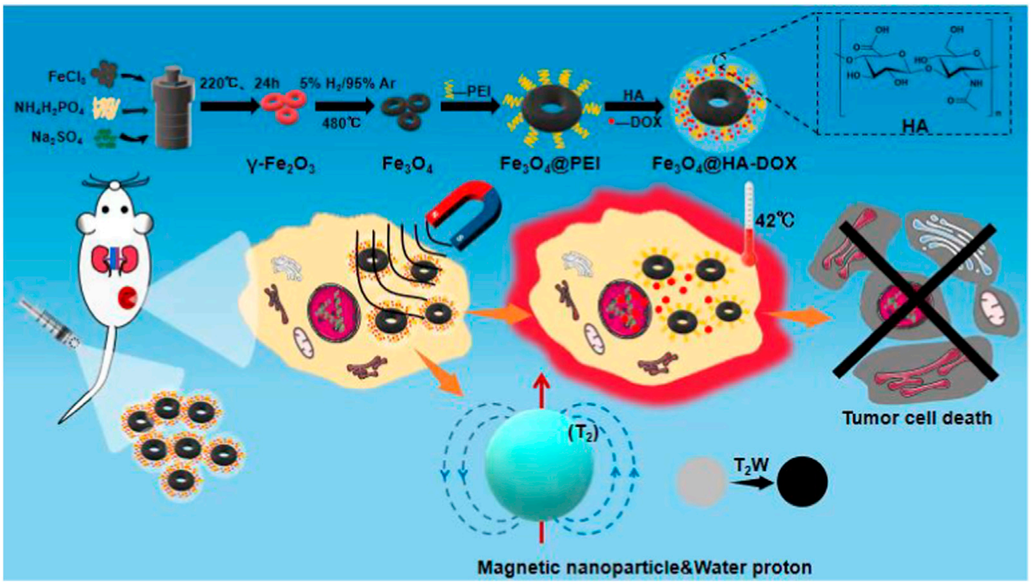

SCHEME 1
Schematic illustration of the nanoring Fe_3O_4@HA-DOX for MRI imaging-guided synergistic MHT-chemo cancer therapy.

with a specific absorption rate of 2390 W/g, and they demonstrated that the NPs could be used as an excellent magneto-thermal agent and nanoenzyme as well for liver tumor inhibition. Despite the great progress made in the field of nanomediated magnetothermal therapy, more time may be needed for its application in the clinic, and there are still challenges to be addressed, such as the low thermal efficiency compared to photothermal and biosafety issues.

Conclusion

In this paper, the one-pot solvothermal method combined with the following reduction reaction was used to prepare ring shape and mono-dispersion Fe_3O_4 nanoparticles. The core-shell nanoring Fe_3O_4@HA loaded with DOX was formed for magnetothermal-chemo cancer therapy and enhancing T2W MRI imaging. Notably, the FVNH shows significantly extremally high magnetothermal conversion efficiency and shoring the transverse relaxation time. Additionally, a thin HA coating was formed on the nanoring surface, which endowed the NPs with a high-capacity of drug loading and triggered releasing abilities. The preliminary results demonstrated that the established vortex nanoring Fe_3O_4-based nanoconstruct might hold great potential for DOX delivery and cancer theranostics.

Data availability statement

The original contributions presented in the study are included in the article/Supplementary Material, further inquiries can be directed to the corresponding authors.

Ethics statement

The animal study was reviewed and approved by The Ethics Committee of the First Affiliated Hospital of Zhengzhou University.

Author contributions

JB wrote the draft manuscript. LX and FZ designed the project. HT, YD, and LD performed the experiments. JB, JL, and HT interpreted the data. JL and KY revised the manuscript. All authors approved the submission the final version.

Funding

This work was financially supported by the National Natural Science Foundation of China (Grant Nos. 81601470).

Conflict of interest

The authors declare that the research was conducted in the absence of any commercial or financial relationships that could be construed as a potential conflict of interest.

Publisher's note

Supplementary material

The Supplementary Material for this article can be found online at: https://www.frontiersin.org/articles/10.3389/fbioe.2022.1005719/full#supplementary-material

References

Ahn, J., Ko, J., Lee, S., Yu, J., Kim, Y., and Jeon, N. L. (2018). Microfluidics in nanoparticle drug delivery; from synthesis to pre-clinical screening. *Adv. Drug Deliv. Rev.* 128, 29–53. doi:10.1016/j.addr.2018.04.001

Al-Jamal, W. T., and Kostarelos, K. (2011). Liposomes: From a clinically established drug delivery system to a nanoparticle platform for theranostic nanomedicine. *Acc. Chem. Res.* 44, 1094–1104. doi:10.1021/ar200105p

Asati, A., Santra, S., Kaittanis, C., and Perez, J. M. (2010). Surface-charge-dependent cell localization and cytotoxicity of cerium oxide nanoparticles. *ACS Nano* 4, 5321–5331. doi:10.1021/nn100816s

Bao, J., Guo, S., Zu, X., Zhuang, Y., Fan, D., Zhang, Y., et al. (2021). Polypyrrole-coated magnetite vortex nanoring for hyperthermia-boosted photothermal/magnetothermal tumor ablation under photoacoustic/magnetic resonance guidance. *Front. Bioeng. Biotechnol.* 9, 721617. doi:10.3389/fbioe.2021.721617

Bao, J., Guo, S., Zu, X., Zhuang, Y., Fan, D., Zhang, Y., et al. (2022). Magnetic vortex nanoring coated with gadolinium oxide for highly enhanced T1-T2 dual-modality magnetic resonance imaging-guided magnetic hyperthermia cancer ablation. *Biomed. Pharmacother.* 150, 112926. doi:10.1016/j.biopha.2022.112926

Barani, M., Bilal, M., Sabir, F., Rahdar, A., and Kyzas, G. Z. (2021). Nanotechnology in ovarian cancer: Diagnosis and treatment. *Life Sci.* 266, 118914. doi:10.1016/j.lfs.2020.118914

Bazak, R., Houri, M., El Achy, S., Kamel, S., and Refaat, T. (2015). Cancer active targeting by nanoparticles: A comprehensive review of literature. *J. Cancer Res. Clin. Oncol.* 141, 769–784. doi:10.1007/s00432-014-1767-3

Cheng, Z., Li, M., Dey, R., and Chen, Y. (2021). Nanomaterials for cancer therapy: Current progress and perspectives. *J. Hematol. Oncol.* 14, 85. doi:10.1186/s13045-021-01096-0

Cryer, A. M., and Thorley, A. J. (2019). Nanotechnology in the diagnosis and treatment of lung cancer. *Pharmacol. Ther.* 198, 189–205. doi:10.1016/j.pharmthera.2019.02.010

Fan, H.-M., Olivo, M., Shuter, B., Yi, J.-B., Bhuvaneswari, R., Tan, H.-R., et al. (2010). Quantum dot capped magnetite nanorings as high performance nanoprobe for multiphoton fluorescence and magnetic resonance imaging. *J. Am. Chem. Soc.* 132, 14803–14811. doi:10.1021/ja103738t

Fang, Z., Li, X., Xu, Z., Du, F., Wang, W., Shi, R., et al. (2019). Hyaluronic acid-modified mesoporous silica-coated superparamagnetic Fe_3O_4 nanoparticles for targeted drug delivery. *Int. J. Nanomedicine* 14, 5785–5797. doi:10.2147/ijn.s213974

Farzin, A., Etesami, S. A., Quint, J., Memic, A., and Tamayol, A. (2020). Magnetic nanoparticles in cancer therapy and diagnosis. *Adv. Healthc. Mat.* 9, 1901058. doi:10.1002/adhm.201901058

Ge, R., Li, X., Lin, M., Wang, D., Li, S., Liu, S., et al. (2016). Fe3O4@ polydopamine composite theranostic superparticles employing preassembled Fe3O4 nanoparticles as the core. *ACS Appl. Mat. Interfaces* 8, 22942–22952. doi:10.1021/acsami.6b07997

Hu, F., Zhang, Y., Chen, G., Li, C., and Wang, Q. (2015). Double-walled Au nanocage/SiO2 nanorattles: Integrating SERS imaging, drug delivery and photothermal therapy. *Small* 11, 985–993. doi:10.1002/smll.201401360

Hussain, A., and Guo, S. (2019). NIR-triggered release of DOX from sophorolipid-coated mesoporous carbon nanoparticles with the phase-change material 1-tetradecanol to treat MCF-7/ADR cells. *J. Mat. Chem. B* 7, 974–985. doi:10.1039/c8tb02673d

Janib, S. M., Moses, A. S., and Mackay, J. A. (2010). Imaging and drug delivery using theranostic nanoparticles. *Adv. Drug Deliv. Rev.* 62, 1052–1063. doi:10.1016/j.addr.2010.08.004

Jia, C.-J., Sun, L.-D., Luo, F., Han, X.-D., Heyderman, L. J., Yan, Z.-G., et al. (2008). Large-scale synthesis of single-crystalline iron oxide magnetic nanorings. *J. Am. Chem. Soc.* 130, 16968–16977. doi:10.1021/ja805152t

Jiang, G., Park, K., Kim, J., Kim, K. S., Oh, E. J., Kang, H., et al. (2008). Hyaluronic acid-polyethyleneimine conjugate for target specific intracellular delivery of siRNA. *Biopolymers* 89, 635–642. doi:10.1002/bip.20978

Kelkar, S. S., and Reineke, T. M. (2011). Theranostics: Combining imaging and therapy. *Bioconjug. Chem.* 22, 1879–1903. doi:10.1021/bc200151q

Lawson, H. D., Walton, S. P., and Chan, C. (2021). Metal–organic frameworks for drug delivery: A Design perspective. *ACS Appl. Mat. Interfaces* 13, 7004–7020. doi:10.1021/acsami.1c01089

Li, J., He, Y., Sun, W., Luo, Y., Cai, H., Pan, Y., et al. (2014). Hyaluronic acid-modified hydrothermally synthesized iron oxide nanoparticles for targeted tumor MR imaging. *Biomaterials* 35, 3666–3677. doi:10.1016/j.biomaterials.2014.01.011

Lim, E.-K., Kim, T., Paik, S., Haam, S., Huh, Y.-M., and Lee, K. (2015). Nanomaterials for theranostics: Recent advances and future challenges. *Chem. Rev.* 115, 327–394. doi:10.1021/cr300213b

Lindley, C., Mccune, J. S., Thomason, T. E., Lauder, D., Sauls, A., Adkins, S., et al. (1999). Perception of chemotherapy side effects cancer versus noncancer patients. *Cancer Pract.* 7, 59–65. doi:10.1046/j.1523-5394.1999.07205.x

Litwin, M. S., and Tan, H.-J. (2017). The diagnosis and treatment of prostate cancer: A review. *JAMA* 317, 2532–2542. doi:10.1001/jama.2017.7248

Luo, Z., Jiang, L., Yang, S., Li, Z., Soh, W. M. W., Zheng, L., et al. (2019). Light-induced redox-responsive smart drug delivery system by using selenium-containing polymer@MOF shell/core nanocomposite. *Adv. Healthc. Mat.* 8, 1900406. doi:10.1002/adhm.201900406

Madamsetty, V. S., Mukherjee, A., and Mukherjee, S. (2019). Recent trends of the bio-inspired nanoparticles in cancer theranostics. *Front. Pharmacol.* 10, 1264. doi:10.3389/fphar.2019.01264

Mccarroll, J., Teo, J., Boyer, C., Goldstein, D., Kavallaris, M., and Phillips, P. (2014). Potential applications of nanotechnology for the diagnosis and treatment of pancreatic cancer. *Front. Physiol.* 5, 2. doi:10.3389/fphys.2014.00002

Ni, W., Zhang, L., Zhang, H., Zhang, C., Jiang, K., and Cao, X. (2022). Hierarchical MOF-on-MOF architecture for pH/GSH-controlled drug delivery and Fe-based chemodynamic therapy. *Inorg. Chem.* 61, 3281–3287. doi:10.1021/acs.inorgchem.1c03855

Pramanik, N., Ranganathan, S., Rao, S., Suneet, K., Jain, S., Rangarajan, A., et al. (2019). A composite of hyaluronic acid-modified graphene oxide and iron oxide nanoparticles for targeted drug delivery and magnetothermal therapy. *ACS Omega* 4, 9284–9293. doi:10.1021/acsomega.9b00870

Prijic, S., Scancar, J., Romih, R., Cemazar, M., Bregar, V. B., Znidarsic, A., et al. (2010). Increased cellular uptake of biocompatible superparamagnetic iron oxide nanoparticles into malignant cells by an external magnetic field. *J. Membr. Biol.* 236, 167–179. doi:10.1007/s00232-010-9271-4

Quinto, C. A., Mohindra, P., Tong, S., and Bao, G. (2015). Multifunctional superparamagnetic iron oxide nanoparticles for combined chemotherapy and hyperthermia cancer treatment. *Nanoscale* 7, 12728–12736. doi:10.1039/c5nr02718g

Semkina, A., Abakumov, M., Grinenko, N., Abakumov, A., Skorikov, A., Mironova, E., et al. (2015). Core–shell–corona doxorubicin-loaded superparamagnetic Fe3O4 nanoparticles for cancer theranostics. *Colloids Surfaces B Biointerfaces* 136, 1073–1080. doi:10.1016/j.colsurfb.2015.11.009

Steichen, S. D., Caldorera-Moore, M., and Peppas, N. A. (2013). A review of current nanoparticle and targeting moieties for the delivery of cancer therapeutics. *Eur. J. Pharm. Sci.* 48, 416–427. doi:10.1016/j.ejps.2012.12.006

Vines, J. B., Yoon, J.-H., Ryu, N.-E., Lim, D.-J., and Park, H. (2019). Gold nanoparticles for photothermal cancer therapy. *Front. Chem.* 7, 167. doi:10.3389/fchem.2019.00167

Waks, A. G., and Winer, E. P. (2019). Breast cancer treatment: A review. *JAMA* 321, 288–300. doi:10.1001/jama.2018.19323

Wen, J., Yang, K., Liu, F., Li, H., Xu, Y., and Sun, S. (2017). Diverse gatekeepers for mesoporous silica nanoparticle based drug delivery systems. *Chem. Soc. Rev.* 46, 6024–6045. doi:10.1039/c7cs00219j

Wu, F., Sun, B., Chu, X., Zhang, Q., She, Z., Song, S., et al. (2019). Hyaluronic acid-modified porous carbon-coated Fe3O4 nanoparticles for magnetic resonance imaging-guided photothermal/chemotherapy of tumors. *Langmuir* 35, 13135–13144. doi:10.1021/acs.langmuir.9b02300

Wu, T., Munro, A. J., Guanjian, L., and Liu, G. J. (2005). Chinese medical herbs for chemotherapy side effects in colorectal cancer patients. *Cochrane Database Syst. Rev.* 2010, CD004540. doi:10.1002/14651858.cd004540.pub2

Yang, L., Shi, P., Zhao, G., Xu, J., Peng, W., Zhang, J., et al. (2020). Targeting cancer stem cell pathways for cancer therapy. *Signal Transduct. Target. Ther.* 5, 8. doi:10.1038/s41392-020-0110-5

Yeh, P.-H., Sun, J.-S., Wu, H.-C., Hwang, L.-H., and Wang, T.-W. (2013). Stimuli-responsive HA-PEI nanoparticles encapsulating endostatin plasmid for stem cell gene therapy. *RSC Adv.* 3, 12922–12932. doi:10.1039/c3ra40880a

Yoo, J., Park, C., Yi, G., Lee, D., and Koo, H. (2019). Active targeting strategies using biological ligands for nanoparticle drug delivery systems. *Cancers* 11, 640. doi:10.3390/cancers11050640

Zhang, C., Wang, W., Liu, T., Wu, Y., Guo, H., Wang, P., et al. (2012). Doxorubicin-loaded glycyrrhetinic acid-modified alginate nanoparticles for liver tumor chemotherapy. *Biomaterials* 33, 2187–2196. doi:10.1016/j.biomaterials.2011.11.045

Zhang, X., Ong'achwa Machuki, J., Pan, W., Cai, W., Xi, Z., Shen, F., et al. (2020a). Carbon nitride hollow theranostic nanoregulators executing laser-activatable water splitting for enhanced ultrasound/fluorescence imaging and cooperative phototherapy. *ACS Nano* 14, 4045–4060. doi:10.1021/acsnano.9b08737

Zhang, X., Xi, Z., Machuki, J. O. A., Luo, J., Yang, D., Li, J., et al. (2019). Gold cube-in-cube based oxygen nanogenerator: A theranostic nanoplatform for modulating tumor microenvironment for precise chemo-phototherapy and multimodal imaging. *ACS Nano* 13, 5306–5325. doi:10.1021/acsnano.8b09786

Zhang, Y., Wang, X., Chu, C., Zhou, Z., Chen, B., Pang, X., et al. (2020b). Genetically engineered magnetic nanocages for cancer magneto-catalytic theranostics. *Nat. Commun.* 11, 5421. doi:10.1038/s41467-020-19061-9

Zhao, S., Yu, X., Qian, Y., Chen, W., and Shen, J. (2020). Multifunctional magnetic iron oxide nanoparticles: An advanced platform for cancer theranostics. *Theranostics* 10, 6278–6309. doi:10.7150/thno.42564

Zhao, Z., Wang, W., Li, C., Zhang, Y., Yu, T., Wu, R., et al. (2019). Reactive oxygen species–activatable liposomes regulating hypoxic tumor microenvironment for synergistic photo/chemodynamic therapies. *Adv. Funct. Mat.* 29, 1905013. doi:10.1002/adfm.201905013

Zhou, P., Zhao, H., Wang, Q., Zhou, Z., Wang, J., Deng, G., et al. (2018). Photoacoustic-enabled self-guidance in magnetic-hyperthermia Fe@ Fe3O4 nanoparticles for theranostics *in vivo*. *Adv. Healthc. Mat.* 7, 1701201. doi:10.1002/adhm.201701201

Zhu, Y., Fang, Y., and Kaskel, S. (2010). Folate-conjugated Fe3O4@SiO2 hollow mesoporous spheres for targeted anticancer drug delivery. *J. Phys. Chem. C* 114, 16382–16388. doi:10.1021/jp106685q

frontiers | Frontiers in Bioengineering and Biotechnology

TYPE Original Research
PUBLISHED 10 October 2022
DOI 10.3389/fbioe.2022.1027868

Advanced nanoparticles that can target therapy and reverse drug resistance may be the dawn of leukemia treatment: A bibliometrics study

Rui Wang[1], Changming Zhao[1], Shuxia Jiang[2], Zhaohua Zhang[2], Chunmei Ban[3], Guiping Zheng[2], Yan Hou[2], Bingjin Jin[4], Yannan Shi[5], Xin Wu[6]* and Qiangqiang Zhao[2]*

[1]Department of Hematology, Shandong Second Provincial General Hospital, Jinan, China, [2]Department of Hematology, The Qinghai Provincial People's Hospital, Xining, China, [3]Department of Hematology, Hematology Department, The People's Hospital of Liuzhou City, Liuzhou, China, [4]Department of Pharmacy, The Qinghai Provincial People's Hospital, Xining, China, [5]Department of General Medicine, Ganmei Hospital, Kunming First People's Hospital, Kunming, China, [6]Department of Spine Surgery, Third Xiangya Hospital, Central South University, Changsha, China

OPEN ACCESS

EDITED BY
Long Bai,
East China University of Science and Technology, China

REVIEWED BY
Yuanyuan Han,
The University of Hong Kong, Hong Kong SAR, China
Jaison Jeevanandam,
Universidade da Madeira, Portugal
Jun Cheng,
University of Texas MD Anderson Cancer Center, United States

*CORRESPONDENCE
Xin Wu,
drxinwu@163.com
Qiangqiang Zhao,
zgxyws@163.com

SPECIALTY SECTION
This article was submitted to Nanobiotechnology, a section of the journal Frontiers in Bioengineering and Biotechnology

RECEIVED 25 August 2022
ACCEPTED 14 September 2022
PUBLISHED 10 October 2022

CITATION
Wang R, Zhao C, Jiang S, Zhang Z, Ban C, Zheng G, Hou Y, Jin B, Shi Y, Wu X and Zhao Q (2022), Advanced nanoparticles that can target therapy and reverse drug resistance may be the dawn of leukemia treatment: A bibliometrics study.
Front. Bioeng. Biotechnol. 10:1027868.
doi: 10.3389/fbioe.2022.1027868

With the development of nanomedicine, more and more nanoparticles are used in the diagnosis and treatment of leukemia. This study aimed to identify author, country, institutional, and journal collaborations and their impacts, assess the knowledge base, identify existing trends, and uncover emerging topics related to leukemia research. 1825 Articles and reviews were obtained from the WoSCC and analyzed by Citespace and Vosviewer. INTERNATIONAL JOURNAL OF NANOMEDICINE is the journal with the highest output. The contribution of FRONTIERS IN BIOENGINEERING AND BIOTECHNOLOGY is also noteworthy. The three main aspects of research in Nanoparticles-leukemia-related fields included nanoparticles for the diagnosis and treatment of leukemia, related to the type and treatment of leukemia, the specific molecular mechanism, and existing problems of the application of nanoparticles in leukemia. In the future, synthesize nano-drugs that have targeted therapy and chemotherapy resistance according to the mechanism, which may be the dawn of the solution to leukemia. This study offers a comprehensive overview of the Nanoparticles-leukemia-related field using bibliometrics and visual methods for the first time, providing a valuable reference for researchers interested in Nanoparticles-leukemia.

KEYWORDS

nanoparticles, target therapy, drug resistance, leukemia, chemotherapy

1 Introduction

Cancer has always been a thorn in the hearts of human beings worldwide, and leukemia is even more worrying for researchers because of its high incidence and low survival rate (Wu et al., 2021a; Wu et al., 2021b). Leukemia is a highly invasive hematological tumor with complex genetic and biological characteristics (Du et al., 2021; Jiang et al., 2022; Wu et al., 2022). There are a variety of treatments for leukemia, including chemotherapy, radiotherapy, stem cell transplantation, immunotherapy, targeted therapy, and so on (Kaldor et al., 1990; Montserrat and Dreger, 2015; Woyach, 2019; Locatelli et al., 2021; Lussana et al., 2021). Although immunotherapy such as Autologous chimeric antigen receptor (CAR) T cells has attracted wide attention from researchers recently, chemotherapy has always been the main treatment for leukemia because of its classic and effectiveness. Chemotherapy is one of the primary means to treat leukemia. However, the clinical application still has the following problems: 1. Chemotherapeutic drugs kill leukemic and normal cells and produce adverse effects, including malnutrition, cancer, and chronic pain. 2. The emergence of drug resistance leads to a significant decline in chemotherapy efficacy and a poor prognosis (Lokody, 2014). How to solve the above problems has become an urgent problem to be solved in this field.

Nanotechnology is widely used in medicine, such as tissue repair, diagnosis, and treatment of diseases (Lin et al., 2020a; Lin et al., 2020b; Zhang et al., 2020; Bai et al., 2021; Chen et al., 2021; Zhao et al., 2022). Professor Feng's team developed a GSH bioimprinted nanocomposite loaded with an FTO inhibitor (GNPIPP12MA). The GNPIPP12MA can not only achieve an anti-leukemia effect by inducing ferroptosis but also enhance the blocking effect of PD-L1 by increasing the infiltration of cytotoxic T cells (Cao et al., 2022). Professor Zhao's team constructs a novel amino acid nanomedicine for the treatment of T-cell acute lymphoblastic leukemia by combining leukemia cell targeting and immune surveillance stimulation (Li et al., 2022). Nanoparticles can not only treat leukemia by transporting small molecular drugs, antibody drugs, and genes but also carry out photodynamic therapy for leukemia through photosensitizers (Shen et al., 2020). Because the physiological structure of a tumor is different from that of normal tissue, nanoparticles can be passively targeted to the tumor by the Enhanced Permeability and Retention Effect (EPR). EPR refers to the phenomenon that some macromolecular substances of a specific size (such as liposomes, nanoparticles, and some macromolecular drugs) are more likely to penetrate into tumor tissue and remain for a long time (compared with normal tissue). At the same time, nanoparticles can also be modified by the cell membrane, ligand, or aptamer to achieve active targeting (Tatar et al., 2016; Tee et al., 2019). However, the research on nano-drugs that can achieve specific targeting and reverse leukemia drug resistance is still in its infancy.

There are many ways to systematically review a research field, among which the bibliometric method is one of the most commonly used approaches. Bibliometric analysis can study the contributions and collaboration of researchers, organizations, nations, and journals qualitatively and quantitatively and assess academic research's developmental status and new tendencies (Zhang et al., 2021). The bibliometric method can also consider conventional reviews, meta-analysis, or experimental studies, whose analysis cannot be performed using other approaches (Petersen et al., 2016; Björnmalm et al., 2017; Izci et al., 2021). Based on these advantages, this method is increasingly used to assess academic tendencies and develop guidelines. Hence, we used bibliometric analysis for evaluating and summarizing Nanoparticles-leukemia studies.

This study aimed to objectively delineate the knowledge field and new trends in Nanoparticles-leukemia research from the following four dimensions using two standard bibliometric tools, CiteSpace and VOSviewer. 1) We intended to quantify and identify general information in Nanoparticles-leukemia studies by studying yearly articles, journals, co-cited journals, nations, organizations, researchers, and co-cited researchers. 2) We strived to identify and study the top 100 most cited articles through co-citation reference analyses to assess the knowledge base of Nanoparticles-leukemia. 3) We aimed to identify the knowledge structure and hotspot evolution through keyword and co-citation reference burst analyses (Jiang et al., 2022). Meanwhile, under the analyses of the journals, countries, and keywords of the former top 100 articles and co-cited journals, combined with the analysis content of 3), the research content and possible new directions in the field of Nanoparticles-leukemia were further determined.

2 Materials and methods

2.1 Study design

This study used bibliometric analysis to study journal papers in Nanoparticles-leukemia. The study is divided into two parts: the first is the study of all the published articles in the Nanoparticles-leukemia field using WOSCC; the second is the analysis of the first 100 highly cited papers in the Nanoparticles-leukemia (Figure 1).

2.2 Eligibility criteria

Inclusion criteria included (Wu et al., 2021a) Basic scientific and clinical studies related to nanoparticles-leukemia (Wu et al., 2021b); Studies on diagnosis, treatment, prognosis or prevention related to nanoparticle-leukemia; and (Wu et al., 2022) Original articles and reviews that are closely related to nanoparticles-

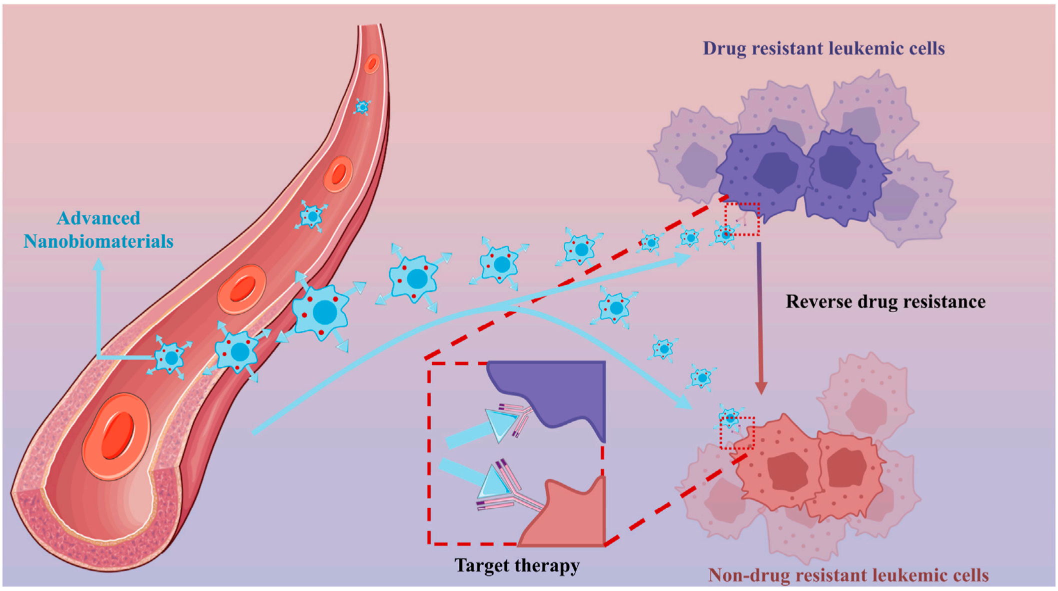

FIGURE 1
Advanced nanobiomaterials that can target therapy and reverse drug resistance.

leukemia. Exclusion criteria were (Wu et al., 2021a) Contents that are not related to nanoparticles-leukemia.

2.3 Data collection

Our team used the WoSCC database as it can offer comprehensive data required by the bibliometric software and is considered the most potent database. Data were acquired from the WoSCC database on 2 August 2022, and the relevant data can be found in Supplementary Materials 1. Our main search terms were "Nanoparticles" and "leukemia" (Lin et al., 2020c; Huang et al., 2022). For specific search terms, please refer to Supplementary Material 2. Part I: All articles relevant to the Nanoparticles-leukemia field were downloaded from WoSCC (Time span from the establishment of WoSCC to 2 August 2022). Part II: Two independent researchers manually screened the top 100 most-cited articles relevant to the Nanoparticles-leukemia field. Search conditions: The language was limited to English, and the type of article was restricted to articles and reviews. The retrieval outcomes were downloaded from the recorded contents of "Full Record and Cited References." (Zhang et al., 2021).

2.4 Data analysis and visualization

The most frequently utilized bibliometric programs are VOSViewer, CiteSpace, SCI2, NetDraw, and HistCite. There is no consensus on the best bibliographic approach. After careful consideration, this study utilized VOSviewer and CiteSpace.

Our team used VOSviewer1.6.15 to determine influential journals, co-cited journals, researchers, co-cited researchers, and associated knowledge graphs based on bibliographic information. Moreover, our team created keyword co-occurrence and clustering diagrams based on text data. First, the data were cleaned. For example, "nanoparticle" and "NPs" were unified to "nanoparticles" in the keyword analysis. The project's other thresholds (T) were set according to different circumstances and marked in the relevant tables and illustrations.

CiteSpace, proposed by Professor Chen Chaomei, is a bibliometric and visualization analysis tool suitable for investigating collaboration, key points, inner architectures, and latent tendencies in a specific field. Hence, our team used CiteSpace6.1.R2 to study and visualize the co-occurrence of nations and organizations, dual maps, high-frequency keyword trends, co-citation references, and citation bursts. The data were cleaned before the investigation; For example, articles from Taiwan were classified as China in the country analyses. The CiteSpace settings are stated below: time span, 1999–2022; years per slice, 1, pruning, minimum spanning tree and pruning sliced networks; selection standards, Top N = 50; and others followed the default.

Microsoft Office Excel 2022 was used to process the annual database of articles. Furthermore, the 2021 journal IF and JCR Division was obtained from the Web of Science in Cites Journal Citation Reports on 11 August 2022.

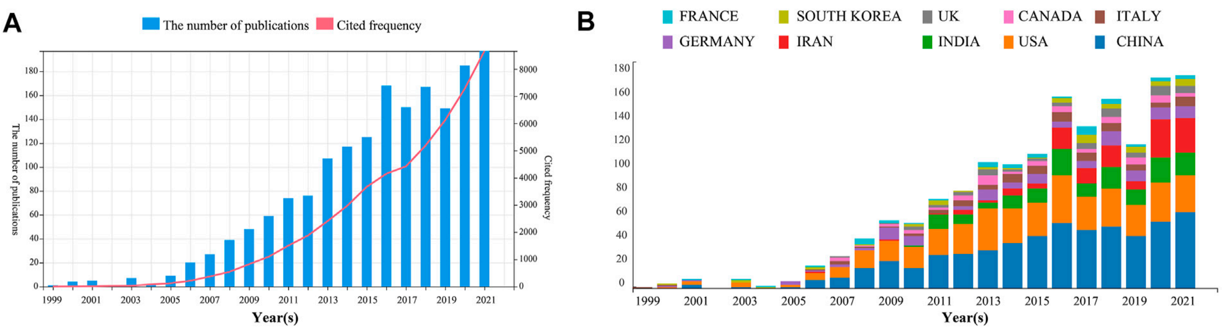

FIGURE 2
(A) Annual publication number and citation frequency of Nanoparticles-leukemia-related studies. **(B)** Composition ratio of the top 10 countries by the publication number.

TABLE 1 The top 10 journals of Nanoparticles-leukemia-related research.

RANK	Journal	N	(%)	IF(2021)	JCR division	Country
1	INTERNATIONAL JOURNAL OF NANOMEDICINE	76	4.14847161572052	7.033	Q1	New Zealand
2	JOURNAL OF CONTROLLED RELEASE	34	1.85589519650655	11.467	Q1	NETHERLANDS
3	MOLECULAR PHARMACEUTICS	33	1.80131004366812	5.364	Q1	United States
4	BIOSENSORS BIOELECTRONICS	32	1.74672489082969	12.545	Q1	United Kingdom
5	RSC ADVANCES	31	1.69213973799127	4.036	Q2	United Kingdom
6	INTERNATIONAL JOURNAL OF PHARMACEUTICS	30	1.63755458515284	6.51	Q1	NETHERLANDS
7	BIOMATERIALS	28	1.52838427947598	15.304	Q1	NETHERLANDS
8	NANOSCALE	26	1.41921397379913	8.307	Q1	United Kingdom
9	ACS NANO	24	1.31004366812227	18.027	Q1	United States
	ANALYTICAL CHEMISTRY	24	1.31004366812227	8.008	Q1	United States
	COLLOIDS AND SURFACES B BIOINTERFACES	24	1.31004366812227	5.999	Q2	NETHERLANDS
10	JOURNAL OF BIOMEDICAL NANOTECHNOLOGY	23	1.25545851528384	3.641	Q3	United States

3 Results

3.1 The annual growth trend and the number of annual cited departments

As per the data acquisition method, our team obtained 1825 articles upon limiting the types of research to articles and reviews and the language to English. Finally, 1825 eligible articles (Supplementary Material 1) published between 1999 and 2022 were selected. From Figure 2A, we can observe that references related to Nanoparticles-leukemia generally showed an increasing trend. It is worth noting that the citations of published articles in 2017–2021 have increased significantly. In addition, we also analyzed the top 10 countries with published articles (Figure 2B): America was leading in publishing articles until 2007 (1999–2007). Since 2008, China has shown great interest in Nanoparticles-leukemia, surpassing the United States to become the country with the most significant number of articles published.

3.2 Journals and co-cited journals

Our team utilized VOSviewer to analyze journals and co-cited journals to find the most influential and vital journals concerning the Nanoparticles-leukemia field. The results revealed that 1825 articles related to this field were published in 595 journals. The INTERNATIONAL JOURNAL OF NANOMEDICINE published the most articles (76, 4.1485%) (Table 1). About the country of the publication, US and United Kingdom accounted for more than half (7/12). Among the top 10 journals, nine were from the Q1 JCR division, and their Impact Factors (IF) exceeded 5 (Table 1). Among the 7,934 commonly cited journals, ten were cited > 1000 times. As presented in Table 2, BLOOD had the most significant

TABLE 2 The top 10 co-cited journals of Nanoparticles-leukemia-related research.

RANK	Co-cited journal	N	IF(2021)	JCR division	Country
1	BLOOD	2458	25.476	Q1	United States
2	JOURNAL OF CONTROLLED RELEASE	2038	11.467	Q1	NETHERLANDS
3	BIOMATERIALS	1845	15.304	Q1	NETHERLANDS
4	CANCER RESEARCH	1715	13.312	Q1	United States
5	PNAS	1524	12.779	Q1	United States
6	ACS NANO	1357	18.027	Q1	United States
7	JOURNAL OF THE AMERICAN CHEMICAL SOCIETY	1248	16.383	Q1	United States
8	NATURE	1123	69.504	Q1	United Kingdom
9	ADVANCED DRUG DELIVERY REVIEWS	1102	17.873	Q1	NETHERLANDS
10	INTERNATIONAL JOURNAL OF NANOMEDICINE	1096	7.033	Q1	New Zealand

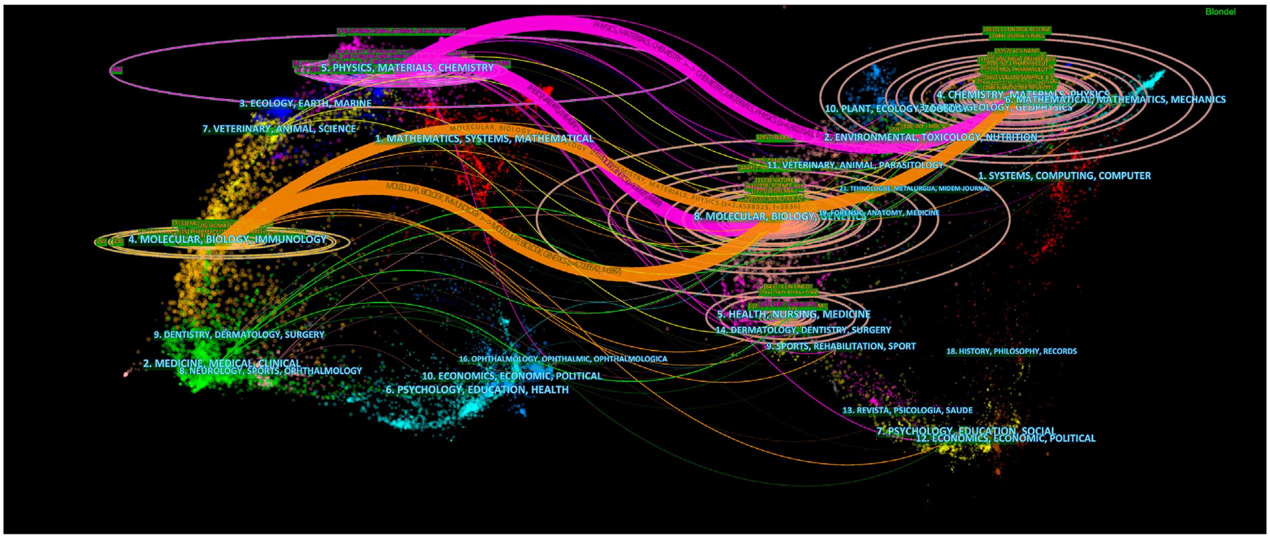

FIGURE 3
The dual-map overlay of journals related to Nanoparticles-leukemia research. Notes: The citing journals were on the left, the cited journals were on the right, and the colored path represents the citation relationship.

number of citations (N = 2,458), followed by JOURNAL OF CONTROLLED RELEASE (N = 2038) and BIOMATERIALS (N = 1845). It is not surprising that the journals with high co-citations are all from the Q1 JCR partition and all have high IF values. Furthermore, consistent with the analysis of high-volume journals, the US and United Kingdom accounted for more than half of the country's distribution, followed by NETHERLANDS.

The journal dual-map overlay represents the topic distribution status of journals (Figure 3). Citation journals are on the left, cited journals are on the right, and the color path indicates the citation relationship. Four primary citation path was determined, which meant that research published in Molecular/Biology/Immunology and Physics/Materials/chemistry journals was predominantly cited by a study published in Molecular/Biology/Immunology and Chemistry/Materials/Physics journals.

3.3 Country/region and institution

A total of 2,174 institutions from 80 countries have published 1825 articles. The most significant number of publications came from China (593, 24.14%), followed by the United States (419, 17.06%) and Japan (161,6.56%) (Table 3). As we have presented in Table 3, the United States, France, and Germany have made indelible contributions in the Nanoparticles-leukemia field (Figure 4A). In addition, according to link color, the United States (1999), Germany (1999), United Kingdom

TABLE 3 The top 10 countries/regions and institutions involved in Nanoparticles-leukemia-related research.

RANK	Country/ region	N	Percent(%)	Centrality	Institution	N	Percent(%)	Country/ region	Centrality
1	PEOPLES R CHINA	593	24.1449511400651	0.03	Southeast Univ	82	2.3768115942029	CHINA	0.1
2	USA	419	17.0602605863192	0.44	Chinese Acad Sci	40	1.15942028985507	CHINA	0.16
3	INDIA	161	6.55537459283388	0.15	Nanjing Univ	34	0.985507246376812	CHINA	0.03
4	IRAN	146	5.94462540716612	0.1	Islamic Azad Univ	29	0.840579710144928	IRAN	0.06
5	GERMANY	108	4.39739413680782	0.18	Ohio State Univ	25	0.72463768115942	United States	0.06
6	ITALY	80	3.25732899022801	0.12	Univ Florida	22	0.63768115942029	United States	0.03
7	CANADA	61	2.48371335504886	0.17	Hunan Univ	20	0.579710144927536	CHINA	0.01
8	SOUTH KOREA	50	2.03583061889251	0.02	Shandong Univ	19	0.550724637681159	CHINA	0.01
9	ENGLAND	49	1.99511400651466	0.12	Sun Yat Sen Univ	18	0.521739130434783	CHINA	0.14
10	FRANCE	45	1.83224755700326	0.19	Shanghai Jiao Tong Univ	18	0.521739130434783	CHINA	0.06
					Jilin Univ	18	0.521739130434783	CHINA	0.02

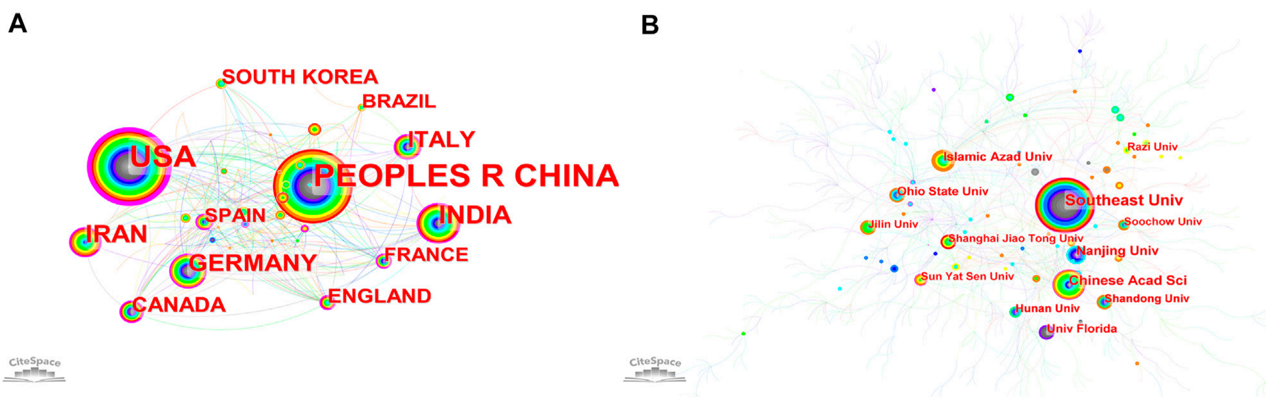

FIGURE 4
The co-occurrence map of **(A)** countries/regions and **(B)** institutions in Nanoparticles-leukemia research (T ≥ 18). Notes: The node's size reflects the co-occurrence frequencies, and the links indicate the co-occurrence relationships. The color of the node and line represent different years. Colors vary from grey to orange as time goes from 1999 to 2022; a node with a purple round means high betweenness centrality (>0.1).

(1999) and China (2000) were the first countries to conduct studies on Nanoparticles-leukemia field. We used minimal spanning tree pruning to clarify the net (Figure 4A). The standard map of unpruned countries contained 80 nodes and 272 links with a density of 0.0861, revealing active collaboration between diverse nations. For example, the United States cooperated with 42 nations, followed by Germany (n = 34) and China (n = 31).

More than half of the top 10 institutions were from China (6/11), followed by the United States (8/11) (Figure 4B) (Table 3). Southeast Univ (82,2.37%) published the most papers, followed by Chinese Acad Sci, Nanjing Univ, and Islamic Azad Univ (Table 3).

3.4 The highly productive author

Eight thousand seven hundred forty-one researchers participated in Nanoparticles-leukemia research. Furthermore, 11 published more than 14 papers. Wang, Xuemei wrote the most articles (n = 40), followed by Chen, Baoan (n = 38), Jiang, hui (n = 18) (Table 4). It includes authors who have authored more than five articles (T ≥ 5) (n = 80) to construct authors (Figure 5). Such knowledge graphs can present high-frequency researchers. As represented in Figure 5, Wang, Xuemei, Chen, Baoan, Jiang, hui, Gao, Feng and, Xia, guohua were closely linked and formed a group of authors with the reddest color, indicating that the group has made outstanding contributions in the field of Nanoparticles-leukemia. Zhang, Yu, and Gu, Ning constituted

TABLE 4 The top 10 authors and co-cited authors of Nanoparticles-leukemia-related research.

RANK	Author	Count	Citation	H-index
1	wang, xuemei	40	1706	64
2	chen, baoan	38	1516	44
3	jiang, hui	18	742	31
4	zhang, yu	18	463	36
5	parang, keykavous	16	342	36
6	gu, ning	15	437	56
7	lee, robert j.	15	837	64
8	tan, weihong	15	2053	129
9	zhang, wei	15	155	11
10	gao, feng	14	591	25
10	xia, guohua	14	334	25

the second largest group of authors. Lee, Robert j. and Zhang, Wei constituted the third largest group of authors.

3.5 Keyword co-occurrence, clustering, and development

VOSviewer was utilized to present keyword co-occurrence (Table 5; Figures 6, 7) and cluster analyses (Figure 6). An Overall 4,124 keywords were abstracted, of which 90 occurred over nine times. The keyword density map (Figure 6) can find high-frequency co-occurrence entries and unveil hotspots in specific academic fields. As presented in Table 5 and Figure 6, "drug delivery systems" is a critical term, appearing 128 times in total (5.58%), followed by apoptosis, AML, gold nanoparticles, cytotoxicity, anti-cancer, targeted therapy, and drug resistance.

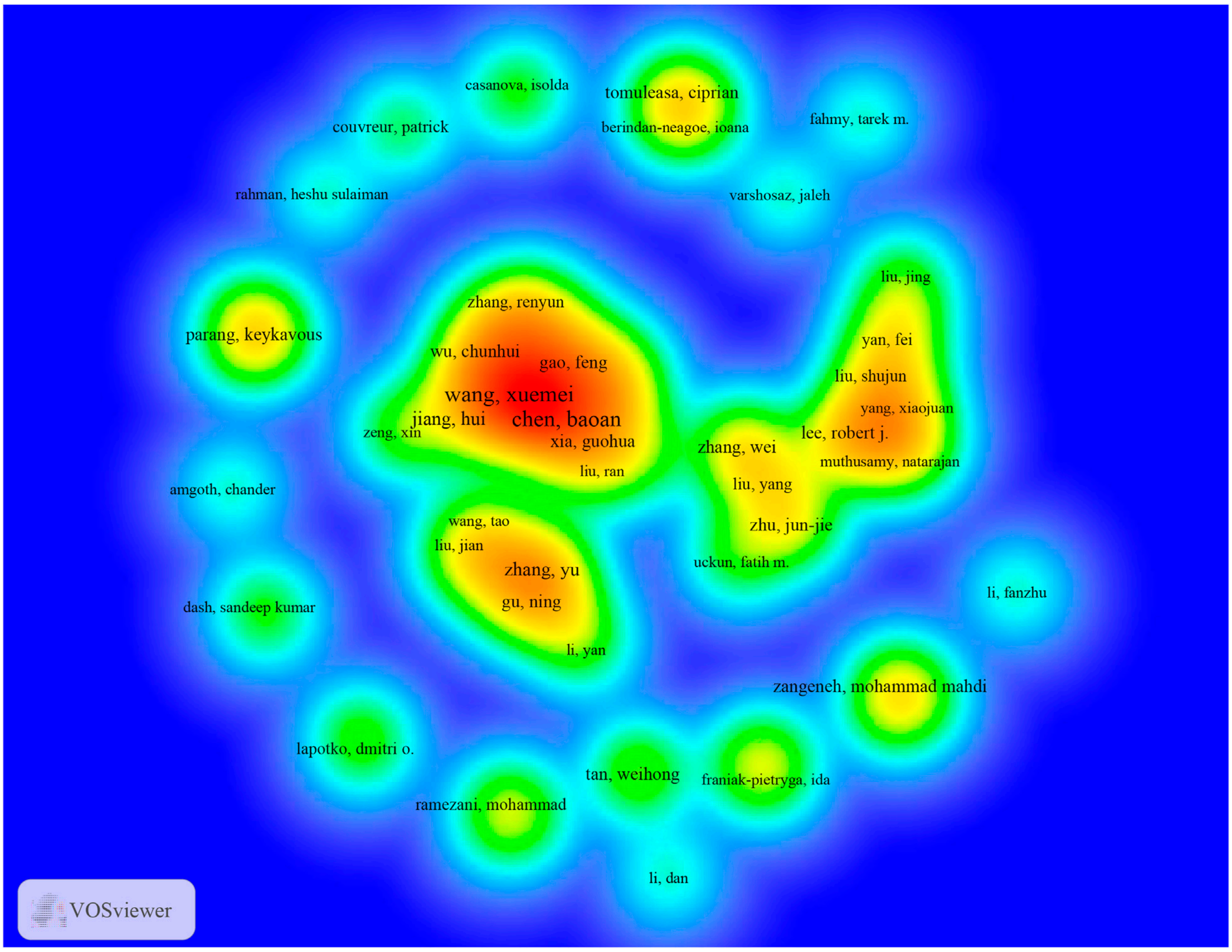

FIGURE 5
The density map of authors in Nanoparticles-leukemia research (T≥5). Notes: The size of the word, round, and the opacity of yellow are positively related to the publication frequency.

TABLE 5 The top 20 keywords of Nanoparticles-leukemia-related research.

RANK	Keyword	Occurrences	N(%)	RANK	Keyword	Occurrences	N(%)
1	nanoparticles	288	12.559965111208	11	nanomedicines	64	2.79110335804623
2	leukemia	226	9.85608373310074	12	liposomes	54	2.3549934583515
3	drug delivery systems	128	5.58220671609246	13	doxorubicin	47	2.0497165285652
4	apoptosis	107	4.66637592673354	14	aptamers	34	1.48277365896206
5	acute myeloid leukemia	85	3.70693414740515	15	magnetic nanoparticles	32	1.39555167902311
6	gold nanoparticles	81	3.53249018752726	16	chitosan nanoparticles	29	1.2647187091147
7	cytotoxicity	78	3.40165721761884	17	silver nanoparticles	28	1.22110771914522
8	anti-cancer	71	3.09638028783253	18	daunorubicin	27	1.17749672917575
9	targeted therapy	66	2.87832533798517	19	reactive oxygen species	26	1.13388573920628
10	drug resistance	64	2.79110335804623	20	chronic myeloid leukemia	24	1.04666375926734

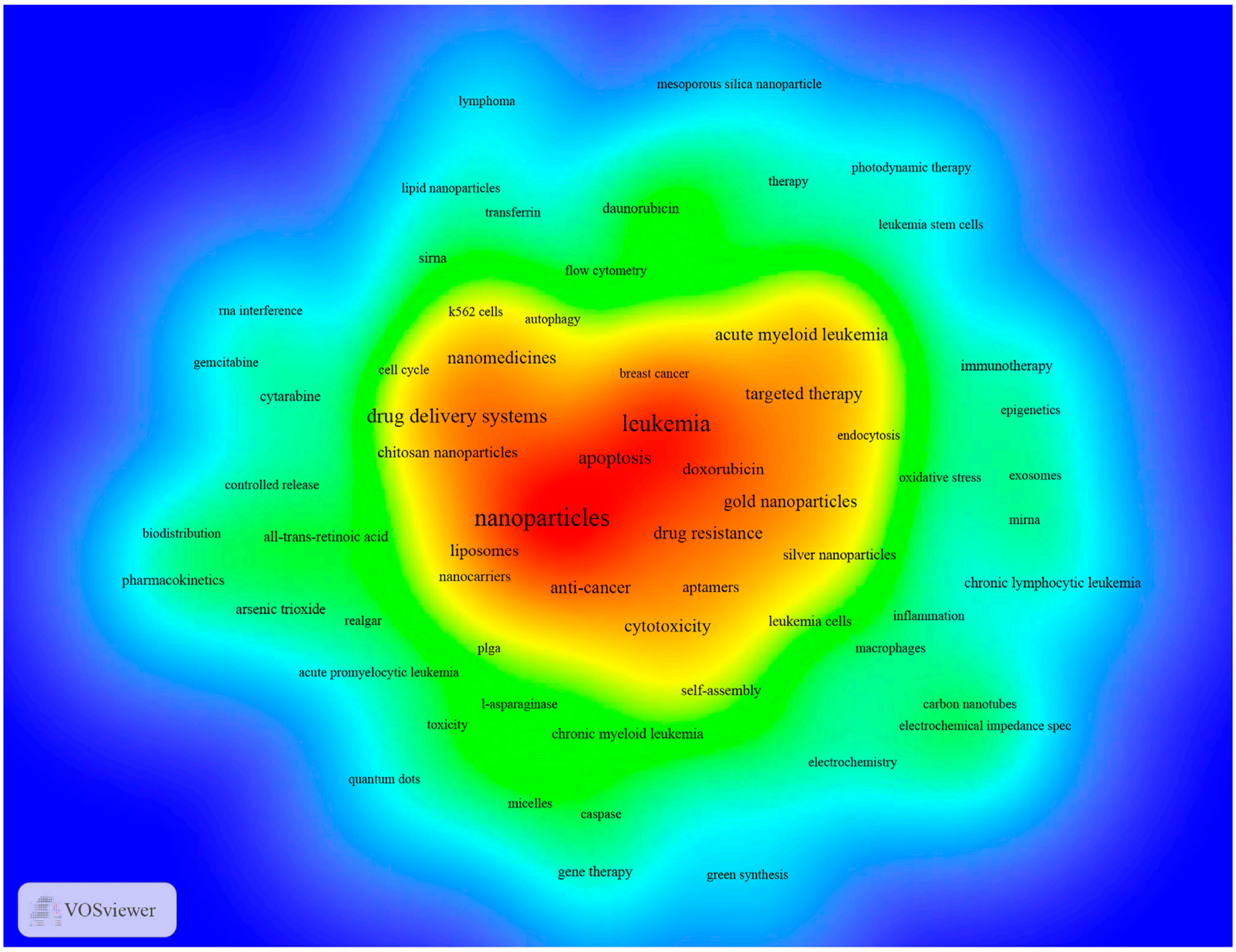

FIGURE 6
The density map of keywords in Nanoparticles-leukemia research (T≥9). Notes: The word's size, round, and red opacity positively relate to the co-occurrence frequency.

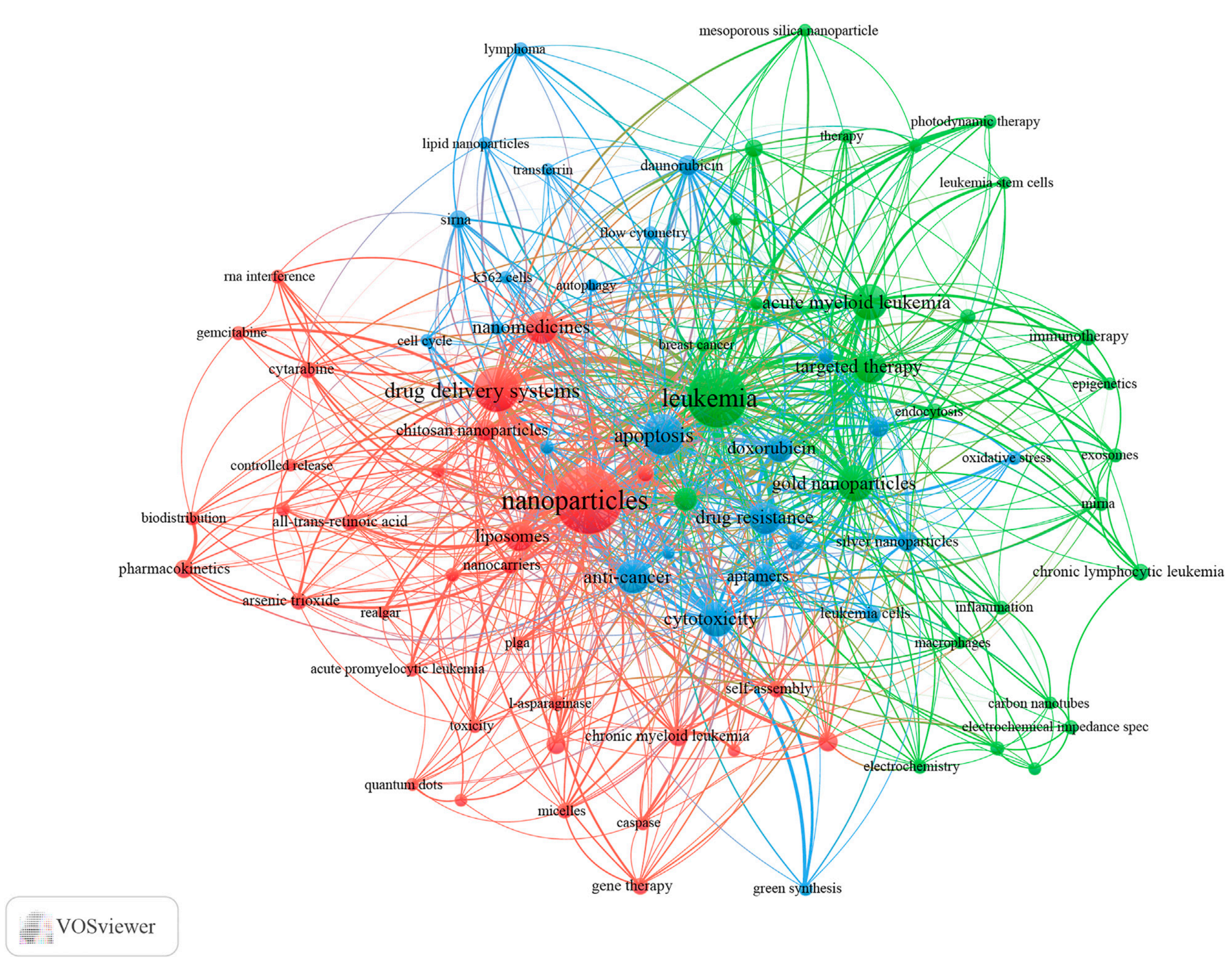

FIGURE 7
Keyword co-occurrence network and clusters in Nanoparticles-leukemia research (Notes: The size of the node and word reflects the co-occurrence frequencies, the link indicates the co-occurrence relationship, and the same color of the node represents the same cluster.

Cluster analysis can reveal the knowledge architecture of a research field (Karwath et al., 2021). The net was separated into three clusters according to the link strength of keyword co-occurrence (Figure 7). The keywords in each cluster were highly homogeneous. Cluster 1 (red) was the most significant cluster with 33 co-occurrence keywords, including nanoparticles, drug delivery systems, nanomedicines, liposomes, chitosan nanoparticles, and nanotechnology. The keywords of Cluster 1 were mainly related to nanoparticles used in the diagnosis and treatment of leukemia. Cluster 2 (green) was primarily associated with the type and treatment of leukemia and included 35 keywords, such as leukemia, acute myeloid leukemia, gold nanoparticles, targeted therapy, magnetic nanoparticles, chemotherapy, immunotherapy, and chronic lymphocytic leukemia. Cluster 3 (blue) focused on Specific molecular mechanisms and existing problems in the application of nanoparticles in leukemia and contained 25 keywords, including apoptosis, cytotoxicity, anti-cancer, drug resistance, doxorubicin, aptamers, silver nanoparticles, daunorubicin, reactive oxygen species, and siRNA.

The keyword with the most powerful citation burst was developed by CiteSpace and could present the citation status of high-frequency keywords. Keywords are sorted by citation strength, with dark blue representing how long the keyword has existed and red representing the time it has been cited in a burst. High-frequency keywords (Top 50) are presented in Figure 8. As per the results, the drug resistance with high citation strength (4.7) has been in a state of citation burst in recent years and may continue to become a research hotspot in the future.

3.6 Co-cited reference and reference burst

Our team used CiteSpace to identify the co-cited references (Table 6). results show that the top 10 co-cited

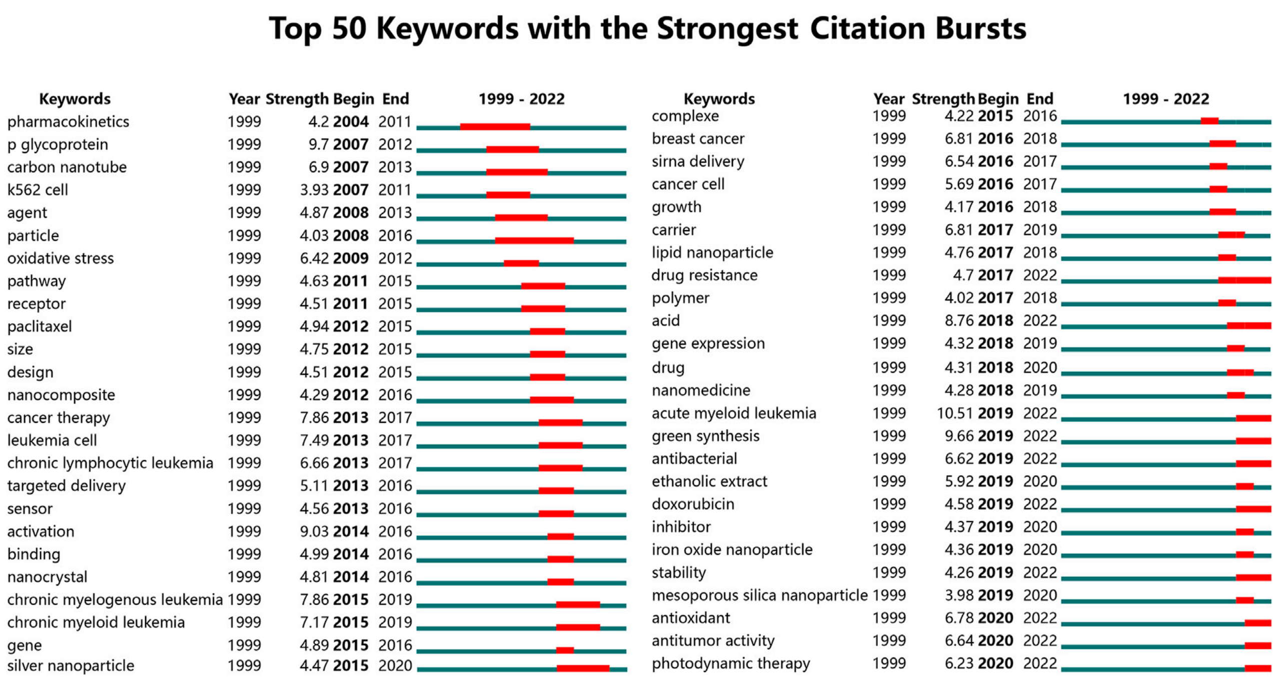

Keywords	Year	Strength	Begin	End	1999 - 2022	Keywords	Year	Strength	Begin	End	1999 - 2022
pharmacokinetics	1999	4.2	**2004**	2011		complexe	1999	4.22	**2015**	2016	
p glycoprotein	1999	9.7	**2007**	2012		breast cancer	1999	6.81	**2016**	2018	
carbon nanotube	1999	6.9	**2007**	2013		sirna delivery	1999	6.54	**2016**	2017	
k562 cell	1999	3.93	**2007**	2011		cancer cell	1999	5.69	**2016**	2017	
agent	1999	4.87	**2008**	2013		growth	1999	4.17	**2016**	2018	
particle	1999	4.03	**2008**	2016		carrier	1999	6.81	**2017**	2019	
oxidative stress	1999	6.42	**2009**	2012		lipid nanoparticle	1999	4.76	**2017**	2018	
pathway	1999	4.63	**2011**	2015		drug resistance	1999	4.7	**2017**	2022	
receptor	1999	4.51	**2011**	2015		polymer	1999	4.02	**2017**	2018	
paclitaxel	1999	4.94	**2012**	2015		acid	1999	8.76	**2018**	2022	
size	1999	4.75	**2012**	2015		gene expression	1999	4.32	**2018**	2019	
design	1999	4.51	**2012**	2015		drug	1999	4.31	**2018**	2020	
nanocomposite	1999	4.29	**2012**	2016		nanomedicine	1999	4.28	**2018**	2019	
cancer therapy	1999	7.86	**2013**	2017		acute myeloid leukemia	1999	10.51	**2019**	2022	
leukemia cell	1999	7.49	**2013**	2017		green synthesis	1999	9.66	**2019**	2022	
chronic lymphocytic leukemia	1999	6.66	**2013**	2017		antibacterial	1999	6.62	**2019**	2022	
targeted delivery	1999	5.11	**2013**	2016		ethanolic extract	1999	5.92	**2019**	2020	
sensor	1999	4.56	**2013**	2016		doxorubicin	1999	4.58	**2019**	2022	
activation	1999	9.03	**2014**	2016		inhibitor	1999	4.37	**2019**	2020	
binding	1999	4.99	**2014**	2016		iron oxide nanoparticle	1999	4.36	**2019**	2020	
nanocrystal	1999	4.81	**2014**	2016		stability	1999	4.26	**2019**	2022	
chronic myelogenous leukemia	1999	7.86	**2015**	2019		mesoporous silica nanoparticle	1999	3.98	**2019**	2020	
chronic myeloid leukemia	1999	7.17	**2015**	2019		antioxidant	1999	6.78	**2020**	2022	
gene	1999	4.89	**2015**	2016		antitumor activity	1999	6.64	**2020**	2022	
silver nanoparticle	1999	4.47	**2015**	2020		photodynamic therapy	1999	6.23	**2020**	2022	

FIGURE 8
Top 50 keywords with the most vigorous citation burst r (sorted by the strength). Notes: The Blue bars mean the published reference; the red bars mean citation burstiness.

TABLE 6 Top 10 co-cited references for Nanoparticles-leukemia-related research.

RANK	ID	Title	Journal	Co-citation	Year	type of article
1	Peer, Dan	Nanocarriers as an emerging platform for cancer therapy	NATURE NANOTECHNOLOGY	54	2007	review
2	Shangguan, Dihua	Aptamers evolved from live cells as effective molecular probes for cancer study	PNAS	48	2006	Article
3	Davis, Mark E.	Nanoparticle therapeutics: an emerging treatment modality for cancer	NATURE REVIEWS DRUG DISCOVERY	41	2008	review
4	Brigger, I	Nanoparticles in cancer therapy and diagnosis	ADVANCED DRUG DELIVERY REVIEWS	38	2002	review
5	Petros, Robby A	Strategies in the design of nanoparticles for therapeutic applications	NATURE REVIEWS DRUG DISCOVERY	30	2010	review
6	Connor, EE	Gold nanoparticles are taken up by human cells but do not cause acute cytotoxicity	SMALL	29	2005	Article
7	Huang, Xiaomeng	Targeted Delivery of microRNA-29b by Transferrin-Conjugated Anionic Lipopolyplex Nanoparticles:A Novel Therapeutic Strategy in Acute Myeloid Leukemia	CLINICAL CANCER RESEARCH	29	2013	Article
8	Blanco, Elvin	Principles of nanoparticle design for overcoming biological barriers to drug delivery	NATURE BIOTECHNOLOGY	29	2015	Article
9	Yechezkel, Barenholz	Doxil®--the first FDA-approved nano-drug: lessons learned	JOURNAL OF CONTROLLED RELEASE	24	2012	review
10	Jinjun Shi	Cancer nanomedicine: progress, challenges and opportunities	NATURE REVIEWS CANCER	23	2017	review

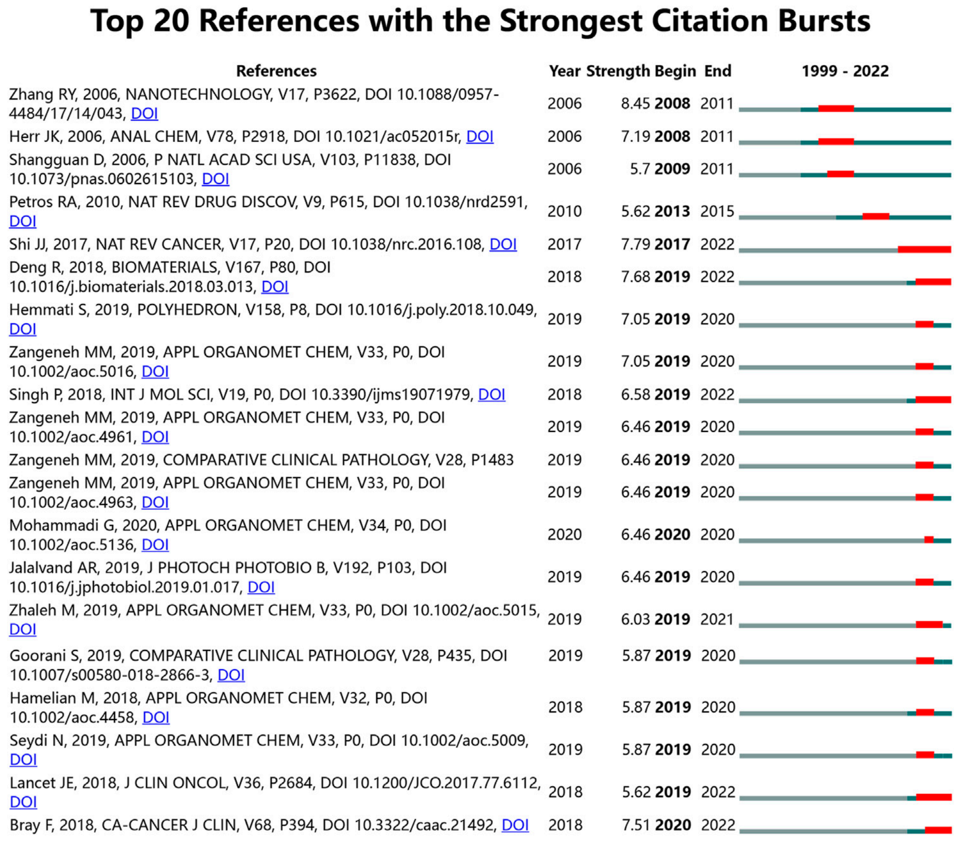

Top 20 References with the Strongest Citation Bursts

References	Year	Strength	Begin	End	1999 - 2022
Zhang RY, 2006, NANOTECHNOLOGY, V17, P3622, DOI 10.1088/0957-4484/17/14/043, DOI	2006	8.45	**2008**	2011	
Herr JK, 2006, ANAL CHEM, V78, P2918, DOI 10.1021/ac052015r, DOI	2006	7.19	**2008**	2011	
Shangguan D, 2006, P NATL ACAD SCI USA, V103, P11838, DOI 10.1073/pnas.0602615103, DOI	2006	5.7	**2009**	2011	
Petros RA, 2010, NAT REV DRUG DISCOV, V9, P615, DOI 10.1038/nrd2591, DOI	2010	5.62	**2013**	2015	
Shi JJ, 2017, NAT REV CANCER, V17, P20, DOI 10.1038/nrc.2016.108, DOI	2017	7.79	**2017**	2022	
Deng R, 2018, BIOMATERIALS, V167, P80, DOI 10.1016/j.biomaterials.2018.03.013, DOI	2018	7.68	**2019**	2022	
Hemmati S, 2019, POLYHEDRON, V158, P8, DOI 10.1016/j.poly.2018.10.049, DOI	2019	7.05	**2019**	2020	
Zangeneh MM, 2019, APPL ORGANOMET CHEM, V33, P0, DOI 10.1002/aoc.5016, DOI	2019	7.05	**2019**	2020	
Singh P, 2018, INT J MOL SCI, V19, P0, DOI 10.3390/ijms19071979, DOI	2018	6.58	**2019**	2022	
Zangeneh MM, 2019, APPL ORGANOMET CHEM, V33, P0, DOI 10.1002/aoc.4961, DOI	2019	6.46	**2019**	2020	
Zangeneh MM, 2019, COMPARATIVE CLINICAL PATHOLOGY, V28, P1483	2019	6.46	**2019**	2020	
Zangeneh MM, 2019, APPL ORGANOMET CHEM, V33, P0, DOI 10.1002/aoc.4963, DOI	2019	6.46	**2019**	2020	
Mohammadi G, 2020, APPL ORGANOMET CHEM, V34, P0, DOI 10.1002/aoc.5136, DOI	2020	6.46	**2020**	2020	
Jalalvand AR, 2019, J PHOTOCH PHOTOBIO B, V192, P103, DOI 10.1016/j.jphotobiol.2019.01.017, DOI	2019	6.46	**2019**	2020	
Zhaleh M, 2019, APPL ORGANOMET CHEM, V33, P0, DOI 10.1002/aoc.5015, DOI	2019	6.03	**2019**	2021	
Goorani S, 2019, COMPARATIVE CLINICAL PATHOLOGY, V28, P435, DOI 10.1007/s00580-018-2866-3, DOI	2019	5.87	**2019**	2020	
Hamelian M, 2018, APPL ORGANOMET CHEM, V32, P0, DOI 10.1002/aoc.4458, DOI	2018	5.87	**2019**	2020	
Seydi N, 2019, APPL ORGANOMET CHEM, V33, P0, DOI 10.1002/aoc.5009, DOI	2019	5.87	**2019**	2020	
Lancet JE, 2018, J CLIN ONCOL, V36, P2684, DOI 10.1200/JCO.2017.77.6112, DOI	2018	5.62	**2019**	2022	
Bray F, 2018, CA-CANCER J CLIN, V68, P394, DOI 10.3322/caac.21492, DOI	2018	7.51	**2020**	2022	

FIGURE 9
Top 20 references with the most powerful citation bursts (sorted by the strength). Notes: The Blue bars mean the published reference; the red bars mean citation burstiness.

references were co-cited ≥ 29 times, three of which were co-cited more than 40 times. The most frequently co-cited reference is a paper written by Peer, Dan, et al. published in NATURE NANOTECHNOLOGY in 2007, entitled "Nanocarriers as an emerging platform for cancer therapy" (Peer et al., 2007), followed by an article entitled "Aptamers evolved from live cells as effective molecular probes for cancer study" (Shangguan et al., 2006). Reference with citation burst is the references often cited over time. In CiteSpace, our team set the burst duration to ≥ 2 years. We identified 99 references with the total citations and selected the top 20 references as the object of analysis. Figure 9 shows that the top 20 burst references were published after 1999 and had high citation outbreaks in 2017–2022. Notably, by 2022, 8 references (32%) were in a state of citation burst. The most substantial citation burst reference was "Synergistic enhancement effect of magnetic nanoparticles on anti-cancer drug accumulation in cancer cells." Zhang, Renyun, and others have maintained a high citation rate since their publication in NANOTECHNOLOGY (Zhang et al., 2006).

3.7 Analysis of journal, countries, and keywords of the top 100 most-cited articles

The top 100 most-cited articles were defined as cited articles with a high correlation with Nanoparticles-leukemia. We analyzed the journals and co-cited journals of the top 100 most-cited articles. (Table 7, Table 8, and Figure 10). Fifteen journals have published more than two articles, of which ACS Nano (n = 10), ANALYTICAL CHEMISTRY (n = 8), and CLINICAL CANCER RESEARCH (n = 5) rank top 3—followed by FRONTIERS IN BIOENGINEERING AND BIOTECHNOLOGY (n = 4).

In the co-cited journals, PROCEEDINGS OF THE NATIONAL ACADEMY OF SCIENCES OF THE UNITED STATES OF AMERICA (n = 233) was the most common, followed by CANCER RESEARCH (n = 217), JOURNAL OF CONTROLLED RELEASE (n = 202), and JOURNAL OF THE AMERICAN CHEMICAL SOCIETY (n = 176). Interestingly, in the top 100 most-cited articles field, FRONTIERS IN BIOENGINEERING AND BIOTECHNOLOGY is not only a

TABLE 7 The top 10 journals of top100 cited articles research.

RANK	Journal	N	IF(2020)	JCR division	Country
1	ACS NANO	10	18.027	Q1	United States
2	ANALYTICAL CHEMISTRY	8	8.008	Q1	United States
3	ADVANCED DRUG DELIVERY REVIEWS	5	17.873	Q1	NETHERLANDS
3	BIOMATERIALS	5	15.304	Q1	NETHERLANDS
4	FRONTIERS IN BIOENGINEERING AND BIOTECHNOLOGY	4	6.064	Q1	NETHERLANDS
5	BIOSENSORS BIOELECTRONICS	3	12.545	Q1	United Kingdom
5	SMALL	3	15.153	Q1	GERMANY
6	INTERNATIONAL JOURNAL OF NANOMEDICINE	2	7.033	Q1	New Zealand
6	JOURNAL OF THE AMERICAN CHEMICAL SOCIETY	2	16.383	Q1	United States
6	MOLECULAR THERAPY	2	12.91	Q1	United States
	NANO LETTERS	2	12.262	Q1	United States
	NANOMEDICINE	2	6.096	Q1	United Kingdom
	NANOMEDICINE NANOTECHNOLOGY BIOLOGY AND MEDICINE	2	6.458	Q2	United States
	PNAS	2	12.779	Q1	United States
	SCIENTIFIC REPORTS	2	4.996	Q2	United Kingdom

high publication volume journal but also a high co-citation journal. Roughly consistent with the overall field analysis, journal analysis of the top 100 most-cited articles identified three primary orange citation paths, which suggests that research published in the Physics/Materials/chemistry and Molecular/Biology/Immunology journal is predominantly cited by a study published in the Molecular/Biology/Genetics and Chemistry/Materials/Physics journal.

We also analyzed the countries with the top 100 most-cited articles (Figure 11). United States ($n = 54$) was the nation with the most papers, followed by China ($n = 29$). China has frequent academic exchanges with the United States, while the United States has ties with ten countries, including CHINA, JAPAN, and GERMANY. To further analyze the development content and trend of the Nanoparticles-leukemia field, we analyzed the keywords of the top 100 articles. The keyword of the top 20 (Table 9) coincided with the top 20 (Table5) in the Nanoparticles-leukemia field, such as targeted therapy, nanoparticles, leukemia, aptamers, drug-resistance, and drug delivery systems, doxorubicin, cytotoxicity, apoptosis, and acute myeloid leukemia. This shows that the primary research content of Nanoparticles-leukemia is related to the above keywords. The net was separated into three clusters according to the link strength of keyword co-occurrence (Figure 12). Cluster 1 (red) was the most significant cluster with 49 co-occurrence keywords, including nanoparticles, acute myeloid-leukemia, drug delivery system, doxorubicin, and aptamers. The theme of Cluster 1 is highly correlated with the design strategy of the nano drug delivery system. Cluster 2 (green) was primarily associated with the specific mechanism and possible hindrance of the anti-cancer effect of nano-drugs and included 16 terms, such as anti-cancer, apoptosis, cytotoxicity, damage, drug resistance, therapy, and toxicity. Cluster 3 (blue) focuses on immunotherapy and targeted therapy related to the nano-drug delivery system and contains 15 terms, such as folate receptor, gene therapy, ligands, liposomal doxorubicin, liposomes, molecular recognition, t-cells, targeted therapy, and tumor-cells.

4 Discussion

4.1 General information

According to data from the WoSCC database, as of 2 August 2022, 8,741 authors from 2,174 institutions in 80 countries have published 1825 studies on Nanoparticles-leukemia in 476 academic journals.

The annual output change and cited frequency are essential indicators of the development trends in this field. In the included literature, Luisa T ondelli et al. constructed polymer nanospheres that can increase leukemia cells' uptake of antisense oligonucleotides (Tondelli et al., 1999). Since then, related articles in the field of Nanoparticles-leukemia have shown an upward trend (Figure 2). Nanoparticles-leukemia-related articles can be separated into 3 phases, namely "budding," "steady growth," and "fast developmental process." "Budding" (1999–2009): The concept of the effect of Nanoparticles on leukemia research is beginning to appear. In these 11 years, no more than 50 articles were published each year, and the annual citation frequency was less than 1000. "Steady growth" (2010–2016): Nanoparticles-leukemia received more attention from scientists, and the output every year increased stably. "Fast developmental process" (2017 to present): At this stage, not only did the number of articles gradually increase steadily but also the citation frequency showed a turning rise, indicating that Nanoparticles-leukemia research has been paid

TABLE 8 The top co-cited 20 journals of top100 cited articles research.

RANK	Co-cited journal	Citations	IF(2021)	JCR division	Country
1	PNAS	233	12.779	Q1	United States
2	CANCER RESEARCH	217	13.312	Q1	United States
3	JOURNAL OF CONTROLLED RELEASE	202	11.467	Q1	NETHERLANDS
4	JOURNAL OF THE AMERICAN CHEMICAL SOCIETY	176	16.383	Q1	United States
5	BIOMATERIALS	156	15.304	Q1	NETHERLANDS
6	ACS NANO	143	18.027	Q1	United States
7	BLOOD	141	25.476	Q1	United States
8	SCIENCE	140	63.714	Q1	United States
9	NATURE	139	69.504	Q1	United Kingdom
10	ANALYTICAL CHEMISTRY	131	8.008	Q1	United States
11	ADVANCED DRUG DELIVERY REVIEWS	125	17.873	Q1	NETHERLANDS
12	JOURNAL OF BIOLOGICAL CHEMISTRY	116	5.486	Q2	AUSTRALIA
13	ANGEWANDTE CHEMIE-INTERNATIONAL EDITION	108	16.823	Q1	GERMANY
14	NANO LETTERS	102	12.262	Q1	United States
15	BIOCONJUGATE CHEMISTRY	92	6.069	Q1	United States
16	NATURE BIOTECHNOLOGY	74	68.164	Q1	United States
17	SMALL	70	15.153	Q1	GERMANY
18	CLINICAL CANCER RESEARCH	69	13.801	Q1	United States
19	LANGMUIR	65	4.331	Q2	United States
20	NATURE REVIEWS CANCER	57	69.8	Q1	United Kingdom
21	MOLECULAR PHARMACEUTICS	56	5.364	Q1	United States
22	NATURE NANOTECHNOLOGY	56	40.523	Q1	United Kingdom
23	NATURE REVIEWS DRUG DISCOVERY	54	112.288	Q1	United Kingdom
24	ADVANCED MATERIALS	52	32.086	Q1	GERMANY
25	JOURNAL OF CLINICAL ONCOLOGY	52	50.717	Q1	United States
26	CELL	48	66.85	Q1	United States
27	NEW ENGLAND JOURNAL OF MEDICINE	48	176.079	Q1	United States
28	INTERNATIONAL JOURNAL OF CANCER	43	7.033	Q2	NEW ZEALAND
29	NANOMEDICINE	42	6.096	Q1	United Kingdom
30	FRONTIERS IN BIOENGINEERING AND BIOTECHNOLOGY	40	6.064	Q1	NETHERLANDS

more attention increasingly by researchers and developed rapidly. Furthermore, the growth trends in this field are promising.

The analysis of journals and co-cited journals (Tables 1, 2) revealed that the INTERNATIONAL JOURNAL OF NANOMEDICINE published the most significant number of studies and obtained more co-cited references in the Nanoparticles-leukemia field. This means that the journal has a strong influence in the field of nano-leukemia. The dual-map overlay of journals represents their theme distributional status (Figure 3). This overlay exhibited four central citation paths from Molecular/Biology/Immunology and Physics/Materials/chemistry journals to Molecular/Biology/Genetic and Chemistry/Materials/Physics co-cited journals. Concurrently, journals at the Q1 JCR division with high IF took up half of the top 10 journals (75%) and co-cited journals (100%), indicating that these journals publish studies on and are vital for Nanoparticles-leukemia associated research. The analysis of countries/institutions related to Nanoparticles-leukemia studies shows (Table 3; Figure 4) that China, the United States, and India are the top three producers.

However, the United States, Germany, France, and Canada could potentially induce revolutionary breakthroughs. Italy, the United States, Germany, and South Korea were the first nations to carry out Nanoparticles-leukemia-related studies, followed by China and France. This shows that the United States has always been fruitful and influential in studying Nanoparticles-leukemia. Notably, China started relatively late but has become one of the most productive contributors in recent years. This may be related to the increased attention due to the high incidence and mortality of Leukemia in China.

Furthermore, cooperation between diverse nations, particularly America, is very active, revealing that research on Nanoparticles-leukemia has aroused widespread concern worldwide, and the United States is the primary cooperation center. The top 11 organizations come from three nations: 8 out of 11 are from

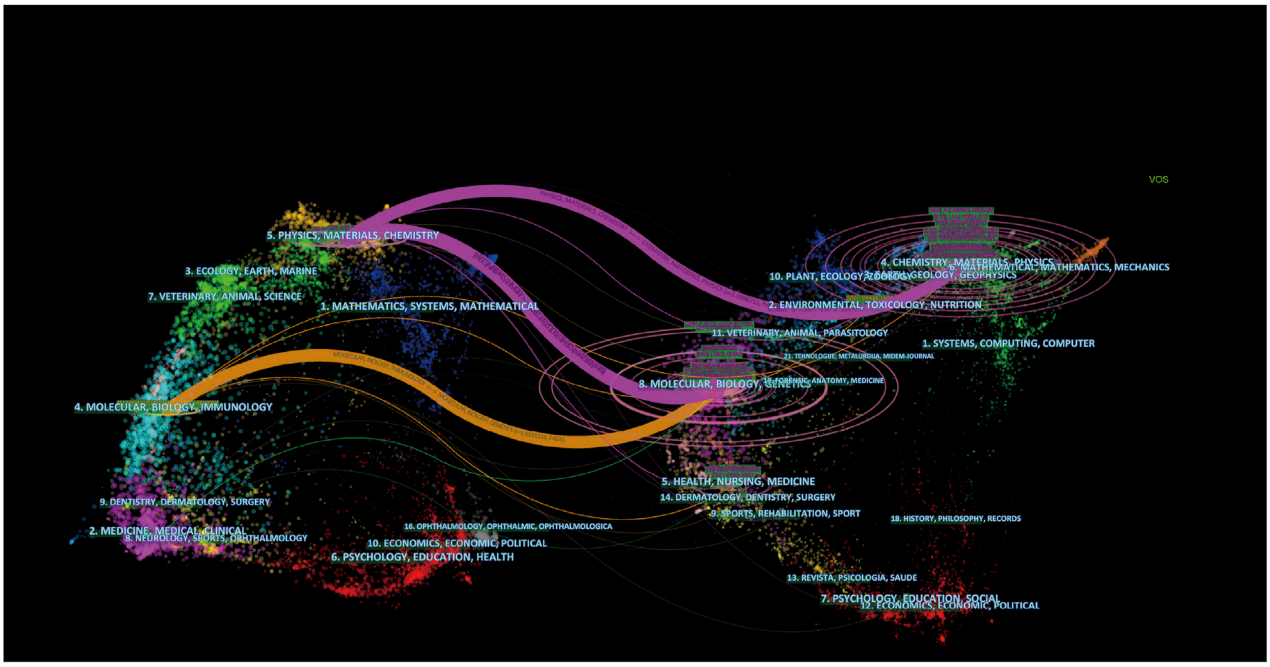

FIGURE 10
The dual-map overlay of journals related to the top 100 most cited references in Nanoparticles-leukemia research. Notes: The citing journals were on the left, the cited journals were on the right, and the colored path represents the citation relationship.

China, 2 out of 11 are from the United States, and one is from Iran. Moreover, our team discovered fruitful collaboration among Southeast Univ, Chinese Acad Sci, Nanjing Univ, and other organizations, which has contributed remarkably to the field of Nanoparticles-leukemia.

Highlighting the contributions of active scholars, such as those who co-appear or co-cite articles in a particular field, can assist researchers in moving forward along this path and offer more directions and guidance. Here (Table 4; Figures 4, 5), wang and Xue mei published the most papers. Additionally, maps of researchers and co-cited researchers provide data regarding the underlying cooperators and powerful academic teams. Scholars have actively collaborated within and between organizations in Nanoparticles-leukemia, particularly among researchers. Overall, 20 scholars from 4 organizations published a critical review titled “Targeted Delivery of microRNA-29b by Transferrin-Conjugated Anionic Lipopolyplex Nanoparticles: A Novel Therapeutic Strategy in Acute Myeloid Leukemia” (Huang et al., 2013). This suggests that these powerful groups might be the underlying cooperators of scholars.

4.2 Knowledge base

The co-cited references have been cited together in other articles. Nevertheless, the knowledge base is a pool of co-cited references cited by relevant academic teams, which is not entirely equal to frequently cited references. In the bibliometric analyses, In the Nanoparticles-leukemia field, there are many overlapping parts in the top 10 high co-cited articles and the top 20 citation burst articles (Table 6; Figure 9). This shows that the knowledge base constructed in this study has a substantial reference value.

In 2007, NATURE NANOTECHNOLOGY published the most co-cited Nanoparticles-leukemia studies by Peer, Dan, et al. (n = 54) (Peer et al., 2007). This article reviews the different mechanisms of targeted delivery of nanomedicines to tumors and reports the research progress of nano-based platforms for treating leukemia. Shangguan, Dihua et al. wrote the second co-citation research on PROCEEDINGS OF THE NATIONAL ACADEMY OF SCIENCES OF THE UNITED STATES OF AMERICA (Shangguan et al., 2006). This study developed a strategy by which a set of aptamers for specific recognition of leukemic cells could be generated, and it is also a Citation Burst article (Strength = 5.7, duration = 2009–2011). Davis, Mark E. et al. (2008) published the third co-cited article in the NATURE REVIEWS DRUG DISCOVERY. (Davis et al., 2008). Unlike the most co-cited reference, this review mainly summarized the application of nanoparticles in preclinical and clinical studies, focusing on the application of nanoparticles in leukemia. The fourth co-cited paper was published in the Nanoparticles in cancer therapy and diagnosis by Brigger et al. (2002). In 2002. This review provides an update on using conventional or long-cycle nanoparticles to target tumors. In 2015, Petros, Robby A

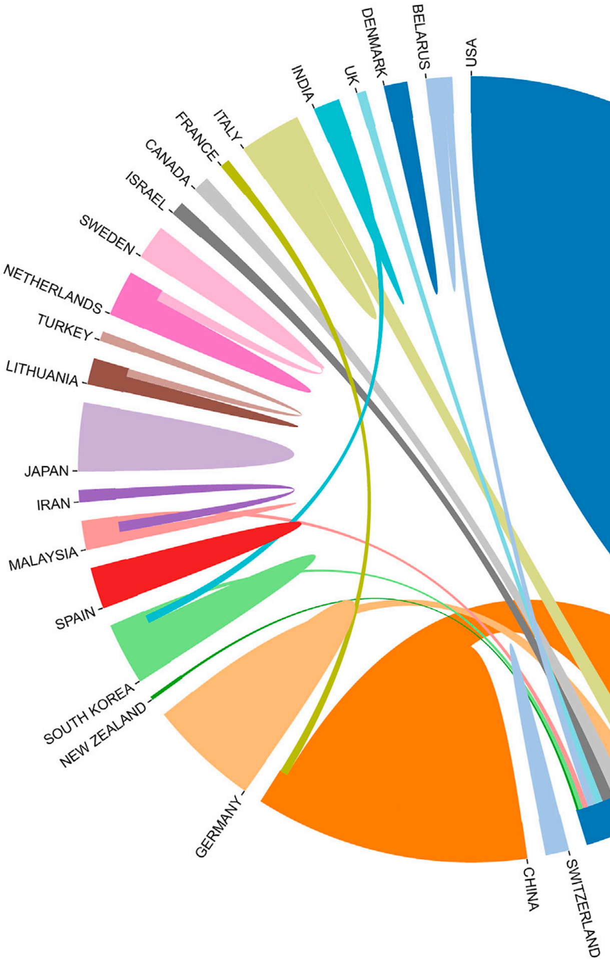

FIGURE 11
Country-to-country relations of Top 100 Most-cited Articles.

TABLE 9 The top 20 keywords of top100 cited articles research.

RANK	Keyword	Occurrences	N(%)	RANK	Keyword	Occurrences	N(%)
1	nanoparticles	32	7.35632183908046	11	in-vivo	10	2.29885057471264
2	leukemia	25	5.74712643678161	12	targeted therapy	8	1.83908045977011
3	expression	12	2.75862068965517	13	cancer-cells	7	1.60919540229885
4	cells	11	2.52873563218391	14	doxorubicin	7	1.60919540229885
5	delivery	11	2.52873563218391	15	aptamers	6	1.37931034482759
6	gold nanoparticles	11	2.52873563218391	16	carbon nanotubes	6	1.37931034482759
7	therapy	11	2.52873563218391	17	cytotoxicity	6	1.37931034482759
8	acute myeloid-leukemia	10	2.29885057471264	18	mechanisms	6	1.37931034482759
9	drug-delivery	10	2.29885057471264	19	drug-resistance	6	1.37931034482759
10	in-vitro	10	2.29885057471264	20	photothermal therapy	6	1.37931034482759

et al. reported the fifth co-cited study in the NATURE REVIEWS DRUG DISCOVERY. (Petros and DeSimone, 2010); this review highlights recent advances that are important for the rational design of such nanoparticles and discusses the challenges to realizing their potential and it is also a Citation Burst article (Strength = 5.62, duration =

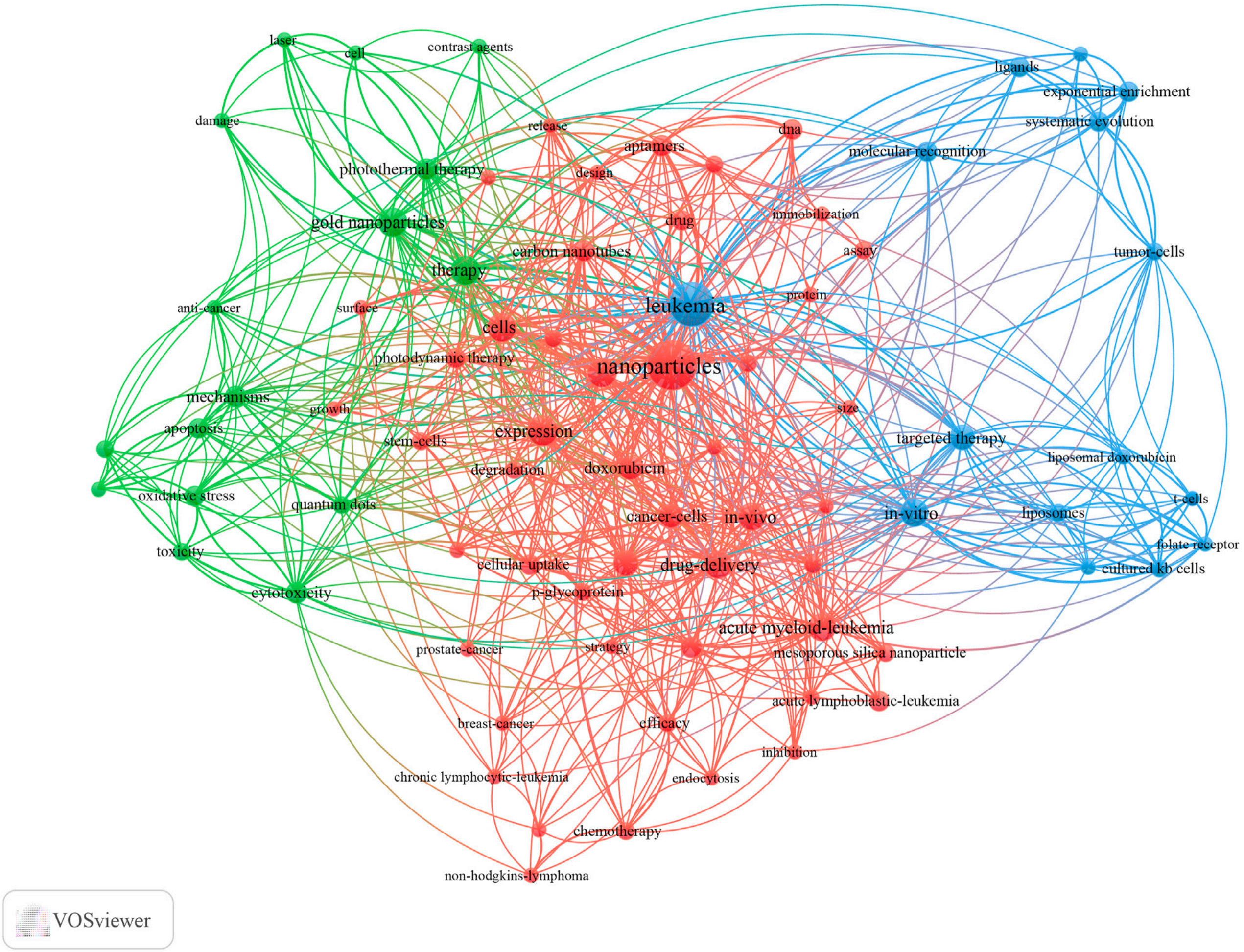

FIGURE 12
Keyword co-occurrence network and clusters in Nanoparticles-leukemia research. Notes: The size of the node and word reflects the co-occurrence frequencies, the link indicates the co-occurrence relationship, and the same color of the node represents the same cluster.

2013–2015). In the sixth article, published by Connor et al. (2005). In 2005, gold nanoparticles are studied in this paper. Although gold nanoparticles can be ingested by leukemia cells and cause cytotoxicity, they can be non-toxic by surface modification. In 2013, CLINICAL CANCER RESEARCH published the seventh co-citation study by Huang et al. (2013). The research team mainly used transferrin-conjugated anionic lipid polymers to construct composite nano-drugs for the treatment of leukemia, which carried a mimic of microRNA-29b. The eighth co-cited article was written by Blanco, Elvin, et al. in NATURE BIOTECHNOLOGY, 2015. (Blanco et al., 2015). This paper mainly reviews the physical obstacles in nanoparticle transport and the solutions to overcome the biological obstacles. It is also explained that the future research focus of nanoparticles in leukemia is to use a nanoparticles-based platform for gene delivery. Notably, it is a Citation Burst article (Strength = 5.33, duration = 2018–2019). In 2012, the JOURNAL OF CONTROLLED RELEASE published the ninth co-citation research completed by Yechezkel, Barenholz. This review summarizes the history and scientific viewpoints of the development of Doxil, as well as the experiences and lessons learned from its development, and discusses its application in leukemia (Zucker et al., 2012). In 2017, the 10th co-cited paper in the NATURE REVIEWS CANCER by Jinjun Shi and others. This review summarizes the historical schedule of significant developments in cancer nanomedicine, predicts the potential markers of the EPR effect and nano therapy effect, and summarizes the clinical application of nanomedicine in leukemia (Deng et al., 2018).

Overall, the top 10 co-cited papers highlighted reviews (six reviews completed in a different year), different nanoparticles used in the treatment of leukemia (Small-Molecule Drugs, Small-Molecule Drugs, Nanoparticles for Gene Therapy, Nanoparticles for Combined Therapy, and Nanoparticles for Photodynamic Therapy), the status of leukemia treatment (Chemotherapy, Radiation Therapy, Radiation Therapy, Targeted Therapy) and Obstacles of nano-drugs in the treatment of leukemia (safety, targeting, inadequate drug release response, drug resistance).

4.3 Hot topic development, knowledge structure, and emerging topics

In bibliometric analysis, keyword/term co-occurrence (Table 5; Figure 6, and Figure 7) can indicate a hot spot in an academic field, and the keyword citation burst (Figure 8) can display the evolutionary process of novel hot spots. High-frequency keywords (Table 5, 9 and Figure 7) include targeted therapy, nanoparticles, leukemia, aptamers, drug resistance, drug delivery systems, doxorubicin, cytotoxicity, apoptosis, and acute myeloid leukemia, which are considered the focus of Nanoparticles-leukemia research. With time, new topics continue to emerge (Figure 8). During the nascent stage (1999–2009), emerging keywords include carbon nanotube, oxidative stress, P-glycoprotein, and so on. This is also in line with the actual situation. At this stage, researchers tried to clarify the pathogenesis of leukemia. In the steady growth phase (2010–2016), These keywords are mainly related to the Researchers who have done much research on nano-drugs in the treatment of cancer, so keywords related to anti-cancer nano-drugs have emerged (cancer therapy, targeted delivery, silver nanoparticle, paclitaxel, and nanocomposite). In the rapid developmental phase (2017–present), with the clinical application of nano-drugs (lipid nanoparticle, liposome, polymer), clinical-related problems (drug resistance, stability) and more nano-synthesis strategies have emerged (green synthesis). Unfortunately, although many studies have focused on solving the problem of drug resistance in leukemia, there is still no good solution.

In addition, keyword clusters can indicate knowledge of the inner architecture and unveil academic frontiers of these disciplines. Cluster analyses show three primary clusters in the field of Nanoparticles-leukemia (Figures 7, 12): nanoparticles for the diagnosis and treatment of leukemia, related to the type and treatment of leukemia, the specific molecular mechanism, and existing problems of the application of nanoparticles in leukemia. As shown earlier, anti-cancer drug resistance remains a significant obstacle to leukemia treatment. It is urgent to explore the mechanisms of drug resistance (multi-drug efflux pumps, drug metabolic enzymes, secondary mutations, remodeling of bone marrow microenvironment, metabolic changes, abnormal activation of signal pathways) and develop targeted and drug-resistant nano-drugs.

Studies presenting strongly-cited breakthroughs (Figure 9) can also characterize new topics in a field. The article with the most vigorous citation burst intensity (strength = 8.45) is a monograph published by Chen Baoan from Southeast University in NANOTECHNOLOGY (Zhang et al., 2006). This article found that magnetic nanoparticles can increase the accumulation of chemotherapeutic drugs in leukemia-resistant cell lines, resulting in different nanoparticles. Different properties of the particles can have wildly different effects on cells. At the same time, to this day, 7 of the 25 highly cited articles are still in a state of the continuous outbreak. These seven references reflect the most recent Nanoparticles-leukemia themes and are, therefore, worthy of further discussion. We rank the eight articles according to the strength of citation bursts, and the first continuous citation of outbreaks paper is also a high Co-cited paper (strength = 7.79), which shows that this paper has an indelible contribution in the field of nano-leukemia (Shi et al., 2017). The second continuous citation of outbreaks paper (strength = 7.68) was published on BIOMATERIALS by Professor Yan Fei of Jilin University, which designed functionalized gold nanoparticles that can treat AML by affecting DNA methylation (Deng et al., 2018). The third continuous citation of outbreaks paper (strength = 7.51) is from the American Cancer Society's Scientific Vice Presiden Ahmedin Jemal, published at CA-A CANCER JOURNAL FOR CLINICIANS. This paper provides a comprehensive overview of global cancer and focuses on the global situation of leukemia (Bray et al., 2018). The fourth-ranked literature (strength = 6.58) is a blockbuster review of INTERNATIONAL JOURNAL OF MOLECULAR SCIENCES published by Ivan Mijakovic of Chalmers University of Technology, which comprehensively summarizes the use of gold nanoparticles in human cancer (Singh et al., 2018).Interestingly, the paper also cited the sixth high co-cited literature and agreed that gold nanoparticles of a particular size might not be toxic to leukemic cells. The fifth-ranked literature (strength = 5.62) is a clinical study published by Ivan Mijakovic and JOURNAL OF CLINICAL ONCOLOGY, which focuses on CPX-351 (a dual liposome encapsulation of cytarabine and daunorubicin) (Lancet et al., 2018). Compared with traditional 7 + 3, CPX-351 can significantly prolong the survival time of leukemia patients with the same safety. This shows that nano-drugs can not only play an anti-cancer role in the theory but also improve patients' quality of life.

To precisely analyze Nanoparticles-leukemia research-related content, we analyzed journals, co-cited journals, and national and keyword analyses of the top most cited 100 articles (Parmar et al., 2019; Mainwaring et al., 2020). The study of journals and co-cited journals (Tables 7, 8) demonstrated that ACS NANO, ANALYTICAL CHEMISTRY, and BIOMATERIALS published the highest number of articles on Nanoparticles-leukemia but also acquired the most co-cited references. The contribution of FRONTIERS IN BIOENGINEERING AND BIOTECHNOLOGY in

Nanoparticles-leukemia research is also noteworthy. In the field of top100, the journal is not only a high-output journal and a highly co-cited journal but is also published as a highly cited journal in this field. Larissa Pereira Brumano summarized the role of L-asparaginase in treating acute lymphoblastic leukemia and the existing methods to improve the biocompatibility and therapeutic efficiency of L-asparaginase (Brumano et al., 2019). This study will facilitate follow-up scholars to gain an in-depth understanding of the mechanisms involved in ASNase treatment to develop new and effective strategies to improve this biopharmaceutical.

The dual-map overlay analyses of the top 100 most-cited articles as well as all articles in the field (Figure 10) show 3 of the primary citation paths from Physics/Materials/chemistry and Molecular/Biology/Immunology co-cited journals to Molecular/Biology/Genetics and Chemistry/Materials/Physics journals, which indicates that Nanoparticles-leukemia studies not only focused on molecular biology but also closely related to the field of materials and physics. The nation-wise analysis findings of the top 100 most-cited papers are consistent with those of all articles in the field, showing that the United States, CHINA, and GERMANY are the largest producers. Additionally, cooperation between the United States and other countries is active, indicating that Nanoparticles-leukemia-related research has attracted worldwide attention.

4.4 The possible focus of future research

The existing treatment methods for leukemia mainly include chemotherapy, radiotherapy, etc. However, the emergence of drug resistance significantly hinders the efficacy of chemotherapy and leads to a poor prognosis, and the side effects caused by poor targeting also make patients miserable. How to solve the chemotherapy resistance, improve the prognosis and improve the quality of life of patients has become a thorny problem. With the rise of nanomedicine and targeted therapy, future researchers can explore the mechanism of drug resistance and active targeting and synthesize nano-drugs that have both targeted therapy and chemotherapy resistance according to the mechanism, which may be the dawn of the solution of leukemia.

5 Limitation

The present study had some inherent flaws in bibliometrics. First, data were acquired from the WoSCC database, excluding some research not in WoSCC. Nevertheless, WoSCC is the most frequently used scientific econometric research database; data from WoSCC can cover the majority of information to a certain extent. Second, all data were acquired *via* bibliometric tools based on machine learning and natural language processing, which may cause biases in other bibliometric studies. Third, in the included article, part of the review also describes diseases other than leukemia, which may lead to analysis deviation. Nevertheless, compared to the most recent conventional reviews, the results herein are consistent and provide scholars with more objective data and insights.

6 Conclusion

In summary, research on Nanoparticles-leukemia is fast-developing, and global collaboration is active, wherein America and China is the primary collaboration center. Currently, the research predominantly highlights the fields of molecular biology, Immunology, physics, materials, and chemistry. The three primary aspects of Nanoparticles-leukemia-related studies include nanoparticles for the diagnosis and treatment of leukemia, the type and treatment of leukemia, the specific molecular mechanism, and existing problems of the application of nanoparticles in leukemia. Future research may be to synthesize nanoparticles with both targeting and reversible drug resistance. Our study is the first to research Nanoparticles-leukemia-associated articles using bibliometrics and knowledge graph systems. INTERNATIONAL JOURNAL OF NANOMEDICINE is the journal with the highest output. The contribution of FRONTIERS IN BIOENGINEERING AND BIOTECHNOLOGY is also noteworthy.In contrast to conventional reviews, the present study offers preliminary and objective insights into Nanoparticles-leukemia studies. We believe that the results of the current report will provide valuable references for future research.

Data availability statement

The original contributions presented in the study are included in the article/supplementary material, further inquiries can be directed to the corresponding authors.

Author contributions

Conceptualization, RW, and CZ; methodology, SJ, and ZZ; software, CB and GZ; validation, YH, BJ, and YS; formal analysis, BJ; investigation, XW; resources, QZ; data curation, XW; writing—original draft preparation, XW; writing—review and editing, XW; visualization, XW; supervision, XW; project administration, XW; funding acquisition, QZ All authors have read and agreed to the published version of the manuscript.

Funding

Central Universities of Central South University funded this research under Grant (No. 2020zzts896). This work was supported by grants from the Project of Kunlun Elite, High-End Innovation and Entrepreneurship Talents of Qinghai Province (2021 No. 13). The guiding project of Qinghai Provincial Health and Family Planning Commission (2018-wjzdx17). This work was supported by the National Natural Science Foundation of China (No. 82260365).

Acknowledgments

XW would like to thank his wife Ethna for her unwavering support of this study.

Conflict of interest

The authors declare that the research was conducted in the absence of any commercial or financial relationships that could be construed as a potential conflict of interest.

Publisher’s note

References

Bai, L., Chen, P., Zhao, Y., Hang, R., Yao, X., Tang, B., et al. (2021). A micro/nano-biomimetic coating on titanium orchestrates osteo/angio-genesis and osteoimmunomodulation for advanced osseointegration. *Biomaterials* 278, 121162. Epub 20211004. doi:10.1016/j.biomaterials.2021.121162

Björnmalm, M., Thurecht, K. J., Michael, M., Scott, A. M., and Caruso, F. (2017). Bridging bio-nano science and cancer nanomedicine. *ACS Nano* 11 (10), 9594–9613. Epub 20170919. doi:10.1021/acsnano.7b04855

Blanco, E., Shen, H., and Ferrari, M. (2015). Principles of nanoparticle design for overcoming biological barriers to drug delivery. *Nat. Biotechnol.* 33 (9), 941–951. doi:10.1038/nbt.3330

Bray, F., Ferlay, J., Soerjomataram, I., Siegel, R. L., Torre, L. A., and Jemal, A. (2018). Global cancer statistics 2018: Globocan estimates of incidence and mortality worldwide for 36 cancers in 185 countries. *CA A Cancer J. Clin.* 68 (6), 394–424. doi:10.3322/caac.21492

Brigger, I., Dubernet, C., and Couvreur, P. (2002). Nanoparticles in cancer therapy and diagnosis. *Adv. Drug Deliv. Rev.* 54 (5), 631–651. doi:10.1016/s0169-409x(02)00044-3

Brumano, L. P., da Silva, F. V. S., Costa-Silva, T. A., Apolinario, A. C., Santos, J., Kleingesinds, E. K., et al. (2019). Development of L-asparaginase biobetters: Current research status and review of the desirable quality profiles. *Front. Bioeng. Biotechnol.* 6, 212. doi:10.3389/fbioe.2018.00212

Cao, K., Du, Y., Bao, X., Han, M., Su, R., Pang, J., et al. (2022). Glutathione-bioimprinted nanoparticles targeting of N6-methyladenosine fto demethylase as a strategy against leukemic stem cells. *Small* 18 (13), e2106558. Epub 20220204. doi:10.1002/smll.202106558

Chen, H., Zheng, D., Pan, W., Li, X., Lv, B., Gu, W., et al. (2021). Biomimetic nanotheranostics camouflaged with cancer cell membranes integrating persistent oxygen supply and homotypic targeting for hypoxic tumor elimination. *ACS Appl. Mat. Interfaces* 13 (17), 19710–19725. Epub 20210423. doi:10.1021/acsami.1c03010

Connor, E. E., Mwamuka, J., Gole, A., Murphy, C. J., and Wyatt, M. D. (2005). Gold nanoparticles are taken up by human cells but do not cause acute cytotoxicity. *Small* 1 (3), 325–327. doi:10.1002/smll.200400093

Davis, M. E., Chen, Z., and Shin, D. M. (2008). Nanoparticle therapeutics: An emerging treatment modality for cancer. *Nat. Rev. Drug Discov.* 7 (9), 771–782. doi:10.1038/nrd2614

Deng, R., Shen, N., Yang, Y., Yu, H. L., Xu, S. P., Yang, Y. W., et al. (2018). Targeting epigenetic pathway with gold nanoparticles for acute myeloid leukemia therapy. *Biomaterials* 167, 80–90. doi:10.1016/j.biomaterials.2018.03.013

Du, A., Wu, X., Gao, Y., Jiang, B., Wang, J., Zhang, P., et al. (2021). M6a regulator-mediated methylation modification patterns and tumor microenvironment infiltration characterization in acute myeloid leukemia. *Front. Immunol.* 12, 789914. Epub 20211123. doi:10.3389/fimmu.2021.789914

Huang, X. M., Schwind, S., Yu, B., Santhanam, R., Wang, H. Y., Hoellerbauer, P., et al. (2013). Targeted delivery of microrna-29b by transferrin-conjugated anionic Lipopolyplex nanoparticles: A novel therapeutic strategy in acute myeloid leukemia. *Clin. Cancer Res.* 19 (9), 2355–2367. doi:10.1158/1078-0432.Ccr-12-3191

Huang, Y., Zhan, Q., Wu, C., Liao, N., Jiang, Z., Ding, H., et al. (2022). Trends and hotspots in nanoparticles for the targeted delivery of nucleic acids: A ten-year bibliometric study. *Front. Pharmacol.* 13, 868398. Epub 20220504. doi:10.3389/fphar.2022.868398

Izci, M., Maksoudian, C., Manshian, B. B., and Soenen, S. J. (2021). The use of alternative strategies for enhanced nanoparticle delivery to solid tumors. *Chem. Rev.* 121 (3), 1746–1803. Epub 20210114. doi:10.1021/acs.chemrev.0c00779

Jiang, D., Wu, X., Sun, X., Tan, W., Dai, X., Xie, Y., et al. (2022). Bone mesenchymal stem cell-derived exosomal microrna-7-5p inhibits progression of acute myeloid leukemia by targeting Osbpl11. *J. Nanobiotechnology* 20 (1), 29. Epub 20220110. doi:10.1186/s12951-021-01206-7

Kaldor, J. M., Day, N. E., Clarke, E. A., Van Leeuwen, F. E., Henry-Amar, M., Fiorentino, M. V., et al. (1990). Leukemia following hodgkin’s disease. *N. Engl. J. Med. Overseas. Ed.* 322 (1), 7–13. doi:10.1056/nejm199001043220102

Karwath, A., Bunting, K. V., Gill, S. K., Tica, O., Pendleton, S., Aziz, F., et al. (2021). Redefining Β-blocker response in heart failure patients with sinus rhythm and atrial fibrillation: A machine learning cluster Analysis. *Lancet* 398 (10309), 1427–1435. Epub 20210830. doi:10.1016/s0140-6736(21)01638-x

Lancet, J. E., Uy, G. L., Cortes, J. E., Newell, L. F., Lin, T. L., Ritchie, E. K., et al. (2018). Cpx-351 (cytarabine and daunorubicin) liposome for injection versus conventional cytarabine plus daunorubicin in older patients with newly diagnosed secondary acute myeloid leukemia. *J. Clin. Oncol.* 36 (26), 2684–2692. doi:10.1200/jco.2017.77.6112

Li, C., You, X., Xu, X., Wu, B., Liu, Y., Tong, T., et al. (2022). A metabolic reprogramming amino acid polymer as an immunosurveillance activator and leukemia targeting drug carrier for T-cell acute lymphoblastic leukemia. *Adv. Sci. (Weinh).* 9 (9), e2104134. Epub 20220126. doi:10.1002/advs.202104134

Lin, C. K., Hsu, Y. T., Brown, K. D., Pokharel, B., Wei, Y., and Chen, S. T. (2020). Residential exposure to petrochemical industrial complexes and the risk of leukemia: A systematic review and exposure-response meta-analysis. *Environ. Pollut.* 258, 113476. Epub 20191122. doi:10.1016/j.envpol.2019.113476

Lin, W., Kampf, N., and Klein, J. (2020). Designer nanoparticles as robust superlubrication vectors. *ACS Nano* 14 (6), 7008–7017. Epub 20200520. doi:10.1021/acsnano.0c01559

Lin, W., Kluzek, M., Iuster, N., Shimoni, E., Kampf, N., Goldberg, R., et al. (2020). Cartilage-inspired, lipid-based boundary-lubricated hydrogels. *Science* 370 (6514), 335–338. doi:10.1126/science.aay8276

Locatelli, F., Zugmaier, G., and von Stackelberg, A. (2021). Blinatumomab vs chemotherapy among children with relapsed acute lymphoblastic leukemia-reply. *Jama* 326 (4), 359–360. doi:10.1001/jama.2021.8154

Lokody, I. (2014). Drug resistance: Overcoming resistance in acute myeloid leukaemia treatment. *Nat. Rev. Cancer* 14 (7), 453–3. doi:10.1038/nrc3776

Lussana, F., Gritti, G., and Rambaldi, A. (2021). Immunotherapy of acute lymphoblastic leukemia and lymphoma with T cell-redirected bispecific antibodies. *J. Clin. Oncol.* 39 (5), 444–455. Epub 20210112. doi:10.1200/jco.20.01564

Mainwaring, A., Bullock, N., Ellul, T., Hughes, O., and Featherstone, J. (2020). The top 100 most cited manuscripts in bladder cancer: A bibliometric analysis (review article). *Int. J. Surg.* 75, 130–138. Epub 20200125. doi:10.1016/j.ijsu.2020.01.128

Montserrat, E., and Dreger, P. (2015). Hope for high-risk chronic lymphocytic leukemia relapsing after allogeneic stem-cell transplantation. *J. Clin. Oncol.* 33 (14), 1527–1529. Epub 20150413. doi:10.1200/jco.2014.60.3282

Parmar, A., Ganesh, R., and Mishra, A. K. (2019). The top 100 cited articles on obsessive compulsive disorder (ocd): A citation analysis. *Asian J. Psychiatr.* 42, 34–41. Epub 20190326. doi:10.1016/j.ajp.2019.03.025

Peer, D., Karp, J. M., Hong, S., FaroKhzad, O. C., Margalit, R., and Langer, R. (2007). Nanocarriers as an emerging platform for cancer therapy. *Nat. Nanotechnol.* 2 (12), 751–760. doi:10.1038/nnano.2007.387

Petersen, G. H., Alzghari, S. K., Chee, W., Sankari, S. S., and La-Beck, N. M. (2016). Meta-analysis of clinical and preclinical studies comparing the anticancer efficacy of liposomal versus conventional non-liposomal doxorubicin. *J. Control. Release* 232, 255–264. Epub 20160422. doi:10.1016/j.jconrel.2016.04.028

Petros, R. A., and DeSimone, J. M. (2010). Strategies in the design of nanoparticles for therapeutic applications. *Nat. Rev. Drug Discov.* 9 (8), 615–627. doi:10.1038/nrd2591

Shangguan, D., Li, Y., Tang, Z. W., Cao, Z. H. C., Chen, H. W., Mallikaratchy, P., et al. (2006). Aptamers evolved from live cells as effective molecular probes for cancer study. *Proc. Natl. Acad. Sci. U. S. A.* 103 (32), 11838–11843. doi:10.1073/pnas.0602615103

Shen, J., Lu, Z. G., Wang, J. Z., Zhang, T. L., Yang, J., Li, Y., et al. (2020). Advances of nanoparticles for leukemia treatment. *ACS Biomater. Sci. Eng.* 6 (12), 6478–6489. doi:10.1021/acsbiomaterials.0c01040

Shi, J. J., Kantoff, P. W., Wooster, R., and Farokhzad, O. C. (2017). Cancer nanomedicine: Progress, challenges and opportunities. *Nat. Rev. Cancer* 17 (1), 20–37. doi:10.1038/nrc.2016.108

Singh, P., Pandit, S., Mokkapati, V., Garg, A., Ravikumar, V., and Mijakovic, I. (2018). Gold nanoparticles in diagnostics and therapeutics for human cancer. *Int. J. Mol. Sci.* 19 (7), 1979. doi:10.3390/ijms19071979

Tatar, A. S., Nagy-Simon, T., Tomuleasa, C., Boca, S., and Astilean, S. (2016). Nanomedicine approaches in acute lymphoblastic leukemia. *J. Control. Release* 238, 123–138. doi:10.1016/j.jconrel.2016.07.035

Tee, J. K., Yip, L. X., Tan, E. S., Santitewagun, S., Prasath, A., Ke, P. C., et al. (2019). Nanoparticles' interactions with vasculature in diseases. *Chem. Soc. Rev.* 48 (21), 5381–5407. doi:10.1039/c9cs00309f

Tondelli, L., Laus, M., Ricca, A., and Citro, G. (1999). Specifically designed polymeric nanospheres increase cellular uptake of unmodified antisense odns. *Nucleosides Nucleotides* 18 (6-7), 1677–1679. doi:10.1080/07328319908044820

Woyach, J. A. (2019). Can combination targeted therapy bring about another paradigm shift in chronic lymphocytic leukemia? *J. Clin. Oncol.* 37 (30), 2711–2713. Epub 20190828. doi:10.1200/jco.19.01718

Wu, X., Li, S., Chen, D., Zheng, G., Zhang, Z., Li, Z., et al. (2022). An inflammatory response-related gene signature associated with immune status and prognosis of acute myeloid leukemia. *Am. J. Transl. Res.* 14 (7), 4898–4917. Epub 20220715.

Wu, X., Zhang, X., Feng, W., Feng, H., Ding, Z., Zhao, Q., et al. (2021). A targeted erythrocyte membrane-encapsulated drug-delivery system with anti-osteosarcoma and anti-osteolytic effects. *ACS Appl. Mat. Interfaces* 13 (24), 27920–27933. Epub 20210614. doi:10.1021/acsami.1c06059

Wu, Z., Zhang, X., Chen, D., Li, Z., Wu, X., Wang, J., et al. (2021). N6-Methyladenosine-Related lncrnas are potential remodeling indicators in the tumor microenvironment and prognostic markers in osteosarcoma. *Front. Immunol.* 12, 806189. Epub 20220112. doi:10.3389/fimmu.2021.806189

Zhang, J., Song, L., Xu, L., Fan, Y., Wang, T., Tian, W., et al. (2021). Knowledge domain and emerging trends in ferroptosis research: A bibliometric and knowledge-map analysis. *Front. Oncol.* 11, 686726. Epub 20210603. doi:10.3389/fonc.2021.686726

Zhang, R. Y., Wang, X. M., Wu, C. H., Song, M., Li, J. Y., Lv, G., et al. (2006). Synergistic enhancement effect of magnetic nanoparticles on anticancer drug accumulation in cancer cells. *Nanotechnology* 17 (14), 3622–3626. doi:10.1088/0957-4484/17/14/043

Zhang, X., Ong'achwa Machuki, J., Pan, W., Cai, W., Xi, Z., Shen, F., et al. (2020). Carbon nitride hollow theranostic nanoregulators executing laser-activatable water splitting for enhanced ultrasound/fluorescence imaging and cooperative phototherapy. *ACS Nano* 14 (4), 4045–4060. Epub 20200410. doi:10.1021/acsnano.9b08737

Zhao, Y., Sun, Y., Hang, R., Yao, R., Zhang, Y., Huang, D., et al. (2022). Biocompatible silane adhesion layer on titanium implants improves angiogenesis and osteogenesis. *Biomater. Adv.* 139, 213033. Epub 20220716. doi:10.1016/j.bioadv.2022.213033

Zucker, D., Andriyanov, A. V., Steiner, A., Raviv, U., and Barenholz, Y. (2012). Characterization of pegylated nanoliposomes Co-remotely loaded with topotecan and vincristine: Relating structure and pharmacokinetics to therapeutic efficacy. *J. Control. Release* 160 (2), 281–289. Epub 20111012. doi:10.1016/j.jconrel.2011.10.003

frontiers | Frontiers in Bioengineering and Biotechnology

TYPE Original Research
PUBLISHED 15 November 2022
DOI 10.3389/fbioe.2022.1069676

OPEN ACCESS

EDITED BY
Long Bai,
East China University of Science and Technology, China

REVIEWED BY
Tongkai Chen,
Guangzhou University of Chinese Medicine, China
Kai Ling,
Shantou University, China
Xiao Sun,
Shandong First Medical University, China

*CORRESPONDENCE
Youhua Xu,
yhxu@must.edu.mo

SPECIALTY SECTION
This article was submitted to Nanobiotechnology, a section of the journal Frontiers in Bioengineering and Biotechnology

RECEIVED 14 October 2022
ACCEPTED 01 November 2022
PUBLISHED 15 November 2022

CITATION
Li Y, Huang C and Xu Y (2022), Colon cancer exosome-derived biomimetic nanoplatform for curcumin-mediated sonodynamic therapy and calcium overload.
Front. Bioeng. Biotechnol. 10:1069676.
doi: 10.3389/fbioe.2022.1069676

Colon cancer exosome-derived biomimetic nanoplatform for curcumin-mediated sonodynamic therapy and calcium overload

Yang Li[1,2,3], Chunyu Huang[4] and Youhua Xu[1,2]*

[1]Faculty of Chinese Medicine, State Key Laboratory of Quality Research in Chinese Medicine, Macau University of Science and Technology, Taipa, Macao, China, [2]School of Pharmacy, State Key Laboratory of Quality Research in Chinese Medicine, Macau University of Science and Technology, Taipa, Macao, China, [3]Department of Gastrointestinal Surgery, Shenzhen People's Hospital The Second Clinical Medical College, Jinan University, The First Affiliated Hospital, Southern University of Science and Technology, Shenzhen, Guangdong, China, [4]Department of Radiation and Medical Oncology, Hubei Key Laboratory of Tumor Biological Behaviors, Hubei Cancer Clinical Study Center, Zhongnan Hospital of Wuhan University, Wuhan, China

Sonodynamic therapy (SDT) possesses unique properties such as being minimally invasive, exhibiting low toxicity, as well as ability to impart the treatment in the deep tissues, and hence has been extensively used. However, inherent defects such as low water-soluble sonosensitizers can limit the clinical application of SDT, and tumor microenvironment (TME) can further compromise the effect of a single SDT. To overcome these challenges, we have designed a bionic nano-system (ECaC) by coating mesoporous calcium carbonate nanoparticles ($CaCO_3$ NPs) and sonosensitizer curcumin (Cur) into tumor-derived exosomes for developing enhanced SDT. Exosome membrane could endow $CaCO_3$ NPs with homologous targeting abilities. In addition, compared with the bare CaCO3 NPs, ECaC showed significant accumulation in the tumor cell species. Subsequently, $CaCO_3$ NPs upon reaching the tumor site can be degraded into Ca^{2+} in response to the acidic microenvironment of the tumor to destroy the cellular mitochondria. Hence, the cellular respiration could be destroyed to be a vulnerable state, causing oxidative stress, enhancing Cur-mediated chemotherapy/SDT. This synergistically dynamic therapy has demonstrated significant anti-tumor effects under *in vitro* and *in vivo* settings without exhibiting any toxic side effects. Our prepared biomimetic nano-system can effectively deliver the hydrophobic Cur to the tumor sites, which holds great promise in field of drug delivery and can broaden the application of exosomes, as this method has a certain enlightenment effect on the subsequent development of exosomes.

KEYWORDS

exosome, curcumin, calcium carbonate, drug delivery, sonodynamic therapy

Introduction

According to the World Health Organization, cancer has become one of the major causes of mortality worldwide, and malignant tumors continue to be the leading cause of death (Zhu et al., 2020; Yu et al., 2021; Zhu et al., 2022a). The different traditional strategies used for tumor treatment display poor selectivity, toxic and side effects, and are generally can be only used in early-stage cancer patients (Baumann et al., 2016). Therefore, it is imperative to develop more effective and safe tumor treatment methods. In the past few decades, the applications of nanotechnology in the field of cancer treatment have developed rapidly (Chen et al., 2021a; Dai et al., 2021; Zhu et al., 2022b). Among them, non-invasive or minimally invasive treatment has become the preferred treatment method for researchers due to its advantages of precise positioning and relatively lesser side effects (Cui et al., 2021; Hu et al., 2021). It has been found that compared with the different traditional treatment methods, photodynamic therapy (PDT) can significantly reduce the toxicity to normal cells during the treatment process (Duo et al., 2021). However, due to the shallow penetration of light, the therapeutic effect of PDT on deeply located tumors located is rather limited. In addition, several photosensitizers display varying degrees of the phototoxicity, which makes them ineffective for the clinical application (Wang et al., 2021a). Sonodynamic therapy (SDT) is a non-invasive treatment method based on the interaction of ultrasound and sonoactive substances (sonosensitizers) (Zhang et al., 2021). In 1989, Yumita et al. first found that some organic substances could generate reactive oxygen radicals under the action of ultrasound, thus proposing the concept of SDT (Zhao et al., 2020). Although application of SDT has been associated with several advantages such as non-invasiveness, targeting, and little damage to normal human tissues, the clinical application effect of SDT is still unsatisfactory (Xu et al., 2020). Therefore, to further improve its therapeutic effect, nanotechnology, which has developed rapidly in recent years, can be utilized.

However, most sonosensitizers are aggregation-prone and weakly targeted, making their delivery very difficult (Liang et al., 2020). It has been established that the potential use of nanotechnology can improve the targeting of sonosensitizers, enhance their ROS yields or ultrasonic cavitation effects, and then promote the development of SDT in the biomedical field (Jiang et al., 2022; Wang et al., 2022). However, nanomaterials rely on the enhanced permeability and retention (EPR) effect to reach the tumor tissues but can be easily cleared by liver and kidney tissues as well as immune system. In recent years, enormous progress has been made in encapsulating nanomaterials with exosome membrane biomimetic technology to achieve specific targeting and avoid immune elimination (Guo et al., 2022; Ma et al., 2022). After the nanoparticles are encapsulated, the proteins on exosomes derived from the different cells are still biologically active, enabling them to escape from immune systems, prolong blood circulation, and directly target the tumor cells (Yang et al., 2021; Yuan et al., 2021). The exosome-encapsulated nanoparticles possess the properties of homologous targeting and homologous adhesion, which can enable them to specifically recognize and accumulate in the tumor tissues (Cao et al., 2019; Wang et al., 2021b). Huang et al. designed a novel tumor-derived biomimetic nanozyme to enhance radiotherapy (RT), and it was found that the tumor cell derived exosome membrane could endow FeS_2 with optimal targeting ability and immune escape ability (Huang et al., 2021). Therefore, utilizing exosomes to deliver sonosensitizer can serve as a promising strategy to achieve SDT.

Calcium-based nanomaterials {such as calcium carbonate ($CaCO_3$), calcium phosphate [$Ca(H_2PO_4)_2$]} have good biocompatibility and biodegradability, and are widely used in chemical, medical and other fields (Bai et al., 2022). Calcium carbonate nanoparticles ($CaCO_3$ NPs) remain stable at neutral pH and decompose into Ca^{2+} and CO_2 at acidic pH, indicating their great potential for pH-responsive drug delivery and tumor therapy (Li et al., 2021). For example, Dong et al. developed monodisperse polyethylene glycol (PEG) modified $CaCO_3$ nanoparticles as multifunctional nanocarriers for loading the photosensitizer [Ce6(Mn)] and chemotherapy drug doxorubicin (DOX) (Dong et al., 2016). The findings of *in vitro* experiments showed that $CaCO_3$@Ce6(Mn)-PEG (DOX) nanoparticles remained stable at the physiological pH of 7.4, but could be rapidly degraded in a slightly acidic environment, and exhibited significant anti-tumor effects during treatment upon exposure to the combination of photodynamic therapy and chemotherapy. Similarly, Chang and co-workers designed a core–shell Cu_2O@$CaCO_3$ nanostructure for the synergistic oncotherapy (Chang et al., 2020). It was observed that Cu_2O@$CaCO_3$ could activate an immune-favorable TME for profound immune responses to simultaneously inhibit tumor distant metastasis and recurrence. Furthermore, Ca^{2+} can effectively destroy the mitochondria, leaving the cells in a vulnerable state, thereby sensitizing the effectiveness of SDT (Tan et al., 2021). In addition, cellular respiration was inhibited and oxygen content increased after the mitochondrial destruction. These properties can make calcium carbonate as a promising compound to cooperate with SDT to achieve tumor therapy.

In this study, by coating porous $CaCO_3$ NPs and Cur with the tumor cell derived exosomes, a composite ECaC nano-system was generated (Scheme 1). The exosome membrane can endow $CaCO_3$ with a new immune evasion ability, which can enable it to actively evade the clearance of organs such as liver and kidney, and specifically targets the tumor site, to facilitate the release Cur and Ca^{2+} in response to the degradation of the tumor's acidic microenvironment. Ca^{2+} can effectively destroy the mitochondria of the tumor cells, thus rendering the cells in a state of inactivation, which is more conducive to the subsequent SDT activated by Cur. Cur also can act as a Ca^{2+} regulator,

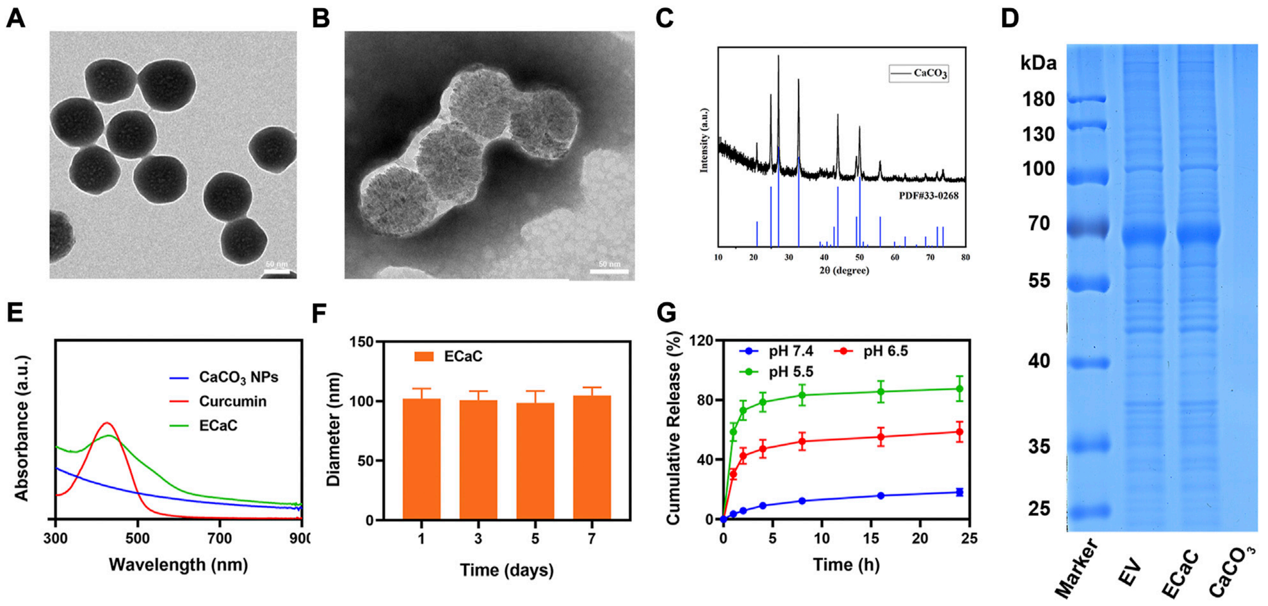

FIGURE 1
(A) TEM image of mesoporous CaCO3 NPs. **(B)** TEM image of ECaC. **(C)** X-ray diffraction (XRD) analysis of CaCO3 NPs. **(D)** Coomassie-stained SDS-PA gel image showing the protein composition of EV, ECaC and CaCO3. **(E)** Absorbance spectrum of CaCO3 NP, Curcumin and ECaC. **(F)** Statistical graph of the measured diameter of ECaC. **(G)** The release of Ca2+ from ECaC after incubation in PBS with different pH values (5.5, 6.5 and 7.4) for several hours.

inhibiting Ca^{2+} efflux by stimulating Ca^{2+} release from the endoplasmic reticulum to the cytoplasm (Zheng et al., 2021). This treatment method can not only achieve the purpose of precise targeting, but also could significantly prolong the metabolic time of Cur and improve the treatment efficiency. Both *in vitro* and *in vivo* experiments have verified that ECaC combined with United States can achieve an optimal tumor treatment effect with good biological safety. This ECaC nano-system possesses useful clinical potential, and our experimental results can further expand the application of exosome-based nano-delivery systems.

Results and discussion

Firstly, porous calcium carbonate nanomaterials ($CaCO_3$ NPs) with uniform size were prepared by using a simple gas diffusion method. The results of transmission electron microscopy (TEM) indicated that the size of $CaCO_3$ NPs was about 92 nm (Figure 1A). Thereafter, after short-term incubation with CT26 cells, ECa was isolated and purified using an exosome kit. Under the similar conditions, Cur was added for co-incubation and purification to obtain ECaC. As shown in Figure 1B, there was a thin exosome membrane formed on the surface of ECaC. X-ray diffraction (XRD) analysis (Figure 1C) showed that the prepared $CaCO_3$ was consistent with the standard card (JCPDS No. 33–0268). X-ray spectroscopy (EDX) (Supplementary Figure S1) result shows that $CaCO_3$ NPs contained three elements namely Ca, O and C. To further verify the successful modification of exosome membranes, we subjected exosomes, ECaC and pure $CaCO_3$ to SDS-PAGE analysis, and the results indicated that there was no protein on the pure material, whereas ECaC and EV exhibited the same proteome (Figure 1D). The exosomes extracted from the tumor cells can successfully target the tumor cells and can be effectively taken up by the parental cells. This can enable rapid release of the $CaCO_3$ and Cur loaded in them to exhibit the significant anti-tumor effects. Figure 1E showed the ultraviolet-visible absorption of various materials, and the results indicated that ECaC retained the characteristic absorption peak of Cur at about 427 nm, indicating that Cur was successfully loaded into ECaC. Moreover, the modification of the exosome membrane can aid to markedly improve the stability of the nanomaterials, as shown in Figure 1F, the particle size of ECaC was unchanged for 7 consecutive days, suggesting its potential for future biomedical applications, which is very important. Although many nanomaterials can exhibit substantial antitumor abilities, their instability can inhibit their future development for clinical use (Zhou et al., 2021). We continued to validate the acid-responsive degradation characteristics of $CaCO_3$, and designed different pH environments to explore the possible release effect of Ca^{2+} in ECaC. As shown in the Figure 1G,

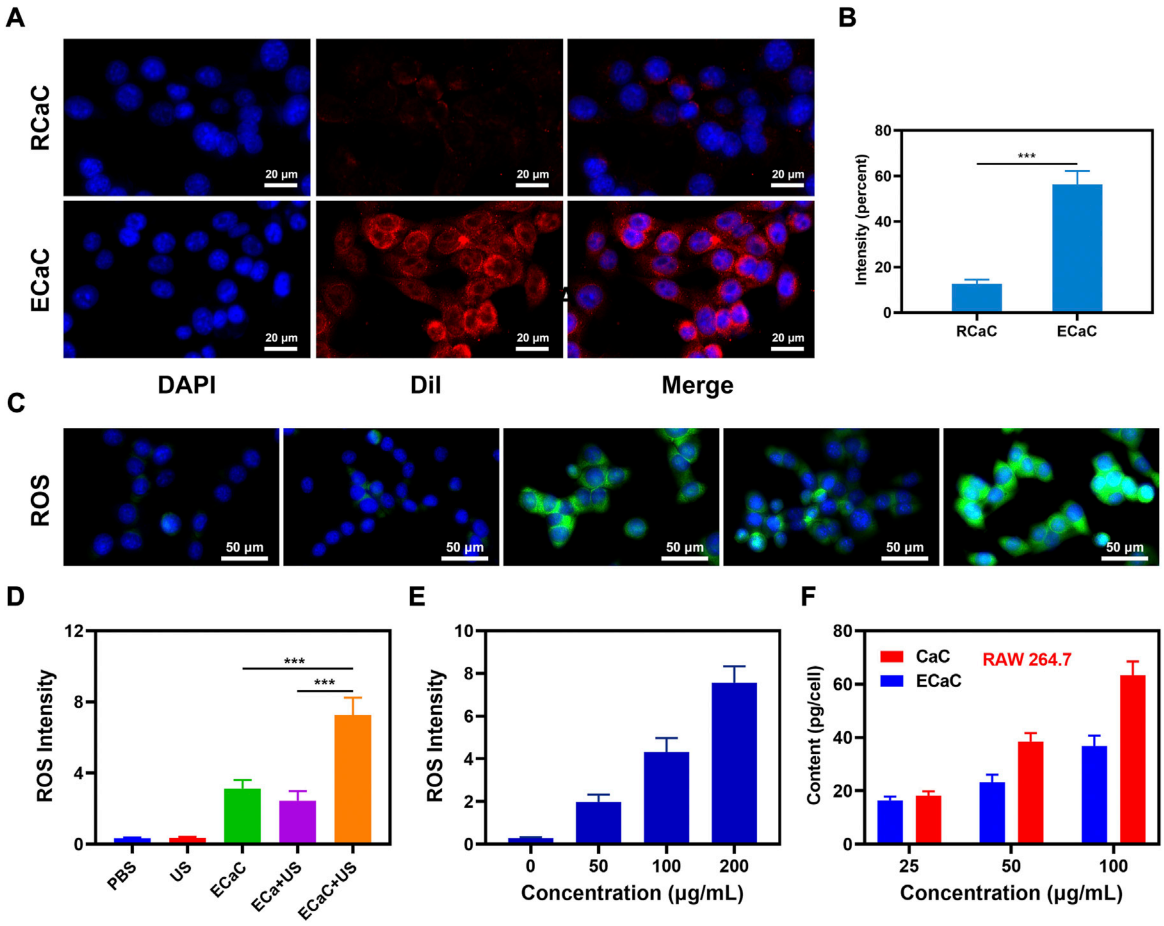

FIGURE 2

(A) Co-localization of DAPI (blue) and Dil (red) for RCaC and ECaC over time in CT26 tumor cells. **(B)** Dil fluorescence intensity of A determined using ImageJ software. **(C)** DCFH-DA fluorescence following the indicated treatments. **(D)** ROS fluorescence intensity of C determined using ImageJ software. **(E)** ROS fluorescence intensity of different ECaC concentration under United States treatment. **(F)** Nanoparticle uptake by RAW 264.7 cells at different incubated concentration. ***$p < 0.001$; Student *t*-test.

CaCO3 released nearly 80% of Ca^{2+} in less than 12 h at pH 5.5. In conclusion, ECaC can actively target the various tumor tissues and can be specifically released in response to the specific microenvironmental properties of the tumors.

In view of the positive results of material characterization experiments, we continued to explore its potential further under *in vitro* settings, and prepared erythrocyte membrane-coated CaC and Cur by a similar method, named RCaC. The ECaC and RCaC were labeled with Dil and subjected to *in vitro* endocytosis experiments. The results showed that ECaC exhibited good targeting, and although RCaC also retained the proteins on the erythrocyte membrane, but it did not display any targeting potential (Figures 2A,B). Supplementary Figure S2 also illustrates the targeting potential of ECaC. In addition, intracellular reactive oxide species (ROS) production was detected using $2'$, $7'$-dichlorodihydrofluorescein diacetate (DCFH-DA), which could be oxidized to $2'$, $7'$-dichlorofluorescein (DCF) with green fluorescence in the presence of ROS. As shown in Figures 2C,D, the PBS and United States groups exhibited relatively weaker green fluorescence, which was primarily caused by the abnormal growth of tumor cells. There was only a slight fluorescence intensity in the ECa + United States group, which was caused by the destruction of the cell mitochondria after Ca^{2+} accumulated into the tumor cells. It is worth noting that ECaC can exhibit a moderate fluorescence effect, ECaC combined with United States can lead to maximal ROS production that can be attributed to the property of chemotherapeutic drug Cur to promote oxidative stress and inhibit the efflux of Ca^{2+}, which can further promote the destruction of mitochondria by Ca^{2+}. A significant ROS generation effect was achieved (Figure 2E), and Cur acted not only as a chemotherapeutic drug to amplify oxidative stress, but also serve as a sonosensitizer to achieve excellent SDT effect to

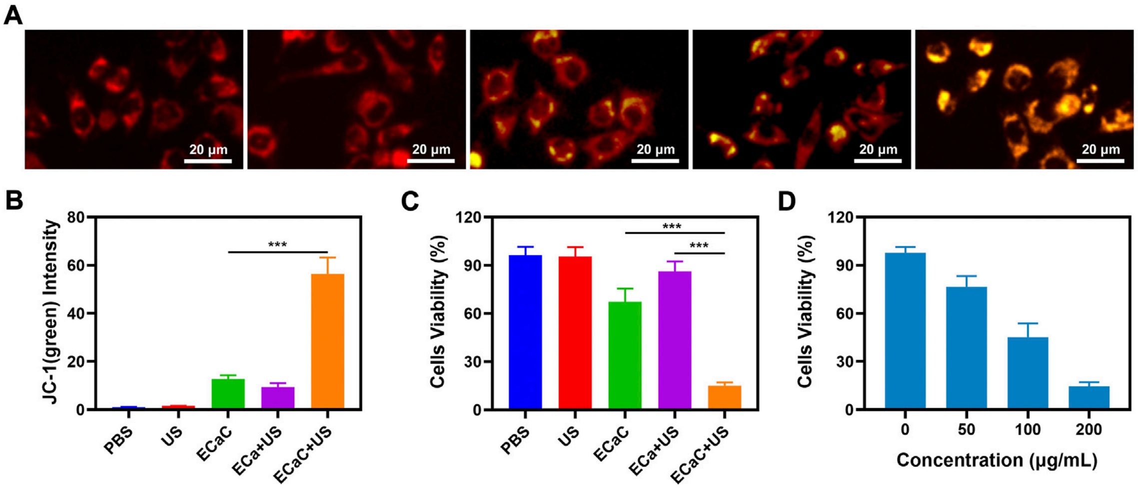

FIGURE 3
(A) JC-1 (green) for JC-1 monomer and red for JC-1 aggregate fluorescence image under different treatment. **(B)** Relative JC-1 (green) intensity in 3A. **(C)** The survival of CT26 cells with Control, United States, ECaC, United States + ECa and United States + ECaC detected by MTT assay. **(D)** The survival of CT26 cells with different ECaC concentration under United States detected by MTT assay. ***$p < 0.001$; Student *t*-test.

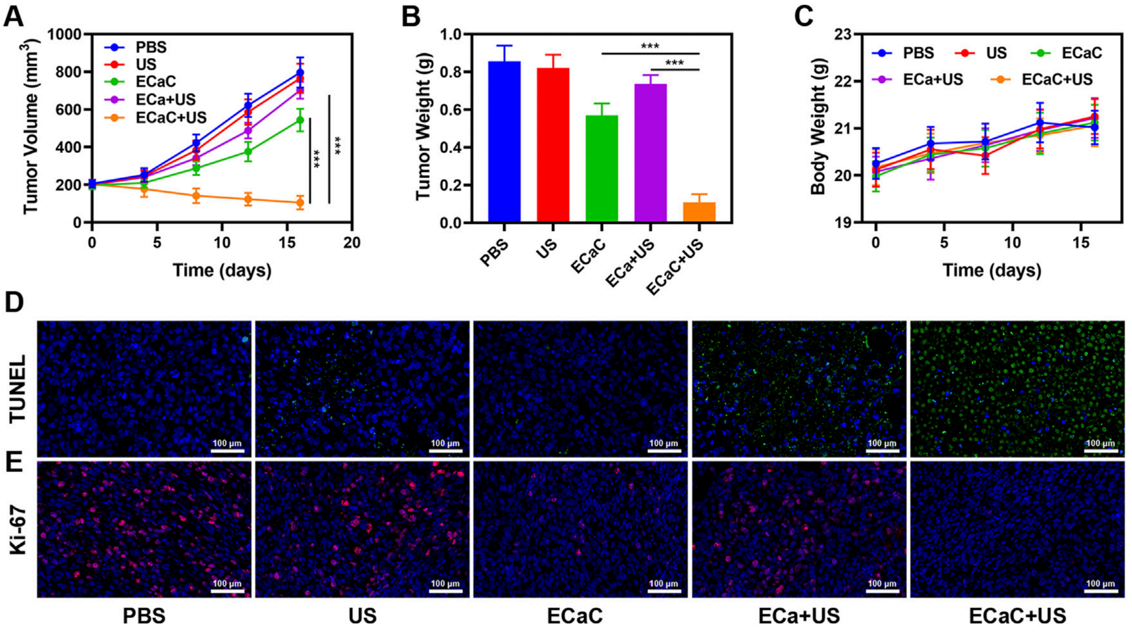

FIGURE 4
(A) Tumor growth curves of different groups of mice after various treatments. **(B)** Average weights of tumors collected from mice at day 16 after various treatments indicated. **(C)** The body weight variation of CT26 tumor-bearing mice during treatment. **(D)** Histological analysis of tumor after various treatments indicated. TUNEL (upper) and **(E)** Ki-67 (bottom) stained slices of tumors were collected from mice one day after various treatments indicated. ***$p < 0.001$; Student *t*-test.

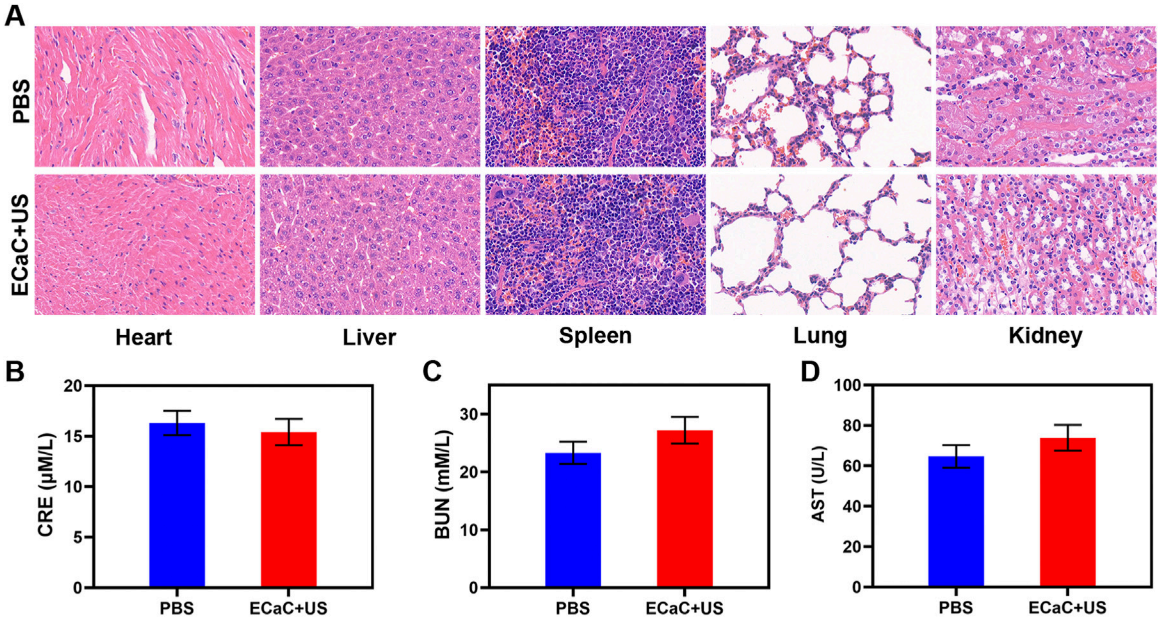

FIGURE 5
(A) Histopathological analysis results (H&E stained images) of the major organs, heart, lung, liver, kidneys, and spleen, of mice that were exposed to different treatments 16 days post-injection. Scale bars: 100 μm. **(B–D)** Liver, kidney and blood function markers: AST, CRE and BUN after various treatments.

enhance ROS content. The immune system can actively recognize and remove the foreign invaders. For example, the macrophages can remove the nanomaterials and pathogens in the form of fixed cells or free cells. We used RAW264.7 cells for entosis experiment, and found that pure CaC was significantly phagocytic, whereas the relative phagocytic amount of ECaC was significantly reduced, indicating that ECaC possessed good immune evasion characteristics (Figure 2F).

The change of the cellular calcium can aid to maintain a dynamic balance due to the combined action of the plasma and cellular mitochondria. When the intracellular calcium content is substantially higher than the normal level, the structure of mitochondria can be damaged, which in turn can compromise the function of mitochondria (Chen et al., 2021b). Hence, the changes in the mitochondrial membrane potential (MMP) in CT26 tumor cells were monitored by using JC-1 (5,5′,6,6′-tetrachloro-1,1′,3,3′-tetraethyl-imidacarbocyanine) probe method. JC dyes can typically accumulate in mitochondria, where they can clump together and fluoresce red. However, when mitochondria are damaged and MMP levels are low, JC monomers are released into the cytoplasm, producing green fluorescence (Zhu et al., 2022c). As shown in Figures 3A,B, PBS and United States groups exhibited red fluorescence. The merged mitochondria fluorescence of ECaC + United States group indicated maximum mitochondrial damage. Thereafter, we used MTT kit to verify the cell viability under the different treatment conditions (Figure 3C). The ECa combined with United States group only exhibited a slight therapeutic effect, but ECaC displayed certain tumor cell killing ability. The Ca^{2+} regulator Cur could stimulate the release of Ca^{2+} from the endoplasmic reticulum to the cytoplasm and can inhibit the outflow of Ca^{2+} from the cytoplasm to the extracellular fluid, enhancing the killing effect of Ca^{2+} on cells. Moreover, Cur itself also exhibited significant chemotherapeutic effects. Similarly, cell viability decreased with increasing ECaC concentration under United States irradiation (Figure 3D). ECaC + United States exhibited the best therapeutic effect, which was primarily caused by Ca overload and Cur-mediated SDT synergy.

The safety of nano-formulations injected into organisms cannot be completely ignored, and the targeted delivery of ECaC to the tumor cells is achieved through the enhanced permeability and retention effect of exosome membrane coating and nanomaterials. Exosome membrane modification can enable ECaC to possess immune evasion ability during blood circulation, thereby avoiding the massive enrichment of ECaC in the normal organs, and thereby avoiding long-term systemic toxicity and toxic side effects. We conducted *in vivo* pharmacokinetic experiments to study the potential effect of exosome membranes on blood retention. As shown in Supplementary Figures S3, S4, both ECaC and RCaC had long cycling properties, while CaC could guarantee a longer Ca retention time. Moreover, *in vivo* organ biodistribution profile showed that a large amount of ECaC reached the tumor site through active targeting 12 h after injection, and exhibited a

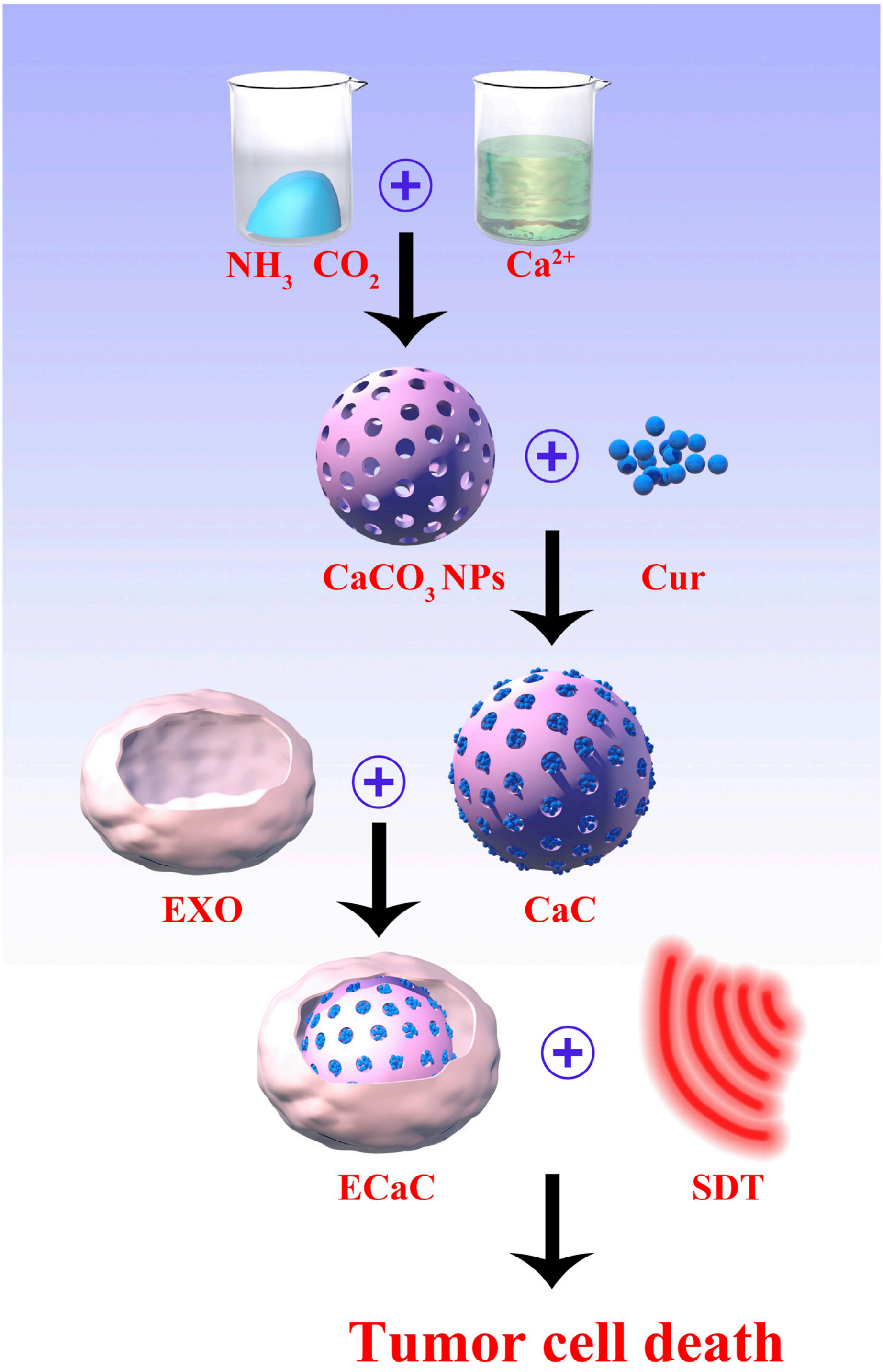

SCHEME 1
The scheme of colon cancer exosome-derived biomimetic nanoplatform for curcumin-mediated sonodynamic therapy and calcium overload.

lower dose accumulation in the liver and kidney than CaC. Based on the above results, we continued to explore ECaC-based *in vivo* anti-tumor effects. In this study, CT26 cells were injected subcutaneously into the mice to establish a CT26 colon cancer subcutaneous tumor model. Once the tumors reached approximately 200 mm^3 in size, tumor-bearing BALB/c mice were randomly assigned into five different groups: 1) PBS; 2) United States; 3) ECaC; 4) ECa + United States and 5) ECaC +

US. Each group was given corresponding treatment. Groups 3, 4 and 5 were administered a 10 mg/kg dose of CaCO3 NPs. After 12 h of intravenous injection, United States irradiation (power density = 1.5 W/cm^2, transducer frequency = 1 MHz, 30% duty cycle, 10 min) was carried out. The tumor volume was measured with the digital calipers after every 4 days and the tumor weight was finally calculated. The results of the study indicated that the tumor volume increased rapidly in the control group, but the tumor growth curve of ECa without Cur combined with United States was only slightly suppressed. In the ECaC group containing the chemotherapeutic drugs Cur and $CaCO_3$ NPs, the initial tumor volume growth in this group exhibited a certain retention effect, but then grew rapidly. The ECaC synergistic United States group showed the maximal tumor suppressor effect, suggesting that the two treatments have a stronger synergistic antitumor effect (Figures 4A,B). In addition, during the treatment period, the weight of the mice in each group increased steadily, and there was no significant change (Figure 4C), indicating that the ECaC system could not cause acute damage to the body. After the treatment cycle, the tumors in the different groups were also harvested and photographed. Deoxynucleotidyl transferase-mediated dUTP nick end labeling (TUNEL) and Ki-67 staining of the tumor slices demonstrated that ECaC combined with United States group exhibited the highest level of tumor cell apoptosis with the lowest level of tumor cell proliferation (Figures 4D,E). After the treatment cycle, mice in all the four groups were euthanized, followed by collection of the major organs for further analysis and blood for biochemical analysis (Figure 5; Supplementary Figures S5, S6). The relevant results of both the experimental group and the conventional control group showed that the mice functioned normally after the treatment, and our treatment method did not show any short-term adverse effects.

Conclusion

In conclusion, a novel nano-biomimetic system for the simultaneous delivery of CaCO3 NPs and the chemotherapeutic drug Cur was designed to achieve robust SDT. ECaCs with exosome membrane modifications could be specifically targeted to the tumor sites, evade clearance by the immune system, and accumulate more effectively at the tumor sites. Subsequently, it can be gradually degraded in the weak acid environment of the tumor, and the Ca^{2+} and Cur are released. After Ca^{2+} causes damage to the mitochondria, the cells are more easily impaired and the Cur-mediated SDT was markedly strengthened. The tumor volume did not increase significantly during the treatment and the main organ parameters of the mice were found to be normal after the treatment, indicating the potential safety of the ECaC system. Overall, ECaCs synthesized by us highlight the promising application of exosomes for drug delivery.

Data availability statement

The original contributions presented in the study are included in the article/Supplementary Material, further inquiries can be directed to the corresponding author.

Ethics statement

The animal study was reviewed and approved by The animal experiments were strictly implemented based on the plan approved and released by the Ministry of Health of China and also approved by the Animal Research Management Committee of Wuhan University.

Author contributions

YL Conceptualization, Writing–original draft, Writing–review and editing. YX Project administration, Funding acquisition. CH Methodology, Validation, Formal analysis, Roles, Writing–original draft.

Acknowledgments

We are grateful for the financial support from the Science, Technology & Innovation Commission of Shenzhen Municipality (No JCYJ20190807144209381).

Conflict of interest

The authors declare that the research was conducted in the absence of any commercial or financial relationships that could be construed as a potential conflict of interest.

Publisher's note

Supplementary material

The Supplementary Material for this article can be found online at: https://www.frontiersin.org/articles/10.3389/fbioe.2022.1069676/full#supplementary-material

References

Bai, S., Lan, Y., Fu, S., Cheng, H., Lu, Z., and Liu, G. (2022). Connecting calcium-based nanomaterials and cancer: From diagnosis to therapy. *Nanomicro. Lett.* 14 (1), 145. doi:10.1007/s40820-022-00894-6

Baumann, M., Krause, M., Overgaard, J., Debus, J., Bentzen, S. M., Daartz, J., et al. (2016). Radiation oncology in the era of precision medicine. *Nat. Rev. Cancer* 16 (4), 234–249. doi:10.1038/nrc.2016.18

Cao, Y., Wu, T., Zhang, K., Meng, X., Dai, W., Wang, D., et al. (2019). Engineered exosome-mediated near-infrared-II region V2C quantum dot delivery for nucleus-target low-temperature photothermal therapy. *ACS Nano* 13 (2), 1499–1510. doi:10.1021/acsnano.8b07224

Chang, M., Hou, Z., Jin, D., Zhou, J., Wang, M., Wang, M., et al. (2020). Colorectal tumor microenvironment-activated bio-decomposable and metabolizable Cu2 O@ CaCO3 nanocomposites for synergistic oncotherapy. *Adv. Mater.*, e2004647.

Chen, F., Yang, B., Xu, L., Yang, J., and Li, J. (2021). A CaO2 @tannic acid-Fe(III) nanoconjugate for enhanced chemodynamic tumor therapy. *ChemMedChem* 16 (14), 2278–2286. doi:10.1002/cmdc.202100108

Chen, N., Fu, W., Zhou, J., Mei, L., Yang, J., Tian, Y., et al. (2021). Mn2+-doped ZrO2@PDA nanocomposite for multimodal imaging-guided chemo-photothermal combination therapy. *Chin. Chem. Lett.* 32 (8), 2405–2410. doi:10.1016/j.cclet.2021.02.030

Cui, X., Lu, G., Fang, F., Xiong, Y., Tian, S., Wan, Y., et al. (2021). Iron self-boosting polymer nanoenzyme for low-temperature photothermal-enhanced ferrotherapy. *ACS Appl. Mat. Interfaces* 13 (26), 30274–30283. doi:10.1021/acsami.1c01658

Dai, Y., Ding, Y., and Li, L. (2021). Nanozymes for regulation of reactive oxygen species and disease therapy. *Chin. Chem. Lett.* 32 (9), 2715–2728. doi:10.1016/j.cclet.2021.03.036

Dong, Z., Feng, L., Zhu, W., Sun, X., Gao, M., Zhao, H., et al. (2016). CaCO3 nanoparticles as an ultra-sensitive tumor-pH-responsive nanoplatform enabling real-time drug release monitoring and cancer combination therapy. *Biomaterials* 110, 60–70. doi:10.1016/j.biomaterials.2016.09.025

Duo, Y., Zhu, D., Sun, X., Suo, M., Zheng, Z., Jiang, W., et al. (2021). Patient-derived microvesicles/AIE luminogen hybrid system for personalized sonodynamic cancer therapy in patient-derived xenograft models. *Biomaterials* 272, 120755. doi:10.1016/j.biomaterials.2021.120755

Guo, W., Wang, T., Huang, C., Ning, S., Guo, Q., Zhang, W., et al. (2022). Platelet membrane-coated C-TiO2 hollow nanospheres for combined sonodynamic and alkyl-radical cancer therapy. *Nano Res.* doi:10.1007/s12274-022-4646-2

Hu, T., Wang, Z., Shen, W., Liang, R., Yan, D., and Wei, M. (2021). Recent advances in innovative strategies for enhanced cancer photodynamic therapy. *Theranostics* 11 (7), 3278–3300. doi:10.7150/thno.54227

Huang, C., Liu, Z., Chen, M., Du, L., Liu, C., Wang, S., et al. (2021). Tumor-derived biomimetic nanozyme with immune evasion ability for synergistically enhanced low dose radiotherapy. *J. Nanobiotechnology* 19 (1), 457. doi:10.1186/s12951-021-01182-y

Jiang, F., Yang, C., Ding, B., Liang, S., Zhao, Y., Cheng, Z., et al. (2022). Tumor microenvironment-responsive MnSiO3-Pt@BSA-Ce6 nanoplatform for synergistic catalysis-enhanced sonodynamic and chemodynamic cancer therapy. *Chin. Chem. Lett.* 33, 2959–2964. doi:10.1016/j.cclet.2021.12.096

Li, Y., Zhou, S., Song, H., Yu, T., Zheng, X., and Chu, Q. (2021). CaCO3 nanoparticles incorporated with KAE to enable amplified calcium overload cancer therapy. *Biomaterials* 277, 121080. doi:10.1016/j.biomaterials.2021.121080

Liang, S., Deng, X., Ma, P., Cheng, Z., and Lin, J. (2020). Recent advances in nanomaterial-assisted combinational sonodynamic cancer therapy. *Adv. Mat.* 32, e2003214. doi:10.1002/adma.202003214

Ma, Y., Zhang, Y., Han, R., Li, Y., Zhai, Y., Qian, Z., et al. (2022). A cascade synergetic strategy induced by photothermal effect based on platelet exosome nanoparticles for tumor therapy. *Biomaterials* 282, 121384. doi:10.1016/j.biomaterials.2022.121384

Tan, X., Huang, J., Wang, Y., He, S., Jia, L., Zhu, Y., et al. (2021). Transformable nanosensitizer with tumor microenvironment-activated sonodynamic process and calcium release for enhanced cancer immunotherapy. *Angew. Chem. Int. Ed. Engl.* 60 (25), 14170–14178. doi:10.1002/ange.202102703

Wang, J., Chen, P., Dong, Y., Xie, H., Wang, Y., Soto, F., et al. (2021). Designer exosomes enabling tumor targeted efficient chemo/gene/photothermal therapy. *Biomaterials* 276, 121056. doi:10.1016/j.biomaterials.2021.121056

Wang, Q., Gao, Z., Zhao, K., Zhang, P., Zhong, Q.-Z., Yu, Q., et al. (2021). Co-delivery of enzymes and photosensitizers via metal-phenolic network capsules for enhanced photodynamic therapy. *Chin. Chem. Lett.* 33, 1917–1922. doi:10.1016/j.cclet.2021.11.040

Wang, S., Zeng, N., Zhang, Q., Chen, M., and Huang, Q. (2022). Nanozyme hydrogels for self-augmented sonodynamic/photothermal combination therapy. *Front. Oncol.* 12, 888855. doi:10.3389/fonc.2022.888855

Xu, T., Zhao, S., Lin, C., Zheng, X., and Lan, M. (2020). Recent advances in nanomaterials for sonodynamic therapy. *Nano Res.* 13 (11), 2898–2908. doi:10.1007/s12274-020-2992-5

Yang, M., Cong, C., Bian, J., Xu, Z., Liu, X., Liu, L., et al. (2021). Photothermal controlled oxygen self-supplying “nano-bombs” via lysosome burst for transcytosis delivery and anti-tumor therapy. *Appl. Mater. Today* 22, 100940. doi:10.1016/j.apmt.2021.100940

Yu, L., Zhang, X., Li, X., Zhang, Z., Niu, X., Wang, X., et al. (2021). A pH-responsive Pt-based nanoradiosensitizer for enhanced radiotherapy via oxidative stress amplification. *Nanoscale* 13 (32), 13735–13745. doi:10.1039/d1nr02043a

Yuan, A., Ruan, L., Jia, R., Wang, X., Wu, L., Cao, J., et al. (2021). Tumor exosome-mimicking iron oxide nanoparticles for near infrared-responsive drug delivery. *ACS Appl. Nano Mat.* 5, 996–1002. doi:10.1021/acsanm.1c03643

Zhang, H., Pan, X., Wu, Q., Guo, J., Wang, C., and Liu, H. (2021). Manganese carbonate nanoparticles-mediated mitochondrial dysfunction for enhanced sonodynamic therapy. *Exploration* 1 (2), 20210010. doi:10.1002/exp.20210010

Zhao, H., Zhao, B., Li, L., Ding, K., Xiao, H., Zheng, C., et al. (2020). Biomimetic decoy inhibits tumor growth and lung metastasis by reversing the drawbacks of sonodynamic therapy. *Adv. Healthc. Mat.* 9 (1), e1901335. doi:10.1002/adhm.201901335

Zheng, P., Ding, B., Jiang, Z., Xu, W., Li, G., Ding, J., et al. (2021). Ultrasound-augmented mitochondrial calcium ion overload by calcium nanomodulator to induce immunogenic cell death. *Nano Lett.* 21 (5), 2088–2093. doi:10.1021/acs.nanolett.0c04778

Zhou, L., Chen, J., Li, R., Wei, L., Xiong, H., Wang, C., et al. (2021). Metal-polyphenol-Network coated prussian blue nanoparticles for synergistic ferroptosis and apoptosis via triggered GPX4 inhibition and concurrent *in situ* bleomycin toxification. *Small* 17 (47), e2103919. doi:10.1002/smll.202103919

Zhu, D., Chen, H., Huang, C., Li, G., Wang, X., Jiang, W., et al. (2022). H2O2 self-producing single-atom nanozyme hydrogels as light-controlled oxidative stress amplifier for enhanced synergistic therapy by transforming “cold” tumors. *Adv. Funct. Mat.* 32, 2110268. doi:10.1002/adfm.202110268

Zhu, D., Ling, R., Chen, H., Lyu, M., Qian, H., Wu, K., et al. (2022). Biomimetic copper single-atom nanozyme system for self-enhanced nanocatalytic tumor therapy. *Nano Res.* 15, 7320–7328. doi:10.1007/s12274-022-4359-6

Zhu, D., Zhang, T., Li, Y., Huang, C., Suo, M., Xia, L., et al. (2022). Tumor-derived exosomes co-delivering aggregation-induced emission luminogens and proton pump inhibitors for tumor glutamine starvation therapy and enhanced type-I photodynamic therapy. *Biomaterials* 283, 121462. doi:10.1016/j.biomaterials.2022.121462

Zhu, Y., Shi, H., Li, T., Yu, J., Guo, Z., Cheng, J., et al. (2020). A dual functional nanoreactor for synergistic starvation and photodynamic therapy. *ACS Appl. Mat. Interfaces* 12 (16), 18309–18318. doi:10.1021/acsami.0c01039

frontiers | Frontiers in Bioengineering and Biotechnology

TYPE Original Research
PUBLISHED 12 January 2023
DOI 10.3389/fbioe.2022.1098923

Bismuth-coated 80S15C bioactive glass scaffolds for photothermal antitumor therapy and bone regeneration

Jianhang Du[2†], Huifeng Ding[1,2†], Shengyang Fu[3†], Dejian Li[2*] and Bin Yu[1*]

[1]Department of Orthopedics, Shanghai Public Health Clinical Center, Fudan University, Shanghai, China, [2]Department of Orthopedics, Shanghai Pudong Hospital, Fudan University Pudong Medical Center, Shanghai, China, [3]Center for Translational Neurodegeneration and Regenerative Therapy, Tongji Hospital, Tongji University School of Medicine, Shanghai, China

OPEN ACCESS

EDITED BY
Long Bai,
East China University of Science and Technology, China

REVIEWED BY
Yingjie Yu,
Beijing University of Chemical Technology, China
Melika Sahranavard,
Materials and Energy Research Center, Iran
Hu Menglong,
Peking University Hospital of Stomatology, China

*CORRESPONDENCE
Dejian Li,
✉ lidejian880820@163.com
Bin Yu,
✉ surgery2010@126.com

†These authors have contributed equally to this work

SPECIALTY SECTION
This article was submitted to Nanobiotechnology, a section of the journal Frontiers in Bioengineering and Biotechnology

RECEIVED 15 November 2022
ACCEPTED 28 December 2022
PUBLISHED 12 January 2023

CITATION
Du J, Ding H, Fu S, Li D and Yu B (2023), Bismuth-coated 80S15C bioactive glass scaffolds for photothermal antitumor therapy and bone regeneration. *Front. Bioeng. Biotechnol.* 10:1098923. doi: 10.3389/fbioe.2022.1098923

Background: Malignant bone tumors usually occur in young people and have a high mortality and disability rate. Surgical excision commonly results in residual bone tumor cells and large bone defects, and conventional radiotherapy and chemotherapy may cause significant side effects. In this study, a bifunctional Bi-BG scaffold for near-infrared (NIR)-activated photothermal ablation of bone tumors and enhanced bone defect regeneration is fabricated.

Methods: In this study, we prepared the Bi-BG scaffold by *in-situ* generation of NIR-absorbing Bi coating on the surface of a 3D-printing bioactive glass (BG) scaffold. SEM was used to analyze the morphological changes of the scaffolds. In addition, the temperature variation was imaged and recorded under 808 nm NIR laser irradiation in real time by an infrared thermal imaging system. Then, the proliferation of rat bone mesenchymal stem cells (rBMSCs) and Saos-2 on the scaffolds was examined by CCK-8 assay. ALP activity assay and RT-PCR were performed to test the osteogenic capacity. For *in vivo* experiments, the nude rat tumor-forming and rat calvarial defect models were established. At 8 weeks after surgery, micro-CT, and histological staining were performed on harvested calvarial samples.

Results: The Bi-BG scaffolds have outstanding photothermal performance under the irradiation of 808 nm NIR at different power densities, while no photothermal effects are observed for pure BG scaffolds. The photothermal temperature of the Bi-BG scaffold can be effectively regulated in the range 26–100°C by controlling the NIR power density and irradiation duration. Bi-BG scaffolds not only significantly induces more than 95% of osteosarcoma cell death (Saos-2) *in vitro*, but also effectively inhibit the growth of bone tumors *in vivo*. Furthermore, they exhibit excellent capability in promoting osteogenic differentiation of rBMSCs and finally enhance new bone formation in the calvarial defects of rats.

Conclusion: The Bi-BG scaffolds have bifunctional properties of photothermal antitumor therapy and bone regeneration, which offers an effective method to ablate malignant bone tumors based on photothermal effect.

KEYWORDS

bismuth, bioactive glass, photothermal antitumor, bone regeneration, 3D printing

1 Introduction

Primary malignant bone tumors such as osteosarcoma and Ewing sarcoma are most common in the adolescent population with a high mortality and disability rate. They can cause large bone defects after surgical treatment. Some bone tumors are still not completely resectable, and therefore are usually treated with post-operative chemotherapy such as metastatic tumors in the spine. However, the lack of targeting of chemotherapy drugs is associated with serious complications such as infection due to bone marrow suppression, femoral head necrosis and nephrotoxicity (Djunic et al., 2011). Long-term chemotherapy can also make tumor cells resistant to drugs. Radiotherapy as a local treatment has limited indications, particularly for spinal tumors where it is contraindicated. It is therefore a great challenge to prepare biomaterials that combine the treatment of bone tumors with bone defect repair.

In recent years, there has been an increasing interest in photothermal therapy (PTT) to kill tumor cells. When a photothermal material absorbs light in the infrared band, the electrons move from the ground state to the excited state and then release energy through non-radiative decay, causing an increase in kinetic energy to heat the local environment of the material (Cao et al., 2013; Li et al., 2013). Photothermal therapy has been considered a very promising method of tumor treatment because it is localized and avoids damage to normal tissue in non-treated areas (Liu et al., 2009; Von Maltzahn et al., 2009; Choi et al., 2011; Melancon et al., 2011).PTT employs photo-absorbing agents to generate heat from light, thus inducing hyperthermia in tumor sites as well as causing protein denaturation and cell membrane disruption, finally resulting in cell death (Cheng et al., 2014a). As effective newborn PTT agents, Bismuth (Bi)-based nanoparticles (NPs) have been intensely investigated in recent years. So far, most research on PTT agents focus on Bi_2Se_3 (Li et al., 2016; Xie et al., 2016), Bi_2S_3 (Wang et al., 2016; Xiao et al., 2016), Cu_3BiS_3 (Yang et al., 2015; Liu et al., 2016), and Bi NPs (Li et al., 2017; Yu X et al., 2017). The photothermal conversion efficiency (η) of these Bi-based NPs is essentially above 30% under NIR laser irradiation. Among them, pure Bi NPs have been demonstrated to exhibit excellent physiological stability, biocompatibility, and extended circulating half-life (Li et al., 2017; Yu X et al., 2017). Due to their strong NIR absorbance as well as the high photothermal conversion efficiency and conversion stability, highly effective *in vivo* photothermal ablation of tumors has been realized under NIR irradiation, without noticeable toxicity (Li et al., 2017; Yu X et al., 2017). Moreover, Bismuth is also used in clinic mainly for the treatment of *H. pylori* infection. It is absorbed orally by the body and distributed primarily to the kidneys, brain, liver and bones. Although it easily forms insoluble precipitates in the stomach, less than .5% is absorbed by the body. Thus, small doses of bismuth rarely cause significant toxic side effects (Leussink et al., 2001).

Bioactive glass is an artificial bone that promotes osteogenesis and provides strong biomechanical properties, while the material is biodegradable. Its main functional elements are Ca, Si, P, and Na. BG is widely used as a bone repair material due to its ability to form a hydroxyapatite layer *in vivo* and to bind biologically to bone tissue (Hench, 1991; Ohtsuki et al., 1992; Hench et al., 1971). In addition, Ca^{2+} and Si^{4+} in bioactive glass promote osteoblast proliferation and differentiation (Gough et al., 2004; Valerio et al., 2004). Yan used a novel method to prepare 80S15C bioactive glass with pores of 5–20 nm, a pore volume of .4 cm^3/g and a surface area of 300 m^2/g (Yan et al., 2006). Zhu et al. (2008) found that 80S15C (a relatively low calcium content) has better biological activity *in vitro* compared to convention; ; al bioactive glass. Our previous study found that 80S15C-coated artificial ligaments had a beneficial effect on tendon-bone healing (Yu B et al., 2017). Therefore, we used 80S15C bioactive glass as a substrate for tumorous bone defects.

To our knowledge, no such bioactive scaffold has been designed with both photothermal anti-tumor effects and osteogenic activity. Therefore, the aim of this study was to design and fabricate a bifunctional scaffold to kill osteosarcoma cells and repair bone defects, making it possible to treat large bone defects caused by surgical resection of bone tumors. In this study, BG scaffolds were firstly prepared by three-dimensional (3D) printing, and Bi was modified to the surface of as-printed scaffolds afterwards (Figure 1A). The effects of NIR laser power and irradiation duration on the photothermal effect of scaffolds were systematically investigated. Then, we evaluated the photothermal antitumor effects of Bi-BG scaffolds *in vitro* and *in vivo*. Furthermore, their osteogenic capacity was investigated *in vitro* and *in vivo*.

2 Materials and methods

2.1 Materials

Tetraethyl orthosilicate (TEOS, 98%), triethylphosphate (TEP, 99%), ethanol, calcium nitrate ($Ca(NO_3)_{24}H_2O$, 99%), sodium borohydride, and bismuth nitrate were purchased from Sinopharm Chemical Reagent (China). Polyvinyl alcohol (PVA, Mn = 70–90 k) was purchased from Sigma-Aldrich. All chemicals were used without further purification.

2.2 Fabrication and characterizations of Bi-coated 80S15C bioactive glass (Bi-BG) scaffolds

The 80S15C BG powder was prepared by the evaporation-induced self-assembly (EISA) method. Firstly, ethyl orthosilicate (TEOS, 53.6 g), $Ca(NO_3)_2$ - 4 H_2O (11.2 g), triethyl phosphate (TEP, 5.84 g) and HCl (.5 M, 8 g) were added to ethanol (480 g) and stirred for 24 h. The resulting solution was poured into a glass Petri dish for evaporation-induced self-assembly at room temperature for 7 days. Subsequently, it is dried in an oven at 60°C for 48 h to obtain BG powder.

In this experiment, an aqueous solution of 10 wt% PVA was used as the adhesive agent for the printing paste preparation. Firstly, 5 g of PVA particles were added to a container containing 45 g of deionized water and stirred for 2 h at room temperature to ensure that the PVA particles were sufficiently swollen to facilitate dissolution. The container was then placed in a water bath whose temperature was gradually increased to 92°C, and stirred until completely dissolved. Finally, allow the PVA solution to cool and reserve for use.

The synthesized BG powder is ground and sieved. Then it was added to the aqueous PVA solution and mixed thoroughly to obtain printable BG/PVA slurry (W_{BG}: W_{PVA} = 1.2:1). The prepared slurry was then transferred into a syringe to print. The needle for printing has an internal diameter of 400 μm, a syringe temperature of 25°C, a pressure of 2–4 bar and a printing speed of 4–8 mm/s. The piston of the syringe squeezed the slurry out of the needle to form a fibrous form, and the final BG/PVA scaffold was printed by layer-by-layer stacking.

BG and Bi-BG scaffolds were viewed by optical microscope. Scanning electron microscopy (SEM) was carried out with a ZEISS Sigma 300 field emission scanning electron microscope with mapping analysis. SEM images and element mapping were monitored on a SU8220 microscope (HITACHI, Japan). FTIR were measured by Thermo Scientific Nicolet iS10 in the range of 4,000–400 cm^{-1}.

2.3 *In Vitro* photothermal effect of Bi-BG scaffolds

To evaluate the photothermal property, the Bi-BG scaffolds were placed in a 48-well culture plate, irradiated by the 808 nm NIR laser (LDT-808, Shanghai Connect Fiber Optics Company) for 5 min, and the temperature variation was imaged and recorded in real time by an infrared thermal imaging system (223S, Fotirc). Different power density of the light was applied, including low (1 W/cm^2), medium (2 W/cm^2), and high (3 W/cm^2). The photothermal effect of the scaffolds in wet condition (PBS) was also evaluated for 10 min. Finally, the photothermal conversion curve over time was plotted using FLIR R&D software.

2.4 *In Vitro* photothermal antitumor effect of Bi-BG scaffolds

All scaffolds were sterilized with ethylene oxide and prepared for use. To evaluate the *in vitro* photothermal anti-tumor effect of the Bi-BG scaffold, Saos-2 cells were inoculated in 48-well plates at a density of 1×10^4 cells per well for 24 h ($n = 4$). For the laser group, the scaffold was placed in the well plate and irradiated with an 808 nm laser (3 W/cm^2) for 10 min, then they were removed. For the no-laser group, the scaffolds were placed in the well plate for 10 min and then removed. Saos-2 cells were then incubated for a further 12 h. The proliferation of Saos-2 cells with the scaffolds was tested using a standard CCK-8 method. The effect of different irradiation time on saos-2 cell viability were further evaluated. The cells were co-cultured with the Bi-BG scaffold for 24 h and then irradiated with a NIR laser at a power density of 3 W/cm^{-2} for 10, 20, and 30 min respectively.

Live/dead cell staining is used to observe the viability of tumor cells after photothermal treatment. Firstly, Saos-2 cells were seeded on round coverslip ($n = 2$). After the cells had grown all over the coverslip, the scaffolds were placed slightly into the well plate. For the laser groups, the scaffolds were exposed to a NIR laser at 3 W/cm^2 for 15 min and then removed. For the no-laser groups, the scaffolds were placed in the well plate for 15 min and then removed. After washed three times with PBS, the cells were stained for 20 min with Calcein AM (Life Technologies, United States) and Ethidium homodimer-1 (Life Technologies, United States). Finally, the status and activity of Saos-2 cells on the coverslip were observed using a single photon laser confocal microscopic imaging system (Leica TCS SP8, Germany).

2.5 *In Vivo* photothermal antitumor effect of Bi-BG scaffolds

A total of 24 female nude mice (Balb/c) of 4–6 weeks were used for this study. Saos-2 cell suspension (5×10^6 cells/each) was injected subcutaneously into the back of nude mice. When the subcutaneous tumor volume reached about 114 mm^3, the nude mice were randomly divided into four groups: BG group, BG + laser group, Bi-BG group and Bi-BG + laser group ($n = 6$). A small incision was carefully made in the skin at the tumor margin and the scaffold (8 mm × 1.5 mm) was inserted into the center of the tumor. The wound was then closed with surgical sutures. After 24 h, the mice in the BG laser and Bi-BG laser groups were anesthetized and irradiated with an 808 nm NIR laser (3 W/cm^{-2}) for 10 min every 3 days. The real-time temperature and *in situ* thermal images at tumor sites of the mice were monitored using an infrared thermographic camera. The tumor volumes of all mice were recorded every other day. Tumor volume (V) = (tumor length) × $(\text{tumor width})^2$/2—scaffold volume; scaffold volume = 60 mm^3. V_0 is the initial tumor volume-scaffold volume at day 0. The relative tumor size = V/V_0.

Finally, tumor specimens were harvested after 2 weeks for hematoxylin and eosin (HE). Tumor cell necrosis rate (TCNR) was calculated according to the formula, TCNR = (1—N/M) × 100%, where M is the mean cell survival rate of normal tumor tissue without treatment and N is the cell survival rate of the scaffold-treated samples. To further verify the *in vivo* biosafety of BG and BI-BG scaffolds, the major organs (heart, liver, spleen, lungs, and kidneys) of all mice were collected for HE staining.

2.6 *In Vitro* osteogenic differentiation of rBMSCs on Bi-BG scaffolds

rBMSCs were used in the following experiments. Firstly, the proliferation of rBMSCs on the scaffold surface was quantitatively assessed using CCK-8 method. Bi and Bi-BG scaffolds were sterilized and placed in 24-well plates, then rBMSCs were inoculated onto the surface of the scaffolds at a density of 1×10^4 per well. Osteogenic differentiation was induced by replacing the complete medium with osteogenic induction solution for 7 and 14 days respectively. At the established time points, 200 μL of cell lysis solution was added to each well and the supernatant was collected after 5 min of lysis on ice. The ALP activity of protein samples was measured at 405 nm according to the instructions (Beyotime, Shanghai). Finally, the protein concentration of the samples was determined by the bicinchoninic acid (BCA) method to standardize the ALP activity.

All scaffolds were sterilized and placed in 6-well plates. 2×10^5 rBMSCs of forth generation were added to each well and the medium was changed every other day. The expression levels of osteogenesis-related genes (OCN, BSP, BMP2, OPN, ALP) were measured by RT-qPCR after 7 and 14 days of incubation, respectively. At the time point of the assay, cells were lysed with 1 mL of Trizol reagent for 15 min to extract RNA after removal of the medium. The RNA was then reverse transcribed into cDNA using iScript cDNA Synthesis kit. Subsequently, the Ct values of the osteogenic genes were detected on a PCR instrument using the SYBR Green PCR Master Mix Kit, with the GAPDH gene as an internal reference. Finally, the expression levels of the osteogenesis-related genes were calculated by the ΔΔCt method.

2.7 *In Vivo* bone regeneration of Bi-BG scaffolds

All experimental procedures described in this study were approved by the Animal Ethics Committee of Fudan University Pudong Medical Center. Eighteen 7-week-old male Sprague Dawley (SD) rats were used for surgery and randomly divided into three groups as follows: 1) Blank control ($n = 6$); 2) BG ($n = 6$), and 3) Bi-BG ($n = 6$). Anesthesia was administered to rats by intraperitoneal injection of 3% (w/v) sodium

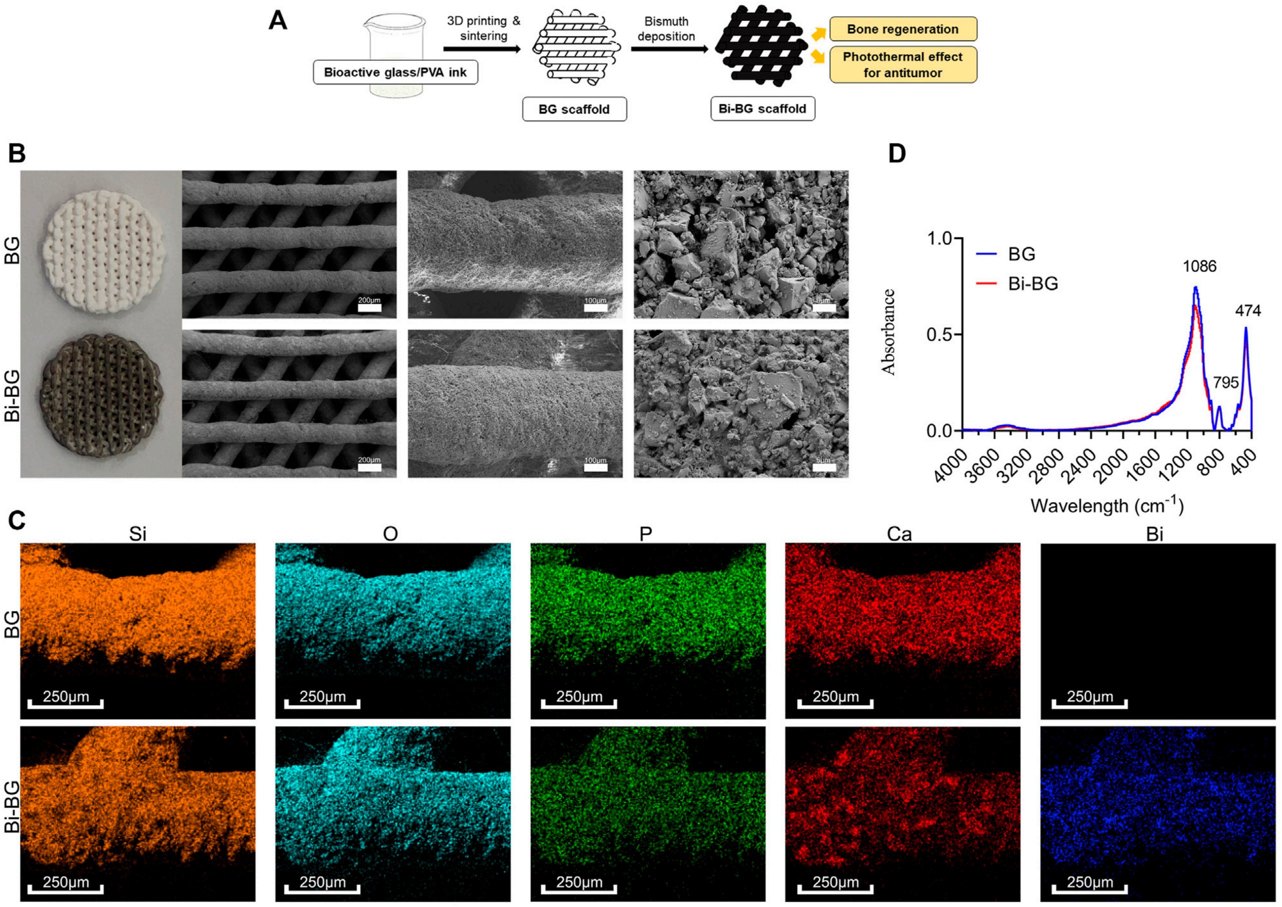

FIGURE 1
Fabrication and characterizations of BG and Bi-BG scaffolds. **(A)** Schematic illustration for the formation of bifunctional Bi-BG scaffolds. **(B)** Photograph and SEM images of 3D printed pure BG and Bi-BG scaffolds; **(C)** Elemental mapping images (Si, O, P, Ca, and Bi elements) of BG and Bi-BG scaffolds; **(D)** FTIR patterns of the scaffolds.

pentobarbital (30 mg/kg). A 1.5-cm sagittal incision is made in the scalp along the median line: the skin and subcutaneous tissues of the rat are incised in sequence, followed by exposure of the skull *via* blunt dissection. Two 5-mm cranial defects were created using an electric torus drill, and then the scaffold material was placed in the defects. Finally, the incision was closed by suturing the periosteum and skin. Each rat was given penicillin intramuscularly for 3 days after surgery. All animals were euthanized by injection of an overdose of sodium pentobarbital 8 weeks after surgery for the following experiments.

All rats were executed 8 weeks after implantation of the scaffolds. The skull was dissected and the surrounding muscles and soft tissues were removed. The newly harvested skull was then scanned using micro-CT (Skyscan1176, Kontich, Belgium) with a resolution of 18 μm to assess the formation of new bone. Finally, 3D images were reconstructed using 3D Creator software to determine bone volume versus total bone volume (BV/TV) and local bone mineral density (BMD). The removed skull was placed in 4% paraformaldehyde for 24 h and then decalcified with 5% nitric acid for 1 week, with the solution changed every other day. This was followed by consecutive dehydration in gradient ethanol (70%–100%) and toluene. The dehydrated samples were embedded using paraffin wax and hardened into paraffin blocks. A slicer (HM 325, Thermo Fisher Scientific) was then used to cut the paraffin blocks to obtain 10 μm thick sections in the sagittal direction. After deparaffinization and hydration, the sections were stained with HE and Masson. Finally, the sections were observed under a microscope and images were captured using a histological digital scanning system (NanoZoomerS210, Hamamatsu) to assess the repair of the skull defect.

2.8 Statistical analyses

All data were collected from three parallel samples and statistically analyzed using Graphpad Prism 10 software. The experimental results are expressed as mean ± standard deviation (mean ± SD). Multiple groups were statistically analyzed by one-way analysis of variance (ANOVA) and Student-Newman-Keuls post-hoc tests. $p < .05$ indicated that there is a statistical difference.

3 Results and discussion

3.1 Preparation and characterization of Bi-BG scaffolds

BG scaffolds were prepared from BG powders *via* 3D printing, which is a rapid and concise technique for complex

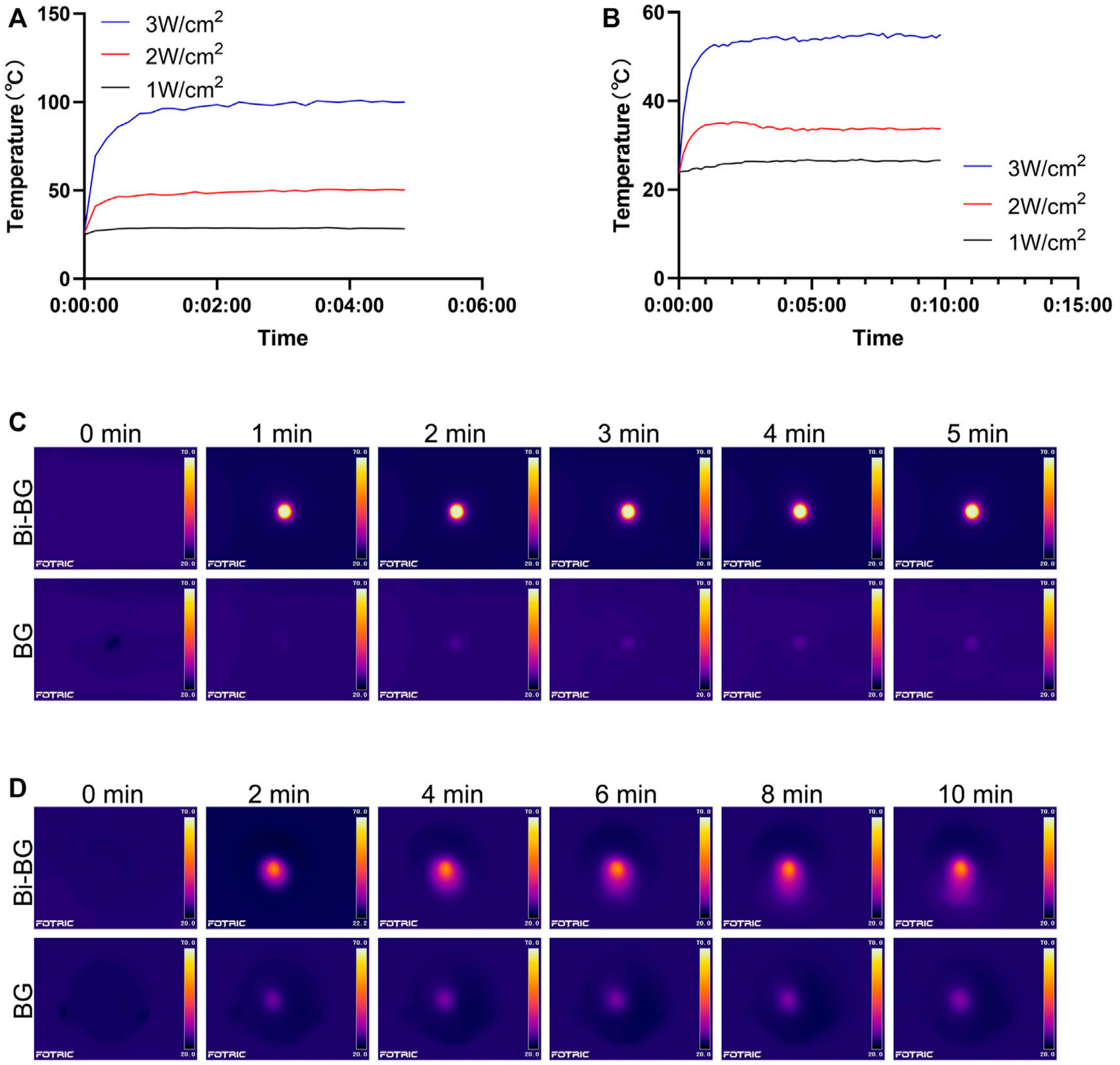

FIGURE 2
Photothermal effect of Bi-BG scaffolds. Heating curves of Bi-BG scaffolds with different laser power irradiation in **(A)** dry state and in **(B)** PBS; infrared thermal images of Bi-BG and BG scaffolds in **(C)** dry state and in **(D)** PBS under 808 nm laser irradiation.

structures forming. We chose the structure with macro-pores (400 μm) (Figure 1b), which has been proved to facilitate cell attachment and migration, nutrient transport, blood vessel growth, and bone formation (Zhu et al., 2015; Rustom et al., 2016). And the crystals could be found on the surface of the scaffolds after sintering. The main elements on scaffolds were Si, O, P, and Ca that were the BG powder composition, and the surface structures seemed to be no different between BG scaffolds after Bi modification (Figure 1b). However, Bi could be detected *via* element analysis with a uniform distribution (Figure 1c). There was no morphological difference that could be attributed to the limited Bi modification on the scaffolds. BG and Bi-BG scaffolds showed similar absorbance peaks evaluated by FTIR (Figure 1d), where the peak on 474 cm^{-1} was the bending vibration absorption peak of Si-O, 795 cm^{-1} was the symmetric stretching vibration peak of Si-O, and 1,086 and 795 cm^{-1} were the asymmetric stretching vibration peak of Si-O-Si. These peaks conformed to the main composition of Si and O in both BG and Bi-BG scaffolds.

As a biocompatible photothermal conversion agent (Chen et al., 2019), Bi has been introduced to surface-modify 3D printed bioactive glass scaffolds to provide them with excellent photothermal properties and enhanced osteogenesis. In this study, we combined 3D printing technology and Bi surface modification to fabricate Bi-BG scaffolds. 3D printing enables good control of the macroporous size and geometry of 80Si15C scaffolds through computer-aided design (CAD). The Bi-BG scaffold can therefore be shaped specifically according to the individual requirements of the patients, compared to other techniques. Bi coatings are easily and firmly deposited on the surface of 3D printed BG scaffolds by direct solution immersion and *in-situ* reduction, which do not damage their macroporous structure. Finally, we have successfully prepared a bifunctional Bi-BG scaffold for bone tumor treatment and the repair of large bone defects.

3.2 Photothermal effect of Bi-BG scaffolds

The photothermal effect of Bi-BG scaffolds was evaluated *in vitro*. It could be found that the Bi-BG scaffolds could induce a temperature rise under NIR irradiation, and the temperature rise could be regulated by laser power (Figure 2A), while the temperature of BG scaffolds stayed at room temperature. Under the high power laser irradiation, the temperature of the Bi-BG scaffolds rises rapidly from room temperature to 100°C in 60 s and remains stable at around 100°C thereafter. In infrared thermal images, the Bi-BG scaffolds showed a more obvious thermal signal compared with BG scaffolds (Figure 2C). Furthermore, when the Bi-BG scaffolds were in wet condition, the temperature could also be raised under NIR irradiation (Figure 2B), but was much lower (53°C) than that in the dry condition (100°C). However, Bi-BG scaffolds still showed a brighter thermal signal than that of BG scaffolds (Figure 2D). These results demonstrated that the Bi modification endowed the excellent photothermal effect to BG scaffolds.

There are many Bi-related photothermal materials, and we have chosen pure Bi NPs because their photothermal conversion efficiency is comparable to, or even higher than, that of other Bi-related materials (Cheng and Zhang, 2018). Studies have shown that Bi not only has strong absorption of NIR laser (808 nm) (Peng et al., 2009), but also efficiently converts it into thermal energy (Peng et al., 2011). Pure Bi NPs can be used as a photothermal agent in cancer therapy because its photothermal effect penetrates the skin and is non-invasive and harmless (Mohan, 2010; Yu X et al., 2017; Li et al., 2017). However, there is no report focusing on the origin of photothermal performance of Bi NPs. As semimetal, Bi NPs not only exhibit the surface plasmon resonances (SPR) effect (Sun et al., 2015; Zhao et al., 2016) which is similar to noble metals, but also have narrow bandgap (Qi et al., 2008; Velasco-Arias et al., 2012) like semiconductors. As a result, we presume that its origin of the photothermal property may be similar with that of Bi_2Se_3 NPs. However, the photothermal mechanism of pure Bi NPs needs to be further investigated, beneficial for improving their photothermal efficacy. In this study, we have successfully fabricated a bifunctional Bi-BG scaffold with excellent photothermal properties to raise the ambient temperature to kill osteosarcoma cells. In addition, the Bi-BG scaffold temperature can be efficiently regulated by controlling the laser power and irradiation time over a wide range from room temperature to 100°C. However, the photothermal effect was found to be significantly lower in wet conditions than in dry conditions. One reason is that the PBS solution in which the scaffold is immersed absorbs some of the NIR and thermal energy. The other is that wet conditions may reduce the thermal conductivity of the Bi-BG scaffold.

3.3 Photothermal effect of Bi-BG scaffolds for killing bone-tumor cells

We investigated the killing effect of the Bi-BG scaffolds on osteosarcoma Saos-2 cells under laser irradiation. The viability of osteosarcoma cells was found to decrease sharply with increasing irradiation time (Figure 3G). After 30 min of laser irradiation, the viability of saos-2 cells dropped to a minimum of .164. However, the cellular viability of the BG groups remained largely unchanged after different irradiation durations. In addition, we performed live-dead cell staining after laser irradiation to further assess the tumor-killing effect of the Bi-BG scaffolds. It can be observed that the Saos-2 cells in the Bi-BG group underwent extensive death after laser irradiation, whereas the Saos-2 cells in the other groups grew well and no significant necrosis was seen (Figure 3H). The above results showed that irradiation time plays a key role in killing osteosarcoma cells. The viability of Saos-2 cells was reduced by 71.5% within 30 min, indicating that the Bi-BG scaffolds have a highly effective photothermal osteosarcoma-killing effect.

3.4 *In Vivo* photothermal therapy of tumor tissue by Bi-BG scaffolds

To evaluate the photothermal anti-tumor effect of the Bi-BG scaffolds *in vivo*, we used Saos-2 osteosarcoma cells to form tumors subcutaneously in nude mice. When the subcutaneous tumor had reached a volume of 114 mm^3, the scaffolds were implanted in it and irradiated with NIR light. As shown in Figures 4A, D, the temperature of the tumor center in the Bi-BG group rises rapidly *in vivo* after irradiation with NIR light and remains above 50°C. Hyperthermia (>50°C) within the tumor causes not only late progressive apoptosis of the tumor cells, but also cell necrosis due to irreversible protein denaturation and cell membrane damage (Nikfarjam et al., 2005; Kirui et al., 2010; Lee et al., 2010; Markovic et al., 2011). In addition, the excellent photothermal performance and thermal conductivity of Bi-BG scaffolds kept the temperature of the tumor tissue edge above 45°C, which induces a state of prolonged cell inactivation (Jaque et al., 2014), thus resulting in tumor growth inhibition. However, the temperature of BG scaffolds changes little after irradiation and remains at room temperature due to their poor NIR absorption efficiency and photothermal conversion properties. It can be found that after laser irradiation, the tumor growth rate of the Bi-BG group was significantly slowed down compared to the other three groups (Figure 4E). In addition, the tumors were removed at day 13 after five times of irradiation and it could be seen that the tumor volume of the Bi-BG laser group was the smallest of all four groups. Finally, the HE staining results showed that a large number of tumor nuclei around the scaffold in the Bi-BG laser group were wrinkled and disappeared, while the tumor tissue in the other three groups was normal (Figure 4B). Quantitative analysis revealed that the Bi-BG group had the highest necrosis rate of tumor tissue around the scaffold reaching 85% (Figure 4F). The above results showed that the fabricated Bi-BG scaffold has outstanding photothermal properties and can efficiently kill saos-2 cells *in vitro* and ablate osteosarcoma tissue *in vivo*. Photothermal therapy can selectively kill tumor cells without damaging normal tissue when not exposed to laser radiation (Cheng et al., 2014a). In this study, “selectivity” involves two aspects. One is being able to control where the Bi-BG scaffold is implanted. In our work, the Bi-BG scaffold was implanted into the center of the tumor tissue. The other one is the ability to control the emission of the NIR laser and the tumor site to be irradiated. Recently, microneedles (MNs) have been combined with various therapy strategies including photodynamic therapy (PDT) and PTT to treat many diseases due to its improved selectivity, and minimal invasiveness and side effects (Zhi et al., 2020). Finally, no significant morphological or pathological changes were found in

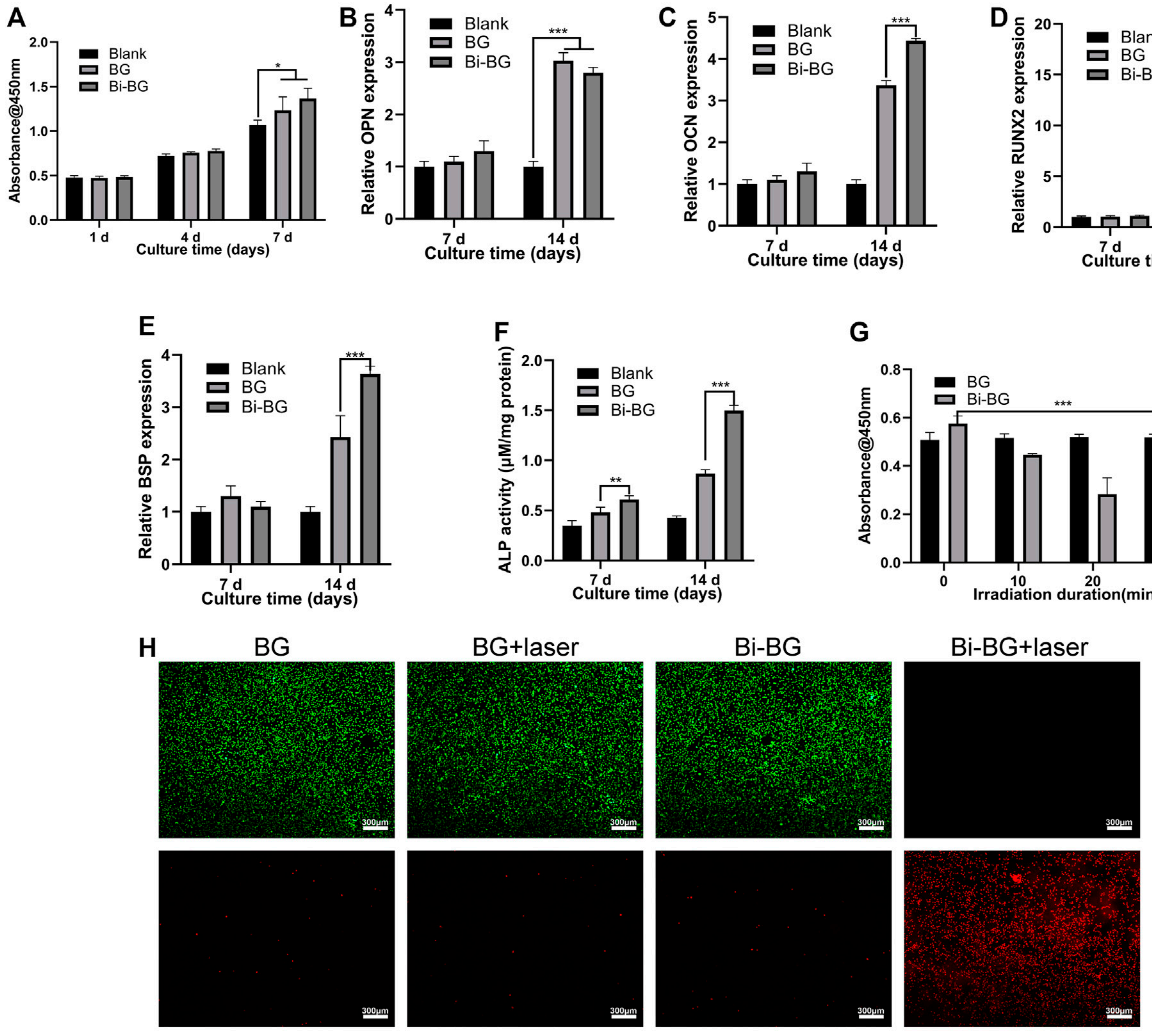

FIGURE 3
In vitro osteogenic and tumor-killing assays. **(A)** Proliferation of rBMSCs incubated on BG and Bi-BG scaffolds for 1, 4, and 7 days; **(B)** osteogenic expression of OPN, **(C)** OCN, **(D)** Runx2, and **(E)** BSP, and **(F)** ALP activity of rBMSCs on the scaffolds for 7 and 14 days ($n = 3$). **(G)** Saos-2 cell viability of on BG and Bi-BG scaffolds treated with different irradiation duration; **(H)** fluorescent images of Saos-2 cells in four groups after 15 min of laser irradiation at 3 W/cm^2. Green represents live cells and red dead (*, **, and *** indicate $p < .05$, $p < .01$, and $p < .001$, respectively).

the major organs of all treatment groups (Figure 4C). Therefore, the Bi-BG scaffolds could effectively inhibit bone tumor growth under NIR laser irradiation with excellent biocompatibility.

3.5 *In Vitro* osteogenic differentiation of rBMSCs for Bi-BG scaffolds

The proliferation of rBMSCs on Bi-BG scaffolds was tested at 1, 4, and 7 days. As shown in Figure 3A, the proliferation viability of rBMSCs of each group increased over time. At day 7, the proliferation viability of BG and Bi-BG groups was significantly higher than that of blank group. More importantly, the proliferation viability of Bi-BG group was statistically higher than that of BG group. These results indicate that the Bi coating on the surface of BG scaffold significantly promoted rBMSC proliferation, which is consistent with the previous studies (Pazarçeviren et al., 2018; Huang et al., 2020). To assess the osteogenic differentiation on Bi-BG scaffolds, the alkaline phosphatase (ALP) activity of rBMSCs was measured at 7 and 14 days of culture. As shown in Figure 3F, the ALP activity of rBMSCs in BG and Bi-BG groups was higher that of blank group. And compared to BG group, the ALP activity of cells on Bi-BG scaffold was significantly higher. In addition, the expression of osteogenic-related genes (OCN, OPN, BSP, RUNX2) (Ivaska et al., 2004; Alford and Hankenson, 2006) of rBMSCs on the scaffold was measured at 7 and 14 days of culture (Figures 3B–E). There was no statistical difference in the expression levels of osteogenesis-related genes of each group at day 7. At day 14, the expression levels of OCN, BSP and RUNX2 in Bi-BG group were significantly higher than those in BG group, but there was no statistical difference in the expression levels of OPN between the two groups. The results show that both BG and Bi-BG scaffolds have favorable osteogenic capacity, which may be attributed to the large pore structure of 3D printed scaffolds that facilitates the

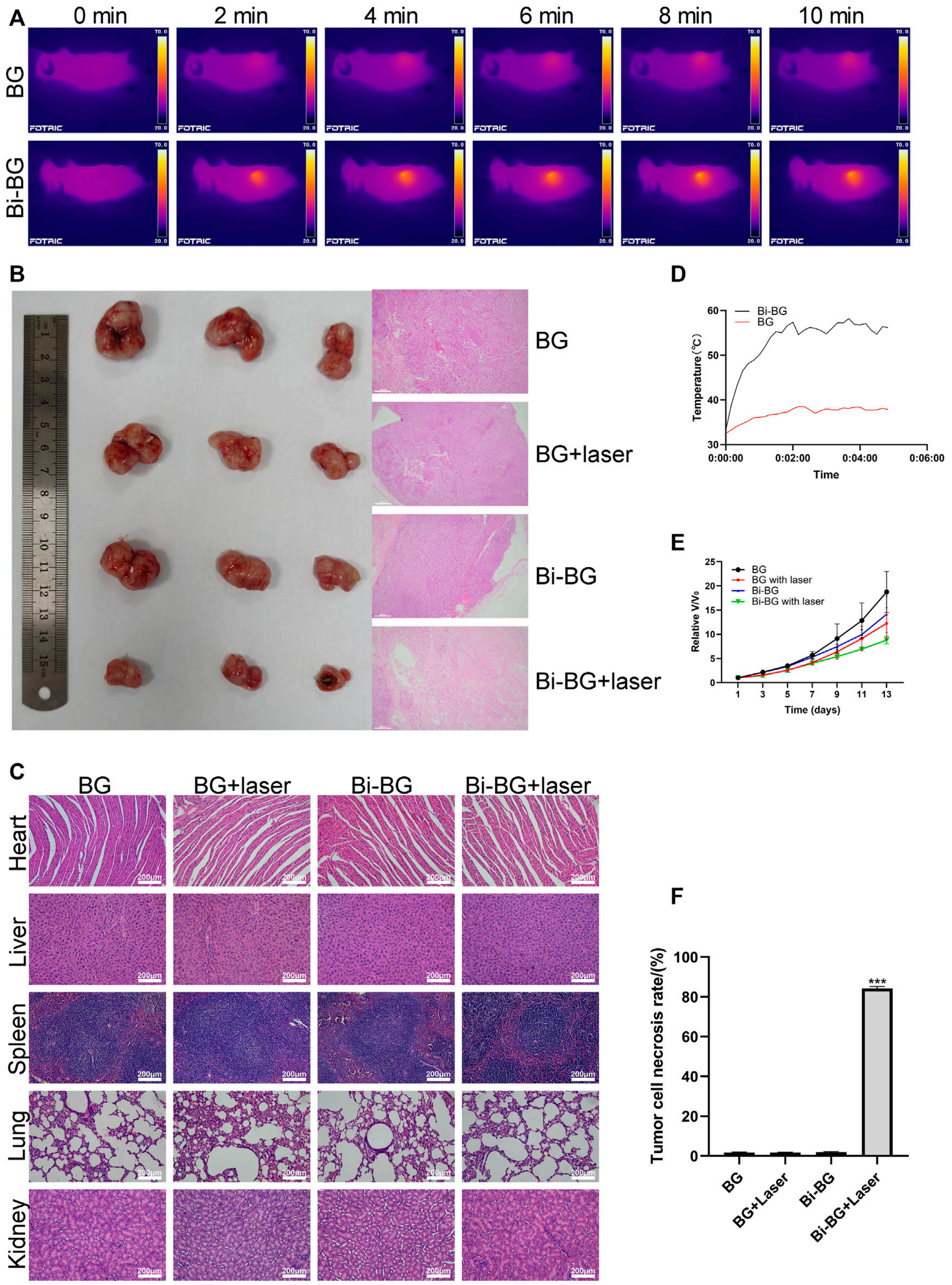

FIGURE 4
In vivo photothermal antitumor effect of Bi-BG scaffolds. **(A)** IR thermal images, **(B)** optical and H&E staining images of tumor in four groups at day 13, **(C)** H&E staining images of major organs from the four groups (scale bar: 100 μm). **(D)** Heating curve of BG and Bi-BG scaffolds in nude mice under 808 nm laser irradiation, **(E)** relative tumor volume change with increasing days of the groups, and **(F)** the tumor cell necrosis rate (TCNR) of four groups.

proliferation, adhesion and osteogenic differentiation of mesenchymal stem cells (Rustom et al., 2016). This is consistent with our previous findings (Zhu et al., 2008; Yu B et al., 2017). And Bi coating on the Bi-BG scaffolds significantly promoted osteogenic differentiation of rBMSCs, which is in line with previous research findings (Wang et al., 2018). This could be explained by the good biocompatibility and chemical stability of the Bi coating (Chiang et al., 2014; Wang et al., 2018).

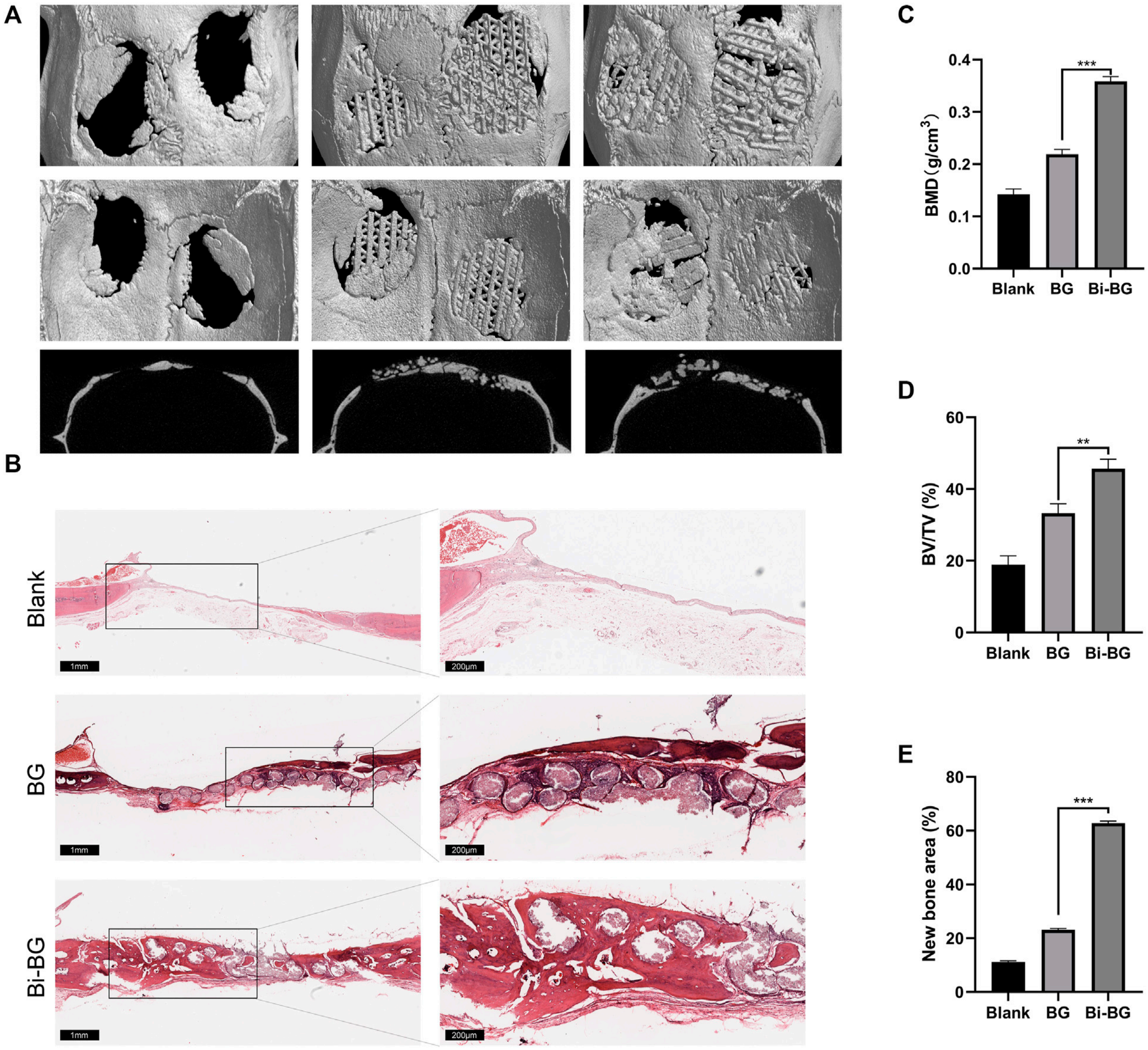

FIGURE 5
In vivo bone regeneration of Bi-BG scaffolds. **(A)** 3D reconstruction and sagittal Micro-CT images of the repaired skulls and **(B)** HE staining images of the blank, BG and Bi-BG groups after 8 weeks' implantation. **(C)** BMD, **(D)** BV/TV, and **(E)** new bone area of each group.

3.6 *In Vivo* bone regeneration for Bi-BG scaffolds

To evaluate the osteogenic capacity of Bi-BG scaffolds *in vivo*, 3D reconstructions were performed on the harvested rat calvarial specimens. As shown in Figure 5A, the Bi-BG scaffolds were well-integrated with the skull defects of the rats and more bone tissue was formed on the scaffolds than the BG scaffolds. Quantitative analysis revealed that the BV/TV and BMD values of Bi-BG group were significantly higher than those of BG and blank groups after 8 weeks (Figures 5C,D). In addition, the HE staining of the calvaria specimens further demonstrated that large amounts of new bone tissue were formed around the Bi-BG scaffolds (Figure 5B). As shown in Figure 5E, Bi-BG group had a considerably higher amount of new bone than BG group. The above results suggested that the modification of Bi coating on BG scaffolds could further promote the regeneration of bone tissue *in vivo*. The results of *in vivo* experiments further validated that the Bi coating on the surface of the Bi-BG scaffolds improves the osteogenic capacity of the scaffold. However, its specific molecular mechanism remains unclear and further research is needed.

It is well known that for bone tissue engineering, large animal models (at least rabbits) should be used, since they can provide relatively large bone defects (Chen et al., 2013; Dong et al., 2013; Kim et al., 2014; Prosecká et al., 2015). However, no such bone cancer models have so far been available in rabbits or larger animals due to immune rejection. Although bone tumor models can be established using nude mice, their bone size is too small for large bone defects. Therefore, in this study, we evaluated the photothermal anti-tumor effect of the Bi-BG scaffold using tumor-bearing nude mouse models to and their bone repair capacity in rabbits. Notably, the hyperthermia induced by photothermal therapy in clinical practice inevitably has a negative impact on surrounding normal bone cells while killing tumor cells. Under laser irradiation, the temperature of photothermal materials typically rises to 41–47°C or higher (Tian et al., 2013; Cheng et al., 2014b; Zhu et al., 2016). Tumor tissue has been shown to be much less tolerant of hyperthermia than normal cells, with the majority of tumor cells having a thermally lethal temperature of 42–43°C.However, normal cells are able to survive such hyperthermia for long periods of time. This may be due to the high metabolic level and low heat dissipation capacity of the tumor, as well as the acidic interstitial environment (Chu and Dupuy, 2014). The results confirmed that the fabricated Bi-BG scaffolds significantly promote the adhesion, proliferation and differentiation of rBMSCs and new bone formation *in vivo*. Therefore, photothermal therapy with the Bi-BG scaffolds has potential applications in facilitating the repair of large bone defects from surgical resection of bone tumors.

4 Conclusion

In conclusion, a bifunctional Bi-BG composite scaffold was successfully prepared by combining 3D printing technology and Bi surface modification, which allows photothermal ablation of bone tumors and enhanced osteogenic capacity. Systematic *in vitro* and *in vivo* evaluation demonstrated that the Bi-BG scaffold exhibited excellent photothermal performance, effectively ablating osteosarcoma cells *in vitro* and inhibiting tumor growth *in vivo* under NIR irradiation. More importantly, the fabricated the Bi-BG scaffold significantly increased new bone formation *in vivo* by promoting osteogenic differentiation of rBMSCs. Our results show that the scaffold can be used for the treatment and repair of large bone defects associated with bone tumors. This work may pave the way for the treatment and repair of tumor-associated tissue defects by developing novel bifunctional scaffolds.

Data availability statement

The original contributions presented in the study are included in the article/Supplementary Material, further inquiries can be directed to the corresponding authors.

Ethics statement

The animal study was reviewed and approved by all experimental procedures described in this study were approved by the Animal Ethics Committee of Fudan University Pudong Medical Center. Written informed consent was obtained from the individual(s) for the publication of any potentially identifiable images or data included in this article.

Author contributions

BY designed the study. JD and SF wrote the paper with help from all the authors. DL and HD were involved in the direction and supervision of this experiment. All the authors have read and approved the final form of the manuscript.

Funding

This work was supported by the funding from the Shanghai Public Health Clinical Center (KY-GW-2021-28), Academic Leaders Training Program of Pudong Health Committee of Shanghai (Grant No.PWRd2017-03), the Outstanding Leaders Training Program of Pudong Hospital affiliated to Fudan University (Grant No. LX202201), the Scientific Research Foundation provided by Pudong Hospital affiliated to Fudan University (Grant No. YJRCJJ201906), the Talents Training Program of Pudong Hospital affiliated to Fudan University (Grant No. PX202001), the Health Industry Clinical Research Project of Shanghai Health Commission (Grant No. 20224Y0393).

Conflict of interest

The authors declare that the research was conducted in the absence of any commercial or financial relationships that could be construed as a potential conflict of interest.

Publisher's note

References

Alford, A. I., and Hankenson, K. D. (2006). Matricellular proteins: Extracellular modulators of bone development, remodeling, and regeneration. *Bone* 38 (6), 749–757. doi:10.1016/j.bone.2005.11.017

Cao, L., Meziani, M. J., Sahu, S., and Sun, Y. P. (2013). Photoluminescence properties of graphene versus other carbon nanomaterials. *Acc. Chem. Res.* 46 (1), 171–180. doi:10.1021/ar300128j

Chen, S-H., Lei, M., Xie, X-H., Zheng, L. Z., Yao, D., Wang, X. L., et al. (2013). PLGA/TCP composite scaffold incorporating bioactive phytomolecule icaritin for enhancement of bone defect repair in rabbits. *Acta Biomater.* 9 (5), 6711–6722. doi:10.1016/j.actbio.2013.01.024

Chen, T., Cen, D., Ren, Z., Wang, Y., Cai, X., Huang, J., et al. (2019). Bismuth embedded silica nanoparticles loaded with autophagy suppressant to promote photothermal therapy. *Biomaterials* 221, 119419. doi:10.1016/j.biomaterials.2019.119419

Cheng, L., Wang, C., Feng, L., Yang, K., and Liu, Z. (2014a). Functional nanomaterials for phototherapies of cancer. *Chem. Rev.* 114 (21), 10869–10939. doi:10.1021/cr400532z

Cheng, L., Liu, J., Gu, X., Gong, H., Shi, X., Liu, T., et al. (2014b). PEGylated WS_2Nanosheets as a multifunctional theranostic agent for *in vivo* dual-modal CT/photoacoustic imaging guided photothermal therapy. *Adv. Mater.* 26 (12), 1886–1893. doi:10.1002/adma.201304497

Cheng, Y., and Zhang, H. (2018). Novel bismuth-based nanomaterials used for cancer diagnosis and therapy. *Chemistry–A Eur. J.* 24 (66), 17405–17418. doi:10.1002/chem.201801588

Chiang, T-Y., Wei, C-K., and Ding, S-J. (2014). Effects of bismuth oxide on physicochemical properties and osteogenic activity of dicalcium silicate cements [J]. *J. Med. Biol. Eng.* 34 (1), 30–35. doi:10.5405/jmbe.1386

Choi, W. I., Kim, J-Y., Kang, C., Byeon, C. C., Kim, Y. H., and Tae, G. (2011). Tumor regression *in vivo* by photothermal therapy based on gold-nanorod-loaded, functional nanocarriers. *ACS Nano* 5 (3), 1995–2003. doi:10.1021/nn103047r

Chu, K. F., and Dupuy, D. E. (2014). Thermal ablation of tumours: Biological mechanisms and advances in therapy. *Nat. Rev. Cancer* 14 (3), 199–208. doi:10.1038/nrc3672

Djunic, I., Elezovic, I., Marinkovic, M., Suvajdzic-Vukovic, N., Tomin, D., Jankovic, G., et al. (2011). Osteolytic lesions marker in multiple myeloma. *Med. Oncol.* 28 (1), 237–240. doi:10.1007/s12032-010-9432-4

Dong, J., Cui, G., Bi, L., Li, J., and Lei, W. (2013). The mechanical and biological studies of calcium phosphate cement-fibrin glue for bone reconstruction of rabbit femoral defects. *Int. J. Nanomedicine* 8, 1317–1324. doi:10.2147/ijn.s42862

Gough, J., Notingher, I., and Hench, L. (2004). Osteoblast attachment and mineralized nodule formation on rough and smooth 45S5 bioactive glass monoliths. *J. Biomed. Mater. Res. Part A* 68 (4), 640–650. doi:10.1002/jbm.a.20075

Hench, L. L. (1991). Bioceramics: From concept to clinic. *J. Am. Ceram. Soc.* 74 (7), 1487–1510. doi:10.1111/j.1151-2916.1991.tb07132.x

Hench, L. L., Splinter, R. J., Allen, W., and Greenlee, T. K. (1971). Bonding mechanisms at the interface of ceramic prosthetic materials. *J. Biomed. Mater Res.* 5 (6), 117–141. doi:10.1002/jbm.820050611

Huang, Z., Liu, C., Lu, Y., Su, H., Wang, Q., Zheng, C., et al. (2020). The treatment effect of highly biocompatible bismuth/strontium/hydroxyapatite/chitosan for osteosarcoma, bacterial and bone defects [J]. *Rev. Chim.* 71, 111–123. doi:10.37358/RC.20.6.8176

Ivaska, K., Hentunen, T. A., Vaaraniemi, J., Ylipahkala, H., Pettersson, K., and Vaananen, H. K. (2004). Release of intact and fragmented osteocalcin molecules from bone matrix during bone resorption *in vitro*. *J. Biol. Chem.* 279 (18), 18361–18369. doi:10.1074/jbc.M314324200

Jaque, D., Maestro, L. M., Del Rosal, B., Haro-Gonzalez, P., Benayas, A., Plaza, J. L., et al. (2014). Nanoparticles for photothermal therapies. *nanoscale* 6 (16), 9494–9530. doi:10.1039/c4nr00708e

Kim, J., Mcbride, S., Dean, D. D., Sylvia, V. L., Doll, B. A., and Hollinger, J. O. (2014). *In vivo*performance of combinations of autograft, demineralized bone matrix, and tricalcium phosphate in a rabbit femoral defect model. *Biomed. Mater.* 9 (3), 035010. doi:10.1088/1748-6041/9/3/035010

Kirui, D. K., Rey, D. A., and Batt, C. A. (2010). Gold hybrid nanoparticles for targeted phototherapy and cancer imaging. *Nanotechnology* 21 (10), 105105. doi:10.1088/0957-4484/21/10/105105

Lee, C., Hong, C., Kim, H., Kang, J., and Zheng, H. M. (2010). TiO2 nanotubes as a therapeutic agent for cancer thermotherapy. *Photochem Photobiol.* 86 (4), 981–989. doi:10.1111/j.1751-1097.2010.00731.x

Leussink, B. T., Slikkerveer, A., Engelbrecht, M. R., Van der Voet, G. B., Nouwen, E. J., De Heer, E., et al. (2001). Bismuth overdosing-induced reversible nephropathy in rats. *Arch. Toxicol.* 74 (12), 745–754. doi:10.1007/s002040000190

Li, J-L., Tang, B., Yuan, B., Sun, L., and Wang, X. G. (2013). A review of optical imaging and therapy using nanosized graphene and graphene oxide. *Biomaterials* 34 (37), 9519–9534. doi:10.1016/j.biomaterials.2013.08.066

Li, Z., Liu, J., Hu, Y., Fan, X., Sun, Y., Yu, M., et al. (2017). Biocompatible PEGylated bismuth nanocrystals: "All-in-one" theranostic agent with triple-modal imaging and efficient *in vivo* photothermal ablation of tumors. *Biomaterials* 141, 284–295. doi:10.1016/j.biomaterials.2017.06.033

Li, Z., Liu, J., Hu, Y., Howard, K. A., Fan, X., Chang, M., et al. (2016). Multimodal imaging-guided antitumor photothermal therapy and drug delivery using bismuth selenide spherical sponge. *ACS Nano* 10 (10), 9646–9658. doi:10.1021/acsnano.6b05427

Liu, J., Wang, P., Zhang, X., Wang, L., Wang, D., Gu, Z., et al. (2016). Rapid degradation and high renal clearance of Cu3BiS3 nanodots for efficient cancer diagnosis and photothermal therapy *in vivo*. *ACS Nano* 10 (4), 4587–4598. doi:10.1021/acsnano.6b00745

Liu, Z., Tabakman, S. M., Chen, Z., and Dai, H. (2009). Preparation of carbon nanotube bioconjugates for biomedical applications. *Nat. Protoc.* 4 (9), 1372–1381. doi:10.1038/nprot.2009.146

Markovic, Z. M., Harhaji-Trajkovic, L. M., Todorovic-Markovic, B. M., Kepic, D. P., Arsikin, K. M., Jovanovic, S. P., et al. (2011). *In vitro* comparison of the photothermal anticancer activity of graphene nanoparticles and carbon nanotubes. *Biomaterials* 32 (4), 1121–1129. doi:10.1016/j.biomaterials.2010.10.030

Melancon, M. P., Zhou, M., and Li, C. (2011). Cancer theranostics with near-infrared light-activatable multimodal nanoparticles. *Acc. Chem. Res.* 44 (10), 947–956. doi:10.1021/ar200022e

Mohan, R. (2010). Green bismuth. *Nat. Chem.* 2 (4), 336. doi:10.1038/nchem.609

Nikfarjam, M., Muralidharan, V., Malcontenti-Wilson, C., and Christophi, C. (2005). The apoptotic response of liver and colorectal liver metastases to focal hyperthermic injury. *Anticancer Res.* 25 (2B), 1413–1419.

Ohtsuki, C., Kokubo, T., and Yamamuro, T. (1992). Mechanism of apatite formation on CaO SiO2P2O5 glasses in a simulated body fluid. *J. Non-Crystalline Solids* 143, 84–92. doi:10.1016/s0022-3093(05)80556-3

Pazarçeviren, A. E., Tahmasebifar, A., Tezcaner, A., Keskin, D., and Evis, Z. (2018). Investigation of bismuth doped bioglass/graphene oxide nanocomposites for bone tissue engineering. *Ceram. Int.* 44 (4), 3791–3799. doi:10.1016/j.ceramint.2017.11.164

Peng, M., Dong, G., Wondraczek, L., Zhang, L., Zhang, N., and Qiu, J. (2011). Discussion on the origin of NIR emission from Bi-doped materials. *J. Non-Crystalline Solids* 357 (11-13), 2241–2245. doi:10.1016/j.jnoncrysol.2010.11.086

Peng, M., Zollfrank, C., and Wondraczek, L. (2009). Origin of broad NIR photoluminescence in bismuthate glass and Bi-doped glasses at room temperature. *J. Phys. Condens. Matter* 21 (28), 285106. doi:10.1088/0953-8984/21/28/285106

Prosecká, E., Rampichová, M., Litvinec, A., Tonar, Z., Kralickova, M., Vojtova, L., et al. (2015). Collagen/hydroxyapatite scaffold enriched with polycaprolactone nanofibers, thrombocyte-rich solution and mesenchymal stem cells promotes regeneration in large bone defect *in vivo*. *J. Biomed. Mater. Res. Part A* 103 (2), 671–682. doi:10.1002/jbm.a.35216

Qi, J., Shi, D., Zhao, J., and Jiang, X. (2008). Stable structures and electronic properties of the oriented Bi nanowires and nanotubes from first-principle calculations. *J. Phys. Chem. C* 112 (29), 10745–10753. doi:10.1021/jp801735g

Rustom, L. E., Boudou, T., Lou, S., Pignot-Paintrand, I., Nemke, B. W., Lu, Y., et al. (2016). Micropore-induced capillarity enhances bone distribution *in vivo* in biphasic calcium phosphate scaffolds. *Acta Biomater.* 44, 144–154. doi:10.1016/j.actbio.2016.08.025

Sun, Y., Zhao, Z., Dong, F., and Zhang, W. (2015). Mechanism of visible light photocatalytic NO$_x$ oxidation with plasmonic Bi cocatalyst-enhanced (BiO)$_2$CO$_3$ hierarchical microspheres. *Phys. Chem. Chem. Phys.* 17 (16), 10383–10390. doi:10.1039/c4cp06045h

Tian, Q., Hu, J., Zhu, Y., Zou, R., Chen, Z., Yang, S., et al. (2013). Sub-10 nm Fe$_3$O$_4$@Cu$_{2-x}$S core–shell nanoparticles for dual-modal imaging and photothermal therapy. *J. Am. Chem. Soc.* 135 (23), 8571–8577. doi:10.1021/ja4013497

Valerio, P., Pereira, M. M., Goes, A. M., and Leite, M. (2004). The effect of ionic products from bioactive glass dissolution on osteoblast proliferation and collagen production. *Biomaterials* 25 (15), 2941–2948. doi:10.1016/j.biomaterials.2003.09.086

Velasco-Arias, D., Zumeta-Dube, I., Diaz, D., Santiago-Jacinto, P., Ruiz-Ruiz, V. F., Castillo-Blum, S. E., et al. (2012). Stabilization of strong quantum confined colloidal bismuth nanoparticles, one-pot synthesized at room conditions. *J. Phys. Chem. C* 116 (27), 14717–14727. doi:10.1021/jp304170k

Von Maltzahn, G., Park, J-H., Agrawal, A., Bandaru, N. K., Das, S. K., Sailor, M. J., et al. (2009). Computationally guided photothermal tumor therapy using long-circulating gold nanorod antennas. *Cancer Res.* 69 (9), 3892–3900. doi:10.1158/0008-5472.can-08-4242

Wang, L., Long, N. J., Li, L., Lu, Y., Li, M., Cao, J., et al. (2018). Multi-functional bismuth-doped bioglasses: Combining bioactivity and photothermal response for bone tumor treatment and tissue repair. *Light Sci. Appl.* 7 (1), 1–13. doi:10.1038/s41377-018-0007-z

Wang, Y., Wu, Y., Liu, Y., Shen, J., Lv, L., Li, L., et al. (2016). BSA-mediated Synthesis of bismuth sulfide nanotheranostic agents for tumor multimodal imaging and thermoradiotherapy. *Adv. Funct. Mater.* 26 (29), 5335–5344. doi:10.1002/adfm.201601341

Xiao, Z., Xu, C., Jiang, X., Zhang, W., Peng, Y., Zou, R., et al. (2016). Hydrophilic bismuth sulfur nanoflower superstructures with an improved photothermal efficiency for ablation of cancer cells. *Nano Res.* 9 (7), 1934–1947. doi:10.1007/s12274-016-1085-y

Xie, H., Li, Z., Sun, Z., Shao, J., Yu, X. F., Guo, Z., et al. (2016). Metabolizable ultrathin Bi$_2$Se$_3$Nanosheets in imaging-guided photothermal therapy. *Small* 12 (30), 4136–4145. doi:10.1002/smll.201601050

Yan, X., Huang, X., Yu, C., Deng, H., Wang, Y., Zhang, Z., et al. (2006). The *in-vitro* bioactivity of mesoporous bioactive glasses. *Biomaterials* 27 (18), 3396–3403. doi:10.1016/j.biomaterials.2006.01.043

Yang, Y., Wu, H., Shi, B., Guo, L., Zhang, Y., An, X., et al. (2015). Hydrophilic Cu$_3$BiS$_3$ nanoparticles for computed tomography imaging and photothermal therapy. *Part. Part. Syst. Charact.* 32 (6), 668–679. doi:10.1002/ppsc.201400238

Yu, B., Pei, P., Yu, B., Li, D., Zhang, X., Huang, J., et al. (2017). Enhance the bioactivity and osseointegration of the polyethylene-terephthalate-based artificial ligament via poly(dopamine) coating with mesoporous bioactive glass. *Adv. Eng. Mater.* 19 (5), 1600708. doi:10.1002/adem.201600708

Yu, X., Li, A., Zhao, C., Yang, K., Chen, X., and Li, W. (2017). Ultrasmall semimetal nanoparticles of bismuth for dual-modal computed tomography/photoacoustic imaging and synergistic thermoradiotherapy. *ACS Nano* 11 (4), 3990–4001. doi:10.1021/acsnano.7b00476

Zhao, Z., Zhang, W., Lv, X., Sun, Y., Dong, F., and Zhang, Y. (2016). Noble metal-free Bi nanoparticles supported on TiO$_2$ with plasmon-enhanced visible light photocatalytic air purification. *Environ. Sci. Nano* 3 (6), 1306–1317. doi:10.1039/c6en00341a

Zhi, D., Yang, T., O'hagan, J., Zhang, S., and Donnelly, R. F. (2020). Photothermal therapy. *J. Control Release* 325, 52–71. doi:10.1016/j.jconrel.2020.06.032

Zhu, X., Feng, W., Chang, J., Tan, Y. W., Li, J., Chen, M., et al. (2016). Temperature-feedback upconversion nanocomposite for accurate photothermal therapy at facile temperature. *Nat. Commun.* 7 (1), 1–10. doi:10.1038/ncomms10437

Zhu, Y., Wu, C., Ramaswamy, Y., Kockrick, E., Simon, P., Kaskel, S., et al. (2008). Preparation, characterization and *in vitro* bioactivity of mesoporous bioactive glasses (MBGs) scaffolds for bone tissue engineering. *Microporous Mesoporous Mater.* 112 (1-3), 494–503. doi:10.1016/j.micromeso.2007.10.029

Zhu, Y., Zhu, R., Ma, J., Weng, Z., Wang, Y., Shi, X., et al. (2015). *In vitro* cell proliferation evaluation of porous nano-zirconia scaffolds with different porosity for bone tissue engineering. *Biomed. Mater.* 10 (5), 055009. doi:10.1088/1748-6041/10/5/055009

frontiers | Frontiers in Bioengineering and Biotechnology

TYPE Original Research
PUBLISHED 03 March 2023
DOI 10.3389/fbioe.2023.1158007

EDITED BY
Long Bai,
East China University of Science and Technology, China

REVIEWED BY
Feng Chen,
Tongji University, China
Xiuhui Wang,
Shanghai University, China

*CORRESPONDENCE
Haidong Zhang,
✉ fsyy00777@njucm.edu.cn
Zhihong Dong,
✉ zhdong@cdu.edu.cn
Chen Yang,
✉ cryangchen@ucas.ac.cn

†These authors have contributed equally to this work and share first authorship

SPECIALTY SECTION
This article was submitted to Nanobiotechnology, a section of the journal Frontiers in Bioengineering and Biotechnology

RECEIVED 03 February 2023
ACCEPTED 23 February 2023
PUBLISHED 03 March 2023

CITATION
Feng Y, Wu M, Zhang H, Xu H, Li H, Chen D, Jiang H, Chang J, Dong Z and Yang C (2023), Mild-temperature photothermal assisted CuSi nanowires for promoting infected wound healing. *Front. Bioeng. Biotechnol.* 11:1158007. doi: 10.3389/fbioe.2023.1158007

Mild-temperature photothermal assisted CuSi nanowires for promoting infected wound healing

Yanping Feng[1,2,3†], Mingzhen Wu[4,3†], Haidong Zhang[5*], He Xu[4], Huili Li[2,3], Dongmin Chen[2,3], Hongyi Jiang[3], Jiang Chang[2,3,4], Zhihong Dong[1*] and Chen Yang[2,3*]

[1]College of Mechanical Engineering, Chengdu University, Chengdu, Sichuan, China, [2]Joint Centre of Translational Medicine, the First Affiliated Hospital of Wenzhou Medical University, Wenzhou, China, [3]Zhejiang Engineering Research Center for Tissue Repair Materials, Wenzhou Institute, University of Chinese Academy of Sciences, Wenzhou, China, [4]College of Chemistry and Materials Sciences, Shanghai Normal University, Shanghai, China, [5]Affiliated Hospital of Nanjing University of Chinese Medicine, Jiangsu Province Hospital of Chinese Medicine, Nanjing, China

In clinical practice, the utilization of antibiotics is still the main approach for the treatment of wound contamination, which lacks the ability to accelerate wound healing and arises the global concern of antimicrobial resistance. Plenty of alternative methods have been explored in recent years due to the fast development of material science. Here, CuO/SiO_2 nanowires (CuSi NWs) with good near-infrared (NIR) photothermal conversion ability are synthesized by a one-step hydrothermal method. The as-prepared CuSi NWs possess excellent antibacterial ability against both *Escherichia coli* (*E. coli*) and *Staphylococcus aureus* (*S. aureus*), which could be enhanced by the assistance of mild photothermal therapy (PTT). Moreover, CuSi NWs at suitable concentrations can promote proliferation, migration, and angiogenic gene expression of human umbilical vein endothelial cells (HUVECs), exhibiting a remarkable pro-vascularization ability. The *in vivo* mouse infect model further proves that the CuSi NWs might be a good candidate for the treatment of infected wounds as the high antibacterial efficiency and accelerated wound healing is obtained.

KEYWORDS

nanowire, anti-bacteria, angiogenesis, infected wound, photothermal therapy

1 Introduction

Treatment of bacterial infection is always an important part in the management of cutaneous wound healing. Severe infection can not only hinder wound healing progress, but also invade deep tissues, causing organ failure or even death (Zilberman and Elsner, 2008; Mei et al., 2021; Zeng et al., 2022). Although antibiotics have been proven as effective methods to deal with bacterial infection for centuries in the clinic, the following drug resistance is becoming a major health and medical crisis (Yu et al., 2018; Bakkeren et al., 2020). On the other hand, even if antibiotics can effectively kill bacteria, they cannot fundamentally accelerate the healing process of the wound, leading to the possibility of secondary infection and the chance to turn acute wounds into chronic wounds. Therefore, a treatment that can both combat bacterial infection and promote wound closure is urgently needed to be developed.

In recent years, non-invasive photothermal therapy (PTT) has been acknowledged as one of the primary alternatives to antibiotics (Doherty et al., 2010; Chen et al., 2020). The principle of PTT is converting light into heat by utilizing photothermal agents to destroy the integrity of pathogenic bacteria while avoiding bacterial resistance (Xu et al., 2019; Huo et al., 2021). The efficiency of photothermal antibacterial is directly related to the temperature, and a high temperature of more than 50°C is usually required for achieving a high antibacterial rate. For example, after NIR irradiation, the temperature of infected sites increased to 56°C which was much higher than surrounding normal skin, and showed excellent antibacterial activity against methicillin-resistant *S. aureus* (MRSA) (Qian et al., 2018). However, the application of hyperthermia may also cause damage to normal tissues, and even delay wound healing, making PTT hard be implemented alone (Xu et al., 2018; Huo et al., 2021; Bai et al., 2023). Therefore, the combination of PPT with other antibacterial treatment methods to achieve high antibacterial efficiency under mild temperatures is becoming the focus of photothermal antibacterial therapy.

Metal ions such as silver (Ag) and copper (Cu) ions are widely used in different antibacterial scenarios including textile fabrics, water treatment, and biomedical applications due to their broad-spectrum antibacterial properties (Chernousova and Epple, 2013; Slavin et al., 2017). For example, Ag ions containing wound dressing are proven effective for multiple microorganisms such as *Staphylococcus aureus* (*S. aureus*), *Escherichia coli* (*E. coli*), and *Candida albicans* (*C. albicans*) (Panacek et al., 2006; Stanic et al., 2011). However, its high cytotoxicity and potential biosafety risks are concerning (Rai et al., 2009; Perdikaki et al., 2016). In contrast, Cu ions showed less antibacterial efficiency but higher biocompatibility. As one of the trace elements of the human body, Cu is essential to maintain homeostasis and the physiological functions of various enzymes such as lysyl oxidase (Das et al., 2015; Das et al., 2016). Moreover, copper ions at low concentrations (0.064–6.4 ppm) can promote endothelial cell proliferation, migration, and vascularization, thus accelerating wound healing (Wu et al., 2013; Kong et al., 2014; Li et al., 2016). However, low concentrations of copper ions have limited antibacterial effects, and combination with other antibacterial means is usually required to achieve the ideal antibacterial therapeutic effect (Ning et al., 2015; Li t al., 2019). For example, Xu Qing et al. developed a PDA-modified Cu-doped mesoporous silica (Cu-MSN), which produced remote "hot ions" effect under the near-infrared (NIR) light and isplayed highly efficient, quick, and long-term inhibition of bacterial pathogens methicillin-resistant *S. aureus* (MRSA) and *E. coli* as well as bacterial biofilm (Xu et al., 2020). More interestingly, the sustained release of Cu and Si ions promoted wound closure by enhancing angiogenesis during the infectious wound healing process. However, the amount of doped Cu in Cu-MSN is limited, which may affect the controllability of Cu ion release. Also, additional photothermal agents such as PDA are required in the above system due to the lack of photothermal covert ability of Cu-MSN, which greatly increases the uncertainty of its practical application.

Herein, we synthesized a copper oxide/silica (CuSi) mixed nanowire (NW) with inherent NIR photothermal properties. The antibacterial effect of CuSi nanowires under NIR light stimulation on both *E.coli* and *S. aureus* was investigated. Meanwhile, the effects of CuSi nanowires on endothelial cell proliferation, migration, and pro-vascularization were studied. Finally, a mouse-infected wound model was established to evaluate the therapeutic effect of CuSi nanowires on promoting infected wound healing. The study provides a new strategy for the treatment of infected wounds. Figure 1.

2 Materials and methods

2.1 Materials

All chemical reagents were from Aladdin Biochemical Technology Co., Ltd. (Shanghai, China) except those otherwise mentioned.

2.2 Preparation of CuSi NWs

CuSi NWs were synthesized following a modified hydrothermal method (Ma et al., 2022). Briefly, 20 mL sodium metasilicate non-ahydrate ($Na_2SiO_3 \cdot 9H_2O$, 0.2 M) and 20 mL copper nitrate trihydrate ($Cu(NO_3) \cdot 3H_2O$, 0.2 M) aqueous solution were mixed evenly into a polyphenylene lined stainless steel autoclave and hydrothermally treated at 200°C for 48 h. Then, the precipitation was collected by centrifugation at 10,000 rpm/min for 5 min. The as-obtained CuSi NWs were rinsed three times with Milli-Q water and freeze-dried in a lyophilizer (SCIENT2-10N/A, Ningbo Xinzhi Biotechnology Co., Ltd., China) for further use.

2.3 Characterization of CuSi NWs

The morphologies of CuSi NWs were observed using a scanning electron microscope (SEM, SU8010, HITACHI, Japan) and the analysis of elements by mapping of energy dispersive spectrometry (EDS) were detected by Phenom scanning electron microscope (Phenom Pharos, Phenom, Netherlands). The X-Ray Diffraction (XRD) patterns of CuSi NWs were collected using an X-ray diffractometer (D8 ADVANCE, Bruker, Germany). Fourier transform infrared (FTIR) spectra of CuSi NWs were measured by an FTIR spectrometer (Tensor II, Bruker, Germany). The ultraviolet-visible-near-infrared (UV-VIS-NIR) absorption spectra of CuSi NWs were tested using a spectrometer (CARY5000, Agilent, United States). To evaluate the ions release concentration of CuSi NWs, CuSi NWs were dispersed in Milli-Q water with weight-to-volume concentrations of 31.25 μg/mL. The aqueous dispersion was diluted, filtrated and collected at different days, then detected by inductively coupled plasma mass spectrometry (ICP).

2.4 Photothermal performance characterization of CuSi NWs

To evaluate the photothermal properties of CuSi NWs, CuSi NWs were dispersed in Milli-Q water with weight-to-volume concentrations of 0.5, 1, 2, 4, and 8 mg/mL, respectively. The samples were then irradiated with an 808 nm laser (Ningbo

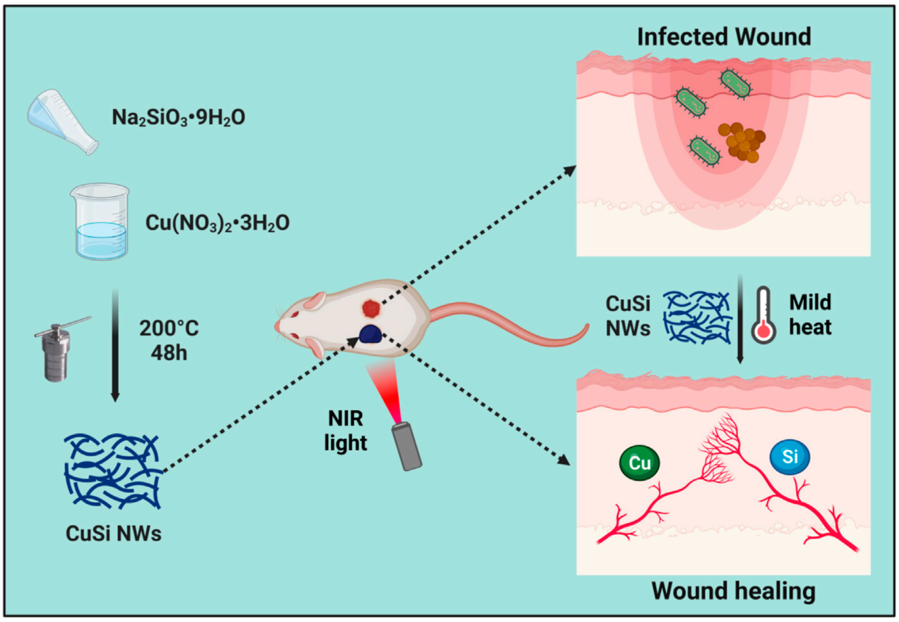

FIGURE 1
CuSi NWs with light-to-heat conversion capability was designed to effectively combat bacteria and simultaneously promote angiogenesis, thereby improving the wound healing rate of infected wounds. The figure was created with BioRender.com.

Yuanming Laser Technology Co., Ltd., China) using the power density of 1 W/cm^{2,} and the corresponding real-time temperature was recorded using an infrared thermal imager (A300, FLIR, United States). In addition, the real-time temperature of CuSi NWs aqueous dispersion (2 mg/mL) under different power densities (0.6, 1, and 1.4 W/cm^2) was also recorded. Finally, to confirm the photothermal stability of the CuSi NWs, a heating cycle test was performed on the 2 mg/mL CuSi NWs dispersion solution. Briefly, the sample was irradiated by the laser at 808 nm using the power density of 1 W/cm^2 for 5 min and then cooled in the air for another 5 min. The whole process was repeated 6 times.

2.5 Effects of CuSi NWs on viability of HUVECs

To evaluate the cytocompatibility of CuSi NWs, human umbilical vein endothelial cells (HUVECs) were purchased from the National Collection of Authenticated Cell Cultures (Shanghai, China) and cultured in Dulbecco's modified eagle medium (DMEM) containing 10% (v/v) fetal bovine serum (FBS) and 1% penicillin/streptomycin (P/S). For cell viability assay, HUVECs were seeded in 96-well cell culture plates with a density of 1 × 10^3 cells/well and incubated at 37°C with the supplement of 5% CO_2 for 24 h. Subsequently, the media were replaced with 100 μL fresh media containing different concentrations of CuSi NWs (125, 62.5, 31.25, 15.625, and 7.8125 μg/mL) to further treat cells for 1, 2, and 3 days, respectively. The CuSi NWs-free culture medium was used as a control. A CCK8 assay kit (40203ES80, YEASEN, China) was then implemented for cell viability assay following the manufacturer's instructions. Briefly, the media were replaced with CCK-8 solution, and the plates were put back into the incubator at 37°C for another 1 h, using a microplate reader (EPOCH2, BioTek, United States) to another 96-well plate for the test of light absorbance at 450 nm.

2.6 Effects of CuSi NWs on migration of HUVECs *in vitro*

HUVECs were seeded in 6-well plates and incubated at 37°C for 24 h. The seeding density of HUVECs was 4.5 × 10^5 cells/well. Then, a 10 μL pipette tip was used to draw a straight line at the bottom of the plate, and the media were refreshed with DMEM containing 1% FBS and 1% P/S, or media containing CuSi NWs (31.25 μg/mL), respectively. Photographs of cells were taken by a microscope (SZ61TR, Olympus, Japan). After treating for another 24 h at 37°C, cells were fixed with 4% paraformaldehyde for 10 min and stained with 0.4% crystal violet for 5 min. Photographs of cells were taken again by the microscope and the cell migration rate was calculated using Image J software.

2.7 Effects of CuSi NWs on tube formation of HUVECs *in vitro*

First, 120 μL of Matrigel™ dilution was added to a 48-well plate and incubated at 37°C for 40 min. Then, HUVECs were seeded onto the well plate with a density of 4 × 10^4 cells/well. DMEM containing 10% FBS and 1% P/S or media containing CuSi NWs (31.25 μg/mL) were used to treat HUVEC for 6 h at 37°C and the normal media were used as the Blank group. Finally, seven randomly selected areas were photographed by the microscope (SZ61TR, Olympus, Japan),

TABLE 1 Primers for gene expression analysis.

Target gene	Forward primer sequence (5′-3′)	Reverse primer sequence (5′-3′)
GAPDH	GATTTGGTCGTATTGGGCG	CTGGAAGATGGTGATGG
bFGF	CAATTCCCATGTGCTGTGAC	ACCTTGACCTCTCAGCCTCA
VEGF	GAAGAAAGTGGTGCCATGGATAG	CCCATGAGTTCCATGCTCAGA
HIF-α	CAACGTGGAAGGTGCTTCA	CGGCTCATAACCCATCAACT

and the tubular length and tube number were analyzed using Image J software.

2.8 The gene expression in HUVECs treated by CuSi NWs

The mRNA expressions of *VEGF*, *bFGF*, and *HIF-1α* in HUVECs were detected by quantitative polymerase chain reaction (qPCR). Briefly, HUVECs (3 × 10^5 cells per well) were seeded on 6-well culture plates and cultured for 24 h. Then, the cells were treated with the above-mentioned media for other 3 days. After that, HUVECs were washed twice with preheated PBS and the mRNA was extracted from cells using an RNA extraction kit (M3211070, YEASEN, Shanghai, China). Subsequently, the extracted RNA was transcribed into cDNA using Hifair®Ⅲ 1st Strand cDNA Synthesis SuperMix for qPCR (gDNA digester plus) (H6201080, YEASEN, Shanghai, China). PCR amplification was further implemented with primers of *VEGF*, *bFGF*, *HIF-1α*, and the housekeeping gene *GAPDH*, which were synthesized by the company of Shenggong, Co., Ltd. (Shanghai, China). The sequences of primers were as Table 1.

2.9 Antibacterial ability of CuSi NWs *in vitro*

Staphylococcus aureus (*S.aureus*) and *Escherichia coli* (E.coli) were used for anti-bacterial experiments. First, *S.aureus* and *E. coli* were cultured with LB broth in a shaker at 37°C for 4 h, and then diluted with saline to the density of 1 × 10^6 CFU/mL. Next, 100 μL saline or saline containing CuSi NWs (62.5 μg/mL) was mixed into 100 μL of bacterial solution. Then for CuSi + NIR group, the obtained samples were irradiated with an 808 nm laser for 15 min and the terminal temperature was maintained at ~ 45°C (monitored by the infrared thermal imager). Then, after incubating the *S.aureus* and *E.coli* solution for another 4 h, the number of bacteria was calculated using the plating method.

2.10 Therapeutic effect of CuSi NWs on infected wounds

Male ICR mice (8-week-old, 30–35 g) were obtained from Zhejiang Animal Center (Zhejiang, China). The animal protocol and experimental procedures were approved by the Animal Research and Ethics Committee of Wenzhou Institute of the University of Chinese Academy of Sciences (Approval Issue No. WIUCAS22102007). A mouse model of infected wounds was established as follows: First, the mice were anesthetized with 1.5% sodium pentobarbital. Then, the hair on the backs was shaved and the nude backs were wiped with iodine. Next, two circular full-thickness wounds on the upper back of the mice were created using a sterilized hole punch (8 mm diameter), and 20 μL *S.aureus* suspension (1 × 10^7 CFU/mL) was added to the wounds to create infectious wounds. The mice were randomly divided into three groups and received different treatments, namely, Blank, CuSi, and CuSi + NIR. For Blank group, 50 μL of PBS solution was applied. For CuSi and CuSi + NIR groups, 50 μL of PBS solution containing CuSi NWs (31.25 μg/mL) was dropped on the infected wound each time, while in the CuSi + NIR group, an 808 nm laser was applied for the photothermal therapy in the first 3 days immediately after the dropping of CuSi NWs suspension. The average temperature of the infected wound irradiated by laser was monitored by the infrared thermal imager and maintained at ~45°C for 15 min. Photographs of wounds were taken at selected time points (Day 0, Day 3, Day 6, and Day 9). In addition, on day 3, the pus from the wound was taken with a disposable sterile cotton swab and transferred into 2 mL of saline. After shaking vigorously, 20 μL of the samples were taken and dispersed on an agar plate for evaluation of bacterial infection of the wound site. On day 9, all mice were sacrificed to obtain skin samples.

2.11 Histological analysis

The obtained tissue samples were fixed in 4% paraformaldehyde for 24 h, then washed with current water, dehydrated by graded ethanol, embedded by paraffin, and cut into 5 μm sections for hematoxylin-eosin (H&E), Masson, and CD31 immunohistochemical staining. For all staining methods, sections were dewaxed and hydrated first. For H&E staining, sections were stained with hematoxylin and eosin following the manufacturer’s instructions (H&E, Sigma-Aldrich). After being captured by microscope (KF-PRO-005, KFBIO, China), the lengths of the wounds were measured using ImageJ software. For Masson staining, sections were stained with Ponceau S and Aniline Blue following the manufacturer’s instructions. After being captured by the microscope, collagen deposition fractions were calculated using Image-Pro Plus software. For immunohistochemical staining, sections were antigen retrieved and antibody anti-CD31 (bs-0196R, Bioss, Beijing, China) was used. The number of blood vessels counted based on the CD31 staining.

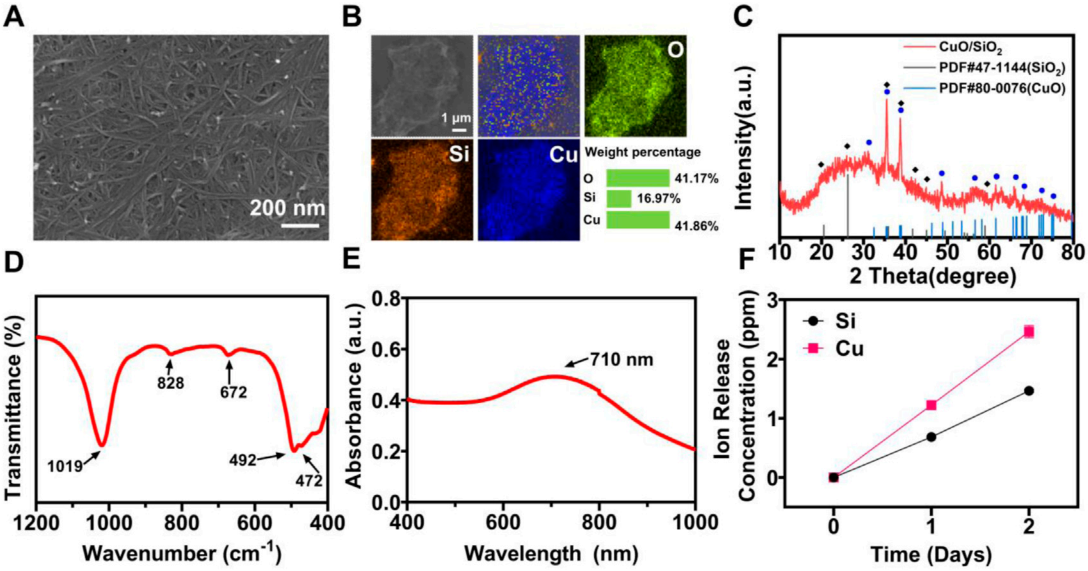

FIGURE 2
Characterization of CuSi NWs. **(A)** SEM image. **(B)** EDS mapping. **(C)** XRD pattern. **(D)** FTIR spectra. **(E)** UV-VIS-NIR spectrograms. **(F)** Accumulated release of Si and Cu ions from CuSi NWs at different days.

2.12 Statistical analysis

All results were expressed as means ± standard error of mean. Multiple comparisons between groups were performed using one-way ANOVA testing with a *post hoc* test. Statistical significance was considered when $^{*}p < 0.05$ or $^{**}p < 0.01$ or $^{***}p < 0.001$ ($^{\#}p < 0.05$ or $^{\#\#}p < 0.01$ or $^{\#\#\#}p < 0.001$).

3 Results

3.1 Characterization of CuSi NWs

CuSi NWs were prepared by a modified hydrothermal reaction method. It can be clearly observed from the scanning electron microscope (SEM) image that the diameter of CuSi NWs was about 10 nm and the length reached about 600 nm (Figure 2A). The energy dispersive spectrometry (EDS) element mapping showed that Cu, Si, and O elements were uniformly distributed in CuSi NWs (Figure 2B). The obtained CuSi NWs were then evaluated by X-ray diffraction (XRD), Fourier-transform infrared spectroscopy (FTIR), and ultraviolet-visible-near-infrared (UV-VIS-NIR) spectrophotometer. It can be found from the XRD pattern that CuSi NWs were mainly constituted by the phase of CuO and SiO_2 (Figure 2C), which was further confirmed by FTIR analysis as the absorption peaks at approximately 1,019, 828, and 472 cm^{-1} were assigned to the different vibration modes of the Si–O–Si or O–Si–O bonds of amorphous SiO_2, while peaks centered at 492 and 672 cm^{-1} indicate cm^{-1} Cu (II)–O species (Lefez et al., 1995; Li et al., 2019) (Figure 2D). In addition, the UV-VIS-NIR absorption spectra showed that CuSi NWs had a broad absorption from the wavelength of 400 nm to 1,000 nm, and a peak at 710 nm was observed (Figure 2E). As shown in Figure 2F, Si ions and Cu ions release concentration from CuSi NWs were about 0.685 ppb and 1.223 ppb per day, respectively.

3.2 Photothermal performance of CuSi NWs

The photothermal performances of CuSi NWs were evaluated under 808 nm laser irradiation. As shown in Figure 3A, the temperature CuSi NWs dispersion (2 mg/mL) rapidly increased from 28.2°C to 61.7°C in 5 min with light irradiation (1 W/cm^2). In contrast, there is no evident temperature increment in pure water with the same treatment. The effect of the CuSi NWs aqueous dispersion concentration and laser power on photothermal performances were further investigated (Figures 3B, C). As expected, the temperature of the dispersion was positively correlated with the concentration of CuSi NWs aqueous dispersion or the power density of the laser. Specially, the maximum temperature of CuSi NWs aqueous dispersion at the concentration of 8 mg/mL could reach 86°C under 5 min' laser irradiation (1 W/cm^2). Moreover, the photothermal stability of CuSi NWs was verified as no particular change in the photothermal effect was noticed after six repetitive laser on/off cycles (Figure 3D).

3.3 Effect of CuSi NWs on proliferation, migration, and pro-vascularization of HUVECs

Human umbilical vein endothelial cells (HUVECs) were used to evaluate the bioactivity of CuSi NWs. Firstly, the activities of HUVECs treated with different concentrations of CuSi NWs (7.8125~125 μg/mL) for 1, 2, and 3 days were evaluated using a

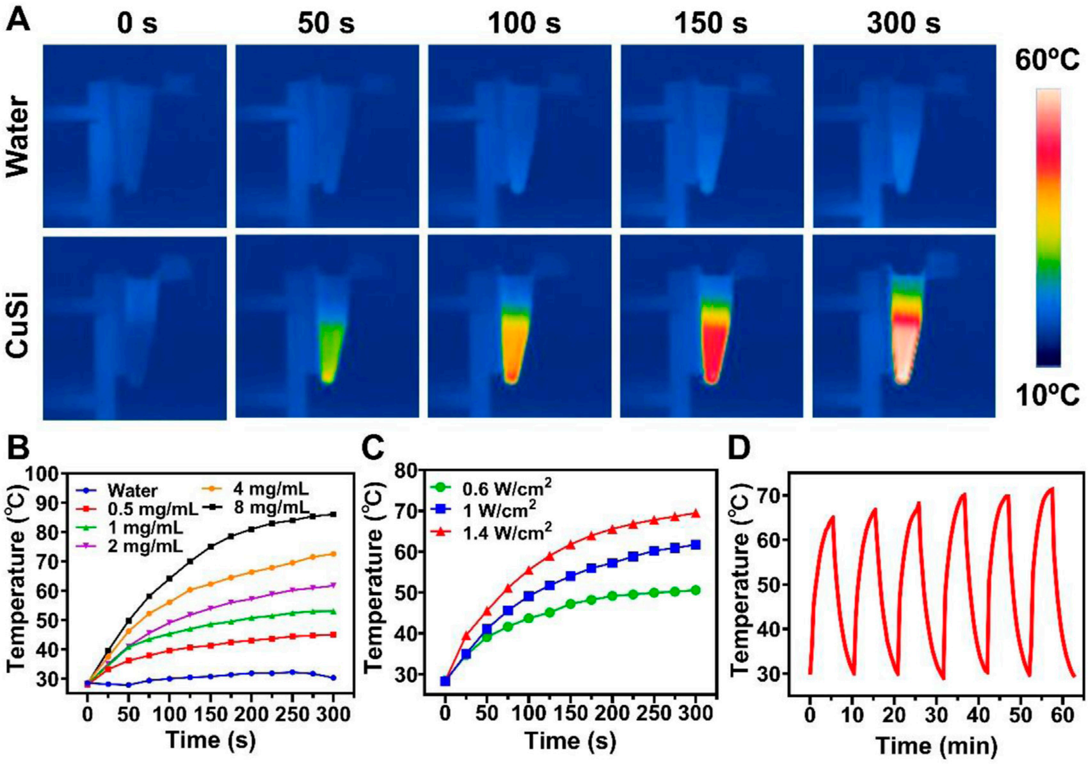

FIGURE 3
Light-to-heat conversion capability of CuSi NWs. **(A)** Representative thermal images of water and CuSi NWs aqueous dispersions under the 808 nm laser irradiation. **(B)** Photothermal heating (1 W/cm^2) curves of different CuSi NWs aqueous dispersions for 5 min. **(C)** Photothermal heating curves of CuSi NWs aqueous dispersion (2 mg/mL) under 808 nm laser irradiation at varying power densities (0.6, 1, and 1.4 W/cm^2). **(D)** Photothermal stability of CuSi NWs aqueous dispersion (six laser on/off cycles).

CCK8 assay, respectively. As shown in Figure 4A, CuSi NWs at high concentrations (62.5 and 125 μg/mL) showed a suppression effect on HUVEC activity. However, CuSi NWs at concentrations of 7.8125, 15.625, and 31.25 μg/mL significantly promoted the proliferation of HUVECs as compared to the Blank group. Notably, CuSi NWs at concentrations of 31.25 μg/mL had the best stimulation on HUVEC activity among all the groups. Therefore, we chose 31.25 μg/mL as the representative group of CuSi NWs for further cell experiments.

The migration of HUVECs with/without the treatment of CuSi NWs was further conducted and the results are presented in Figures 4B, C. In contrast to the Blank group, CuSi NWs promoted faster migration of HUVECs with a rate increment of 32.06%. Furthermore, the CuSi NWs were proved to significantly stimulate more tube formation of HUVECs *in vitro*. As shown in Figure 4D, more formed vascular rings were observed after the treatment of CuSi NWs. The corresponding quantitative analysis further confirmed the conclusion as the tube length was increased by 68.72% compared with Blank group when the Blank group was normalized (Figure 4E). Moreover, the effect of CuSi NWs on activating the expression of pro-angiogenic genes in HUVECs was evaluated, which exhibited that after treating with CuSi NWs, significantly higher expression of *bFGF*, *VEGF*, and *HIF-1α* was observed in HUVECs as compared to that in Blank group, implying the pro-angiogenic ability of CuSi NWs (Figure 4F).

3.4 Antibacterial performance of CuSi NWs

The antibacterial properties of CuSi NWs with/without NIR light irradiation were verified using both gram-positive (*S.aureus*) and gram-negative (*E.coli*) bacteria. As shown in Figures 5A, B, CuSi NWs alone had a broad antibacterial ability as they can suppress the growth of both *S.aureus* and *E.coli.* Such antibacterial performance could be further enhanced under the NIR light irradiation. The corresponding quantitative analysis displayed that the bacteria inhibitive rate of CuSi NWs alone were 38.69% ± 2.34% and 70.93% ± 3.22% against *S.aureus* and *E.coli*, respectively, which increased to 99.35% ± 0.16% and 94.19% ± 4.27% after the treatment of NIR light irradiation. The results proved that CuSi NWs and mild heat may produce a synergistic effect on killing bacteria.

3.5 Effect of CuSi NWs on infected wound healing

To evaluate the photothermal therapeutic effect of CuSi NWs on the repair of infected wounds. We first established a mouse-infected wound model by the contamination of *S. aureus.* Three groups were implemented including Blank, CuSi, and CuSi + NIR. For the treatment of CuSi + NIR, the photothermal threatment was applied by using NIR light 15 min/day at the first 3 days, raised

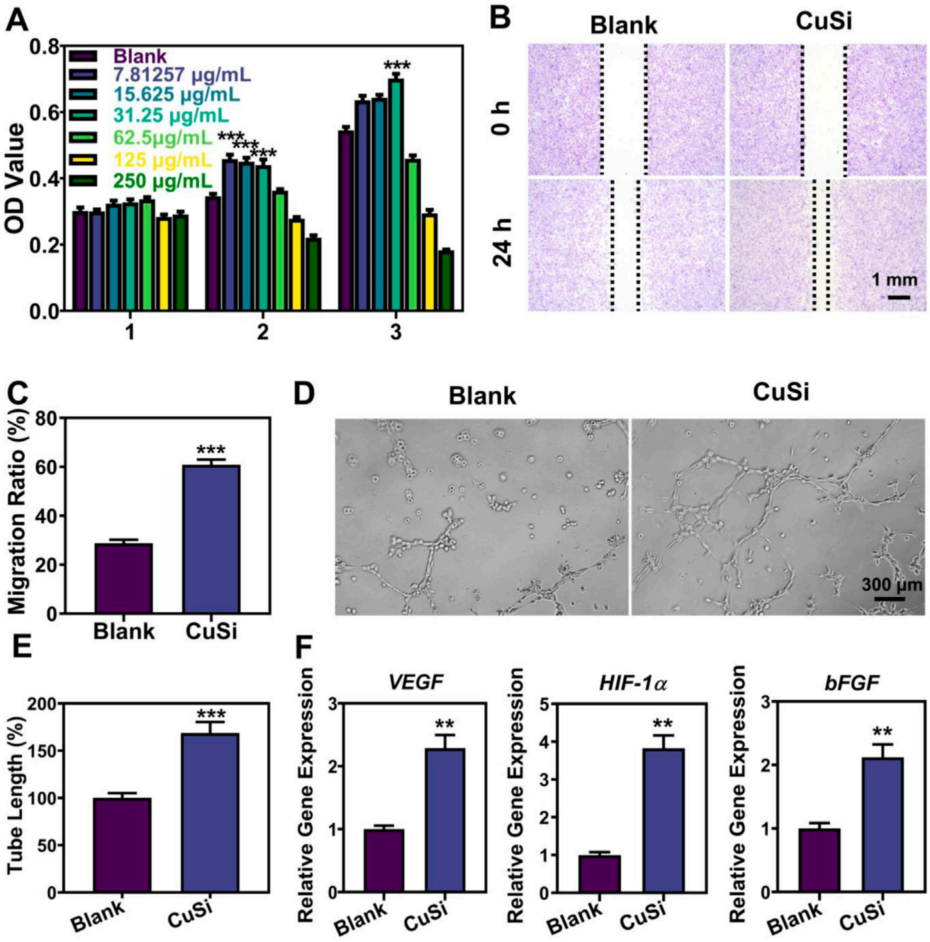

FIGURE 4
Effects of CuSi NWs on the proliferation, migration, and pro-angiogenesis of HUVECs. **(A)** Cell viability of HUVEC after treatment with different CuSi NWs concentrations (*n* = 6). **(B)** Representative cell migration photos after treatment with/without CuSi NWs for 24 h. **(C)** Quantification of cell migration rate (*n* = 8). **(D)** Representative newly formed tubes after treatment with/without CuSi NWs for 6 h. **(E)** Quantification of tube length (*n* = 7). The Blank group was normalized. **(F)** Angiogenic genes (*VEGF*, *HIF-1α* and *bFGF*) expression in HUVECs after treatment with CuSi for 3 days (*n* = 3). *$p < 0.1$, **$p < 0.01$ or ***$p < 0.001$.

the temperature of wound to about 45°C, then add CuSi NWs suspension every 2 days afterwards (Figure 6A). As shown in Figure 6B, the temperature of the wound surface in CuSi + NIR group increased from 35.3°C to 47.6°C in 15 min. After treatment for 3 days, the residual bacteria in each group were collected for plate counting (Figure 6C). The bacterial viabilities in CuSi group and CuSi + NIR group were 50.36% ± 49.66% and 7.49% ± 3.49%, respectively, indicating the synergistic antibacterial effect of Cu ions and hyperthermia.

The wound healing process of each group was further displayed in Figures 6D, E. Both CuSi and CuSi + NIR could facilitate wound healing as compared to Blank group, while CuSi + NIR had the best stimulation effect among all groups. Through quantitative statistics (Figure 6F), it can be found that the wound areas in CuSi + NIR group were always the smallest among all groups at each time point, indicating the best wound healing ability of CuSi + NIR. Specifically, the wound closure rate in CuSi + NIR group on day 3, 5, 7, and 9 were 67.33% ± 10.26%, 72.68% ± 15.48%, 85.32% ± 6.9%, and 92.69% ± 2.14% respectively. Whereas, the corresponding wound closure rates were 41.49% ± 22.82%, 59.37% ± 18.57%, 70.76% ± 15.36%, and 80.21% ± 4.6% in Blank group, and 49.58% ± 18.41%, 64.65% ± 10.8%, 75.82% ± 9.7%, and 85.63% ± 5.76% in CuSi group.

In addition, histological analysis was performed to assess the quality of the repaired wounds with different treatments. Figures 7A, B show the H&E staining and corresponding quantification of the repaired wounds. Compared with the Blank group, both CuSi and CuSi + NIR stimulated less granulation tissue in the defect area, indicating better therapeutic effects on the maturation of granulation tissue, especially for CuSi + NIR group, in which the best dermal formation, epithelization, and hair follicle regeneration were observed. The Masson's staining further revealed that both CuSi and CuSi + NIR promoted more collagen deposition in the wounds compared with the Blank group, while CuSi + NIR had the best collagen deposition outcomes among all groups (Figures 7C, D). Moreover, the newly formed vessels were evaluated by immunohistochemistry staining of CD31. As shown in Figures 7E, F, more neovascularization was observed in the CuSi + NIR

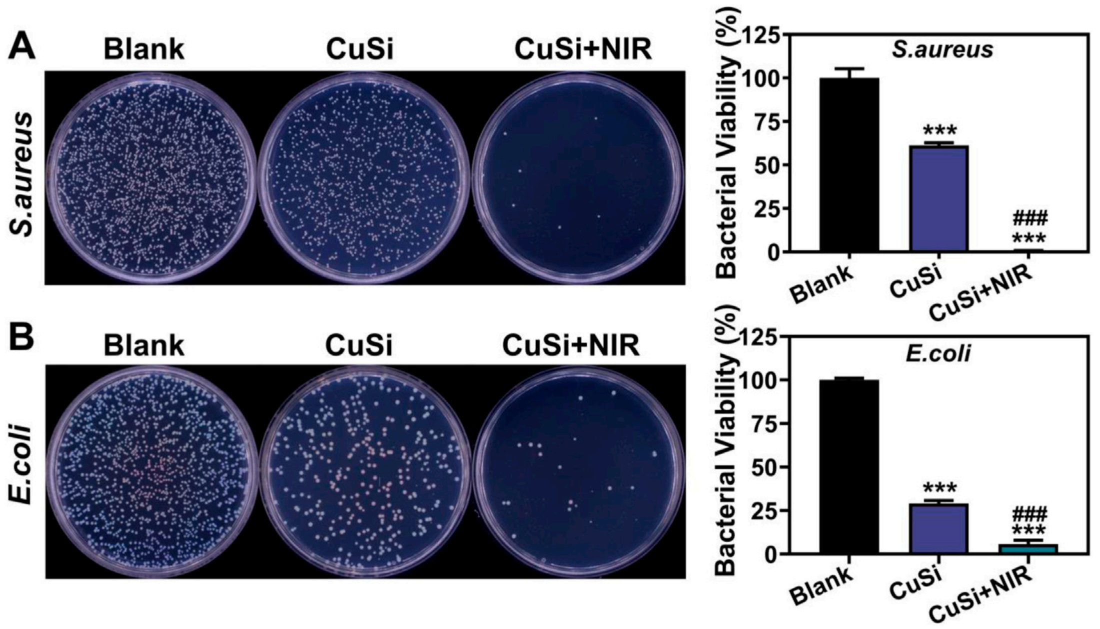

FIGURE 5
Antibacterial activity of CuSi NWs against *S. aureus* and *E. coli*. **(A)** Representative photos and bacterial viability percentage of *S. aureus* with different treatments ($n = 3$). **(B)** Representative photos and bacterial viability percentage of *E. coli* with different treatments ($n = 3$). The Blank group was normalized. $^{*}p < 0.1$, $^{**}p < 0.01$ or, $^{***}p < 0.001$ vs. Blank group; $^{\#}p < 0.05$ or $^{\#\#}p < 0.01$ or $^{\#\#\#}p < 0.001$ vs. CuSi group.

group compared with both Blank and CuSi groups, indicating that the best angiogenic effect of mild heat-assisted CuSi NWs.

4 Discussion

As one-dimensional nanomaterials, NWs usually display unique optical, electronic, or mechanical properties due to the high transverse to longitudinal ratio structure and two-dimensional confinement, making them widely applied in multiple areas including tissue regeneration (Cao et al., 2018; Jones et al., 2018; Huang et al., 2021). Previous studies demonstrated that hydroxyapatite NWs could accelerate hemostasis and wound healing due to the excellent hydrophilicity, release of blood coagulation factor Ca^{2+}, and flexibility to composite with other materials, while silver NWs showed a high-efficiency eradication rate against various bacteria including *E. coli* and *S. aureus*, and high potential as an antibacterial ingredient for wound dressing due to the sustained release of Ag ions (Sun et al., 2018; Wan et al., 2020; Zheng et al., 2022). However, none of these NWs possess antibacterial activity and skin-beneficial bioactivity simultaneously. Our proposal of CuSi NWs showed the advantages as high antibacterial efficiency and high bioactivity of angiogenesis were accomplished at the same time with the assistance of mild photothermal therapy. The *in vitro* antibacterial/cellular experiments and the *in vivo* animal experiments fully demonstrated that CuSi NWs might be a good candidate for the treatment of infected wounds.

The high antibacterial performance of CuSi NWs is mainly attributed to the combination of PTT and sustained Cu ions. Both of them were widely reported as broad-spectrum antibacterial strategies. However, their antibacterial mechanism is different. For photothermal antibacterial therapy, the photothermal agent is required to convert light to generating heat, thereby killing bacteria through the thermal effects including rupturing cell membranes, evaporating cell fluid evaporation, and destroying cellular protein/enzyme (Yang et al., 2017; Xu et al., 2019). NIR light is usually implemented in the process due to the good tissue penetration ability and high biosafety depending on the power density (Geng et al., 2018; Chen et al., 2020). Unlike PTT, Cu ions can kill bacteria by destroying the cell membrane/DNA through an electrostatic interaction or generating reactive oxygen species (ROS), and the efficiency is positively related to the concentration of Cu ions (Ning et al., 2015; Perdikaki et al., 2016; Slavin et al., 2017; Li et al., 2019). Since neither of these two methods is satisfactory as a single strategy in the treatment of bacteria-infected wounds due to concerning the possible negative effects on normal tissues by high temperature or high concentrations of Cu ions, recent investigations have elaborated that the combination of PTT and Cu ions might produce a “hot Cu ion” effect by improving the antibacterial efficiency and reducing the side effects of PPT and Cu ions when used alone (Xu et al., 2020; Xu et al., 2021). The “hot Cu ion” effect has been proven to be not only effective to common bacteria, but also the drug-resistance bacteria. A recent study exhibited that the “hot Cu ion” effect could even significantly inhibit the formation of biofilms due to the direct synergetic antibacterial effect of heat and Cu ions and the indirect pro-inflammatory effect by inducing macrophage towards M1 phenotype (Xu et al., 2021). However, the temperature used in this study is about 50°C, which is still far away from absolute safety (Xu et al., 2018; Fan et al., 2019). Notably, the temperature used in our study (45–47°C) has been proven safe

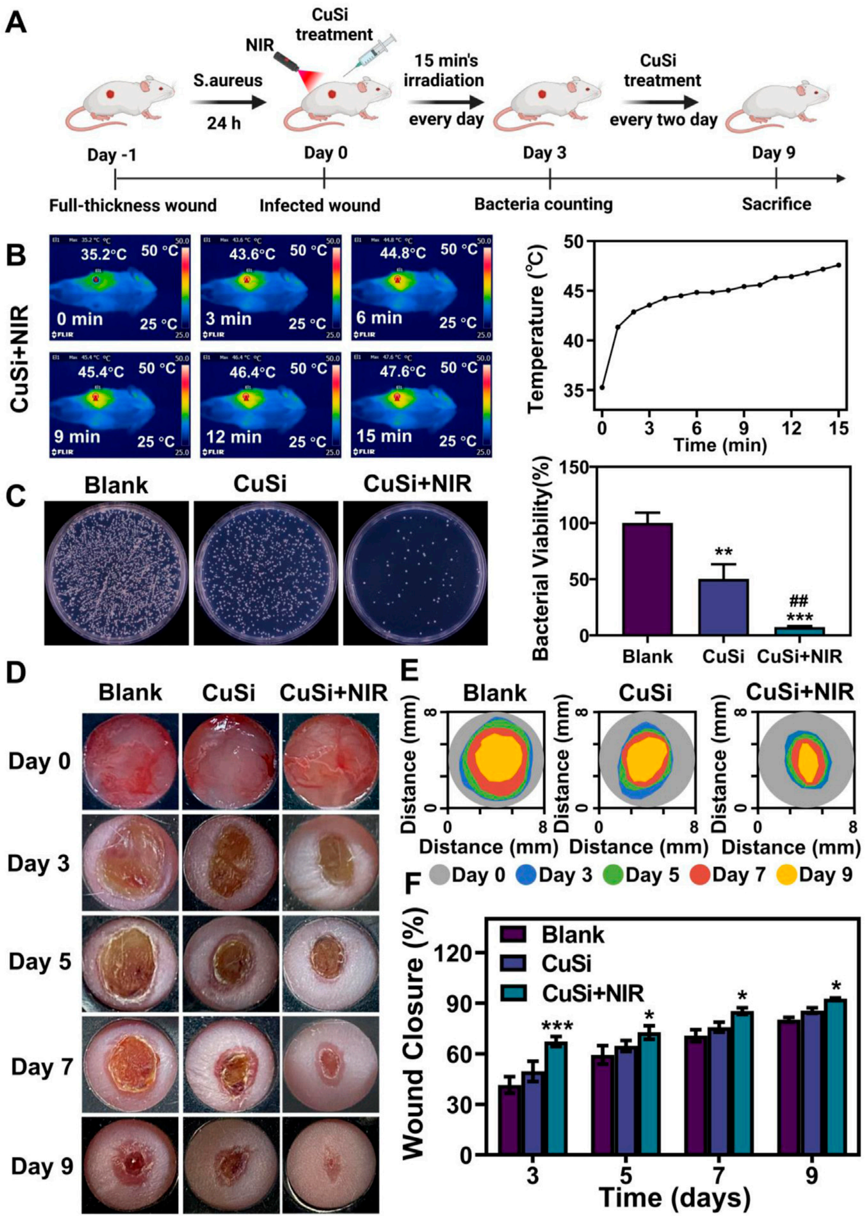

FIGURE 6
Treatment of infected wounds with CuSi NWs. **(A)** Schematic diagram of the protocol for the establishment of an infection model and the course of treatment. **(B)** Representative thermal images and the corresponding photothermal heating curves of the wound site treated with CuSi NWs under the irradiation of NIR light. **(C)** Representative photos and bacterial viability of *S. aureus* in wound site after different treatments ($n = 6$). The Blank group was normalized. **(D)** Representative photos, **(E)** size markers, and **(F)** quantitative closure rate of the wounds with different treatments on day 3, 5, 7, and 9, respectively ($n = 6$). Figure 5A was created with BioRender.com. $^{*}p < 0.1$, $^{**}p < 0.01$, or $^{***}p < 0.001$ vs. Blank group; $^{\#}p < 0.05$ or $^{\#\#}p < 0.01$ or $^{\#\#\#}p < 0.001$ vs. CuSi group.

for multiple tissues as a mild temperature in the application of PTT (Ma et al., 2020; Yang et al., 2020). Whereas the antibacterial efficacy of CuSi + NIR group is still high (~99.35% against *S. aureus* and ~94.19% against *E. coli in vitro*, and 92.51% against *S. aureus in vivo*), which is comparable and even better to other PPT combined strategies (Yuan et al., 2015; Li et al., 2017).

Apart from combating bacteria, promoting neovascularization is also important for the regeneration of injured skin. Numerous attempts have been made to improve the angiogenic ability of wound dressing and incorporation with angiogenic growth factors is one of the most direct and effective approaches (Song et al., 2021; Xie et al., 2023). However, the inherent disadvantages of proteins including the high cost, short half-lives, and low stability limit their clinical practice. Our previous studies demonstrated that silicate biomaterials usually possessed strong pro-vascularized ability including promoting proliferation, migration, and angiogenic gene expression of endothelial cells due to the sustained release of Si ions (Li and Chang, 2013; Zhou et al., 2018). Several silicate bioglasses or bioceramics and their composted materials have

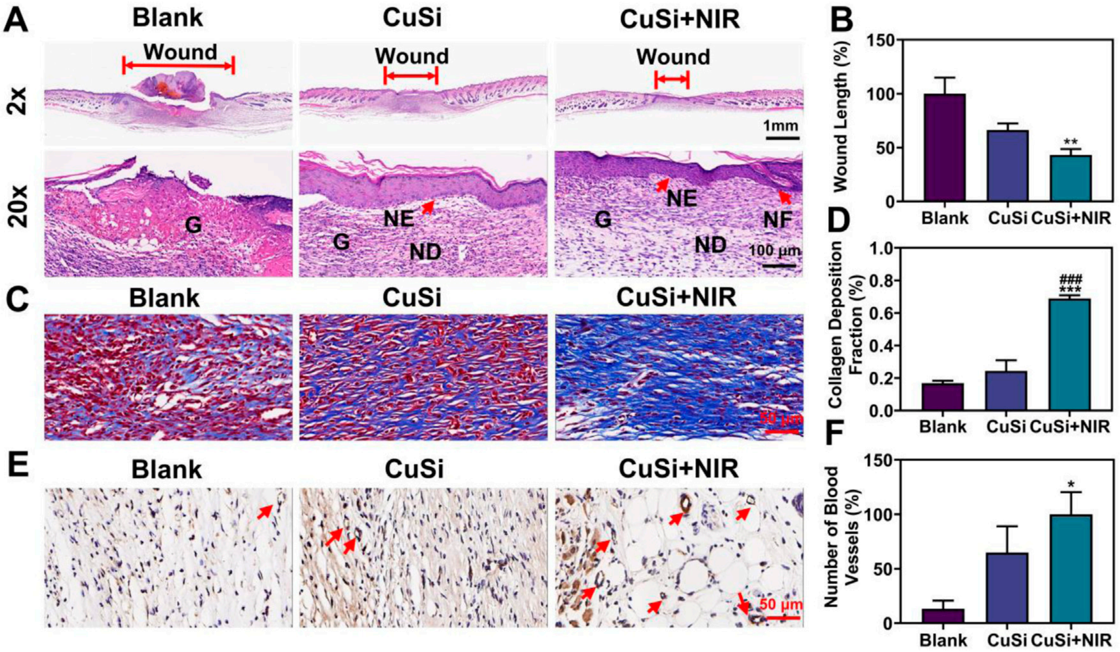

FIGURE 7

Histological analysis of wound sections after 9 days with different treatments. **(A)** H&E staining. The length of the red arrow represents the length of the unhealed wound bed (G: granulation tissue; NE: neoepidermis; ND: neodermis; HF: hair follicles). **(B)** Statistics of wound bed granulation length (n = 5). The Blank group was normalized. **(C)** Masson staining. **(D)** Statistics of collagen deposition distribution (n = 5). **(E)** Immunohistochemical staining pictures against CD31 and **(F)** the statistics of neovessel numbers (n = 5). The CuSi + NIR group was normalized in **(F)**. Arrows indicate blood vessels. $^{*}p < 0.1$, $^{**}p < 0.01$ or $^{***}p < 0.001$ vs. Blank group; $^{\#}p < 0.05$ or $^{\#\#}p < 0.01$ or $^{\#\#\#}p < 0.001$ vs. CuSi group.

been developed as wound dressings with enhanced angiogenic ability for different wound healing including infected wounds, burn wounds, and diabetic wounds (Fan et al., 2022). More interestingly, by combining with the different metal elements, the bioactive of silicate materials could be further enhanced. For instance, Cu ions play a vital role in vascularization, which are mainly existed in the form of Cu-binding proteins in human body and show stimulatory effects on new vessel formation by activating several angiogenic pathways including the *HIF-VEGF* signaling pathway as Cu ions can stabilize the *HIF-1α* by preventing its degradation (Kong et al., 2014). The combination of Cu and Si ions may produce a synergistic effect on stimulating angiogenesis and facilitate the regeneration of injured tissues, which have been verified in different defect tissues such as bone, skin, and endometrium (Yang et al., 2021a; Yang et al., 2021b; Dong et al., 2022). Our present study research proved that CuSi NWs could significantly promote the expression of *VEGF*, *HIF-1α*, and *bFGF* in HUVECs and stimulated more neovascularization in the newly formed dermal tissue, which may also be ascribed to the synergetic angiogenic effect of Cu and Si ions.

Although we have successfully fabricated a new CuSi NW and demonstrated its potential therapeutic capacity in treating cutaneous infectious wounds *via* both *in vitro* and *in vivo* experiments. There are still some issues or limitations that need to be solved or improved in further studies. First, CuSi NWs suspension was applied in this study, which would precipitate after a while and may affect the final therapeutic effects. Composite material such as incorporating CuSi NWs into a commercial hydrogel matrix or an electrospinning film may be a better choice. Second, more biosafety analysis should be conducted since several potential risks were involved in this system including the utilized NIR light and possible nanotoxicity. Finally, the underlying mechanism of the enhanced wound healing ability of CuSi NWs should be explored as endothelial cell is only one of the cells that participate in wound repair and angiogenesis is also one of the factors that affect wound healing.

5 Conclusion

In summary, we proposed a NIR light-assisted approach to treat infected wounds based on the newly synthesized photothermal agent of CuSi NWs, which could not only effectively combat bacteria, but also promote angiogenesis and facilitate wound healing due to the sustained release of bioactive Cu and Si ions. Our results suggested that CuSi NWs have the potential for rapidly erasing bacterial infections and prominently promoting wound healing.

Data availability statement

The original contributions presented in the study are included in the article/supplementary material, further inquiries can be directed to the corresponding authors.

Ethics statement

The animal study was reviewed and approved by the Animal Research and Ethics Committee of Wenzhou Institute of the University of Chinese Academy of Sciences (Approval Issue No. WIUCAS22102007).

Author contributions

YF and MW performed the main experiments and analyzed the data, wrote the manuscript, HL, DC and HJ performed the animal experiment, HX and JC revised the manuscript, HZ, ZD, and CY formulated the hypothesis, designed the research, revised the manuscript provide the fund support.

Funding

This research was supported by National Natural Science Foundation of China (32271386), the Wenzhou Science and Technology Major Project (ZY2022028), the Wenzhou Science and Technology Project (Y20220142), Chengdu Municipal Technological Innovation R&D Project (2021-YF05-01871-SN), Project of Chengdu Municipal Health Commission (2021059), Zhejiang Engineering Research Center for Tissue Repair Materials (WIUCASZZXF21001), the seed grants from the Wenzhou Institute, University of Chinese Academy of Sciences (WIUCASQD2020013, WIUCASQD2021030), and the funding from the First Affiliated Hospital of Wenzhou Medical University.

Acknowledgments

Also, we thank Scientific Research Center of Wenzhou Medical University for consultation and instrument availability that supported this work.

Conflict of interest

The authors declare that the research was conducted in the absence of any commercial or financial relationships that could be construed as a potential conflict of interest.

Publisher's note

References

Bai, X. T., Yang, Y., Zheng, W., Huang, Y., Xu, F. X., and Bao, Z. H. (2023). Synergistic photothermal antibacterial therapy enabled by multifunctional nanomaterials: Progress and perspectives. *Mater. Chem. Front.* 7 (3), 355–380. doi:10.1039/d2qm01141g

Bakkeren, E., Diard, M., and Hardt, W. D. (2020). Evolutionary causes and consequences of bacterial antibiotic persistence. *Nat. Rev. Microbiol.* 18 (9), 479–490. doi:10.1038/s41579-020-0378-z

Cao, W. T., Chen, F. F., Zhu, Y. J., Zhang, Y. G., Jiang, Y. Y., Ma, M. G., et al. (2018). Binary strengthening and toughening of MXene/cellulose nanofiber composite paper with nacre-inspired structure and superior electromagnetic interference shielding properties. *ACS Nano* 12 (5), 4583–4593. doi:10.1021/acsnano.8b00997

Chen, Y., Gao, Y. J., Chen, Y., Liu, L., Mo, A. C., and Peng, Q. (2020). Nanomaterials-based photothermal therapy and its potentials in antibacterial treatment. *J. Control. Release* 328, 251–262. doi:10.1016/j.jconrel.2020.08.055

Chernousova, S., and Epple, M. (2013). Silver as antibacterial agent: Ion, nanoparticle, and metal. *Angew. Chem. Int. Ed.* 52 (6), 1636–1653. doi:10.1002/anie.201205923

Das, A., Chen, G. F., Kim, H. W., Varadarajan, S., Youn, S. W., Yang, J., et al. (2015). Identification of novel copper-dependent wound repair mechanism: Role of copper transport protein antioxidant 1. *Circulation* 132, A13113. doi:10.1161/circ.132.suppl_3.13113

Das, A., Sudhahar, V., Chen, G. F., Kim, H. W., Youn, S. W., Finney, L., et al. (2016). Endothelial antioxidant-1: A key mediator of copper-dependent wound healing *in vivo*. *Sci. Rep.* 6, 33783. doi:10.1038/srep33783

Doherty, C. B., Doherty, S. D., and Rosen, T. (2010). Thermotherapy in dermatologic infections. *J. Am. Acad. Dermatol.* 62 (6), 909–927. doi:10.1016/j.jaad.2009.09.055

Dong, C. L., Yang, C., Younis, M. R., Zhang, J., He, G., Qiu, X. D., et al. (2022). Bioactive NIR-II light-responsive shape memory composite based on cuprorivaite nanosheets for endometrial regeneration. *Adv. Sci.* 9 (12), 2102220. doi:10.1002/advs.202102220

Fan, C., Xu, Q., Hao, R. Q., Wang, C., Que, Y. M., Chen, Y. X., et al. (2022). Multi-functional wound dressings based on silicate bioactive materials. *Biomaterials* 287, 121652. doi:10.1016/j.biomaterials.2022.121652

Fan, X. L., Li, H. Y., Ye, W. Y., Zhao, M. Q., Huang, D. N., Fang, Y., et al. (2019). Magainin-modified polydopamine nanoparticles for photothermal killing of bacteria at low temperature. *Colloids Surf. B* 183, 110423. doi:10.1016/j.colsurfb.2019.110423

Geng, B. J., Yang, D. W., Pan, D. Y., Wang, L., Zheng, F. F., Shen, W. W., et al. (2018). NIR-responsive carbon dots for efficient photothermal cancer therapy at low power densities. *Carbon* 134, 153–162. doi:10.1016/j.carbon.2018.03.084

Huang, G. J., Yu, H. P., Wang, X. L., Ning, B. B., Gao, J., Shi, Y. Q., et al. (2021). Highly porous and elastic aerogel based on ultralong hydroxyapatite nanowires for high-performance bone regeneration and neovascularization. *J. Mat. Chem. B* 9 (5), 1277–1287. doi:10.1039/d0tb02288h

Huo, J., Jia, Q., Huang, H., Zhang, J., Li, P., Dong, X., et al. (2021). Emerging photothermal-derived multimodal synergistic therapy in combating bacterial infections. *Chem. Soc. Rev.* 50 (15), 8762–8789. doi:10.1039/d1cs00074h

Jones, R. S., Draheim, R. R., and Roldo, M. (2018). Silver nanowires: Synthesis, antibacterial activity and biomedical applications. *Appl. Sci.* 8, 673. doi:10.3390/app8050673

Kong, N., Lin, K. L., Li, H. Y., and Chang, J. (2014). Synergy effects of copper and silicon ions on stimulation of vascularization by copper-doped calcium silicate. *J. Mat. Chem. B* 2 (8), 1100–1110. doi:10.1039/c3tb21529f

Lefez, B., Souchet, R., Kartouni, K., and Lenglet, M. (1995). Infrared reflection study of CuO in thin oxide films. *Thin Solid Films* 268 (1-2), 45–48. doi:10.1016/0040-6090(95)06872-4

Li, H., Ban, L., Wang, Z., Meng, P., Zhang, Y., Wu, R., et al. (2019a). Regulation of Cu species in CuO/SiO_2 and its structural evolution in ethynylation reaction. *Nanomaterials* 9 (6), 842. doi:10.3390/nano9060842

Li, H. Y., and Chang, J. (2013). Stimulation of proangiogenesis by calcium silicate bioactive ceramic. *Acta Biomater.* 9 (2), 5379–5389. doi:10.1016/j.actbio.2012.10.019

Li, J., Zhai, D., Lv, F., Yu, Q., Ma, H., Yin, J., et al. (2016). Preparation of copper-containing bioactive glass/eggshell membrane nanocomposites for improving angiogenesis, antibacterial activity and wound healing. *Acta Biomater.* 36, 254–266. doi:10.1016/j.actbio.2016.03.011

Li, K., Xia, C., Qiao, Y., and Liu, X. (2019b). Dose-response relationships between copper and its biocompatibility/antibacterial activities. *J. Trace Elem. Med. Biol.* 55, 127–135. doi:10.1016/j.jtemb.2019.06.015

Li, L. Y., Fu, L. M., Ai, X. C., Zhang, J. P., and Zhou, J. (2017). Design and fabrication of temperature-sensitive nanogels with controlled drug release properties for enhanced photothermal sterilization. *Chem. - Eur. J.* 23 (72), 18092–18186. doi:10.1002/chem.201705256

Ma, H., Yang, C., Ma, Z., Wei, X., Younis, M. R., Wang, H., et al. (2022). Multiscale hierarchical architecture-based bioactive scaffolds for versatile tissue engineering. *Adv. Healthc. Mat.* 11 (13), e2102837. doi:10.1002/adhm.202102837

Ma, L., Zhou, Y., Zhang, Z., Liu, Y., Zhai, D., Zhuang, H., et al. (2020). Multifunctional bioactive Nd-Ca-Si glasses for fluorescence thermometry, photothermal therapy, and burn tissue repair. *Adv. Sci.* 6 (32), eabb1311. doi:10.1126/sciadv.abb1311

Mei, L., Zhu, S., Liu, Y., Yin, W., Gu, Z., and Zhao, Y. (2021). An overview of the use of nanozymes in antibacterial applications. *Chem. Eng. J.* 418, 129431. doi:10.1016/j.cej.2021.129431

Ning, C. Y., Wang, X. L., Li, L. H., Zhu, Y., Li, M., Yu, P., et al. (2015). Concentration ranges of antibacterial cations for showing the highest antibacterial efficacy but the least cytotoxicity against mammalian cells: Implications for a new antibacterial mechanism. *Chem. Res. Toxicol.* 28 (9), 1815–1822. doi:10.1021/acs.chemrestox.5b00258

Panacek, A., Kvitek, L., Prucek, R., Kolar, M., Vecerova, R., Pizurova, N., et al. (2006). Silver colloid nanoparticles: Synthesis, characterization, and their antibacterial activity. *J. Phys. Chem. B* 110 (33), 16248–16253. doi:10.1021/jp063826h

Perdikaki, A., Galeou, A., Pilatos, G., Karatasios, I., Kanellopoulos, N. K., Prombona, A., et al. (2016). Ag and Cu monometallic and Ag/Cu bimetallic nanoparticle-graphene composites with enhanced antibacterial performance. *ACS Appl. Mat. Interfaces.* 8 (41), 27498–27510. doi:10.1021/acsami.6b08403

Qian, W., Yan, C., He, D., Yu, X., Yuan, L., Liu, M., et al. (2018). pH-triggered charge-reversible of glycol chitosan conjugated carboxyl graphene for enhancing photothermal ablation of focal infection. *Acta Biomater.* 69, 256–264. doi:10.1016/j.actbio.2018.01.022

Rai, M., Yadav, A., and Gade, A. (2009). Silver nanoparticles as a new generation of antimicrobials. *Biotechnol. Adv.* 27 (1), 76–83. doi:10.1016/j.biotechadv.2008.09.002

Slavin, Y. N., Asnis, J., Hafeli, U. O., and Bach, H. (2017). Metal nanoparticles: Understanding the mechanisms behind antibacterial activity. *J. Nanobiotechnol.* 15, 65. doi:10.1186/s12951-017-0308-z

Song, J., Chen, Z., Liu, Z., Yi, Y., Tsigkou, O., Li, J., et al. (2021). Controllable release of vascular endothelial growth factor (VEGF) by wheel spinning alginate/silk fibroin fibers for wound healing. *Mat. Des.* 212, 110231. doi:10.1016/j.matdes.2021.110231

Stanic, V., Janackovic, D., Dimitrijevic, S., Tanaskovic, S. B., Mitric, M., Pavlovic, M. S., et al. (2011). Synthesis of antimicrobial monophase silver-doped hydroxyapatite nanopowders for bone tissue engineering. *Appl. Surf. Sci.* 257 (9), 4510–4518. doi:10.1016/j.apsusc.2010.12.113

Sun, T. W., Zhu, Y. J., and Chen, F. (2018). Hydroxyapatite nanowire/collagen elastic porous nanocomposite and its enhanced performance in bone defect repair. *RSC Adv.* 8 (46), 26218–26229. doi:10.1039/c8ra03972k

Wan, Y. Z., Yang, S. S., Wang, J., Gan, D. Q., Gama, M., Yang, Z. W., et al. (2020). Scalable Synthesis of robust and stretchable composite wound dressings by dispersing silver nanowires in continuous bacterial cellulose. *Compos. Part B* 199, 108259. doi:10.1016/j.compositesb.2020.108259

Wu, C. T., Zhou, Y. H., Xu, M. C., Han, P. P., Chen, L., Chang, J., et al. (2013). Copper-containing mesoporous bioactive glass scaffolds with multifunctional properties of angiogenesis capacity, osteostimulation and antibacterial activity. *Biomaterials* 34 (2), 422–433. doi:10.1016/j.biomaterials.2012.09.066

Xie, X. F., Lei, H., and Fan, D. D. (2023). Antibacterial hydrogel with PH-responsive microcarriers of slow-release VEGF for bacterial infected wounds repair. *J. Mat. Sci. Technol.* 144, 198–212. doi:10.1016/j.jmst.2022.09.062

Xu, J. W., Yao, K., and Xu, Z. K. (2019). Nanomaterials with A Photothermal effect for antibacterial activities: An overview. *Nanoscale* 11 (18), 8680–8691. doi:10.1039/c9nr01833f

Xu, Q., Chang, M. L., Zhang, Y., Wang, E. D., Xing, M., Gao, L., et al. (2020). PDA/Cu bioactive hydrogel with "hot ions effect" for inhibition of drug-resistant bacteria and enhancement of infectious skin wound healing. *ACS Appl. Mat. Interfaces.* 12 (28), 31255–31269. doi:10.1021/acsami.0c08890

Xu, Q., Jiang, F., Guo, G. Y., Wang, E. D., Younis, M. R., Zhang, Z. W. B., et al. (2021). Targeted hot ion therapy of infected wound by glycol chitosan and polydopamine grafted Cu-SiO$_2$ nanoparticles. *Nano Today* 41, 101330. doi:10.1016/j.nantod.2021.101330

Xu, X., Liu, X., Tan, L., Cui, Z., Yang, X., Zhu, S., et al. (2018). Controlled-temperature photothermal and oxidative bacteria killing and acceleration of wound healing by polydopamine-assisted Au-hydroxyapatite nanorods. *Acta Biomater.* 77, 352–364. doi:10.1016/j.actbio.2018.07.030

Yang, C., Ma, H. S., Wang, Z. Y., Younis, M. R., Liu, C. Y., Wu, C. T., et al. (2021a). 3D printed wesselsite nanosheets functionalized scaffold facilitates NIR-II photothermal therapy and vascularized bone regeneration. *Adv. Sci.* 8, 2100894. doi:10.1002/advs.202100894

Yang, C., Younis, M. R., Zhang, J., Qu, J. L., Lin, J., and Huang, P. (2020). Programmable NIR-II photothermal-enhanced starvation-primed chemodynamic therapy using glucose oxidase-functionalized ancient pigment nanosheets. *Small* 16 (25), 2001518. doi:10.1002/smll.202001518

Yang, C., Zheng, R., Younis, M. R., Shao, J. D., Fu, L. H., Zhang, D. Y., et al. (2021b). NIR-II light-responsive biodegradable shape memory composites based on cuprorivaite nanosheets for enhanced tissue reconstruction. *Chem. Eng. J.* 419, 129437. doi:10.1016/j.cej.2021.129437

Yang, Y., He, P., Wang, Y., Bai, H., Wang, S., Xu, J. F., et al. (2017). Supramolecular radical anions triggered by bacteria *in situ* for selective photothermal therapy. *Angew. Chem. Int. Ed. Engl.* 56 (51), 16457–16460. doi:10.1002/ange.201708971

Yu, S. M., Li, G. W., Liu, R., Ma, D., and Xue, W. (2018). Dendritic Fe$_3$O$_4$@Poly(dopamine)@PAMAM nanocomposite as controllable NO-releasing material: A synergistic photothermal and no antibacterial study. *Adv. Funct. Mat.* 28 (20), 1707440. doi:10.1002/adfm.201707440

Yuan, P., Ding, X., Guan, Z., Gao, N., Ma, R., Jiang, X. F., et al. (2015). Plasmon-coupled gold nanospheres for two-photon imaging and photoantibacterial activity. *Adv. Healthc. Mater* 4 (5), 674–678. doi:10.1002/adhm.201400524

Zeng, W. N., Wang, D., Yu, Q. P., Yu, Z. P., Wang, H. Y., Wu, C. Y., et al. (2022). Near-infrared light-controllable multifunction mesoporous polydopamine nanocomposites for promoting infected wound healing. *ACS Appl. Mat. Interfaces.* 14 (2), 2534–2550. doi:10.1021/acsami.1c19209

Zheng, Y., Ma, W., Yang, Z., Zhang, H., Ma, J., Li, T., et al. (2022). An ultralong hydroxyapatite nanowire aerogel for rapid hemostasis and wound healing. *Chem. Eng. J.* 430, 132912. doi:10.1016/j.cej.2021.132912

Zhou, Y., Gao, L., Peng, J., Xing, M., Han, Y., Wang, X., et al. (2018). Bioglass activated albumin hydrogels for wound healing. *Adv. Healthc. Mater* 7 (16), e1800144. doi:10.1002/adhm.201800144

Zilberman, M., and Elsner, J. J. (2008). Antibiotic-eluting medical devices for various applications. *J. Control. Release* 130 (3), 202–215. doi:10.1016/j.jconrel.2008.05.020

frontiers | Frontiers in Bioengineering and Biotechnology

TYPE Original Research
PUBLISHED 10 March 2023
DOI 10.3389/fbioe.2023.1160703

Check for updates

OPEN ACCESS

EDITED BY
Weifeng Lin,
Weizmann Institute of Science, Israel

REVIEWED BY
Han Liu,
Shanghai University, China
Hu Menglong,
Peking University Hospital of Stomatology, China
Ying Yang,
University of Michigan, United States

*CORRESPONDENCE
Xing Zhang,
✉ xinzhang@ukaachen.de
Qun Zhao,
✉ qzhao@ukaachen.de
Xinhong Wang,
✉ xinhonghot@126.com

†These authors have contributed equally to this work

SPECIALTY SECTION
This article was submitted to Nanobiotechnology, a section of the journal Frontiers in Bioengineering and Biotechnology

RECEIVED 07 February 2023
ACCEPTED 28 February 2023
PUBLISHED 10 March 2023

CITATION
Zhang X, Zhao Q, Zhou N, Liu Y, Qin K, Buhl EM, Wang X, Hildebrand F, Balmayor ER and Greven J (2023), Osteoblast derived extracellular vesicles induced by dexamethasone: A novel biomimetic tool for enhancing osteogenesis *in vitro*.
Front. Bioeng. Biotechnol. 11:1160703.
doi: 10.3389/fbioe.2023.1160703

Osteoblast derived extracellular vesicles induced by dexamethasone: A novel biomimetic tool for enhancing osteogenesis *in vitro*

Xing Zhang[1*†], Qun Zhao[1*†], Nan Zhou[1], Yu Liu[1], Kang Qin[1], Eva Miriam Buhl[2], Xinhong Wang[3*], Frank Hildebrand[1], Elizabeth R. Balmayor[1†] and Johannes Greven[1†]

[1]Department of Orthopedics, Trauma and Reconstructive Surgery, University Hospital RWTH Aachen, Aachen, Germany, [2]Electron Microscopy Facility, Institute of Pathology and Medical Clinic II, University Hospital RWTH Aachen, Aachen, Germany, [3]Department of Orthopedics, The Affliated Huai'an Hospital of Xuzhou Medical University, Huai'an Second People's Hospital, Huai'an, Jiangsu, China

Extracellular vesicles (EVs) are newly appreciated communicators involved in intercellular crosstalk, and have emerged as a promising biomimetic tool for bone tissue regeneration, overcoming many of the limitations associated with cell-based therapies. However, the significance of osteoblast-derived extracellular vesicles on osteogenesis has not been fully established. In this present study, we aim to investigate the therapeutic potential of extracellular vesicles secreted from consecutive 14 days of dexamethasone-stimulated osteoblasts ($\text{OB-EV}_{\text{Dex}}$) to act as a biomimetic tool for regulating osteogenesis, and to elucidate the underlying mechanisms. $\text{OB-EV}_{\text{dex}}$ treated groups are compared to the clinically used osteo-inductor of BMP-2 as control. Our findings revealed that $\text{OB-EV}_{\text{Dex}}$ have a typical bilayer membrane nanostructure of, with an average diameter of 178 ± 21 nm, and that fluorescently labeled $\text{OB-EV}_{\text{Dex}}$ were engulfed by osteoblasts in a time-dependent manner. The proliferation, attachment, and viability capacities of $\text{OB-EV}_{\text{Dex}}$-treated osteoblasts were significantly improved when compared to untreated cells, with the highest proliferative rate observed in the $\text{OB-EV}_{\text{Dex}}$ + BMP-2 group. Notably, combinations of $\text{OB-EV}_{\text{Dex}}$ and BMP-2 markedly promoted osteogenic differentiation by positively upregulating osteogenesis-related gene expression levels of *RUNX2*, *BGLAP*, *SPP1*, *SPARC*, *Col 1A1*, and *ALPL* relative to BMP-2 or $\text{OB-EV}_{\text{Dex}}$ treatment alone. Mineralization assays also showed greater pro-osteogenic potency after combined applications of $\text{OB-EV}_{\text{Dex}}$ and BMP-2, as evidenced by a notable increase in mineralized nodules (calcium deposition) revealed by Alkaline Phosphatase (ALP), Alizarin Red Alizarin Red staining (ARS), and von Kossa staining. Therefore, our findings shed light on the potential of $\text{OB-EV}_{\text{Dex}}$ as a new therapeutic option for enhancing osteogenesis.

KEYWORDS

extracellular vesicles, dexamethasone stimulation, intercellular crosstalk, osteoblastic differentiation, osteogenesis, bone regeneration

1 Introduction

Bone defects, caused by traumatic injuries, age-associated disorders, infections, and surgical resections, have been a global medical and socioeconomic challenge that severely impairs the natural bone healing process (Dimitriou et al., 2011; El-Rashidy et al., 2017). The current "gold standard" treatment algorithm in clinical settings for augmenting bone regeneration involves applications of autologous and allogeneic bone grafting (Roseti et al., 2017). Mostly these approaches have positive clinical outcomes; however, they are associated with several limitations including limited availability, risk of disease transmission, donor site morbidity, and unexpected immunoreaction, among others that may result in malunion (Ng et al., 2017; Schmidt, 2021). Bone morphogenetic protein-2 (BMP-2), a potent osteoinductive cytokine, was believed to be "near-perfect" in achieving bone induction; however, it simultaneously has accrued a worrisome side effect profile, such as ectopic bone formation, osteoclast-mediated bone resorption, and inappropriate adipogenesis (James et al., 2016). Thus, there is an urgent need to develop alternative therapeutic strategies that can mitigate risks and simultaneously augment bone regeneration.

Cell-based therapies are attractive as a promising alternative solution since they attempt to mimic and improve the body's natural regenerative potential for bone repair (Buzhor et al., 2014). Stem cell-based therapies have been broadly reported, however, clinical success is restricted owing to insurmountable hurdles associated with high costs, ethical concerns, low homing efficacy of transplanted cells, and variations in differentiation capacities (Walmsley et al., 2016; Ho-Shui-Ling et al., 2018). Faced with these limitations, the development of novel biological approaches for bone regeneration that retain many of the advantages of cell-based approaches, with the aim of achieving functional osteogenesis, is of vital importance.

Extracellular vesicles (EVs), one of the cell-secreted factors, have sparked increasing interest as a potential therapeutic tool for regenerative medicine in the past decades (van Niel et al., 2018; Liu et al., 2022). EVs are a group of cell-derived vesicles with sizes ranging from 30 to 1,000 nm, that can be broadly categorized into three major subtypes based on the putative biological pathways: Exosomes, microvesicles, and apoptotic bodies (Li et al., 2021). Nowadays, the biological implications of EVs dramatically evolved, switching from the original concept of secreting cellular wastes/debris to a regulated means of biological information exchange based on cellular needs and status. Accumulating evidence indicated that EVs play a crucial role in intercellular communication by transporting complex cargoes, such as nucleic acids (mRNA or microRNA), functional proteins, lipids, and biologically active molecules to target cells (Théry et al., 2009; Lin et al., 2022; van Niel et al., 2022). Thereby regulating tissue metabolism, homeostasis, and development by so-called horizontal transfer driven by receptor-ligand interactions and endocytosis (Colombo et al., 2014). Such unique features make EVs a potential candidate for restoring bone defects and augmenting bone regeneration.

In recent years, EVs have exhibited great promise in regenerative medicine as biomimetic tools for inducing lineage-specific stem cell differentiation (Alqurashi et al., 2021; Hade et al., 2021). Besides, the considerable utility of stem cells-derived EVs in improving osteogenesis has been extensively reported (Narayanan et al., 2016; Huang et al., 2017; Pizzicannella et al., 2019). It has been reported that EVs exerted a crucial role in amplifying microRNA (miR-29a, miR-3, etc.) cargoes transport to recipient cells, thereby enhancing their osteogenic differentiation (Huang et al., 2017; Hu et al., 2020; Lu et al., 2020). A recent study revealed that osteoblast-derived EVs play a physiologic role in interacting with other cells (monocytes and osteoclasts) in the bone microenvironment (Cappariello et al., 2018). Moreover, Davies et al. (2017) reported the favorable biological effect of EVs derived from osteoblasts, a potent osteo-inductive capacity that elicits enhanced stem cell mineralization to modulate osteogenesis. These findings suggest an effective intercellular communication mediated by EVs in the osteogenic microenvironment.

Numerous studies have evaluated the specific roles of MSC-derived EVs; however, it is surprising that, to date, only a very limited number of studies investigate the role of osteoblast-derived EVs. Previous literature reported that dexamethasone can dramatically enhance the middle-to-late stage of osteoblastic differentiation of hBMSC (Martins et al., 2010); EVs secreted from mineralizing osteoblasts (late differentiation) have also been identified to have a high pro-osteogenic potency (Cui et al., 2016). In this context, we put forward the hypothesis that EVs derived from synchronized late-stage osteoblast differentiation caused by 14 days of dexamethasone stimulation (OB-EV_{Dex}) would present an exceptional osteo-promoting capacity for improved osteogenesis.

In this study, we aim to investigate the osteogenic potential of dexamethasone-induced OB-EV_{Dex} on osteogenesis and explore their potential utility as biomimetic tools to accelerate bone augmentation. Furthermore, the therapeutic role of OB-EV_{Dex} was validated by examining the proliferation, viability, growth, and osteoblastic differentiation capacities of osteoblasts after OB-EV_{Dex} treatment. This study may open a new horizon for exploring EVs in regenerative medicine for restoring bone defects in a shorter period of treatment time or bringing up the possibility of non-union treatment.

2 Materials and methods

2.1 Cell culture under normal conditions and osteogenic conditions

Porcine osteoblasts (OB) were isolated according to a previously published protocol with a slight modification (Bakker and Klein-Nulend, 2012; Perpétuo et al., 2019). Osteoblast cells were routinely cultured in growth medium (GM) containing basal Dulbecco's Modified Eagle Medium (DMEM, Invitrogen, Carlsbad, CA, United States) supplemented with 10% fetal bovine serum (FBS), 1% double-antibiotics (penicillin/streptomycin), and maintained at 37°C in a humidified 5% CO_2 atmosphere. Isolated cells were passaged until passage 3–5 for subsequent experiments. For osteogenic induction, osteoblasts were maintained and treated with a common osteogenic induction medium (OM) supplemented with 100 nM dexamethasone, 10 mM β-glycerophosphate, and 100 µM L-ascorbic acid-2-phosphate.

Osteoblasts were seeded on the commercially available particulate bone graft substitutes (biphasic calcium phosphate, BCP) with the particle size of 0.5–2 mm (maxresorb®, botiss biomaterials GmbH, Zossen, Germany). BCP granules have a chemical composition of 60% hydroxyapatite (HA) and 40% β-tricalcium phosphate (β-TCP) and displayed good stability with a porosity of about 80%, interconnectivity, and rough surfaces, which is beneficial to the adhesion and growth of seeded osteoblasts. For sterilization, the BCP granules were rinsed with sterile deionized water, and then sterilized by overnight incubation in 70% ethanol as well as 1 h of UV exposure.

2.2 Isolation and characterization of OB-EV$_{\text{Dex}}$

2.2.1 Isolation

Prior to OB-EV$_{\text{Dex}}$ extraction, porcine osteoblasts were plated at an initial density of 40,000 cells/well in the 6-well plates. Afterwards, dexamethasone (500 nM) was supplemented into the GM medium to sustainably stimulate osteoblast cells for 14 consecutive days in order to generate OB-EV$_{\text{Dex}}$. Only dexamethasone as an osteogenic stimulant was chosen. Commonly employed β-glycerophosphate and L-ascorbic acid-2-phosphate were not used in our study. Thereby, the obtained results will be correlated specifically to dexamethasone later on. At day 14, dexamethasone-stimulated osteoblast cells were rinsed with a serum-free medium and maintained under serum-free conditions for another 24 h. Subsequently, the dexamethasone-stimulated conditioned medium was collected and subjected to a series of differential centrifugation at 300 g, ×2,000 g, and ×5,000 g for 15 min at 4°C, respectively, to eliminate remnant cells, followed by filtration through a 0.22 μm filter for removal of excess cell debris. The supernatant was harvested and centrifuged twice at ×20,000 g in a sterile Ultra-Clear™ tube (Beckman Coulter, Brea, CA, United States) for 90 min for purification. Finally, OB-EV$_{\text{Dex}}$ were pelleted by ultracentrifugation at ×100,000 g for 90 min, resuspended in filtered PBS, and stored at −80°C for further use.

2.2.2 Characterization examinations of OB-EV$_{\text{Dex}}$

The concentration and size distribution of OB-EV$_{\text{Dex}}$ were determined by transmission electron microscopy (TEM) and nanoparticle tracking analysis (NTA) with a NanoSight NS300 (Malvern, Worcestershire, United Kingdom) with 545 nm laser. For NTA, the OB-EV$_{\text{Dex}}$ suspension was assessed using a NanoSight NS-300 instrument to acquire size distribution plots and corresponding concentration (particles/mL). For TEM observations, the harvested OB-EV$_{\text{Dex}}$ resuspended in 10 μL of Hepes buffer (0.1 M, pH 7.4) were allowed to absorb onto the glow discharged formvar-carbon-coated nickel grids (Maxtaform, 200 mesh, Plano, Wetzlar, Germany) for 10 min. After that, samples on grids were stained by placing shortly on a drop of 0.5% uranyl acetate in distilled water (DW). After air drying, samples were examined using a TEM LEO 906 (Carl Zeiss, Oberkochen, Germany), operating at an acceleration voltage of 60 kV. To maintain consistency, the isolated OB-EV$_{\text{Dex}}$ were resuspended in 100 μL of DPBS after which an equal number and concentration of OB-EV$_{\text{Dex}}$ were ensured for each experiment.

2.3 Cytotoxicity assay of bone graft granules and OB-EV$_{\text{Dex}}$

The Cell Counting Kit-8 (CCK-8, Sigma-Aldrich, Steinheim, Germany) assay was performed to assess the potential cytotoxicity of bone graft BCP granules towards OB cells in the presence or absence of OB-EV$_{\text{Dex}}$. The concentration of EVs used was around 5–6 × 10^9 particles/mL. Osteoblast cells were seeded in 96-well plates with a density of 5,000 cells/well and incubated at 37°C overnight to adhere to plates, after which they were exposed to varying concentrations of DMEM medium suspension containing BCP granules (25, 50, 75, 100, 200, 500, 1,000, 2000, and 3,000 μg/mL) and cultured for 1, 4, and 7 days. Afterward, DMEM medium was removed, and 10 μL of CCK-8 solutions was introduced into each well and incubated for another 2 h. Parallel sets of wells with freshly cultured, non-treated cells served as negative controls. Optical densities were determined at 450 nm wavelength through a microplate reader (Infinite M200, Tecan, Switzerland). Besides, the absorbance of cells simultaneously treated with BCP granules and OB-EV$_{\text{Dex}}$ was measured following the same testing procedures.

2.4 OB-EV$_{\text{Dex}}$ cellular internalization

With regards to endocytosis experiments, isolated OB-EV$_{\text{Dex}}$ were marked with a molecular fluorescent lectin probe, Wheat Germ Agglutinin Conjugates (WGA, Alexa Fluor® 488 conjugate, Invitrogen, Carlsbad, CA, United States), which selectively binds to the sialic acid on the membranes for the labeling. Prior to the experiments, osteoblasts at a density of 5 × 10^4/dish were seeded onto each confocal dish (VWR GmbH, Darmstadt, Germany) and incubated for 24 h. In brief, OB-EV$_{\text{Dex}}$ were centrifuged and collected, after which recommended amounts of probe solution were applied for labeling EVs. Labeling of the EVs was performed following the instructions provided with the lectin probe. Fluorescently labeled OB-EV$_{\text{Dex}}$ were rinsed thrice with DPBS and centrifuged at ×20,000 g for 90 min to remove excess probes. Fluorescently labeled OB-EV$_{\text{Dex}}$ were dispersed in DMEM and then supplemented into cell-seeded confocal dishes at 37°C for 1, 4, 12, and 72 h incubation. Finally, the amount of fluorescently labeled OB-EV$_{\text{Dex}}$ internalized into cells was evaluated *via* a confocal laser scanning microscope (CLSM, LSM 710, Carl Zeiss MicroImaging GmbH, Jena, Germany).

2.5 Cell attachment and proliferation under various treatment groups

Sterilized BCP granules were placed on confocal dishes after which OB cells were seeded at a density of 20,000 cells/well. Cells randomly received the following treatments: 1) only BCP granules (control), 2) BMP-2 loaded BCP granules (BMP-2), 3) BCP granules plus OB-EV$_{\text{Dex}}$ (OB-EV$_{\text{Dex}}$), and 4) BMP-2 loaded BCP granules plus OB-EV$_{\text{Dex}}$ (BMP-2+OB-EV$_{\text{Dex}}$). After various treatments for 1, 4, and 7 days, cell attachment and proliferation of OB cells were evaluated. Firstly, calcein AM/DAPI staining was performed. In brief, cells were stained using 5 μM of fluorescence dye (Calcein AM, PromoCell GmbH, Heidelberg, Germany) for 40 min without light. DAPI staining dye (Invitrogen, Karlsruhe, Germany) was used at

10 μg/mL final concentration. Cells were stained at the indicated time-points and subsequently visualized *via* a fluorescence microscope (Leica DM IRB, Wetzlar, Germany). In addition, a CCK-8 assay was also performed. OB cells were cultured on BCP granules in 48-well plates at an initial density of 2×10^4 cells/well and subjected to four above-mentioned treatments for 1, 4, and 7 days prior to evaluation with the CCK-8 kit.

2.6 Cell viability analysis

OB cells were cultured on BCP granules under the four above-mentioned treatments (please see 2.5) at an initial density of 2×10^4 cells/well for 1, 4, and 7 days. At each predetermined time point, the medium was removed, the cells were rinsed, and labeled with the Live/Dead Cell Viability Assay kit (PromoCell GmbH, Heidelberg, Germany) containing 2 μM calcein AM and 4 μM ethidium homodimer-III (EthD-III), as per the manufacturer's instructions. Images were captured by a fluorescent microscope fitted with appropriate exciter and emitter filters to evaluate live and dead cells, which had been labeled with green and red fluorescence, respectively. Cell survival rate was calculated according to the following equation: Cell survival rate (%) = $[N_{live}/N_{dead} + N_{live}] \times 100\%$, where N_{live} is the number of live cells, and N_{dead} is the number of dead cells.

2.7 Evaluation of cell growth and morphology

After incubation for 7 days, we assessed cell morphologies on BCP granules under the four applied treatments. For this evaluation, cells were seeded at an initial density of 2×10^4 cells/well. Cell morphology was investigated through cytoskeleton staining and scanning electron microscopy (SEM, ESEM XL 30 FEG, FEI, Eindhoven, Netherlands). With regards to cytoskeleton staining, OB cells were subjected to co-staining with Rhodamine Phalloidin (ThermoFisher, Grand Island, NY, United States) and DAPI, which aid in visualizing F-actin and cell nuclei. Briefly, cells were rinsed with DPBS, fixed in 4% paraformaldehyde, followed by permeabilizing with 0.1% Triton X-100 and blocking with 1% BSA solution. After that, cells were co-stained with the indicated fluorescent regents and visualized *via* a CLSM under Ex/Em (540/565 nm) wavelength. For SEM observation, OB cells in various treatment groups were treated with an SEM fixation solution without light and dehydrated through varying gradient ethanol. Lastly, the morphologies of OB cells were detected *via* SEM after spray-coating with 4 nm thick gold.

2.8 Osteogenic differentiation and osteogenic potential validation

2.8.1 Alkaline Phosphatase (ALP) activity assay and ALP staining

OB cells were cultured on the BCP granules in OM medium and subjected to four different treatments for indicated durations. OM medium was chosen to induce osteogenic differentiation. ALP activities of OB cells in the various studied groups were quantitatively determined using an ALP Activity Assay Kit (PromoKine, PromoCell Gmbh, Heidelberg, Germany), which uses pnitrophenyl phosphate (pNPP) as the phosphatase substrate. Besides, the microplate reader was used for measuring the absorbance (O.D. value) at 405 nm. The ALP activities were calculated as the following equation: ALP activity = A/V/T, whereby A is the amount of pNP generated by OB cells, V is the volume of cell samples, and T is the reaction time. ALP staining was performed at 7 and 14 days after culture. Initially, OB cells under the various treatments were rinsed thrice with DPBS and fixed for 2 min at room temperature, followed by addition of ALP staining solution (Abcam, Cambridge, United Kingdom) in darkness for 30 min.

2.8.2 *In vitro* mineralization assessment

After incubation for 14 days, Alizarin red staining (ARS, Thermo Fisher, Waltham, MA, United States) and von Kossa staining (Sigma-Aldrich, St. Louis, MO, United States) were performed to evaluate mature mineralized nodules during late phase of osteogenic differentiation (Kwon et al., 2014). For ARS staining, OB cells subjected to the various studied treatments were washed using DPBS, fixed in 2% paraformaldehyde, and then stained with ARS working solution. Culture plates were imaged *via* an optical microscope. Mineralized nodules are shown as a dark red center and light red peripheral area. For von Kossa staining, OB cells were rinsed with DPBS and fixed in 2% paraformaldehyde for 15 min, followed by staining with a freshly prepared 5% silver nitrate solution for 40 min under UV exposure. After that, cells were immersed in fresh 5% sodium carbonate to indicate minerals and matrix of calcium deposits. Lastly, positive calcium deposits with brownish-blackish color were photographed using an optical microscope.

2.9 Expressions of related osteogenic marker genes during osteogenic differentiation

The OB cells under four different groups at an initial density of 20,000 cells/well were maintained in the osteogenic induction medium in confocal culture dishes for 0, 3, 7, and 14 days. At various predetermined time points, cells were obtained, and their osteogenic differentiation was assessed by examining the expression levels of osteogenesis-related genes of type 1A1 collagen (*Col 1A1*), *ALPL*, osteocalcin (*BGLAP*), osteopontin (*SPP1)*, osteonectin (*SPARC*), runt-related transcription factor 2 (*RUNX2*) through quantitative real-time PCR (qRT-PCR). In brief, a commercial RNA extraction kit (TRIzol, Invitrogen, Carlsbad, CA, United States) was utilized to extract and collect total RNA from OB cells in the various studied groups. The extracted RNA was reverse transcribed to cDNA using an RNA-to-cDNA kit (Thermo Fisher, Waltham, MA, United States). Then, a SYBR™ Green Master Mix Kit (Thermo Fisher, Waltham, MA, United States) was used for performing qRT-PCR on a CFX96 real-time PCR detection system (BioRad, Hercules, CA, United States). Primer sequences used in this assay are shown in Table 1. *GAPDH* was regarded as a housekeeping gene.

2.10 Statistical analysis

Experimental data are shown as the mean ± standard deviation (SD). Statistical analysis was carried out using SPSS 22.0 software

TABLE 1 Primer sequences used for qRT-PCR.

Gene	Forward primer sequences	Reverse primer sequences
RUNX2	GAGAGTAGGTGTCCCGCCT	GAAGTCAGAGGTGGCAGTGT
BGLAP	GCAGCCTTCGTGTCCAAGCA	GCCTCCTGGAAGCCGATGTGAT
SPP1	ACCGATCCGACGAGTCTCATCAC	ACCTCAGTCCATAGACCACACTATCC
SPARC	ACCTGGACTACATCGGACCTTGC	GCTTCTCATTCTCGTGGATCTCCTTCA
Col 1A1	GACATCCCACCAGTCACCTG	CACCCTTAGCACCAACAGCA
ALPL	AGCCTTCCTGAAAGAGGATTGG	GCCAGTACTTGGGGTCTTTCT
GAPDH	GTGAAGGTCGGAGTGAACGGATT	ACCATGTAGTGGAGGTCAATGAAGG

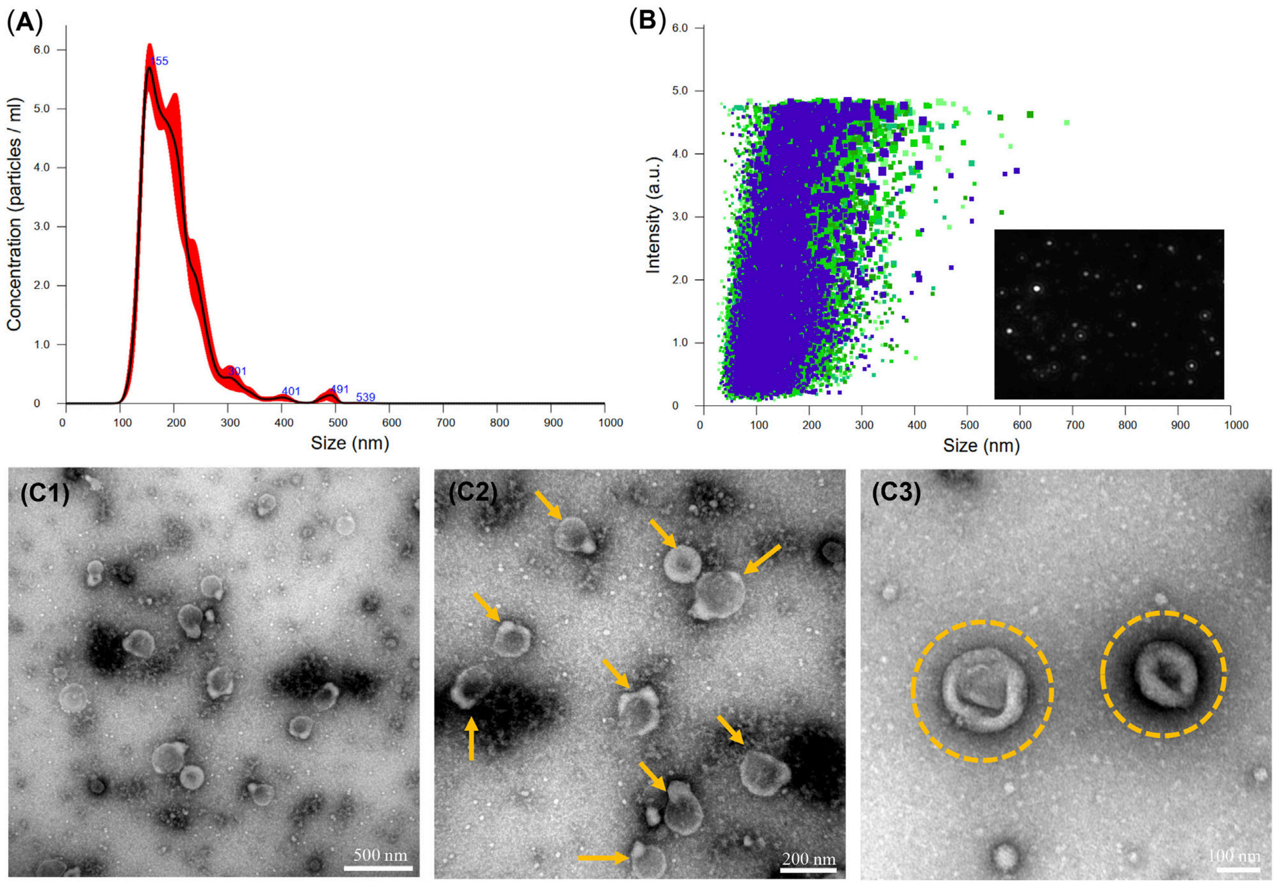

FIGURE 1
(A, B) Nanoparticle tracking analysis (NTA) of the obtained OB-EV$_{\text{Dex}}$ revealing their size distribution, particle concentration, and intensity. **(C1-C3)** Transmission electron microscopy (TEM) images of isolated OB-EV$_{\text{Dex}}$ at low and high magnification. Yellow arrows indicate the presence of OB-EV$_{\text{Dex}}$; yellow circles indicate OB-EV$_{\text{Dex}}$ showing a typical double-membrane nanostructure with spheroid shape.

(Armonk, NY, United States) and ORIGIN 9.0 software (Northampton, MA, United States). Student's t-test and two-way ANOVA are applied to compare the significance among two groups or multiple groups. $p < 0.05$ was considered as the minimal level of significance, $p < 0.01$ was regarded as the medium level of significance, and $p < 0.001$ was indicated as the high level of significance.

3 Results

3.1 OB-EV$_{\text{Dex}}$ characterization and cellular internalization

The EV$_{\text{Dex}}$ isolated from dexamethasone-stimulated OB cells were characterized for concentration and size distribution by NTA

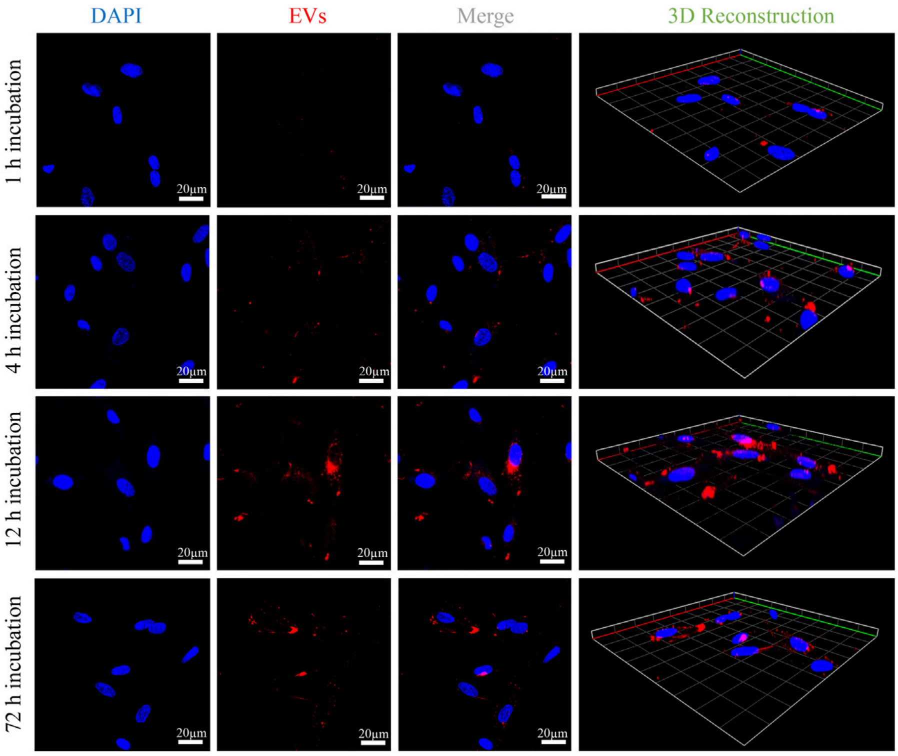

FIGURE 2
Confocal microscopy observations of cellular uptakes of fluorescently labeled OB-EV$_{Dex}$ by osteoblasts after 1, 4, 12, and 72 h incubation. 3D reconstruction images of z-stack recorded by confocal microscopy. Fluorescently labeled OB-EV$_{Dex}$ were detected as red fluorescence; cell nuclei were detected as blue fluorescence. Scale bar: 20 μm.

and TEM analysis. Figures 1A, B clearly verified the presence of a heterogeneous population of OB-EV$_{Dex}$, mainly ranging from 100 to 500 nm, as revealed by NTA analysis. Of note, one primary population was identified, whose average diameter was roughly 178 ± 21 nm. After standardized OB-EV$_{Dex}$ preparation, OB-EV$_{Dex}$ concentrations were established to be around 6×10^9 particles/mL in each fraction. The identity and sizes of OB-EV$_{Dex}$ were further confirmed through TEM examination (Figures 1C1–1C3). This revealed the diameters of spherical vesicles to be 150–200 nm, which is in accordance with the NTA results. OB-EV$_{Dex}$ exhibited a uniform distribution and a typical double-membrane nanostructure with spheroid shape, as also revealed by TEM analysis (Figure 1C3). These findings confirmed the successful isolation of OB-EV$_{Dex}$.

To justify that OB-EV$_{Dex}$ could interact with OB cells, the cellular uptake of fluorescently labelled EV$_{Dex}$ by OB cells was assessed by confocal laser scanning microscopy (CLSM). Figure 2 shows an apparent increment of the red fluorescence signal with prolonged incubation time (from 1 to 12 h). In fact, the red fluorescence signal from wheat germ agglutinin (WGA)-labeled OB-EV$_{Dex}$ confirmed the presence of the EV$_{Dex}$, that were assembled in the cell cytoplasm, validating that a large amount of labeled EV$_{Dex}$ were taken up by OB cells. It was noteworthy that the increase in red fluorescence inside OB cells exhibited a time-dependent pattern. Of note, WGA-labeled red signals were the most intense when incubation time reached 12 h in comparison to other times. The 3D reconstruction images visually indicated the distribution of labeled EVs inside OB cells with increasing time. The majority of OB-EV$_{Dex}$ were located in the cytoplasm and around the cellular nucleus. Notably, after 72 h post-incubation, there is a decrease in the intensity of red signals, attributable to the fact that these OB-EV$_{Dex}$ were metabolized by the host cells.

3.2 Cytotoxicity assessment, cell attachment and proliferation of osteoblasts upon OB-EV$_{Dex}$ stimulation

A schematic diagram of key isolation procedures, the internalization mechanism of OB-EV$_{Dex}$, and how OB-EV$_{Dex}$ influences osteogenic differentiation by transferring a complex cargo is sketched in Figure 3A. Prior to the cell experiments, the potential cytotoxicity of bone graft granules in the presence or absence of OB-EV$_{Dex}$ was examined *via* the standard Cell Counting Kit-8 (CCK-8) assay. As shown in Figure 3B, the cell viability of osteoblasts after treatment of BCP granules suspension did not show an obvious decline in a wide concentration range from 25 to 3,000 μg/mL. Noticeably, the cell viability was constantly higher than 85% even at the highest concentration of 3,000 μg/mL with or without OB-EV$_{Dex}$. These findings imply no present cytotoxicity of the bone BCP granules used nor of the OB-EV$_{Dex}$, which is beneficial for applications with regard to osteoblast-dependent osteogenesis.

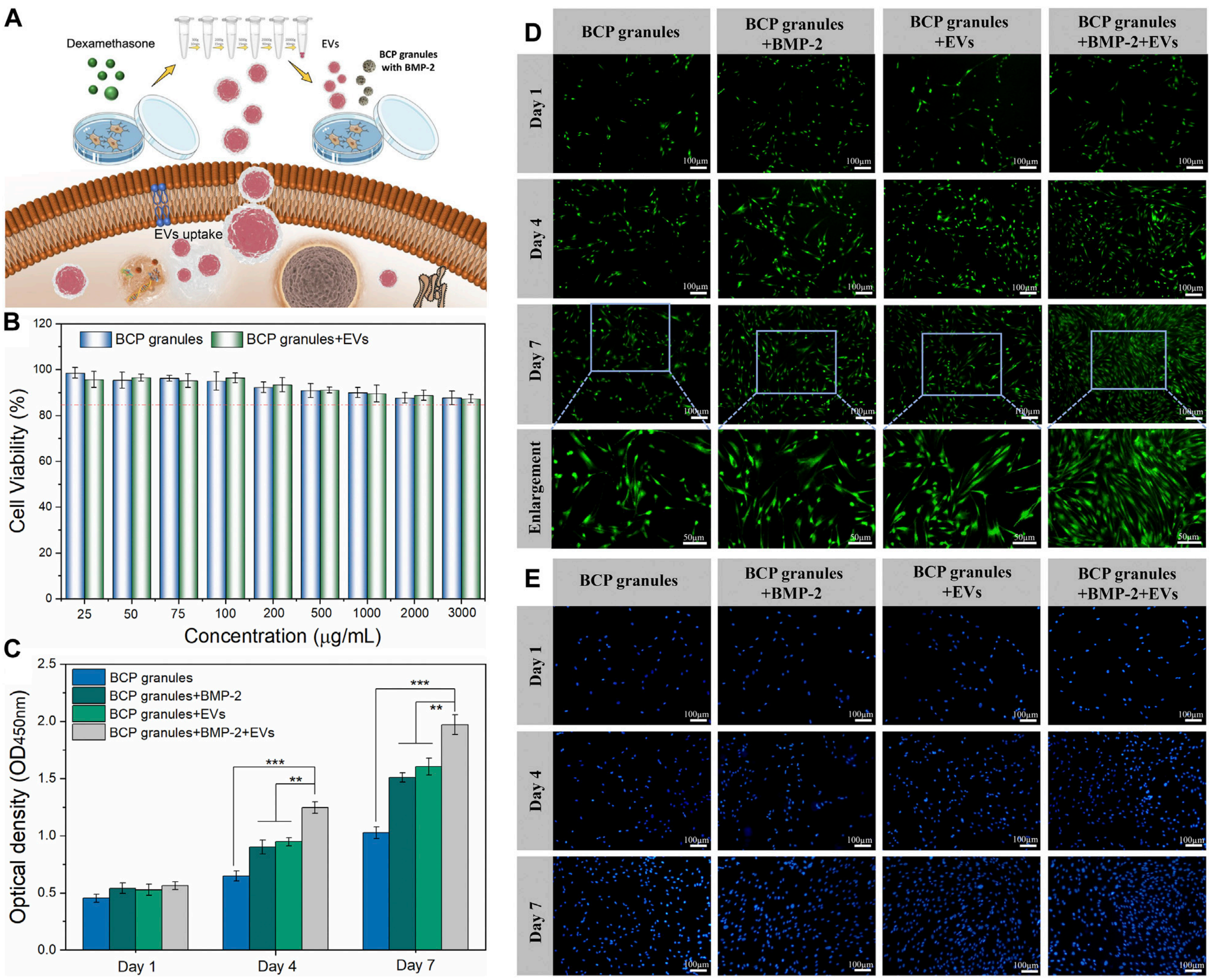

FIGURE 3
(A) Schematic illustration of key isolation steps of OB-EV$_{Dex}$, internalization mechanism, and how OB-EV$_{Dex}$ influence the osteogenic differentiation by transferring a complex cargo. **(B)** Cell viability of OB cells incubated with varying concentrations of bone granules suspension ranging from 25 to 3,000 μg/mL in the presence or absence of OB-EV$_{Dex}$ (n = 3). Cell proliferation of OB cells on the BCP granules under various treatments measured by CCK-8 assay **(C)**, Calcein AM staining **(D)**, and DAPI staining **(E)** after 1, 4, and 7 days of culture (n = 3). Scale bar: 100 μm.

To prove cell attachment and proliferation on the bone BCP granules with or without OB-EV$_{Dex}$, CCK-8 assay, DAPI staining, and Calcein AM staining were adopted to evaluate proliferative effects under various treatments after 1, 4, and 7 days of culture. As displayed in Figure 3D, the cell density (green fluorescence) significantly increased in various treatment groups with prolonged culturing time, especially on days 4 and 7 after seeding. The cell number and proliferation rate in the BMP-2+OB-EV$_{Dex}$ group were significantly higher relative to other groups on the seventh day. Nevertheless, no apparent difference in cell number was observed between the BMP-2 group and the OB-EV$_{Dex}$ group. Comparatively, the control group displayed the worst proliferation at all time-points. Besides, a similar uptrend of cell number in various treatment groups was detectable by DAPI staining assay (Figure 3E). The proliferative effects after various interventions were quantitatively examined by CCK-8 assay at designated time points (Figure 3C). At 4- and 7- days post-cultivation, optical density (OD value) of the BMP-2+OB-EV$_{Dex}$ group was determined to be significantly higher than those of the BMP-2 and OB-EV$_{Dex}$ groups ($p < 0.01$). Conversely, the control group had the lowest OD values at predetermined time intervals.

3.3 Influence of OB-EV$_{Dex}$ on the viability, growth, and cell morphology

The viability of OB cells under various interventions was evaluated by Calcein AM/EthD-III co-staining assay after 7 days of culture. Figure 4A showed that numerous live cells (green) were detected while a few dead cells (red) were scattered on these granules in the various treatment groups on the seventh day. The density of live cells was highest and pronouncedly amplified in the BMP-2+OB-EV$_{Dex}$ group when compared to other treatment groups. Furthermore, the live cell and dead cell status were emphasized

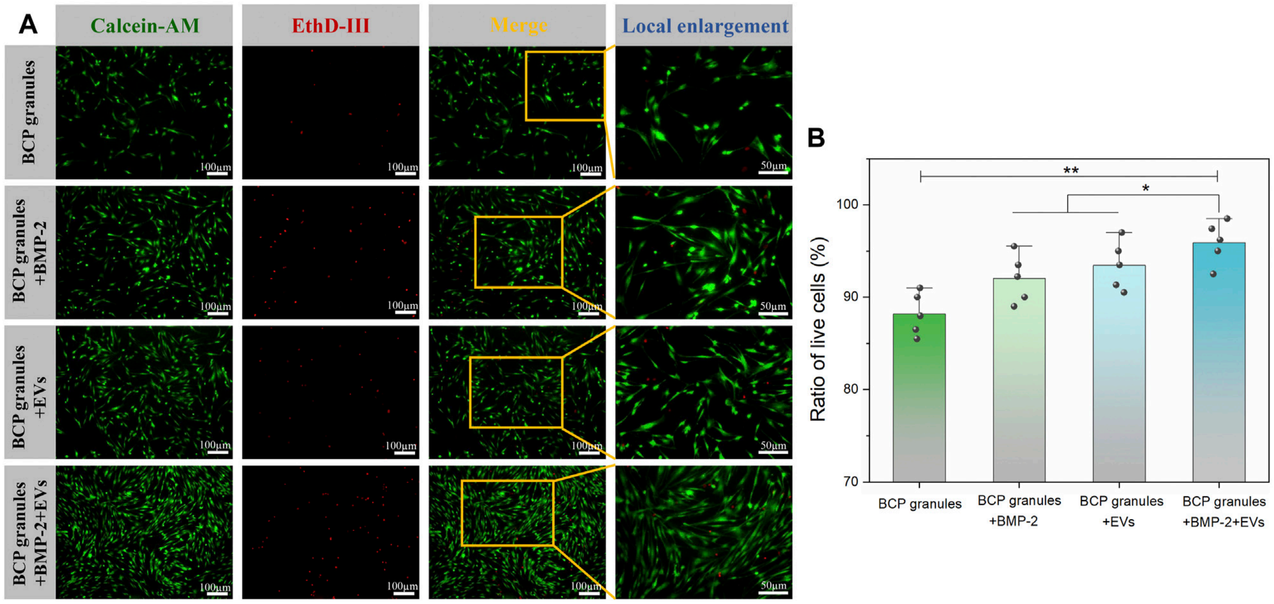

FIGURE 4
(A) Viability of OB cells under various interventions was evaluated by Calcein AM/EthD-III co-staining assay after 7 days of culture. Green fluorescence stands for live cells, and red fluorescence stands for dead cells. **(B)** Corresponding ratio of live cells versus dead cells, which was determined by ImageJ software at low magnification (×10) from five different random regions (n = 5).

in local enlargement images. To directly determine cell viabilities under various interventions, the ratio of live cells to dead cells from five different randomly selected regions was calculated by the ImageJ software (Figure 4B). As expected, cell viability in the BMP-2+OB-EV_{Dex} group was highest, reaching 96.2%, whereas OB-EV_{Dex} and BMP-2 groups had lower viabilities, about 94.1%, and 92.8%, respectively.

Morphological traits of OB cells on bone BCP granular materials after 7 days of cultivation were examined by CLSM and SEM analysis. OB cells were fluorescently labeled by cytoskeletal staining with Rhodamine Phalloidin and DAPI, which indicated F-actin and cell nuclei (Figure 5A). Particularly, OB cells in the OB-EV_{Dex} group majorly presented a typical spindle-like morphology, with some filamentous pseudopodia; however, OB cells in the control group did not display such a typical morphology and apparently fewer cytoskeletons were found. Notably, an organized cytoskeleton network with a multitude of well-spreading OB cells was only detected in the BMP-2+OB-EV_{Dex} group. Meanwhile, these OB cells treated with the dual stimuli of BMP-2 and OB-EV_{Dex} displayed a relatively ordered distribution of the cytoskeleton layer along BCP granules.

SEM observations shown in Figure 5B indicated that OB cells in the BMP-2+OB-EV_{Dex} group exhibited a well-spreading morphology in response to the dual-stimuli. Moreover, OB cells developed an even stretched and elongated spindle-like shape with multiple prominent filopodia to tightly get hold on granules substrate surfaces. Conversely, OB cells in the granular materials group exhibited a polygonal morphology. No distinguishable difference in the cell morphologies could be identified between the BMP-2+OB-EV_{Dex} group and the OB-EV_{Dex} group.

3.4 Validation of osteogenic potential of OB-EV_{Dex} during osteogenic differentiation

ALP staining and ALP activity were used to qualitatively and quantitatively analyze the osteogenic capacity of OB cells after various treatments after 7 and 14 days of cultivation. As illustrated in Figure 6A, the OB-EV_{Dex} and BMP-2 groups both produced a certain area of lavender-colored cobalt oxide precipitation on the 14th day. This confirms that EV_{Dex} or BMP-2 stimuli had a certain osteoinductive ability. Notably, the whole field of OB cells in the BMP-2+EV_{Dex} group was totally covered with lavender colored precipitation, suggesting that ALP levels were substantially elevated by the combined applications of OB-EV_{Dex} and BMP-2. Furthermore, ALP activities in all treatment groups progressively increased over the course of time (from 7 to 14 days). Besides, on the 14th day, ALP activities in the BMP-2+OB-EV_{Dex} group were significantly higher than those in the OB-EV_{Dex} and BMP-2 group ($p < 0.05$) by nearly 1.5 times (Figure 6B), while ALP activities in the OB-EV_{Dex} group was comparable to that in the BMP-2 group on either seventh or 14th day.

The mineralized nodules (calcium deposition) were detected by Alizarin Red and von Kossa staining after culturing for 2 weeks Figure 6A showed that small amounts of mineralized nodules were sparsely scattered in the OB-EV_{Dex} and BMP-2 groups, indicating the certain osteogenic potentials of OB-EV_{Dex} and/or BMP-2. In comparison, a substantial increase in cell-mediated calcium depositions (red or black precipitates) in the BMP-2+OB-EV_{Dex} group was observed on the 14th day. At that time, calcium deposition speckles appeared larger, reddish-brown, and tended to agglomerate on a large scale. In addition, according to the

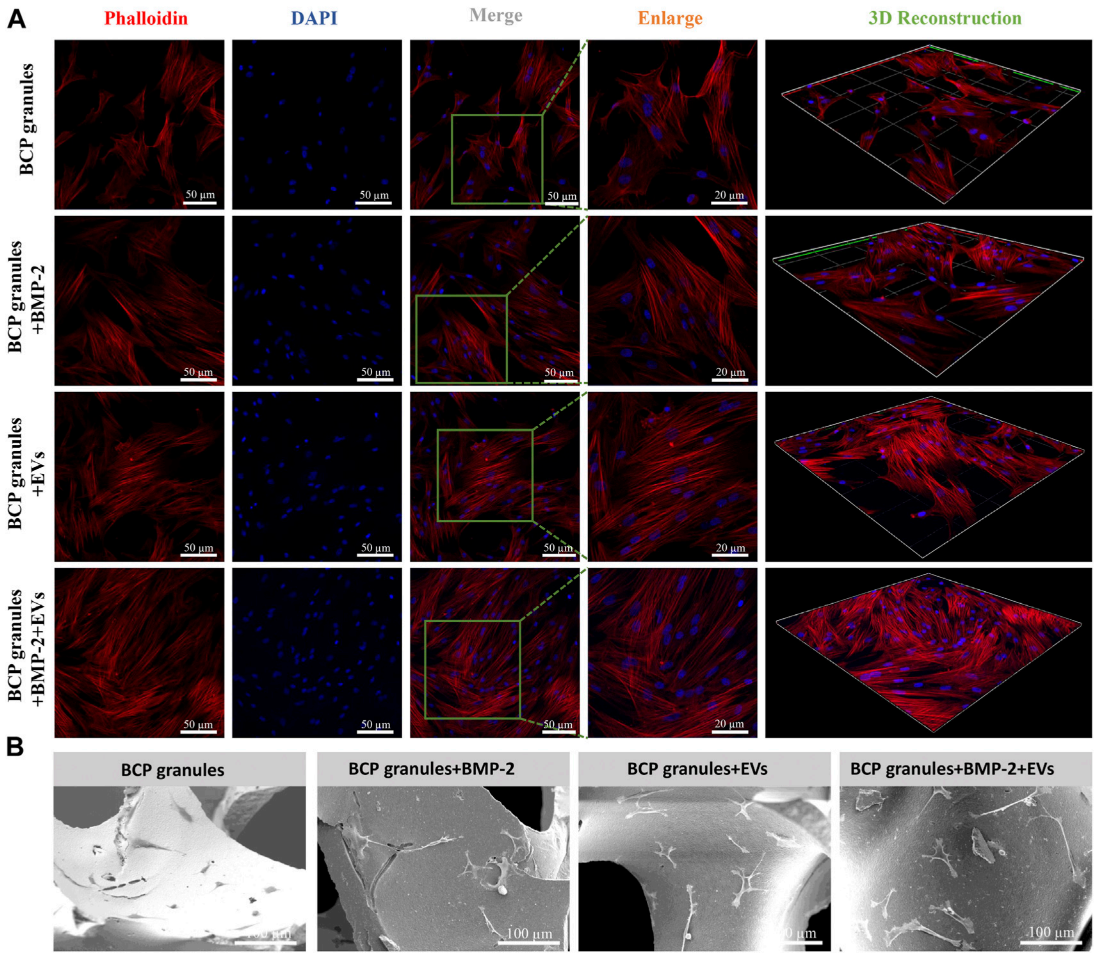

FIGURE 5
(A) Cell morphological observations of OB cells growth on bone BCP granules under various treatments after 7 days of cultivation *via* CLSM. OB cells were fluorescently labeled by cytoskeletal staining with Rhodamine Phalloidin and DAPI, which indicate F-actin (red) and cell nuclei (blue). Scale bar: 50 or 20 μm. **(B)** Representative SEM images of OB cells on bone BCP granules under various treatments after 7 days of cultivation. Scale bar: 100 μm.

semiquantitative results of the Alizarin Red staining, we found that the BMP-2+OB-EV$_{Dex}$ group produces much denser mineralized nodules and a higher degree of mineralization level on the 14th day than those in the OB-EV$_{Dex}$ and BMP-2 group, as evidenced by absorbance at 582 nm (Figure 6C).

3.5 OB-EV$_{Dex}$ significantly upregulate osteogenic marker gene expressions

The expression levels of major osteogenic marker genes of *RUNX2*, *BGALP*, *SPP1*, *SPARC*, *Col 1A1*, and *ALPL* in OB cells under the various studied interventions were measured on days 7 and 14 by performing qRT-PCR (Figures 6D–I). It was noted that *RUNX2* expression levels in all treatment groups were significantly higher on day 7 relative to day 14. In addition to *RUNX2*, significantly upregulated expressions of selected genes of *Col 1A1*, *ALPL*, *BGALP*, *SPP1*, and *SPARC* were noted over the course of time. Notably, the BMP-2+OB-EV$_{Dex}$ treatment resulted in a remarkably elevated expression of *Col 1A1* (Figure 6H) relative to the BMP-2 and OB-EV$_{Dex}$ groups ($p < 0.01$). *BGLAP* and *SPP1*, two typical markers of late-stage biomineralization, exhibited an extremely similar time-dependent uptrend with *Col 1A1* expressions, especially for the BMP-2+OB-EV$_{Dex}$ group (Figures 6E, F). Besides, it was evident that on either day 7 or 14, mRNA expression levels of *ALPL* in the OB-EV$_{Dex}$ group were comparable to those of the BMP-2 group. These findings mentioned above were in accordance with biomineralization experiments.

4 Discussion

Substantial research has uncovered that MSCs-derived EVs exhibited great promise in regenerative medicine since they are able to induce lineage-specific stem cell differentiation and accelerate new bone tissue formation and regeneration (Alqurashi et al., 2021; Hade et al., 2021). Despite numerous studies reporting “the specific roles of MSC-derived EVs”, however, it is surprising that, to date, only a very limited number of investigations deal with the role of osteoblast-derived EVs in bone biology (Cappariello et al., 2018; Man et al., 2022).

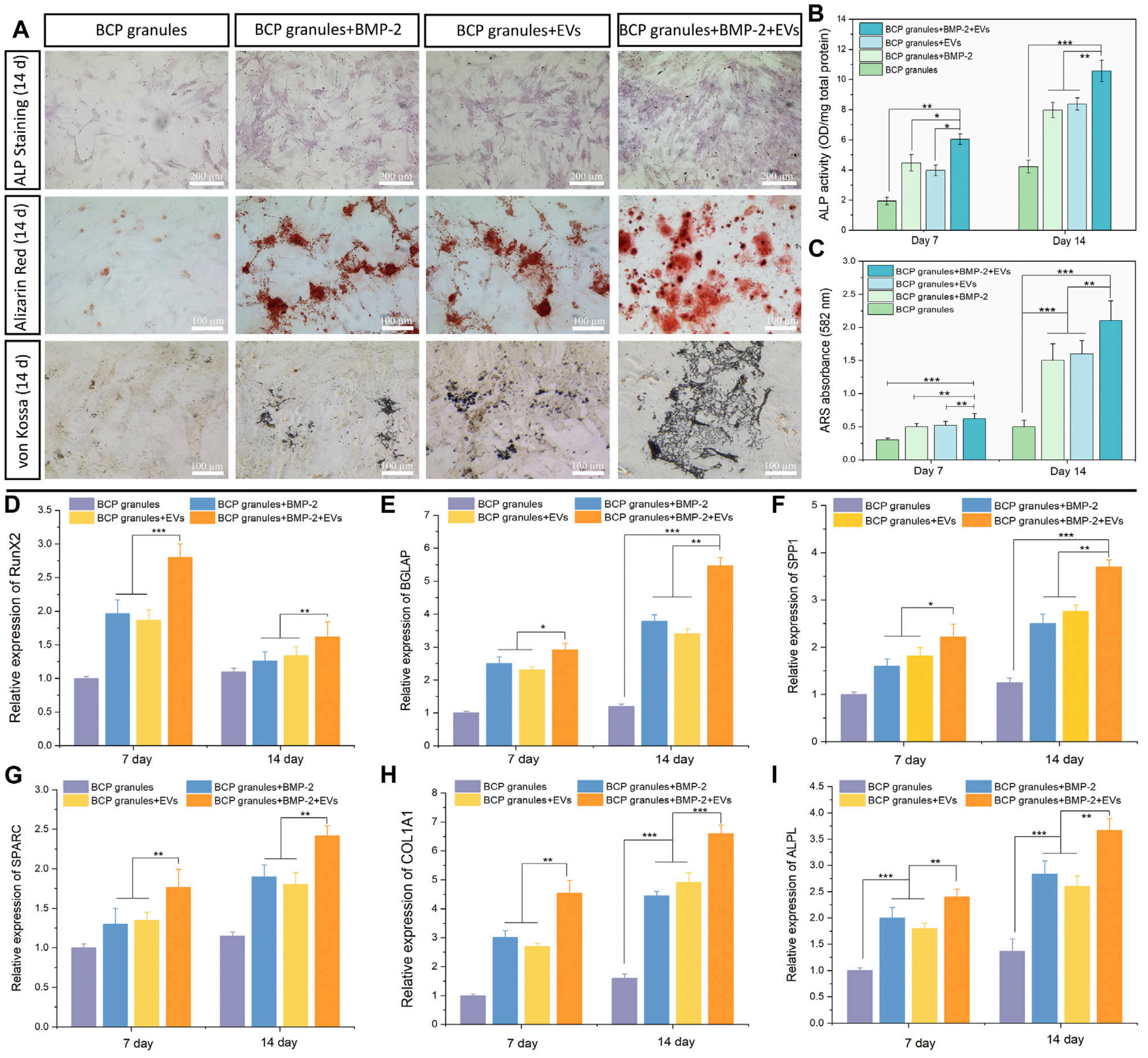

FIGURE 6
Osteogenic potential validation. **(A)** Biomineralization analysis of osteoblasts for different treatment groups measured by Alkaline Phosphatase staining, Alizarin Red staining and von Kossa staining on day 14. Scale bar: 100 or 200 μm. **(B)** Quantitative ALP activity and **(C)** colorimetric quantitative of Alizarin Red staining (ARS) after 7 or 14 days of culture (n = 3). Relative mRNA expression of selected osteogenic markers of **(D)** *RunX2*, **(E)** *BGLAP*, **(F)** *SPP1*, **(G)** *SPARC*, **(H)** *COL 1A1*, and **(I)** *ALPL* in osteoblasts after various treatments for 7 or 14 days, measured by quantitative RT-PCR (n = 3). $*p < 0.05$, $**p < 0.01$, and $***p < 0.001$.

In the present study, we provided insights into some of the potentials of EVs secreted from consecutive 14 days of dexamethasone-stimulated osteoblasts (OB-EV$_{Dex}$) for osteogenesis. With regard to OB-EV$_{Dex}$ endocytosis, it was observed that a sufficient amount of fluorescently labeled OB-EV$_{Dex}$ were taken up by porcine osteoblasts in a time-dependent pattern and mainly distributed in the perinuclear region. This is in line with the concept that effective cellular uptakes of extracellular vesicles are of vital significance for performing biological effects (Tkach and Théry, 2016).

Considering that the capacity for proliferation, attachment, and migration of transplanted cells is of most significance in boosting tissue regeneration (Monaco et al., 2011; Ma et al., 2019), we, therefore, evaluated the proliferative effects of OB-EV$_{Dex}$ on osteoblast cells. Our findings have demonstrated that OB-EV$_{Dex}$ significantly enhanced OB surface attachment and proliferation when compared to untreated cells. Interestingly, OB-EV$_{Dex}$ treatment resulted in a comparable pro-proliferative effect with that found in the BMP-2 group. The obtained results of the control and BMP-2 group are in line with findings known from the literature (Luppen et al., 2003) and therefore indicated that the found results for the OB-EV$_{Dex}$ treatment group are not related to any artifact. The increased cell number and proliferation rate in the BMP-2+OB-EV$_{Dex}$ group compared to the BMP-2 or OB-EV$_{Dex}$

group demonstrate that the cell proliferation effect was obviously strengthened due to the synergistic amplifying effect of OB-EV_{Dex} and BMP-2. This contradicts some of the known effects of dexamethasone in regard to the suppression of osteoblast proliferation but, on the other hand, shows possible counteracting effects of OB-EV_{Dex} restoring not only late-phase but also early-phase osteogenic effects. In addition, cell viability is a vital metric for the evaluation of cellular behaviors (Zhang et al., 2019). We speculate that the high cell viability (96.2%) found in the BMP-2+OB-EV_{Dex} group might be attributed to the synergistic amplifying proliferative effect supporting the cell with proteins driving the early and late onset of ossification. Furthermore, osteoblast-derived EVs were recently shown to regulate cell-to-cell communication such as by stimulating and facilitating the recruitment of endogenous cells, which greatly benefits bone tissue restoration (Man et al., 2021).

Cellular morphological traits influenced by osteogenic microenvironments are regarded as a vital indicator in assessing the cell-material/microenvironment interactions (Zhu et al., 2021). Our study found that OB cells in the OB-EV_{Dex} group developed an even stretched and elongated spindle-like morphology with some filamentous pseudopodia to get hold on BCP granules substrate surfaces more tightly. In addition, OB cells in the control group only exhibited a polygonal morphology. Accumulating evidence indicates that the filamentous pseudopodium is highly involved in cell adhesion, stretching, spreading, and proliferation (Yom-Tov et al., 2014; Yan et al., 2019; Chen et al., 2021). Interestingly, a mass of adhered osteoblasts with a well-organized cytoskeleton network was only found in the BMP-2+OB-EV_{Dex} group. This might be due to a combinational stimulating effect from OB-EV_{Dex} and BMP-2, which might induce more filopodia formation supporting cell adhesions to granules matrix surfaces and simultaneously making the OB cells produce an extremely dense cytoskeleton layer throughout the cells themselves.

Nevertheless, biological mineralization is an extremely complex, multiple-stage biological process (Matta et al., 2019). In our study, the results of intensity and number of mineralized nodules (calcium deposition) indicate that BMP-2+OB-EV_{Dex} treatment exhibited a greater pro-osteogenic potency than solely OB-EV_{Dex} or BMP-2 treatment. This suggests a crucial role of dual-stimuli from OB-EV_{Dex} and BMP-2 in strengthening osteoblastic differentiation of OB cells by elevating calcium deposition levels, likely due to the significant enrichment of pro-mineralization proteins associated with OB-EV_{Dex}, including, e.g., annexins as reported by Davies et al. (2019).

Our findings provided strong evidence that the combinations of OB-EV_{Dex} and BMP-2 were considerably superior at enhancing ALP activities when compared to OB-EV_{Dex} or BMP-2 alone. This suggests that the combination of OB-EV_{Dex} and BMP-2 presents increased pro-osteogenic effects, especially at the early or middle phase of osteogenic differentiation and mineralization (Vimalraj, 2020). Moreover, our study discovered that *RUNX2* expression is positively influenced in the OB-EV_{Dex}-treated groups. This could be explained by the fact that *RUNX2* is a crucial transcription factor that activates the early osteogenesis differentiation phase (Bruderer et al., 2014), which is an essential step for the initiation of bone regeneration. The upregulation of *RUNX2* expression might be one of the closest explanations for the counteracting effect of OB-EV_{Dex} towards the suppressive effect of dexamethasone. In addition, it was observed that the combination of EV_{Dex} and BMP-2 engenders a maximum activating effect to elevate *Col 1A1* matrix protein expression levels, thereby facilitating the maturation of osteogenic mineralization (Yan et al., 2019; Man et al., 2021). In addition to *RUNX2* and *Col 1A1*, the expression of other selected marker genes of *ALPL*, *BGLAP*, *SPP1*, and *SPARC* all exhibited a significant upregulation over time, especially for the BMP-2+OB-EV_{Dex} group. In contradiction to that, Uenaka et al. (2022) found that differentiated osteoblasts release a subset of small EVs in order to inhibit bone formation and enhance osteoclastogenesis. These findings might not be applicable to what we found here, due to the fact that they focused on native OB-EVs and a different subset of EVs (diameter of 200–400 nm).

Taken together, our findings reported here revealed that OB-EV_{Dex} significantly amplify pro-osteogenic processes while promoting the osteoblastic differentiation by upregulating the expressions of crucial osteogenesis-related marker genes, as well as mineralization nodules and ALP activity. Besides, it is noteworthy that the most apparent pro-osteogenic differentiation capacity in upregulating gene expressions was evoked by OB-EV_{Dex} together with BMP-2. On the basis of above evidence, we reasoned that irrespective of any clinical challenges, the prospective use of dexamethasone-induced OB-EV_{Dex} could function as a novel osteogenic accelerator for treating, or at least alleviating the symptoms of bone defects in future clinical practice. It may be possible that OB-EV_{Dex} can be a promising candidate that circumvent the limitations associated with traditional cell-based therapies, such as limited cell sources, immunogenicity, low survival of transplanted cells. Altogether, this study provides a solid foundation for advancing OB-EV_{Dex} towards the clinical translation.

Although our study has demonstrated the pronounced potential of OB-EV_{Dex} to act as a new modified biological tool for improving osteogenesis, it still presents a few restrictions. First, we did not identify the most exact components inside OB-EV_{DEX} responsible for improving the *in vitro* osteogenesis, and therefore, further research is required for the exploration the underlying mechanism. Second, we did not assess the influence of OB-EV_{Dex} on bone restoration and regeneration *in vivo*, which may provide better direct evidence about the therapeutic potential of OB-$EV_{Dex.}$ Nevertheless, the findings reported in this study are crucial for EVs-related osteogenesis in the frame of bone tissue engineering.

5 Conclusion

In our study, dexamethasone-stimulated osteoblast-derived EVs (OB-EV_{Dex}) could markedly promote osteoblastic differentiation by positively upregulating crucial osteogenic genes, but also significantly augment capacities for *in vitro* proliferation, attachment, and viability of osteoblasts. Of note, the pro-osteogenic effects mediated by OB-EV_{Dex} were comparable to those of individual BMP-2 treatment. In addition, the combinational applications of OB-EV_{Dex} and BMP-2 were more advantageous in stimulating proliferation, differentiation, and biomineralization, when compared to OB-EV_{Dex} or BMP-2 treatment alone, resulting in notable increases in calcium nodules during osteogenesis. Taken together, our findings elucidate the potential of dexamethasone-induced OB-EV$_{Dex}$ as a prospective therapeutic option for enhancing osteogenesis.

Data availability statement

The original contributions presented in the study are included in the article/supplementary material, further inquiries can be directed to the corresponding authors.

Author contributions

XZ conceived the study, performed all experiments, wrote and drafted the manuscript alone. XZ, QZ, and NZ collected and analyzed data. XZ, QZ, YL, KQ, XW, and JG discussed and interpreted results. XW helped with data curation, manuscript revision and editions. JG coordinated and supervised experiments. EMB assisted with TEM characterization for OBEVD$_{ex}$. FH and EB provided financial, institutional support, supervised the study, and performed corrections and editions to the manuscript draft to its final version. The final version of the manuscript was reviewed and approved by all authors.

Funding

The project was partially funded by the Deutsche Forschungsgemeinschaft (DFG, German Research Foundation)—Project Number 429837092. The author, XZ, is finically funded and supervised by China Scholarship Council (CSC) under Grant 202008080053.

Acknowledgments

The authors are grateful to Hiltrud Königs-Werner from Institute of Pathology and Medical Clinic II, University Hospital RWTH Aachen for supporting TEM evaluations. The authors thank to Dr. rer. nat. Sabrina Ernst from the Confocal Microscopy Facility, a core facility of the Interdisciplinary Center for Clinical Research (IZKF) Aachen within the Faculty of Medicine at RWTH Aachen University for her valuable assistance.

Conflict of interest

The authors declare that the research was conducted in the absence of any commercial or financial relationships that could be construed as a potential conflict of interest.

Publisher's note

References

Alqurashi, H., Ortega Asencio, I., and Lambert, D. W. (2021). The emerging potential of extracellular vesicles in cell-free tissue engineering and regenerative medicine. *Tissue Eng. Part B Rev.* 27 (5), 530–538. doi:10.1089/ten.TEB.2020.0222

Bakker, A. D., and Klein-Nulend, J. (2012). Osteoblast isolation from murine calvaria and long bones. *Methods Mol. Biol.* 816, 19–29. doi:10.1007/978-1-61779-415-5_2

Bruderer, M., Richards, R. G., Alini, M., and Stoddart, M. J. (2014). Role and regulation of RUNX2 in osteogenesis. *Eur. Cell Mater* 28, 269–286. doi:10.22203/ecm.v028a19

Buzhor, E., Leshansky, L., Blumenthal, J., Barash, H., Warshawsky, D., Mazor, Y., et al. (2014). Cell-based therapy approaches: The hope for incurable diseases. *Regen. Med.* 9 (5), 649–672. doi:10.2217/rme.14.35

Cappariello, A., Loftus, A., Muraca, M., Maurizi, A., Rucci, N., and Teti, A. (2018). Osteoblast-derived extracellular vesicles are biological tools for the delivery of active molecules to bone. *J. Bone Min. Res.* 33 (3), 517–533. doi:10.1002/jbmr.3332

Chen, D., Dunkers, J. P., Losert, W., and Sarkar, S. (2021). Early time-point cell morphology classifiers successfully predict human bone marrow stromal cell differentiation modulated by fiber density in nanofiber scaffolds. *Biomaterials* 274, 120812. doi:10.1016/j.biomaterials.2021.120812

Colombo, M., Raposo, G., and Théry, C. (2014). Biogenesis, secretion, and intercellular interactions of exosomes and other extracellular vesicles. *Annu. Rev. Cell Dev. Biol.* 30, 255–289. doi:10.1146/annurev-cellbio-101512-122326

Cui, Y., Luan, J., Li, H., Zhou, X., and Han, J. (2016). Exosomes derived from mineralizing osteoblasts promote ST2 cell osteogenic differentiation by alteration of microRNA expression. *FEBS Lett.* 590 (1), 185–192. doi:10.1002/1873-3468.12024

Davies, O. G., Cox, S. C., Azoidis, I., McGuinness, A. J. A., Cooke, M., Heaney, L. M., et al. (2019). Osteoblast-derived vesicle protein content is temporally regulated during osteogenesis: Implications for regenerative therapies. *Front. Bioeng. Biotechnol.* 7, 92. doi:10.3389/fbioe.2019.00092

Davies, O. G., Cox, S. C., Williams, R. L., Tsaroucha, D., Dorrepaal, R. M., Lewis, M. P., et al. (2017). Annexin-enriched osteoblast-derived vesicles act as an extracellular site of mineral nucleation within developing stem cell cultures. *Sci. Rep.* 7 (1), 12639. doi:10.1038/s41598-017-13027-6

Dimitriou, R., Jones, E., McGonagle, D., and Giannoudis, P. V. (2011). Bone regeneration: Current concepts and future directions. *BMC Med.* 9, 66. doi:10.1186/1741-7015-9-66

El-Rashidy, A. A., Roether, J. A., Harhaus, L., Kneser, U., and Boccaccini, A. R. (2017). Regenerating bone with bioactive glass scaffolds: A review of *in vivo* studies in bone defect models. *Acta Biomater.* 62, 1–28. doi:10.1016/j.actbio.2017.08.030

Hade, M. D., Suire, C. N., and Suo, Z. (2021). Mesenchymal stem cell-derived exosomes: Applications in regenerative medicine. *Cells* 10 (8), 1959. doi:10.3390/cells10081959

Ho-Shui-Ling, A., Bolander, J., Rustom, L. E., Johnson, A. W., Luyten, F. P., and Picart, C. (2018). Bone regeneration strategies: Engineered scaffolds, bioactive molecules and stem cells current stage and future perspectives. *Biomaterials* 180, 143–162. doi:10.1016/j.biomaterials.2018.07.017

Hu, H., Dong, L., Bu, Z., Shen, Y., Luo, J., Zhang, H., et al. (2020). miR-23a-3p-abundant small extracellular vesicles released from Gelma/nanoclay hydrogel for cartilage regeneration. *J. Extracell. Vesicles* 9 (1), 1778883. doi:10.1080/20013078.2020.1778883

Huang, C., Geng, J., and Jiang, S. (2017). MicroRNAs in regulation of osteogenic differentiation of mesenchymal stem cells. *Cell Tissue Res.* 368 (2), 229–238. doi:10.1007/s00441-016-2462-2

James, A. W., LaChaud, G., Shen, J., Asatrian, G., Nguyen, V., Zhang, X., et al. (2016). A review of the clinical side effects of bone morphogenetic protein-2. *Tissue Eng. Part B Rev.* 22 (4), 284–297. doi:10.1089/ten.TEB.2015.0357

Kwon, J. S., Kim, S. W., Kwon, D. Y., Park, S. H., Son, A. R., Kim, J. H., et al. (2014). *In vivo* osteogenic differentiation of human turbinate mesenchymal stem cells in an injectable *in situ*-forming hydrogel. *Biomaterials* 35 (20), 5337–5346. doi:10.1016/j.biomaterials.2014.03.045

Li, Q., Yu, H., Sun, M., Yang, P., Hu, X., Ao, Y., et al. (2021). The tissue origin effect of extracellular vesicles on cartilage and bone regeneration. *Acta Biomater.* 125, 253–266. doi:10.1016/j.actbio.2021.02.039

Lin, Z., Xiong, Y., Meng, W., Hu, Y., Chen, L., Chen, L., et al. (2022). Exosomal PD-L1 induces osteogenic differentiation and promotes fracture healing by acting as an immunosuppressant. *Bioact. Mater* 13, 300–311. doi:10.1016/j.bioactmat.2021.10.042

Liu, H., Zhang, Q., Wang, S., Weng, W., Jing, Y., and Su, J. (2022). Bacterial extracellular vesicles as bioactive nanocarriers for drug delivery: Advances and perspectives. *Bioact. Mater* 14, 169–181. doi:10.1016/j.bioactmat.2021.12.006

Lu, G. D., Cheng, P., Liu, T., and Wang, Z. (2020). BMSC-derived exosomal miR-29a promotes angiogenesis and osteogenesis. *Front. Cell Dev. Biol.* 8, 608521. doi:10.3389/fcell.2020.608521

Luppen, C. A., Smith, E., Spevak, L., Boskey, A. L., and Frenkel, B. (2003). Bone morphogenetic protein-2 restores mineralization in glucocorticoid-inhibited MC3T3-E1 osteoblast cultures. *J. Bone Min. Res.* 18 (7), 1186–1197. doi:10.1359/jbmr.2003.18.7.1186

Ma, T., Fu, B., Yang, X., Xiao, Y., and Pan, M. (2019). Adipose mesenchymal stem cell-derived exosomes promote cell proliferation, migration, and inhibit cell apoptosis via Wnt/β-catenin signaling in cutaneous wound healing. *J. Cell Biochem.* 120 (6), 10847–10854. doi:10.1002/jcb.28376

Man, K., Brunet, M. Y., Federici, A. S., Hoey, D. A., and Cox, S. C. (2022). An ECM-mimetic hydrogel to promote the therapeutic efficacy of osteoblast-derived extracellular vesicles for bone regeneration. *Front. Bioeng. Biotechnol.* 10, 829969. doi:10.3389/fbioe.2022.829969

Man, K., Brunet, M. Y., Fernandez-Rhodes, M., Williams, S., Heaney, L. M., Gethings, L. A., et al. (2021). Epigenetic reprogramming enhances the therapeutic efficacy of osteoblast-derived extracellular vesicles to promote human bone marrow stem cell osteogenic differentiation. *J. Extracell. Vesicles* 10 (9), e12118. doi:10.1002/jev2.12118

Martins, A., Duarte, A. R., Faria, S., Marques, A. P., Reis, R. L., and Neves, N. M. (2010). Osteogenic induction of hBMSCs by electrospun scaffolds with dexamethasone release functionality. *Biomaterials* 31 (22), 5875–5885. doi:10.1016/j.biomaterials.2010.04.010

Matta, C., Szűcs-Somogyi, C., Kon, E., Robinson, D., Neufeld, T., Altschuler, N., et al. (2019). Osteogenic differentiation of human bone marrow-derived mesenchymal stem cells is enhanced by an aragonite scaffold. *Differentiation* 107, 24–34. doi:10.1016/j.diff.2019.05.002

Monaco, E., Bionaz, M., Hollister, S. J., and Wheeler, M. B. (2011). Strategies for regeneration of the bone using porcine adult adipose-derived mesenchymal stem cells. *Theriogenology* 75 (8), 1381–1399. doi:10.1016/j.theriogenology.2010.11.020

Narayanan, R., Huang, C. C., and Ravindran, S. (2016). Hijacking the cellular mail: Exosome mediated differentiation of mesenchymal stem cells. *Stem Cells Int.* 2016, 1–11. doi:10.1155/2016/3808674

Ng, J., Spiller, K., Bernhard, J., and Vunjak-Novakovic, G. (2017). Biomimetic approaches for bone tissue engineering. *Tissue Eng. Part B Rev.* 23 (5), 480–493. doi:10.1089/ten.TEB.2016.0289

Perpétuo, I. P., Bourne, L. E., and Orriss, I. R. (2019). Isolation and generation of osteoblasts. *Methods Mol. Biol.* 1914, 21–38. doi:10.1007/978-1-4939-8997-3_2

Pizzicannella, J., Diomede, F., Gugliandolo, A., Chiricosta, L., Bramanti, P., Merciaro, I., et al. (2019). 3D printing PLA/gingival stem cells/EVs upregulate miR-2861 and -210 during osteoangiogenesis commitment. *Int. J. Mol. Sci.* 20 (13), 3256. doi:10.3390/ijms20133256

Roseti, L., Parisi, V., Petretta, M., Cavallo, C., Desando, G., Bartolotti, I., et al. (2017). Scaffolds for bone tissue engineering: State of the art and new perspectives. *Mater Sci. Eng. C Mater Biol. Appl.* 78, 1246–1262. doi:10.1016/j.msec.2017.05.017

Schmidt, A. H. (2021). Autologous bone graft: Is it still the gold standard? *Injury* 52, S18–s22. doi:10.1016/j.injury.2021.01.043

Théry, C., Ostrowski, M., and Segura, E. (2009). Membrane vesicles as conveyors of immune responses. *Nat. Rev. Immunol.* 9 (8), 581–593. doi:10.1038/nri2567

Tkach, M., and Théry, C. (2016). Communication by extracellular vesicles: Where we are and where we need to go. *Cell* 164 (6), 1226–1232. doi:10.1016/j.cell.2016.01.043

Uenaka, M., Yamashita, E., Kikuta, J., Morimoto, A., Ao, T., Mizuno, H., et al. (2022). Osteoblast-derived vesicles induce a switch from bone-formation to bone-resorption *in vivo*. *Nat. Commun.* 13 (1), 1066. doi:10.1038/s41467-022-28673-2

van Niel, G., Carter, D. R. F., Clayton, A., Lambert, D. W., Raposo, G., and Vader, P. (2022). Challenges and directions in studying cell-cell communication by extracellular vesicles. *Nat. Rev. Mol. Cell Biol.* 23 (5), 369–382. doi:10.1038/s41580-022-00460-3

van Niel, G., D'Angelo, G., and Raposo, G. (2018). Shedding light on the cell biology of extracellular vesicles. *Nat. Rev. Mol. Cell Biol.* 19 (4), 213–228. doi:10.1038/nrm.2017.125

Vimalraj, S. (2020). Alkaline phosphatase: Structure, expression and its function in bone mineralization. *Gene* 754, 144855. doi:10.1016/j.gene.2020.144855

Walmsley, G. G., Ransom, R. C., Zielins, E. R., Leavitt, T., Flacco, J. S., Hu, M. S., et al. (2016). Stem cells in bone regeneration. *Stem Cell Rev. Rep.* 12 (5), 524–529. doi:10.1007/s12015-016-9665-5

Yan, Y., Cheng, B., Chen, K., Cui, W., Qi, J., Li, X., et al. (2019). Enhanced osteogenesis of bone marrow-derived mesenchymal stem cells by a functionalized silk fibroin hydrogel for bone defect repair. *Adv. Healthc. Mater* 8 (3), e1801043. doi:10.1002/adhm.201801043

Yom-Tov, O., Seliktar, D., and Bianco-Peled, H. (2014). Cell morphology in injectable nanostructured biosynthetic hydrogels. *J. Biomed. Mater Res. A* 102 (12), 4371–4379. doi:10.1002/jbm.a.35134

Zhang, X., Yin, X., Luo, J., Zheng, X., Wang, H., Wang, J., et al. (2019). Novel hierarchical nitrogen-doped multiwalled carbon nanotubes/cellulose/nanohydroxyapatite nanocomposite as an osteoinductive scaffold for enhancing bone regeneration. *ACS Biomater. Sci. Eng.* 5 (1), 294–307. doi:10.1021/acsbiomaterials.8b00908

Zhu, G., Zhang, T., Chen, M., Yao, K., Huang, X., Zhang, B., et al. (2021). Bone physiological microenvironment and healing mechanism: Basis for future bone-tissue engineering scaffolds. *Bioact. Mater* 6 (11), 4110–4140. doi:10.1016/j.bioactmat.2021.03.043

frontiers | Frontiers in Bioengineering and Biotechnology

TYPE Original Research
PUBLISHED 16 March 2023
DOI 10.3389/fbioe.2023.1163405

OPEN ACCESS

EDITED BY
Long Bai,
East China University of Science and Technology, China

REVIEWED BY
Yani Liu,
Huazhong University of Science and Technology, China
Han Liu,
Shanghai University, China
Min / Pan,
Shenzhen Hospital of Guangzhou University of Chinese Medicine, China

*CORRESPONDENCE
Yongping Lu,
✉ luyongp@163.com

†These authors have contributed equally to this work and share first authorship

SPECIALTY SECTION
This article was submitted to Nanobiotechnology, a section of the journal Frontiers in Bioengineering and Biotechnology

RECEIVED 10 February 2023
ACCEPTED 08 March 2023
PUBLISHED 16 March 2023

CITATION
Chen J, Yang Y, Li Y, Xu L, Zhao C, Chen Q and Lu Y (2023), Targeted microbubbles combined with low-power focused ultrasound promote the thrombolysis of acute deep vein thrombosis.
Front. Bioeng. Biotechnol. 11:1163405.
doi: 10.3389/fbioe.2023.1163405

Targeted microbubbles combined with low-power focused ultrasound promote the thrombolysis of acute deep vein thrombosis

Jianfu Chen[1†], Yuan Yang[1†], Yunyan Li[2], Lirong Xu[2], Chun Zhao[2], Qi Chen[3] and Yongping Lu[2*]

[1]Kunming Medical University, Kunming, Yunnan, China, [2]Department of Ultrasound, The Affiliated Hospital of Yunnan University (The Second People's Hospital of Yunnan Province), Kunming, Yunnan, China, [3]School of Clinical Medicine, Dali University, Dali, Yunnan, China

Introduction: The side effects of conventional therapy for acute deep vein thrombosis (DVT) are severe, with inflammatory reactions playing a pivotal role. It is particularly important to explore new ways of treatment thrombosis by targeting inflammatory factors.

Methods: A targeted microbubble contrast agent was prepared using the biotin-avidin method. The 40 DVT model rabbits were established and divided into four groups according to different treatment regimens. The four coagulation indexes, TNF-α, and D-dimer content of experimental animals were measured before modeling and before and after treatment, and the thrombolysis was assessed by ultrasound imaging. Finally, the results were verified by pathology.

Results and Discussion: Fluorescence microscopy verified the successful preparation of targeted microbubbles. Among the groups, PT, APTT, and TT in Group II-IV were longer than those in Group I (all $p < 0.05$). FIB and D-dimer content were lower than those in Group I (all $p < 0.05$), and TNF-α content in Group IV was lower than that in Group I-III (all $p < 0.05$). Pairwise comparison before modeling and before treatment and after treatment showed that, after treatment, the PT, APTT, and TT in Group II-IV were longer than those before modeling (all $p < 0.05$). The contents of FIB and D-dimer were lower than those before modeling and before treatment (all $p < 0.05$). The content of TNF-α decreased significantly only in Group IV, but increased in the other three groups. Targeted microbubbles combined with Low-power focused ultrasound can reduce inflammation, significantly promote thrombolysis, and provide new ideas and methods for the diagnosis and treatment of acute DVT.

KEYWORDS

targeted microbubbles, low-power focused ultrasound, ultrasonic irradiation, acute deep vein thrombosis, thrombolysis

1 Introduction

Venous thromboembolism has been ranked as the third most common cause of disability and cardiovascular death in the world, encompassing deep vein thrombosis (DVT) and pulmonary embolism (PE), which frequently occur due to trauma, stress, pregnancy, and postoperative complications (Khan et al., 2021; Jackson et al., 2022). Due to the intensive study of thrombosis, venous thrombosis has been revealed be closely associated with the inflammatory response of the venous wall. Slowed blood flow, hypoxia, inflammatory cell activation, and the release of various active substances correlated with thrombosis (Poredos and Poredos, 2022). Studies have revealed that TNF-α is closely linked to the interaction between leukocytes and endothelial cells (Aguilar et al., 2021). In the initial stage of thrombosis, TNF-α induces the expression of adhesion molecules on the surface of endothelial cells. Therefore, the inflammatory response can be neutralized by inhibiting TNF-α. The use of antibody to TNF-α is one of the most effective methods to reduce neutrophil infiltration (Presicce et al., 2020). Aue et al. (2011) found that the upregulation of TNF-α was significantly related to thrombosis, and the upregulation degree was more predictive than the medical history of non-drug-related (DVT).

The above descriptions indicate that TNF-α can be used as a target for thrombosis therapy. Anti-inflammatory and targeted therapy of thrombosis can be achieved by using bioactive materials (Liu et al., 2022a) or ultrasound microbubble contrast agents labeled with targeting guides. The combination of a microbubble contrast agent and ultrasound targeted microbubble destruction (UTMD) technology can deliver bioactive substances to various targets non-invasively and specifically (Liu et al., 2022b). At present, it is mainly used in the treatment of heart disease, tumors, and atherosclerotic plaque (Zhang et al., 2021; He et al., 2022). UTMD technology breaks up targeted microbubbles and releases large amounts of therapeutic substances in the target area, which optimizes the local treatment effect while reducing systemic side effects (Yang et al., 2019; Xu et al., 2022).

There is no doubt that ultrasound can accelerate thrombolysis. Both high-frequency ultrasound and low-power ultrasound can significantly promote thrombolysis (Notten et al., 2020; Avgerinos et al., 2021). Microbubbles combined with thrombolytic medication, such as urokinase (UK) or tissue plasminogen activator, can further enhance the success rate of thrombolysis (Wang et al., 2019; Wang et al., 2020). Studies have demonstrated that UTMD can mechanically remove dialysis grafts with thrombosis in experimental animals even without the delivery of any substance (Liang et al., 2021). Ultrasound with a frequency greater than 0.5 MHz can enhance the dissolution of thrombus *in vitro* (Ebben et al., 2015), and the study by Zhong et al. (2019) has confirmed that ultrasound can accelerate thrombolysis *in vivo*. In recent years, microbubbles carrying medication to treat thrombosis have also become a research hotspot.

Microbubbles carrying the antibody of TNF-α played multiple roles in thrombolytic therapy. Firstly, targeted microbubbles were an ultrasound contrast agent, which could effectively identify thrombus through ultrasound contrast imaging and evaluate the thrombolytic effect. Secondly, the monoclonal antibody to TNF-α carried by targeted microbubbles bound the local TNF-α produced by thrombus and alleviated the inflammatory response. Finally, the cavitation effect and thermal effect generated by breaking the microbubble through UTMD technology stimulated the regeneration of blood vessels, loosened the internal structure of thrombus, and promoted the effect of thrombolytic drugs.

In this study, an animal model of DVT was established and treated by low-power ultrasound combined with targeted microbubbles (MBt) bearing TNF-α antibody and UK. UTMD technology promoted monoclonal antibodies to TNF-α release from MBt and alleviated inflammation and subsequent chain reaction. At the same time, the cavitation effect produced by ultrasonic crushing microbubbles also promoted thrombus dissolution, in the hope of achieving the effect of complete dissolution of thrombus, recanalization, and providing new ideas for thrombus treatment.

2 Materials and methods

2.1 Establishment of thrombus model

In this experiment, 40 healthy adult Japanese white rabbits were used to make the acute DVT model. The experimental animals were supplemented according to the principle of randomization, if some of them died during the experiment.

Firstly, the rabbit inferior vena cava was exposed and dissociated. The dissociative segment was from the lower part of the renal vein bifurcation to the upper part of the iliac vein bifurcation. Thread was threaded under the renal vein bifurcation. The self-made needle tube was positioned parallel to the inferior vena cava. The vena cava and needle tube were ligated with a suture. After ligation, the needle tube was removed to ensure the identical stenosis rate of each rabbit. The distal blood vessel was clamped with a vascular clamp and removed 30 min later, at which point the abdomen was sutured. Finally, Philips Ultrasonic diagnostic instrument (EPIQ 5, Holland) was used to observe and confirm the inferior vena cava thrombosis.

2.2 Reagents

2.2.1 UK

UK (100,000 IU/bottle, Wuhan Renfu Pharmaceutical Co., Ltd.) was dissolved and diluted with normal saline, and slowly injected through the rabbit ear vein at a proportion of 10,000 IU/kg.

2.2.2 Targeted microbubble contrast agent

USphere™ Labeler microbubble (particle size: 492.66 nm ± 41.68 nm, marked avidin, Taiwan, China Boxin Biotechnology Co., Ltd.) was placed in the room for 30 min. After it returned to room temperature, 100 uL monoclonal antibody of TNF-α (marked biotin and FAM fluorescent group, Nanjing Zhongding Biotechnology Co., Ltd.) was injected into it. The mixture was oscillated for 40 s in an oscillator until it became white microbubbles.

2.3 Grouping and treatment of experimental animals

2.3.1 Grouping

There were 40 rabbits randomly divided into four groups, with 10 rabbits in each group. Group I: ultrasonic irradiation; Group II: UK + ultrasonic irradiation; Group III: UK + control microbubbles (MBc) + ultrasonic irradiation; Group IV: UK + MBt + ultrasonic irradiation.

The treatment time of the above four groups was 3 days. After the final treatment, the experimental animals were killed and the thrombus tissue was taken.

2.3.2 Treatment method

Ultrasonic irradiation was performed using a Low-Power Focused Ultrasound Device (Chongqing Ronghai Ultrasonic Medical Engineering Co., Ltd.). The frequency was 0.7 MHz, the power was 2.0 w/cm^2, and the vascular lumen of thrombus segment was irradiated continuously for 20 min. UK's dose was 10,000 IU/kg; MBc's dose: 0.05 mL/kg; MBt's dose: 0.05 mL/kg, and all reagents were injected through the auricular vein of rabbits.

2.4 Evaluation of DVT

After the final treatment, DVT was detected and evaluated by color Doppler flow imaging (CDFI) and Contrast-Enhanced Ultrasound (CEUS), and the patency of the inferior vena cava was analyzed.

2.5 Laboratory index

The thrombin time (TT), prothrombin time (PT), activated partial thrombin time (APTT), and fibrinogen (FIB) in peripheral blood of experimental animals was measured before modelling, before treatment, and after treatment respectively. The content of D-dimer and TNF-α was detected by enzyme-linked immunosorbent assay (ELISA).

2.6 Pathological examination

IVC thrombus was removed, fixed with 4% paraformaldehyde, and embedded in paraffin. Hematoxylin-eosin staining was used to observe the morphology of the thrombus.

2.7 Statistical analyses

The experimental data were analyzed using SPSS 23.0 statistical software. The measurement data were expressed as mean ± standard deviation. Multiple samples were compared by one-way ANOVA, pairwise comparison by LSD-*t* test. The difference was considered statistically significant at $p < 0.05$.

3 Result

3.1 Identification of targeted microbubble contrast agent

Under the light microscope, the MBc and MBt were regular in shape, uniform in size and distribution (Figures 1A, C), and there was no obvious morphological difference between them. The MBc had no fluorescence imaging under the inverted fluorescence interference microscope (Figure 1B), while the MBt showed obvious green fluorescence (Figure 1D), indicating that the TNF-α antibody was successfully coupled with USphere™ Labeler microbubble contrast agent.

3.2 Evaluation of ultrasonic imaging

3.2.1 Evaluation of DVT by CDFI

Before treatment, solid hypoechoic thrombus was in the veins of the thrombosed segment (marked by the white arrow), and CDFI showed that there was no obvious blood flow signal in the veins in Group I-IV (Figures 2A–D). After treatment, there was still solid hypoechoic thrombus in the vein (marked by the white arrow). CDFI showed that there was a little discontinuous color blood flow signal around the thrombus in Group I (Figure 2E). Part of the vein was solid hypoechoic (marked by the white arrow) and the other part recanalized and enabled the accelerated color flow signal to pass through in Group II (Figure 2F). There was almost no thrombus in the vein of Group III, and continuous color blood flow signal passed through the vessel (Figure 2G). The thrombus in Group IV was completely dissolved, the wall structure was clear, and patency of the blood flow signal was returned (Figure 2H).

3.2.2 Evaluation of DVT by CEUS

Before treatment, CEUS showed that there was no obvious contrast agent in the veins of the thrombus segment of experimental animals in Group I-IV, but contrast agent could be seen in the surrounding tissue (Figures 3A–D). After treatment, CEUS showed that there was a very small amount of contrast agents around the thrombus in Group I (Figure 3E, marked by the red arrow). The contrast agent could pass through part of the vein (marked by the red arrow), while the other part was still blocked by the thrombus in Group II (Figure 3F). In Group III, the venous lumen was basically recanalized allowing the contrast agent to pass through (Figure 3G, marked by the red arrow). The vein was totally unobstructed, and the contrast agent passed through the blood vessel smoothly in Group IV (Figure 3H, marked by the red arrow).

The above results proved that before treatment, there was thrombus in the inferior vena cava of rabbits in Group I-IV. After treatment, there was little thrombolysis and recanalization of blood vessel in Group I; there was partial thrombolysis in Group II; the thrombus in Group III was almost dissolved; and the blood vessel in Group IV were entirely recanalized and the blood flow was unobstructed. This indicated that the treatment methods in Group I-IV were progressively effective.

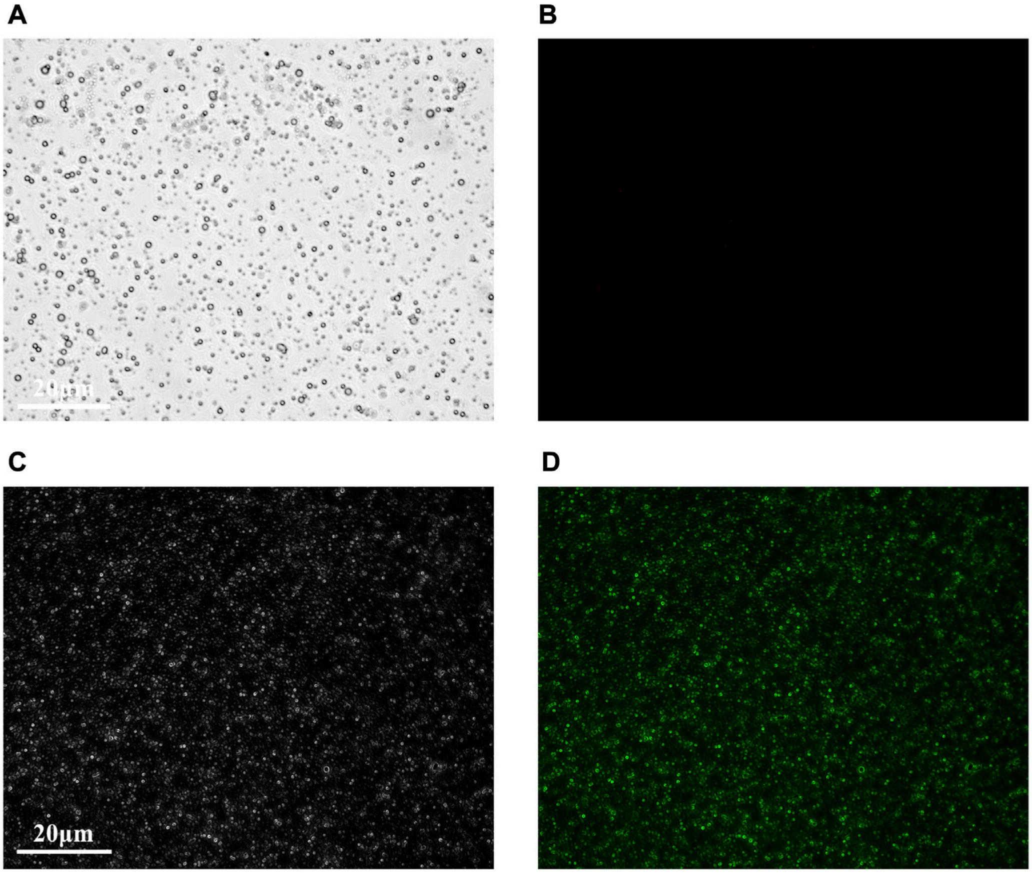

FIGURE 1
Fluorescence microscopic images of control microbubbles **(A,B)** and targeted microbubbles **(C,D)**. **(A,C)** were bright field images and **(B,D)** were FAM fluorescence images. Scale bar = 20 μm.

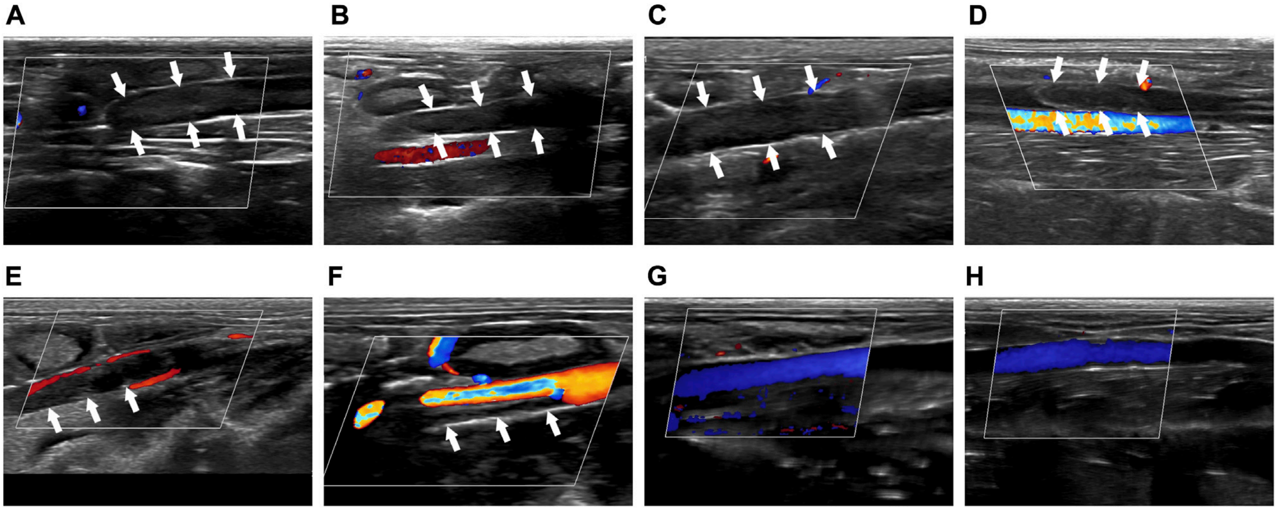

FIGURE 2
Comparison of imaging by CDFI of thrombus before and after treatment. **(A–D)** Corresponded to the Group I-IV before treatment. **(E–H)** Corresponded to the Group I-IV after treatment. The white arrow indicated the thrombus in the blood vessel.

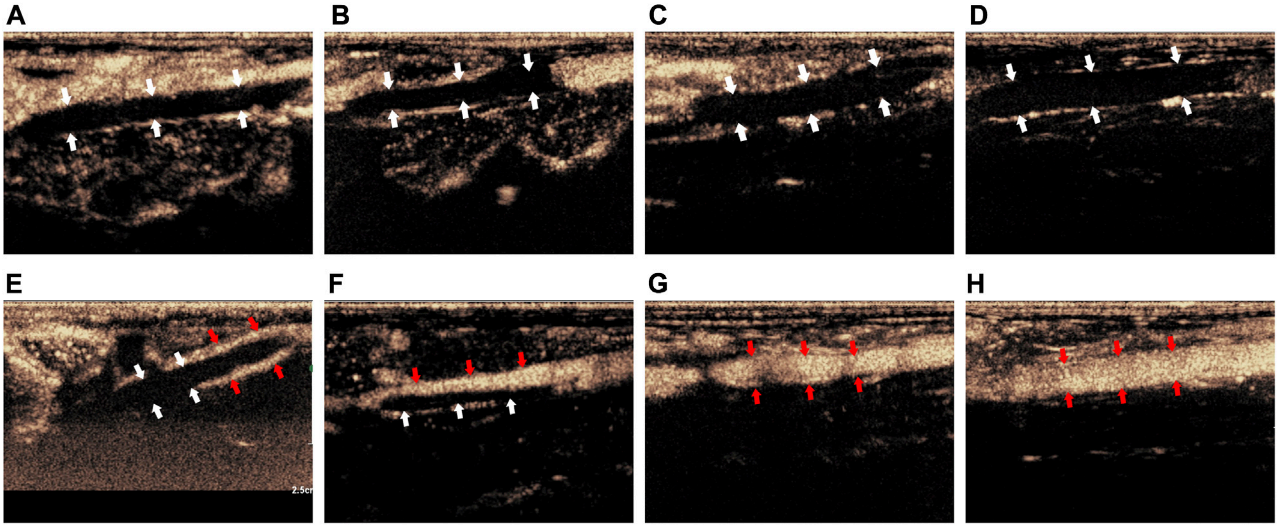

FIGURE 3
Comparison of imaging by CEUS of the thrombus before and after treatment. **(A–D)** Corresponded to the Group I-IV before treatment; **(E–H)** corresponded to the Group I-IV after treatment. The white arrow indicated the thrombus in the blood vessel, the red arrow indicated the contrast agent that passes through the vessel after recanalization.

TABLE 1 The D-dimer content in each group (ng/ml, $\bar{x}$ ± s).

Group	Before modeling	Before treatment	After treatment
Group I	24.470 ± 3.4533	50.633 ± 6.820$^{\triangledown}$	47.383 ± 3.872$^{\triangledown}$
Group II	23.509 ± 3.882	47.552 ± 6.466$^{\triangledown}$	32.512 ± 4.373$^{*\triangledown\blacktriangledown}$
Group III	24.231 ± 4.476	46.892 ± 4.961$^{\triangledown}$	30.324±4.387$^{*\triangledown\blacktriangledown}$
Group IV	25.212 ± 4.227	46.613 ± 6.789$^{\triangledown}$	28.923 ± 4.866$^{*\blacktriangledown}$

$^{*}p < 0.05$ compared with Group I. $^{\triangledown}p < 0.05$ compared with Before modeling. $^{\blacktriangledown}p < 0.05$ compared with Before treatment.

3.3 The D-dimer content in each group

The comparison of D-dimer content in Group I-IV showed that, after treatment, the D-dimer content of rabbits in Group II-IV was lower than that in Group I ($p < 0.05$). However, there was no significant difference in D-dimer content among Group I-IV before modeling and treatment ($p > 0.05$) Table 1.

Pairwise comparison of D-dimer content before modeling, before treatment, and after treatment showed that, before treatment, the D-dimer content of rabbits in Group I-IV was higher than that before modeling ($p < 0.05$). After treatment, the D-dimer content of rabbits in Group I-III was higher than that before modeling ($p < 0.05$), and that of rabbits in Group II-IV was lower than that before treatment ($p < 0.05$). There was no statistical significance among other groups ($p > 0.05$).

3.4 The TNF-α content in each group

Comparison of TNF-α content in Group I-IV showed that, after treatment, the TNF-α content in Group I -III was lower than that in Group IV ($p < 0.05$), but before modeling and treatment, the TNF-α content of rabbits in Group I-IV was not statistically significant ($p > 0.05$) Table 2.

Pairwise comparison of TNF-α content before modeling, before treatment, and after treatment showed that, before treatment, the TNF-α content of rabbits in Group I-IV was higher than that before modeling ($p < 0.05$). After treatment, the TNF-α content of rabbits in Group I-III was higher than that before modeling and treatment ($p < 0.05$); the TNF-α content of rabbits in Group IV was lower than that before treatment ($p < 0.05$), and there was no significant difference among other groups ($p > 0.05$). It showed that only the level of inflammatory factors in Group IV decreased, and the other groups had no significant effect on the inflammatory response.

3.5 Results of four indexes of coagulation in peripheral blood of rabbits

3.5.1 PT in each group

Comparison of PT Group I-IV showed that, after treatment, PT of rabbits in Group II-IV was longer than that of Group I ($p < 0.05$); before modeling and treatment, PT of rabbits in Group I-IV was not statistically significant ($p > 0.05$). It showed that the use of UK could

TABLE 2 The TNF-α content in each group (pg/mL, $\bar{x}$ ± s).

Group	Before modeling	Before treatment	After treatment
Group I	12.662 ± 1.979	55.270 ± 7.771$^{\triangledown}$	67.082 ± 8.457$^{*\triangledown\blacktriangledown}$
Group II	11.908 ± 1.901	54.373 ± 7.942$^{\triangledown}$	63.169 ± 4.788$^{*\triangledown\blacktriangledown}$
Group III	12.366 ± 1.879	59.933 ± 8.572$^{\triangledown}$	65.437 ± 8.462$^{*\triangledown\blacktriangledown}$
Group IV	13.144 ± 1.837	55.603 ± 8.502$^{\triangledown}$	15.922 ± 4.369$^{\blacktriangledown}$

$^{*}p < 0.05$ compared with Group IV. $^{\triangledown}p < 0.05$ compared with Before modeling. $^{\blacktriangledown}p < 0.05$ compared with Before treatment.

TABLE 3 PT in each (s, $\bar{x}$ ± s).

Group	Before modeling	Before treatment	After treatment
Group I	7.098 ± 0.592	7.488 ± 0.603	7.479 ± 0.690
Group II	7.022 ± 0.601	7.351 ± 0.547	8.084 ± 0.447$^{*\triangledown}$
Group III	7.244 ± 0.476	7.532 ± 0.610	7.962 ± 0.362$^{*\triangledown}$
Group IV	7.303 ± 0.521	7.704 ± 0.687	8.011 ± 0.356$^{*\triangledown}$

$^{*}p < 0.05$ compared with Group I. $^{\triangledown}p < 0.05$ compared with Before modeling.

TABLE 4 APTT in each group (s, $\bar{x}$ ± s).

Group	Before modeling	Before treatment	After treatment
Group I	13.822 ± 1.419	13.204 ± 1.002	13.588 ± 1.441
Group II	13.593 ± 1.046	12.967 ± 1.426	16.304 ± 2.433$^{*\triangledown\blacktriangledown}$
Group III	14.023 ± 0.611	13.844 ± 1.512	16.408 ± 2.130$^{*\triangledown\blacktriangledown}$
Group IV	13.851 ± 0.773	13.710 ± 1.328	16.878 ± 2.010$^{*\triangledown\blacktriangledown}$

$^{*}p < 0.05$ compared with Group I. $^{\triangledown}p < 0.05$ compared with Before modeling. $^{\blacktriangledown}p < 0.05$ compared with Before treatment.

prolong PT, but the use of contrast medium did not affect PT (Table 3).

Pairwise comparison of PT before modeling, before treatment, and after treatment showed that, after treatment, PT of rabbits in Group II-IV was higher than that before modeling ($p < 0.05$), and there was no statistical significance among other groups ($p > 0.05$).

3.5.2 APTT in each group

Comparison of APTT in Group I-IV showed that, after treatment, the APTT of rabbits in Group II-IV was longer than that in Group I ($p < 0.05$), while before modeling and treatment, the APTT of rabbits in Group I-IV was not statistically significant ($p > 0.05$). It showed that the use of UK could prolong APTT, but the use of contrast medium did not affect APTT (Table 4).

Pairwise comparison of APTT of rabbits before modeling, before treatment, and after treatment showed that, after treatment, APTT of rabbits in Group II-IV was higher than that before modeling and before treatment ($p < 0.05$), and there was no statistical significance among other groups ($p > 0.05$).

3.5.3 TT in each group

Comparison of TT in Group I-IV showed that, after treatment, the TT of rabbits in Group II-IV was longer than that of Group I ($p < 0.05$), while before modeling and treatment, the TT of rabbits in Group I-IV was not statistically significant ($p > 0.05$). It showed that the use of UK could prolong TT, but the use of contrast medium did not affect TT (Table 5).

Pairwise comparison of TT before modeling, before treatment, and after treatment showed that, after treatment, the TT of rabbits in Group II-IV was higher than that before modeling and before treatment ($p < 0.05$), and there was no statistical significance among other groups ($p > 0.05$).

3.5.4 The FIB content in each group

Comparison of FIB content in Group I-IV showed that, after treatment, the FIB content of rabbits in Group II-IV was lower than that in Group I ($p < 0.05$), but before modeling and treatment, the FIB content of rabbits in Group I-IV was not statistically significant ($p > 0.05$) (Table 6).

Pairwise comparison of FIB content before modeling before treatment and after treatment showed that, before treatment, the FIB content of rabbits in Group I-IV was higher than that before modeling ($p < 0.05$). After treatment, the FIB content of rabbits in Group I was higher than that before modeling ($p < 0.05$), the FIB content of rabbits in Group II-IV was less than that before treatment ($p < 0.05$), and there was no statistical significance among other groups ($p > 0.05$).

TABLE 5 TT in each group (s, $\overline{x} \pm s$).

Group	Before modeling	Before treatment	After treatment
Group I	27.664 ± 5.261	26.039 ± 3.167	26.832 ± 4.209
Group II	28.211 ± 4.376	27.050 ± 3.447	$35.739 \pm 5.550^{*\triangledown\blacktriangledown}$
Group III	28.878 ± 5.540	28.111 ± 2.624	$32.986 \pm 4.437^{*\triangledown\blacktriangledown}$
Group IV	30.843 ± 3.631	28.681 ± 1.902	$35.102 \pm 4.513^{*\triangledown\blacktriangledown}$

$^{*}p < 0.05$ compared with Group I. $^{\triangledown}p < 0.05$ compared with Before modeling. $^{\blacktriangledown}p < 0.05$ compared with Before treatment.

TABLE 6 The FIB content in each group (g/L, $\overline{x} \pm s$).

Group	Before modeling	Before treatment	After treatment
Group I	1.087 ± 0.190	$2.102 \pm 0.289^{\triangledown}$	$1.944 \pm 0.331^{\triangledown}$
Group II	1.122 ± 0.231	$1.882 \pm 0.337^{\triangledown}$	$1.272 \pm 0.241^{*\blacktriangledown}$
Group III	1.154 ± 0.227	$1.971 \pm 0.268^{\triangledown}$	$1.104 \pm 0.223^{*\blacktriangledown}$
Group IV	1.202 ± 0.279	$1.983 \pm 0.330^{\triangledown}$	$1.027 \pm 0.276^{*\blacktriangledown}$

$^{*}p < 0.05$ compared with Group I. $^{\triangledown}p < 0.05$ compared with Before modeling. $^{\blacktriangledown}p < 0.05$ compared with Before treatment.

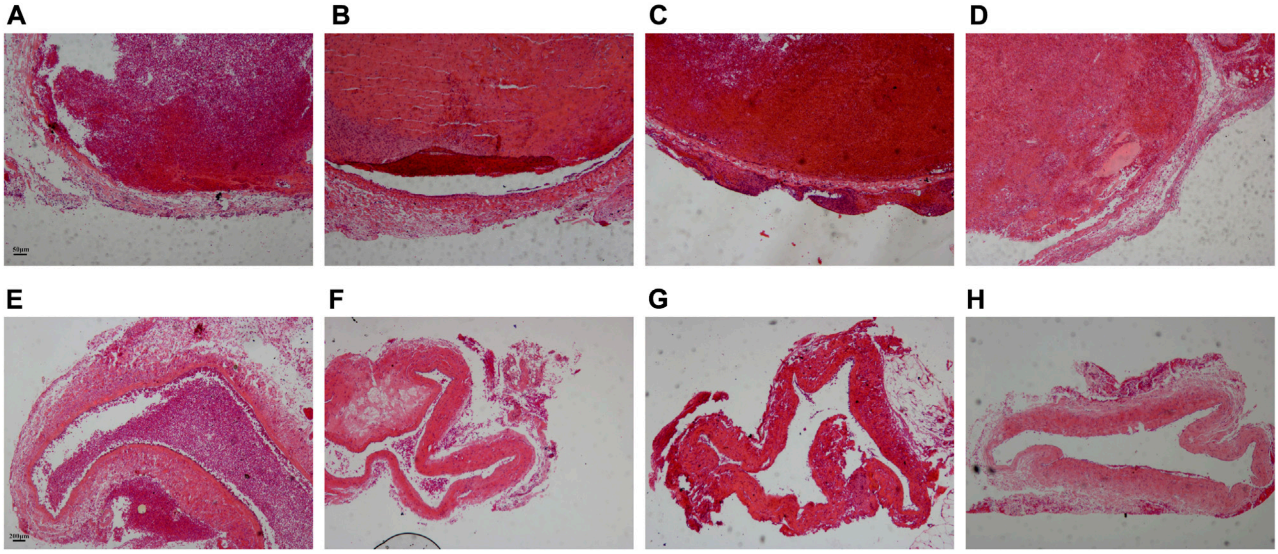

FIGURE 4
Comparison of pathological results of the thrombus before and after treatment. **(A–D)** Corresponded to the Group I-IV before treatment. Scale bar = 50 μm. **(E–H)** Corresponded to the Group I-IV after treatment. Scale bar = 200 μm.

3.6 Hematoxylin-eosin staining of thrombus

Before treatment, the thrombus in the vascular lumen was uniform in texture and consisted of a large amount of red-stained cellulose interwoven in a network to form a fibrous mesh, which was filled with dense red blood cells. The boundary between the thrombus and vessel wall was clear, and there was no significant difference in the thrombus among Group I-IV (Figures 4A–D).

After treatment, the thrombus was reduced in all four experimental groups, and the density of red blood cells in the thrombus decreased. Only a small thrombus was dissolved in Group I, and the thrombus structure was looser than that before treatment, especially around the thrombus (Figure 4E). Most of the thrombi were dissolved except for a tiny remnant on one side of the blood vessel in Group II (Figure 4F). The thrombus was basically dissolved and the vessel wall structure was clear in Group III (Figure 4G). The thrombus was completely dissolved in

Group IV and there was no obvious thrombus in the vein (Figure 4H).

4 Discussion

The application of ultrasound in thrombus therapy was first noted in 1976 (Trübestein et al., 1976). The pivotal mechanism is that the cavitation effect produced by ultrasonic irradiation promotes thrombolysis. Sonic flow generated by low-frequency ultrasound causes mechanical displacement of the thrombus and exposes the fiber structure inside the thrombus to thrombolytic medicine. The micro jet caused by the cavitation effect generates a shear force on the surface of the thrombus and then dissolves the thrombus (Pan et al., 2023).

In recent years, research on the application of ultrasound targeted contrast agents has improved rapidly (Liu et al., 2022c). CEUS is a highly secure inspection technology developed in recent years. The principle of this method is that ultrasound contrast agents reflect ultrasound and create different echo signals for the diagnosis of related diseases. MBt contrast agents are not only used for the diagnosis of diseases, but also carry genes or medicine to treat various diseases (Han et al., 2022). MBt swiftly expands and ruptures under the action of low-power focused ultrasound, then releases the genes or medication, so as to increase the local medicine concentration and enhance the efficacy without systemic side effects (Yu et al., 2020; Liu et al., 2023).

Many studies have verified that there is a close connection between inflammation and venous thrombosis (Weitz and Chan, 2020; Stark and Massberg, 2021). TNF-α is one of the critical factors in many diseases complicated with venous thrombosis (Zheng et al., 2021). It plays a vital role in mediating inflammatory events related to venous thrombosis, including early inflammatory response and neutrophil infiltration into the venous wall. Previous studies confirmed that the TNF-α content continued to rise after thrombosis. And the MBt contrast agent carrying monoclonal antibodies against IL-6, IL-8, and TNF-α was successfully prepared. Therefore, this research followed the preceding preparation method of MBt contrast agent, prepared MBt carrying TNF-α antibody, and selected TNF-α as the target to study the treatment of DVT.

This study concluded that there was no significant difference in PT, APTT, and TT of rabbits in each group before modeling and treatment, but the contents of FIB, D-dimer, and TNF-α increased significantly before treatment. Although relevant literature (Heestermans et al., 2021) reported that Pt and APTT would be shortened after thrombosis, the four indexes of coagulation were affected by numerous factors. Pt and APTT were not the most sensitive indicators to predict thrombosis. The relationship between thrombosis and the fibrinolytic system was complicated. In addition, this experimental model was an acute phase thrombus model. Therefore, these two indicators did not change significantly in this research after thrombosis. As the most sensitive index for clinical prediction of thrombosis, the contents of D-dimer and FIB increased markedly after thrombosis.

After treatment with different schemes, the four coagulation indexes and D-dimer content in Group I did not change significantly compared with that before treatment. But the content of TNF-α increased compared with those before treatment, indicating that ultrasonic irradiation did not increase the risk of bleeding or activate the fibrinolytic system *in vivo*, and had no effect on inflammatory reactions. The PT, APTT, and TT in Group II-IV were longer than those before and after modeling, while the contents of FIB and D-dimer were significantly lower than those before modeling and before treatment, indicating that the use of UK to treat thrombosis could also increase the risk of bleeding. Among the four groups, only the TNF-α content in Group IV decreased significantly after treatment, indicating that TNF-α content increased with the extension of thrombosis time, and MBt effectively reduced the level of the inflammatory factors.

Meanwhile, there was no significant difference in the four indexes of coagulation and the contents of D-dimer and TNF-α among the rabbits in Group I-IV before modeling and before treatment. After treatment, the PT, APTT, and TT of rabbits in Group II-IV were longer than those in Group I, and the contents of FIB and D-dimer of rabbits in Group II-IV were lower than those in Group I; in addition, there was no significant difference in the four indexes of coagulation and the content of D-dimer among Group II-IV. It showed that both MBc and MBt would not cause changes in the coagulation system. As for the content of TNF-α, Group IV was higher than Group I-III, but there was no significant difference among Group I-III. It showed that in thrombotic diseases, the increase of inflammatory factor level was not only related to thrombosis, but may also be linked to reperfusion injury after thrombolysis.

Through the analysis of CDFI, CEUS, and pathological results, the study found that the thrombolysis of focused ultrasound alone was limited. When focused ultrasound was combined with UK, the thrombus was partially dissolved. With the addition of a microbubble contrast agent, the thrombus almost disappeared, which indicated that the treatment method significantly accelerated the thrombolysis and promoted the recanalization of blood vessels. Furthermore, the combination of UK, focused ultrasound, and MBt produced the best therapeutic effect. More MBt accumulates locally in the thrombus through an antigen-antibody reaction, facilitating the therapeutic effect of UK on the thrombus, so as to completely dissolve the thrombus while alleviating the inflammatory response.

Combined with previous studies, we found that CEUS can be used not only to diagnose thrombosis but also to treat it. The thrombolytic effect of ultrasound was one of its clinical applications, which mainly depended on the cavitation effect to enhance the efficacy of thrombolytic medicine (Porter et al., 2017; Ma et al., 2020). Relevant studies showed that a microbubble contrast agent, as an artificially added cavitation core, could enhance the induced ultrasonic cavitation effect and improve the thrombolytic effect of ultrasound (Yang and Zhou, 2017).

In summary, this study had some innovations for thrombosis treatment. At first, the combination of targeted microbubbles and UK was innovatively used in the study of acute DVT. Thrombus was diagnosed by ultrasound imaging and treated at the same time. This treatment has been rarely reported. Secondly, TNF-α was used as the target of thrombus to attract a large number of targeted microbubbles to enrich locally in the thrombus and neutralize the inflammatory response, which was another innovative way to treat thrombus. This experiment opens up new ways to study the effect of UTMD technology targeting inflammatory factors on thrombosis and provides new ideas for the diagnosis and treatment of acute DVT.

This study has a few limitations in experimental design. This experiment only treated acute thrombosis, ignoring the long-term damage of thrombus. By extending the experimental time, we will prepare animal models of thrombosis in the subacute and chronic phases and conduct therapeutic studies on them. Secondly, using low-power focused ultrasound to thrombi could affect the perfusion of microcirculation of the surrounding tissues. The main concern in the experiment was the recanalization of vascular lumen. We will study the damage to the vessel wall of the thrombus segment and use more refined ultrasound irradiation to avoid damage to the tissue surrounding the thrombus.

Data availability statement

The original contributions presented in the study are included in the article/Supplementary Material, further inquiries can be directed to the corresponding author.

Ethics statement

The animal study was reviewed and approved by The animal study was reviewed and approved by the Ethics Committee of Kunming Medical University (Ethical Approval No. KMMU20220861).

Author contributions

JC, YY, and YyL conducted the experiments and analyzed the results, JC and YY drafted the manuscript. LX organized the database. CZ and QC performed the statistical analysis. YyL and YpL revised the manuscript and contributed to the design and concept of the study. All authors participated in the revision, reading, and review of the manuscript.

Funding

This study was supported by the Construction of Engineering Research Center of Higher Education in Yunnan Province (2021), Yunnan Provincial Science and Technology Department - Kunming Medical University Joint Fund key program (grant number 202001AY070001-008), Yunnan Provincial Science and Technology Department - Kunming Medical University Joint Fund general program (grant number 202201AY070001-271, 202201AY070001-273).

Conflict of interest

The authors declare that the research was conducted in the absence of any commercial or financial relationships that could be construed as a potential conflict of interest.

Publisher's note

References

Aguilar, G., Córdova, F., Koning, T., Sarmiento, J., Boric, M. P., Birukov, K., et al. (2021). Tnf-A-activated enos signaling increases leukocyte adhesion through the S-nitrosylation pathway. *Am. J. Physiol-Heart C.* 321 (6), H1083–H1095. doi:10.1152/ajpheart.00065.2021

Aue, G., Nelson Lozier, J., Tian, X., Cullinane, A. M., Soto, S., Samsel, L., et al. (2011). Inflammation, tnfα and endothelial dysfunction link lenalidomide to venous thrombosis in chronic lymphocytic leukemia. *Am. J. Hematol.* 86 (10), 835–840. doi:10.1002/ajh.22114

Avgerinos, E. D., Jaber, W., Lacomis, J., Markel, K., McDaniel, M., Rivera-Lebron, B. N., et al. (2021). Randomized trial comparing standard versus ultrasound-assisted thrombolysis for submassive pulmonary embolism: The sunset spe trial. *Jacc-Cardiovasc Inte* 14 (12), 1364–1373. doi:10.1016/j.jcin.2021.04.049

Ebben, H. P., Nederhoed, J. H., Slikkerveer, J., Kamp, O., Tangelder, G. W., Musters, R. J., et al. (2015). Therapeutic application of contrast-enhanced ultrasound and low-dose urokinase for thrombolysis in a porcine model of acute peripheral arterial occlusion. *J. Vasc. Surg.* 62 (2), 477–485. doi:10.1016/j.jvs.2014.02.057

Han, L., Mengmeng, L., Tao, Z., Xinru, L., Hao, Z., Zhen, G., et al. (2022). Engineered bacterial extracellular vesicles for osteoporosis therapy. *Chem. Eng. J.* 450, 138309. doi:10.1016/j.cej.2022.138309

He, Y., Dong, X. H., Zhu, Q., Xu, Y. L., Chen, M. L., and Liu, Z. (2022). Ultrasound-triggered microbubble destruction enhances the radiosensitivity of glioblastoma by inhibiting pgrmc1-mediated autophagy *in vitro* and *in vivo*. *Mil. Med. Res.* 9 (1), 9. doi:10.1186/s40779-022-00369-0

Heestermans, M., Naudin, C., Mailer, R. K., Konrath, S., Klaetschke, K., Jämsä, A., et al. (2021). Identification of the factor xii contact activation site enables sensitive coagulation diagnostics. *Nat. Commun.* 12 (1), 5596. doi:10.1038/s41467-021-25888-7

Jackson, C. D., Cifu, A. S., and Burroughs-Ray, D. C. (2022). Antithrombotic therapy for venous thromboembolism. *Jama-J. Am. Med. Assoc.* 327 (21), 2141–2142. doi:10.1001/jama.2022.7325

Khan, F., Tritschler, T., Kahn, S. R., and Rodger, M. A. (2021). Venous thromboembolism. *Lancet* 398 (10294), 64–77. doi:10.1016/s0140-6736(20)32658-1

Liang, Z., Chen, H., Gong, X., Shi, B., Lin, L., Tao, F., et al. (2021). Ultrasound-induced destruction of nitric oxide-loaded microbubbles in the treatment of thrombus and ischemia-reperfusion injury. *Front. Pharmacol.* 12, 745693. doi:10.3389/fphar.2021.745693

Liu, H., Geng, Z., and Su, J. (2022). Engineered mammalian and bacterial extracellular vesicles as promising nanocarriers for targeted therapy. *Extracell. Vesicles Circ. Nucl. Acids* 3 (1), 63–86. doi:10.20517/evcna.2022.04

Liu, H., Zhang, H., Han, Y., Hu, Y., Geng, Z., and Su, J. (2022). Bacterial extracellular vesicles-based therapeutic strategies for bone and soft tissue tumors therapy. *Theranostics* 12 (15), 6576–6594. doi:10.7150/thno.78034

Liu, H., Zhang, H., Wang, S., Cui, J., Weng, W., Liu, X., et al. (2023). Bone-targeted bioengineered bacterial extracellular vesicles delivering sirna to ameliorate osteoporosis. *Compos Part B Eng.* 255, 110610. doi:10.1016/j.compositesb.2023.110610

Liu, H., Zhang, Q., Wang, S., Weng, W., Jing, Y., and Su, J. (2022). Bacterial extracellular vesicles as bioactive nanocarriers for drug delivery: Advances and perspectives. *Bioact. Mater* 14, 169–181. doi:10.1016/j.bioactmat.2021.12.006

Ma, L., Wang, Y., Zhang, S., Qian, X., Xue, N., Jiang, Z., et al. (2020). Deep penetration of targeted nanobubbles enhanced cavitation effect on thrombolytic capacity. *Bioconjugate Chem.* 31 (2), 369–374. doi:10.1021/acs.bioconjchem.9b00653

Notten, P., Arnoldussen, C., Brans, R., de Smet, A., Tick, L. W., van de Poel, M. H. W., et al. (2020). Association of successful ultrasound-accelerated catheter-directed thrombolysis with postthrombotic syndrome: A post hoc analysis of the cava trial. *Thromb. Haemost.* 120 (8), 1188–1199. doi:10.1055/s-0040-1713171

Pan, Y., Li, Y., Li, Y., Zheng, X., Zou, C., Li, J., et al. (2023). Nanodroplet-coated microbubbles used in sonothrombolysis with two-step cavitation strategy. *Adv. Healthc. Mater* 12 (6), e2202281. doi:10.1002/adhm.202202281

Poredos, P., and Poredos, P. (2022). Involvement of inflammation in venous thromboembolic disease: An update in the age of covid-19. *Semin. Thromb. Hemost.* 48 (1), 093–099. doi:10.1055/s-0041-1732372

Porter, T. R., Xie, F., Lof, J., Powers, J., Vignon, F., Shi, W., et al. (2017). The thrombolytic effect of diagnostic ultrasound-induced microbubble cavitation in acute carotid thromboembolism. *Invest. Radiol.* 52 (8), 477–481. doi:10.1097/rli.0000000000000369

Presicce, P., Cappelletti, M., Senthamaraikannan, P., Ma, F., Morselli, M., Jackson, C. M., et al. (2020). Tnf-signaling modulates neutrophil-mediated immunity at the feto-maternal interface during lps-induced intrauterine inflammation. *Front. Immunol.* 11, 558. doi:10.3389/fimmu.2020.00558

Stark, K., and Massberg, S. (2021). Interplay between inflammation and thrombosis in cardiovascular pathology. *Nat. Rev. Cardiol.* 18 (9), 666–682. doi:10.1038/s41569-021-00552-1

Trübestein, G., Engel, C., Etzel, F., Sobbe, A., Cremer, H., and Stumpff, U. (1976). Thrombolysis by ultrasound. *Clin. Sci. Mol. Med. Suppl.* 3, 697s–8s. doi:10.1042/cs051697s

Wang, F., Shi, T., and Su, C. (2019). Ultrasound with microbubble contrast agent and urokinase for thrombosis. *Ultrasound Med. Biol.* 45 (3), 859–866. doi:10.1016/j.ultrasmedbio.2018.10.021

Wang, S., Guo, X., Xiu, W., Liu, Y., Ren, L., Xiao, H., et al. (2020). Accelerating thrombolysis using a precision and clot-penetrating drug delivery strategy by nanoparticle-shelled microbubbles. *Sci. Adv.* 6 (31), eaaz8204. doi:10.1126/sciadv.aaz8204

Weitz, J. I., and Chan, N. C. (2020). Novel antithrombotic strategies for treatment of venous thromboembolism. *Blood* 135 (5), 351–359. doi:10.1182/blood.2019000919

Xu, Y., Liu, R., Yang, H., Qu, S., Qian, L., and Dai, Z. (2022). Enhancing photodynamic therapy efficacy against cancer metastasis by ultrasound-mediated oxygen microbubble destruction to boost tumor-targeted delivery of oxygen and renal-clearable photosensitizer micelles. *Acs Appl. mater inter* 14 (22), 25197–25208. doi:10.1021/acsami.2c06655

Yang, H., Sun, Y., Wei, J., Xu, L., Tang, Y., Yang, L., et al. (2019). The effects of ultrasound-targeted microbubble destruction (utmd) carrying il-8 monoclonal antibody on the inflammatory responses and stability of atherosclerotic plaques. *Biomed. Pharmacother.* 118, 109161. doi:10.1016/j.biopha.2019.109161

Yang, W., and Zhou, Y. (2017). Effect of pulse repetition frequency of high-intensity focused ultrasound on *in vitro* thrombolysis. *Ultrason. sonochem* 35, 152–160. doi:10.1016/j.ultsonch.2016.09.014

Yu, G. Z., Istvanic, F., Chen, X., Nouraie, M., Shiva, S., Straub, A. C., et al. (2020). Ultrasound-targeted microbubble cavitation with sodium nitrite synergistically enhances nitric oxide production and microvascular perfusion. *Ultrasound Med. Biol.* 46 (3), 667–678. doi:10.1016/j.ultrasmedbio.2019.10.012

Zhang, C., Chen, S., Li, Q., Wu, J., Qiu, F., Chen, Z., et al. (2021). Ultrasound-targeted microbubble destruction mediates gene transfection for beta-cell regeneration and glucose regulation. *Small* 17 (31), e2008177. doi:10.1002/smll.202008177

Zheng, X., Liu, H., Ma, M., Ji, J., Zhu, F., and Sun, L. (2021). Anti-thrombotic activity of phenolic acids obtained from salvia miltiorrhiza F. Alba in tnf-A-stimulated endothelial cells via the nf-?b/jnk/P38 mapk signaling pathway. *Arch. Pharm. Res.* 44 (4), 427–438. doi:10.1007/s12272-021-01325-7

Zhong, Y., Zhang, Y., Xu, J., Zhou, J., Liu, J., Ye, M., et al. (2019). Low-intensity focused ultrasound-responsive phase-transitional nanoparticles for thrombolysis without vascular damage: A synergistic nonpharmaceutical strategy. *Acs Nano* 13 (3), 3387–3403. doi:10.1021/acsnano.8b09277

frontiers | Frontiers in Bioengineering and Biotechnology

TYPE Original Research
PUBLISHED 18 April 2023
DOI 10.3389/fbioe.2023.1171450

OPEN ACCESS

EDITED BY
Long Bai,
East China University of Science and Technology, China

REVIEWED BY
Liming Wang,
Saitama Medical University, Japan
Jing Huang,
Affiliated Hospital of Guangdong Medical University, China
Wei Xie,
Hefei Comprehensive National Science Center, China
Xiumei Huang,
Indiana University Bloomington,
United States

*CORRESPONDENCE
Guoxin Li,
✉ gzliguoxin@163.com
Yanfeng Hu,
✉ yfenghu@qq.com

†These authors have contributed equally to this work

SPECIALTY SECTION
This article was submitted to Nanobiotechnology, a section of the journal Frontiers in Bioengineering and Biotechnology

RECEIVED 22 February 2023
ACCEPTED 31 March 2023
PUBLISHED 18 April 2023

CITATION
Wang H, Niu H, Luo X, Zhu N, Xiang J, He Y, Chen Z, Li G and Hu Y (2023), Radiosensitizing effects of pyrogallol-loaded mesoporous or-ganosilica nanoparticles on gastric cancer by amplified ferroptosis.
Front. Bioeng. Biotechnol. 11:1171450.
doi: 10.3389/fbioe.2023.1171450

Radiosensitizing effects of pyrogallol-loaded mesoporous or-ganosilica nanoparticles on gastric cancer by amplified ferroptosis

Hongwei Wang[1,2†], Hongyan Niu[3†], Xi Luo[1†], Nan Zhu[1], Jingfeng Xiang[1], Yan He[4], Zhian Chen[1], Guoxin Li[1]* and Yanfeng Hu[1]*

[1]Department of General Surgery, Guangdong Provincial Key Laboratory of Precision Medicine for Gastrointestinal Tumor, Nanfang Hospital, The First School of Clinical Medicine, Southern Medical University, Guangzhou, China, [2]Department of General Surgery, Longgang Central Hospital of Shenzhen, Shenzhen, China, [3]Department of Clinical Laboratory, The Affiliated Huai'an Hospital of Xuzhou Medical University and Huai'an Second People's Hospital, Huai'an, China, [4]Department of Pathology, Longgang Central Hospital of Shenzhen, Shenzhen, China

Radiotherapy (RT) incorporated multidisciplinary treatment is producing excellent clinical results, but its efficacy in treating late-stage gastric cancer is constrained by radioresistance and RT-related toxicity. Especially, since reactive oxygen species are the pivotal effectual molecules of ionizing radiation, improving ROS production by nanoparticles and other pharmacological modulation to amplify oxidation of polyunsaturated fatty acids and subsequent ferroptotic cell death is shown to enhance cancer cell radioresponse. Herein, we constructed a nanosystem by loading Pyrogallol (PG), a polyphenol compound and ROS generator, into mesoporous organosilica nanoparticles named as MON@*p*G. The nanoparticles exhibit proper size distribution with amplified ROS production and substantial glutathione depletion under X-ray radiation in gastric cancer cell line. Meanwhile, MON@PG enhanced radiosensitivity of gastric cancer in xenograft tumor model by ROS-mediated accumulation of DNA damage and apoptosis. Furthermore, this augmented oxidative process induced mitochondrial dysfunction and ferroptosis. In summary, MON@PG nanoparticles show the capacity to improve RT potency in gastric cancer by disrupting redox balance and augmenting ferroptosis.

KEYWORDS

gastric cancer, radiosensitivity, ROS generation, GSH depletion, ferroptosis

1 Introduction

Although gastric cancer (GC) incidence and mortality have decreased in recent decades, GC remains one of the greatest tumor burdens and the third most common reason for cancer-related deaths globally (Siegel et al., 2022). In spite of recent breakthroughs in therapeutic modalities and immunotherapy reagents, treating locally progressed and metastatic GC is still problematic and challenging (Yu et al., 2019; Chiaravalli et al., 2022). According to the latest evidence, preoperative radiation (RT) for GC can have a favorable therapeutic effect, although the adjuvant RT has proven otherwise (Lee et al., 2021;

Lordick et al., 2021). As an efficient and secure mode of therapy for gastric cancer hemorrhaging, palliative radiation have a satisfied hemostatic effect with positive overall survival rate (Takeda et al., 2022). However, GC possesses affluent lymphatic network and peritoneal metastatic tendency, the delivery of sufficient radiation to tumor sites but tolerable dose to adjacent tissues is not always achievable for planning target volumes, which seriously impairs the treatment efficacy of RT in clinical practice (Mondlane et al., 2018; Wang et al., 2021; Mao and Zhang, 2022).

Ionizing radiation induces cancer death *via* endogenous oxidative damage caused by elevated intracellular levels of reactive oxygen species (ROS) and direct DNA double-strand breaks (DSBs) (Zou et al., 2017). By breaking multiple molecular targets, orchestrating peroxidation reaction and meddling with the mitochondrial membrane integrity, radiation-induced ROS prompts metabolic disturbances in the energy homeostasis (Yang et al., 2021). However, glutathione (GSH), a pivotal role in radical scavenging and electrophile elimination, can effectively remove excess ROS to protect cells against oxidation threat. Clearly, the everlasting tug of war between ROS and GSH is crucial for tumor resilience to radiation challenge (Liu et al., 2022).

As characterized by hypoxia with overabundant H_2O_2 and glutathione (GSH) (Geng et al., 2001; Rouschop et al., 2013; Wang et al., 2013), tumor microenvironment (TME) cultivate the proliferation, survival, and migration of tumor cells by expansion of aberrant tumor blood vessels (Finger and Giaccia, 2010). Hypoxia diminishes ROS generation by reprogramming mitochondrial energy consumption (Harada et al., 2012). Robust DNA repair and damage-bypass mechanisms within the hypoxic TME have been identified as important promoters of tumor progression despite treatment efforts (Brown and Wilson, 2004; Yoshimura et al., 2013).

Ferroptosis is defined as regulated necrosis catalyzed by iron that occurs when ROS initiate immoderate peroxidation of polyunsaturated fatty acids (PUFA) (Dixon et al., 2014). During the process lipid hydroperoxides disintegrate into reactive wastes such as malondialdehydes (MDA), which by cross-coupling may deactivate proteins involved in membrane integrity to promote ferroptosis (Lu, 2009). Glutathione peroxidase 4 (GPX4) retaines special capacity to detoxify hydroperoxides to shield biomembranes from oxidative stress, which can be inactivated by depletion of intracellular glutathione (GSH) (Tsaturyan et al., 2022).

Various innovative strategies, including photothermal agents and photosensitizer with catalysis properties, have been explored to promote oxygenation in TME (Yu N. et al., 2018; Espinosa et al., 2018; Xu et al., 2018). Many nanoparticles radiosensitizer have been customized to overcome hypoxia-induced RT resistance by enhancing ROS generation and inducing ferroptosis (Dou et al., 2018; Li et al., 2018; Hassannia et al., 2019; Lyu et al., 2020). Mesoporous organosilica nanoparticles (MON) has been an encouraging alternative to traditional platforms in drug delivery, due to its ample surface area, low toxicity, decent biocompatibility (Zhang F. et al., 2021; Zhang et al., 2022). Particularly, GSH-responsive biodegradable MON carriers has show promising potential in tumor-specific drug release due to the reducing property of TME with higher GSH level (Yu L. et al., 2018).

Herein, we construct a novel nanocomposites (MON@PG) by docking pyrogallol to MON in order to sensitize GC cells to ionizing radiation. Pyrogallol (PG), a trihydroxybenzene compound, has shown antineoplastic effect many cancer cells including gastric cancer by disrupting the cellular redox equilibrium (Park et al., 2008). Notably, studies have shown that PG can promote ROS generation in a concentration dependent manner along with significant consumption of intracellular GSH (Mahmoud et al., 2022). As shown in Scheme 1, the controlled release of PG from MON@PG in cancer cells was achieved by matrix degradation in response to GSH. The unloaded PG induces ROS burst and GSH exhaustion, which amplifies the ROS-mediated DNA damage, mitochondrial dysfunction, lipid peroxidation and ferroptosis under irradiation. Essentially, the constructed MON@PG represent a promising approach to tilt redox balance in favor of sensitized radioresponse of GC.

2 Materials and methods

2.1 Materials

Tetraethoxysilane, cetyltrimethylammonium tosylate (CTAT), triethanolamine (TEA), γ-chloropropyl trimethoxysilane (CP), bis [3-(triethoxysilyl)propyl]tetrasulfide (TESPT), 3-aminopropyltriethoxysilane (APTES), sulforhodamine B (SRB), polyacrylic acid (PAA), dichloromethane, pyrogallol were acquired from MilliporeSigma (St Louis, USA). Selenium powder, sodium powder, sodium borohydride ($NaBH_4$), ammonium nitrate (NH_4NO_3), anhydrous sodium sulfate, 30% H_2O_2, and ethanol (anhydrous) were purchased from Guidechem (Hangzhou, China). C18PMH-PEG was purchased from Ruixi Biotech, Inc. (Xi'an, China). Trypsin-EDTA (0.25%), Hoechst 33,342 (Hoechst), DAPI, Fetal bovine serum (FBS) and DMEM medium were supplied by Thermo Fisher Scientific Inc. (Waltham, USA). Antibiotic/antimycotic solution was purchased from Beyotime Biotech. Inc. (Shanghai, China).

2.2 Cell lines and animals

The American Type Culture Collection was the supplier of mouse stomach cancer cell line (MFC) cells and human gastric cancer cell line (MKN45), which were then cultured in DMEM with 1% antibiotic/antimycotic solution and 10% FBS. Female Balb/c mice (age 4–5 weeks) and New Zealand rabbits (male, 25 weeks old, 2.–2.5 kg) were purchased from Experimental Animal Centre of Guangdong Province.

2.3 Synthesis of MON@PG

According to earlier reports, bis [3-(triethoxysilyl)propyl] diselenide (BTESePD) was properly prepared (Zhang F. et al., 2021). Then, 0.8 g CTAT and 0.2 g TEA were stirred to dissolve in 40 mL deionized water at 80°C for 30 min, before 1.0 g BTESePD and 4.0 g tetraethoxysilane were added dropwise into 3 mL ethanol and stirred for 3 more hours. The products were collected and rinsed with ethanol for three times before extracted with 1% NH_4NO_3 ethanol solution for 12 h. Next, 5 mg PG was dissolved in 0.5 mL

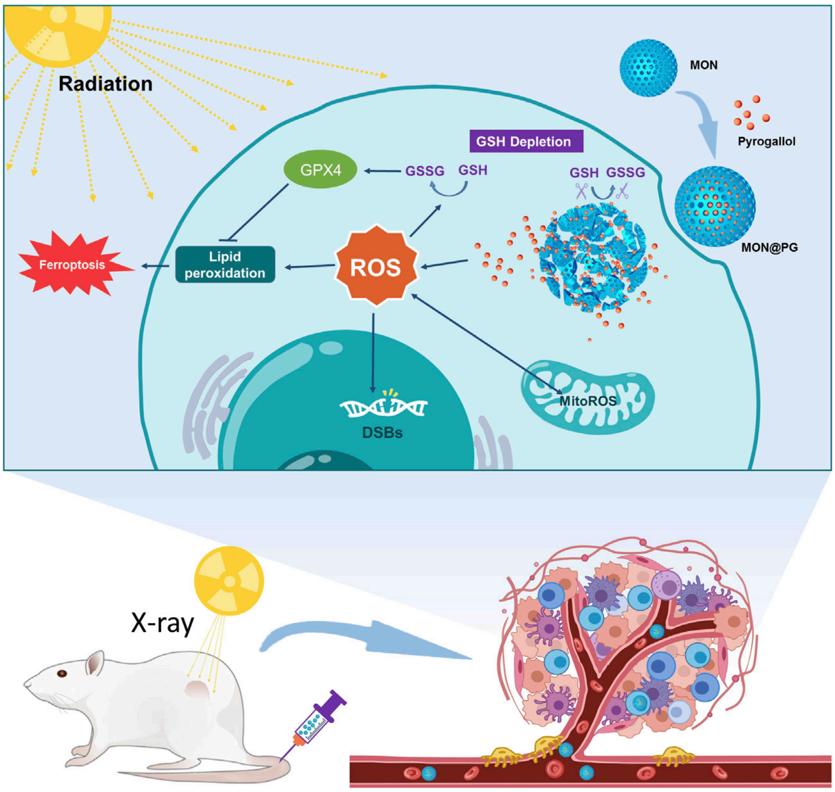

SCHEME 1
Illustration of MON@PG nanplatform as a radiosensitizer by enhanced tumor ferroptosis. Prepared MON@PG enter the tumor cells and disintegrate in GSH-rich cytoplasm. The released PG boost ROS generation and GSH depletion, leading to amplified lipid peroxidation and ferroptosis under X-ray irradiation.

DMSO and mixed with 20 mg MON under sonication prior to be shaken at 500 rpm at 37°C over night to obtain PG loaded MON. Moreover, 20 mg C18PMH-PEG was added to the MON@PG solution and stirred for 1 h before blow drying to prepare more water-soluble and biocompatible reagent.

2.4 GSH-responsive drug release

Inductively coupled plasma optical emission spectroscopy (ICP-OES, Pekin-Elmer, USA) was applied to measure the PG yield. The equation, drug loading content (%) = mass of PG in MON@PG/ mass of MON@PG, was used to calculate the drug loading content. MON@PG was dissolved in 10 mM GSH solution at 37 °C to analyze the drug release capability by ICP-OES over a 50-h period.

2.5 Characterization of MON@PG

The elemental mapping and surface morphology of the MON@ PG were investigated *via* a transmission electron microscope (TEM, S-450, Hitachi Limited, Japan). Particle Size And Zeta Potential Analyzer (Malvern Panalytical, United Kingdom) was applied to measure the average size of the nanocomposite. The optical properties of MON@PG was analyzed by UV–Vis spectroscopy (UV-2600, Shimadzu Vietnam Co., Ltd., Japan). Elemental composition of MON was investigated by energy dispersive spectroscopy (EDS, Oxford Instruments, United Kingdom).

2.6 Biocompatibility evaluation

MON@PG with different concentration were incubated in rabbit whole blood in a 96-well plate at 37 °C for 1 h before centrifuged at 1,000 *g* for 3 min. The absorbance of supernatant was measured by a microplate reader (Multiskan SkyHigh, Thermo Fisher Scientific Analyzers, USA) at 540 nm. PBS and Triton X −100 were used as negative control and positive control. Hemolysis rate (HR) of each well was calculated as follow: HR (%) = $(OD_1 - OD_2)/(OD_3 - OD_2) \times 100$, where OD_1, OD_2 and OD_3 were the absorbances of MON@PG, negative control, and positive control.

2.7 Cell viability

Cell counting kit-8 (CCK-8, Beyotime Biotech, China) was applied to measure the cell viability by a microplate reader. MFC cells was planted in 96-well plates and cultured for 12 h. Following the addition of different concentrations of MON@PG (PG concentrations of 10, 20, 40, 60, and 80 μmol/L) to each well, the plates were either exposed to radiation (4 Gy, Varian Clinac 23EX

Linear Accelerator) or not. After 24 h, cell viability was calculated at wavelength of 450 nm with optical density.

2.8 Intracellular ROS generation and GSH depletion

DCFH-DA fluorogenic dye was used to measure intracellular peroxyl, hydroxyl, and other ROS activity. MFC cells were planted in 12-well plates and cultured for 12 h before incubated with MON@PG (50 μM) for 12 h, during of which the plates underwent irradiation or not. Next, treated cells were stained with DCFH-DA for 30 min before observation under fluorescence microscopy. The average fluorescence intensity was assessed following flow cytometry protocols.

To detect the intracellular GSH level, cells treated with various concentrations of MON@PG (PG concentration of 10, 20, 40, 60, and 80 μmol/L) with or without irradiation for 24 h were collected for total glutathione content analysis by Total Glutathione Assay Kit (Beyotime Biotech, China).

2.9 *In vitro* Antitumor assay

Cytotoxicity of different treatment groups was detected by EdU cell proliferation assay. MFC cells were seeded in 12-well plates and cultured for 12 h before incubated with MON@PG (50 μM) for 12 h, during of which the plates underwent irradiation or not. Next, treated cells were stained with YF®555 Click-iT EdU Imaging Kits (Biorigin Inc., China) following the manufacturer's protocol and imaged *via* fluorescence microscopy.

To measure the cell apoptosis rate, MFC cells were cultured in 6-well plates before incubated with MON@PG (50 μM), meanwhile the plates were either exposed to radiation or not. After 24 h, treated cells were collected and labelled by an AnnexinV-FITC/PI kit (Beyotime Biotech, China) following the manufacturer's protocol prior to flow cytometry analysis.

2.10 DNA damage and comet assay

γ-H2AX, as known as phospho-H2AX, is a marker of DSBs that can be used to detect DNA damage after irradiation. MFC cells were cultured in 6-well plates before incubated with MON@PG (50 μM), meanwhile the plates were either exposed to radiation or not. After 24 h, the treated cells were fixed with 4% paraformaldehyde for 15 min before treated with 0.3% Triton X-100 solution for permeabilization. Next, cells were incubated with γ-H2AX antibody (1:150; Affinity Biosciences) overnight at 4°C before cultured with Cy3-labeled secondary antibody (goat anti-rabbit, 1:200; Invitrogen) and Hoechst. Inverted phase contrast fluorescence microscope was used for imaging.

For comet assay, MFC cells were cultured in 6-well plates before incubated with MON@PG (50 μM), meanwhile the plates were either exposed to radiation or not. The treated cells were suspended in low melting point agarose before layered on frosted slides that have been previously coated with normal melting point agarose. Then, the coated slides were immersed in cold lysis buffer at 4°C for 2 h. Next, slides were soaked in fresh alkaline electrophoresis buffer for 40 min before electrophoresis at a field strength of 20 V for 30 min. Finally, slides were stained with propidium iodide for 25 min and analyzed with fluorescence microscopy. Tail DNA (%) was calculated following the equation: Tail DNA (%) = Tail intensity/(Head intensity + Tail intensity) ×100.

2.11 Evaluation of mitochondrial function

MFC cells were cultured in 6-well plates before incubated with MON@PG (50 μM), meanwhile the plates were either exposed to radiation or not. After 24 h, following the manufacturer's protocols, the treated cells were collected and tested by a MMP assay kits with JC-1 (Beyotime Biotech, China) and a mitoROS kit (AAT Bioquest, China).

2.12 Detection of mitochondrial permeability transition pore

GC cells (MFC) were first seeded in CLSM culture dishes and cultured for 12 h, then incubated with MON@PG (50 μM) for 4 h before irradiation. After 24 h, following the protocol of a mitochondrial permeability transition pore (mPTP) assay kit (Beyotime Biotech, China), GC cells were stained by Calcein AM, then fixed in paraformaldehyde (4%) for 15 min and labeled with Hoechst for 20 min before CLSM imaging (LSM 880, Zeiss, Germany).

2.13 Detection of lipid peroxidation

MFC cells were seeded in a CLSM culture dishes and cultured for 24 h. Then, cells were incubated for 12 h with the PBS and MON@PG with or without X-ray irradiation (4 Gy). To measure lipid peroxidation, the cells were incubated with C11 BODIPY 581/591 (Abclonal, China) for 1 h and washed twice with PBS to remove excess dye. Representative images were subsequently acquired by CLSM. Additionally, C11-BODIPY591/581 staining was combined with flow cytometry to measure lipid peroxidation in MKN45 cells. Furthermore MDA level was quantified *via* a thiobarbituric acid assay kit (Beyotime Biotech, China) as per manufacturer's instructions.

2.14 Western blot analysis

GPX4 and Cleaved Caspase-3 protein (17KD) expression level were assessed by Western blot analysis with GAPDH as internal reference control. Protein extraction from pre-treated cells (MFC or MKN45) were separated by SDS-PAGE and transferred onto polyvinylideneifluoride (PVDF) membranes before PBS-5% BSA blocking. After incubating at 4°C with GPX4 (1:500, Abcam, USA), Anti-Cleaved Caspase-3 (ab2302, 1:500, Abcam), and GAPDH (1:1000, Abcam) antibodies overnight, the PVDF membranes were then washed and incubated with secondary antibodies (HRP Conjugate, 1:2000, Abcam) at room temperature before

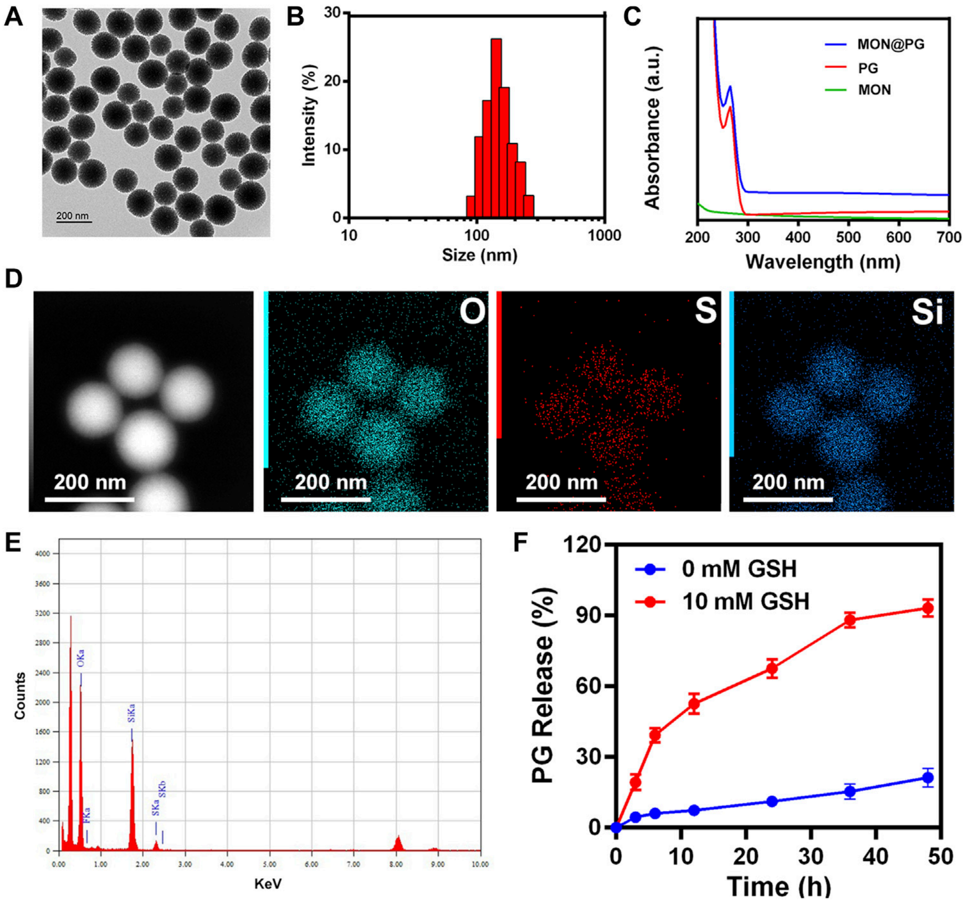

FIGURE 1
Characterization of MON@PG nanoplatform. **(A)** TEM images of MON@PG nanoplatform. **(B)** Dynamic light scattering (DLS) of MON@PG. **(C)** UV–Vis spectra of free PG and MON@PG. **(D)** Element mapping images of MON. **(E)** EDS spectrogram of MON. **(F)** Drug release profiles of MON@PG in the present or absent of 10 mM GSH. Outcomes are presented as mean ± SD (n = 3).

visualization under chemiluminescent Western blot detection System (Tanon, China).

2.15 *In vivo* antitumor effect of MON@PG

All animal protocols were approved by Animal Care and Use Committeeof Southern Medical University. For tumor inoculation, female Balb/c mice (age 4–5 weeks) were subcutaneously injected with MFC cells (1×10^7) in the left hind limb. When the tumor volume reached approximately 40 mm^3, the mouse tumor-bearing models were randomized into four groups: PBS, RT, MON@PG, MON@PG plus RT. The mice were subsequently injected with nanocompsites *via* the tail vein at 14 and 18 days after tumor-bearing, and then treated twice with or without 4 Gy of X-ray at 15 and 19 days after tumor-bearing. Tumor volume was recorded every 2 days until sacrifice and calculated as follows: length × $width^2 \times 0.5$. On day 26, the tumors were harvested and weighted for HE staining and TUNEL immunohistochemistry.

2.16 Statistical analysis

Results are represented as mean ± standard deviation (SD). Representative immunofluorescence images are shown in the figures. The therapeutic differences between two treatment groups were analyzed by Student's t-test. To analyze the differences among multiple groups, one-way ANOVA and Tukey's HSD Test for multiple comparisons was utilized. Differences between groups were calculated *via* SPSS 20.0 (IBM Corp., USA) and considered statistically significant when *p*-values <0.05. At least three times each of the experiments were repeated.

3 Results and discussion

3.1 Synthesis and characterization of MON@PG

According to earlier studies (Lu et al., 2018; Guo W et al., 2020), MON nanocarrier were constructed using the sol-gel technique and

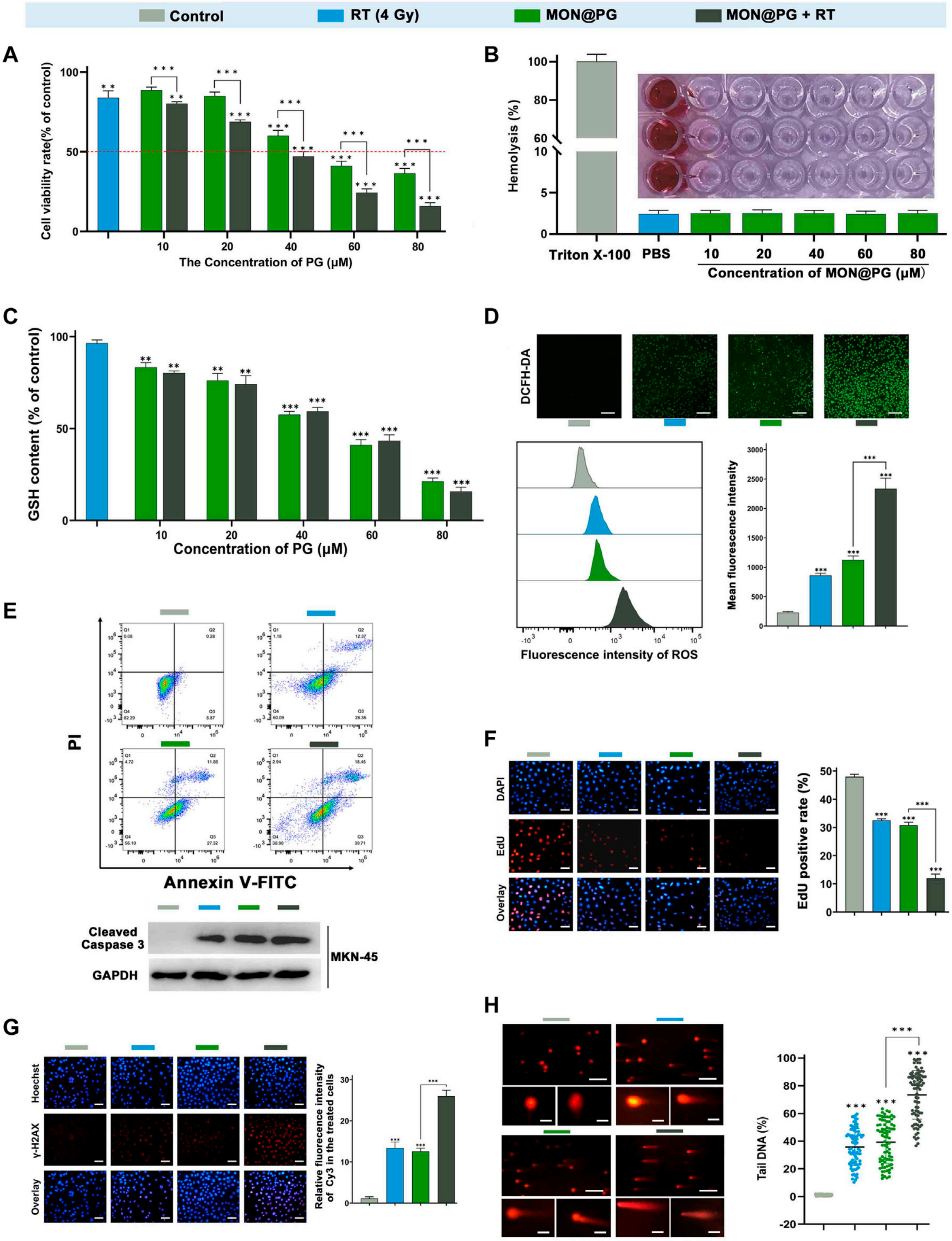

FIGURE 2
In vitro antitumor efficacy of MON@PG in MFC cells with different treatments. **(A)** Cell viabilities of different treatment groups measured by CCK-8 assays. **(B)** Hemolysis assay of different concentrations of MON@PG incubated with red blood cells extracted from rabbits. **(C)** The GSH content of MFC cells following treatments of various concentrations of MON@PG with or without RT. **(D)** Fluorescence microscopic images of DCFH-DA stained MFC cells (upper). Flow cytometry (lower left) and related analysis (lower right) of DCFH-DA fluorescence following different treatments. Scale bars: 100 μm. **(E)** Cell apoptosis flow cytometry (upper) of MFC and Western blotting of cleaved caspase-3 in MKN45 cells (lower) following different treatments. **(F)** EdU images (left) and associated analysis (right) in different treatment groups. Scale bars: 30 μm. **(G)** γH2AX immunofluorescence images (left) and associated analysis (right) of DNA damage levels in different treatment groups. **(H)** Comet assay of PI fluorescence stained DNA damage accumulation (left) and related analysis (right) in different treatment groups. Scale bars: 200 μm; embedded inset: 5 μm.Scale bars: 30 μm. Outcomes are displayed as mean ± SD (n = 3, $^{***}p < 0.001$).

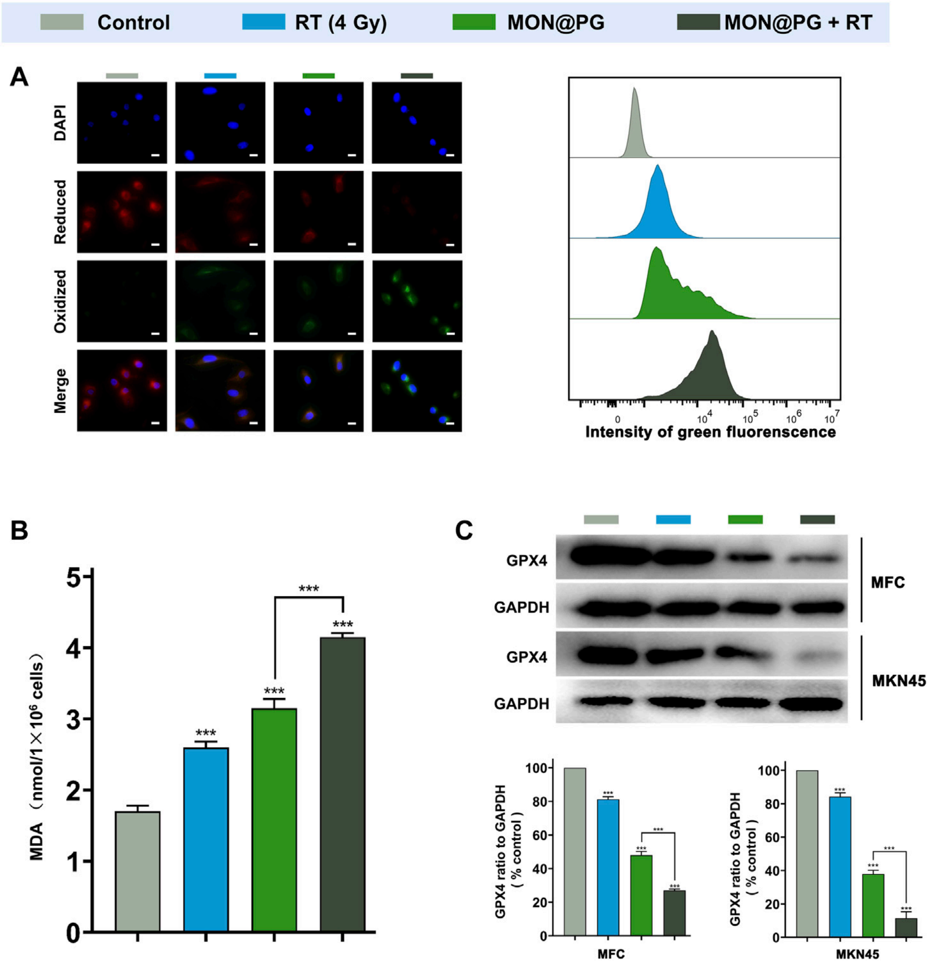

FIGURE 3
Ferroptosis levels of MFC cells with various treatments. **(A)** Representative CLSM fluorescence images of C11-BODIPY (581/591) reported lipid peroxidation (left) and flow cytometry of its green fluorescence (right). Scale bars: 10 μm. **(B)** MDA assay of MFC cells following different treatments. **(C)** Western blot Imaging and Analysis of GPX4 protein expression in both MFC and MKN45 cells. Outcomes are displayed as mean ± SD (n = 3, ***$p < 0.001$).

ethanol. The consistent spherical morphology and monodispersion of MON@PG were visible in TEM pictures, with the average particle size being around 142 nm (Figure 1A&B). The absorption spectrum of MON@PG revealed PG specific absorption (peak at 280 nm) using UV-Vis spectroscopy (Figure 1C). After centrifuging and magnetically stirring PG into the produced MON nanocarrier to create MON@PG nanocomplexes, the presence of Si, O, and S in the mesoporous nanostructure is highlighted in the EDS spectra of MON (Figure 1E), which is corroborated by element mapping images (Figure 1D). Together, these findings demonstrated that the construction of PG-loaded MON nanocomposites was successful.

Despite progress in nanodrug delivery systems, effective cancer targeting and immediate drug release continues to be a challenge (Lu et al., 2018). In this study, as the BTESePD and tetraethoxysilane in MON framework provide rich selenium content to form coordination sites for PG, the disulfide rebridging nanoparticles displayed biodegradable characteristic in GSH-containing environment. The rapid release of PG (>60% after 20 h) was achieved in the presence of 10 mM GSH, which resembled the intracellular reductive environment, whereas in the absence of GSH, less than 30% of PG were released after 50 h (Figure 1F). Since GC cells and its microenvironment possess rich GSH content (Goroshinskaya et al., 2020), the MON@PG nanosystem proved to be reduction-sensitive and active tumor-targeting.

3.2 *In vitro* radiosensitizing antitumor effect of MON@PG

As reactive metabolic byproducts of the cellular respiratory chain, ROS are ubiquitous signaling mediators in cell stress and development. Cellular redox equilibrium and metabolic homeostasis could be disturbed as a direct result of dynamic ROS generation. The connections among ROS-meditated signaling pathway crosstalk, TME transformation in GC, epithelial-mesenchymal transition, radio-resistance, and recurrence of GC has been extensively established (Gu et al., 2018). To protect mammalian cells from ROS-induced oxidative damage, GSH as a predominant non-enzyme antioxidant is vital for the reactions needed to eliminate

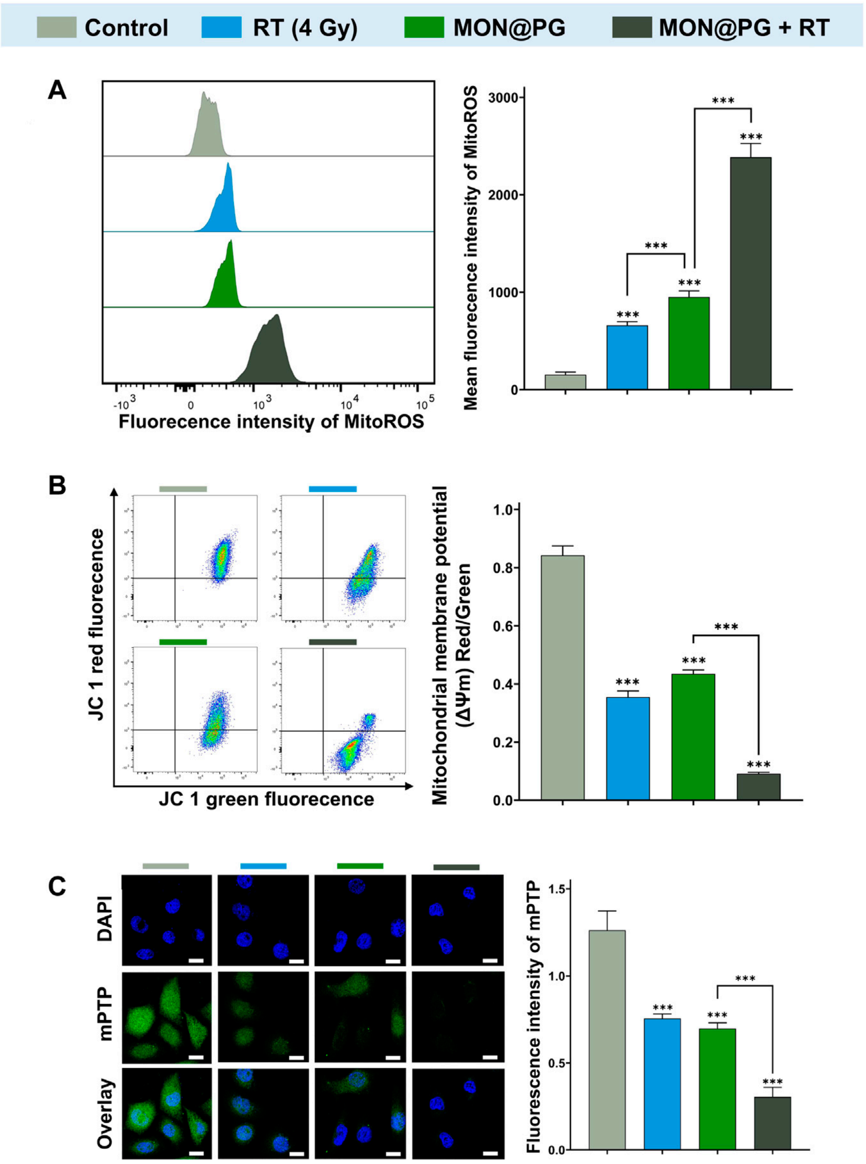

FIGURE 4
Mitochondrial dysfunction induced by MON@PG combined with irradiation. **(A)** MitoROS level of different treatment groups: flow cytometry imaging (left) and associated analysis (right). **(B)** Flow cytometry of JC-1 fluorescence (left) and associated statistical analysis (right) of different treatment groups. **(C)** Representative mPTP CLSM fluorescence images of treated GC cells (left) and associated statistical analysis (right). Scale bars: 10 μm. Outcomes are displayed as mean ± SD (n = 3, ****p* < 0.001).

cascading ROS storms. Researchers have attempted to diminish radioresistance of cancer cell by deactivating GSH-orchestrated DSBs self-repair (Mao et al., 2022; Zhou et al., 2022). Many Innovative nanocatalytic reagents stimulated massive ROS production which surmounted GSH-coordinated antioxidation to initiate cytochrome c release, mitochondrial malfunction, and eventually apoptosis of radioresistant cancer cells (Liu et al., 2022).

As a natural substance, PG has been use as a additive in drug manufacturing. By disrupting the balance of ROS and GSH, pyrogallol has been shown to have antitumor effect against lung cancer cells, HeLa cervical adenocarcinoma cells, colon cancer cells and gastric cancer cells (Mahmoud et al., 2022). According to Park WH et al., considerable ROS augmentation was seen along with dose-dependent suppression of cell proliferation in SNU-484 gastric cancer cells. The GSH content, however, is only depleted when the PG concentration rises to 80 μM (Park et al., 2008).

In this study, a CCK-8 kit was employed to determine the vitality of GC cells following various intervention to quantify the cytotoxity effect. Since it has been established that MON has excellent biocompatibility (Guo et al., 2022), the cytotoxicity MON@PG exhibited was consistent with previous study (Figure 2A) (Park et al., 2008). Besides, the results also showed that MON@PG nanocomposites did not cause obvious hemolysis at any tested concentrations (Figure 2B). Once combined to irradiation, a dose-dependent increase in MON@PG's cytotoxicity was observed in MFC cells. To evaluate GSH depletion property of

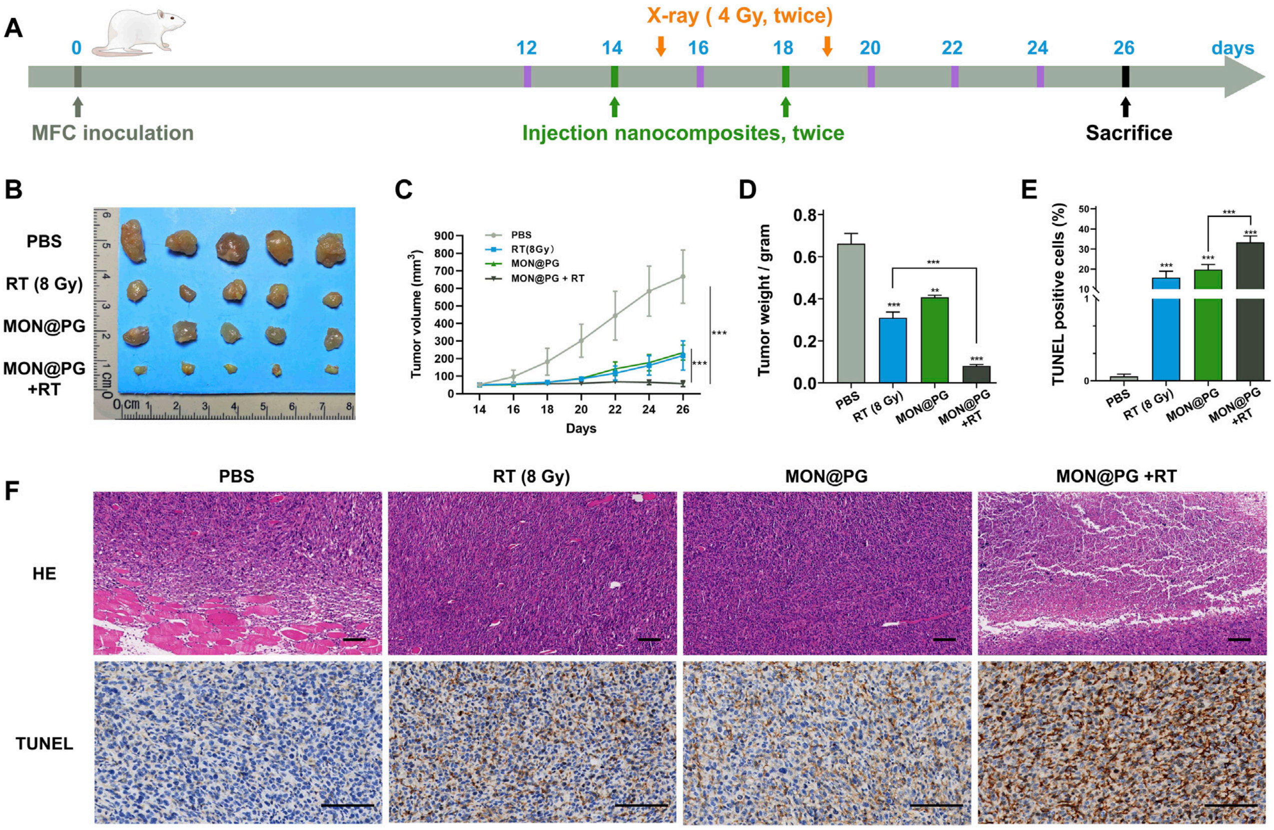

FIGURE 5

The therapeutic efficacy of MON@PG combined with radiotherapy in MFC CDX models. **(A)** Schematic illustration of therapeutic experiments CDX models. The arrows point out the schedule of tail-vein injection (green) and X-ray radiation (orange). **(B)** Measurements of tumor masses after sacrifice in different treatment groups (n = 5). **(C)** Tumor volume growth curves of mice from different groups. **(D)** Weights of tumors from different groups. **(E)** Quantitative analysis of percentage of TUNEL positive cells. **(F)** HE and TUNEL staining images of tumors samples in different treatment groups. Scale barss: 100 μm. Statistical analysis: two-tailed, unpaired Student's t-test, $^{***}p < 0.001$.

MON@PG, a panel of different concentration of MON@PG was applied to treat cells following RT protocol. The GSH content of the cells treated with MON@PG progressively fell from 83.3% to 21.1% as the concentration increased while the MON@PG plus RT group showed a decrease from 80.2% to 17.7%, which show no significant change. Moreover 4 Gy irradiation alone only have a minimal effect on GSH content after 24 h (Figure 2C), suggesting MON@PG possess excellent GSH consumption ability independent of irradiation. Considering this, MON@PG containing PG (50 mM, 10 μg/mL) was selected for the following tests.

2′,7′-dichlorofluorescin diacetate (DCFH-DA) fluorogenic dye, which is cell permeant before deacetylated by esterases to a non-fluorescent compound, was further employed to measure intracellular ROS level. As shown in Figure 2D, control group showed weak fluorescence, while the RT and MON@PG groups showed minimal intensity. Once combined with MON@PG to ionizing radiation, the intracellular green fluorescence significantly increased, indicating that MON@PG and RT could generate ROS synergistically. Furthermore, the intracellular ROS intensity was quantified using flow cytometry. Correspondingly, MON@PG plus irradiation group showed roughly 2.2 and 2.6 fold increase of ROS level respectively, compared to control group (Figure 2D). Taken together, MON@PG significantly enhance the intracellular ROS burst generated by ionizing radiation. Furthermore, a drastically decreased GSH concentration limited cell radical scavenging activity and allowed cascading ROS attack, activating apoptosis signalling pathways (Redza-Dutordoir and Averill-Bates, 2016). As shown in Figure 2E, MON@PG plus RT led to 1.6-fold greater level of overall apoptosis (about 57.9%) than RT and 1.6-fold higher level than MON@PG (about 39%) respectively. Furthermore, the apoptosis-inducing effects was confirmed by Western blot analysis as combined treatment group showed highest expression of active caspase-3, which is a key mediator of apoptosis-inducing protease pathway (Figure 2E) (Porter and Janicke, 1999).

EdU test was further applied to measure the inhibition of cell proliferation following different MON@PG treatments. EdU (5-ethynyl-2′-deoxyuridine), a nucleoside analog of thymidine, can be specifically incorporated into DNA of dividing cells to measure *de novo* DNA synthesis. We discovered that the EdU fluorescence (red) positive cells in MON@PG with irradiation group were significantly lower than that of MON@PG or radiation alone, suggesting that MON@PG improved the antitumor effect of irradiation (Figure 2F). Furthermore, the expression of γ-H2AX was measured since it is a

DSB sensitive biomarker that is significantly expressed throughout the nucleotide excision repair process and therefore indicates DNA damage (Mah et al., 2010). Because of the combination therapy's ability to produce ROS which can damage nuclear DNA, MON@PG plus RT increased the expression level of γ-H2AX by 1.6-times higher than RT group and by 1.8-folds compared to MON@PG alone (Figure 2G). Furthermore, the comet assay was performed to examine double DNA strand breaks. When DNA is damaged, the DNA pieces move and create comet-like patterns (Olive and Banath, 2006). In MFC cells treated with MON@PG plus irradiation, the frequency of DNA strand rupture was 72.82%, and the DNA fragments exhibited comet-shaped tails instead of the smooth edges and complete nuclei in control group (Figure 2H). When coupled with RT irradiation, the MON@PG generated an amplified lethal effect on cancer cells by significantly tilting redox balance, which may directly induce ferroptosis (Bano et al., 2022).

3.3 *In vitro* MON@PG plus RT induced ferroptosis

Previous studys have shown that anti-oxidant GSH acts as cofactor with GPX4 to reduce lipid hydroperoxides. The depletion of GSH deactivates GPX4 leading to cumulation of ROS-mediated lipid peroxide and ferroptotic cell death (Lu, 2009; Dixon et al., 2014; Hassannia et al., 2019). To further evaluate the cytotoxic lipid peroxidation triggerd by MON@PG, the C11-BODIPY lipid peroxidation sensor was used to detect the peroxidated PUFA products in the MFC cells treated with PBS, MON@PG and irradiation. Oxidied C11-BODIPY causes a shift of fluorescence intensity from 590 nm (red) to 510 nm (green). As seen in Figure 3A, MON@PG plus RT group showd the strongest green fluorescence whcih is about 2 folds of the intensity in RT and MON@PG group, indicating the highest lipid peroxidation level among all groups. This finding was further confirmed by C11-BODIPY staining with flow cytometery analyses. Additionally, MDA as the final products of PUFA peroxidation is commonly used as a marker of oxidative stress in cells (Tsaturyan et al., 2022). As illustrated in Figure 3B, compared with other treatment groups, the MDA level increased significantly in MON@PG plus RT group. Furthermore, GPX4 employs GSH to neutralize the toxity of PUFA peroxides and protects cells from ferroptosis (Zhang Y. et al., 2021). The expression of GPX4 protein in MON@PG plus irradiation group showed the lowest expression in this study (Figure 3C), suggesting that GPX4 was downregulated after MON@PG plus radiation exposure. From these results, we inferred that the MON@PG-sensitized RT significantly induced ferroptosis of tumor cells by disrupted redox homeostasis and GPX4 downregulation, which may lay an experimental foundation for application of MON@PG in future chemoradiotherapy.

3.4 MON@PG induced mitochondrial dysfunction

Since the mitochondrial electron transport chain is the primary location of ROS synthesis, it has been established that mitochondria is one of the a main targets for ROS damage (West et al., 2011). Studies have revealed that bacterial DNA-like motifs exist in mitochondrial DNA (mtDNA), and that these motifs are essential for the activation of antigen-presenting dendritic cells for the innate antitumor immune response (Fogal et al., 2010; Gao et al., 2017). Since PG can target mitochondria in a variety of cancers according to earlier findings (Park, 2016; Revathi et al., 2019), mitochondria may be one of the possible targets of MON@PG plus radiation treatment. To detect ROS production in the mitochondria, a red superoxide indicator (MitoROS 580) that is tailored to mitochondria ROS detection was utilized. As depicted in Figure 4A, only mild red fluorescence of MitoROS 580 was observed in the MON@PG or RT group compared to control group, however a potent red fluorescence was observed in MON@PG treated cells once exposed to radiation, indicating that A significant amount of ROS was produced in cell mitochondria. Loss of MMP (ΔΨm), a useful biomarker for evaluating mitochondrial function, may indicate a change in mitochondrial permeability (West et al., 2011; Zacharioudakis and Gavathiotis, 2022). Therefore, the MMP of different MON@PG treatments was measured *via* flow cytometry by calculating the ratio of fluorescence intensity (red/green) after JC-1 labeling. The MON@PG plus irradiation groups had the lowest ratio compared to RT and MON@PG alone group, further demonstrating that MON@PG sensitized RT can significantly increase the permeability of mitochondrial membrane of targeted cells (Figure 4B).

Cytosolic mtDNA, a especially robust pathogen related molecular patterns that activates numerous innate immune sensors, is particularly susceptible to mitoROS attack due to shortage of histone formation (Guo Y et al., 2020). Since mPTP is essential for mtDNA to disseminate from mitochondria into cytosol, an mPTP assay kit was applied to measure the impact of MON@PG-induced MitoROS on the mitochondrial membrane permeability. This assay employs cobalt chloride to quench the Calcein fluorescence except for mitochondrial matrix after staining the entire cell with Calcein AM (green fluorescence). Cobalt cannot penetrate if the inner mitochondrial membrane is intact, and the mitochondrial matrix glows green. The Calcein fluorescence is muted and no fluorescence is seen if the mitochondrial membrane is damaged. In the present study, almost no green fluorescence was seen in the MON@PG plus irradiation groups compared to control group and monotherapeutic groups (Figure 4C), showing that the combined treatment considerably damaged the mitochondrial structural integrity and its membrane barrier. Taken together, MON@PG may serve as a potential radiosensitizer for the radiotherapy of gastric cancer. However, it is still unclear how MON@PG acts as an antitumor nanoplatform under irraditaion in experimental animal models.

3.5 *In vivo* radiosensitizing effects of MON@PG

The antitumor effect of MON@PG was evaluated on mouse cancer models *in vivo*. Balb/c mice models with MFC cell derived xenograft were established and randomized into four groups when the tumor volume reached 40 mm^3 (Figure 5A). During a 26-day observation period along with irradiation and intravenous injection of PBS and MON@PG, tumor growth parameters was measured every 2 days. MON@PG plus RT group showed a significant reduction in tumor growth with a 91.5% decrease in tumor volume compared with control group, whereas the RT alone group showed an mild antitumor effect (67.4%) (Figure 5B&C). Furthermore, average tumor weight in MON@PG plus RT group significantly decreased compared to other groups (Figure 5D), suggesting that MON@PG may serve as a potential radiosensitizer of *in vivo* tumor growth under radiotherapy.

To further verify the promising therapeutic effect pathologically, tumor samples were stained with Hematoxylin-Eosin Stain (HE) and terminal deoxynucleotidyl transferase-mediated deoxyuridine triphosphate-nick end labeling (TUNEL) staining. MON@PG plus RT group exhibited profound necrosis on HE staing while control group showed cancer cells that spreads into muscle. In TUNEL assay that has been designed to recognize DNA degradation in apoptotic tissues, the tumor samples from MON@PG plus RT group showed increased cancer cell apoptosis (dark brown staining) compared with other groups (Figure 5E &F). These results indicated that the MON@PG were highly effective in radiotherapy for gastric cancer.

4 Conclusion

Herein, we constructed an nanoplatform by loading PG into mesoporous organosilica nanoparticles to boost both intracellular and mitochondrial ROS level, deplete GSH and downregulate GPX4. This GSH-responsive degradable nanoplatform possess tumor targeting property and elevates intracellular ROS accumulation, which causes DNA fragmentation and mitochondrial dysfunction. Hence, the MON@PG nanoplatform successfully inhibited cancer proliferation *in vitro* and *in vivo* by inducing ferroptotic cell death to sensitized radiotherapy, offering a promising alternative chemoradiotherapy for late-stage gastric cancer treatment.

Data availability statement

The original contributions presented in the study are included in the article/Supplementary Material, further inquiries can be directed to the corresponding authors.

Ethics statement

The animal study was reviewed and approved by Animal Care and Use Committee of Southern Medical University.

Author contributions

Conceptualization: JX, YH and ZC, GL and YH; Data curation: HW, HN and XL; Funding acquisition, GL and YH; Investigation: HW, HN, XL, GL and YH; Methodology: HW, HN, XL, NZ, JX, YH and ZC; Project administration: GL and YH; Supervision: GL and YH; Writing–original draft: HW; Writing–review and editing: GL and YH. The published version of the manuscript have been read and consented by all authors.

Funding

This work is sponsored by National Natural Science Foundation of China (82272062; 82001948; 81971746), Guangdong Provincial Key Laboratory of Precision Medicine for Gastrointestinal Cancer (2020B121201004), Guangdong Basic and Applied Basic Research Foundation (2022A1515010462), Key-Area Research and Development Program of Guangdong Province (2021B0101420005), Guangdong Provincial Major Talents Project (2019JC05Y361), Guangzhou Basic and Applied Basic Research Foundation (SL 2022A04J02053).

Acknowledgments

The authors would like to expressed their deep appreciation to Wenxiang Feng for their efforts in nanoparticle synthesis and Weihong Guo for the technical guidance.

Conflict of interest

The authors declare that the research was conducted in the absence of any commercial or financial relationships that could be construed as a potential conflict of interest.

Publisher's note

References

Bano, I., Horky, P., Abbas, S. Q., Majid, M., Bilal, A. H. M., Ali, F., et al. (2022). Ferroptosis: A New road towards cancer management. *Molecules* 27 (7), 2129. doi:10.3390/molecules27072129

Brown, J. M., and Wilson, W. R. (2004). Exploiting tumour hypoxia in cancer treatment. *Nat. Rev. Cancer* 4 (6), 437–447. doi:10.1038/nrc1367

Chiaravalli, M., Spring, A., Agostini, A., Piro, G., Carbone, C., and Tortora, G. (2022). Immunogenic cell death: An emerging target in gastrointestinal cancers. *Cells* 11 (19), 3033. doi:10.3390/cells11193033

Dixon, S. J., Patel, D. N., Welsch, M., Skouta, R., Lee, E. D., Hayano, M., et al. (2014). Pharmacological inhibition of cystine-glutamate exchange induces endoplasmic reticulum stress and ferroptosis. *Elife* 3, e02523. doi:10.7554/eLife.02523

Dou, Y., Liu, Y., Zhao, F., Guo, Y., Li, X., Wu, M., et al. (2018). Radiation-responsive scintillating nanotheranostics for reduced hypoxic radioresistance under ROS/NO-mediated tumor microenvironment regulation. *Theranostics* 8 (21), 5870–5889. doi:10.7150/thno.27351

Espinosa, A., Curcio, A., Cabana, S., Radtke, G., Bugnet, M., Kolosnjaj-Tabi, J., et al. (2018). Intracellular biodegradation of Ag nanoparticles, storage in ferritin, and protection by a Au shell for enhanced photothermal therapy. *ACS Nano* 12 (7), 6523–6535. doi:10.1021/acsnano.8b00482

Finger, E. C., and Giaccia, A. J. (2010). Hypoxia, inflammation, and the tumor microenvironment in metastatic disease. *Cancer Metastasis Rev.* 29 (2), 285–293. doi:10.1007/s10555-010-9224-5

Fogal, V., Richardson, A. D., Karmali, P. P., Scheffler, I. E., Smith, J. W., and Ruoslahti, E. (2010). Mitochondrial p32 protein is a critical regulator of tumor metabolism via maintenance of oxidative phosphorylation. *Mol. Cell Biol.* 30 (6), 1303–1318. doi:10.1128/MCB.01101-09

Gao, Z., Li, Y., Wang, F., Huang, T., Fan, K., Zhang, Y., et al. (2017). Mitochondrial dynamics controls anti-tumour innate immunity by regulating CHIP-IRF1 axis stability. *Nat. Commun.* 8 (1), 1805. doi:10.1038/s41467-017-01919-0

Geng, L., Donnelly, E., McMahon, G., Lin, P. C., Sierra-Rivera, E., Oshinka, H., et al. (2001). Inhibition of vascular endothelial growth factor receptor signaling leads to reversal of tumor resistance to radiotherapy. *Cancer Res.* 61 (6), 2413–2419.

Goroshinskaya, I. A., Surikova, E. I., Frantsiyants, E. M., Nemashkalova, L. A., Kachesova, P. S., Chudilova, A. V., et al. (2020). Glutathione system in the blood of gastric cancer patients with various tumor histotypes and prevalence of the disease. *J. Clin. Oncol.* 38 (15), e16534. doi:10.1200/JCO.2020.38.15_suppl.e16534

Gu, H., Huang, T., Shen, Y., Liu, Y., Zhou, F., Jin, Y., et al. (2018). Reactive oxygen species-mediated tumor microenvironment transformation: The mechanism of radioresistant gastric cancer. *Oxid. Med. Cell Longev.* 2018, 1–8. doi:10.1155/2018/5801209

Guo W, W., Chen, Z., Chen, J., Feng, X., Yang, Y., Huang, H., et al. (2020). Biodegradable hollow mesoporous organosilica nanotheranostics (HMON) for multi-mode imaging and mild photo-therapeutic-induced mitochondrial damage on gastric cancer. *J. Nanobiotechnology* 18 (1), 99. doi:10.1186/s12951-020-00653-y

Guo, W., Chen, Z., Li, Z., Huang, H., Ren, Y., Zhao, B., et al. (2022). Improved immunotherapy for gastric cancer by nanocomposites with capability of triggering Dual-Damage of Nuclear/Mitochondrial DNA and cGAS/STING-Mediated innate immunity. *Chem. Eng. J.* 443, 136428. doi:10.1016/j.cej.2022.136428

Guo Y, Y., Gu, R., Gan, D., Hu, F., Li, G., and Xu, G. (2020). Mitochondrial DNA drives noncanonical inflammation activation via cGAS-STING signaling pathway in retinal microvascular endothelial cells. *Cell Commun. Signal* 18 (1), 172. doi:10.1186/s12964-020-00637-3

Harada, H., Inoue, M., Itasaka, S., Hirota, K., Morinibu, A., Shinomiya, K., et al. (2012). Cancer cells that survive radiation therapy acquire HIF-1 activity and translocate towards tumour blood vessels. *Nat. Commun.* 3, 783. doi:10.1038/ncomms1786

Hassannia, B., Vandenabeele, P., and Vanden Berghe, T. (2019). Targeting ferroptosis to iron out cancer. *Cancer Cell* 35 (6), 830–849. doi:10.1016/j.ccell.2019.04.002

Lee, J., Byun, H. K., Koom, W. S., Lee, Y. C., and Seong, J. (2021). Efficacy of radiotherapy for gastric bleeding associated with advanced gastric cancer. *Radiat. Oncol.* 16 (1), 161. doi:10.1186/s13014-021-01884-5

Li, N., Yu, L., Wang, J., Gao, X., Chen, Y., Pan, W., et al. (2018). A mitochondria-targeted nanoradiosensitizer activating reactive oxygen species burst for enhanced radiation therapy. *Chem. Sci.* 9 (12), 3159–3164. doi:10.1039/c7sc04458e

Liu, T., Sun, L., Zhang, Y., Wang, Y., and Zheng, J. (2022). Imbalanced GSH/ROS and sequential cell death. *J. Biochem. Mol. Toxicol.* 36 (1), e22942. doi:10.1002/jbt.22942

Lordick, F., Nilsson, M., and Leong, T. (2021). Adjuvant radiotherapy for gastric cancer-end of the road? *Ann. Oncol.* 32 (3), 287–289. doi:10.1016/j.annonc.2020.12.006

Lu, N., Fan, W., Yi, X., Wang, S., Wang, Z., Tian, R., et al. (2018). Biodegradable hollow mesoporous organosilica nanotheranostics for mild hyperthermia-induced bubble-enhanced oxygen-sensitized radiotherapy. *ACS Nano* 12 (2), 1580–1591. doi:10.1021/acsnano.7b08103

Lu, S. C. (2009). Regulation of glutathione synthesis. *Mol. Asp. Med.* 30 (1-2), 42–59. doi:10.1016/j.mam.2008.05.005

Lyu, M., Zhu, D., Kong, X., Yang, Y., Ding, S., Zhou, Y., et al. (2020). Glutathione-depleting nanoenzyme and glucose oxidase combination for hypoxia modulation and radiotherapy enhancement. *Adv. Healthc. Mater* 9 (11), e1901819. doi:10.1002/adhm.201901819

Mah, L. J., El-Osta, A., and Karagiannis, T. C. (2010). γH2AX: A sensitive molecular marker of DNA damage and repair. *Leukemia* 24 (4), 679–686. doi:10.1038/leu.2010.6

Mahmoud, G. A., Ali, H. E., and Radwan, R. R. (2022). Design of pH-responsive polymeric nanocarrier for targeted delivery of pyrogallol with enhanced antitumor potential in colon cancer. *Arch. Biochem. Biophys.* 731, 109431. doi:10.1016/j.abb.2022.109431

Mao, H., Wen, Y., Yu, Y., Li, H., Wang, J., and Sun, B. (2022). Bioinspired nanocatalytic tumor therapy by simultaneous reactive oxygen species generation enhancement and glutamine pathway-mediated glutathione depletion. *J. Mater Chem. B* 11, 131–143. doi:10.1039/d2tb02194c

Mao, Y., and Zhang, T. (2022). Knockdown of SHMT2 enhances the sensitivity of gastric cancer cells to radiotherapy through the Wnt/β-catenin pathway. *Open Life Sci.* 17 (1), 1249–1255. doi:10.1515/biol-2022-0480

Mondlane, G., Ureba, A., Gubanski, M., Lind, P. A., and Siegbahn, A. (2018). Estimation of risk of normal-tissue toxicity following gastric cancer radiotherapy with photon- or scanned proton-beams. *Anticancer Res.* 38 (5), 2619–2625. doi:10.21873/anticanres.12503

Olive, P. L., and Banáth, J. P. (2006). The comet assay: a method to measure DNA damage in individual cells. *Nat. Protoc.* 1 (1), 23–9. doi:10.1038/nprot.2006.5

Park, W. H., Park, M. N., Han, Y. H., and Kim, S. W. (2008). Pyrogallol inhibits the growth of gastric cancer SNU-484 cells via induction of apoptosis. *Int. J. Mol. Med.* 22 (2), 263–268.

Park, W. H. (2016). Pyrogallol induces the death of human pulmonary fibroblast cells through ROS increase and GSH depletion. *Int. J. Oncol.* 49 (2), 785–792. doi:10.3892/ijo.2016.3543

Porter, A. G., and Janicke, R. U. (1999). Emerging roles of caspase-3 in apoptosis. *Cell Death Differ.* 6 (2), 99–104. doi:10.1038/sj.cdd.4400476

Redza-Dutordoir, M., and Averill-Bates, D. A. (2016). Activation of apoptosis signalling pathways by reactive oxygen species. *Biochim. Biophys. Acta* 1863 (12), 2977–2992. doi:10.1016/j.bbamcr.2016.09.012

Revathi, S., Hakkim, F. L., Ramesh Kumar, N., Bakshi, H. A., Sangilimuthu, A. Y., Tambuwala, M. M., et al. (2019). *In vivo* anti cancer potential of pyrogallol in murine model of colon cancer. *Asian Pac J. Cancer Prev.* 20 (9), 2645–2651. doi:10.31557/apjcp.2019.20.9.2645

Rouschop, K. M., Dubois, L. J., Keulers, T. G., van den Beucken, T., Lambin, P., Bussink, J., et al. (2013). PERK/eIF2α signaling protects therapy resistant hypoxic cells through induction of glutathione synthesis and protection against ROS. *Proc. Natl. Acad. Sci. U. S. A.* 110 (12), 4622–4627. doi:10.1073/pnas.1210633110

Siegel, R. L., Miller, K. D., Fuchs, H. E., and Jemal, A. (2022). Cancer statistics, 2022. *CA Cancer J. Clin.* 72 (1), 7–33. doi:10.3322/caac.21708

Takeda, K., Sakayauchi, T., Kubozono, M., Katagiri, Y., Umezawa, R., Yamamoto, T., et al. (2022). Palliative radiotherapy for gastric cancer bleeding: A multi-institutional retrospective study. *BMC Palliat. Care* 21 (1), 52. doi:10.1186/s12904-022-00943-2

Tsaturyan, V., Poghosyan, A., Toczylowski, M., and Pepoyan, A. (2022). Evaluation of malondialdehyde levels, oxidative stress and host-bacteria interactions: *Escherichia coli* and Salmonella derby. *Cells* 11 (19), 2989. doi:10.3390/cells11192989

Wang, J., Sun, X., Mao, W., Sun, W., Tang, J., Sui, M., et al. (2013). Tumor redox heterogeneity-responsive prodrug nanocapsules for cancer chemotherapy. *Adv. Mater* 25 (27), 3670–3676. doi:10.1002/adma.201300929

Wang, X., Wang, W. H., Wang, S. L., Song, Y. W., Liu, Y. P., Tang, Y., et al. (2021). Efficacy and toxicity of capecitabine combined with intensity-modulated radiotherapy after D1/D2 lymph node dissection in patients with gastric cancer. *World J. Gastrointest. Oncol.* 13 (10), 1532–1543. doi:10.4251/wjgo.v13.i10.1532

West, A. P., Shadel, G. S., and Ghosh, S. (2011). Mitochondria in innate immune responses. *Nat. Rev. Immunol.* 11 (6), 389–402. doi:10.1038/nri2975

Xu, J., Han, W., Yang, P., Jia, T., Dong, S., Bi, H., et al. (2018). Tumor microenvironment-responsive mesoporous MnO2-coated upconversion nanoplatform for self-enhanced tumor theranostics. *Adv. Funct. Mater.* 28 (36), 1803804. doi:10.1002/adfm.201803804

Yang, P., Luo, X., Li, J., Zhang, T., Gao, X., Hua, J., et al. (2021). Ionizing radiation upregulates glutamine metabolism and induces cell death via accumulation of reactive oxygen species. *Oxid. Med. Cell Longev.* 2021, 1–22. doi:10.1155/2021/5826932

Yoshimura, M., Itasaka, S., Harada, H., and Hiraoka, M. (2013). Microenvironment and radiation therapy. *Biomed. Res. Int.* 2013, 1–13. doi:10.1155/2013/685308

Yu, J., Huang, C., Sun, Y., Su, X., Cao, H., Hu, J., et al. (2019). Effect of laparoscopic vs open distal gastrectomy on 3-year disease-free survival in patients with locally advanced gastric cancer: The CLASS-01 randomized clinical trial. *JAMA* 321 (20), 1983–1992. doi:10.1001/jama.2019.5359

Yu, L., Chen, Y., Lin, H., Du, W., Chen, H., and Shi, J. (2018a). Ultrasmall mesoporous organosilica nanoparticles: Morphology modulations and redox-responsive biodegradability for tumor-specific drug delivery. *Biomaterials* 161, 292–305. doi:10.1016/j.biomaterials.2018.01.046

Yu, N., Wang, Z., Zhang, J., Liu, Z., Zhu, B., Yu, J., et al. (2018b). Thiol-capped Bi nanoparticles as stable and all-in-one type theranostic nanoagents for tumor imaging and thermoradiotherapy. *Biomaterials* 161, 279–291. doi:10.1016/j.biomaterials.2018.01.047

Zacharioudakis, E., and Gavathiotis, E. (2022). Mitochondrial dynamics proteins as emerging drug targets. *Trends Pharmacol. Sci.* 44, 112–127. doi:10.1016/j.tips.2022.11.004

Zhang, F., Chen, F., Yang, C., Wang, L., Hu, H., Li, X., et al. (2021a). Coordination and redox dual-responsive mesoporous organosilica nanoparticles amplify immunogenic cell death for cancer chemoimmunotherapy. *Small* 17 (26), 2100006. doi:10.1002/smll.202100006

Zhang, J., Jiang, D., Lyu, M., Ren, S., Zhou, Y., and Cao, Z. (2022). Synergistic radiosensitization mediated by chemodynamic therapy via a novel biodegradable peroxidases mimicking nanohybrid. *Front. Oncol.* 12, 872502. doi:10.3389/fonc.2022.872502

Zhang, Y., Swanda, R. V., Nie, L., Liu, X., Wang, C., Lee, H., et al. (2021b). mTORC1 couples cyst(e)ine availability with GPX4 protein synthesis and ferroptosis regulation. *Nat. Commun.* 12 (1), 1589. doi:10.1038/s41467-021-21841-w

Zhou, X., Li, X., Wu, B., Chen, Z., and Chen, L. (2022). Biomimetic CuS nanoparticles for radiosensitization with mild photothermal therapy and GSH-depletion. *Front. Oncol.* 12, 1054608. doi:10.3389/fonc.2022.1054608

Zou, Z., Chang, H., Li, H., and Wang, S. (2017). Induction of reactive oxygen species: An emerging approach for cancer therapy. *Apoptosis* 22 (11), 1321–1335. doi:10.1007/s10495-017-1424-9

Frontiers in Bioengineering and Biotechnology

TYPE Original Research
PUBLISHED 02 May 2023
DOI 10.3389/fbioe.2023.1191014

EDITED BY
Long Bai,
East China University of Science and Technology, China

REVIEWED BY
Shrey Sindhwani,
University of Toronto, Canada
Xin Li,
Leibniz Institute for Interactive Materials (DWI), Germany
Wei Xie,
Hefei Comprehensive National Science Center, China
Jinyuan Liu,
South Dakota School of Mines and Technology, United States

*CORRESPONDENCE
Huawei Yang,
✉ Lordyhw@163.com
Ying Cui,
✉ cuiying819@163.com
Lei Yao,
✉ yaolei7915@126.com

†These authors have contributed equally to this work

RECEIVED 21 March 2023
ACCEPTED 18 April 2023
PUBLISHED 02 May 2023

CITATION
Ning S, Mo J, Huang R, Liu B, Fu B, Ding S, Yang H, Cui Y and Yao L (2023), Injectable thermo-sensitive hydrogel loaded hollow copper sulfide nanoparticles for ROS burst in TME and effective tumor treatment.
Front. Bioeng. Biotechnol. 11:1191014.
doi: 10.3389/fbioe.2023.1191014

Injectable thermo-sensitive hydrogel loaded hollow copper sulfide nanoparticles for ROS burst in TME and effective tumor treatment

Shipeng Ning[1†], Jianlan Mo[2†], Rong Huang[1†], Benkun Liu[3], Bicheng Fu[3], Shuaijie Ding[4], Huawei Yang[1]*, Ying Cui[5]* and Lei Yao[3]*

[1]Guangxi Medical University Cancer Hospital, Nanning, China, [2]Department of Anesthesiology, Maternal and Child Health Hospital of Guangxi Zhuang Autonomous Region, Nanning, China, [3]Department of Thoracic Surgery, Harbin Medical University Cancer Hospital, Harbin, China, [4]Department of Gastrointestinal Surgery and Department of Geriatrics, Shenzhen People's Hospital (The Second Clinical Medical College, Jinan University, The First Affiliated Hospital, Southern University of Science and Technology), Shenzhen, Guangdong, China, [5]Department of Radiation Oncology, Harbin Medical University Cancer Hospital, Harbin, China

Introduction: Lung cancer the most prevalent cause of cancer-related deaths, and current therapies lack sufficient specificity and efficacy. This study developed an injectable thermosensitive hydrogel harboring hollow copper sulfide nanoparticles and β-lapachone (Lap) (CLH) for lung tumor treatment.

Methods: The hydrogel-encapsulated CLH system can remotely control the release of copper ions (Cu^{2+}) and drugs using photothermal effects for non-invasive controlled-release drug delivery in tumor therapy. The released Cu^{2+} consumes the overexpressed GSH in TME and the generated Cu^{+} further exploits the TME characteristics to initiate nanocatalytic reactions for generating highly toxic hydroxyl radicals. In addition, in cancer cells overexpressing Nicotinamide adenine dinucleotide (phosphate): quinone oxidoreductase 1 (NQO1), Lap can catalyze the generation of hydrogen peroxide (H_2O_2) through futile redox cycles. H_2O_2 is further converted into highly toxic hydroxyl radicals via the Fenton-like reaction, leading to a burst of reactive oxygen species in TME, which further enhances the therapeutic effect of chemokines.

Results: Analysis of the antitumor efficacy in a subcutaneous A549 lung tumor model mice showed a significant delay in tumor growth and no systemic toxicity was detected.

Discussion: In conclusion, we have established a CLH nanodrug platform that enables efficient lung tumor therapy through combined photothermal/chemodynamic therapy (CDT) treatment and self-supplying H_2O_2 to achieve cascade catalysis, leading to explosive amplification of oxidative stress.

KEYWORDS

lung cancer, hydrogel, β-lapachone, CDT, self-supplies H_2O_2

Introduction

In recent years, the incidence of lung cancer has been increasing steadily, with mortality rates for lung cancer remaining high (Sugarbaker and DaSilva, 2011). Non-small cell lung cancer (NSCLC) accounts for approximately 80% of lung cancer, of which early NSCLC accounts for only 20%–30%, and surgery is the main treatment (Milano et al., 2014; Evison et al., 2015; Vallone et al., 2017). However, the adverse reactions of chemotherapy drugs limit wide clinical application, so it is paramount to develop a novel lung cancer therapeutic option. Being an emerging and effective cancer treatment strategy, chemodynamic therapy (CDT) has recently attracted a lot of attention in the field of cancer treatment (Yu et al., 2021; Deng et al., 2022; Peng et al., 2023). It converts weakly oxidized hydrogen peroxide (H_2O_2) into highly cytotoxic hydroxyl groups (·OH) *in situ* within tumor region via a Fenton/Fenton-like reaction, thereby inducing apoptosis and inhibiting tumor growth (Shen et al., 2018; Dong et al., 2019). In contrast to conventional therapies, CDT is not dependent on intracellular oxygen content and does not require exogenous energy such as X-rays, continuous light and ultrasound input, which not only effectively avoids the limited penetration depth of light and radiation from X-rays, but also overcomes the inherent barrier of hypoxia within tumor area. In addition, CDT is less toxic to normal cells and can achieve specific killing of tumor cells, and therefore has great potential for application in tumor therapy. However, CDT research is still in its infancy and the therapeutic effect is not yet ideal. Methods for effectively improving the therapeutic effect of CDT is still an important research direction (Yu et al., 2020; Yang et al., 2021). In addition, GSH overexpressed within tumor microenvironment (TME), as an important antioxidant in cells, can scavenge the generated hydroxyl radicals (·OH) and weaken the cellular redox effect (Zhu et al., 2018; Zhu et al., 2022a), and this antioxidant defense of cancer cells becomes a major obstacle for CDT effectiveness (Franco et al., 2007; Chang et al., 2019; Wu et al., 2020).

At present, research on the use of nanomedicines for tumor treatment is emerging endlessly (Zhu et al., 2020; Zhu et al., 2021a; Chen et al., 2022a; Dai et al., 2022; Li et al., 2022; Opoku-Damoah et al., 2022; Xiang et al., 2022; Cao et al., 2023; Lu et al., 2023; Ning et al., 2023). Iron-based nanomaterials were widely used as classical Fenton reaction catalysts in CDT studies (Feng et al., 2020; Cheng et al., 2021). However, reaction of Fe^{2+}-mediated Fenton reaction is relatively inefficient and strongly dependent on the acidic environment, thus the reaction efficiency is low within weakly acidic TME, resulting in slow generation of reactive oxygen species and limited therapeutic effects (Lin et al., 2020). In recent years, it has been found that besides Fe^{2+} catalyzing the decomposition of H_2O_2 to produce OH, other transition metal ions such as Mn^{2+}, Cu^{2+} and Co^{2+} could also accelerate or replace Fe^{2+} to play this role (Liu et al., 2018; Fu et al., 2019; Sang et al., 2020). Among these metal elements, Cu^{2+} is renowned for its excellent properties. Firstly, as a cofactor of many natural enzymes in living organisms, copper has excellent biocompatibility and is widely involved in biochemical reactions *in vivo*. Moreover, it has been reported within literature that copper ion-like Fenton reactions have a broader pH range than Fe^{3+}. More importantly, the conversion of Cu^{2+} to Cu^{+} can effectively consume intracellular GSH and reducing loss of ROS, with reduced Cu + reacting with H_2O_2 in tumor cells to produce OH, thus improving CDT efficiency and enhancing anti-tumor effects (Wu et al., 2019a; Ma et al., 2019). CuS, as a naturally occurring inorganic mineral, is not only capable of releasing Cu^{2+} under acidic conditions, though it can also react with H_2O_2 in tumor sites to produce ROS for CDT (Liu et al., 2021). Moreover, as one of the first-developed inorganic semiconductor photothermal reagents, CuS nanoparticles are able to convert irradiated near-infra-red (NIR) light into energy through local plasmon resonance effect (Liang et al., 2019; Ding et al., 2022). By delivering CuS nanoparticles (NPs) to the tumor tissue, photothermal therapy (PTT) can be performed through thermal effects when the tumor is exposed to NIR laser irradiation. Therefore, the combination therapy of PTT and CDT, based on CuS nanoparticles, could achieve excellent synergistic therapeutic effects. In addition to the Fenton-like properties of the metastable metal itself, the Fenton reaction rate is also dependent on the concentration of the reactant substance, such as the concentration of H_2O_2 (Cun et al., 2022; Deng et al., 2022). Although the H_2O_2 content in tumor sites is higher than for normal tissue (Zhu et al., 2022b; Zhu et al., 2022c), the limited content still regulates the rate of Fenton-like reactions, thus limiting the therapeutic effect of CDT.

The natural compound β-lapachone (Lap), chemically known as 3,4-dihydro-2,2-dimethyl-2H-naphtho [1,2-b]-pyran-5,6-dione, belongs to the group of 1,2-naphthoquinones (Cun et al., 2022). Lap retains a wide range of biological and pharmacological effects, with its pharmacological actions including antibacterial, anti-inflammatory, anticancer, and anti-angiogenic. The main cytotoxic mechanism of Lap is through NADP(H)-quinone oxidoreductase l (NQ01) bioactivation, which generates reactive oxygen species through a quinone-hydroquinone-quinone redox cycle process. The consumption of 60 mol of NAD(P)H per mole of Lap in approximately 2 min generates >120 mol of equivalent H_2O_2 (Wang et al., 2019). However, low solubility of Lap in water (0.038 mg/mL), short plasma half-life (24 min), narrow therapeutic window and the tendency to develop methemoglobinemia beyond the window, all greatly limit its application.

Herein, we have developed a CLH nanohydrogel system that amplifies oxidative stress through cascade catalysis by co-loading CuS nanoparticles and Lap into agarose hydrogels. The hydrogel delivery system can exist in the tumor site for a long time, avoiding the trouble and trauma of repeated injection in the tumor (Scheme 1) (Qiu et al., 2018; Wu et al., 2019b; Zhu et al., 2021b). This CLH system, with the excellent photothermal conversion efficiency of CuS NPs, is able to convert NIR light into thermal energy, leading to tumor warming and thus photothermal therapy, leading to tumor ablation. Agarose hydrogels has temperature sensitive characteristics (Qiu et al., 2018; Zhang et al., 2022), combined with the photothermal properties of CuS, to achieve demand-controlled Lap release. The acidic TME can accelerate the degradation of CuS NPs, and the released Cu^{2+} generates Fenton-like reaction with H_2O_2. Cu^{2+} can consume overexpressed GSH inside tumor tissue through redox reaction to generate Cu+, which further catalyzes H_2O_2 to generate cytotoxic OH radicals. Through this synergistic effect, intracellular ROS levels were significantly increased and oxidative stress was amplified. Meanwhile, the

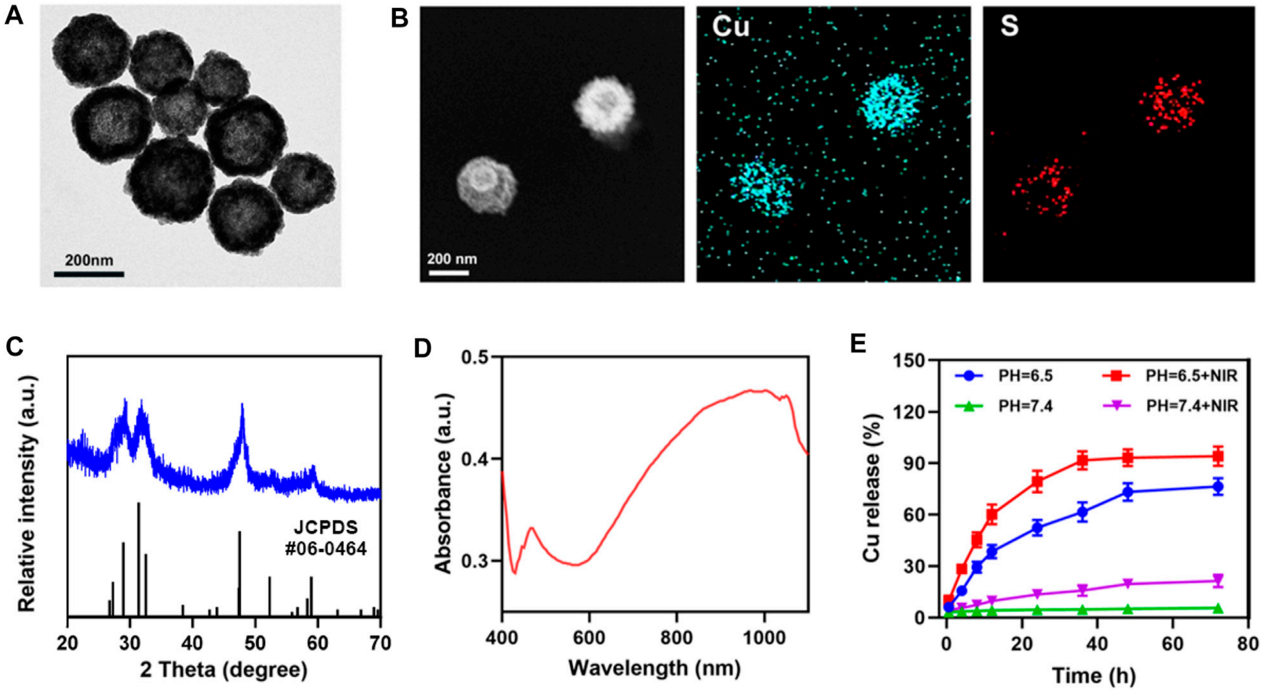

FIGURE 1
(A) TEM image, and **(B)** corresponding elemental mapping images of CuS. **(C)** XRD pattern of CuS. **(D)** CuS absorbance spectra. **(E)** Release profiles of copper ions in weak acidic and neutral environments, with or without irradiation (808 nm, 0.5 W cm^{-2}).

released Lap underwent a useless redox cycle in the presence of NQO1 and efficiently produced H_2O_2, which not only directly caused DNA damage, though also further increased the rate of Fenton-like reaction by self-supplying H_2O_2, thus enhancing the killing ability of CDT on tumor cells. *In vitro* and *in vivo* anti-tumor analysis of subcutaneous A549 lung tumors in murines showed that CLH significantly inhibited tumor growth, without adverse effects - such as inflammatory reactions. The system is combined with synergistic photothermal/chemical kinetics to induce H_2O_2 self-supply and achieve reactive oxygen species burst through cascade catalysis, thus achieving effective tumor treatment effects.

Results and discussion

Transmission electron microscopy (TEM) analysis revealed the morphology and size distribution of CuS NPs. A hollow nanostructure of CuS was observed. Studies have shown that this hollow CuS has higher photothermal conversion efficiency (30%) (Zhang et al., 2019) (Figure 1A). Their elemental mapping illustrates the Cu and S elements in CuS (Figure 1B). The powder X-ray diffraction (XRD) characterization also proved the phase structures of the obtained CuS nanocrystals. The patterns of obtained CuS Janus were consistent with the standard data of hexagonal phase CuS (JCPDS no. 06-0464) (Figure 1C). As shown in Figure 1D, the CuS dispersion exhibited a strong absorption band within NIR region, which could render the capability of CuS for photothermal conversion. Furthermore, this group examined the effect of laser in weak acidic and neutral environments on the release of copper ions, using inductively-coupled plasma optical emission spectrometry (Figure 1E), demonstrating that the 808 nm laser irradiation is capable of accelerating the release of copper ions in an acidic environment.

The CLH platforms are prepared by co-encapsulating laplachones and preparing CuS NPs in FDA-approved agaroses, which are then characterized by scanning electron microscopy (SEM) (Figure 2A). Due to the elastic deformation ability of the hydrogel, it gradually dissolves on heating. When the temperature returns to ambient level, the hydrogel solidifies, consistent with the rheological curve within Figure 2B. Subsequently, the photothermal conversion properties of CLH hydrogel platforms, containing various doses of CuS NPs, were investigated by exposing them to a NIL-II laser for 7 minutes. It is worth noting that studies have shown that the safe laser power is lower than 0.6W cm^{-2}, so it is appropriate for us to adopt 0.5 W cm^{-2} power here (Li et al., 2021). The dose- and time-dependent temperature rise curves were demonstrated (Figure 2C). The infrared thermal imaging technology further verifies that CLH has obvious temperature rise after irradiation, and also proves its excellent photothermal properties (Supplementary Figure S1). In addition, the experimental results also prove that CLH has good photothermal stability (Supplementary Figure S2). Combined with the excellent photothermal properties of CuS NPs, when irradiated with an 808 nm laser, the temperature of the hydrogel platform increased, resulting in liquefaction of the gel and consequent drug release (Figure 2D). Once the irradiation is halted, the temperature drops, the hydrogel solidifies, and release of the stored drug is halted, thus

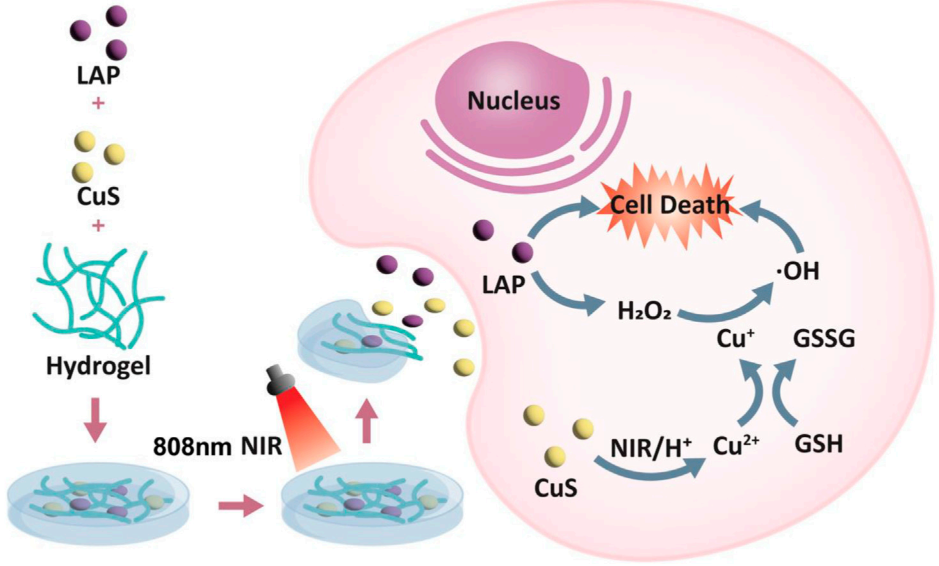

SCHEME 1
Schematic illustration of injectable thermo-sensitive hydrogel loaded hollow copper sulfide nanoparticles for reactive oxygen species burst within TME and attaining effective tumor treatment.

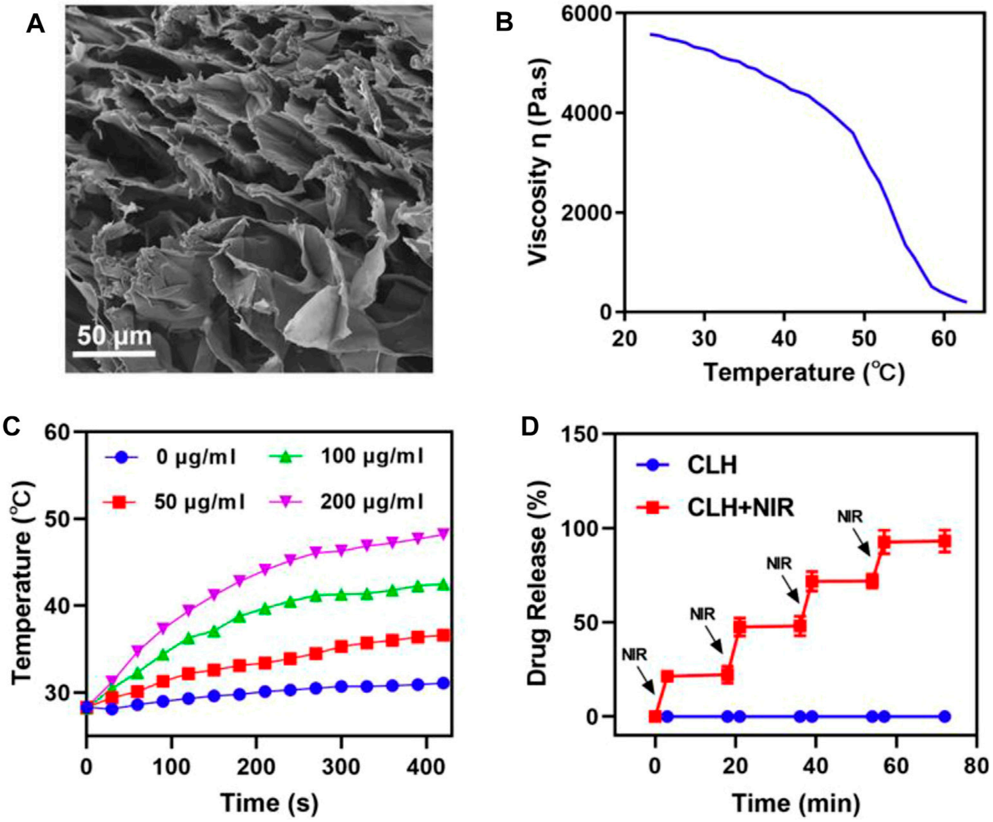

FIGURE 2
(A) Representative SEM images of CLH. **(B)** Viscosity measurements of reversibility for CLH during temperature jumps, from 23.17°C to 62.82°C. **(C)** Heating curves of varying CLH doses upon 808 nm laser at 0.5 W/cm^2. **(D)** The CLH release profile, with or without 808 nm laser irradiation, with black arrows indicating irradiation time points.

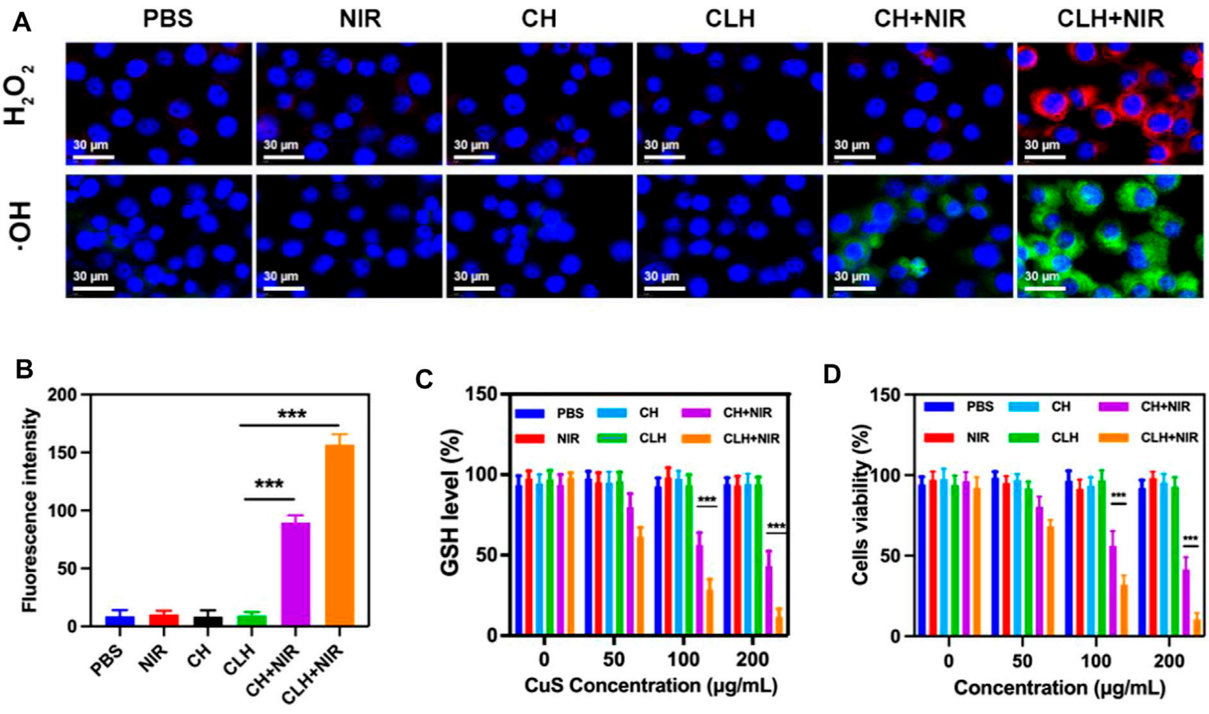

FIGURE 3
(A) Fluorescence images of ROS production in A549 cells following various treatments. **(B)** Fluorescence intensity of OH from Figure 3A. **(C)** The effect of different formulations on intracellular GSH levels ($n = 3$). **(D)** Cytotoxicity of differing doses of CuS NPs on A549 cells. ($n = 3$). $^{*}p < 0.05$, $^{**}p < 0.01$, $^{***}p < 0.005$; Student's t-test.

achieving CuS NPS-mediated photothermal controlled drug release/delivery.

Given the good photothermal effect of the CLH platform, this study subsequently explored the apoptotic effect of CLH *in vitro*. As mentioned previously, the main mechanism of tumor apoptosis by CLH could be the dissolution of hydrogel under light and the release of Lap. This latter event can catalyze the production of H_2O_2 through an ineffective redox cycle, in-turn catalyzed by the overexpression of NQO1 in tumor tissue. The generated H_2O_2 can not only cause direct tumor damage, though can also be further converted into highly toxic hydroxyl radicals via Fenton-like reactions, leading to the outbreak of reactive oxygen species within TME. In addition, Cu^{2+} can also deplete excess GSH within tumor region, further enhancing the production of ROS. Since ROS is a key factor within the induction of apoptosis by this CLH platform, this study first detected intracellular hydrogen peroxide and OH production in different treatment groups, using a hydrogen peroxide assay kit/hydroxyphenyl fluorescein (HPF). This study also prepared a CuS-coated hydrogel (CH) as a control group to further compare test results. The control group, laser group, CH group and CLH group alone hardly produced fluorescence signals (Figures 3A, B), probably since the drug could not function under the hydrogel wrapping. The combined CH + NIR group produced moderate OH fluorescence, though no H_2O_2 fluorescence was produced, indicating that the hydrogel dissolved under 808 nm laser irradiation and the released Cu^{2+} exerted the combined CDT and PTT. The CLH platform, constructed by adding Lap to the hydrogel platform, produced the strongest H_2O_2 fluorescence and OH fluorescence under the laser, which further demonstrated that lap-like can generate H_2O_2 within tumor region/s to further amplify the Fenton-like mediated oxidative stress. Typically, GSH is overexpressed within *in situ* tumor tissue to meet the redox homeostasis required for their growth, and its depletion of ROS is therefore considered a major obstacle to tumor therapy (Zhu et al., 2022a; Chen et al., 2022b; Opoku-Damoah et al., 2022). To determine how the prepared CLH synergized with NIR radiation to deplete glutathione, this study examined GSH levels across differing treatment groups (Figure 3C). The GSH levels within CH + NIR and CLH + NIR groups were significantly decreased, possibly due to the depletion of intracellular GSH levels by Cu^{2+}, while Lap could also produce a noticeable level of H_2O_2 to promote GSH depletion, further enhancing the therapeutic effect of CDT. Consequently, this study performed treatment combinations containing various doses of CuS on A549 tumor cells and assessed cellular viability through MTT assay (Figure 3D). Cells within control, laser and CLH treatment groups did not exhibit any significant cytotoxicity, which also indicated satisfactory biocompatibility for CLH. The CH + NIR group produced moderate cytotoxicity onto A549 cultures, whereas under 808 nm laser irradiation, CLH treatment produced significant cytotoxicity. Cell death was further enhanced with increasing CuS concentration, indicating that CLH-based apoptosis was concentration dependent. Thus, such assays demonstrated that this combined treatment strategy could compensate the deficiency of H_2O_2 within tumor mass, through Lap self-supply of H_2O_2 and depletion of GSH within tumor cells through Cu^{2+}, thus further amplifying oxidative stress

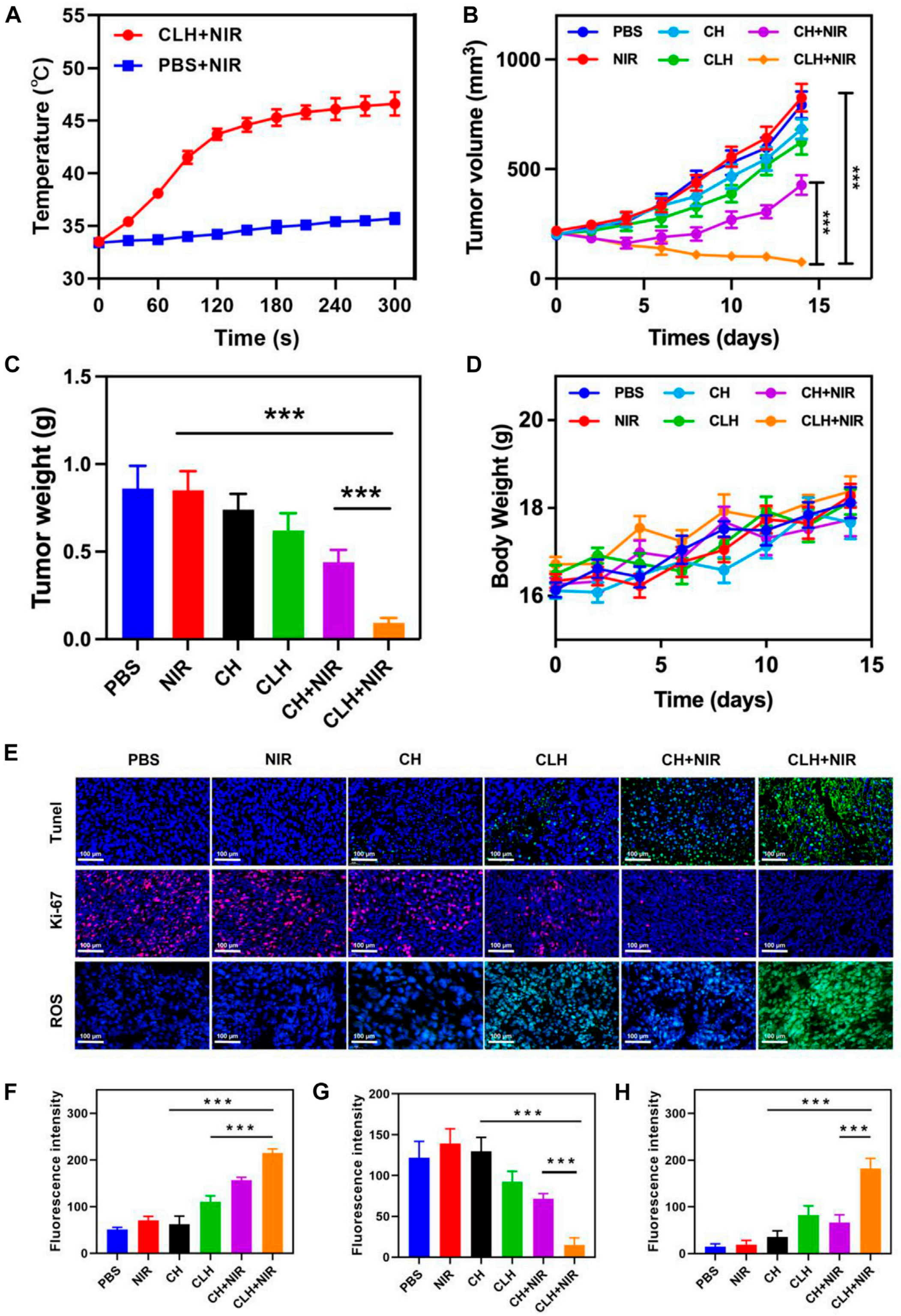

FIGURE 4
(A) Upon being irradiated with 808 nm laser at 0.5 W/cm^{-2} for 5 minutes, the temperature elevated in murines having A549 tumor, within specified treatment groups (*n* = 5). **(B)** Tumor-volume change curves of A549 tumor-bearing female BALB/C nude murines following various treatments (*n* = 5). **(C)** Tumor weight of A549 tumor-bearing female BALB/C nude murines following different treatments (*n* = 5). **(D)** Murine weight changes in different vivo treatments (*n* = 5). **(E)** TUNEL, Ki-67 and ROS immunofluorescence staining in tumor region of each group post-treatments. **(F)** TUNEL, **(G)** Ki-67 and **(H)** ROS fluorescence intensity.

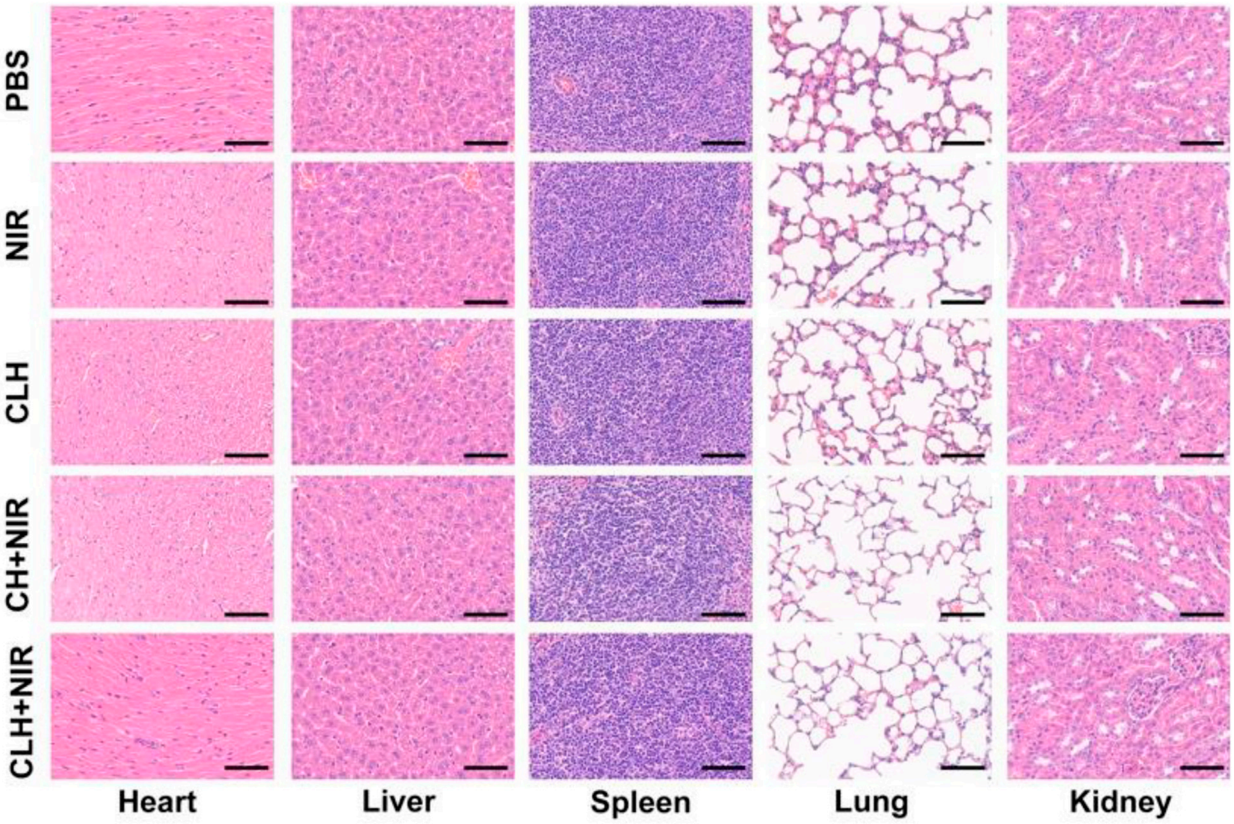

FIGURE 5
H&E staining of major organs post-treatments. Scale bars: 100 μm.

and improving the therapeutic effect. CuS can kill tumor cells significantly only at higher concentrations. On the one hand, it shows that CuS has good biological safety, and on the other hand, it suggests that direct injection of hydrogel into tumor to make it highly enriched may obtain better therapeutic effect.

Prior to probing the *in vivo* treatment effect of CLH, this study initially probed for *in vivo* photothermal effect. Following treatment of A549 murines with PBS and CLH respectively, tumor tissue was irradiated with an 808 nm laser for 5 min, and the increase in tumor temperature was recorded by infrared thermography within different treatment groups. Tumor temperature within CLH group reached 46.6°C within 5 min of 808 nm laser irradiation. Conversely, tumor temperature rose by only 2.3°C following PBS administration within identical irradiation settings (Figure 4A). The skin thickness of nude mice is about 550 μm thick (~30 μm skin, ~220 μm leather, ~300 μm subcutaneously) (Calabro et al., 2011; Byers et al., 2017), so the surface vasculature of the tumor implanted subcutaneously is visible. The 808 nm laser used in this work belongs to the near-infrared region, which can reach the position 5 mm below the skin, and the distance increases with the increase of the spot area (Zhao et al., 2018; Chu et al., 2022). Therefore, PTT can be used for tumor treatment with high clinical application potential. From one perspective, high temperature allow CLH to release CuS NPs and Lap for controlled drug release, while conversely, high temperatures also destroy proteins and selected active substances within tumor tissue, allowing tumor ablation. In addition, CLH is expected to effectively inhibit tumor growth by enhancing the synergistic effect of oxidative stress and glutathione depletion in tumor tissues. Hydrogels containing CuS NPs alone (CH) were prepared as a control group. A549 tumor-bearing nude murines were randomly divided into six groups: 1) PBS; 2) NIR; 3) CH; 4) CLH; 5) CH + NIR; and 6) CLH + NIR. Each treatment group was monitored for tumor volume every 2 days throughout the observation period. As shown in Figures 4B, C, there was no significant inhibition of tumor growth by single application of PBS or 808 nm laser irradiation. In contrast, the CH group had a slight inhibitory effect on tumor growth, which seemed to contradict the results of *in vitro* cytotoxicity tests. In contrast, the CH and CLH groups had a slight inhibitory effect on tumor growth, which seemed to contradict the results of *in vitro* cytotoxicity tests. In fact, hydrogels are decomposed slowly *in vivo* through bioenzyme activity (Qiu et al., 2018; Zhu et al., 2022b; Zhang et al., 2022), and a small amount of CuS NPs released have some inhibitory effect on tumor growth through ROS produced by CDT, while CLH prepared by adding Lap into the hydrogel platform seems to be able to further inhibit tumor growth. The killing effect of CH + NIR group on tumor tissue was further enhanced, which may be because the photothermal effect of CuS under light can accelerate the release of Cu2+, further improve the efficiency of CDT, and thus produce more ROS. However, due to the limited H_2O_2 content of the tumor tissue, this resulted in low CDT efficiency and did not completely inhibit tumor growth. Notably, the addition of Lap to the hydrogel platform and the preparation of CLH produced a significant inhibition of tumor proliferation under 808 nm irradiation, since Lap could catalyse the production of H_2O_2 through a futile redox cycle, in-turn catalysed by tumor tissue overexpression of NQO1. H_2O_2 was further converted to highly toxic hydroxyl radicals through the Fenton-like reaction, leading to a burst of reactive oxygen species in TME, which also validates the ability of CLH + NIR to amplify oxidative stress and complete inhibition of tumor growth. Efficacy following various treatments was further assessed by TdT-mediated dUTP nick-end labeling (TUNEL) staining and Ki-67 staining (Figures 4E–G). In contrast to the control and laser groups, which showed no significant changes in cell status, the TUNEL results showed significant apoptosis/necrosis in both the CLH and CH + NIR groups (Figure 4F). However, the degree of apoptosis and necrosis within CLH + NIR group was significantly higher than for other treatment groups, consistent with the trend of tumor growth. Ki-67 staining was commonly used to detect the proliferation status of cancer cells (Zhu et al., 2021a; Duo et al., 2021), and the results were consistent with the TUNEL results, confirming that the combined photothermal/chemical kinetic synergistic effect of CLH + NIR induced H_2O_2 self-supply, in order to achieve reactive oxygen species burst through cascade catalysis and thereby leading to apoptosis of tumor cells. We verified the production of ROS in tumors (Figures 4E and H). The results showed that CLH + NIR group could produce a large amount of reactive oxygen species in the tumor. Therefore, the anti-tumor effect of CLH system was the synergistic effect of ROS and heat. All groups caused no significant body weight loss (Figure 4D). The histopathology changes of major organs including liver, heart, kidney, spleen, lung and brain were collected and investigated post-H&E staining (Figure 5). There were no obvious physiological and morphological changes and inflammatory responses in five groups. And we conducted further blood biochemical analysis (Supplementary Figure S3), all the indicators were normal. This result shows that the health of the mice was not affected after the treatment. The results demonstrated that no organ damage was observed, further confirming the good biocompatibility of CLH.

Conclusion

In conclusion, our development of injectable thermosensitive hydrogel-loaded hollow copper sulfide nanoparticles and Lap can be used for reactive oxygen species burst in TME and effective tumor therapy. This platform was effective in generating heat under NIL-II radiation, resulting in dissolution of the hydrogel and release of CuS and lap to the tumor site. The acidic TME can accelerate the degradation of CuS NPs. Cu^{2+} can consume the overexpressed GSH in tumor tissues through redox reactions to generate Cu^+, which further catalyzes H_2O_2 to generate cytotoxic hydroxyl radicals. Through this synergistic effect, intracellular ROS levels were significantly increased and oxidative stress was amplified. Simultaneously, under the action of NQO1, the released Lap undergoes a redundant redox cycle to efficiently produce H_2O_2, which causes not only direct DNA damage, though also further improve the Fenton-like reaction rate through self-supply of H_2O_2, thereby enhancing the apoptotic ability of CDT to tumor cells. This platform, combined with photothermal/chemokinetic synergism, induces H_2O_2 self-supply and achieves reactive oxygen species burst through cascade catalysis, thus significantly inhibiting the growth of subcutaneous A549 lung tumors in murines. In the future, this CLH-mediated reactive oxygen burst strategy is expected to enhance traditional tumor therapies. Reactive oxygen species outbreaks within tumor cells often induce non apoptotic death modes such as immunogenic death, pyroptosis, and ferroptosis. Therefore, CLH has great potential in enhancing tumor immunotherapy and reversing tumor chemoradiotherapy resistance.

Data availability statement

The original contributions presented in the study are included in the article/Supplementary Material, further inquiries can be directed to the corresponding authors.

Ethics statement

The animal study was reviewed and approved by Shenzhen people's hospital.

Author contributions

Conceived and designed the experiments: SN, BF, SD, and YC performed the experiments: LY, JM, and BL contributed reagents/materials/analysis tools: SN, BF, SD, and YC revised the polished the article: SN, BF, SD, and YC.

Funding

This work was supported by National Natural Science Foundation of China (81860464).

Conflict of interest

The authors declare that the research was conducted in the absence of any commercial or financial relationships that could be construed as a potential conflict of interest.

Publisher's note

Supplementary material

The Supplementary Material for this article can be found online at: https://www.frontiersin.org/articles/10.3389/fbioe.2023.1191014/full#supplementary-material

References

Byers, R. A., Fisher, M., Brown, N. J., Tozer, G. M., and Matcher, S. J. (2017). Vascular patterning of subcutaneous mouse fibrosarcomas expressing individual VEGF isoforms can be differentiated using angiographic optical coherence tomography. *Biomed. Opt. express* 8 (10), 4551–4567. doi:10.1364/boe.8.004551

Calabro, K. W., Curtis, A., Galarneau, J.-R., Krucker, T., and Bigio, I. J. (2011). Gender variations in the optical properties of skin in murine animal models. *J. Biomed. Opt.* 16 1, 011008. doi:10.1117/1.3525565

Cao, X., Luo, Q., Song, F., Liu, G., Chen, S., Li, Y., et al. (2023). Effects of oxidative torrefaction on the physicochemical properties and pyrolysis products of hemicellulose in bamboo processing residues. *Industrial Crops Prod.* 191, 115986. doi:10.1016/j.indcrop.2022.115986

Chang, M., Wang, M., Wang, M., Shu, M., Ding, B., Li, C., et al. (2019). A multifunctional cascade bioreactor based on hollow-structured Cu2 MoS4 for synergetic cancer chemo-dynamic therapy/starvation therapy/phototherapy/immunotherapy with remarkably enhanced efficacy. *Adv. Mater.* 31 (51), e1905271. doi:10.1002/adma.201905271

Chen, G., Xu, Q., Feng, Z., Xu, Q., Zhang, X., Yang, Y., et al. (2022). Glutamine antagonist synergizes with electrodynamic therapy to induce tumor regression and systemic antitumor immunity. *ACS Nano* 16 (1), 951–962. doi:10.1021/acsnano.1c08544

Chen, J., Chen, T., Fang, Q., Pan, C., Akakuru, O. U., Ren, W., et al. (2022). Gd2O3/b-TiO2 composite nanoprobes with ultra-high photoconversion efficiency for MR image-guided NIR-II photothermal therapy. *Exploration* 2 (6), 20220014. doi:10.1002/exp.20220014

Cheng, J., Zhu, Y., Xing, X., Xiao, J., Chen, H., Zhang, H., et al. (2021). Manganese-deposited iron oxide promotes tumor-responsive ferroptosis that synergizes the apoptosis of cisplatin. *Theranostics* 11 (11), 5418–5429. doi:10.7150/thno.53346

Chu, Y., Xu, X. Q., and Wang, Y. (2022). Ultradeep photothermal therapy strategies. *J. Phys. Chem. Lett.* 13 (41), 9564–9572. doi:10.1021/acs.jpclett.2c02642

Cun, J. E., Pan, Y., Zhang, Z., Lu, Y., Li, J., Pan, Q., et al. (2022). Photo-enhanced upcycling H2O2 into hydroxyl radicals by IR780-embedded Fe3O4@MIL-100 for intense nanocatalytic tumor therapy. *Biomaterials* 287, 121687. doi:10.1016/j.biomaterials.2022.121687

Dai, H., Fan, Q., and Wang, C. (2022). Recent applications of immunomodulatory biomaterials for disease immunotherapy. *Exploration* 2 (6), 20210157. doi:10.1002/exp.20210157

Deng, H., Zhang, J., Yang, Y., Yang, J., Wei, Y., Ma, S., et al. (2022). Chemodynamic and photothermal combination therapy based on dual-modified metal–organic framework for inducing tumor ferroptosis/pyroptosis. *ACS Appl. Mater. interfaces* 14 (21), 24089–24101. doi:10.1021/acsami.2c00574

Ding, D., Mei, Z., Huang, H., Feng, W., Chen, L., Chen, Y., et al. (2022). Oxygen-independent sulfate radical for stimuli-responsive tumor nanotherapy. *Adv. Sci.* 9, e2200974. doi:10.1002/advs.202200974

Dong, Z., Feng, L., Chao, Y., Hao, Y., Chen, M., Gong, F., et al. (2019). Amplification of tumor oxidative stresses with liposomal Fenton catalyst and glutathione inhibitor for enhanced cancer chemotherapy and radiotherapy. *Nano Lett.* 19 (2), 805–815. doi:10.1021/acs.nanolett.8b03905

Duo, Y., Zhu, D., Sun, X., Suo, M., Zheng, Z., Jiang, W., et al. (2021). Patient-derived microvesicles/AIE luminogen hybrid system for personalized sonodynamic cancer therapy in patient-derived xenograft models. *Biomaterials* 272, 120755. doi:10.1016/j.biomaterials.2021.120755

Evison, M., Britton, S., Al-Najjar, H., Shah, R., Crosbie, P., and Booton, R. (2015). Pathological variables in resected NSCLC tumours: Predictors of survival? *J. Thorac. Oncol.* 10 (9), S435.

Feng, L., Liu, B., Xie, R., Wang, D., Qian, C., Zhou, W., et al. (2020). An ultrasmall SnFe2O4 nanozyme with endogenous oxygen generation and glutathione depletion for synergistic cancer therapy. *Adv. Funct. Mater.* 31 (5), 2006216. doi:10.1002/adfm.202006216

Franco, R., Panayiotidis, M. I., and Cidlowski, J. A. (2007). Glutathione depletion is necessary for apoptosis in lymphoid cells independent of reactive oxygen species formation. *J. Biol. Chem.* 282 (42), 30452–30465. doi:10.1074/jbc.m703091200

Fu, L. H., Hu, Y. R., Qi, C., He, T., Jiang, S., Jiang, C., et al. (2019). Biodegradable manganese-doped calcium phosphate nanotheranostics for traceable cascade reaction-enhanced anti-tumor therapy. *ACS Nano* 13, 13985–13994. doi:10.1021/acsnano.9b05836

Li, X., Hetjens, L., Wolter, N., Li, H., Shi, X., and Pich, A. (2022). Charge-reversible and biodegradable chitosan-based microgels for lysozyme-triggered release of vancomycin. *J. Adv. Res.* 43, 87–96. doi:10.1016/j.jare.2022.02.014

Li, X., Sun, H., Li, H., Hu, C., Luo, Y., Shi, X., et al. (2021). Multi-Responsive biodegradable cationic nanogels for highly efficient treatment of tumors. *Adv. Funct. Mater.* 31 (26), 2100227. doi:10.1002/adfm.202100227

Liang, S., Deng, X., Chang, Y., Sun, C., Shao, S., Xie, Z., et al. (2019). Intelligent hollow Pt-CuS Janus architecture for synergistic catalysis-enhanced sonodynamic and photothermal cancer therapy. *Nano Lett.* 19 (6), 4134–4145. doi:10.1021/acs.nanolett.9b01595

Lin, L., Wang, S., Deng, H., Yang, W., Rao, L., Tian, R., et al. (2020). Endogenous labile iron pool-mediated free radical generation for cancer chemodynamic therapy. *J. Am. Chem. Soc.* 142 (36), 15320–15330. doi:10.1021/jacs.0c05604

Liu, W., Xiang, H., Tan, M., Chen, Q., Jiang, Q., Yang, L., et al. (2021). Nanomedicine enables drug-potency activation with tumor sensitivity and Hyperthermia Synergy in the Second near-infrared Biowindow. *ACS Nano* 15 (4), 6457–6470. doi:10.1021/acsnano.0c08848

Liu, Y., Zhen, W., Jin, L., Zhang, S., Sun, G., Zhang, T., et al. (2018). All-in-One theranostic nanoagent with enhanced reactive oxygen species generation and modulating tumor microenvironment ability for effective tumor eradication. *ACS Nano* 12 (5), 4886–4893. doi:10.1021/acsnano.8b01893

Lu, Y., Luo, Q., Jia, X., Tam, J. P., Yang, H., Shen, Y., et al. (2023). Multidisciplinary strategies to enhance therapeutic effects of flavonoids from Epimedii Folium: Integration of herbal medicine, enzyme engineering, and nanotechnology. *J. Pharm. Analysis* 13 (3), 239–254. doi:10.1016/j.jpha.2022.12.001

Ma, B., Wang, S., Liu, F., Zhang, S., Duan, J., Li, Z., et al. (2019). Self-assembled copper–amino acid nanoparticles for *in situ* glutathione "AND" H2O2 sequentially triggered chemodynamic therapy. *J. Am. Chem. Soc.* 141 (2), 849–857. doi:10.1021/jacs.8b08714

Milano, M. T., Strawderman, R. L., Venigalla, S., Ng, K., and Travis, L. B. (2014). Non-small-cell lung cancer after breast cancer A population-based study of clinicopathologic characteristics and survival outcomes in 3529 women. *J. Thorac. Oncol.* 9 (8), 1081–1090. doi:10.1097/jto.0000000000000213

Ning, S., Zhang, T., Lyu, M., Lam, J. W. Y., Zhu, D., Huang, Q., et al. (2023). A type I AIE photosensitiser-loaded biomimetic nanosystem allowing precise depletion of cancer stem cells and prevention of cancer recurrence after radiotherapy. *Biomaterials* 295, 122034. doi:10.1016/j.biomaterials.2023.122034

Opoku-Damoah, Y., Zhang, R., Ta, H. T., and Xu, Z. P. (2022). Therapeutic gas-releasing nanomedicines with controlled release: Advances and perspectives. *Exploration* 2 (5), 20210181. doi:10.1002/exp.20210181

Peng, H., Yao, F., Zhao, J., Zhang, W., Chen, L., Wang, X., et al. (2023). Unraveling mitochondria-targeting reactive oxygen species modulation and their implementations in cancer therapy by nanomaterials. *Exploration* 2023, 20220115. doi:10.1002/exp.20220115

Qiu, M., Wang, D., Liang, W., Liu, L., Zhang, Y., Chen, X., et al. (2018). Novel concept of the smart NIR-light-controlled drug release of black phosphorus nanostructure for cancer therapy. *Proc. Natl. Acad. Sci. U. S. A.* 115 (3), 501–506. doi:10.1073/pnas.1714421115

Sang, Y., Cao, F., Li, W., Zhang, L., You, Y., Deng, Q., et al. (2020). Bioinspired construction of a nanozyme-based H2O2 homeostasis disruptor for intensive chemodynamic therapy. *J. Am. Chem. Soc.* 142 (11), 5177–5183. doi:10.1021/jacs.9b12873

Shen, Z., Liu, T., Li, Y., Lau, J., Yang, Z., Fan, W., et al. (2018). Fenton-reaction-acceleratable magnetic nanoparticles for ferroptosis therapy of orthotopic brain tumors. *ACS Nano* 12 (11), 11355–11365. doi:10.1021/acsnano.8b06201

Sugarbaker, D. J., and DaSilva, M. C. (2011). Diagnostic workup of lung cancer. *Surg. Oncol. Clin.* 20 (4), 667–679. doi:10.1016/j.soc.2011.08.003

Vallone, S., Beunders, I., and Szmytke, E. (2017). Lung cancer patient needs in different countries. *Lung Cancer Manag.* 6 (1), 1–4. doi:10.2217/lmt-2017-0005

Wang, S., Yu, G., Wang, Z., Jacobson, O., Lin, L. S., Yang, W., et al. (2019). Enhanced antitumor efficacy by a cascade of reactive oxygen species generation and drug release. *Angew. Chem.* 58 (41), 14758–14763. doi:10.1002/anie.201908997

Wu, H., Chen, F., You, C., Zhang, Y., Sun, B., and Zhu, Q. (2020). Smart porous core-shell cuprous oxide nanocatalyst with high biocompatibility for acid-triggered chemo/chemodynamic synergistic therapy. *Small* 16 (45), e2001805. doi:10.1002/smll.202001805

Wu, H., Liu, L., Song, L., Ma, M., Gu, N., and Zhang, Y. (2019). Enhanced tumor synergistic therapy by injectable magnetic hydrogel mediated generation of Hyperthermia and highly toxic reactive oxygen species. *ACS Nano* 13 (12), 14013–14023. doi:10.1021/acsnano.9b06134

Wu, W., Yu, L., Jiang, Q., Huo, M., Lin, H., Wang, L., et al. (2019). Enhanced tumor-specific disulfiram chemotherapy by *in situ* Cu2+ chelation-initiated nontoxicity-to-toxicity transition. *J. Am. Chem. Soc.* 141 (29), 11531–11539. doi:10.1021/jacs.9b03503

Xiang, X., Feng, X., Lu, S., Jiang, B., Hao, D., Pei, Q., et al. (2022). Indocyanine green potentiated paclitaxel nanoprodrugs for imaging and chemotherapy. *Exploration* 2 (4), 20220008. doi:10.1002/exp.20220008

Yang, B., Yao, H., Tian, H., Yu, Z., Guo, Y., Wang, Y., et al. (2021). Intratumoral synthesis of nano-metalchelate for tumor catalytic therapy by ligand field-enhanced coordination. *Nat. Commun.* 12 (1), 3393. doi:10.1038/s41467-021-23710-y

Yu, P., Li, X., Cheng, G., Zhang, X., Wu, D., Chang, J., et al. (2021). Hydrogen peroxide-generating nanomedicine for enhanced chemodynamic therapy. *Chin. Chem. Lett.* 32 (7), 2127–2138. doi:10.1016/j.cclet.2021.02.015

Yu, X. A., Lu, M., Luo, Y., Hu, Y., Zhang, Y., Xu, Z., et al. (2020). A cancer-specific activatable theranostic nanodrug for enhanced therapeutic efficacy via amplification of oxidative stress. *Theranostics* 10 (1), 371–383. doi:10.7150/thno.39412

Zhang, H., Chen, Y., Cai, Y., Liu, J., Liu, P., Li, Z., et al. (2019). Paramagnetic CuS hollow nanoflowers for T2-FLAIR magnetic resonance imaging-guided thermochemotherapy of cancer. *Biomaterials Sci.* 7 (1), 409–418. doi:10.1039/c8bm01412d

Zhang, T., Liu, Z., Tang, W., Zhu, D., Lyu, M., Lam, J. W. Y., et al. (2022). Mitochondria-targeting Type I AIE photosensitizer combined with H2S therapy: Uninterrupted hydroxyl radical generation for enhancing tumor therapy. *Nano Today* 46, 101620. doi:10.1016/j.nantod.2022.101620

Zhao, J., Zhong, D., and Zhou, S. (2018). NIR-I-to-NIR-II fluorescent nanomaterials for biomedical imaging and cancer therapy. *J. Mater. Chem. B* 6 (3), 349–365. doi:10.1039/c7tb02573d

Zhu, D., Chen, H., Huang, C., Li, G., Wang, X., Jiang, W., et al. (2022). H_2O_2 self-producing single-atom nanozyme hydrogels as light-controlled oxidative stress amplifier for enhanced synergistic therapy by transforming “cold” tumors. *Adv. Funct. Mater.* 32 (16), 2110268. doi:10.1002/adfm.202110268

Zhu, D., Duo, Y., Meng, S., Zhao, Y., Xia, L., Zheng, Z., et al. (2020). Tumor-exocytosed exosome/aggregation-induced emission luminogen hybrid nanovesicles facilitate efficient tumor penetration and photodynamic therapy. *Angew. Chem.* 59, 2–10.

Zhu, D., Ling, R., Chen, H., Lyu, M., Qian, H., Wu, K., et al. (2022). Biomimetic copper single-atom nanozyme system for self-enhanced nanocatalytic tumor therapy. *Nano Res.* 15 (8), 7320–7328. doi:10.1007/s12274-022-4359-6

Zhu, D., Zhang, J., Luo, G., Duo, Y., and Tang, B. Z. (2021). Bright bacterium for hypoxia-tolerant photodynamic therapy against orthotopic colon tumors by an interventional method. *Adv. Sci.* 8 (15), 2004769. doi:10.1002/advs.202004769

Zhu, D., Zhang, T., Li, Y., Huang, C., Suo, M., Xia, L., et al. (2022). Tumor-derived exosomes co-delivering aggregation-induced emission luminogens and proton pump inhibitors for tumor glutamine starvation therapy and enhanced type-I photodynamic therapy. *Biomaterials* 283, 121462. doi:10.1016/j.biomaterials.2022.121462

Zhu, D., Zheng, Z., Luo, G., Suo, M., Li, X., Duo, Y., et al. (2021). Single injection and multiple treatments: An injectable nanozyme hydrogel as AIEgen reservoir and release controller for efficient tumor therapy. *Nano Today* 37, 101091. doi:10.1016/j.nantod.2021.101091

Zhu, P., Chen, Y., and Shi, J. (2018). Nanoenzyme-augmented cancer sonodynamic therapy by catalytic tumor oxygenation. *ACS Nano* 12 (4), 3780–3795. doi:10.1021/acsnano.8b00999

frontiers | Frontiers in Bioengineering and Biotechnology

TYPE Original Research
PUBLISHED 05 May 2023
DOI 10.3389/fbioe.2023.1173169

OPEN ACCESS

EDITED BY
Weifeng Lin,
Weizmann Institute of Science, Israel

REVIEWED BY
Longgang Wang,
Yanshan University, China
Shufang Chang,
Chongqing Medical University, China
Jiaqi Zhao,
Shanghai Fourth People's Hospital, China

*CORRESPONDENCE
Xiaojie Zhang,
✉ xjzzhang@sjtu.edu.cn
Xiaojun Cai,
✉ c1x2j34@163.com
Yuanyi Zheng,
✉ zhengyuanyi@sjtu.edu.cn

RECEIVED 24 February 2023
ACCEPTED 25 April 2023
PUBLISHED 05 May 2023

CITATION
Liu Z, Li J, Bian Y, Zhang X, Cai X and Zheng Y (2023), Low-intensity pulsed ultrasound reduces lymphedema by regulating macrophage polarization and enhancing microcirculation.
Front. Bioeng. Biotechnol. 11:1173169.
doi: 10.3389/fbioe.2023.1173169

Low-intensity pulsed ultrasound reduces lymphedema by regulating macrophage polarization and enhancing microcirculation

Zihao Liu[1], Jia Li[1], Yu Bian[1], Xiaojie Zhang[2]*, Xiaojun Cai[1]* and Yuanyi Zheng[1]*

[1]Department of Ultrasound in Medicine, Shanghai Jiao Tong University School of Medicine Affiliated Sixth People's Hospital, Shanghai, China, [2]Department of Neurology, Shanghai Jiao Tong University School of Medicine Affiliated Sixth People's Hospital, Shanghai, China

Background: Conventional therapies reduce lymphedema but do not cure it because they cannot modulate the pathophysiology of secondary lymphedema. Lymphedema is characterized by inflammation. We hypothesized that low-intensity pulsed ultrasound (LIPUS) treatment could reduce lymphedema by enhancing anti-inflammatory macrophage polarization and microcirculation.

Methods: The rat tail secondary lymphedema model was established through the surgical ligation of lymphatic vessels. The rats were randomly divided into the normal, lymphedema, and LIPUS treatment groups. The LIPUS treatment (3 min daily) was applied 3 days after establishing the model. The total treatment period was 28 days. Swelling, fibro adipose deposition, and inflammation of the rat tail were evaluated by HE staining and Masson's staining. The photoacoustic imaging system and laser Doppler flowmetry were used to monitor microcirculation changes in rat tails after LIPUS treatment. The cell inflammation model was activated with lipopolysaccharides. Flow cytometry and fluorescence staining were used to observe the dynamic process of macrophage polarization.

Results: After 28 days of treatment, compared with the lymphedema group, the tail circumference and subcutaneous tissue thickness of rats in the LIPUS group were decreased by 30%, the proportion of collagen fibers and the lymphatic vessel cross-sectional area was decreased, and tail blood flow was increased significantly. Cellular experiments revealed a decrease in $CD86^+$ macrophages (M1) after LIPUS treatment.

Conclusion: The transition of M1 macrophage and the promotion of microcirculation could be responsible for the beneficial effect of LIPUS on lymphedema.

KEYWORDS

macrophage polarization, low-intensity pulsed ultrasound, circulation, lymphedema, inflammation

1 Introduction

Lymphedema is a progressive disease caused by lymphatic transport dysfunction primarily because of external or congenital abnormalities. At the late stage of lymphedema, patients experience tissue fibrosis, fat deposition and inflammation, decreased quality of life (QOL), and recurrent infections. Secondary lymphedema is a common complication of cancer treatment (Rockson et al., 2019). Recently, with the advancement of cancer treatment technology, the life expectancy of cancer survivors has increased, leading to lifelong lymphedema in approximately one-fifth of patients undergoing cancer treatment (Fish et al., 2020). Lymphedema patients experience associated symptoms such as chronic pain, dysfunction, repeated skin infections, poor body shape, depression, and anxiety, which can seriously affect their quality of life and mental health (Ahmed et al., 2008). Lymphedema imposes a substantial biomedical burden; therefore, it is crucial to investigate effective treatment options.

The primary therapeutic objective of secondary lymphedema is to improve the patient's quality of life. Lymphedema treatment can be divided into surgical and conservative treatments (Schaverien and Coroneos, 2019). Surgical treatment methods such as venous lymphatic anastomosis have demonstrated some promise. However, surgical injury and the risk of infection reduce patient acceptance. The objective of conservative treatments, such as manual lymphatic drainage and skin care, is to reduce the accumulation of lymph in the tissues through various measures, reduce edema, and prevent disease progression. Conservative treatments are reportedly not able to have a therapeutic effect on lymphatic structures (Devoogdt et al., 2023). These treatments cannot effectively treat lymphedema, and the effect was unsatisfactory (Sanal-Toprak et al., 2019; Liang et al., 2020). Because of the complexity of current treatment methods and the need for lifelong treatment, lymphedema patients often experience poor compliance. These factors contributed to the patients' poor QOL (Farncombe et al., 1994). After recovering from cancer surgery, secondary lymphedema patients urgently need a convenient and effective treatment method that can improve their QOL.

Studies have demonstrated that inflammation is a key component of the pathophysiology of lymphedema. Lymphatic obstruction and lymph siltation can continuously irritate the edematous site, resulting in chronic inflammation and exacerbating lymphedema (Grada and Phillips, 2017). When lymphedema occurs, lymph stasis leads to lymphangitis, accompanied by upregulation of inflammatory factors (Yuan et al., 2019). Because of the stimulation of the inflammatory environment, macrophages infiltrate the fusion sites and clear tissue fragments. Traditionally, macrophages are divided into two subgroups: M1 macrophages and M2 macrophages (Trus et al., 2020). Activated M1 macrophages engulf and destroy microorganisms, which is essential for pathogen resistance, but M1 macrophages simultaneously release high levels of proinflammatory factors, such as TNF- α, Interleukin 6 (IL-6), and IL-1 β (Viola et al., 2019).

The expression of inflammatory factors increased at the site of lymph node obstruction, macrophages were polarized by the stimulation of the inflammatory microenvironment, and there was a high expression of polarized M1 macrophages (Liu et al., 2014). The M1 macrophages aggravate the expression of inflammation response. Severe inflammatory responses lead to more severe tissue damage and fibrosis. (Yunna et al., 2020).

Ultrasonic therapy—a form of physical therapy—has made significant progress in recent years because of its unique non-invasive treatment and user-friendly application (Yang et al., 2019). Ultrasound treatment has numerous effects (Jiang et al., 2019). Through the vibration, loosening, and shock of the lesion, ultrasonic therapy can cause cell and tissue movement, produce mechanical effect through internal massage, promote metabolism, strengthen circulation (Yang et al., 2019; Joiner et al., 2022), improve tissue nutrition, and alleviate body inflammation (Ling et al., 2017).

LIPUS can potentially reduce tissue inflammation by regulating macrophage polarization and reducing M1 polarization (Zhang et al., 2019). Theoretically, the mechanical stress of LIPUS may reduce the inflammatory response after lymphedema treatment.

The objective of our study was to provide an experimental basis for the application of LIPUS treatment to patients with secondary lymphedema and then evaluate the microcirculation and macrophage inflammation.

2 Materials and methods

2.1 Animals

A total of 18 male SD rats (age: 6 weeks; weight: 220–250 g) were obtained from the Animal Laboratory of Shanghai Jiao Tong University Affiliated Sixth People's Hospital. All animals were housed at 22°C room temperature with a 24-h light/dark cycle. Animal operating protocols were followed in accordance with the laboratory of Shanghai Jiao Tong University Affiliated Sixth People's Hospital (No. DWLL 2022–0601).

2.2 Rat model of tail lymphedema

The rats were randomly divided into three groups ($n = 6$): the normal group, the lymphedema group, and the LIPUS treatment group. To construct a rat tail lymphedema model, we anesthetized the rats with pentobarbital sodium (50 mg/kg intraperitoneal injection). To demonstrate the lymphatic network, we injected 0.1 mL of 2% methylene blue solution intradermally into the end of the rat tail. After disinfecting the skin, a 1 cm circular incision was made at 13 cm–14 cm from the end of the tail. After removing the skin and subcutaneous tissue, the dermis and superficial lymphatic network were eliminated. The collecting lymphatics under the deep fascia on both sides were eliminated. The muscles, tendons, bones, and main subdermal vessels were not injured (Jin et al., 2021).

2.3 LIPUS treatment of lymphedema

The treatment group received ultrasound therapy with the WED-100 all-digital ultrasound therapy instrument (Shenzhen Welld Medical Electronics Co., Ltd.). During ultrasound treatment, the probe was centered on the surgical stump of the

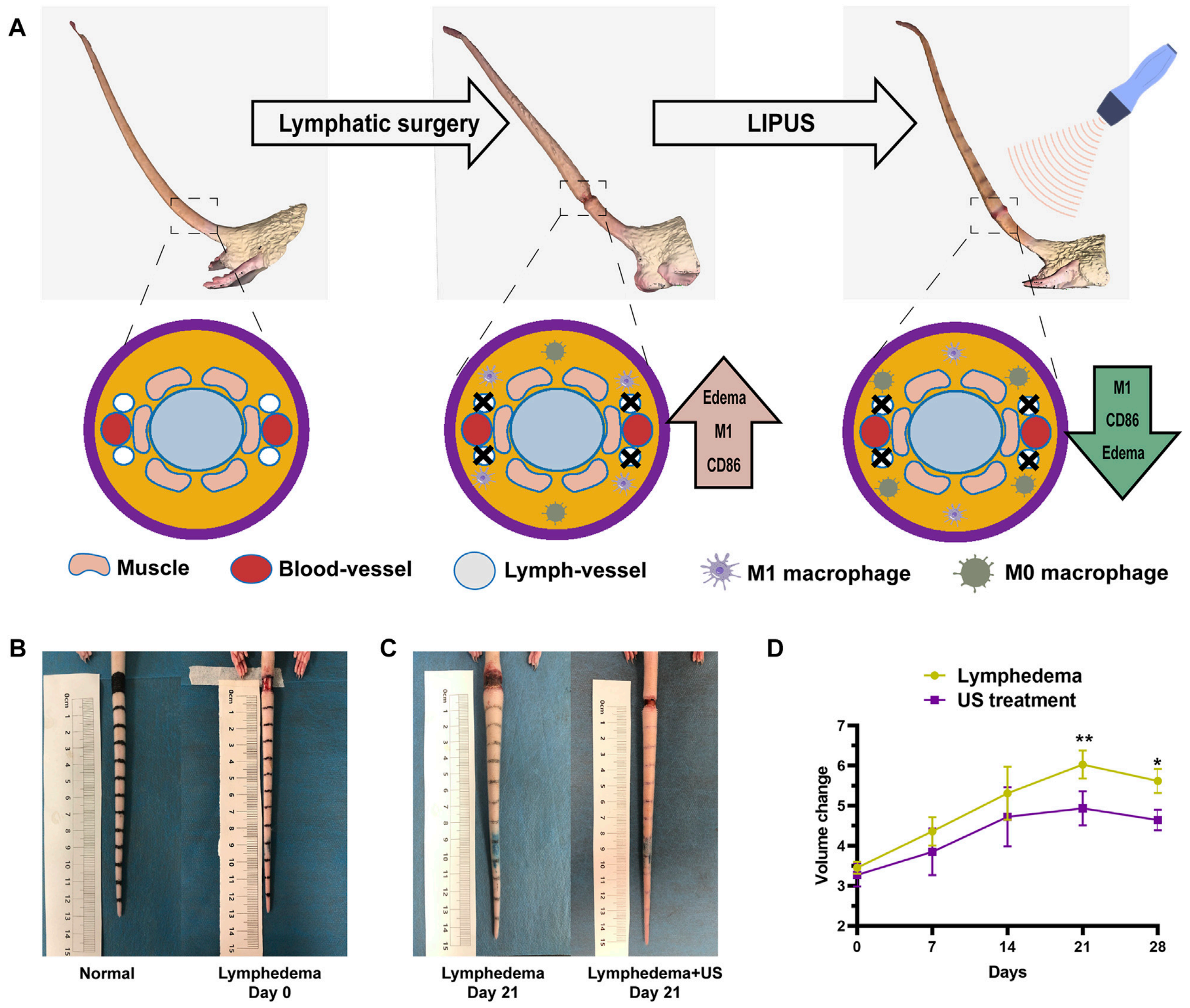

FIGURE 1
The tail volume of the ultrasonic treatment group and the non-treatment group. **(A)** 3D simulation of acquired lymphedema surgery. The lymphatic network was eliminated. **(B)** Bright-field images of the acquired lymphedema surgery. **(C)** Images of the control group and LIPUS group on day 21. **(D)** The lymphedema tail volume responses of the LIPUS treatment group and the non-treatment group after a treatment course of 28 days. The volume was measured by the drainage method.

lymphatic vessel in the rat tail. Each ultrasonic treatment was administered daily for 3 min (Figure 1A).

LIPUS device parameters: Effective ultrasonic intensity of 0.5 mW/cm^2; working ultrasonic frequency of 1.0 MHz, 10 ms pulse repetition period; the therapeutic probe is 2 cm^2. During LIPUS treatment, the rats were anesthetized with isoflurane. The LIPUS probe was carefully fixed on the tail's skin. The coupling gel was applied to ensure that the sensors were in contact.

2.4 ELISA

Excessive pentobarbital sodium is used to euthanize rats and the edema tissue (the skin and subcutaneous tissue) of tail at 13 cm–14 cm was collected. The serum level of VEGF-C were measured using the appropriate kit at day 21. The serum level of IL-1, TNF-α were measured 3 days after LIPUS treatment. All methods were performed according to the manufacturer's protocol.

2.5 Immunohistochemistry and histology

The skin tissue of the rat tail at the surgical incision was sectioned on day 28 post-surgery, and HE staining was used to observe the thickness of the skin and the subcutaneous tissue. Masson's staining was used to evaluate the formation of collagen fibers.

Anti-Lyve-1 (ab36993) was used to stain LECs. Nuclei were stained with DAPI (Vector Laboratories). All images were measured using ImageJ (National Institutes of Health, NIH).

2.6 Cells LIPUS treatment

The raw264.7 cells were seeded in 6-well plates, cultured for 1 day, and then the medium was replaced with one containing lipopolysaccharides (LPS). Ultrasound treatment was initiated after the medium replacement. LIPUS device parameters: Effective ultrasonic intensity of 0.3–0.5 mW/cm^2, working ultrasonic frequency of 1.0 MHz, and treatment duration of 3 min daily.

2.7 Flow cytometry

For macrophage polarization analysis, the raw264.7 cells were labeled with FITC-conjugated anti-CD86 [BU63] (ab77276, Abcam). Flow cytometry data were analyzed and presented using the FlowJo software (Flowjo LLC, Ashland, OR, United States).

2.8 Microcirculatory assessment

The tail blood flow of rats in the treatment groups was evaluated using laser Doppler blood flow imaging and a photoacoustic imaging system. Infrared images were used to monitor temperature fluctuations.

2.9 Statistics analysis

All data were statistically analyzed with GraphPad Prism 8 (GraphPad, Chicago, IL, United States). The data are expressed as means ± SD or SEM for continuous variables. For comparing the values of the three groups, the one-way ANOVA method was used. A *p*-value of <0.05 was considered statistically significant.

2.10 Study approval

The rats in each group were anesthetized so that the tissues in their tails could be sampled for all experiments. This study was approved by the Animal Welfare Ethics Committee of Shanghai Sixth People's Hospital. All methods were conducted according to relevant guidelines and regulations.

3 Results

3.1 Low-intensity pulsed ultrasound (LIPUS) reduced the edema and fibrosis of rat tail lymphedema

The rat tail volume (Figure 1D) was measured on days 0, 7, 14, 21, and 28. The tail volume of the ultrasonic treatment group and the non-treatment group exhibited significant differences after the operation (Figures 1B,C), with the largest difference (18%) on day 21 after the operation. The volume was measured by the drainage method. The histological analysis revealed that the thickness of subcutaneous tissue at the lymphedema site (Figure 2A) in the LIPUS treatment group decreased by 30% (HE staining) (Figure 2B) on day 28 after the operation of rat tail lymphatic vessels. The thickness of subcutaneous fibrous tissue decreased by 10% after ultrasonic treatment (Masson's staining) (Figures 2C, D).

3.2 LIPUS reduced the lymphatic hyperplasia of rat tail lymphedema

On day 28 after lymphatic vessel surgery, the skin and subcutaneous tissue were collected for homogenization, and the VEGF-C level of the LIPUS group was increased (Figure 3B), indicating that LIPUS treatment toadied in the growth of damaged lymphatic vessels.

The lyve-1 staining (Figure 3A) revealed lymphatic hyperplasia. The lymphatic vessels in the LIPUS treatment group exhibited a smaller cross-sectional area, whereas the lymphatic vessels of the lymphedema group exhibited a significantly expanded cross-sectional area and were swollen and thickened. The enhanced microcirculation might be the reason for the improved degree of lymphatic obstruction.

3.3 LIPUS reduced inflammation by regulating macrophage polarization

A cellular model was used to study the cellular function of LIPUS. The raw264.7 cells were harvested using LPS (10 ng/mL), and then the expression of the phenotypic marker—CD86—associated with M1 macrophages was examined using flow cytometry. After the ultrasound treatment, the CD86 phenotype of LPS-treated raw264.7 cells decreased by 22% (Figure 4B).

iNOS was mainly expressed in M1 macrophage (Figure 4C). Compared with and without the LIPUS group, LIPUS reduced the iNOS fluorescence intensity (Figures 4D, E).

3.4 LIPUS promote microcirculation

After LIPUS treatment, the photoacoustic imaging system (Figure 5C) and the laser Doppler flowmetry (LDF) (Figure 5D) revealed an increase in the blood flow of the rat tail. Infrared temperature measurement was used to measure the temperature of the rat tail. The temperature increased after LIPUS but did not rise after reaching 44°C (Figures 5A, B). The skin and subcutaneous tissue could be heated to promote microcirculation.

4 Discussion

Ultrasonic examination—the most prevalent medical imaging modality worldwide (Wang et al., 2020)—is abundant, safe, portable, and inexpensive. In addition to rapidly expanding beyond traditional radiology and cardiology practices, Ultrasound also plays a unique role in treating various diseases. With such early visions, FRY et al. (1955) developed focused ultrasound, utilizing its ability to penetrate deeply into the human body and provide tight energy deposition in focused areas. Initial success with a therapeutic

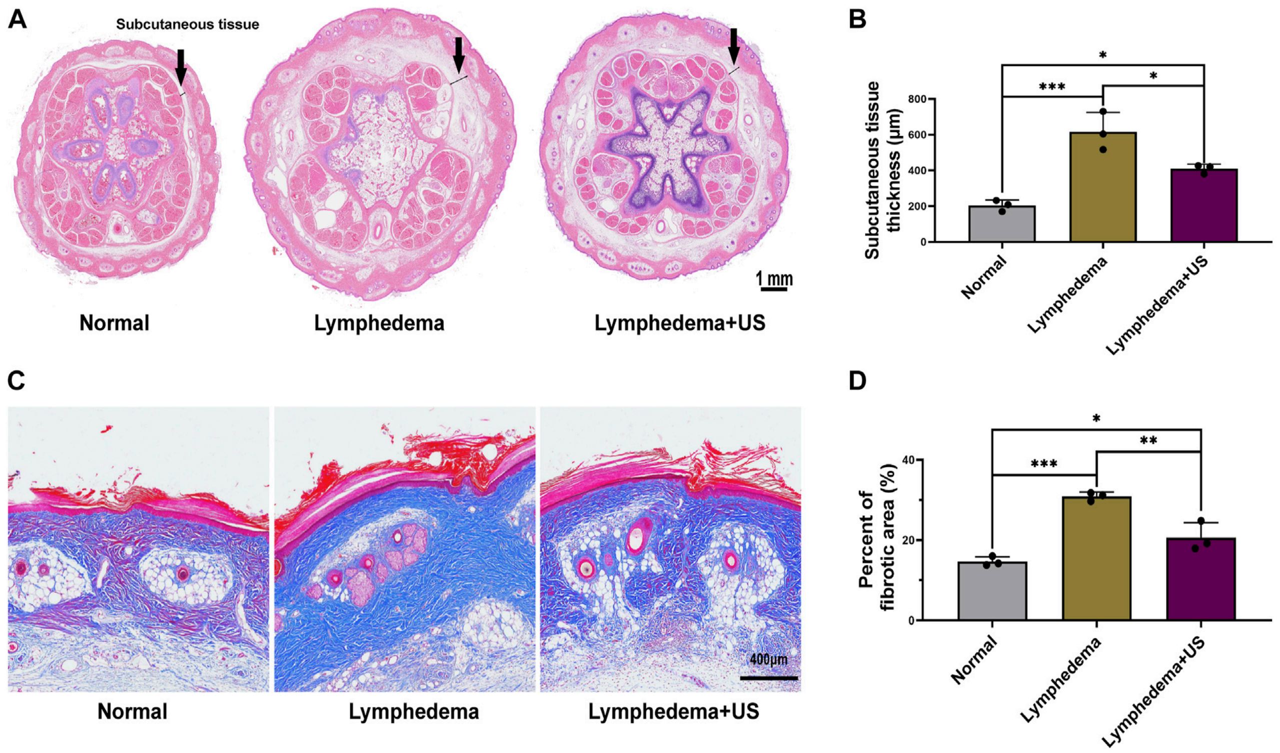

FIGURE 2
Histological photomicrographs of lymphedema site of the control and LIPUS groups. **(A,B)** HE staining showing the thickness of subcutaneous tissue at the lymphedema site, scale bar = 1 mm. **(C)** Masson's staining to evaluate fibrotic tissue deposition revealed a decrease in fibrosis after LIPUS, scale bar = 400 μm. **(D)** Percent of the fibrotic area at the lymphedema site ($p < 0.05$, $n = 3$).

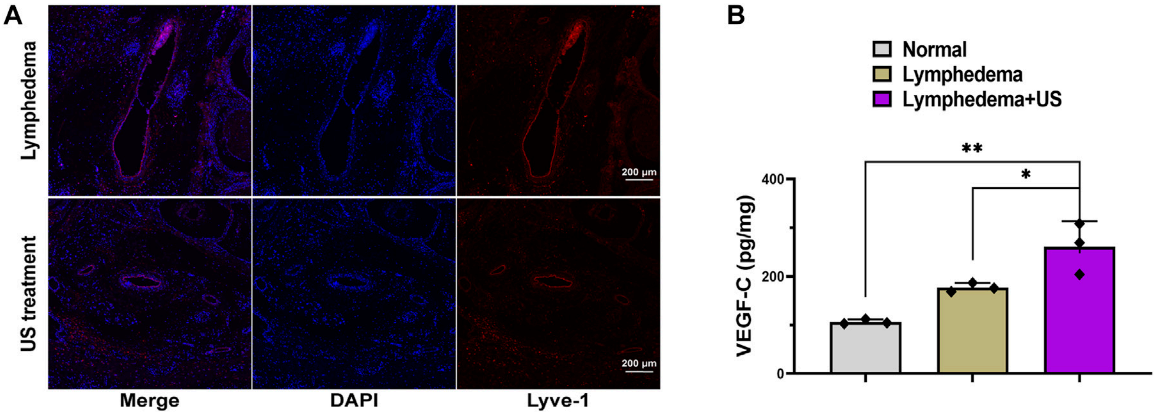

FIGURE 3
Lymphatic vessel in lymphedema tail after LIPUS treatment. **(A)** Immunofluorescence staining for LYVE-1 (red) showing lymphatic vessel 3 weeks after LIPUS, scale bar = 200 μm; LYVE-1: lymphatic vessel endothelial hyaluronan receptor 1. **(B)** The VEGF-C level at the lymphedema site. ($p < 0.05$, $n = 3$).

intervention was reported after its implementation. After years of significant progress, LIPUS was approved by the FDA for several diseases (Schandelmaier et al., 2017). Studies have demonstrated that LIPUS can reduce inflammation and accelerate vascular damage repair, and it has been widely used to treat various diseases (Harrison and Alt, 2021). Similarly, our results demonstrated that LIPUS could reduce secondary lymphedema by accelerating blood circulation and reducing inflammation.

We verified that LIPUS intervention significantly reduced the swelling in the rat tails model after lympectomy. The results

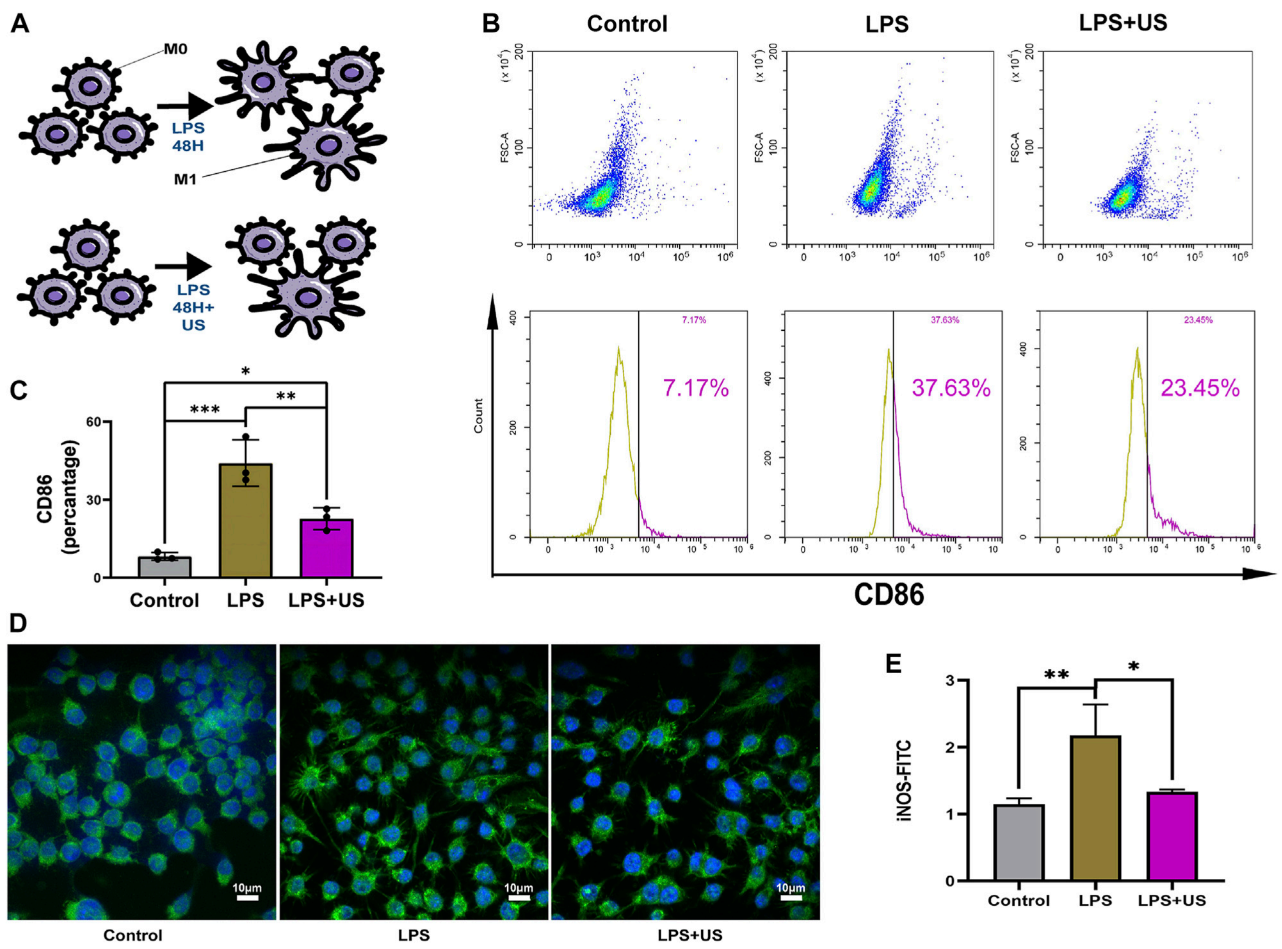

FIGURE 4
Cell experiments to examine the effect of LIPUS on macrophage polarization. **(A)** LIPUS regulates macrophage polarization. **(B,C)** The raw 264.7 cells were treated with LPS and LIPUS. Flow cytometry was performed to determine the percentage of CD86$^+$ macrophages ($p < 0.05$, $n = 3$). **(D,E)** The intensity of fluorescence staining of iNOS.

demonstrated the effectiveness of LIPUS treatment in relieving lymphedema. However, the volume of the rat tail began to differ significantly after 21 days, indicating that LIPUS treatment requires a certain course of treatment. In the acute swelling period, emergency treatment may still be required, and LIPUS is more suitable for medium- and long-term treatment. Second, the difference between treatment groups diminished over time, possibly due to the self-limitation of the rat tail lymphedema model.

Guilherme et al. (Cuadrado et al., 2021) found that inflammation precedes fat deposition in lymphedema, indicating the importance of inflammatory macrophages in lymphedema. Studies have reported that LIPUS inhibits inflammatory responses by reducing the proportion of M1 macrophages. Ultrasound may affect the polarization of macrophages by inhibiting the production of pro-inflammatory cytokines such as interleukin-33 (IL-33), IL-6, IL-8, and IL-1β and suppressing intracellular signaling such as extracellular signal-regulated kinase (ERK) and MAPK (Zhang et al., 2020; Iacoponi et al., 2023). Similarly, our cellular experiments confirmed that LIPUS could alter the polarization of macrophages in response to inflammatory stimulation. Kusuyama et al. (2019) reported that LIPUS inhibited inflammatory cytokines such as IL-1 and TNF- α. This finding is consistent with our conclusion: repolarization may be one of the major causes of LIPUS that can reduce lymphedema inflammation.

In lymphedema, subcutaneous tissue thickening was the most significant pathological change. Moreover, fibrosis is crucial for pathological changes. Studies have demonstrated that fibrosis occurs not only in subcutaneous fat but also in lymph and neonatal lymphatic vessels. Fibrosis seriously affects the function of lymphatic vessels and aggravates lymphedema. Animal model studies of lymphedema demonstrated that many neonatal lymphatic vessels appeared in the lymphedema lesion 2 weeks after model creation, but the neonatal lymphatic vessel was irregular. The irregular lumens hindered the function of lymphatic function. After LIPUS intervention, the thickness of the subcutaneous tissue and fat layer of the tail decreased, tissue fibrosis diminished, and lymphatic function improved, demonstrating the effectiveness of LIPUS in relieving lymphedema.

Lymphatic obstruction leads to an increased degree of swelling in lymphedema. Patrick et al. (Mucka et al., 2016) found that reduced vascular permeability could hinder lymphatic drainage and aggravate

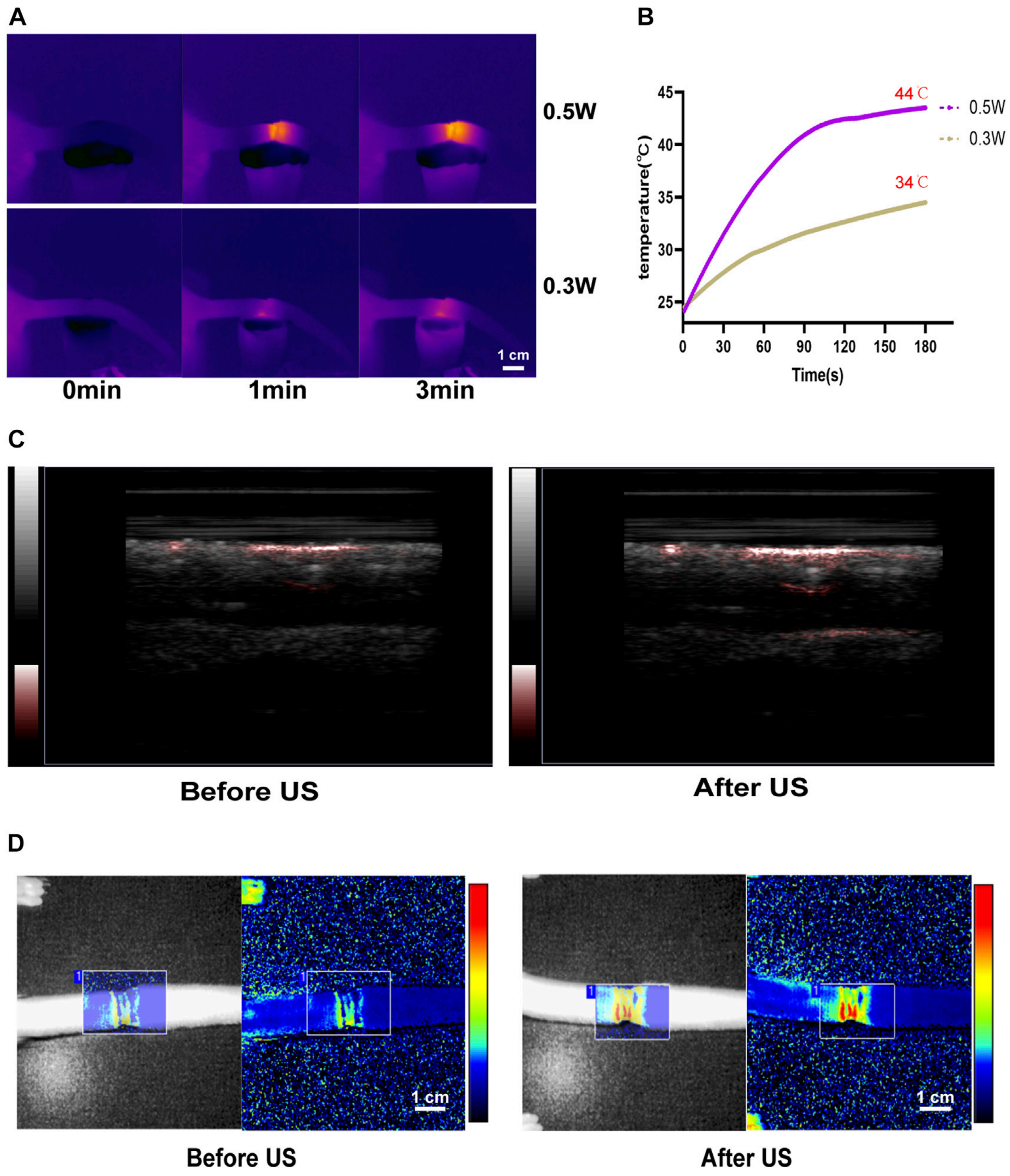

FIGURE 5
LIPUS enhances microcirculation in lymphedema tails. **(A,B)** The temperature of rat tail after LIPUS increase in different power density. **(C)** The blood flow of the rat tail increased after LIPUS treatment in the photoacoustic imaging system. **(D)** The blood flow of the rat tail increased after LIPUS treatment in the laser Doppler flowmetry (LDF).

lymphoedema swelling in Nrp2 deficient mice. In our study, the LIPUS treatment could promote microcirculation, improve vascular permeability, and increase blood flow; this is the short-term effect of ultrasound treatment (Kösters et al., 2017). Through mechanical stimulation, endogenous friction could promote blood and lymphatic circulation, improve the expression of VEGF-C, and accelerate the repair and lymphatic regeneration (Cheung et al., 2006). In the progression of lymphedema, lymphatic circulation disorder is the most important aggravating factor. We used LIPUS to stimulate the local circulatory ability, accelerate the lymphatic function of collateral compensation or stricture, and accelerate the repair function of the lymphatic system.

Our study revealed the relieving effect of LIPUS on secondary lymphedema. The results demonstrated that LIPUS could reduce lymphedema by regulating macrophage polarization and enhancing microcirculation. This finding offers a promising therapeutic way for lymphedema in the future. To overcome the existing ultrasonic treatment equipment, our team are working on a wearable ultrasound treatment device. It is also a practical attempt to improve the quality of life (QOL) of lymphedema patients.

Data availability statement

The original contributions presented in the study are included in the article/Supplementary Material, further inquiries can be directed to the corresponding authors.

Ethics statement

The animal study was reviewed and approved by the Animal Welfare Ethics Committee of Shanghai Sixth People's Hospital.

Author contributions

All authors participated in the design of concept, hypothesis, and aims of the study. XZ, XC, and YZ: conceptualization, funding acquisition, methodology, project administration, resources, supervision, validation, and writing—review and editing. All authors contributed to the article and approved the submitted version.

Funding

This work was supported by the Key Project of the National Natural Science Foundation of China (No. 82030050).

Acknowledgments

The authors are grateful for all those who have contributed.

Conflict of interest

Publisher's note

Supplementary material

The Supplementary Material for this article can be found online at: https://www.frontiersin.org/articles/10.3389/fbioe.2023.1173169/full#supplementary-material

References

Ahmed, R. L., Prizment, A., Lazovich, D., Schmitz, K. H., and Folsom, A. R. (2008). Lymphedema and quality of life in breast cancer survivors: The Iowa women's health study. *J. Clin. Oncol.* 26, 5689–5696. doi:10.1200/JCO.2008.16.4731

Cheung, L., Han, J., Beilhack, A., Joshi, S., Wilburn, P., Dua, A., et al. (2006). An experimental model for the study of lymphedema and its response to therapeutic lymphangiogenesis. *BioDrugs* 20, 363–370. doi:10.2165/00063030-200620060-00007

Cuadrado, G. A., de Andrade, M., Ariga, S. K., de Lima, T. M., and Souza, H. P. (2021). Inflammation precedes fat deposition in an experimental model of lymphedema. *Lymphat. Res. Biol.* 19, 116–125. doi:10.1089/lrb.2020.0061

Devoogdt, N., Thomis, S., De Groef, A., Heroes, A. K., Nevelsteen, I., Gebruers, N., et al. (2023). The effectiveness of fluoroscopy-guided manual lymph drainage as part of decongestive lymphatic therapy on the superficial lymphatic architecture in patients with breast cancer-related lymphoedema: A randomised controlled trial. *Cancers (Basel)* 15, 1545. doi:10.3390/cancers15051545

Farncombe, M., Daniels, G., and Cross, L. (1994). Lymphedema: The seemingly forgotten complication. *J. Pain Symptom Manage* 9, 269–276. doi:10.1016/0885-3924(94)90105-8

Fish, M. L., Grover, R., and Schwarz, G. S. (2020). Quality-of-Life outcomes in surgical vs nonsurgical treatment of breast cancer-related lymphedema: A systematic review. *JAMA Surg.* 155, 513–519. doi:10.1001/jamasurg.2020.0230

Fry, W. J., Barnard, J. W., Fry, E. J., Krumins, R. F., and Brennan, J. F. (1955). Ultrasonic lesions in the mammalian central nervous system. *Science* 122, 517–518. doi:10.1126/science.122.3168.517

Grada, A. A., and Phillips, T. J. (2017). Lymphedema: Pathophysiology and clinical manifestations. *J. Am. Acad. Dermatol* 77, 1009–1020. doi:10.1016/j.jaad.2017.03.022

Harrison, A., and Alt, V. (2021). Low-intensity pulsed ultrasound (LIPUS) for stimulation of bone healing - a narrative review. *Injury* 52 (2), S91–S96. doi:10.1016/j.injury.2021.05.002

Iacoponi, F., Cafarelli, A., Fontana, F., Pratellesi, T., Dumont, E., Barravecchia, I., et al. (2023). Optimal low-intensity pulsed ultrasound stimulation for promoting anti-inflammatory effects in macrophages. *Apl. Bioeng.* 7, 016114. doi:10.1063/5.0137881

Jiang, X., Savchenko, O., Li, Y., Qi, S., Yang, T., Zhang, W., et al. (2019). A review of low-intensity pulsed ultrasound for therapeutic applications. *IEEE Trans. Biomed. Eng.* 66, 2704–2718. doi:10.1109/TBME.2018.2889669

Jin, S., Zhang, C., Gao, M., Wang, T., Li, L., Yang, G., et al. (2021). Validation of laser scanning confocal microscopy as a diagnostic method for lymphedema using a rat model. *Lasers Med. Sci.* 36, 811–819. doi:10.1007/s10103-020-03106-y

Joiner, J. B., Kren, N. P., Durham, P. G., McRee, A. J., Dayton, P. A., and Pylayeva-Gupta, Y. (2022). Low-intensity focused ultrasound produces immune response in pancreatic cancer. *Ultrasound Med. Biol.* 48, 2344–2353. doi:10.1016/j.ultrasmedbio.2022.06.017

Kösters, A. K., Ganse, B., Gueorguiev, B., Klos, K., Modabber, A., Nebelung, S., et al. (2017). Effects of low-intensity pulsed ultrasound on soft tissue micro-circulation in the foot. *Int. Orthop.* 41, 2067–2074. doi:10.1007/s00264-017-3574-3

Kusuyama, J., Nakamura, T., Ohnishi, T., Albertson, B. G., Ebe, Y., Eiraku, N., et al. (2019). Low-intensity pulsed ultrasound promotes bone morphogenic protein 9-induced osteogenesis and suppresses inhibitory effects of inflammatory cytokines on cellular responses via Rho-associated kinase 1 in human periodontal ligament fibroblasts. *J. Cell. Biochem.* 120, 14657–14669. doi:10.1002/jcb.28727

Liang, M., Chen, Q., Peng, K., Deng, L., He, L., Hou, Y., et al. (2020). Manual lymphatic drainage for lymphedema in patients after breast cancer surgery: A systematic review and meta-analysis of randomized controlled trials. *Med. Baltim.* 99, e23192. doi:10.1097/MD.0000000000023192

Ling, L., Feng, X., Wei, T., Wang, Y., Wang, Y., Zhang, W., et al. (2017). Effects of low-intensity pulsed ultrasound (LIPUS)-pretreated human amnion-derived mesenchymal stem cell (hAD-MSC) transplantation on primary ovarian insufficiency in rats. *Stem Cell. Res. Ther.* 8, 283. doi:10.1186/s13287-017-0739-3

Liu, Y. C., Zou, X. B., Chai, Y. F., and Yao, Y. M. (2014). Macrophage polarization in inflammatory diseases. *Int. J. Biol. Sci.* 10, 520–529. doi:10.7150/ijbs.8879

Mucka, P., Levonyak, N., Geretti, E., Zwaans, B., Li, X., Adini, I., et al. (2016). Inflammation and lymphedema are exacerbated and prolonged by neuropilin 2 deficiency. *Am. J. Pathol.* 186, 2803–2812. doi:10.1016/j.ajpath.2016.07.022

Rockson, S. G., Keeley, V., Kilbreath, S., Szuba, A., and Towers, A. (2019). Cancer-associated secondary lymphoedema. *Nat. Rev. Dis. Prim.* 5, 22. doi:10.1038/s41572-019-0072-5

Sanal-Toprak, C., Ozsoy-Unubol, T., Bahar-Ozdemir, Y., and Akyuz, G. (2019). The efficacy of intermittent pneumatic compression as a substitute for manual lymphatic drainage in complete decongestive therapy in the treatment of breast cancer related lymphedema. *Lymphology* 52, 82–91. doi:10.2458/lymph.4629

Schandelmaier, S., Kaushal, A., Lytvyn, L., Heels-Ansdell, D., Siemieniuk, R. A., Agoritsas, T., et al. (2017). Low intensity pulsed ultrasound for bone healing: Systematic review of randomized controlled trials. *BMJ* 356, j656. doi:10.1136/bmj.j656

Schaverien, M. V., and Coroneos, C. J. (2019). Surgical treatment of lymphedema. *Plast. Reconstr. Surg.* 144, 738–758. doi:10.1097/PRS.0000000000005993

Trus, E., Basta, S., and Gee, K. (2020). Who's in charge here? Macrophage colony stimulating factor and granulocyte macrophage colony stimulating factor: Competing factors in macrophage polarization. *Cytokine* 127, 154939. doi:10.1016/j.cyto.2019.154939

Viola, A., Munari, F., Sánchez-Rodríguez, R., Scolaro, T., and Castegna, A. (2019). The metabolic signature of macrophage responses. *Front. Immunol.* 10, 1462. doi:10.3389/fimmu.2019.01462

Wang, S., Hossack, J. A., and Klibanov, A. L. (2020). From anatomy to functional and molecular biomarker imaging and therapy: Ultrasound is safe, ultrafast, portable, and inexpensive. *Invest. Radiol.* 55, 559–572. doi:10.1097/RLI.0000000000000675

Yang, C., Li, Y., Du, M., and Chen, Z. (2019). Recent advances in ultrasound-triggered therapy. *J. Drug Target* 27, 33–50. doi:10.1080/1061186X.2018.1464012

Yuan, Y., Arcucci, V., Levy, S. M., and Achen, M. G. (2019). Modulation of immunity by lymphatic dysfunction in lymphedema. *Front. Immunol.* 10, 76. doi:10.3389/fimmu.2019.00076

Yunna, C., Mengru, H., Lei, W., and Weidong, C. (2020). Macrophage M1/M2 polarization. *Eur. J. Pharmacol.* 877, 173090. doi:10.1016/j.ejphar.2020.173090

Zhang, B., Chen, H., Ouyang, J., Xie, Y., Chen, L., Tan, Q., et al. (2020). SQSTM1-dependent autophagic degradation of PKM2 inhibits the production of mature IL1B/IL-1β and contributes to LIPUS-mediated anti-inflammatory effect. *Autophagy* 16, 1262–1278. doi:10.1080/15548627.2019.1664705

Zhang, Z. C., Yang, Y. L., Li, B., Hu, X. C., Xu, S., Wang, F., et al. (2019). Low-intensity pulsed ultrasound promotes spinal fusion by regulating macrophage polarization. *Biomed. Pharmacother.* 120, 109499. doi:10.1016/j.biopha.2019.109499

frontiers | Frontiers in Bioengineering and Biotechnology

TYPE Original Research
PUBLISHED 11 May 2023
DOI 10.3389/fbioe.2023.1169124

OPEN ACCESS

EDITED BY
Long Bai,
East China University of Science and Technology, China

REVIEWED BY
Kunyu Zhang,
South China University of Technology, China
Johannes Greven,
University Hospital RWTH Aachen, Germany
Angela Jedlovszky-Hajdu,
Semmelweis University, Hungary

*CORRESPONDENCE
Yong Mei Chen,
✉ chenyongmei@sust.edu.cn

†These authors have contributed equally to this work

RECEIVED 18 February 2023
ACCEPTED 28 April 2023
PUBLISHED 11 May 2023

CITATION
Yang K, Wei W, Gao LT, Zhao XY, Liu Z, Li J, Li H, Miyatake H, Ito Y and Chen YM (2023), Dynamic and self-biodegradable polysaccharide hydrogel stores embryonic stem cell construct under ambient condition.
Front. Bioeng. Biotechnol. 11:1169124.
doi: 10.3389/fbioe.2023.1169124

Dynamic and self-biodegradable polysaccharide hydrogel stores embryonic stem cell construct under ambient condition

Kuan Yang[1†], Wei Wei[1†], Li Ting Gao[1†], Xin Yi Zhao[1], Zhenqi Liu[2], Jianhui Li[3], Haopeng Li[4], Hideyuki Miyatake[5], Yoshihiro Ito[5] and Yong Mei Chen[1]*

[1]College of Bioresources Chemical and Materials Engineering, National Demonstration Center for Experimental Light Chemistry Engineering Education, Shaanxi University of Science and Technology, Xi'an, China, [2]College of Chemistry, Xi'an Jiaotong University, Xi'an, China, [3]Department of Surgical Oncology, Shaanxi Provincial People's Hospital, Xi'an, China, [4]Second Affiliated Hospital of Xi'an Jiaotong University, Xi'an Jiaotong University, Xi'an, China, [5]Nano Medical Engineering Laboratory, RIKEN Cluster for Pioneering Research, Emergent Bioengineering Materials Research Team, RIKEN Center for Emergent Matter Science, Wako, Japan

The proper microenvironment is critical for the storage and transportation of embryonic stem cells (ESCs). To mimic a dynamic 3D microenvironment as it exists *in vivo* and consider "off-the-shelf" availability reaching the destination, we proposed an alternative approach that allows for facile storage and transportation of stem cells in the form of ESCs-dynamic hydrogel construct (CDHC) under ambient conditions. To form CDHC, mouse embryonic stem cells (mESCs) were *in-situ* encapsulated within a polysaccharide-based dynamic and self-biodegradable hydrogel. After storing CDHC in a sterile and hermetic environment for 3 days and then transferring to a sealed vessel with fresh medium for another 3 days, the large and compact colonies retained a 90% survival rate and pluripotency. Furthermore, after transporting and arriving at the destination, the encapsulated stem cell could be automatically released from the self-biodegradable hydrogel. After continuous cultivation of 15 generations of retrieved cells, automatically released from the CDHC, the mESCs underwent 3D encapsulation, storage, transportation, release, and continuous long-term subculture; resumed colony forming capacity and pluripotency were revealed by stem cell markers both in protein and mRNA levels. We believe that the dynamic and self-biodegradable hydrogel provides a simple, cost-effective, and valuable tool for storing and transporting "ready-to-use" CDHC under ambient conditions, facilitating "off-the-shelf" availability and widespread applications.

KEYWORDS

dynamic polysaccharide hydrogel, self-biodegradation, embryonic stem cell construct, storage, ambient condition

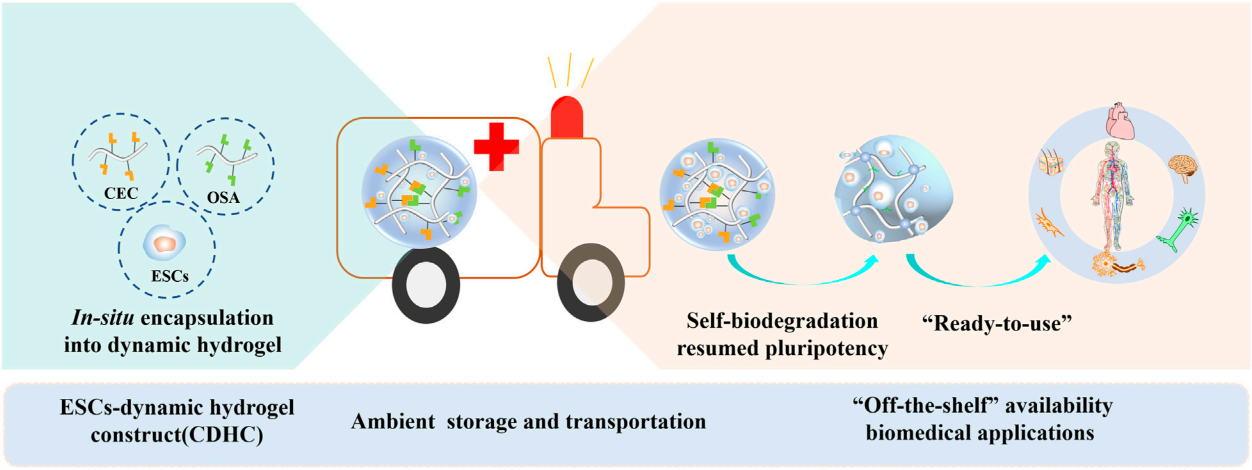

GRAPHICAL ABSTRACT

Highlights

- ESCs-dynamic hydrogel construct (CDHC) could be constructed through *in-situ* encapsulation of embryonic stem cells (ESCs) into polysaccharide based dynamic and self-biodegradable hydrogel.
- Large and compact colonies developed after storing and transportation of CDHC under ambient conditions.
- Automatically released ESCs resumed colony forming capacity and pluripotency.
- Storage and transportation of "ready-to-use" CDHC under ambient conditions facilitats "off-the-shelf" availability and widespread biomedical applications.

To mimic the dynamic 3D microenvironment in vivo and consider "off-the-shelf" availability reaching the destination, we propose an alternative approach to produce ESCs-dynamic hydrogel construct (CDHC), simultaneously considering storage and transportation of stem cells under ambient conditions. The mESCs undergone 3D encapsulation, storage, transportation, automatical release and continuous long-term subculture, resumed colony forming capacity and pluripotency, revealing stem cell markers both in protein and mRNA levels.

1 Introduction

A suitable microenvironment is crucial for the storage and transport of embryonic stem cells (ESCs), as they are highly active and the pluripotency of ESCs is very sensitive to disturbance by various stimuli. ESCs encapsulation in hydrogels has enormous potential for biomedical applications, including cell-based medicine, cytotherapy, tissue engineering, regenerative medicine, drug screening, and genetic disease research (Xue et al., 2018; Fang et al., 2021). Pluripotent ESCs are derived from the inner cell mass of pre-implantation embryos and display the unique properties of infinite proliferation, self-renewal, and multidirectional differentiation (Fu et al., 2021; Hoang et al., 2022). Hydrogels, that mimic the extracellular matrix (ECM) microenvironment, possess high moisture content, excellent material transfer ability, and a soft tissue-like elastic modulus. These properties enable them to protect encapsulated cells from external force and immune rejection (Wang M. et al., 2022), at the same time, they facilitate cell survival and function by promoting the transport of oxygen and nutrients, while also expelling secreted molecules and metabolic wastes (Rosales and Anseth, 2016; Huang et al., 2017).

A crucial step before usage is necessary for the quick availability of various applications: efficient storage of cell-laden hydrogel and reliable preservation for sustaining ESCs pluripotency. However, there are still logistical and bioprocessing challenges that need to be addressed to preserve stem cells (Murray and Gibson, 2022; Zhao et al., 2022). Storage methods can significantly affect cell performances, especially ESCs with stress sensitivities (e.g., external force, chemical substances, and temperature change). Cryopreservation is used to full fill the tasks of long-term storage and long-distance transportation associated with several biological and technical issues, including harsh conditions, uneconomical facilities, and complex procedures (Liu M. et al., 2022; Liu Z. et al., 2022; Zhan et al., 2022). Therefore, the major bottleneck is the safe and efficient implementation of ESCs storage and transportation under ambient conditions (Jiang et al., 2017; Guo et al., 2022), as well as the widespread applications of "off-the-shelf" availability.

We consider that an alternate strategy through the creation of a "ready-to-use" ESCs-hydrogel construct (CDHC) may overcome these obstacles, which can be done through the storage of stem cells within dynamic hydrogel via *in-situ* encapsulating of cells under physiological conditions. Meanwhile, the storage of stem cells encapsulated in dynamic hydrogels with the properties of biocompatibility and self-biodegradability may allow generating cell-biomaterial construct, which potentially realizes automatic cell release for "off-the-shelf" availability. The strategy does not require uneconomic facilities and cumbersome operating procedures. This "off-the-shelf" associated with transportation between the sites of manufacture and the destinations facilitates to use of CDHC directly. Designing the platform to realize the above ideal is an ongoing challenge. Self-healing hydrogels crosslinked via dynamically reversible bonds have the features of restoring their integrated structures and functionalities after damage. Because dissociation and association or recombination of reversible interactions between polymer chains can reestablish the dynamic equilibrium of networks to self-repair damaged regions (Wei et al., 2014; Rizwan et al., 2021), these reversible features of dynamic hydrogels mimic the intrinsic structural dynamics of the ECM microenvironment and soft tissues (Wei et al., 2020; Lou and Mooney, 2022). While existing strategies focus on dynamic hydrogels as biomaterials for the biomedical field (Wei et al., 2014; Wei et al., 2015; Rosales and Anseth, 2016; Wei et al., 2016; Wei et al., 2020; Zheng et al., 2021; Li S. et al., 2022; Eftekhari-Pournigjeh et al., 2022; Wang et al., 2023), much less effort has been exerted to formally evaluate the storage and transportation potentials of cell-dynamic hydrogel construct in which ESCs are encapsulated in dynamic and self-biodegradable hydrogels.

Here, we propose a “ready-to-use” ESCs-hydrogel construct based on a dynamic polysaccharide hydrogel, that considers both the storage and transport of ESCs and the “off-the-shelf” availability for widespread applications. Because encapsulation of stem cells in polysaccharide hydrogels is an enabling technology for producing “off-the-shelf” cell-biomaterial constructs, permitting the automatic release of stem cells in the process of self-biodegradation of polysaccharide hydrogels while maintaining their viability and phenotype for biomedical applications and basic research.

In view of the fact that 1) ESCs can be conveniently encapsulated *in-situ* in dynamic hydrogel under physiological conditions by mixing cell suspension and cell culture medium solving polysaccharides. 2) Synergistic effect of self-biodegradation and reversible bonding can accommodate the drastic volume expansion of growing colonies 3D encapsulated in polymer networks. 3) Superb biocompatibility and self-biodegradability of polysaccharides and dynamic bonds ensure high quality of ESCs-hydrogel constructs and automatically released cells for “off the shelf” availability. We developed a facile and economical approach to produce ESCs-dynamic hydrogel construct simultaneously considering the storage and transportation of stem cells under ambient conditions, as well as “off-the-shelf” availability for automatically released cells to their destination.

We fabricated a self-healing polysaccharide-based CEC-l-OSA hydrogel (“l” means “linked-by”) crosslinked by Schiff base reaction with imide bonds, in which oxidized sodium alginate (OSA) and N-carboxyethyl chitosan (CEC) were used as biocompatible and biodegradable backbones for *in-situ* encapsulation of ESCs. It is demonstrated that CEC-l-OSA hydrogel significantly promoted clonal expansion and preserved good pluripotency of the encapsulated mESCs which were subjected to storage in a sealed vessel for 3 days and then transferred to a fresh medium for another 3 days. Furthermore, the mESCs automatically released from dynamic hydrogel sustained pluripotency during continuous cultivation for 15 generations (over 25 days) with cell passaging every 5 days. The synergistic effect of self-biodegradation and reversibly crosslinked polymer networks of the hydrogel can provide a dynamic microenvironment and spaces to accommodate the growth of mESCs clonal and retain pluripotency.

This approach is facile for realizing short-term cell storage and express transportation of stem cells between different institutions under ambient conditions. Most importantly, after arriving at the destination, the characteristics of the stem cells were not changed, and the CDHC can be directly used without any further treatment. Our findings highlight that dynamic and self-biodegradable hydrogel provides a versatile and practical tool of facile, economical, and reliable stem cell-biomaterial construct to support the storage and “ready-to-use” properties of ESCs, facilitating “off-the-shelf” availability and widespread applications in biomedical fields and research.

2 Materials and methods

2.1 Materials

Chitosan (CAS: 9012-76-4, degree of deacetylation 86%, Mw = 200,000 Da) was purchased from Tokyo Kasei Kogyo Co., Ltd. Sodium alginate (CAS: 9005-38-3, >350 mpa.s) was ordered from Alfa Aesar. Sodium periodate (CAS: 7790-28-5) was bought from Sigma-Aldrich and acrylic acid (CAS:79-10-7) was obtained from Aladdin Biochemical Technology (Shanghai, Co., Ltd). All chemical reagents were analytical grade and used without further purification.

2.2 Synthesis and characterization of CEC and OSA

CEC was synthesized through Michael’s addition reaction, and OSA was synthesized by oxidation of sodium periodate, according to our previously reported method (Wei et al., 2015). The degree of substitution of the amino group in CEC is 48%. The oxidation degree of OSA is 50% determined by hydroxylamine hydrochloride titration. The details are available in the Supplementary Materials (Supplementary Materials S1–S3).

2.3 Preparation of CEC-l-OSA hydrogel

To prepare the dynamic hydrogel swelling solution in the same environment as the culture medium of stem cells, CEC (2 wt%, 4.5 ml) and OSA (10 wt%, 0.5 ml) solution were prepared using Dulbecco’s modified Eagles’ medium (DMEM, Gibco) culture medium (10% fetal bovine serum (FBS, Invitrogen), penicillin/streptomycin (Cellgro), respectively. The uniformly dynamic hydrogel could be obtained by homogeneously mixing the above solution at 37°C or under ambient conditions (25°C, 1013.25 kPa) while fixing the equimolar ratio of the reactive groups (M_{-NH2}: M_{-CHO} = 1).

2.4 Characterization of dynamic behaviors

Macroscopic dynamic behaviors like injection, self-healing, and remodeling of the CEC-l-OSA hydrogel were tested by gel extrusion and incision healing experiments. The microscopic dynamic behavior of the hydrogel and CDHC was monitored by rheological measurements at 37°C (S4).

2.5 Storage and transportation of 3D cultured mESCs in hydrogel

The routine culture of mESCs is described in the Supplementary Materials. To fabricate CDHC in which mESCs were 3D encapsulated into the matrix of dynamic hydrogel, mESCs were dissociated to single cells and suspended in DMEM medium containing CEC and OSA under sterile conditions, keeping cell density in the hydrogel was 3×10^6 cell/ml. The CDHC was stored in a sterile and hermetic environment for 3 days and then transferred into a sealed vessel with fresh medium for another 72 h to simulate transportation under ambient conditions. The encapsulated mESCs automatically released from the self-biodegradable hydrogel after the processes of storage and transportation. Collecting the released cells, the cells were subcultured according to the method of routine culture. The first generation of retrieved cells were denoted as S+T+P0, and the cells that continued to culture for 7 and 15 generations were denoted as S+T+P7 and S+T+P15, respectively. Calculation of the cell doubling time of different generations through software (www.doubling-time.com).

2.6 Cell viability and immunocytochemistry

Live/dead staining was used to assess cell viability. For immunocytochemistry, the 2D and 3D cultured mESCs in dynamic hydrogel were incubated with primary antibodies including OCT3/4 (1:200, Santa Cruz), NANOG (1:400, Abcam), SSEA-1 (1:200, Santa Cruz) followed by fluorescence secondary antibodies (Supplementary Table S1). Cell nuclei were stained with 4′,6-diamidino-2-phenylindole (DAPI, 1:1000, Sigma). Staining results were observed by laser confocal microscope (S5).

2.7 ALP detection and quantitative RT-PCR

Undifferentiated mESCs were identified by both qualitative and quantitative alkaline phosphatase (ALP) analyses. Quantitative RT-PCR reactions for NANOG, Oct3/4, DPPA5α, and Sox2 were performed using the Thermal Cycler Dice Real-Time PCR System (Takara) (S6, S8, Supplementary Table S2).

2.8 Statistical analysis

Each experiment was repeated three times. Data were analyzed by Excel (Microsoft) through conducting unpaired and independent Student's *t*-test for comparison between independent two groups. $p < 0.05$ was considered statistically significant.

3 Results and discussion

3.1 Experiment strategy

The strategy of fabricating "ready-to-use" CDHC in advance, using self-healing hydrogel crosslinked by reversible bonds as mimetics of structurally dynamic ECM microenvironment and soft tissues, and then storage under physiological conditions as an "off-the-shelf" availability for biomedical applications is shown in Figure 1. To *in-situ* build CDHC meeting the actual demand of cell storage and subsequent "ready-to-use" applications, ESCs laden CEC-l-OSA hydrogels were facilely fabricated by mixing a cell suspension, OSA (Figures 1Ai) and CEC (Figures 1Aii) dissolved in the culture medium of stem cells under physiological conditions (pH = 7.4, 37°C). The *in-situ* gelation could be realized by crosslinking polysaccharide backbones via Schiff base reaction between the aldehyde groups from OSA and the amino groups from CEC (Figures 1Aiii). Imide bond is a preferable option to fabricate dynamic hydrogel for assembling ambient storage "ready-to-use" CDHC, because the Schiff base reaction is known as the reversible and biocompatible crosslinking between the polysaccharides, conforming to biomedical applications (Wei et al., 2015; Wei et al., 2016). The ESCs-hydrogel construct could be quickly formed by homogeneous mixing cell suspension and polysaccharide solution for 120 s, which is suitable for homogeneous 3D cell encapsulation. It has been reported that stiff hydrogel hinders the colony growth of encapsulated mESCs, while comparatively, soft hydrogel facilitates the growth of mESC colonies (Ranga et al., 2014; Choi et al., 2016; Marco-Dufort and Tibbitt, 2019), thus, we purposed to fabricate a dynamic hydrogel with low stiffness providing a suitable living microenvironment for ESCs.

Self-biodegradation is important to release mESCs from CDHC. CEC-l-OSA hydrogel crosslinked by imine bonds can self-biodegrade in cell culture medium at 7 days due to a fast hydrolysis rate (Rizwan et al., 2021). In general, pH 4.5 is ideal for the formation of a stable Schiff base. However, the dissociation of the imine bond is stimulated when pH is greater than or less than 4.5. A 3D cell culture was performed under physiological conditions (pH = 7.4). In this case, the hydrogel crosslinked by dynamic imine bond is in a state of slow hydrolysis. Thus, after 6 days of incubation, most cells could be released from the hydrogel. The CDHC was stored in a sealed vessel under an ambient environment for 3 days and then transferred to a fresh medium for another 72 h. The colonies could be harvested after undergoing these processes, owing to partial self-biodegradation of the polysaccharide hydrogel. It is considered that hydrolytic degradation and enzymes produced by the cells may contribute to the degradation of polymer networks.

The synergistic effect of the dynamic hydrogel, including reversibly crosslinked polymer networks and self-biodegradation, provides a dynamic microenvironment and growing space for accommodating mESCs clonal expansion and maintaining pluripotency (Hozumi et al., 2018). After continuous cultivation of 15 generations with passaging released or retrieved cells every 5 days, the mESCs could maintain pluripotency over a long term (25 days), confirmed by ALP staining, immunofluorescence assay of pluripotency (OCT3/4, NANOG, SSEA-1), and RT-PCR analysis of expression marker (NANOG, Dppa5 α, Sox2). The dynamic and self-biodegradable hydrogel provides a tool of facile, cost-effective, and reliable "ready-to-use" CDHC to support short-term ESCs storage and "off-the-shelf" availability, facilitating widespread applications in biomedical applications and research (Figure 1B).

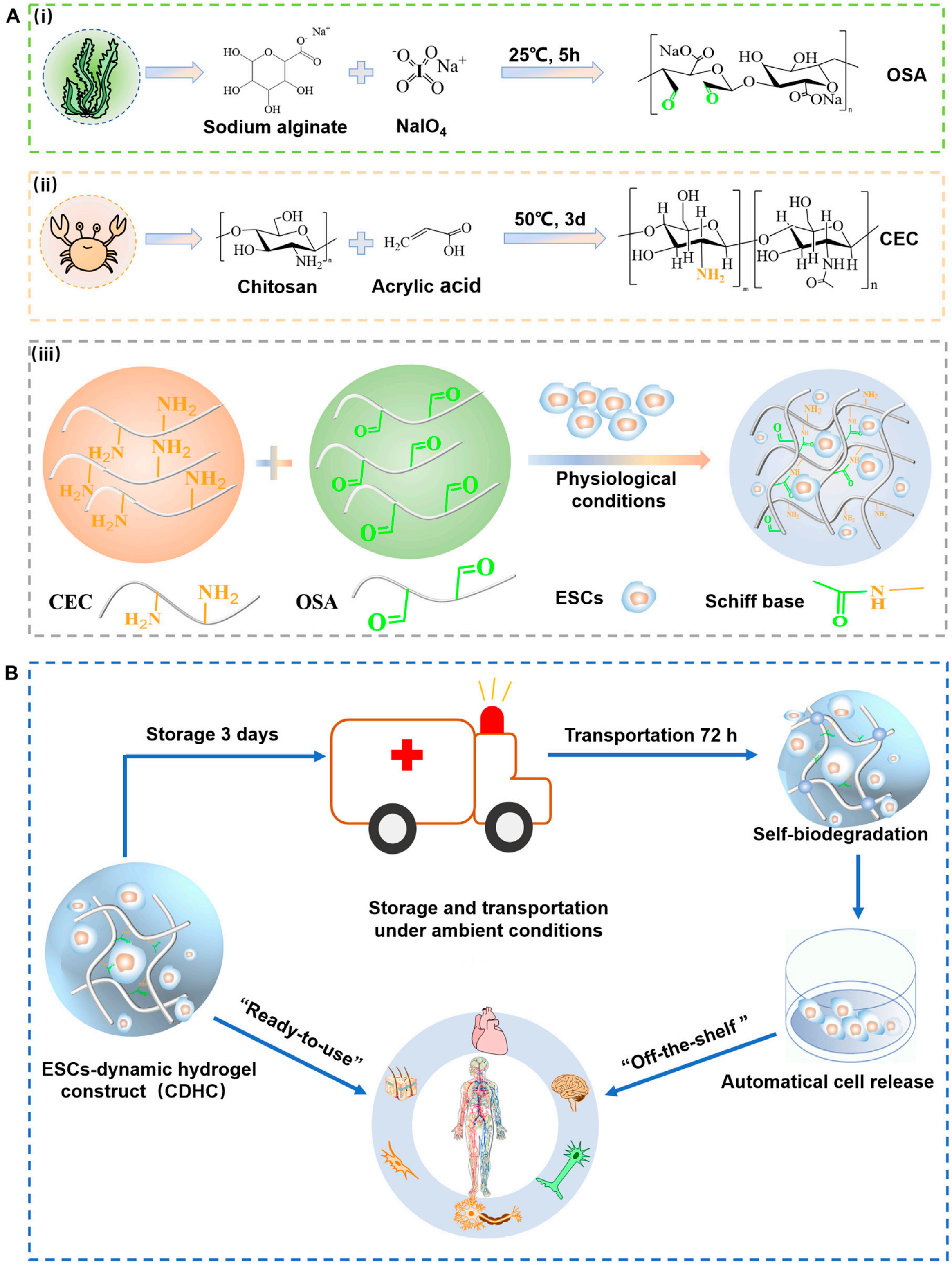

FIGURE 1
The strategy of storage and transportation of mESCs-dynamic hydrogel construct (CDHC) under ambient conditions. **(A)** Synthesis of **(Ai)** CEC and **(Aii)** OSA, **(Aiii)** fabrication of ESCs-hydrogel construct via encapsulating the cells into CEC-l-OSA hydrogel under physiological conditions. **(B)** The ambient storage and transportation of ESCs-hydrogel construct based on dynamic polysaccharide hydrogel for "off-the-shelf" applications in the biomedical field and research.

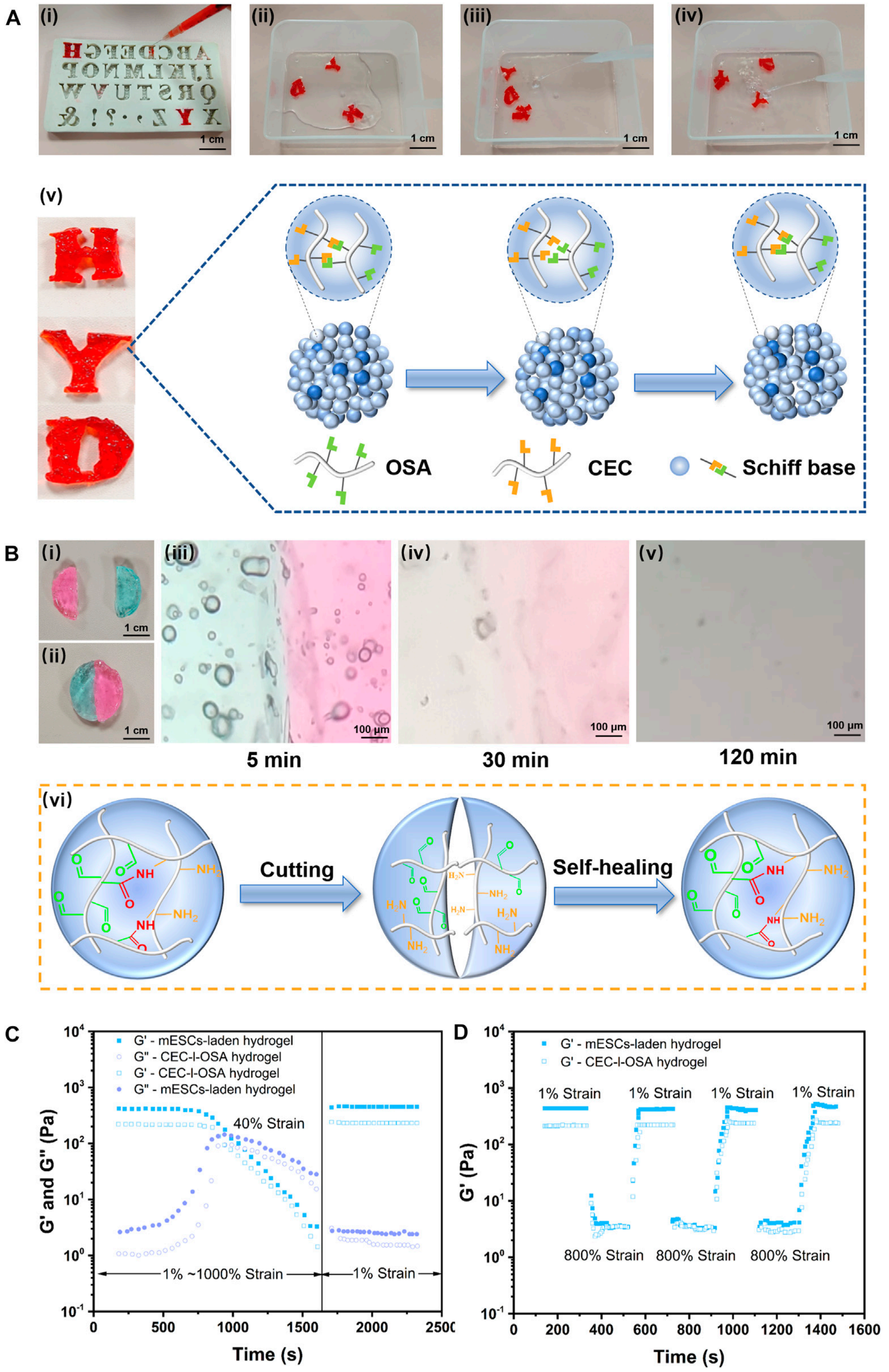

FIGURE 2
Versatile injectability, remodeling, and self-healing of the dynamic hydrogel and mESCs-hydrogel construct. **(A)** The hydrogel stained with food color red *in-situ* gelation into a syringe and squeezed out into the "H", "Y", and "D" templates (Scale bar: 1 cm) **(Ai)**, then the extruded gel particles were self-healed and remodeled to form integrated capitals after 5 min at 37°C without any external intervention (Scale bar: 100 μm) **(Aii)**. The self-healed gel capitals could withstand the impact force generated by water flow without splitting **(Aiii, Aiv)**. **(Av)** Schematic illustration of self-healing and integrity of the remodeled gel capitals constituted by extruded gel particles via dynamic imide bonds. **(B)** Photographs **(Bi, Bii)** (Scale bar: 1 cm), optical microscope images **(Aiii, Aiv, Av)** (Scale bar: 1 cm), and schematic illustrations highlighted dynamic imide bonds **(Avi)** of self-healing of two half disc hydrogels died by methylene blue and rhodamine, respectively. The rheological analysis of the dynamic hydrogel loading or without cells when stain change from 1% to 1000% at 10 rad/s **(C)** and alternating strains (1% and 800%) for three cycles with 200s intervals **(D)**.

3.2 Dynamic behaviors of hydrogel matrix and CDHC

The reversible crosslinking mechanism of imide bonds between the aldehyde and amino groups endows the hydrogel with excellent capabilities including injectability, self-healing, and remodeling (Wei et al., 2016). The macroscopic tests were performed to simultaneously evaluate these capabilities. As shown in Figures 2Ai (Supplementary Movie S1), the hydrogel stained with red food coloring was *in-situ* formed into a 26-gauge syringe and then extruded through a needle into a capital template with the shapes of "H", "Y", and "D". The dynamic hydrogel could be facilely squeezed through a needle, owing to easy breakage of dynamic bonds under shear stress during injection. The extruded hydrogel particles automatically self-healed to form new integrities with the same shapes as the capitals, via dynamic imine bonds for 5 min at 37°C without any external interventions (Figures 2Aii). Noteworthy, the self-healed and remodeling hydrogels with capital shapes constituted by gel particles were stable enough to endure PBS flush and maintain their shapes without splitting, demonstrating the self-healed and remodeled hydrogel could withstand the impact force (Figures 2Aiii,iv). A schematic illustration of self-healing and integrity of the remodeled gel capitals constituted by extruded gel particles via dynamic imide bonds is shown in Figures 2Av.

To further macroscopically observe the details of the healing interface, a disc-like piece of the hydrogel was cut into half from the middle (Figures 2Bi), and half dyed methylene blue, half stained with rhodamine, then they were autonomously healed for 5 min under 37°C when combined the two parts with different color (Figures 2Bii). Moreover, the boundary of contacting interface during the healing processes was observed under a microscope at ambient temperature. Initially, the boundary between the different colored pieces was very clear (Figures 2Biii), while the boundary became blurred over time, the interface became a blur and the colors diffused into each other after 30 min (Figures 2Biv). At last, the contacting interface almost disappeared after 120 min. The colors gradually disappeared due to washing out water soluble dyes in PBS solution (Figures 2Bv). These tests demonstrated good injectability and excellent self-healing capability of the CEC-l-OSA hydrogel when exposed to physiological saline (Wang Y. et al., 2022). Figures 2Bvi schematically illustrates the corresponding mechanism of self-healing depending on dynamic imide bonds.

To investigate the effect of 3D loading mESCs on the dynamic and self-healing performances of the hydrogel, we analyzed the rheological behaviors of CDHC, and compared it to a pristine CEC-l-OSA hydrogel (Wei et al., 2015). The rheological analysis in strain amplitude sweep tests at 10 rad/s revealed that, when increasing strain amplitude from 1% to 1000%, the storage modulus (G′) of the as-prepared CDHC significantly descended from 430.83 Pa to 3.28 Pa, whereas the corresponding loss modulus (G″) ascended from 2.64 Pa to 27.98 Pa. Similar, the G′ of the pristine dynamic hydrogel descended from 226.73 Pa to 1.46 Pa, while the corresponding G″ ascended from 1.07 Pa to 15.47 Pa. The results made clear that the mechanical properties of CDHC were higher than pristine hydrogel, meanwhile, the change tendency of G′ and G″ of the CEC-l-OSA hydrogel loading or without cells were similar within the increase of strain amplitude (1%–1000%) (Figure 2C). In addition, when the strain rose from 1% to 40%, and G′ kept at high values, which was significantly higher than the corresponding G″ maintaining at the low lever for both dynamic hydrogel and mESCs-hydrogel construct, indicating elastic-like gel behavior of the associated or crosslinked polysaccharides. Further rising strain to 40%, G′ value began to decrease, meanwhile, G″ value increased with strain growth, and the intersection points of G′ and G″ values of the two hydrogel samples appeared. At this point, the mechanical property of the samples was in the state of gel-to-sol transition, owing to the damage of some reversible imine bonds of polymer networks under relatively high strain. Moreover, when strain continued to rise from 40% to 1000%, most dynamic imide bonds were broken under high strain, leading to translation from the state of gel to sol with the drop of both G′ and G″ values. This liquid-like behavior is derived from the disassociation or uncrosslinking of polysaccharide chains under high stains (Li R. et al., 2022; Liang et al., 2022).

To further confirm the self-healing performance of CDHC, the samples were tested by alternating low (1%) and high (800%) shear strains with 200s intervals and compared with the pristine CEC-l-OSA hydrogel (Figure 2D). In these processes, the hydrogels underwent a transition between the state of gel and sol under alternating shear strains, respectively. When the shear strain rose from 1% to 800%, the CEC-l-OSA hydrogel loading or without cells exhibited the same trend, that is, the G′ values of both samples rapidly decreased dramatically about two orders of magnitude due to shear-thinning. This phenomenon demonstrates that the network structure of the dynamic hydrogels was destroyed under large strain, and the samples underwent a gel-sol transition. The dissociation of imide bonds among polysaccharide chains is believed to contribute to fast stress relaxation of the dynamic covalently crosslinked hydrogel. On the other hand, when the shear strain declined from 800% to 1%, the G′ value almost fully restored to the initial level of gel state instantaneously, as associations or recovery of dissociated dynamic polymer networks.

The above consequences confirm that the excellent self-healing performance of the CEC-l-OSA hydrogel could be maintained when 3D encapsulation of mESCs. Moreover, the G′ value (430.83 Pa) of CDHC was higher than that of the dynamic hydrogel (G′ = 226.73 Pa), which is attributed to the fact that the dynamic hydrogel can wonderfully accommodate the stem cells into dynamic polymer networks after 3D cell encapsulation. The cells take up a certain space in the 3D polymer networks, improving the mechanical strength of the cell-biomaterial construct to a certain extent. The aforementioned fast relaxation, shear-thinning, and self-healing behaviors of CDHC, which is similar to CEC-l-OSA hydrogel, confirmed that the hydrogel encapsulated mESCs inherited self-healing property of the dynamic hydrogel, and the dynamic polysaccharide networks enabled rearrangement to accommodate loading cells.

3.3 Storage and transportation of CDHC under ambient condition

To simulate the processes of cell storage, the as-prepared CDHC in which mESCs encapsulated in the CEC-l-OSA hydrogel (3×10^6 cell/ml cells, MEF-conditioned medium containing LIF and mESC specific serum) was stored in a sterile and hermetic

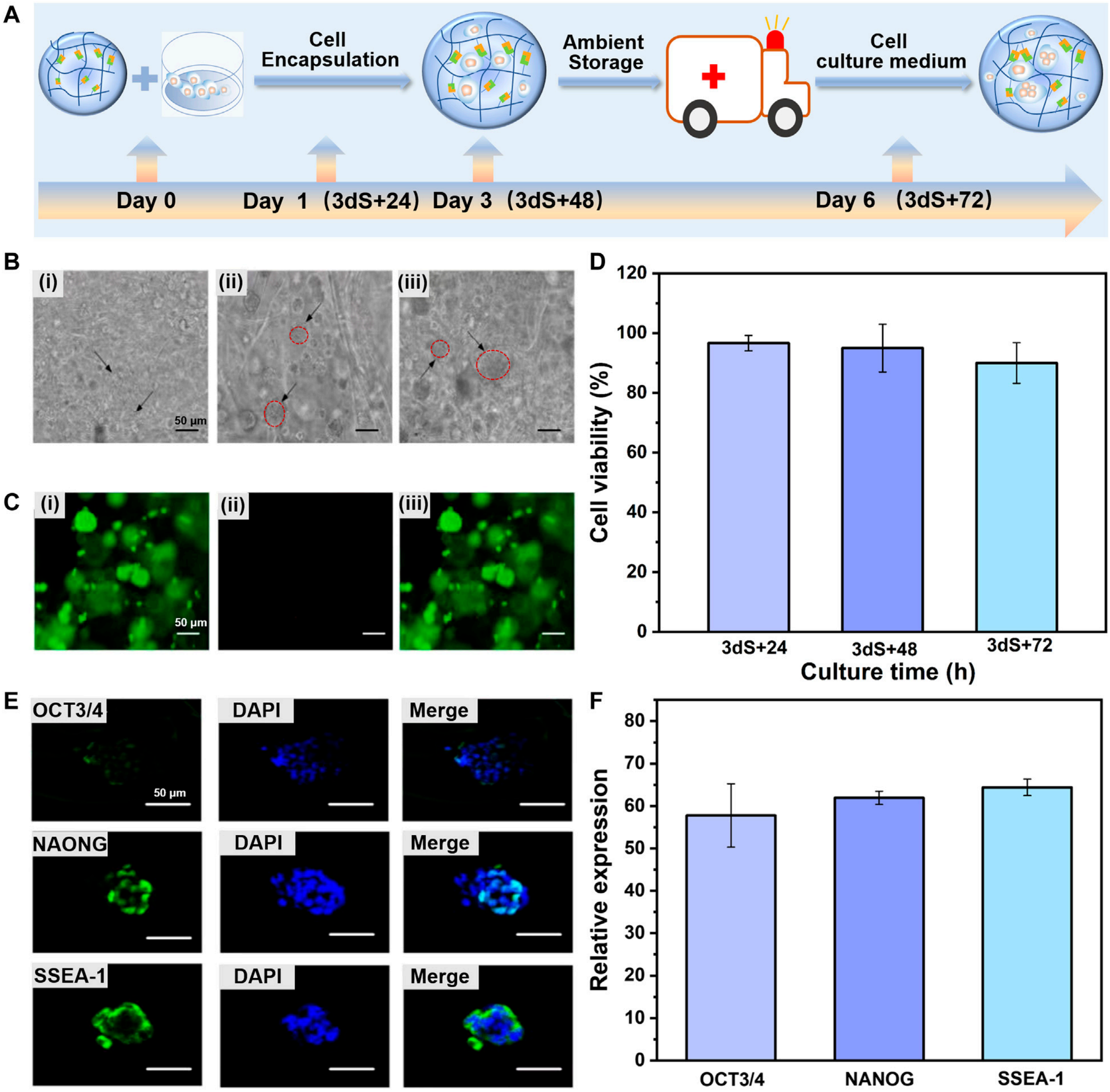

FIGURE 3
Dynamic hydrogel supports colony expansion and pluripotency of encapsulated mESCs during storage and transportation of mESCs-hydrogel construct at ambient conditions. **(A)** Schematic illustration of the time scale of storage and transportation of mESCs-hydrogel construct. **(B)** Optical microscope images of ESCs encapsulated in hydrogel after storage and then continuous incubation in fresh cell culture medium to transportation for 3 dS+24 h **(Bi)**, 3 dS+48 h **(Bii)**, and 3 dS+72 h **(Biii)** (Scale bar: 50 μm). **(C)** The live/dead staining images of encapsulated mESCs continuously cultured 3 dS+72 h, live cells **(Ci)**, dead cells **(Cii)**, and merge image **(Ciii)** (Scale bar: 50 μm). **(D)** The viability of encapsulated ESCs continuously cultured for 3 dS+24 h, 3 dS+48 h, and 3 dS+72 h. The immunofluorescence staining **(E)** (Scale bar: 50 μm) and relative expression **(F)** for OCT3/4, NAONG, SSEA-1 of encapsulated mESCs continuously cultured for 3 dS+72 h. The data is presented as the means ± SD, n = 12.

environment under ambient temperature for 3 days without adding more culture medium, to reduce the activity of the stem cells and temporarily make cells become quiescent. Subsequently, to simulate cell transportation process, the CDHC was transferred into a sealed vessel filled with fresh cell culture medium and continuously incubated for another 72 h (typically 3 days for domestic delivery) without refreshments under ambient temperature. The corresponding samples during transportation time points of 24, 48, and 72 h was denoted as 3 dS + 24 h, 3 dS + 48 h, and 3 dS + 72 h, respectively. Figure 3A schematic illustration of the time scale of storage and transportation of CDHC. Meanwhile, the colony growth and immunofluorescence staining of pluripotency markers (OCT3/4, NANOG, and SSEA-1) were recorded. The bright-field images showed that mESCs were uniformly distributed within the hydrogel matrix, and colony size increased during the transportation process of continuous incubation after storage. The colonies gradually increased from *c.a.* 5 μm in diameter for 3 dS + 24 h to *c.a.* 60 μm after 3 dS + 72 h transportation, meanwhile, the formation of tight spherical colonies was witnessed, confirming that the dynamic hydrogel promotes robust colony growth during the processes of storage and transportation (Figure 3B). The growth of large and compact colonies was presumably attributed to microenvironment synergistic effects of viscoelastic CEC-l-OSA hydrogel, including dynamic polymer networks, softness, and self-biodegradation, which provide a remodeling surrounding, minimum mechanical interference and stress relaxation.

Furthermore, live/dead staining assay at the transportation time point of 3 dS + 72 h revealed that the majority of mESCs 3D cultured within the dynamic hydrogel adapted and facilitated colony growth, and remained at more than 90% cell viability (acridine orange labels live cells green), whereas very few apoptotic cells (propidium iodide labels dead cells red) (Figure 3C). As shown in Figure 3D, the cell viability was 96.92%, 95.02%, and 90.67% for 3 dS + 24 h, 3 dS + 48 h, and 3 dS + 72 h transportation time points, respectively. The transported stem cells preserved a high survival rate, confirming the cytocompatibility of CEC-l-OSA hydrogel. Pluripotency is the most valuable property to support extensive applications of CDHC. The results of immunofluorescence staining of several representative pluripotency markers demonstrated that substantial expression of OCT3/4, NANOG, and SSEA-1 of the mESCs colony grown within the dynamic hydrogel in 3D cultured for 3 dS + 72 h transportation time point (Figures 3E, F), indicating that the transported stem cells retained the expression of ESCs markers at the protein level, The results showed that the mESCs could express pluripotency marker normally after the processes of encapsulation, storage, and transportation, which proved that 3D culture of the encapsulated mESCs in the dynamic hydrogel could maintain the pluripotency of mESCs well. The above-mentioned results indicate that the dynamic property of polymer networks and transport of sufficient nutrients and oxygen within the self-biodegradable hydrogels could robustly support colony expansion and pluripotency of the 3D encapsulated mESCs during storage and transportation.

3.4 Pluripotency of released mESCs from dynamic hydrogel

The ultimate goal of this study is to fabricate CDHC for applications in biomedical fields and research, thus, the features of stem cells like normal proliferation and pluripotency should not be compromised during the period of storage and transportation under ambient conditions (Mei et al., 2010; Celiz et al., 2014). To this end, the properties of mESCs released from dynamic hydrogel were analyzed. Indeed, in our system, the encapsulated stem cells could be automatically released from the CEC-l-OSA hydrogel after the processes of 3 days of storage and further 72 h transportation, owing to the self-biodegradation of the dynamic hydrogel.

Based on the capabilities of automatical cell release and self-biodegradation, mESCs could be facilely harvested or retrieved from hydrogel after transportation within a certain period, without using any enzymes or external stimuli. These merits facilitate to obtain of a biocompatible "off-the-shelf" construct of ESCs-dynamic hydrogel. To further evaluate the proliferation and stemness of released mESCs during long-term culture, the behaviors of doubling time (the time of doubling cell number of its initial value) and pluripotency of the mESCs automatically released from the hydrogel after 3 days storage and 120 h transportation, was evaluated after further incubation. The morphology and doubling time of the mESCs just released from hydrogel (denoted as S+T+P0), and the cells after continued culture for 7 and 15 generations (denoted as S+T+P7, S+T+P15) with cell passaging every 5 days were characterized. The results showed that the stem cells released from hydrogel, both freshly released S+T+P0 cells (Figures 4Aii) and continuously cultured for S+T+P7 (Figures 4Aiii) and S+T+P15 (Figures 4Aiv) generations, could form spherical and compact colonies and had no obvious morphological difference comparing with the stem cells cultured by routine culture (control group) (Figures 4Ai). At the same time, the released stem cells were still enabled to proliferate with culture time, the doubling time was 32.87%, 28.24%, and 29.77%, respectively, for S+T+P0, S+T+P7, S+T+P15 generations which were not significantly different from that of routinely cultured mESCs (29.25%) under the same cell seeding density (Figure 4E). The above results proved that the retrieved mESCs undergone storage and transportation can not only sustain proliferation but also ensure a high biological activity to form colonies, that is, at the same level as that of routinely cultured mESCs.

To judge whether the mESCs automatically released from the hydrogel still retained pluripotency, ALP staining, a specific and sensitive method for phenotypic assessment of ESCs by determination of the activity of alkaline phosphatase, was used to preliminarily detect the pluripotency of released stem cells. As shown in Figure 4C, the retrieved mESCs (S+T+P0) and the stem cells after continuing to culture as S+T+P7 and S+T+P15 generations were stained brown-red under the action of ALP reagent, like routinely cultured stem cells without hydrogel encapsulation and before storage/transportation. The quantitative test of ALP staining results further showed that there was no significant difference in the activity of alkaline phosphatase between the retrieved mESCs and routinely cultured stem cells without hydrogel encapsulation and before storage/transportation (Figure 4F). The above results preliminarily proved that the released stem cells could resume normal capabilities of colony formation and pluripotency.

To further demonstrate the retrieved mESCs could maintain pluripotency after long-term subculture, the stem cell markers both in protein and mRNA levels were analyzed. The compact and well-defined colonies formed by the stem cells with S+T+P0, S+T+P7, and S+T+P15 generations when cultured for 48 h, and the colonies exhibited robust immunofluorescence staining for Oct3/4, NANOG, and SSEA-1 (Figure 4D). At the same time, there was no significant difference in their expression levels compared with the routine passaging of mESCs. To quantitatively verify the pluripotency of the released mESCs with long-term passaging, we next analyzed the expression of pluripotency of related genes S+T+P15 generation using RT-PCR detection. Consisting with the results of immunofluorescence staining, the RT-PCR analysis also showed significantly higher expression levels of NANOG, Dppa5a, and Sox2, and there was no significant difference in the expression compared with

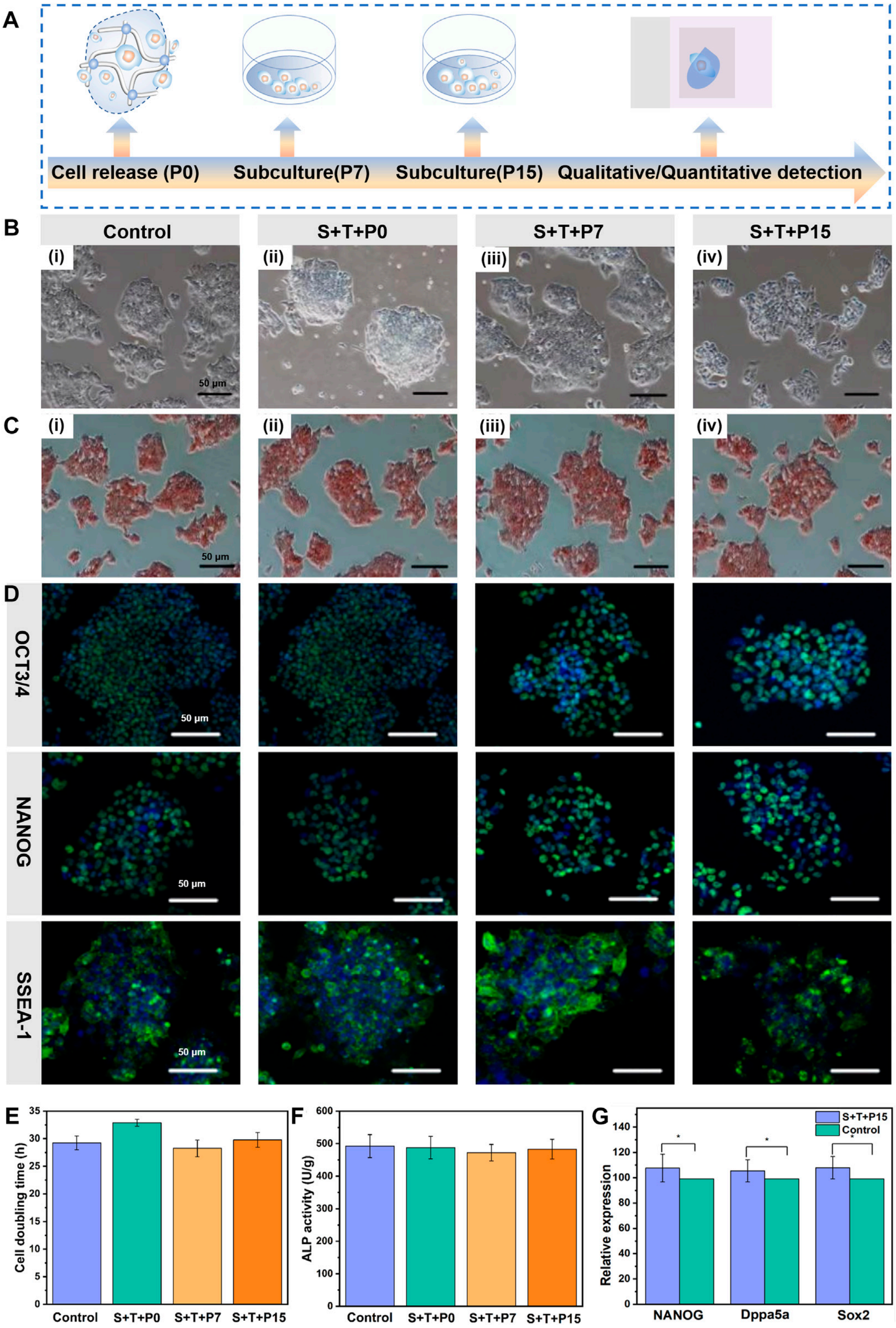

FIGURE 4
Pluripotency of automatically released mESCs from the dynamic hydrogel. **(A)** Schematic illustration of the time scale of continuous subculture and quantitative detection of released mESCs. **(B)** Optical microscope images, **(C)** ALP staining images, **(D)** Immunofluorescence staining of routinely cultured ESCs without hydrogel encapsulation and before storage/transportation **(Bi)**, S+T+P0 **(Bii)**, S+T+P7 **(Biii)**, and S+T+P15 **(Biv)** (Scale bar: 50 μm). **(E)** Cell doubling time, **(F)** ALP activity, and **(G)** Relative expression for NANOG, Dppa5a, Sox2 of routinely cultured ESCs without hydrogel encapsulation and before storage/transportation (control) and S+T+P15. The data are presented as the means ± SD, n = 12, $^{*}p < 0.05$.

routinely passaged stem cells, indicating released mESCs maintained functional pluripotency after 25 days continuous culture (Figure 4F). In Figure 4G, the S+T+P15 group was the mESCs automatically released from the dynamic hydrogel after 3 days of storage and 120 h transportation, and continued culture for 15 generations (denoted as S+T+P7, S+T+P15). Due to the dynamic hydrogel that could support the self-renewal and differentiation of ESCs in biomimetic 3D and dynamic environments, the S+T+P15 group has higher expression of NANOG, Dppa5a, Sox2 than the routinely cultured ESCs without hydrogel encapsulation and before storage/transportation (control group). Due to the dynamic hydrogel that could support the self-renewal and differentiation of ESCs in biomimetic 3D and dynamic environments (Xu et al., 2022), these findings together indicate that the CEC-l-OSA hydrogel could be an effective dynamic culture platform for the ESCs-hydrogel construct that can keep the pluripotency of stem cells at both protein and gene levels.

4 Conclusion

The approaches of safe storage and transportation of ESCs for reliable preservation of stem cell survival and pluripotency is a bottleneck to the distribution of stem cells for biomedical applications and research. However, the current cryopreservation involves ice crystal formation, toxic cryoprotective agents, and cold chain management, which are technically challenging and financially expensive. The goal of this study is to design a facile and efficient approach for the storage and transportation of ESCs under ambient conditions. To this end, we proposed an alternative approach taking into consideration of ambient storage, transportation, and "off-the-shelf" availability simultaneously. That is, storage and transportation of stem cells facilely in the form of CDHC, through encapsulating ESCs within dynamic and self-biodegradable polysaccharide hydrogel. Conclusions could be drawn from the results that our facile and economic approach only involves *in-situ* encapsulation of stem cells inside dynamic polysaccharide hydrogel, storage, and transportation for a few days under ambient conditions. The large and tight spherical colonies with an expression of pluripotency markers (OCT3/4, NANOG, and SSEA-1) formed in dynamic hydrogel after storage and subsequently transformation, and the viability of mESCs remained >90%. Moreover, the automatically released stem cells resumed typical capabilities of colony formation and pluripotency after long-term continuous culture (25 days) confirmed by stem cell markers both in protein and mRNA (NANOG, Dppa5a, and Sox2) levels. This preservation approach of ESCs-hydrogel construct is easy to scale up for generation, storage, and transportation of a large number of biocompatible and self-biodegradable ESCs-hydrogel construct under ambient conditions, having wide potentials in biomedical applications and research as "off-the-shelf" availability.

Data availability statement

The datasets presented in this study can be found in online repositories. The names of the repository/repositories and accession number(s) can be found in the article/Supplementary Material.

Author contributions

YC conception and design, administrative support the work. KY, WW, LG, XZ, and ZL performed all the experiments and collected and assembled data. KY, JL, HL, HM, and YI data analysis and interpretation. KY wrote the article draft and editing. YC contributed to the manuscript revision overview and correction. All authors listed have made a substantial, direct, and intellectual contribution to the work and approved it for publication. All authors contributed to the article and approved the submitted version.

Funding

This work was supported by Key Intergovernmental Special Projects of the National Key R & D Plan of the People's Republic of China (2022YFE0104200); International Science & Technology Key Research and Development Program of Shaanxi (2020KWZ-006); High-end foreign expert introduction plan (G20200241017); The research project grant of the joint logistic support force (BLB18J014); YC is grateful for the startup funds from Shaanxi University of Science and Technology.

Conflict of interest

The authors declare that the research was conducted in the absence of any commercial or financial relationships that could be construed as a potential conflict of interest.

Publisher's note

Supplementary material

The Supplementary Material for this article can be found online at: https://www.frontiersin.org/articles/10.3389/fbioe.2023.1169124/full#supplementary-material

References

Celiz, A. D., Smith, J. G. W., Langer, R., Anderson, D. G., Winkler, D. A., Barrett, D. A., et al. (2014). Materials for stem cell factories of the future. *Nat. Mater* 13 (6), 570–579. doi:10.1038/nmat3972

Choi, B., Park, K. S., Kim, J. H., Ko, K. W., Kim, J. S., Han, D. K., et al. (2016). Stiffness of hydrogels regulates cellular reprogramming efficiency through mesenchymal-to-epithelial transition and stemness markers. *Macromol. Biosci.* 16 (2), 199–206. doi:10.1002/mabi.201500273

Eftekhari-Pournigjeh, F., Saeed, M., Rajabi, S., Tamimi, M., and Pezeshki-Modaress, M. (2022). Three-dimensional biomimetic reinforced chitosan/gelatin composite scaffolds containing PLA nano/microfibers for soft tissue engineering application. *Int. J. Biol. Macromol.* 19 (S0141), 1028–1037. doi:10.1016/j.ijbiomac.2022.11.165

Fang, Y., Shi, L., Duan, Z., and Rohani, S. (2021). Hyaluronic acid hydrogels, as a biological macromolecule-based platform for stem cells delivery and their fate control: A review. *Int. J. Biol. Macromol.* 189, 554–566. doi:10.1016/j.ijbiomac.2021.08.140

Fu, J., Warmflash, A., and Lutolf, M. P. (2021). Stem-cell-based embryo models for fundamental research and translation. *Nat. Mater* 20 (2), 132–144. doi:10.1038/s41563-020-00829-9

Guo, J., Amini, S., Lei, Q., Ping, Y., Agola, J. O., Wang, L., et al. (2022). Robust and long-term cellular protein and enzymatic activity preservation in biomineralized mammalian cells. *ACS Nano* 16 (2), 2164–2175. doi:10.1021/acsnano.1c08103

Hoang, D. M., Pham, P. T., Bach, T. Q., Ngo, A. T. L., Nguyen, Q. T., Phan, T. T. K., et al. (2022). Stem cell-based therapy for human diseases. *Signal Transduct. Target Ther.* 7 (1), 272. doi:10.1038/s41392-022-01134-4

Hozumi, T., Kageyama, T., Ohta, S., Fukuda, J., and Ito, T. (2018). Injectable hydrogel with slow degradability composed of gelatin and hyaluronic acid cross-linked by schiff's base formation. *Biomacromolecules* 19 (2), 288–297. doi:10.1021/acs.biomac.7b01133

Huang, G., Li, F., Zhao, X., Ma, Y., Li, Y., Lin, M., et al. (2017). Functional and biomimetic materials for engineering of the three-dimensional cell microenvironment. *Chem. Rev.* 117 (20), 12764–12850. doi:10.1021/acs.chemrev.7b00094

Jiang, B., Yan, L., Miao, Z., Li, E., Wong, K. H., and Xu, R. H. (2017). Spheroidal formation preserves human stem cells for prolonged time under ambient conditions for facile storage and transportation. *Biomaterials* 133, 275–286. doi:10.1016/j.biomaterials.2017.03.050

Li, R., Zhou, C., Chen, J., Luo, H., Li, R., Chen, D., et al. (2022a). Synergistic osteogenic and angiogenic effects of KP and QK peptides incorporated with an injectable and self-healing hydrogel for efficient bone regeneration. *Bioact. Mater* 18, 267–283. doi:10.1016/j.bioactmat.2022.02.011

Li, S., Dong, Q., Peng, X., Chen, Y., Yang, H., Xu, W., et al. (2022b). Self-healing hyaluronic acid nanocomposite hydrogels with platelet-rich plasma impregnated for skin regeneration. *ACS Nano* 16 (7), 11346–11359. doi:10.1021/acsnano.2c05069

Liang, Y., Xu, H., Li, Z., Zhangji, A., and Guo, B. (2022). Bioinspired injectable self-healing hydrogel sealant with fault-tolerant and repeated thermo-responsive adhesion for sutureless post-wound-closure and wound healing. *Nano-Micro Lett.* 14 (1), 185. doi:10.1007/s40820-022-00928-z

Liu, M., Chen, C., Yu, J., Zhang, H., Liang, L., Guo, B., et al. (2022a). The gelatin-based liquid marbles for cell cryopreservation. *Mater. Today Bio* 17, 100477. doi:10.1016/j.mtbio.2022.100477

Liu, Z., Zheng, X., and Wang, J. (2022b). Bioinspired ice-binding materials for tissue and organ cryopreservation. *J. Am. Chem. Soc.* 144 (13), 5685–5701. doi:10.1021/jacs.2c00203

Lou, J., and Mooney, D. J. (2022). Chemical strategies to engineer hydrogels for cell culture. *Nat. Rev. Chem.* 6 (10), 726–744. doi:10.1038/s41570-022-00420-7

Marco-Dufort, B., and Tibbitt, M. W. (2019). Design of moldable hydrogels for biomedical applications using dynamic covalent boronic esters. *Mat. Today Chem.* 12, 16–33. doi:10.1016/j.mtchem.2018.12.001

Mei, Y., Saha, K., Bogatyrev, S. R., Yang, J., Hook, A. L., Kalcioglu, Z. I., et al. (2010). Combinatorial development of biomaterials for clonal growth of human pluripotent stem cells. *Nat. Mater* 9 (9), 768–778. doi:10.1038/nmat2812

Murray, K. A., and Gibson, M. I. (2022). Chemical approaches to cryopreservation. *Nat. Rev. Chem.* 6 (8), 579–593. doi:10.1038/s41570-022-00407-4

Ranga, A., Gobaa, S., Okawa, Y., Mosiewicz, K., Negro, A., and Lutolf, M. P. (2014). 3D niche microarrays for systems-level analyses of cell fate. *Nat. Commun.* 14 (5), 4324. doi:10.1038/ncomms5324

Rizwan, M., Baker, A. E. G., and Shoichet, M. S. (2021). Designing hydrogels for 3D cell culture using dynamic covalent crosslinking. *Adv. Healthc. Mater* 10 (12), e2100234. doi:10.1002/adhm.202100234

Rosales, A. M., and Anseth, K. S. (2016). The design of reversible hydrogels to capture extracellular matrix dynamics. *Nat. Rev. Mater* 1 (2), 15012. doi:10.1038/natrevmats.2015.12

Wang, J., Cheng, H., Chen, W., Han, P., Yao, X., Tang, B., et al. (2023). An injectable, self-healing composite hydrogel with enhanced near-infrared photo-antibacterial therapeutic effects for accelerated wound healing. *Chem. Eng. J.* 452, 139474. doi:10.1016/j.cej.2022.139474

Wang, M., Guo, Y., Deng, Z., and Xu, P. (2022a). Engineering elastic bioactive composite hydrogels for promoting osteogenic differentiation of embryonic mesenchymal stem cells. *Front. Bioeng. Biotechnol.* 10, 1022153–1022215. doi:10.3389/fbioe.2022.1022153

Wang, Y., Li, X., Yuan, J., Wang, X., Tao, K., and Yan, J. (2022b). A bionic self-assembly hydrogel constructed by peptides with favorable biosecurity, rapid hemostasis and antibacterial property for wound healing. *Front. Bioeng. Biotechnol.* 10, 901534–901611. doi:10.3389/fbioe.2022.901534

Wei, Z., Schnellmann, R., Pruitt, H. C., and Gerecht, S. (2020). Hydrogel network dynamics regulate vascular morphogenesis. *Cell Stem Cell* 27 (5), 798–812.e6. doi:10.1016/j.stem.2020.08.005

Wei, Z., Yang, J. H., Liu, Z. Q., Xu, F., Zhou, J. X., Zrinyi, M., et al. (2015). Novel biocompatible polysaccharide-based self-healing hydrogel. *Adv. Funct.* 25 (9), 1352–1359. doi:10.1002/adfm.201401502

Wei, Z., Yang, J. H., Zhou, J., Xu, F., Zrinyi, M., Dussault, P. H., et al. (2014). Self-healing gels based on constitutional dynamic chemistry and their potential applications. *Chem. Soc. Rev.* 43 (23), 8114–8131. doi:10.1039/c4cs00219a

Wei, Z., Zhao, J., Chen, Y. M., Zhang, P., and Zhang, Q. (2016). Self-healing polysaccharide-based hydrogels as injectable carriers for neural stem cells. *Sci. Rep.* 6, 37841. doi:10.1038/srep37841

Xu, X., Feng, Q., Ma, X., Deng, Y., Zhang, K., Ooi, H. S., et al. (2022). Dynamic gelatin-based hydrogels promote the proliferation and self-renewal of embryonic stem cells in long-term 3D culture. *Biomaterials* 289, 121802. doi:10.1016/j.biomaterials.2022.121802

Xue, X., Sun, Y., Resto-Irizarry, A. M., Yuan, Y., Aw Yong, K. M., Zheng, Y., et al. (2018). Mechanics-guided embryonic patterning of neuroectoderm tissue from human pluripotent stem cells. *Nat. Mater* 17 (7), 633–641. doi:10.1038/s41563-018-0082-9

Zhan, L., Han, Z., Shao, Q., Etheridge, M. L., Hays, T., and Bischof, J. C. (2022). Rapid joule heating improves vitrification based cryopreservation. *Nat. Commun.* 13 (1), 6017. doi:10.1038/s41467-022-33546-9

Zhao, Y., Shi, Y., Yang, H., Liu, M., Shen, L., Zhang, S., et al. (2022). Stem cell microencapsulation maintains stemness in inflammatory microenvironment. *Int. J. Oral. Sci.* 14 (1), 48. doi:10.1038/s41368-022-00198-w

Zheng, J., Wei, Z., Yang, K., Lu, Y., Lu, P., Zhao, J., et al. (2021). Neural stem cell-laden self-healing polysaccharide hydrogel transplantation promotes neurogenesis and functional recovery after cerebral ischemia in rats. *ACS Appl. Bio Mater* 4 (4), 3046–3054. doi:10.1021/acsabm.0c00934

Frontiers in Bioengineering and Biotechnology

TYPE Original Research
PUBLISHED 07 July 2023
DOI 10.3389/fbioe.2023.1225937

OPEN ACCESS

EDITED BY
Long Bai,
East China University of Science and Technology, China

REVIEWED BY
Jiulong Zhao,
Naval Medical University, China
Hao Ye,
ETH Zürich, Switzerland
Yang Zhu,
Fuzhou University, China

*CORRESPONDENCE
Qinqin Huang,
✉ qqhuang@zzu.edu.cn
Xiang Li,
✉ lixiang_suda@126.com
Hongtao Zhang,
✉ zhtzzu@zzu.edu.cn

†These authors have contributed equally to this work

RECEIVED 20 May 2023
ACCEPTED 23 June 2023
PUBLISHED 07 July 2023

CITATION
Wang S, Fei H, Ma Y, Zhu D, Zhang H, Li X and Huang Q (2023), Cu-doped polypyrrole hydrogel with tumor catalyst activity for NIR-II thermo-radiotherapy.
Front. Bioeng. Biotechnol. 11:1225937.
doi: 10.3389/fbioe.2023.1225937

Cu-doped polypyrrole hydrogel with tumor catalyst activity for NIR-II thermo-radiotherapy

Shile Wang[1†], Haotian Fei[2†], Yuhong Ma[3†], Daoming Zhu[4], Hongtao Zhang[5,6]*, Xiang Li[7,8]* and Qinqin Huang[1]*

[1]The Research and Application Center of Precision Medicine, The Second Affiliated Hospital of Zhengzhou University, Zhengzhou, China, [2]Department of Pharmacy/Evidence-Based Pharmacy Center, West China Second University Hospital, Sichuan University, Chengdu, Sichuan, China, [3]Department of Psychiatry, Huaian No. 3 People's Hospital, Huai'an, Jiangsu, China, [4]Department of Electronic Science and Technology, School of Physics and Technology, Wuhan University, Wuhan, China, [5]Blood Purification Center, The People's Hospital of Zhengzhou University, Zhengzhou, China, [6]Blood Purification Center, Henan Provincial People's Hospital, Zhengzhou, China, [7]Department of Central Laboratory and Precision Medicine Center, The Affiliated Huai'an Hospital of Xuzhou Medical University and Huai'an Second People's Hospital, Huai'an, China, [8]Department of Nephrology, The Affiliated Huai'an Hospital of Xuzhou Medical University and Huai'an Second People's Hospital, Huai'an, China

Introduction: Radiotherapy (RT) is one of the key methods for treating breast cancer. However, the effect of single RT is often poor because of insufficient deposition of X-rays in tumor sites and radiation resistance induced by the abnormal tumor microenvironment (overexpression of glutathione (GSH)). The development of multifunctional RT sensitizers and synergetic therapeutic strategies is, therefore, a promising area for enhancing the anticancer effect of RT.

Methods: In this study, a multifunctional nanozyme hydrogel based on Cu-doped polypyrrole (CuP) was designed to work concertedly with a second near-infrared thermal RT. The CuP-based hydrogel (CH) reached the tumor site when injected *in-situ* and achieved long-term storage.

Results: Once stimulated with 1064-nm laser irradiation, the heated and softened hydrogel system released CuP nanozyme to provide photothermal therapy, thereby inhibiting the repair of DNA damage caused by RT. In addition, CuP with dual nanozyme activity depleted the intracellular GSH to reduce the antioxidant capacity of the tumor. Moreover, CuP converted H_2O_2 to produce ·OH to directly kill the tumor cells, thus enhancing the capability of low-dose RT to inhibit tumor growth. *In vivo* experiments showed that the CH system used in combination with a low-power 1064-nm laser and low-dose RT (4 Gy) exhibited good synergistic anticancer effects and biological safety.

Discussion: As a new light-responsive hydrogel system, CH holds immense potential for radio-sensitization.

KEYWORDS

radiotherapy, nanozyme, hydrogel, photothermal therapy, ROS

Introduction

Cancer is one of the most life-threatening diseases in the world (Li et al., 2022). Approximately 70% of patients with cancer need radiotherapy (RT) (Limoli and Vozenin, 2023; Lin et al., 2023; Wu et al., 2023). RT mainly uses high-energy X-rays or γ-rays to induce DNA damage and cell apoptosis, thus resulting in tumor ablation (Secchi et al., 2023). When an adequate dose of radiation is used to locally irradiate the cancer tissue, it fights against cancer cells and effectively combats the disease. However, high-dose radiation can also cause damage to the normal cells in the vicinity, which is a concern in the development of RT (Ni et al., 2018; Gao et al., 2022). With the advancements in nanomedicine, several new cancer treatments, such as photothermal therapy (PTT), photodynamic therapy (PDT), and gene therapy, have emerged (Wang et al., 2022a; Wang et al., 2022b; Sun et al., 2022; Zhao et al., 2022). Of these, PTT is a kind of treatment method that uses a photothermal agent to convert light energy into heat energy under the irradiation of external light sources, such as near-infrared (NIR) laser (Ye et al., 2019; Zhu Y. et al., 2022). This irradiation increases the temperature of the tumor site, thus ablating the tumor. Owing to its high selectivity, low invasion, and high efficiency, PTT has been employed widely (Zhu et al., 2023a). The heat generated during PTT not only directly kills tumor cells but also acts as an RT sensitizer. First, hyperthermia induces double-strand breaks in the DNA, thus leading to protein aggregation and inhibiting the repair of DNA damage induced by ion radiation (Wang et al., 2021). Second, the high temperature kills S-phase cells that display the lowest sensitivity to radiation (Lyu et al., 2021). Third, the mild photothermal effect accelerates the blood flow in the tumor, thus increasing the oxygenation in the hypoxic part of the tumor and improving the sensitivity of tumor cells to RT (Lyu et al., 2019). Therefore, the concerted use of PTT/RT has good prospects.

The antitumor effect of PTT/RT is limited to a great extent by the complexity of the tumor physiological environment (poor permeability of the radiosensitizer in RT) and its limitation (limited conversion efficiency of the photothermal agent) (Yin et al., 2017; Cheng et al., 2021; Lan et al., 2021). Owing to the rapid growth and metabolism of tumor cells, the tumor microenvironment (TME) tends to be acidic, with low oxygen and elevated H_2O_2 levels (Ren et al., 2020; Zhu D. et al., 2022). Based on these characteristics, a reasonably designed nanozyme system can generate toxic substances in tumors via endogenous properties or exogenous stimulation to kill tumor cells, thereby improving the effects of thermal RT on tumors (Ji et al., 2021; Jiang et al., 2022). In recent years, nanomaterials have gained widespread attention in the field of tumor therapy (Ye et al., 2019; Ren et al., 2020; Sun et al., 2021; Zhao et al., 2022; Chen et al., 2023). The physicochemical response characteristics of nanomaterials are combined with the catalytic activity of enzymes, such as glutathione oxidase (GSH-OXD) and peroxidase (POD) (Zhu Y. et al., 2021; Zhu et al., 2023a; Zhu et al., 2023b). Hence, the development of multifunctional nanozymes can provide a promising weapon for enhancing tumor treatment. Intracellular GSH can offer protection against radiation, including free radical removal, peroxide reduction, and protein mercaptan, to maintain the reduced state (Chang et al., 2020). Emerging studies have shown that mixed-valence copper-based nanomaterials can specifically catalyze the conversion of GSH into glutathione disulfide in tumors in response to the TME, thereby restoring the sensitivity of cells to X-rays. In addition, a Cu^+-mediated pod-like reaction converts H_2O_2 into highly toxic OH to destroy mitochondria, which makes cells more vulnerable to radiation attack (Zhang et al., 2011).

Photothermal agents are generally injected intravenously to deliver them to tumor tissues, and although the biocompatibility and targeting of most photothermal agents can be improved via modification, their efficacy remains unsatisfactory (Dai et al., 2022; Zhuang et al., 2022). Furthermore, the systemic toxicity of nanomaterials, which often leads to unavoidable side effects, should be considered (Xu et al., 2022). Hydrogel is a three-dimensional network polymer that has been widely used in the biomedical field. The functions of the hydrogel include sustained drug release, cell delivery vehicle, and tissue engineering (Hou et al., 2018). Injectable hydrogels with injectable and *in situ* gelling properties are of great interest owing to their biocompatibility, ease of handling, and non-invasive mode of administration via injection (Wu et al., 2019). Such hydrogels exhibit properties that are superior to those of preformed hydrogels. The hydrogel carrying the cargo can prolong the sustained release time of the cargo, immensely reduce the toxicity and systemic side effects, centralize the administration concentration, and augment the utilization rate of the drug (Zhu D. et al., 2021; Zhang et al., 2022). Injectable hydrogels are clinically appealing because they significantly reduce patient discomfort, risk of infection, recovery time, and treatment costs (Chen et al., 2020). For example, Zhang designed light-responsive black phosphorus (BP)-based hydrogel to achieve controlled release of the BP and enable safe photothermal therapy (Qiu et al., 2018). Therefore, light-responsive hydrogels are expected to become the preferred medium for controlled-release nanomaterials.

In this study, Cu-doped polypyrrole (CuP), a copper-based multifunctional nanozyme was synthesized and loaded into agarose hydrogel to form a CuP-based hydrogel (CH) to achieve sensitization treatment for breast cancer using a second near-infrared (NIR-II) photothermal synergistic RT (Scheme 1). CH reached the focal area directly when injected intratumorally and accumulated *in situ* after gelation. After irradiation with 1064-nm laser (0.5 W/cm^2), CH converted light energy into heat energy, thereby enabling accurate and deep penetration of NIR-II PTT. Moreover, the thermally responsive hydrogel gradually softened and released the CuP nanozyme. CuP reduced GSH in the TME and converted H_2O_2 to generate highly toxic OH, destroy the redox steady state, and greatly enhance the effect of subsequent RT. Both *in vitro* cell experiments and *in vivo* animal model experiments showed that the designed CH system achieved satisfactory synergistic therapeutic effects. Furthermore, the combination of a relatively low radiation dose (only 4Gy) and a laser power of 0.5 W/cm^2 resulted in almost no adverse effects during the treatment cycle. This finding confirmed the long-term reliability of the CH system and provided novel insights for the multiple sensitization study of RT for 4T1 tumors.

Results and discussion

In this study, $CuCl_2$ was used as an oxidation catalyst instead of $FeCl_3$. *In situ* chemical oxidative polymerization was used to trigger the polymerization of pyrrole monomer at room temperature, and polyvinyl alcohol (PVA) was used as a stabilizer to avoid the infinite growth of CuP. As shown in Figure 1A, transmission electron microscopy (TEM) revealed that the synthesized CuP exhibited good dispersion, uniform size, and spherical characteristics. When the elemental mapping images were analyzed, the major

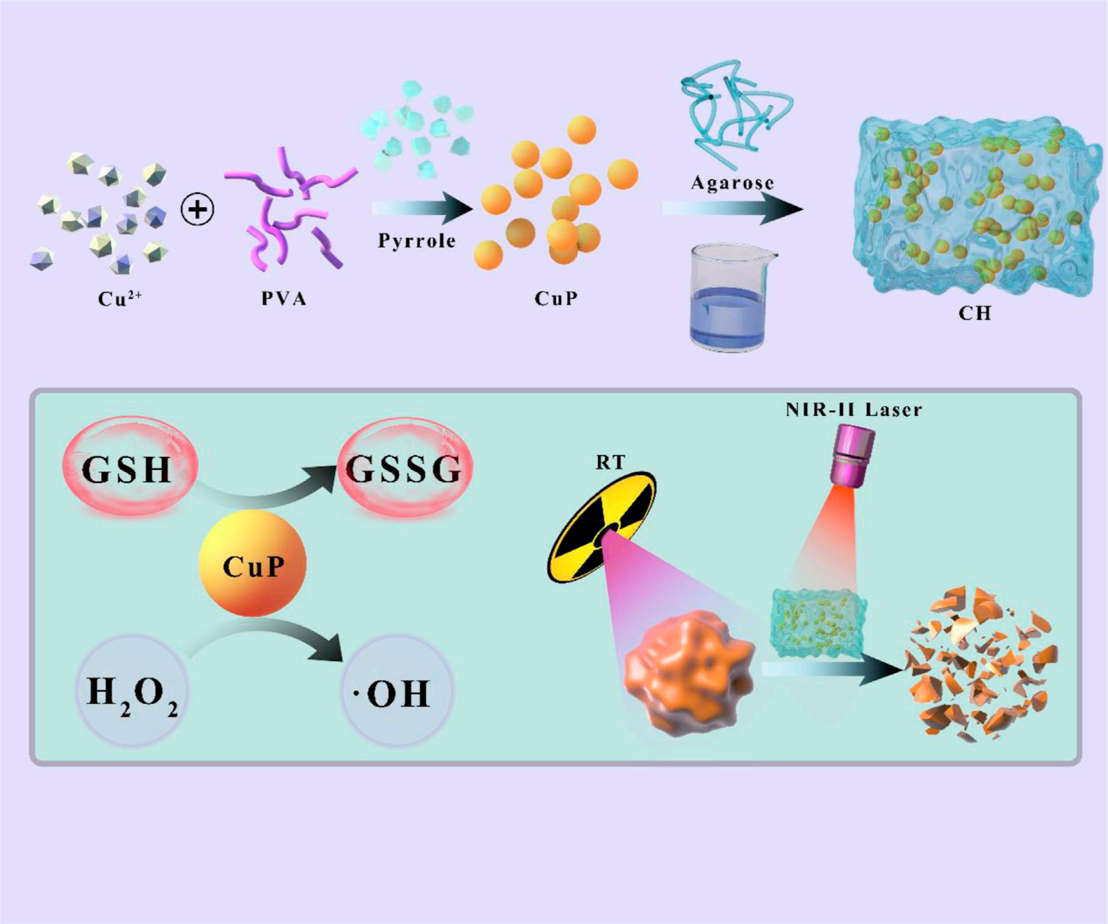

SCHEME 1
Schematic illustration of Cu-Doped polypyrrole hydrogel with tumor catalyst activity for NIR-II thermo-radiotherapy.

elements Cu, C, and N were distributed (Figure 1B). The size of the CuP nanozyme was controlled to approximately 100 nm by improving the PVA content (Figure 1C). The stability of nanocomposites in solution is critical to achieving a good therapeutic effect (Su et al., 2021; Yang et al., 2022). The zeta potential of the CuP obtained by repeated preparation is almost unchanged (Figure 1D). Hence, the average hydrodynamic diameter change of CuP dispersed in PBS was measured for 1 week using dynamic light scattering (DLS). Figure 1E presents the hydrodynamic diameter of CuP that was measured for seven consecutive days. The results confirmed the long-term stability of the prepared nanozyme. As depicted in Figure 1F, the UV–vis spectra showed that CuP had a broad absorption band in the 1,000–1,100 nm range. The absorption spectrum of CuP irradiated with a 1064-nm laser did not change significantly, which indicates that CuP has excellent photothermal conversion stability. Transition metals with multivalent states, such as Cu and Co, have been proven to exhibit catalytic activity in tumor-specific therapy, thus destroying the redox homeostasis in the TME (Ren et al., 2020). To confirm that CuP displayed POD-like enzymatic activity, methylene blue (MB) was used as a probe for the preliminary evaluation of the degradation ability of CuP for MB at different temperatures. The results demonstrated that the POD-like activity of a given concentration of CuP increased with the increase in temperature. It is worth noting that when the temperature reached 45°C, the degradation rate of MB reached approximately 50% in 20 min (Figure 1G). To adapt to the internal oxidative stress of cell growth and survival, cancer cells regulate their ROS level by upregulating antioxidants such as GSH (Sang et al., 2020). Hence, GSH is highly expressed in tumor cells, which affects their sensitivity to RT to a certain extent. DTNB was used as a probe to test the GSH–OXD-like activity of CuP. The findings suggested that the consumption of GSH by CuP increased with time, which could be attributed to the redox reaction between GSH and the active site of Cu^{2+} (Figure 1H).

For further experiments, injectable hydrogels were prepared by mixing CuP and agarose solutions as vehicles for enhancing PTT/RT. The rheological properties of CH were examined at different temperatures. The results showed that the hydrogel gradually softened with the increase in temperature and the storage modulus continued to decrease, thus leading to the controlled release of CuP in the hydrogel (Figure 2A). When the temperature and injection time were controlled, CH gelled rapidly *in situ* in the tumor. Owing to the excellent optical

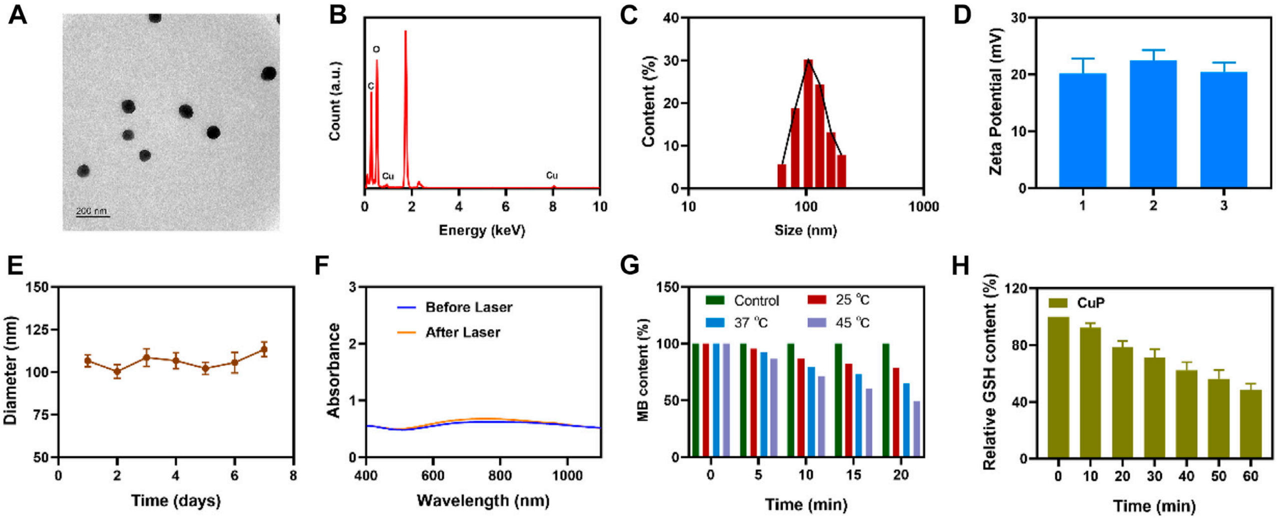

FIGURE 1
(A) TEM image of CuP **(B)** Energy dispersive spectroscopy (EDS) of CuP **(C)** Hydrodynamic diameter of CuP in water **(D)** The zeta potential of CuP suspended in PBS **(E)** DLS diameter of CuP within 7 days **(F)** UV-vis-NIR absorbance spectra of CuP aqueous dispersions before and after 1,064 nm laser irradiation for 20 min **(G)** MB depletion profile treated with or without CuP at different temperature (RT, 37°C, and 45°C) **(H)** The relative GSH content of the supernatant after the reaction of GSH and CuP.

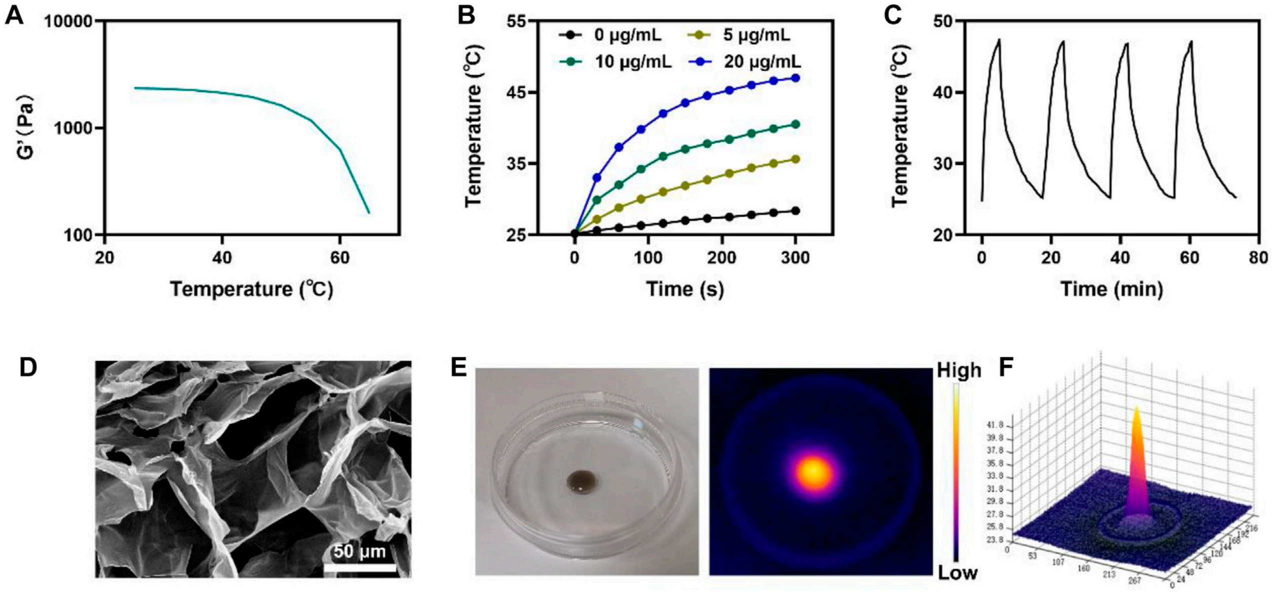

FIGURE 2
(A) Temperature-dependent Rheological curves for the prepared CH **(B)** Temperature changes of CuP NPs at various concentrations under a 5 min irradiation from a 1,064 nm laser at 0.5 W/cm^2 **(C)** Heating curve of CH for four cycles having a 0.5 W/cm^2 power intensity under irradiation by 1,064 nm laser **(D)** SEM image of the CH **(E)** The photographic pictures represent the morphology of the prepared CH and IR image during laser irradiation **(F)** Relevant 3D temperature diagram in 2 E.

absorption of CuP in the NIR II region and its ability to respond to the conversion of light energy into heat energy, the photothermal heating capacities of CuP and CH were evaluated comprehensively using the photothermal imaging system. Figure 2B portrays the heating effect of CuP at different concentrations under the irradiation of a 1064-nm laser (0.5 W/cm^2). The temperature of the aqueous solution of CuP (20 μg/mL) increased gradually under irradiation for 5 min and finally reached 46 °C (Figure 2B). In contrast, the temperature of the deionized aqueous solution did not increase perceptibly. This finding signifies that CuP, a photothermal agent, plays a key role in photothermal stability under laser irradiation. Furthermore, according to the

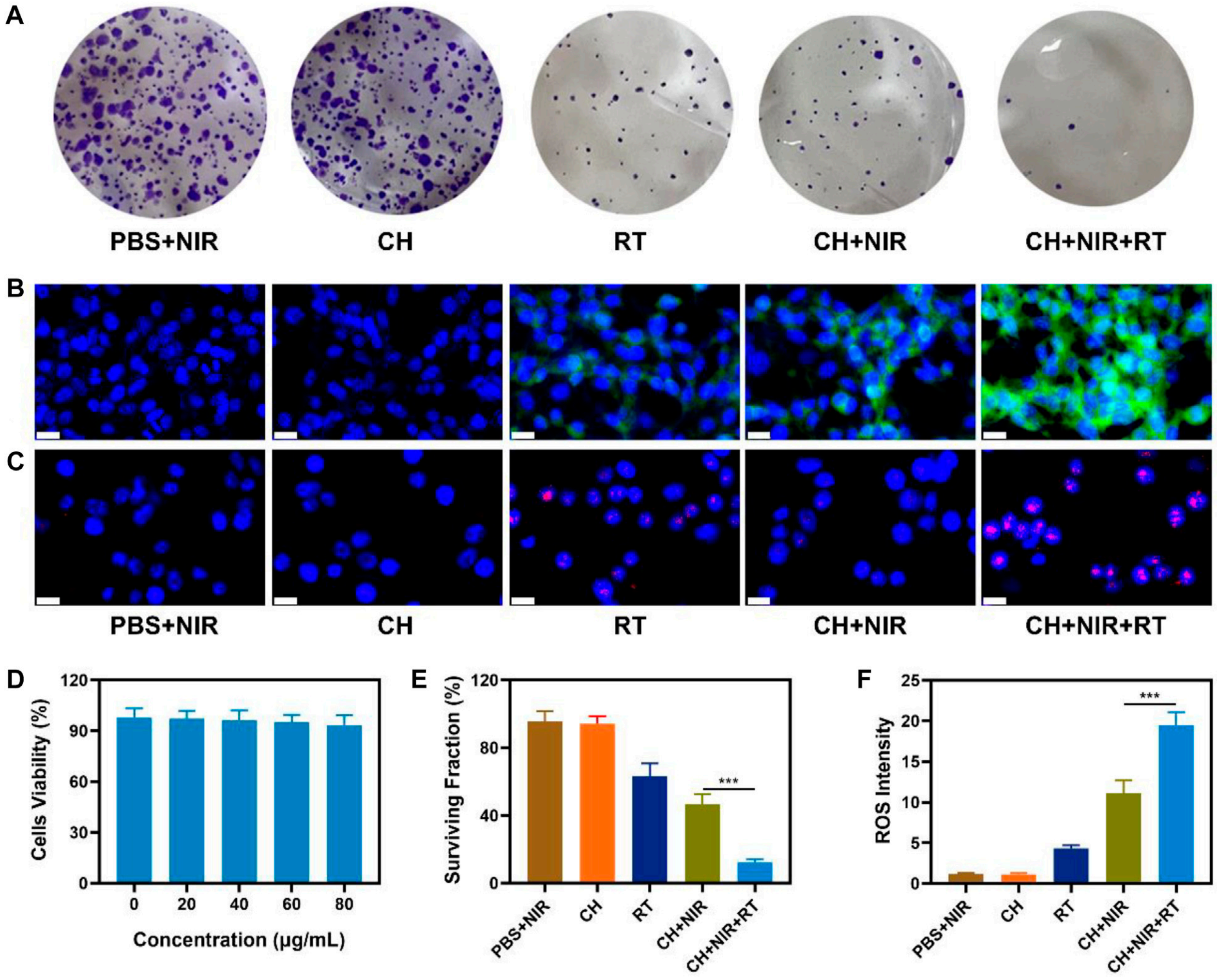

FIGURE 3
(A) Colony of 4T1 cells treated with different formulations and the irradiation dose was 4 Gy **(B)** CLSM images of DCFH-DA-stained 4T1 cells after treatment with different formulations. Scale bars: 20 μm **(C)** Detection of 4T1 cells' DNA damage through immunofluorescence staining of γ-H_2AX, induced by different formulations. Scale bars: 20 μm **(D)** Dark cytotoxicity of CH on 4T1 cells **(E)** *In vitro* cytotoxicity of different formulations against 4T1 cells **(F)** Corresponding quantitative analysis of ROS generation in 3A. ***$p < 0.005$; Student's t-test.

temperature changes in the four heating–cooling cycles of 1064-nm laser irradiation with a power of 0.5 W/cm^2 for 5 min (Figure 2C), the heating effect remained mostly unchanged until the end of the cycle. This result indicates that CuP has good photothermal stability. Therefore, the prepared CuP displays good photothermal conversion ability and photothermal stability under the irradiation of a 1064-nm laser, thus denoting its great potential in the PTT application. Scanning electron microscope (SEM) revealed the three-dimensional network structure of the hydrogel. The complex pore structure can accommodate more carriers (Figure 2D). Hence, the photothermal heating ability of CH was tested. CH was dropped at the center of a Petri dish and irradiated with a 1064-nm laser (Figure 2E). The infrared thermogram and 3D thermogram showed that the heating effect was significant (Figure 2F). The above results demonstrate that CuP has a good heating effect under 1064-nm laser irradiation. The CuP is an excellent photothermal agent that could be used synergistically with multimodal therapy for tumors.

In view of the aforementioned properties of CuP, the TME modulation ability and *in vitro* anticancer outcomes of CH were evaluated. The photothermal therapeutic effect and radiosensitization ability of CuP were investigated using 4T1 cells as a model. First, the high performance of the CH synergistic multimodal treatment was confirmed using a clone formation experiment. As shown in Figure 3A, PBS + NIR and CH groups had high cell populations, whereas RT and CH + NIR groups formed relatively fewer colonies. Compared with these groups, CH synergistic NIR + RT formed fewer cell clusters and had a lower survival fraction, which was significantly different compared with CH + NIR. Studies have reported that when irradiating cells with X-rays, RT can directly damage DNA molecules in the nucleus or indirectly damage them by producing various reactive oxygen molecules with water molecules. In this study, DCFH-DA probes were used to explore the reactive oxygen species (ROS) induced by various groups. Upon entering the cells, DCFH-DA is hydrolyzed by intracellular esterase to produce DCFH, which is in turn oxidized

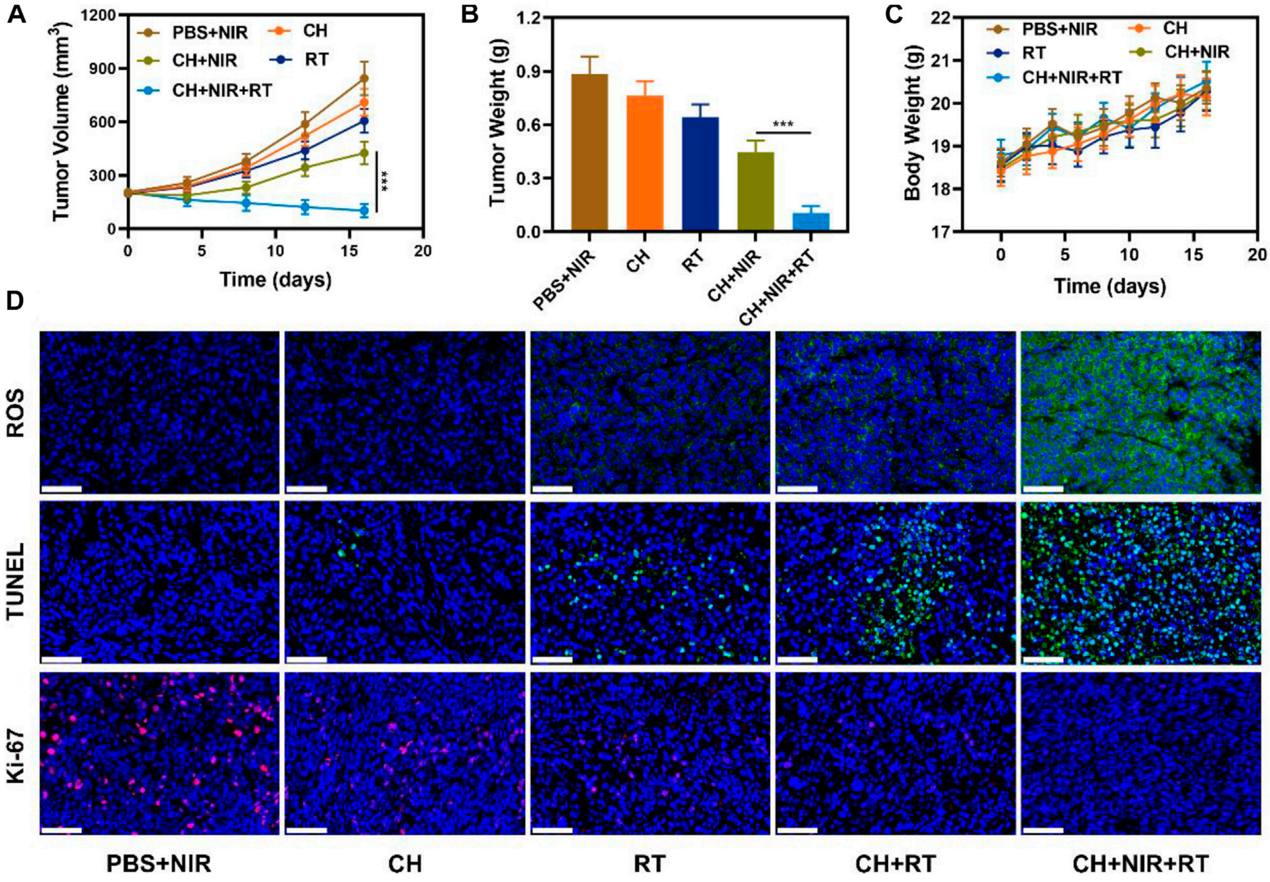

FIGURE 4
(A) Tumor volume changes and **(B)** tumor weights **(C)** Body weight changes of treated mice **(D)** ROS, TUNEL and Ki-67 stained tumor sections from the indicated treatment groups. Scale bars: 50 μm $^{***}p < 0.005$; Student's t-test.

by ROS to produce DCF that emits green fluorescence (Zhu et al., 2020). The RT group induced weak green fluorescence, as shown in Figures 3B,F. On the contrary, the CH + NIR group produced moderate green fluorescence, which could be attributed to the fact that CH subjected to laser radiation facilitates photothermal therapy by destroying the TME. CuP reduced the intracellular GSH content and converted the abundant H_2O_2 to produce OH, which led to increased oxidative stress and, eventually, increased ROS level. The brightest green fluorescence was achieved in the CH + NIR + RT group, which indicates that the heating effect of PTT could effectively promote the sensitization of RT to generate more ROS. X-ray induced double-strand breaks in the DNA, and H_2AX served as the sensitivity index for monitoring double-strand breaks in the DNA. The red fluorescence in the CH + NIR + RT group was the most significant of all groups, which indicates that its nuclear DNA was most damaged (Figures 3C, Supplementary Figure S1). Furthermore, to investigate whether CH has good biocompatibility, its cytotoxicity was studied *in vitro* using 4T1 cells. MTT test results showed that even if the concentration of CuP reached 80 μg/mL (Figure 3D), it displayed low cytotoxicity toward 4T1 cells and that the cell viability remained >90%. CH-mediated PTT inhibited the repair of DNA damage after RT. CuP in the hydrogel system not only exhibited POD-like activity and produced highly toxic OH to destroy cell activity but also reduced the GSH content and made tumor cells more sensitive to ROS, thereby accentuating the radio-sensitization effect (Figure 3E). This combined strategy can augment the therapeutic efficacy by transforming non-toxic CH into a toxic therapeutic system via light stimulation and increasing the sensitivity of tumor cells to X-rays.

Considering the encouraging results for the validation experiments of photothermal agent and multifunctional nanozyme, the *in vivo* antitumor ability was investigated. 4T1 tumor-bearing mice were constructed via the subcutaneous injection of 4T1 cells in BALB/c mice. The mice were randomly assigned to the following five groups: 1) PBS + NIR, 2) CH, 3) RT, 4) CH + NIR, and 5) CH + NIR + RT. Tumor volumes were recorded every 4 days after providing the corresponding treatment, as shown in Figure 4A. The tumor volumes increased rapidly over time in the PBS + NIR group and were slightly inhibited by RT. On the contrary, the tumor volumes were inhibited during the first week in the CH + NIR-treated mice. Non-etheless, the treatment was not effective in the following week, and there was a rapid increase in the tumor volume. This result suggests that the combination of CH and photothermal therapy was inadequate to destroy tumor cell growth. In the CH + NIR + RT group, the tumor volume was significantly inhibited during the whole treatment cycle. CH was initially enriched in the tumor area, and after irradiation with the highly penetrating 1064-nm laser, the light energy was converted into heat energy, which destroyed the activity of tumor cells to a certain extent. Moreover, the high temperature enhanced the nanozyme activity of CuP, which converted H_2O_2 to produce more OH. This killed the tumor tissue and depleted GSH, the reducing substance, which made the tumor cells more sensitive to RT. After the 16th day of treatment, the mice were sacrificed and their tumors were weighed. As shown in Figures 4B, Supplementary Figure S2, the tumor weight was significantly reduced in the treatment group compared with that in the control group, which agreed with the tumor growth curve. Notable changes in body weights were not seen in any of the mice during the treatment cycle, which affirms that the regimen was not considered toxic and did not cause substantial harm to the mice (Figure 4C). To further examine the mechanism of killing the tumor cells, the tumor tissue was subjected to various staining analyses at the end of the treatment. The CH + NIR + RT group exhibited the strongest apoptotic signal and the weakest proliferative signal, together with a high content and density of ROS (Figure 4D). These findings allude that this therapeutic regimen achieved the optimal antitumor effects. To further confirm the *in vivo* safety of the system, H&E staining was performed on the main organs (heart, liver, spleen, lung, and kidney) of the mice. As illustrated in Supplementary Figure S3, compared with the PBS group, there were no significant pathological changes in the main organs of mice treated with CH + NIR + RT. This finding signifies that the treatment system has good biocompatibility and would not cause significant damage to the mice. Based on these observations, we believe that CH is a good photothermal agent and radiosensitizer, with good application potential for treating breast cancer.

Conclusion

In this study, a Cu-doped polypyrrole-based hydrogel with tumor catalytic activity was designed for enhanced NIR-II PTT and RT. After IR stimulation, the non-toxic CH turned into a toxic treatment system. The softened CH released CuP to deplete the GSH in the TME, thereby alleviating the antioxidant capability and catalyzing the production of OH from intracellular H_2O_2 to kill tumor cells. The oxidative stress was thus amplified, and the approach worked concertedly with the subsequent RT to achieve a good antitumor effect. This treatment system, when combined with low-dose RT, can commendably inhibit tumor growth during the entire treatment cycle. In addition, the availability and biological safety of CH make it an extremely promising agent in clinical therapy.

Data availability statement

The original contributions presented in the study are included in the article/Supplementary Material, further inquiries can be directed to the corresponding authors.

Ethics statement

The animal experiments were carried out according to the protocol approved by the Ministry of Health in People's Republic of PR China and were approved by the Administrative Committee on Animal Research of the Wuhan University.

Author contributions

SW Methodology, Validation, Formal analysis; HF Conceptualization, Writing—review and editing; YM Writing—original draft, Writing—review and editing; DZ Formalanalysis, Data curation; HZ Formal analysis, Data curation, Writing—review and editing; XL Conceptualization, Writing—review and editing, Project administration; QH: Funding acquisition, Investigation, Writing—original draft. All authors contributed to the article and approved the submitted version.

Funding

The authors are grateful for the financial support from the Cultivation of High-level Internationalized Talents Project, 22180007.

Conflict of interest

The authors declare that the research was conducted in the absence of any commercial or financial relationships that could be construed as a potential conflict of interest.

Publisher's note

Supplementary material

The Supplementary Material for this article can be found online at: https://www.frontiersin.org/articles/10.3389/fbioe.2023.1225937/full#supplementary-material

References

Chang, M., Hou, Z., Jin, D., Zhou, J., Wang, M., Wang, M., et al. (2020). Colorectal tumor microenvironment-activated bio-decomposable and metabolizable Cu2 O@ $CaCO_3$ nanocomposites for synergistic oncotherapy. *Adv. Mater.* 32, e2004647. doi:10.1002/adma.202004647

Chen, M., Tan, Y., Dong, Z., Lu, J., Han, X., Jin, Q., et al. (2020). Injectable anti-inflammatory nanofiber hydrogel to achieve systemic immunotherapy post local administration. *Nano Lett.* 20, 6763–6773. doi:10.1021/acs.nanolett.0c02684

Chen, Z., Zheng, X., Zhao, J., Tang, J., Hu, L., and Wang, S. (2023). Glucose oxidase-loaded colloidal stable WS2 nanobowls for combined starvation/photothermal therapy of colorectal tumors. *Int. J. Pharm.* 636, 122848. doi:10.1016/j.ijpharm.2023.122848

Cheng, Y., Wen, C., Sun, Y. Q., Yu, H., and Yin, X. B. (2021). Mixed-Metal MOF-derived hollow porous nanocomposite for trimodality imaging guided reactive oxygen species-augmented synergistic therapy. *Adv. Funct. Mater.* 31 (37), 2104378. doi:10.1002/adfm.202104378

Dai, J., Wu, M., Xu, Y., Yao, H., Lou, X., Hong, Y., et al. (2022). Platelet membrane camouflaged AIEgen-mediated photodynamic therapy improves the effectiveness of anti-PD-L1 immunotherapy in large-burden tumors. *Bioeng. Transl. Med.* 8, e10417. doi:10.1002/btm2.10417

Gao, J., Wang, Z., Guo, Q., Tang, H., Wang, Z., Yang, C., et al. (2022). Mitochondrion-targeted supramolecular "nano-boat" simultaneously inhibiting dual energy metabolism for tumor selective and synergistic chemo-radiotherapy. *Theranostics* 12 (3), 1286–1302. doi:10.7150/thno.67543

Hou, M., Yang, R., Zhang, L., Zhang, L., Liu, G., Xu, Z., et al. (2018). Injectable and natural humic acid/agarose hybrid hydrogel for localized light-driven photothermal ablation and chemotherapy of cancer. *ACS Biomaterials Sci. Eng.* 4 (12), 4266–4277. doi:10.1021/acsbiomaterials.8b01147

Ji, S., Jiang, B., Hao, H., Chen, Y., Dong, J., Mao, Y., et al. (2021). Matching the kinetics of natural enzymes with a single-atom iron nanozyme. *Nat. Catal.* 4 (5), 407–417. doi:10.1038/s41929-021-00609-x

Jiang, C., He, T., Tang, Q., He, J., Ren, Q., Zhang, D.-Y., et al. (2022). Nanozyme catalyzed cascade reaction for enhanced chemodynamic therapy of low-H2O2 tumor. *Appl. Mater. Today* 26, 101357. doi:10.1016/j.apmt.2021.101357

Lan, J.-S., Liu, L., Zeng, R.-F., Qin, Y.-H., Hou, J.-W., Xie, S.-S., et al. (2021). Tumor-specific carrier-free nanodrugs with GSH depletion and enhanced ROS generation for endogenous synergistic anti-tumor by a chemotherapy-photodynamic therapy. *Chem. Eng. J.* 407, 127212. doi:10.1016/j.cej.2020.127212

Li, Q., Wu, T. T., Fan, X. W., Guo, X. B., Jiang, W., and Fan, K. L. (2022). Multifaceted nanozymes for synergistic antitumor therapy: A review. *Mater. Des.* 224, 111430. doi:10.1016/j.matdes.2022.111430

Limoli, C. L., and Vozenin, M.-C. (2023). Reinventing radiobiology in the light of FLASH radiotherapy. *Reinventing Radiobiology Light FLASH Radiotherapy* 7 (1), 1–21. doi:10.1146/annurev-cancerbio-061421-022217

Lin, T. A., Wei, L.-J., and Ludmir, E. B. (2023). Radiotherapy alone vs radiotherapy with concurrent chemoradiotherapy and survival of patients with low-risk nasopharyngeal carcinoma. *JAMA* 329 (3), 261. doi:10.1001/jama.2022.21033

Lyu, M., Chen, M., Liu, L., Zhu, D., Wu, X., Li, Y., et al. (2021). A platelet-mimicking theranostic platform for cancer interstitial brachytherapy. *Theranostics* 11 (15), 7589–7599. doi:10.7150/thno.61259

Lyu, M., Zhu, D., Li, Y., and Quan, H. (2019). Bimetallic nanodots for tri-modal CT/MRI/PA imaging and hypoxia-resistant thermoradiotherapy in the NIR-II biological windows. *Biomaterials* 233, 119656. doi:10.1016/j.biomaterials.2019.119656

Ni, K., Lan, G., Veroneau, S. S., Duan, X., Song, Y., and Lin, W. (2018). Nanoscale metal-organic frameworks for mitochondria-targeted radiotherapy-radiodynamic therapy. *Nat. Commun.* 9 (1), 4321. doi:10.1038/s41467-018-06655-7

Qiu, M., Wang, D., Liang, W., Liu, L., Zhang, Y., Chen, X., et al. (2018). Novel concept of the smart NIR-light-controlled drug release of black phosphorus nanostructure for cancer therapy. *Proc. Natl. Acad. Sci. U. S. A.* 115 (3), 501–506. doi:10.1073/pnas.1714421115

Ren, S. Z., Wang, B., Zhu, X. H., Zhu, D., Liu, M., Li, S. K., et al. (2020). Oxygen self-sufficient core-shell metal-organic framework-based smart nanoplatform for enhanced synergistic chemotherapy and photodynamic therapy. *ACS Appl. Mater. interfaces* 12 (22), 24662–24674. doi:10.1021/acsami.0c08534

Sang, Y., Cao, F., Li, W., Zhang, L., You, Y., Deng, Q., et al. (2020). Bioinspired construction of a nanozyme-based H2O2 homeostasis disruptor for intensive chemodynamic therapy. *J. Am. Chem. Soc.* 142 (11), 5177–5183. doi:10.1021/jacs.9b12873

Secchi, V., Cova, F., Villa, I., Babin, V., Nikl, M., Campione, M., et al. (2023). Energy partitioning in multicomponent nanoscintillators for enhanced localized radiotherapy. *ACS Appl. Mater. interfaces* 15, 24693–24700. doi:10.1021/acsami.3c00853

Su, X., Cao, Y., Liu, Y., Ouyang, B., Ning, B., Wang, Y., et al. (2021). Localized disruption of redox homeostasis boosting ferroptosis of tumor by hydrogel delivery system. *Mater. Today Bio* 12, 100154. doi:10.1016/j.mtbio.2021.100154

Sun, J., Wang, J., Hu, W., Wang, Y., Zhang, Q., Hu, X., et al. (2022). A porous bimetallic Au@Pt core-shell oxygen generator to enhance hypoxia-dampened tumor chemotherapy synergized with NIR-II photothermal therapy. *ACS Nano* 16, 10711–10728. doi:10.1021/acsnano.2c02528

Sun, M., Ye, H., Shi, Q., Xie, J., Yu, X., Ling, H., et al. (2021). Both-in-one hybrid bacteria suppress the tumor metastasis and relapse via tandem-amplifying reactive oxygen species-immunity responses. *Adv. Healthc. Mater.* 10 (21), 2100950. doi:10.1002/adhm.202100950

Wang, S., Yang, Y., Wu, H., Li, J., Xie, P., Xu, F., et al. (2022a). Thermosensitive and tum or microenvironment activated nanotheranostics for the chemodynamic/photothermal therapy of colorectal tumor. *J. Colloid Interface Sci.* 612, 223–234. doi:10.1016/j.jcis.2021.12.126

Wang, S., Zeng, N., Zhang, Q., Chen, M., and Huang, Q. (2022b). Nanozyme hydrogels for self-augmented sonodynamic/photothermal combination therapy. *Front. Oncol.* 12, 888855. doi:10.3389/fonc.2022.888855

Wang, Z., Zeng, W., Chen, Z., Suo, W., Quan, H., and Tan, Z. J. (2021). An intratumoral injectable nanozyme hydrogel for hypoxia-resistant thermoradiotherapy. *Colloids surfaces. B, Biointerfaces* 207, 112026. doi:10.1016/j.colsurfb.2021.112026

Wu, H., Liu, L., Song, L., Ma, M., Gu, N., and Zhang, Y. (2019). Enhanced tumor synergistic therapy by injectable magnetic hydrogel mediated generation of hyperthermia and highly toxic reactive oxygen species. *ACS Nano* 13, 14013–14023. doi:10.1021/acsnano.9b06134

Wu, Y., Zhu, K., Zhang, X., Du, W., Song, J., and Yang, H. (2023). Emerging plasmonic nanoparticles and their assemblies for cancer radiotherapy. *Adv. drug Deliv. Rev.* 194, 114710. doi:10.1016/j.addr.2023.114710

Xu, Y., Feng, K., Zhao, H., Di, L., Wang, L., and Wang, R. (2022). Tumor-derived extracellular vesicles as messengers of natural products in cancer treatment. *Theranostics* 12 (4), 1683–1714. doi:10.7150/thno.67775

Yang, X., Wang, S., Zhang, X., Ye, C., Wang, S., and An, X. (2022). Development of PVA-based microsphere as a potential embolization agent. *Biomater. Adv.* 135, 112677. doi:10.1016/j.msec.2022.112677

Ye, H., Wang, K., Wang, M., Liu, R., Song, H., Li, N., et al. (2019). Bioinspired nanoplatelets for chemo-photothermal therapy of breast cancer metastasis inhibition. *Biomaterials* 206, 1–12. doi:10.1016/j.biomaterials.2019.03.024

Yin, W., Li, J., Ke, W., Zha, Z., and Ge, Z. (2017). Integrated nanoparticles to synergistically elevate tumor oxidative stress and suppress antioxidative capability for amplified oxidation therapy. *ACS Appl. Mater. interfaces* 9 (35), 29538–29546. doi:10.1021/acsami.7b08347

Zhang, D.-F., Zhang, H., Shang, Y., and Guo, L. (2011). Stoichiometry-controlled fabrication of Cu_xS hollow structures with Cu_2O as sacrificial templates. *Cryst. Growth & Des.* 11 (9), 3748–3753. doi:10.1021/cg101283w

Zhang, T., Liu, Z., Tang, W., Zhu, D., Lyu, M., Lam, J. W. Y., et al. (2022). Mitochondria-targeting Type I AIE photosensitizer combined with H2S therapy: Uninterrupted hydroxyl radical generation for enhancing tumor therapy. *Nano Today* 46, 101620. doi:10.1016/j.nantod.2022.101620

Zhao, J., Ye, H., Lu, Q., Wang, K., Chen, X., Song, J., et al. (2022). Inhibition of post-surgery tumour recurrence via a sprayable chemo-immunotherapy gel releasing PD-L1 antibody and platelet-derived small EVs. *J. nanobiotechnology* 20 (1), 62. doi:10.1186/s12951-022-01270-7

Zhu, D., Chen, H., Huang, C., Li, G., Wang, X., Jiang, W., et al. (2022b). H2O2 self-producing single-atom nanozyme hydrogels as light-controlled oxidative stress amplifier for enhanced synergistic therapy by transforming "cold" tumors. *Adv. Funct. Mater.* 32, 2110268. doi:10.1002/adfm.202110268

Zhu, D., Lyu, M., Jiang, W., Suo, M., Huang, Q., and Li, K. (2020). A biomimetic nanozyme/camptothecin hybrid system for synergistically enhanced radiotherapy. *J. Mater. Chem. B* 8 (24), 5312–5319. doi:10.1039/d0tb00676a

Zhu, D., Zheng, Z., Luo, G., Suo, M., Li, X., Duo, Y., et al. (2021b). Single injection and multiple treatments: An injectable nanozyme hydrogel as AIEgen reservoir and release controller for efficient tumor therapy. *Nano Today* 37, 101091. doi:10.1016/j.nantod.2021.101091

Zhu, Y., Gong, P., Wang, J., Cheng, J., Wang, W., Cai, H., et al. (2023b). Amplification of lipid peroxidation by regulating cell membrane unsaturation to enhance chemodynamic therapy. *Angew. Chem.* 62 (12), e202218407. doi:10.1002/anie.202218407

Zhu, Y., Pan, Y., Guo, Z., Jin, D., Wang, W., Liu, M., et al. (2023a). Photothermal enhanced and tumor microenvironment responsive nanozyme for amplified cascade enzyme catalytic therapy. *Adv. Healthc. Mater.* 12 (7), e2202198. doi:10.1002/adhm.202202198

Zhu, Y., Wang, W., Cheng, J., Qu, Y., Dai, Y., Liu, M., et al. (2021a). Stimuli-responsive manganese single-atom nanozyme for tumor therapy via integrated cascade reactions. *Angew. Chem.* 60 (17), 9566–9574. doi:10.1002/ange.202017152

Zhu, Y., Wang, Z., Zhao, R., Zhou, Y., Feng, L., Gai, S., et al. (2022a). Pt decorated $Ti_3C_2T_x$ MXene with NIR-II light amplified nanozyme catalytic activity for efficient phototheranostics. *ACS Nano* 16 (2), 3105–3118. doi:10.1021/acsnano.1c10732

Zhuang, W. R., Wang, Y., Lei, Y., Zuo, L., Jiang, A., Wu, G., et al. (2022). Phytochemical engineered bacterial outer membrane vesicles for photodynamic effects promoted immunotherapy. *Nano Lett.* 22 (11), 4491–4500. doi:10.1021/acs.nanolett.2c01280

Frontiers in
Bioengineering and Biotechnology

Accelerates the development of therapies, devices, and technologies to improve our lives

A multidisciplinary journal that accelerates the development of biological therapies, devices, processes and technologies to improve our lives by bridging the gap between discoveries and their application.

Discover the latest Research Topics

See more →

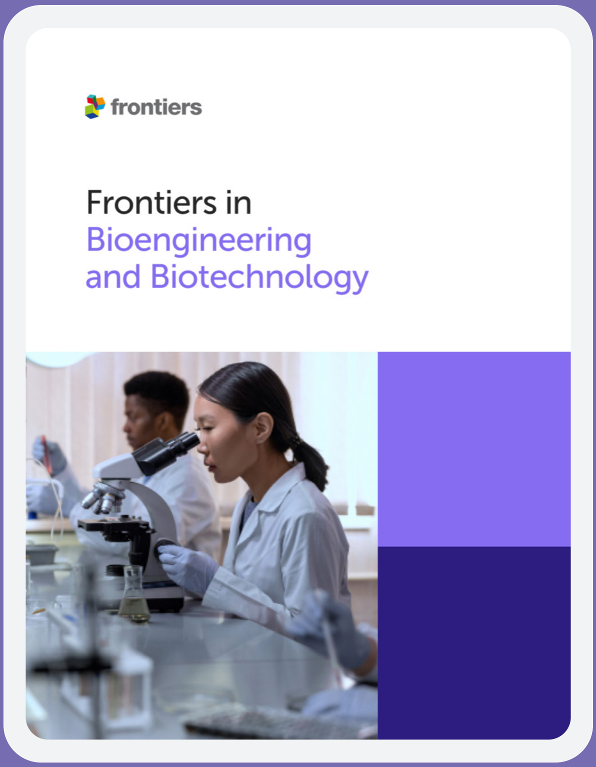

frontiers

Frontiers in
Bioengineering
and Biotechnology

Frontiers

Avenue du Tribunal-Fédéral 34
1005 Lausanne, Switzerland
frontiersin.org

Contact us

+41 (0)21 510 17 00
frontiersin.org/about/contact

frontiers | Research Topics